Springer Theses
Recognizing Outstanding Ph.D. Research

Edoardo Baldini

Nonequilibrium Dynamics of Collective Excitations in Quantum Materials

Springer

Springer Theses

Recognizing Outstanding Ph.D. Research

Aims and Scope

The series "Springer Theses" brings together a selection of the very best Ph.D. theses from around the world and across the physical sciences. Nominated and endorsed by two recognized specialists, each published volume has been selected for its scientific excellence and the high impact of its contents for the pertinent field of research. For greater accessibility to non-specialists, the published versions include an extended introduction, as well as a foreword by the student's supervisor explaining the special relevance of the work for the field. As a whole, the series will provide a valuable resource both for newcomers to the research fields described, and for other scientists seeking detailed background information on special questions. Finally, it provides an accredited documentation of the valuable contributions made by today's younger generation of scientists.

Theses are accepted into the series by invited nomination only and must fulfill all of the following criteria

- They must be written in good English.
- The topic should fall within the confines of Chemistry, Physics, Earth Sciences, Engineering and related interdisciplinary fields such as Materials, Nanoscience, Chemical Engineering, Complex Systems and Biophysics.
- The work reported in the thesis must represent a significant scientific advance.
- If the thesis includes previously published material, permission to reproduce this must be gained from the respective copyright holder.
- They must have been examined and passed during the 12 months prior to nomination.
- Each thesis should include a foreword by the supervisor outlining the significance of its content.
- The theses should have a clearly defined structure including an introduction accessible to scientists not expert in that particular field.

More information about this series at http://www.springer.com/series/8790

Edoardo Baldini

Nonequilibrium Dynamics of Collective Excitations in Quantum Materials

Doctoral Thesis accepted by
the École Polytechnique Fédérale de Lausanne, Switzerland

Springer

Author
Dr. Edoardo Baldini
Department of Physics
Massachusetts Institute of Technology
Cambridge, MA
USA

Supervisors
Prof. Majed Chergui
École Polytechnique Fédérale
de Lausanne (EPFL)
Lausanne
Switzerland

Prof. Fabrizio Carbone
École Polytechnique Fédérale
de Lausanne (EPFL)
Lausanne
Switzerland

ISSN 2190-5053 ISSN 2190-5061 (electronic)
Springer Theses
ISBN 978-3-319-77497-8 ISBN 978-3-319-77498-5 (eBook)
https://doi.org/10.1007/978-3-319-77498-5

Library of Congress Control Number: 2018934895

Printed on acid-free paper

This Springer imprint is published by the registered company Springer International Publishing AG
part of Springer Nature
The registered company address is: Gewerbestrasse 11, 6330 Cham, Switzerland

Nothing in life is to be feared, it is only to be understood. Now is the time to understand more, so that we may fear less.

—Marie Skłodowska Curie

To my parents, Luisella and Primo
In memory of Teresa, Francesco and Silvio

Supervisors' Foreword

One of the historical goals of condensed matter physics is to explain the *diversity* that characterizes different quantum states of matter in the condensed phase. Understanding its origin would unravel new quantum phenomena, with a potential for advanced functionalities in devices. At the core of this diversity lies a subtle balance between different forces on a microscopic scale. Such forces govern the coupling among the fundamental particles that characterize the material properties. As a result, the interplay between the constituent particles makes the study of condensed matter an intrinsic many-body problem.

In order to address the details of the many-body problem, in the early twentieth century, band theory provided a first intuitive classification of the quantum mechanical behavior of electrons in solids, leading to the distinction between metals and band insulators. However, most complex solids nowadays escape this simple classification, requiring more advanced and refined models for treating the interactions among several elementary excitations. These solids are currently referred to as "Quantum materials", as their fundamental properties arise from a complex interplay between electron–boson interactions and electron–electron correlations. Phenomena such as high-temperature superconductivity; spin, charge, and orbital ordering; metal–insulator transitions, colossal magnetoresistance, and many others are believed to be direct manifestations of this phenomenology.

The most promising strategy to reveal the details of complex many-body systems is understanding the spectrum of their elementary excitations, since the latter reflect the balance among the forces within the solid. Some of these elementary excitations can still be described as fermionic particles with renormalized properties, i.e., dressed of interactions. Other elementary excitations, mostly of bosonic nature, involve a cooperative, wave-like motion of many particles in the system simultaneously. These are dubbed "collective excitations", which represent the main topic of this book. The spectrum of the elementary excitations, similarly to the underlying interactions, depends on a number of external parameters that can be tuned at will. For example, it is well known that the energy, linewidth, and intensity

of a collective excitation can vary as a function of temperature, pressure, magnetic or electric field, and chemical doping depending on the specific material that is investigated. This in turn reflects how the combination of several microscopic forces inside the solid is affected by the same subset of external parameters. More recently, another external parameter has become available, which can be tuned to investigate and modify the properties of quantum materials: Light. Indeed, photons in the form of short, tailored light pulses interact with matter and can prepare a system in a highly nonequilibrium state that depends on the nature of the photoexcitation process itself. As a result, the dynamical response of a system can be followed with a temporal resolution comparable to the timescale of the relevant microscopic processes in the material.

In this book, Dr. Baldini focuses on the role of collective excitations in governing the properties of quantum materials beyond conventional band theory, namely strongly interacting metals and insulators, and strongly correlated superconductors and multiferroics. In so doing, he develops a novel spectroscopic technique that relies on ultrafast broadband optical probes in the visible and deep-ultraviolet range. This cutting-edge approach has a main advantage over other conventional spectroscopic probes, as it allows to simultaneously track high-energy collective modes (such as plasmons and excitons) in the frequency domain and low-energy collective modes (such as phonons, magnons, and exotic charge-density excitations) in the time domain. The dynamical behavior of these collective excitations in turn unveils the real-time evolution of complex many-body phenomena occurring in the solid at low energies. As such, the methodology implemented by Dr. Baldini hits deep inside the paradigm of correlated electron systems and allowed him to obtain a number of important results. To name a few, the first observation of the phonon-mediated mechanism connecting distinct electronic subsystems in the multiband superconductor MgB_2, the discovery of strongly bound excitons in anatase TiO_2, and the use of the latter excitons to detect the interfacial electron transfer in dye-sensitized systems.

All the results presented in this book are cast and described in a broad perspective, providing an extensive and simplified introduction to concepts. At the same time, deep physical insights are offered by the combination of novel experimental data and state-of-the-art theoretical calculations. The book reads like an advanced treatise in condensed matter physics that, by a few examples, explains topics of huge interest in the field, discussed with a critical eye and a very original vision. It also contains an exhaustive and rich list of references. The high quality of Dr. Baldini's work has also been recognized by the members of the jury that evaluated his thesis, comprising distinguished names in the field such as Prof. Anthony James Leggett (Nobel Prize in Physics 2003—University of Illinois at Urbana-Champaign, USA), Prof. Thomas Elsaesser (Head of the Max Born Institute, Germany), Prof. Joël Mesot (Head of the Paul Scherrer Institute, Switzerland), and Prof. Vincenzo Savona (Director of the Doctoral program in Physics at EPFL, Switzerland). The thesis has been also awarded the prestigious

Dimitris N. Chorafas Prize 2017, which is assigned for outstanding work in selected fields in the engineering sciences, medicine, and the natural sciences. We are convinced that this work provides a highly valuable reference textbook for any scientist starting a project in this field of research and in particular young ones.

Lausanne, Switzerland
December 2017

Prof. Majed Chergui
Prof. Fabrizio Carbone

Abstract

Revealing the emergence and the dynamics of collective excitations in complex matter is a subject of pivotal importance, as it provides insight into the strength and spatial distribution of interactions and correlations. At the same time, collectivity lies at the origin of several cooperative phenomena in many-body systems, which can lead to profound transformations, instabilities and, eventually, phase transitions. Mapping the interactions of the collective bosonic excitations with the fermionic particles and among themselves leads to the comprehension of the many-body problem. In this thesis, we investigate the dynamics of collective excitations in strongly interacting and correlated systems by means of ultrafast broadband optical spectroscopy. Within this approach, a material is set out-of-equilibrium by an ultrashort laser pulse, and the photoinduced changes in its optical properties are subsequently monitored with a delayed probe pulse, covering a broad spectral region in the visible or in the ultraviolet. Collective excitations can be unraveled either in the frequency domain as spectral features across the probed range or in the time domain as coherent modes triggered by the pump pulse. Studying the renormalization and temporal evolution of these collective excitations gives access to the hierarchy of low-energy phenomena occurring in the solid during its path toward the thermodynamic equilibrium. This framework is explored in a number of prototypical materials with an increasing degree of internal complexity beyond conventional band theory. Among the most remarkable results obtained in this work, we observe crosstalk phenomena between distinct electronic subsystems in MgB_2, discover bound excitons coupled to the phonon bath in anatase TiO_2, provide a selective and quantitative estimate of the electron–phonon coupling in La_2CuO_4, reveal precursor superconducting effects in $NdBa_2Cu_3O_{7-\delta}$ and unravel a lattice-mediated mechanism behind the magnetic order melting in the multiferroic $TbMnO_3$.

Keywords Ultrafast Optical Spectroscopy · Many-Body Physics
Collective Excitations · Strongly Correlated Electron Systems

Parts of this thesis have been published in the following journal articles:

1. E. Baldini, T. Palmieri, E. Pomarico, G. Auböck, M. Chergui, "*Clocking the Ultrafast Electron Cooling in Anatase Titanium Dioxide Nanoparticles*", ACS Photonics, DOI: 10.1021/acsphotonics.7b00945 (2018).
2. E. Baldini, A. Mann, L. Benfatto, E. Cappelluti, A. Acocella, V. M. Silkin, S. V. Eremeev, A. B. Kuzmenko, S. Borroni, T. Tan, X. X. Xi, F. Zerbetto, R. Merlin, F. Carbone, "*Real-Time Observation of Phonon-Mediated σ-π Interband Scattering in MgB_2*", Physical Review Letters 119, 097002 (2017).
3. E. Baldini, T. Palmieri, T. Rossi, M. Oppermann, E. Pomarico, G. Auböck, M. Chergui, "*Ultrafast Interfacial Electron Injection Probed by a Substrate-Specific Excitonic Signature*", Journal of American Chemical Society 139, 11584–11589 (2017).
4. E. Baldini, A. Dominguez, L. Chiodo, E. Sheveleva, M. Yazdi-Rizi, C. Bernhard, A. Rubio, M. Chergui, "*Anomalous Anisotropic Exciton Temperature Dependence in Rutile TiO_2*", Physical Review B 96, 041204(R) (2017).
5. E. Baldini, L. Chiodo, A. Dominguez, M. Palummo, S. Moser, M. Yazdi-Rizi, G. Auböck, B. P. P. Mallett, H. Berger, A. Magrez, C. Bernhard, M. Grioni, A. Rubio, M. Chergui, "*Strongly Bound Excitons in Anatase TiO_2 Single Crystals and Nanoparticles*", Nature Communications 8, 13 (2017).
6. E. Baldini, A. Mann, B. P. P. Mallett, C. Arrell, F. van Mourik, T. Wolf, D. Mihailovic, J. Tallon, C. Bernhard, J. Lorenzana, F. Carbone, "*Clocking the Onset of Bilayer Coherence in a High-T_C Cuprate*, Physical Review B 95, 024501 (2017).
7. E. Baldini, A. Mann, S. Borroni, C. Arrell, F. van Mourik, F. Carbone, "*A Versatile Setup for Ultrafast Broadband Optical Spectroscopy on Strongly Correlated Quantum Systems*", Structural Dynamics 3, 064301 (2016).
8. A. Mann, E. Baldini, A. Tramontana, E. Pomjakushina, K. Conder, C. Arrell, F. van Mourik, J. Lorenzana, F. Carbone "*Probing the Electron-Phonon Interaction in Correlated Systems with Coherent Lattice Fluctuation Spectroscopy*", Physical Review B 92, 035147 (2015).

Acknowledgements

Writing the acknowledgements of this book is a challenge by itself. The risk is to condense in a few words the sense of gratitude that built up over the past years for the people who made this work possible. Here, I will try to address this task despite the limited space available.

My deepest gratitude goes first and foremost to my thesis advisors, Majed Chergui and Fabrizio Carbone. During these years, they taught me that the seek for knowledge and the intellectual honesty are the two cornerstones on which a real scientist should rely. I owe my passion and motivation toward science to them, as they have been excellent mentors.

A debt of gratitude is owed to Angel Rubio for the central role played in this work and the visionary discussions at the border between theory and experiment. Our collaboration has solid roots, and it will bring to new exciting projects. I acknowledge Christian Bernhard, José Lorenzana, and Roberto Merlin for guiding me in the interpretation of many results and for the beautiful interaction of these years, and Anthony James Leggett, Thomas Elsaesser, Joël Mesot, and Vincenzo Savona for improving the quality of this work with their precious suggestions. A special note goes to Tania Palmieri, as her close support in everyday life bridged the years from Pavia to the writing of this book. A deep thank is devoted to Andreas Mann, the long-standing companion of my scientific life at EPFL, as our friendship has gone beyond our nightshifts in the lab, and to Andre al Haddad for being a wonderful officemate and a loyal friend. I express my sincere appreciation to Christopher Arrell, Gerald Auböck, and Frank van Mourik, whose support and dedication have been crucial for the success of many experiments, and to Monique Bassin and Leonor Camporeale for making my life at EPFL lighter. I also thank Giulia Mancini, José Ojeda, Gianmaria Vanacore, and Luca Longetti for their friendship, all people in LSU and LUMES for creating a warm environment, and all the other colleagues at the physics and the chemistry departments for the insightful conversations. Thanks also to Ambra Garlaschelli, the most asymmetric artist I know, who enthusiastically accepted to draw the cartoon of the experiment on a

broken symmetry phase and realized a piece of art. A special gratitude goes to Crystal Lynn Morton, for her warm support during the final steps of this book.

Last but most importantly, special words go to the people who have always encouraged me from far away. My parents and grandparents first, as this book can be considered as the reflection of their efforts in providing me a constant and unconditional support. Finally, my friends Valentina Baldrighi, Sebastiano Bianco, Isabella Bossolino, Alessandro Emmi, Iacopo Fonte, Lorenzo Iotti, Daniele Sartori and Micol Usardi, for being always present despite the distance.

Contributions

This work could have not been possible without the invaluable help of many scientists all around the world. This highlights how, in our field, people can gather and start working together driven by a common interest to reach a final goal. This represents the most beautiful aspect of science and still embodies its *collective* purpose.

Sample Preparation

Prof. Xiaoxing Xi—The Pennsylvania State University, USA
Dr. Arnaud Magrez—EPFL, Switzerland
Dr. Helmuth Berger—EPFL, Switzerland
Dr. Seyed M. Koohpayeh—Johns Hopkins University, USA
Dr. Ekaterina Pomjakushina—Paul Scherrer Institute, Switzerland
Dr. Kazimierz Conder—Paul Scherrer Institute, Switzerland
Dr. Thomas Wolf—Karlsruhe Institute of Technology, Germany
Dr. Teng Tan—The Pennsylvania State University, USA

Experiments

Prof. Christian Bernhard—University of Fribourg, Switzerland
Prof. Roberto Merlin—University of Michigan, USA
Prof. Marco Grioni—EPFL, Switzerland
Prof. Steven Lee Johnson—ETHZ, Switzerland
Prof. Dirk van der Marel—University of Geneva, Switzerland
Prof. Dragan Mihailovic—Jozef Stefan Institute, Slovenia
Prof. Pascal Ruello—University of Maine, France
Prof. Jeffrey L. Tallon—Victoria University of Wellington, New Zealand
Dr. Frank van Mourik—EPFL, Switzerland
Dr. Andreas Mann—EPFL, Switzerland
Dr. Gerald Auböck—EPFL, Switzerland
Dr. Christopher Arrell—EPFL, Switzerland
Dr. Enrico Pomarico—EPFL, Switzerland
Dr. Hannelore Rittmann-Frank—EPFL, Switzerland

Dr. Malte Oppermann—EPFL, Switzerland
Dr. Benjamin P. P. Mallett—University of Fribourg, Switzerland
Dr. Meghdad Yazi-Rizi—University of Fribourg, Switzerland
Dr. Simon Karl Moser—EPFL, Switzerland
Dr. Jan Helbing—University of Zurich, Switzerland
Dr. Alexey Kuzmenko—University of Geneva, Switzerland
Dr. Fabio Santomauro—EPFL, Switzerland
Dr. Teresa Kubacka—ETHZ, Switzerland
Ms. Tania Palmieri—EPFL, Switzerland
Ms. Evgeniia Sheveleva—University of Fribourg, Switzerland
Mr. Thomas Rossi—EPFL, Switzerland
Mr. Simone Borroni—EPFL, Switzerland
Ms. Ingalena Bucher—EPFL, Switzerland

Theory

Prof. Angel Rubio—MPI for the Structure and Dynamics of Matter, Germany
Prof. José Lorenzana—University of Rome "La Sapienza", Italy
Prof. Francesco Zerbetto—University of Bologna, Italy
Prof. Vyacheslav Silkin—Universidad del Pas Vasco, Spain
Dr. Letizia Chiodo—Università Campus Bio-Medico di Roma, Italy
Dr. Adriel Dominguez—MPI for the Structure and Dynamics of Matter, Germany
Dr. Maurizia Palummo—University of Rome "Tor Vergata", Italy
Dr. Lara Benfatto—University of Rome "La Sapienza", Italy
Dr. Emmanuele Cappelluti—University of Rome "La Sapienza", Italy
Dr. Angela Acocella—University of Bologna, Italy
Dr. Cedric Weber—King's College London, United Kingdom
Dr. Michael Sentef—MPI for the Structure and Dynamics of Matter, Germany
Dr. Thomas Brumme—MPI for the Structure and Dynamics of Matter, Germany
Dr. Chao Ma—Hunan University, China
Dr. Sergey V. Eremeev—Tomsk State University, Russia

Contents

Acronyms

2D	Two-Dimensional
3D	Three-Dimensional
AFM	Antiferromagnetic
ARPES	Angle-Resolved Photoemission Spectroscopy
BCS	Bardeen-Cooper-Schrieffer
BGR	Bandgap Renormalization
BSE	Bethe-Salpeter Equation
BZ	Brillouin Zone
CAP	Coherent Acoustic Phonon
CDW	Charge-Density Wave
CPM	Cross-Phase Modulation
CT	Charge-Transfer
DFT	Density Functional Theory
DMFT	Dynamical Mean Field Theory
DOS	Density of States
DP	Deformation Potential
EELS	Electron Energy Loss Spectroscopy
ES	Excited State
ET	Electron Transfer
FIR	Far-infrared
FT	Fourier Transform
GGA	Generalized Gradient Approximation
GS	Ground State
GVD	Group Velocity Dispersion
ISRS	Impulsive Stimulated Raman Scattering
JT	Jahn-Teller
KK	Kramers-Kronig
LC	Ligand-Centred
LDA	Local Density Approximation
MIR	Mid-infrared

MLCT Metal-to-Ligand Charge Transfer
NOPA Noncollinear Optical Parametric Amplifier
NP Nanoparticle
OD Overdoped
OP Optimally Doped
PBE Perdew-Burke-Ernzerhof
PG Pseudogap
QP Quasiparticle
REXS Resonant Elastic X-ray Scattering
RIXS Resonant Inelastic X-ray Scattering
RPA Random Phase Approximation
RT Room Temperature
SC Superconducting
SDW Spin-Density Wave
SE Spectroscopic Ellipsometry
SHG Second Harmonic Generation
STM Scanning Tunneling Microscopy
STS Scanning Tunneling Spectroscopy
SVD Singular Value Decomposition
SW Spectral Weight
TE Thermoelastic
TEM Transmission Electron Microscopy
UD Underdoped
UV Ultraviolet
ZPR Zero-Point Renormalization
ZRS Zhang-Rice Singlet
ZSA Zaanen-Sawatzky-Allen

List of Figures

List of Tables

Introduction

In physics, the term "collective excitations" refers to fictitious particles, mostly of bosonic nature, that do not center around individual particles, but involve a cooperative, wave-like motion of many particles in the system simultaneously. This motion is governed by the global interaction among the constituent particles. As such, collective excitations express the paradigm of the many-body problem, which represents one of the most fascinating yet challenging topics in condensed matter physics.

A major interest in revealing the emergence and dynamics of collective behavior comes from theoretical physics, since the collective excitations give access to the strength and spatial distribution of fundamental interactions and correlations in matter. At the same time, collectivity lies at the origin of several cooperative phenomena in many-body systems, which can cause profound transformations, instabilities, and, eventually, phase transitions. Understanding the interactions of the collective excitations with the fermionic particles and among themselves leads to the comprehension of the many-body problem.

A second area of interest is that of technology, as collective excitations hold huge promise for future developments and applications, especially in relation to energy sciences, health sciences, data storage, and signal processing. The dream is to engineer novel devices where collective modes can be efficiently generated, manipulated, and detected, similarly to what occurs in electronics with the electrons and in photonics with the photons. While this task has already been accomplished in the specific case of plasmonics, its extension to other collective excitations of interest is far from being reached. Prominent examples include excitonics, which is key to the future of photovoltaics; phononics, which can lead to novel functionalities for quantum materials through the control of their lattice modes; magnonics, which can open the doors to the use of magnons as information carriers in magnetic storage devices; and polaritonics, which is expected to bridge the gap between electronics and photonics for high-speed signal processing applications.

The first crucial step toward this technological goal involves a complete mapping and understanding of the physics behind collective excitations. In this regard,

spectroscopy represents the ideal tool through which physicists can gain insights into the quantum world. Nowadays, advanced spectroscopic methods are providing detailed information on the physics of complex materials under equilibrium conditions, unveiling the subtle effects associated with strong interactions and correlations. Although this approach still represents the primary and most valuable tool for revealing the electronic structure and behavior of matter, it provides only a time-averaged picture of the underlying physics. As a result, this hinders the possibility to directly observe dynamical phenomena that are at the heart of many fundamental processes, such as the transport of charges or the immediate response of a system to external stimuli. Moreover, the separation of overlapping spectroscopic features with different origins is not obvious at equilibrium, especially when the material properties result from the coexistence or the competition between distinct exotic phases of matter.

This calls for the development of experimental methods that can disentangle the contributions of the different degrees of freedom on the basis of their timescale. In real materials, such a nonequilibrium approach can be realized through the development and use of ultrafast spectroscopy. In this scenario, an initial impulsive perturbation sets the system far from the equilibrium, and the coupling among different electronic and structural excitations can be subsequently followed in real time with a variety of probes. One of the main frontiers in the field involves the *dynamical* investigation of collective excitations. Mapping the temporal evolution of these modes is highly desirable, as it bears the signature of the low-energy phenomena occurring in the system during its path to reach the thermodynamic equilibrium. This framework embodies the main subject of this thesis and, as such, it is explored in a number of prototypical materials. Within our approach, the fingerprint of the collective excitations of interest is revealed in the optical spectrum of the system, either in the frequency or in the time domain. Indeed, ultrafast broadband optical spectroscopy represents a powerful tool for accessing the dynamics of collective excitations lying at very different energy scales, thus unraveling the details of interactions and correlations in quantum many-body systems. To this end, the structure of the present thesis is organized to study several candidate materials where strong electron–boson interactions and electron–electron correlations act alone or simultaneously to determine the underlying properties. In this regard, we describe these solids by increasing the degree of internal complexity beyond conventional band theory.

Chapter 1 introduces the basic concepts behind the quantum many-body problem, namely the interplay between the electron–boson interaction and the electron–electron correlations. We show how the intrinsic nature of the many-body problem leads to the emergence of collective excitations and we briefly describe the electrodynamic properties of the collective modes of interest for this thesis. We finally discuss the main prospects and frontiers for the physics of collective excitations in quantum many-body systems, which involves their study and control under nonequilibrium conditions using tailored laser pulses.

Chapter 2 describes how the many-body problem can be addressed experimentally via the spectroscopic investigation of the elementary excitation spectrum

in quantum materials. The need for extending the spectroscopic study under nonequilibrium conditions is justified, and the current state of knowledge on the many-body processes occurring out-of-equilibrium is also described. Finally, ultrafast broadband optical spectroscopy is presented as the main experimental approach adopted in the framework of this thesis. In this regard, strong emphasis is given to the technical details of the used experimental setups.

Chapter 3 is devoted to the study of strong electron–phonon interaction in multiband anisotropic Fermi liquids. We investigate the case of MgB_2, which is a prototypical example of two-band superconductor in the strong coupling regime. By tracking the renormalization of a high-energy plasmon with sub-picosecond time resolution, we reveal the dynamics of the interband scattering process connecting the two bands and we elucidate its microscopic origin. This also allows us to highlight hot phonon effects involving extremely fast timescales in the system.

Chapter 4 deals with the description of band insulators in the intermediate-to-strong electron–phonon coupling regime. We focus our attention on anatase TiO_2 and reveal the central role played by many-body correlations in stabilizing collective charge excitations in the form of strongly bound excitons. We demonstrate the universality of our finding in the typical samples used for applications and we gain information on the low-energy carrier dynamics in the material by monitoring how the exciton signature renormalizes over time. Finally, we get first important insights into the exciton–phonon coupling mechanism in this system and we propose a possible application involving the detection of the excitonic feature.

Chapter 5 introduces the concept of strong electron–electron correlations by presenting a set of experiments on the charge-transfer insulator La_2CuO_4. This material represents the undoped parent compound of one cuprate family, and its properties arise from a complex interplay between electron–electron correlations and electron–phonon interactions. Here, we investigate the latter coupling by detecting how different coherent optical phonons modify the spectral properties of the material in the vicinity of its fundamental gap. We set the basis for a selective estimate of the electron–phonon matrix elements using this methodology, which can be extended to other classes of strongly correlated quantum systems.

Chapter 6 extends the investigation of cuprates, focusing on the superconducting phase in an underdoped crystal of the bilayer material $NdBa_2Cu_3O_{7-\delta}$. Here, the main challenge is to disentangle the contributions of distinct competing phases, which are represented by the superconducting and the pseudogap correlations. By interrogating the system out-of-equilibrium, the different states can be separated through their characteristic timescales, and undetected features related to precursor pairing correlations above T_C can be directly revealed. The signatures of the precursor state manifest both in the incoherent transient reflectivity response and in the anomalies of specific coherent optical phonon modes.

Chapter 7 addresses the physics of cooperation in multiferroic manganites. Here, our aim is to elucidate the hierarchy of phenomena following photoexcitation across the fundamental gap of $TbMnO_3$, which lead to a delayed melting of its cycloid spin order. We observe a complex collective structural response, which we assign to anti-Jahn-Teller polaron formation. We propose that these long-lived self-trapped

carriers hinder the emission of magnons and other spin-flip mechanisms. Thus, the energy is stored in the lattice via its ultrafast reorganization and subsequently transferred to the spin subsystem, causing the magnetic order melting. The coherent collective response also allows us to gain insights into one of the long-standing questions in manganite physics, namely the origin of the fundamental charge gap.

Chapter 1
Strong Interactions and Correlations

One of the most intriguing yet challenging fields of research in contemporary condensed matter physics is the investigation of many-body effects in strongly correlated quantum systems. This class of materials provides an excellent playground for discovering exotic phenomena involving charge, lattice, spin and orbital degrees of freedom and leading to extraordinarily varied chemical and physical properties. Understanding electronic correlations in prototypical systems like cuprates and manganites can pave the route to the potential design and engineering of novel materials with tailored functionalities. As a consequence, the main goal of current research is to identify the underlying mechanisms shared by these solids, so that their emerging phenomena can be accounted for by new theoretical models. In this Chapter, we describe the current status of understanding of the paradigm behind these systems. In Sect. 1.1, we put strong emphasis on the role played by the excitation spectrum in reflecting the signature of the many-body interactions and correlations that simultaneously act in the solid. In this regard, we provide some prototypical examples by gradually increasing the degree of complexity from the weakly correlated Fermi liquids to the systems governed by an intermediate correlations regime, which is the most difficult to address on both the theoretical and experimental sides. In Sect. 1.2, we introduce the concept of collective excitations in many-body systems, and explain why their study can provide valuable insights in the behaviour of complex materials, and open up new avenues for technological developments. Finally, in Sect. 1.3, we give a perspective on the intriguing frontiers offered by the physics of collective excitations for addressing long-standing problems in condensed matter research and for reaching the control of the material functionalities at ultrafast timescales.

E. Baldini, *Nonequilibrium Dynamics of Collective Excitations in Quantum Materials*,
Springer Theses, https://doi.org/10.1007/978-3-319-77498-5_1

1.1 The Paradigm of Strong Interactions and Correlations

The search for a complete theoretical framework to capture the physics of strong interactions and correlations in complex materials is an old problem faced by condensed matter physics. It has deep roots in the history of physics soon after the formulation of the band theory by Bethe, Sommerfeld and Bloch [1–3]. Band theory provided an intuitive yet profound description of the quantum mechanical behaviour of electrons in solids, leading to explain the origin of the difference between metals and insulators. One of the cornerstones of this theory is the assumption of a free electron model in metals, in which the interactions among electrons are completely neglected. It is therefore natural to believe that the first considerations on the transport and photoconductivity properties of NiO created a huge surprise in the physics community [4]. While band theory was predicting NiO to behave as a metal, experimental data were pointing towards a heavily insulating scenario. Peierls and Mott readily recognized that the breakdown of band theory in the description of NiO had to be related somehow to the presence of an incomplete d electron shell in the transition metal ions [5], whose main role is to produce a non-negligible Coulomb interaction among the electrons. This observation opened the doors to new frontiers in condensed matter physics and led to coin the term "Mott insulator" to describe a solid violating band theory.

Since then, a number of systems has been found to contradict the expectations of band theory. The simplest examples of metals at low temperatures could be readily treated within the framework of Landau's theory of Fermi liquids [6], where the role of electron-electron interactions was reduced to small corrections of susceptibilities of the free electron gas. Bardeen-Cooper-Schrieffer (BCS) theory of phonon-mediated superconductivity [7] and the subsequent extension by Eliashberg [8] unveiled the need of considering the electron-boson interaction for explaining the superconducting (SC) instability in Fermi liquids. It was soon recognized that the physics of more complex solids with incomplete d- or f- electron shells required the inclusion of both electron-boson interactions and electron-electron correlations, which could not be simply considered as weak perturbations of the free electron gas regime. Although this called for the search of more exotic microscopic mechanisms beyond band theory, for long time the task of extending the quantum theory of solids was just considered as a mere puzzle for theorists, without any possible implications for the field of technology. New enthusiasm towards this area of research followed the unexpected discovery of a variety of exotic electronic phenomena, such as high-temperature (high-T_C) superconductivity [9] and colossal magnetoresistance [10], which hold huge promise for the development of future devices and applications. Indeed, such phenomena are thought to be governed by two distinctive and common features, that have been revealed by a number of spectroscopies: (i) The presence of strong interactions (strong electron-boson coupling), which gives rise to effects like polaronic transport, incipient charge- and spin-density wave (CDW, SDW) instabilities and renormalizations of the electronic structure [11]; (ii) A subtle interplay between low- and high-energy scales, whose origin lies in the strong

electronic correlations spreading the material's spectral-weight (SW) over a wide energy range [12].

Corollary to these features is the dual nature that electrons exhibit in these materials [13]. For example, in most situations, itinerant carriers originating from wavefunction hybridization are found to coexist with localized carriers generated by boson-mediated carrier dressing, electron-electron repulsion and intrinsic inhomogeneities. Unravelling the details of this duality would shed light on many of the unsolved enigmas of contemporary condensed matter physics.

As the main source of uncertainty lies in the electronic structure of many materials, experimental probes of the many-body electron motion and energetics have been widely applied [12, 14, 15]. The deep understanding of a solid's excitation spectrum in response to an external perturbation provides a benchmark for tests of theoretical models and can lead to the comprehension of the elusive ground state (GS) properties of the material. It is therefore pivotal to clarify the effects that strong interactions and correlations produce on the electronic structure of a solid, which become apparent in the so-called one- and two-particle excitation spectra of the material. The one-particle excitation spectrum results from the removal or the addition of an electron in the solid and represents a signature of charged excitations that can be probed by photoemission and inverse-photoemission spectroscopies [14]. The two-particle excitation spectrum arises instead from the interaction between the solid and a low-energy light field (i.e. with a photon energy below the material ionization threshold), resulting in the creation of neutral excitations that are detectable by optical probes [12].

To introduce a qualitative picture of how the electron-boson interaction and the electron-electron correlation renormalize the electronic structure of a material, it is instructive to consider first the example of Fermi liquids. In the simplest picture, the Fermi liquid quasiparticles, obeying the Pauli exclusion principle, reside in a partially filled parabolic band (Fig. 1.1a). The electrodynamic response of the system can be described by the Drude model [16], in which the complex optical conductivity is expressed as

$$\sigma(\omega) = \frac{\widetilde{n}e^2\tau_D}{m_b}\frac{1}{1-i\omega\tau_D} = \frac{\sigma_{dc}}{1-i\omega\tau_D}, \tag{1.1}$$

where e is the electronic charge, $\widetilde{n}$ is the effective carrier density, and m_b is the band mass of the carriers (which typically differs from the free electron mass m_e), $1/\tau_D$ is the scattering rate, and σ_{dc} is the dc conductivity that can be probed by transport. From this description, it results that the electrodynamic response of the Fermi liquid is characterized by the emergence of a Lorentzian peak centered around zero frequency and related to intraband processes (red feature in Fig. 1.1d). The contribution of interband transitions (blue feature in Fig. 1.1d) is found to arise at higher energies and is typically well reproduced by band structure calculations. The electronic kinetic energy in a Fermi liquid is proportional to the SW associated with the intraband Drude contribution.

To describe the emergence of electron-boson coupling, a milestone is represented by Eliashberg theory of interactions [8]. The presence of a strong interaction with a bosonic collective mode at Ω_0 leads to a renormalization of the electronic

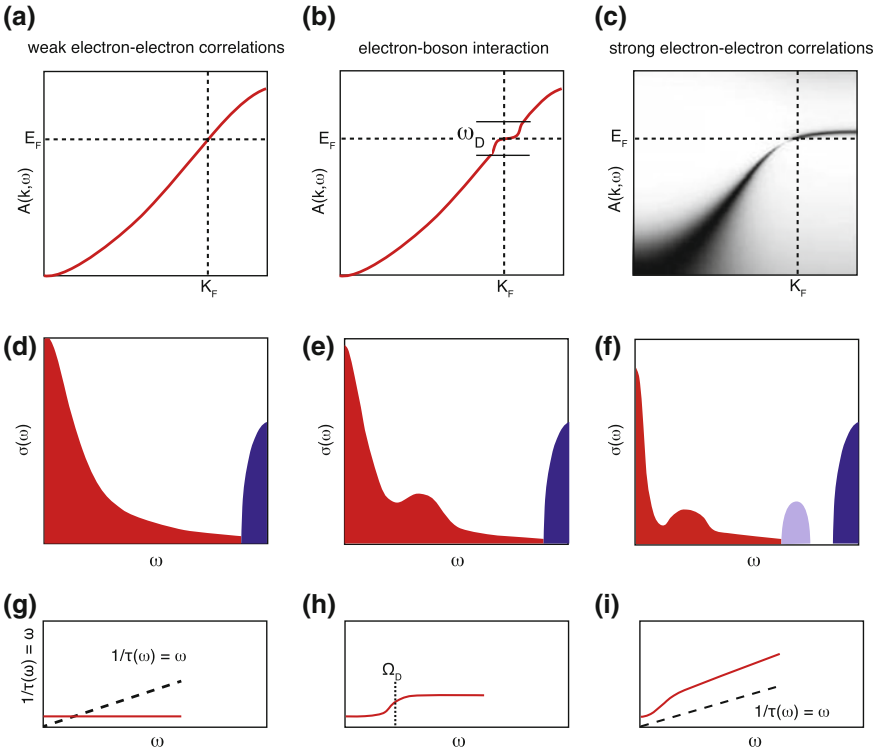

Fig. 1.1 Schematic diagram representing the impact of electron-boson interaction and electron-electron correlations on the one- and two-particle excitation spectrum of a solid. In the top panels, the momentum-resolved single-particle spectral function is shown for **a** a weakly correlated, **b** an interacting and **c** a correlated material. The two particle spectral function is represented in the three cases in Panels (**d**), (**e**) and (**f**), respectively. Panels (**g**), (**h**) and (**i**) display the frequency-dependent scattering rate retrieved in the three different cases. The figure has been adapted from Ref. [12]

energy-momentum dispersion near the Fermi level E_F (Fig. 1.1b). The spectral shape of the optical conductivity undergoes a marked change, revealing an absorption sideband at $\omega > \Omega_0$ (Fig. 1.1e). This absorption sideband can take the form of a satellite progression or can merge into a broad incoherent background as the electron-boson coupling strength increases. In any case, the SW associated with this sideband is transferred from the coherent Drude peak, thus conserving the total SW of the system typically below 1 eV. Consequently, electron-boson interaction alone does not alter the kinetic energy with respect to the Fermi liquid scenario. The frequency-dependent scattering rate $1/\tau_D(\omega)$ shows a step in the proximity of Ω_0, which is the signature of an enhanced scattering probability at higher energies (Fig. 1.1h). The same concept of electron-boson interaction is also central to the physics of insulators, as excitons and high-energy interband transitions can display strong couplings to other collective modes, modifying their profile [17].

We conclude by discussing the case of strong electron-electron correlations. Once correlations are introduced, they manifest as a pronounced broadening of the energy-momentum dispersion relation far from from E_F (Fig. 1.1c), thus suggesting that the concept of weakly damped Landau quasiparticles does not hold over the entire energy range. This leads to a remarkable reduction of the low-energy SW compared to band-structure expectations, suppressing the value of the kinetic energy. Importantly, the SW removed from the coherent Drude response is transferred to high energies of the order of the on-site Coulomb energy U and/or of interband transitions (violet feature in Fig. 1.1f). At the same time, large values of the scattering rate are reached and become evident in the two-particle excitation spectrum (Fig. 1.1i).

In the following sections, we focus on several examples that will be extensively treated in the framework of this Thesis. All these examples involve scenarios in which the electron-boson interaction and the electron-electron correlations act either separately or simultaneously to offer a variety of emergent phenomena in quantum many-body systems.

1.1.1 Electron-Phonon Interaction in the Strong Coupling Regime

By adopting an increasing degree of complexity in the many-body problem, the first type of interaction that can be considered is the one that establishes among electrons and phonons. Although this interaction is present to a certain extent in all solids, it is its magnitude and structure that lead to remarkable consequences on the behaviour of some materials. In general, the electron-phonon interaction describes how the energy of an electronic charge is affected by alterations of the atomic positions in the encompassing medium, and can be written in the form

$$V_{ep} = \frac{1}{\sqrt{\Omega}} \sum_{\mathbf{k},\mathbf{q},\eta} M_\eta(\mathbf{k}+\mathbf{q},\mathbf{k}) A_{\mathbf{q},\eta} c^\dagger_{\mathbf{k}+\mathbf{q},\sigma} c_{\mathbf{k},\sigma}\,, \tag{1.2}$$

where $A_{\mathbf{q},\eta} = a_{\mathbf{q},\eta} + a^\dagger_{\mathbf{-q},\eta}$. The operators $c^\dagger_{\mathbf{k}+\mathbf{q},\sigma}\ c_{\mathbf{k},\sigma}$ describe scattering of an electron with spin σ from the band state $\mathbf{k}$ to $\mathbf{k+q}$, while destroying $a_{\mathbf{q},\eta}$ or creating $a^\dagger_{\mathbf{-q},\eta}$ a phonon in band η with wave vector $\mathbf{q}$. The main task for theory and experiment is to derive expressions and reveal the details of the matrix element $M_\eta(\mathbf{k}+\mathbf{q},\mathbf{k})$ regulating this process.

In the presence of a sizeable coupling, the atoms of the lattice undergo a local displacement around the electron during its propagation through the crystal. This, in turn, can have a tremendous impact on the behaviour of the system, producing instabilities of the electronic structure towards other phases of matter or strongly renormalizing the charge dynamics. In the following, we describe two remarkable manifestations of this interaction, namely the phonon-driven SC instability in conventional metals and the concept of polarons in the specific case of insulators. Here,

only the salient features that are relevant to the topics of the following Chapters will be discussed. A more detailed description of the quantum many-body theory behind the electron-phonon interaction is provided in books such as Refs. [18–20].

The electron-phonon interaction has acquired renewed interest from the late 1950s, right after the formulation of the BCS theory of superconductivity [7]. According to the BCS theory, the SC transport in conventional metals is realized upon the formation of bound pairs of electrons (i.e. Cooper pairs) via the exchange of virtual phonons. This interaction is frequency dependent and becomes attractive for specific frequency regions. As a result, only the electrons within a Debye energy of the Fermi surface undergo pairing, thus becoming part of a many-electron eigenfunction describing the GS of the superconductor. The success of this theory lies in the correct description of the SC properties of *weak* superconductors, in which the magnitude of the electron-phonon interaction is rather small. Further extensions of this theory by Eliashberg [8] allowed to capture the properties of those materials that lie in the *strong* coupling regime, such as lead and tin [21]. The parameter discriminating the weak and the strong coupling regimes is represented by the electron-phonon mass enhancement factor λ [22]. The discovery of new classes of superconductors, such as cuprates [9] and pnictides [23], has shed light on the fragility of the BCS framework in providing a universal description of the SC state of matter. Despite this limitation, BCS theory still represents one of the most valuable successes of many-body physics and its influence persists even today in the formulation of novel theories of superconductivity.

In this regard, more recent examples of phonon-mediated superconductivity at $T_C > 35$ K have paved the route to new applications of BCS/Eliashberg theories. The discovery of superconductivity at 39 K in the layered system MgB_2 [24] and that at 203 K in H_2S under pressure [25] have come as huge surprises to the physics community. While the case of H_2S is still under intense debate at the time of writing to clarify the strength of the electron-phonon coupling, the lattice anharmonicity and the involvement of multiple bands in the SC properties [26, 27], the case of MgB_2 has reached a general consensus concerning its main properties. It is nowadays well established that MgB_2 represents a prototypical example of two-band superconductor [28–37], in which two distinct electronic bands (the σ and π bands) crossing E_F contribute to the SC properties by offering distinct coupling strengths with the phonon degrees of freedom [38–42]. In other words, MgB_2 embodies a rare type of phonon-mediated two-band superconductor in the strong coupling regime and, as such, has been the perfect playground to go beyond the established Eliashberg theory by implementing its anisotropic version [28, 43]. The phonon of interest is the optical boron stretching branch along the Γ-A direction in the BZ, which gives rise to a pronounced peak around 70 meV in the Eliashberg function $\alpha^2F(\omega)$ and is characterized by a large degree of anharmonicity [40, 44]. Besides governing the SC properties of MgB_2, this phonon mode is also expected to play a central role in the normal state properties of the material, offering an off-diagonal scattering channel that connects the two bands. This phonon-mediated interband scattering process is intimately related to the electron-phonon coupling mechanism and has remained elusive over time, despite 15 years of research on MgB_2. As this mechanism reflects

a dynamical manifestation of the electron-phonon coupling, it cannot be addressed directly via equilibrium spectroscopy, thus requiring the intrinsic time resolution of ultrafast spectroscopies to be unraveled. The first excursion of this Thesis towards the comprehension of the electron- phonon coupling mechanism involves the real-time observation of the phonon-mediated σ-π interband scattering in MgB_2, to which Chap. 3 is devoted. To track the dynamics of this process, we rely on the renormalization of a high-energy plasmon mode that can be detected by measuring the material transient reflectivity [45].

Besides the BCS/Eliashberg theory of superconductivity, another key manifestation of the electron-phonon coupling in solids is the emergence of polarons. The motion of an electronic charge through the lattice generates a potential well that, after overcoming a threshold and becoming sufficiently deep, can even bind the carrier itself. In this situation, the carrier is said to "self-trap", i.e. it is bound in the well that it induces and cannot escape without a significant movement of the ions. The unit comprising the self-trapped carrier and the associated pattern of displaced ions is typically known as "polaron". The polaronic coupling results in a renormalization of the bare electron mass, velocity, and scattering processes, thus leading to a slow motion of the self-trapped carrier along the crystal. The polaron model is an old topic in condensed matter physics, dating back to the pioneering work of Landau and Pekar [46]. The subsequent developments by Fröhlich, Holstein and Feynman aimed at a classification of the polaron species in terms of large, small and intermediate, depending on the extension of the polaron wavefunction over the crystal lattice [47–50]. The Fröhlich model relies on the coupling with (polar) optical phonon modes, whose parameters (like the longitudinal phonon quantum energy) can be obtained via infrared spectroscopy [47]. The Holstein model depicts instead a situation where the electron-phonon interaction is local [48, 49]. The interplay between the electron-phonon coupling and the presence of defects/impurities in the crystal lattice can also give rise to more complex scenarios of electron localization [51].

The polaron problem has been subsequently extended to more exotic cases in which an agile body interacts with a relatively deformable environment. In this regard, one of the frontiers is represented by the study of the polaronic coupling between an exciton and the surrounding atoms [17]. Nowadays, this still represents a hard task, since it implies to understand the combined effects of electron-hole correlations and phonon coupling. This problem is addressed in Chap. 4, where we discover strongly bound excitons in anatase TiO_2 and set the basis for the detailed description of their interaction with the polar modes of the lattice. Another example of interest is offered by materials in which an electron occupies one of the empty degenerate e_g levels on a transition metal ion in an octahedral crystal field. The lattice reacts locally by undergoing a Jahn-Teller (JT) distortion, thus lowering the energy cost associated with the presence of the excess charge. The electron dressed by this JT displacement is known as JT polaron [20]. On the contrary, in lattices where a collective JT distortion is already at play, the presence of an excess carrier can lead to the local relaxation or even removal of the JT distortion. The latter situation is referred to as anti-JT polaron [52]. This concept led to the initial search and discovery of high-T_C superconductivity [9], following the prediction that high-T_C values could

be found in JT-distorted materials due to the condensation of a bipolaronic charged Bose liquid. This subject will be discussed in Chaps. 5 and 7.

We remark that both the BCS-Eliashberg theory of superconductivity and the polaron model provide an elegant framework to describe the effects produced by the electron-phonon interaction but neglect the possible coexistence of strong electron-electron correlations. The interplay between the electron-phonon interaction and the electron-electron correlation, with disorder tipping the balance on a local scale, is expected to give rise to a variety of exotic phenomena that are hardly captured by current theoretical models. In this regard, estimating the electron-phonon coupling in a correlated material for specific lattice modes can contribute advancing our knowledge on the preferential phonons to which the electronic excitations are mainly coupled. In this Thesis, we make the first step to this purpose, by evaluating the electron-phonon matrix elements in La_2CuO_4 for a specific mode. The extension of this approach to many lattice modes and across a material phase diagram can in turn provide valuable inputs for simplified theoretical models such as the Hubbard-Holstein model [53–57].

1.1.2 Interplay between Low- and High-Energy Scales in Cuprates

Elucidating the origin of high-T_C superconductivity in cuprates is probably the most studied, yet unsolved, problem faced by condensed matter physics. The interest in addressing this long-standing open question is driven mostly by fundamental research rather than by applications. Cuprates have always represented a novel paradigm for broadening the frontiers of solid state physics, offering unique phenomena that are not shared simultaneously by other classes of materials: Unconventional superconductivity [58, 59], stripe/nematic/CDW order formation [60–66], opening of a pseudogap (PG) [67–70], precursor and critical phenomena [71–75], strange metal behaviour [76, 77], dichotomy of the charge carrier nature [78], possible quantum criticality [79, 80], Mott physics [59, 81, 82], electronic phase separation. The emergence of such a variety of electronic phases is mostly associated with the extreme sensitivity that cuprates manifest towards external parameters and stimuli. This sensitivity is reflected in the complexity of the cuprate phase diagram, which is shown in Fig. 1.2. This has been adapted from very recent works in literature at the time of writing, and it represents the state-of-the-art of the knowledge on cuprate physics [66, 83].

A possible explanation behind this exotic behaviour is that cuprates are characterized by an intermediate regime of electronic correlations, which connects the extreme Mott insulator and Fermi liquid scenarios [84, 85]. This imposes several limitations to theory, as both the independent particle picture and the fully correlated Mott regime fail miserably in describing the microscopic properties of these compounds. Moreover, an intermediate-to-strong electron-boson interaction is expected to play a substantial role in the renormalization of the charge dynamics, as in most

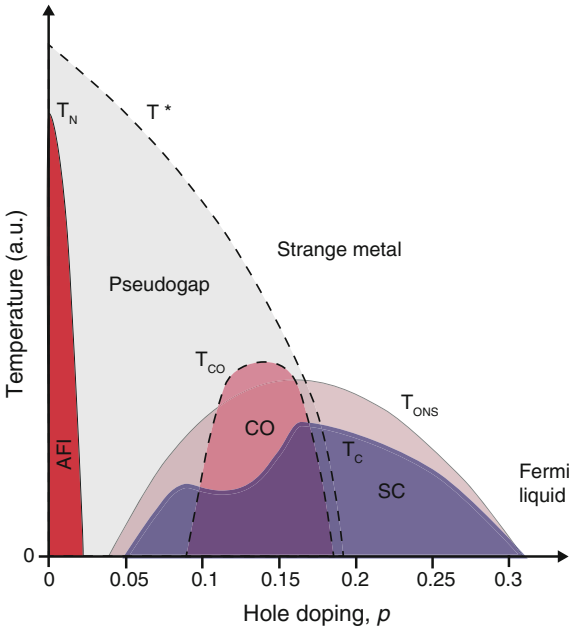

Fig. 1.2 Tentative phase diagram for the cuprates as a function of temperature and hole doping on the CuO_2 planes. The temperature scale T_N defines the Néel temperature for the AFM Mott insulating phase. The temperature scale T^* describes the emergence of the PG, which competes with the SC phase. The latter settles below the temperature T_C and extends from $p = 0.05$ to $p = 0.32$. Below T_{CO}, some form of short-range charge ordering arises as another competing phase and leads to the suprression of T_C. T_{ONS} represents the temperature below which SC phase fluctuations can be detected. In the normal phase, cuprates are considered as strange metals to account for non-Fermi liquid behaviour. In the extreme overdoped region, Fermi liquid behaviour is retrieved. The phase diagram has been adapted from a combination of those reported in Refs. [66, 83]

transition metal oxides (TMOs) [11]. Among the prominent bosonic excitations that have been identified or proposed, we can mention phonons, magnons, Josephson plasmons, excitons and polarization waves, and each of these collective excitations can generate a field that substantially affects the transport and the interactions of the fermionic particles. As a result, it is this lying in the "*world of the intermediate*" that makes cuprate physics so elusive and puzzling to both theory and experiment. As an additional element, disorder modifies the balance among the different forces on a local scale and leads to an intrinsic degree of inhomogeneity even in high quality single crystals [86]. All these subtle microscopic features concur in making cuprates the ideal playground for testing theories of cooperation and/or competition among several order parameters at a macroscopic scale.

The current Paragraph has neither the ambition, nor the intention, of providing a rigorous description of the complex physics behind the cuprates. Its goal is twofold: (i) To briefly illustrate how the physics of the electron-boson interactions and the electron-electron correlations have given foundation to two distinct schools of

thought in the past for understanding unconventional superconductivity in cuprates; (ii) To connect this long-standing debate to the framework of this Thesis.

In regard to the first task, it is crucial to recall the main conclusion hold by the BCS theory of superconductivity and by its extensions for describing the so-called "conventional pairing mechanism" [7, 8]. In this scenario, low-energy virtual phonons act as a glue between two electrons, providing a retarded attractive interaction between them and leading to the formation of Cooper pairs. In cuprates, the role of the retarded interactions have been widely considered after the discovery that the formation of Cooper pairs is still valid and lies behind the mechanism of superconductivity (which is a priori not obvious). This has led to the search for the glue lying at the origin of high-T_C superconductivity. As this glue cannot be provided solely by lattice vibrations, other frameworks involving spin fluctuations/polarization, electric polarization or charge density have been put forward [87–89]. This picture resembles the conventional mechanism, in which the mediating virtual phonons are replaced by a different low-energy glue of bosonic nature. Experimental data of ARPES and optics showed the presence of a peak in the electron-boson coupling function at ∼60 meV, which may be related to a spin resonance or to a phonon mode [90–93]. Additional modelling of the optical data also provided evidence for the decreased contribution of the 60 meV peak for increasing doping and for the presence of a broader contribution extending to higher energies (300 meV) [94]. This observation may support the idea that the pairing glue involves some kind of electronic degrees of freedom, such as spin, charge or orbital fluctuations.

In an opposite scenario, the existence of the retarded interactions has been doubted and a completely different mechanism involving non-retarded interactions associated with high-energy electronic scales has been proposed [95, 96]. Here, the most important element is represented by the proximity of the SC state to the Mott phase. Since the significant timescale of the interactions taking part to the pairing is the inverse of the Mott-Hubbard energy U (which lies in the range of some eV), such interaction can therefore be considered instantaneous. This is well depicted by the famous cartoon reported by Anderson in Ref. [95] and shown in Fig. 1.3a, representing an elephant (Mott-Hubbard energy scale U), a mammoth (superexchange interaction J) and a little mouse (electron-phonon coupling λ) in a refrigerator. "*We have a mammoth and an elephant in our refrigerator—do we care much if there is also a mouse?*" Consistent with this high-energy picture, a variety of studies showed that the physics of cuprates is not governed by processes living at energies close to E_F alone. The underlying "Mottness is at the origin of the SW transfer between high- and low energies detected by a number of studies [59, 97–101]. These peculiar effects have been found to set in around T_C and involve surprisingly high energies, from the mid-infrared (MIR) to the visible range. Remarkably, transfers of SW from the interband spectral region are not expected to occur in the conventional BCS picture and imply that the Ferrell-Glover-Tinkham sum rule is not satisfied within the intraband region alone [59, 102].

A different framework involving the high-energy scales, known as "the MIR scenario", was put forward on theoretical basis [103–105]. In this picture, it was postulated that superconductivity in cuprates is driven by a saving of the inter-conduction

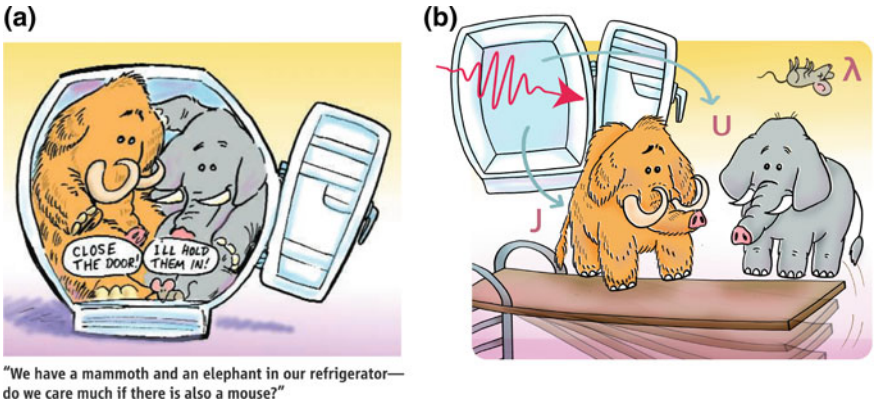

Fig. 1.3 **a** Cartoon showing a mammoth, an elephant and a mouse inside a refrigerator. The elephant, the mammoth and the mouse embody the Mott-Hubbard energy U, the superexchange interaction J and the electron-phonon coupling λ, respectively, thus setting a direct comparison among the magnitude of the three energy scales in cuprates. The image has been reprinted with permission from Ref. [95], credits of Joe Sutliff. **b** Cartoon representing the concept behind our ultrafast broadband optical spectroscopy experiment to unveil the importance of the different energy scales to the SC pairing mechanism in cuprates. A light pulse opens the refrigerator and the SC condensate is set out-of-equilibrium. The oscillations of the SC condensate will resonate on the energy scale/scales that is/are playing a role in the pairing mechanism

electron Coulomb energy, and specifically in the part associated with long wavelengths ($\mathbf{q} \leq 0.3$ Å^{-1}) and MIR frequencies (0.6–1.8 eV). In other words, *all* or *most of* the SC condensation energy comes from saving the Coulomb energy in this particular wavevector- and energy regime. The decrease in Coulomb energy would reflect an enhanced screening caused by the Cooper pair formation, as the latter modifies the bare density response function of the system. From these argument, it is evident that this scenario results in a strong modification of the electrodynamic properties of the system [104], producing remarkable changes in the MIR loss function (i.e. in the region that mainly involves the contributions from the conduction electrons in the CuO_2 planes and is characterized by a broad feature known as MIR peak). Experimentally, these changes can be detected as sizeable modifications in the loss function measured by optics at $\mathbf{q} = 0$ [78, 106] or as large drops in the electron scattering cross-section probed by differential transmission Electron Energy Loss Spectroscopy (EELS) at finite $\mathbf{q}$.

To settle the controversy behind the origin of superconductivity in cuprates and to elucidate possible synergies between different mechanisms, one needs a technique that can monitor both the electron-boson interaction and the high-energy scales. In the context of this Thesis, we make a first step towards this goal by using a nonlinear optical technique out-of-equilibrium, based on the pump-probe spectroscopy method (described in details in Chap. 2). This approach has two main strengths: (i) to disentangle the contributions of the different electron-boson scattering channels on the basis of their characteristic timescales; (ii) the possibility to set *specific* col-

lective excitations out-of-equilibrium using a laser pump pulse and subsequently monitor their impact on other degrees of freedom using a delayed optical probe pulse. In Chap. 2, we will refer to the first observable as the "incoherent response" of pump-probe spectroscopy, and to the second observable as the "coherent response". In the latter case, when the collective excitation is represented for example by an optical phonon, this technique can provide a very selective and quantitative estimate of the electron-phonon coupling matrix elements. When the collective excitation is represented by the pair-breaking Bogoliubov mode [107], this technique can obtain information on possible pairing actors in superconductivity, by studying how the perturbed condensate affects and couples to other elementary excitations [108, 109]. In the language of the cartoon of Fig. 1.3a, this is like opening the refrigerator using a light pulse and setting superconductivity out-of-equilibrium. Therefore, the oscillating SC condensate can be considered as a trampoline. By monitoring how the elephant and the mammoth react to the oscillations of the SC condensate, one can gain information on the pair-mediating or the pair-breaking mechanism (Fig. 1.3b). Using this technique in optimally doped (OP) $La_{2-x}Sr_xCuO_4$, it has been recently shown that the Bogoliubov mode couples to a high-energy excitation lying on the Mott scale, i.e. the remnant of the CT excitation [108]. Due to the crucial involvement of collective modes in our approach, a substantial part of this Chapter is devoted to discuss the physics of collective excitations in solid matter. The main limitations imposed by our approach are: (i) the limited spectral range that can be monitored; (ii) the possibility to study collective excitations only in the long-wavelength limit, i.e. at $\mathbf{q} = 0$. The first drawback can be overcome by extending the probing region to cover the THz, MIR or the ultraviolet (UV) spectral ranges [110, 111]. The second restriction will be possibly released by the future development of the x-ray/electron analogues of the technique, which are expected to give access to a wider $\mathbf{q}$-range of the elementary excitations.

At the time of writing, the task is therefore to set the basis for these future developments to occur, while gaining novel insights into the physics of cuprates. In Chap. 5, we investigate the electron-phonon matrix elements in the undoped parent compound La_2CuO_4, where superconductivity and density wave effects are quenched and the system is electronically governed by Mott physics. In Chap. 6, we also demonstrate that our nonequilibrium method becomes a sensitive probe to the onset of fluctuating phenomena, like precursor SC correlations. In this regard, we also show how the emergence of precursor SC effects renormalizes some features in the bosonic excitation spectrum of a cuprate. In other words, the modification of the bosonic spectrum encodes the onset of short-range SC correlations.

In conclusion, addressing the physics of cuprates still remains a formidable task after thirty years since their discovery. Despite the disagreement between the different theoretical frameworks, a general consensus has been reached on the experimental side, in that the elementary excitation spectrum hides the fundamental manifestation of the mechanism behind superconductivity. This calls for the implementation of novel experimental techniques that can reveal new details imprinted on the elementary excitation spectrum with unprecedented time (spectral) and spatial (momentum) resolution.

1.1.3 Cooperative Phenomena in Manganites

Another intriguing manifestation of the balance between interactions and correlations is the emergence of cooperative phenomena in a wide class of oxides. Cooperative mechanisms lie at the heart of exotic electronic instabilities governing the properties of numerous materials at the macroscopic scale. Prototypical systems for the study of these effects are the manganites, which, similarly to cuprates, are also controlled by Mott physics and by an extreme sensitivity to the external conditions.

Since the 1990s, the main open question in the physics of mixed-valence manganites has been represented by the microscopic explanation of their colossal magnetoresistance, i.e. the colossal reduction of the electric resistivity that doped manganites undergo upon application of a magnetic field [10]. However, it was soon realized that addressing this problem had to involve another change of paradigm in the field of strongly correlated quantum systems. Indeed, manganites represent a fertile ground for the coexistence and mutual coupling among different order parameters, which complicates the description of the phenomena at the origin of the colossal magnetoresistance. As a result, in the last years, the focus of much research has been shifted to understand at first the complex relationship among the different degrees of freedom in the undoped parent compounds.

In these Mn^{3+} solids, the electronic properties arise from the subtle balance among a number of relevant energy scales [112, 113]. The on-site effective Coulomb interaction and the charge-transfer (CT) energy, embodied respectively by the Mott-Hubbard energy scale U and Δ, govern the electronic behaviour of the system within the framework of intermediate-to-strong electronic correlations. The intra-atomic exchange term, represented by the Hund coupling, is also relatively strong and implies that all electron spins must be aligned within the d^4 configuration. The electron-phonon interaction lies at the heart of the orbital ordering in the material through the cooperative JT distortion of the lattice and strongly renormalizes the charge transport via polaronic coupling. The antiferromagnetic (AFM) superexchange interaction plays a fundamental role in defining the spin ordering pattern of the system. The coexistence of all these energy scales reflects in the richness and complexity characterizing the spectra of the elementary excitations in the undoped manganites [114, 115]. Assigning all these excitations is highly desirable, because they could play a crucial role in multiband Hubbard models used to capture the properties of the unconventional states developed upon doping. Despite huge efforts, this task still remains a real challenge. Experimentally, features associated with distinct phenomena often overlap and give rise to overcrowded spectra, thus hindering their clear assignment [115]. Moreover, the evolution of the spectroscopic signatures as a function of external parameters, crucial for unravelling many-body effects at play, are often too complicated to be reproduced even with phenomenological models. This makes manganites very elusive and ambiguous materials even to the most advanced experimental probes. A prototypical example of this ambiguity regards the classification of these solids within the Zaanen-Sawatzky-Allen (ZSA) scheme [114–118]. Since manganites, similarly to cuprates, also lie in the "*land of the intermediate*", their salient properties become

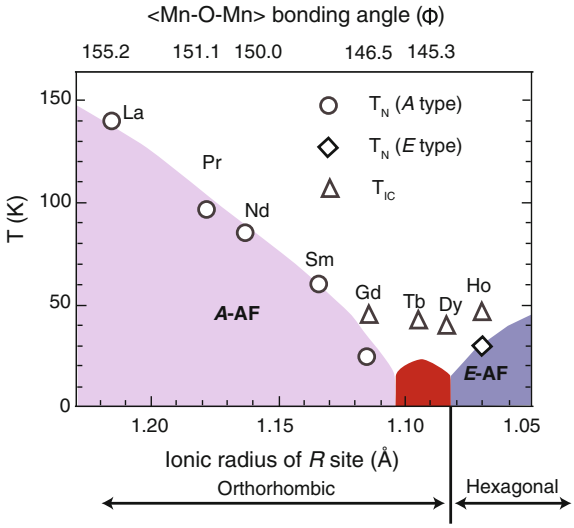

Fig. 1.4 Schematic magnetic phase diagram of $RMnO_3$ as a function of the R^{3+} ion size, adapted from Ref. [119]. The evolution of the A-type AFM ordering, the incommensurate spin ordering and the E-type AFM ordering temperatures are displayed using open circles, open triangles and open diamonds, respectively. The red area highlights the region where the commensurate spin order and ferroelectric property emerges

hard to capture on the theory side with simplified model Hamiltonians or *ab initio* calculations.

Despite imposing a limitation to a detailed understanding of the physics behind these materials, such an internal complexity opens up new frontiers for the observation of exotic phenomena. Indeed, it becomes clear that key to this goal is to modify the energy landscape and the balance among the different interactions by applying an internal or an external perturbation. The simplest degree of freedom that can be varied is represented by the rare-earth ion R in the formula $RMnO_3$ of orthorhombic manganites. What can appear in first instance as an innocent substitution leads in reality to a dramatic rearrangement of the structural, electronic, orbital and magnetic properties of the solid. Despite preserving the insulating character of the manganite, rare-earth substitution causes a strong structural deviation from the ideal perovskite lattice and eventually leads to a structural phase transition from orthorhombic to hexagonal. This is shown in the phase diagram of Fig. 1.4, which has been adapted from Ref. [119]. More interestingly, this structural distortion has profound consequences on magnetism, activating new paths for the spin interaction among different Mn^{3+} ions. The AFM ordering changes from A-type to E-type across the transition, but a small portion of the phase diagram involves more interesting spin patterns in correspondence of $TbMnO_3$ and $DyMnO_3$. Indeed, when the emerging magnetic interactions retain a competing character, magnetic frustration precludes simple spin ordering to establish and the system reorganizes with exotic chiral spin patterns to save energy. Thus, these unconventional spin orderings are a beautiful result of the interplay between the physics of cooperation and competition among several degrees of freedom. It is in these conditions that novel unexpected and fascinating phenomena can arise, the most subtle of which is the development of a ferroelectric polarization inside the manganite, thus giving rise to multiferroicity. At first

sight this effect is counter-intuitive, as ferroelectricity and magnetism are generally mutually exclusive or competing order parameters. In the manganites, instead, the ferroelectric polarization rises as a secondary order parameter which is induced by the presence of the spiral order via the inverse Dzyaloshinskii-Moriya interaction and it is further stabilized by specific lattice displacements [120–122]. As multiferroicity in the manganites is a manifestation of the concept of multiple coupled order parameters, novel hybrid magnon-phonon modes (known as "electromagnons") are expected to appear in the excitation spectrum of the system [123]. Studying these collective modes is attracting much interest as a way to reveal all the sources and symmetry of the magnetoelectric coupling [124–127].

From the previous discussion, it becomes evident that the central task in solving the paradigm of manganites is to establish the "*cause-effect*" relationship behind their phenomenology. To this aim, a powerful approach is to investigate this relationship directly in the time domain, in which the different elementary excitations of the solid appear with distinct timescales. This approach relies on the use of a tailored pump pulse to set the manganite in a nonequilibrium state, followed by a delayed pulse that probes the evolution of the system. In the simplest scheme, one can separate the contributions related to the different degrees of freedom (charge, lattice, spin, orbital) depending on their characteristic temporal response, which is already a remarkable result. This is the playground of single- or two-colour pump-probe spectroscopy, whose application on the manganites has provided a wealth of information on the electron-lattice/electron-spin interactions, the spin order melting or the generation of coherent bosonic modes as phonons and orbitons [128–130]. More advanced ultrafast methods allow to selectively monitor an observable associated with a specific degree of freedom or to gain spectrally-resolved insights into the nonequilibrium response of the system. In the manganites, the former framework has elucidated the complex interplay among different order parameters, following the selective melting of the charge, orbital or spin order in real time [131, 132]. In contrast, spectrally-resolved nonequilibrium studies have never been applied to manganites. Mapping the ultrafast renormalization of the elementary excitation spectrum is highly desirable, as it can (i) reveal the presence of dynamical processes manifesting only in a specific spectral region; (ii) unveil subtle shifts of the SW associated with many-body effects; (iii) find novel observables contributing to the assignment of ambiguous spectral features. These are the main goals behind the experiments presented in Chap. 7 of this Thesis on the multiferroic manganite $TbMnO_3$. Using high-energy photons covering the broad spectral range of the intersite *d-d* transitions, we are able to reveal the temporal hierarchy of low-energy phenomena leading to the melting of the cycloid spin-order after photoexcitation. Moreover, by studying the behaviour of the coherent collective modes of the material, we also gain insights into one of the unsolved problems behind the physics of insulating manganites, i.e. the character of their fundamental gap.

All these arguments lead to conclude that the nonequilibrium approach is a very promising scheme for shedding light on some controversial aspects of the manganite physics. In this regard, our conclusions for manganites are very similar to the ones we have drawn for cuprates in the previous section. On the contrary, the main difference between the two classes of materials upon perturbation with an optical pump

pulse lies in the fact that doped manganites are more prone than cuprates to exhibit interesting photoinduced phase transitions [128, 133–135]. Although this feature is simply related to the rich phase diagrams shown by the manganites as a function of doping, it still justifies the efforts to realize the light-induced control of phase transitions in an ultrafast fashion. A different framework will be presented at the end of this Chapter, as the resonant excitation of specific collective modes is paving the route for the observation of even more exotic phenomena in both classes of solids. Once again, this in turn confirms the importance of describing the role of collective excitations in many-body systems, which is the subject of the following Section.

1.2 The Role of Collective Excitations in Many-Body Systems

From the previous Sections, it emerges that the general challenge in condensed matter physics is to approach the problem of many particles in complex systems. In a few cases, the physics of a many-body system can be still treated within the single-particle approximation by considering each particle as not the original electron but as a fermionic quasiparticle that becomes dressed of many-body interactions. As we have already mentioned in Sect. 1.1, this is the cornerstone of Landau's theory of Fermi liquids, which applies to the situation of weakly interacting particles in a metal [6]. The breakdown of the Fermi liquid approach naturally leads to novel scenarios, which typically involve the presence of strong interactions, strong correlations and lower dimensionality. In these exotic cases, a deep and complete comprehension of the system becomes a formidable task.

The approach that is commonly adopted is therefore to construct a minimal theoretical model that is able to capture the salient properties of a specific material. However, for unravelling the hidden details of a many-body system, a different strategy must be used, which involves predicting and understanding the excitation spectrum of the material. Indeed, elementary excitations result from the balance among several forces inside the solid and govern all the relevant physical properties, such as the transport mechanisms and the response of the system to external perturbations. In other words, elementary excitations represent the signature of the many-body system. Some of these elementary excitations can be still traced back to the quasiparticle concept and associated with an effective mass and a characteristic lifetime. However, there also exists another kind of fictitious particles, mostly of bosonic nature, which are known under the name of "collective modes". These excitations do not center around individual particles, but involve a cooperative, wave-like motion of many particles in the system simultaneously. This motion is therefore governed by the global interaction among the constituent particles. Most collective excitations (e.g. phonons, plasmons, magnons...) are intrinsic to the solid, while others arise as a consequence of the interaction with an external field. For example, the strong coupling of the electromagnetic field with a collective excitation carrying an

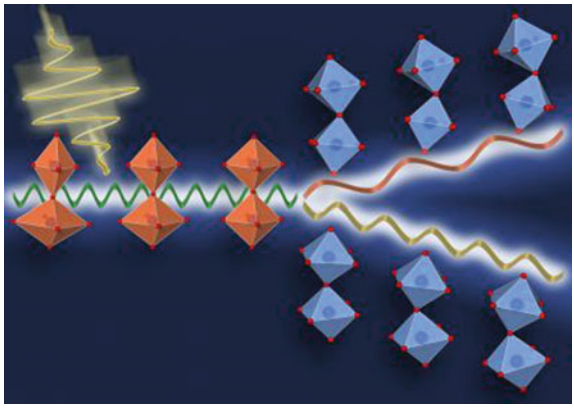

Fig. 1.5 Phononics, example of a novel research field involving the use of collective excitations for technological purposes. Credits of Joerg M. Harms, Max Planck Institute for the Structure and Dynamics of Matter, Hamburg

electric- or magnetic-dipole moment results in the emergence of "polaritons" [136], which are hybrid modes characterized by unique quantum optical properties [137–139]. While collective excitations are present to some extent in all solids, it is in the case of strongly correlated systems that collectivity gives rise to a rich variety of emergent phenomena and leads to profound transformations depending on the external conditions [140]. This aspect has been widely described in Sects. 1.1.2 and 1.1.3. Thus, investigating the physics of collective modes in complex solids can reveal invaluable information on the many-body problem in the presence of cooperative or competing interactions.

Besides embodying the paradigm of the many-body problem, collective modes hold a huge promise for new technological developments and applications, especially in relation to energy sciences, health sciences, data storage and signal processing. The dream is to engineer novel devices where collective modes can be efficiently generated, manipulated and detected, similarly to what occurs in electronics with the electrons and in photonics with the photons [141–144].

First steps towards this goal have been made in the field of plasmonics, which has now become a reality [145]. Plasmonics deals with the interaction between the electromagnetic field and peculiar transverse collective modes known as surface plasmons. The latter are coherent oscillations of delocalized electrons, which set at the interface between two materials where the real part of the dielectric function changes sign across the interface [146]. Surface plasmons possess remarkable properties, including strongly enhanced local fields, dramatic sensitivity to the modification of the local environment and the ability to localize energy to tiny volumes not restricted by the wavelength of the exciting light. For these reasons, the generation, manipulation and detection of surface plasmons is nowadays exploited in several applications, the most famous of which is the surface plasmon resonance for detecting nanometer changes in thickness, density fluctuations or molecular adsorption [147].

Following the successful example of plasmonics, new areas of research are quickly emerging to explore the potential of collective excitations. For example, excitonics is now viewed as an ideal route for mediating the flow of energy at the nanoscale

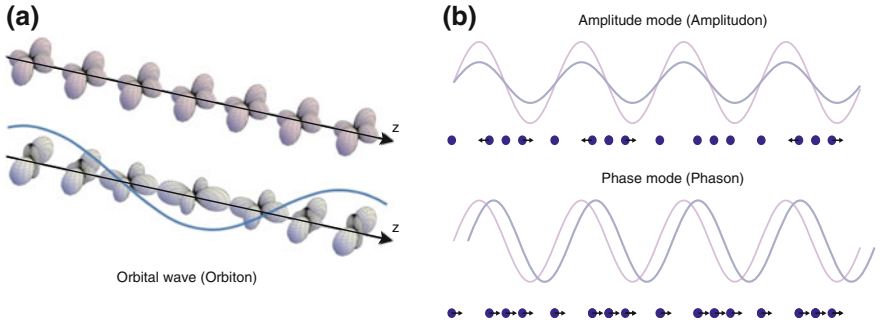

Fig. 1.6 Pictorial representation of emergent collective modes in condensed matter systems. **a** Orbital waves (orbitons) in orbitally-ordered materials, involving a periodic modulation in the shape of the electronic clouds (adapted from Ref. [152]). **b** Amplitude and phase modes (amplitudon and phason) in a CDW system. Pink lines denote the static CDW, grey lines depict the change occurring in the CDW. Blue dots are the ions and the arrows indicate their motion

in photovoltaic materials, since strongly localized excitons are relatively immune to longer-range structural defects and disorder [148]. Phononics (Fig. 1.5) is gradually establishing as a powerful tool for controlling the structure of materials, thus tailoring their functionalities [149]. Magnonics is a promising field that aims to use propagating spin waves, i.e. magnons, as information carriers in devices [150]. Finally, polaritonics is expected to bridge the gap between electronics and photonics (100 GHz–10 THz) or to go beyond photonics (>300 THz) for high-speed signal processing applications, by exploiting the coupling between the electromagnetic field and transverse polarization fields inside the solid (e.g. those from transverse optical phonons or from excitons) [151].

Such a technological perspective for the physics of collective excitations naturally leads to an important question concerning the fate of this area of research. Are there other collective excitations that can provide a valuable platform for facing future challenges in technology? The answer to this question is deeply intertwined with the fundamental concept of spontaneous symmetry breaking in condensed matter [153]. Whenever the symmetry of a system spontaneously breaks, an order parameter establishes in the lowest-energy phase and collective modes naturally emerge as low-lying excitations. The higher is the complexity of the order parameter, the more exotic is the nature of the collective modes arising in the system. In this framework sits the research on strongly correlated quantum systems, as these materials are natural candidates to search for new collective modes that can be manipulated and controlled by external stimuli. A prototypical example is provided by the orbitally-ordered manganites, where emerging collective modes are orbital waves named orbitons (displayed in Fig. 1.6a), involving a periodic modulation in the shape of the electronic clouds [152]. CDW systems offer a valuable platform for exploring collective modes of hybrid electronic-structural character [154], like the amplitude mode of the CDW (amplitudon), involving periodic changes in the charge density amplitude throughout the lattice, or the phase mode (phason), which gives rise to a translation of the

condensate (shown in Fig. 1.6b). Finally, more exotic collective modes of electronic origin emerge in the physics of superconductors. Prominent examples involve: the Higgs mode, a neutral excitation associated with the amplitude of the SC gap [155, 156]; the Anderson-Bogoliubov mode, which involves charge and phase fluctuations of the SC condensate [107]; the Leggett mode, consisting of dynamic oscillations of Cooper pairs between two distinct superfluids [157].

In the following sections, we put emphasis on the collective excitations that will play a fundamental role in the framework of this Thesis, namely plasmons, excitons and phonons.

1.2.1 Plasmons

Plasmons are quantized collective oscillations of the charge density that arise in a plasma, i.e. a system of mobile charged particles interacting with one another via Coulomb forces. In metals and highly-doped semiconductors, the plasma is represented by the electron density and plasmons emerge as collective excitations of the many-electron system, leading to a coherent motion of all particles with a common frequency and wave-vector [158]. As a result, these modes play a fundamental role in the electrodynamics of solids and their study provides valuable information on intrinsic many-body phenomena governing the physics of materials.

Depending on the character of the collective excitation, plasmons can be transverse or longitudinal modes. Prototypical examples of transverse plasmons are the surface plasmons in metallic thin films/nanoparticles (NPs) [146] or a particular type of Josephson plasmons in high-T_C cuprate superconductors [159]. The transverse nature of these collective modes allows them to absorb light, thus becoming detectable in the absorption spectrum of a material. Examples of longitudinal plasmons are the conventional bulk plasmons of metals and doped semiconductors, which arise in correspondence of the zero-crossings of the dispersive part of the material dielectric function $\epsilon_1(\mathbf{q}, \omega)$. As the longitudinal nature of these waves prevents their direct excitation by photon absorption, their observation becomes possible only via photon- or electron inelastic scattering [160, 161]. In the last decades, these probes have established as a powerful tool for investigating the charge-density response function of metals, unveiling the details of the dielectric screening and the associated crystal potential, local-field, and exchange-correlation effects.

In the following, we focus our discussion only on the longitudinal plasma modes, since in Chap. 3 the renormalization of a high-energy longitudinal plasmon is monitored to track the low-energy carrier dynamics of the two-band superconductor MgB_2.

The origin of the concept of longitudinal plasma oscillations lies in the semiclassical Drude model of the electron conduction in metals, in order to explain the cut-off response of the reflectivity above a certain frequency ω_p [16, 162]. A striking implication of the free carrier model is that the dielectric constant changes from negative

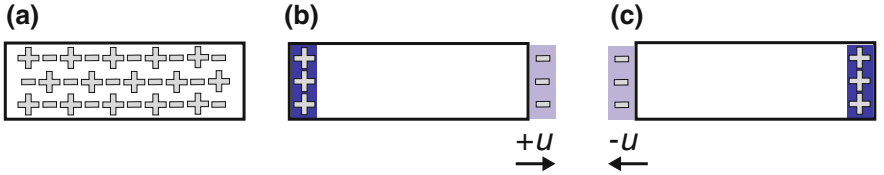

Fig. 1.7 Schematic representation of a metallic slab sustaining longitudinal plasma oscillations. **a** At equilibrium, a perfect compensation of the positive ion and negative electron charges occurs along the whole metallic slab. **b**, **c** Collective displacements of the electron gas in one direction or the other are shown. This in turn creates positive and negative surface charge layers, depicted in blue and violet, respectively. In the presence of a collective electronic displacement, a restoring force sets in and gives rise to oscillations at a frequency ω_p

to positive as the frequency goes through ω_p. Within the Drude model, the plasma frequency of the free-electron gas takes the form

$$\omega_p = \sqrt{\frac{ne^2}{\epsilon_0 m_0}}, \tag{1.3}$$

where n is the number of electrons per unit volume, e is the electron charge, ϵ_0 is the vacuum permittivity and m_0 is the bare electron mass. From Eq. 1.3, it follows that very large values of n lead to a high plasma frequency, which can be even pushed to the UV spectral region. This implies that, in the absence of other absorption processes, the reflectivity drops abruptly above ω_p and some of the light can be transmitted through the metal. In doped semiconductors, it is the presence of impurities that leads to a free-carrier plasma reflectivity edge, lying typically in the infrared [163]. In this case, Eq. 1.3 has to be modified to account for the carrier effective mass and the background polarizability of the bound electrons.

From the semiclassical framework of the Drude model, plasmons arise as oscillations of the whole displaced electron gas with respect to the fixed lattice of positive ions [16] (Fig. 1.7). These collective oscillations proceed with a frequency ω_p and can be sustained only in the absence of dissipative phenomena. In reality, the inspection of the plasmon energy-momentum dispersion relation allows to highlight the presence of dissipative mechanisms. For small values of the wave vector $\mathbf{q}$, the lack of single-particle excitations in the region of the plasma oscillations leads to a negligible damping; for larger $\mathbf{q}$, the plasmon dispersion curve merges into the continuum of single-electron excitations at a wavevector $\mathbf{q}_c$ and for $\mathbf{q} > \mathbf{q}_c$ the oscillations will be damped and decay into the single-particle continuum (Landau damping) [164]. A notable exception to this behaviour is offered by the c-axis plasmon mode of MgB_2, which reappears periodically in higher BZs due to the strong coupling between the single-particle and collective excitation channels [45]. As already observed, this mode will be subject of investigation in Chap. 3, although in the $\mathbf{q} = 0$ limit.

Finally, the renormalization of the bare plasma frequency as a function of temperature can offer valuable information on peculiar many-body processes occurring in

a system. In single-band metals, the bare plasma frequency is expected to decrease for increasing temperature [165–167]. In multiband systems with electron- and hole-like bands and strong electron-boson coupling, the carrier density n in every band depends on the details of the electron-boson interaction. As a result, the temperature dependence of n (i.e. the size of the Fermi surface) is strictly related to the thermal activation of the interaction processes [168, 169]. An analogous scenario will be proposed also in Chap. 3 for explaining the anomalous behaviour of the a- and c-axis bare plasma frequencies of MgB_2.

1.2.2 Excitons

Excitons represent collective excitations emerging in a non-metallic system. An ideal exciton can be considered as an electrically neutral quantum of electronic excitation energy, travelling in the periodic structure of a crystal. As such, it can be viewed as a bound electron-hole pair that involves the transport of energy, but not of a net charge. As the exciton arises just in the presence of both the electron and the hole, its existence is intimately related to the absorption of a light field at a given frequency. The collective nature of an exciton provides a clear manifestation during the absorption of light. Differently from single-particle optical transitions, in which only one single-particle state gets excited by the incident light field and all the other states do not participate (Fig. 1.8a), the excitonic transition is a "collective" one, which involves many states of the electronic band structure. A simple cartoon for this phenomenon is shown in Fig. 1.8b.

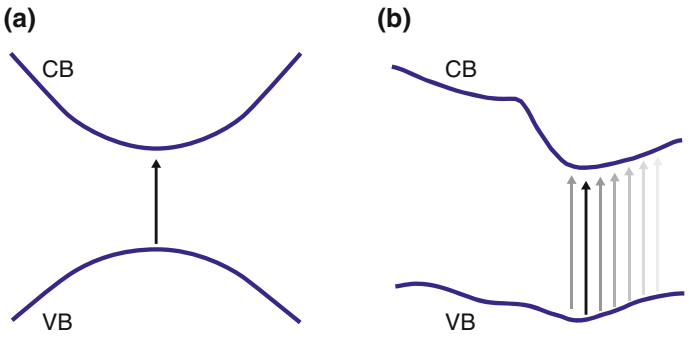

Fig. 1.8 **a** Schematic representation of single-particle optical transitions, in which only an individual particle is excited by the incident light and all the other states are silent; **b** Schematic representation of a "collective" excitation associated with an excitonic transition, in which many states participate. The arrow shading indicates the strengths of the different transitions. As a result, the excitation energy becomes smaller than the bandgap since the collective character of the response is energetically stable

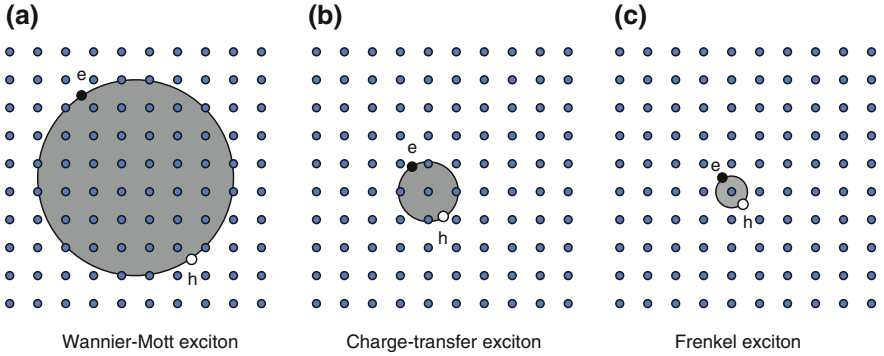

Fig. 1.9 Schematic representation of the wavefunction for **a** a Wannier-Mott, **b** a CT and **c** a Frenkel exciton

A necessary condition for this many-state transition to occur and for the exciton to form is that the electron and hole group velocities are the same, i.e. that the gradients of the CB and the VB are identical in a specific portion of the BZ. As a consequence, while the excitation energy of a single-particle transition is just the difference between the initial and final single-particle states, the excitation energy of an excitonic transition is lower than the fundamental band gap. The stabilization energy with respect to the uncorrelated particle-hole limit is the fingerprint for the collective nature of the state created in the absorption process and is typically known as the "exciton binding energy" (E_B). This quantity measures the strength of the electron-hole interaction giving rise to the peculiar bound state, in which the electron and hole are found to move together with the same group velocity.

From the discussion above, it follows that the rigorous determination of E_B relies on the estimate of the fundamental energy gap for both charged (single-particle) and neutral (two-particle) excitations. The former gap, known as "electronic gap" (E_{el}), can be measured by a combination of photoemission and inverse photoemission spectroscopy; the latter gap, the so-called "optical gap" (E_{opt}), can be extracted by optical spectroscopy. It follows that E_B can be simply defined as

$$E_B = E_{el} - E_{opt}. \tag{1.4}$$

Depending on the value of E_B and the spread of the wavefunction, excitons in condensed matter can be classified under different types. Wannier-Mott excitons represent hydrogenic electron-hole pairs delocalized over several unit cells of the lattice and arise in semiconductors with high dielectric constant (Fig. 1.9a). The other extreme is represented by Frenkel excitons, which correspond to a correlated electron-hole pair localized on a single lattice site and mostly prevail in solid rare gases and molecular solids (Fig. 1.9c). Intermediate between these two regimes is a number of exotic excitations that are typically referred to as CT excitons. In the language of molecular physics, CT excitons form when the electron and the hole

occupy adjacent molecules in a molecular structure of an organic semiconductor [170]; on the other hand, in the language of strong electron correlations, CT excitons embody the lowest-energy neutral excitation that is found in insulating TMOs, involving an electron in the transition metal *3d* orbitals and a hole in the oxygen *2p* orbitals [171, 172]. Irrespective of the origin, the concept of CT exciton is always related to a transfer of charge from one atomic site to another, thus spreading the wavefunction over several unit cells and retaining an intermediate character between the Wannier-Mott and Frenkel limits (Fig. 1.9b).

Studying these collective electronic excitations is of great importance, as it provides detailed information about the magnitude and spatial distribution of the electron-hole correlations. The natural technique to probe excitons is represented by optical spectroscopy at low temperature, as the excitons manifest as narrow peaks preceding the absorption continuum [163]. Thus, optical spectroscopy alone can reveal the nature of the lowest-energy charge excitations of an insulator, provided that the fundamental gap has a direct character. In the presence of a fundamental indirect gap, the determination of E_B by optical spectroscopy alone is hindered and the situation becomes more complex. We will illustrate an example of such a scenario in Chap. 4. Additional information on the exciton energy-momentum dispersion, which offers a precise estimate of the exciton transport properties, are instead provided by resonant inelastic x-ray scattering (RIXS) and EELS [171, 172].

To describe the properties of the neutral excitations occurring upon photon absorption or scattering, in the last decade much progress has been made by *ab initio* theoretical calculations. One of the main achievements for theory has been the inclusion of the screened electronhole interaction involved in the formation of excitons. This interaction is described in the so-called BetheSalpeter equation (BSE), which solves for the neutral excitation energies as the poles of a two-particle Green's function [173]. The solution of the BSE typically begins with a many-body electronic structure calculation to solve for the single-particle quasielectron and quasihole. The BSE formalism subsequently introduces an interaction term that mixes the two types of charged transitions. Despite being computationally demanding, this technique proved successful in reproducing the salient feature of the experimental optical spectra of standard semiconductors and TMOs [174].

Novel frontiers in fundamental exciton research involve the study of exciton physics in the presence of strong interactions and correlations in complex materials. Excitons are high-energy bosonic collective excitations and, as such, they are more prone to undergo severe renormalizations upon interaction with other particles in a material. In the past, a body of work focused on the renormalization processes that the exciton experience in simple semiconductors upon chemical- or photo-doping [175]. Several single-particle and many-body effects as Pauli blocking, exciton screening and carrier-induced bandgap renormalization (BGR) were identified experimentally and modelled theoretically. More remarkably, research in this area successfully identified the sources of optical nonlinearity occurring in bulk semiconductors and nanostructures, opening the doors to the use of excitonic materials for applications and technology [176]. Extending these concepts to the case of strongly interacting and correlated quantum systems is not trivial, as excitons are likely to interact with the

phonon field or with other elementary excitations [17]. On the experimental side, one needs to reveal the fingerprints of such exotic interactions by performing extensive temperature studies or by applying state-of-the-art techniques. On the theory side, suitable extension of the BSE should be developed in order to include the effects of electron-phonon interaction or of a finite doping. In the framework of this Thesis, these concepts will be deeply explored in Chap. 4, in which we report on the experimental discovery and the complete theoretical modelling of bound excitonic quasiparticles in the strongly interacting d^0 insulator anatase TiO_2. In this regard, the application of advanced ultrafast spectroscopic techniques paves the route toward a selective and quantitative estimate of the exciton-phonon interaction, an aspect which has never been accessible via conventional steady-state methods.

1.2.3 Phonons

Collective excitations of the atoms in a solid are known as phonons. These modes play a fundamental role in the physics of a crystal, determining its thermodynamic, transport and electrodynamic properties. The description of phonons within the quantum theory of solids has been the subjects of numerous books [18–20] and it is out of the scope of this Thesis. In Sect. 1.1.1, we have already explored some remarkable manifestations of the electron-phonon interactions in the strong coupling regime. Here, in this section, we restrict our discussion to another aspect of primary importance for the development of the following Chapters, namely the impact that phonons have on the electrodynamic properties of materials. In this regard, it is useful to distinguish between two separate effects: the direct manifestation of phonon modes in the infrared or in the Raman spectra of a material [160] and the signature that phonons leave on the high-energy charge excitations of the solid (like the optical bands of polarons, excitons and uncorrelated particle-hole excitations) [17].

In the first scenario, insightful information on the phonon degrees of freedom at $\mathbf{q} = 0$ can be retrieved either via direct absorption or via scattering of the electromagnetic radiation by a phonon mode in the crystal. Direct absorption relies on a dipole-allowed process and is achieved by shining a resonant infrared field on the crystal. As the electromagnetic waves are transverse, they can couple to the transverse optic phonon modes of the solid at $\mathbf{q} = 0$, which thus become observable in infrared spectroscopy. In contrast, the spontaneous inelastic scattering of radiation by phonons is a nonlinear process (quadratic in the electric field) and is typically achieved using photons in the visible or near-infrared range, which interact with the polarizable electron density and the bonds in the solid. As a consequence, the system is maintained in a virtual energy state for a short period of time before releasing a new photon (which is inelastically scattered). The signature of the phonon mode is left on the scattered photon, which possesses lower (Stokes) or higher (anti-Stokes) energy than the incoming photon [160].

From the above arguments, a phonon is named infrared/Raman-active if its excitation involves the absorption/scattering of the incident electromagnetic radiation in

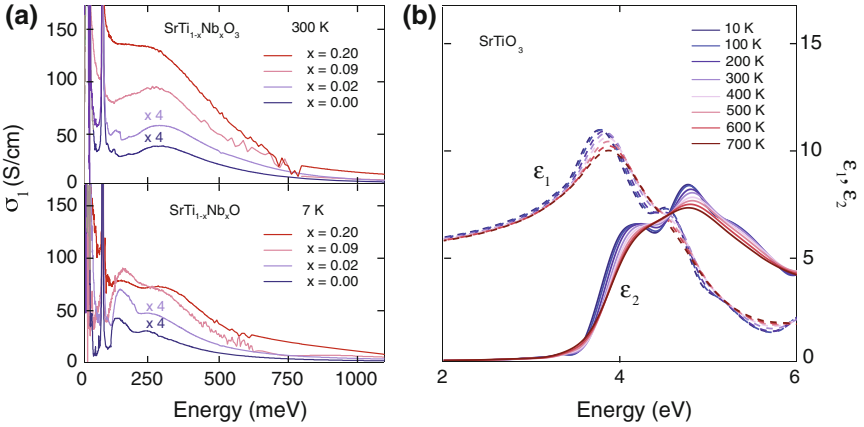

Fig. 1.10 **a** Real part of the optical conductivity in $SrTi_{1-x}Nb_xO_3$ samples at 300 and 7 K for different values of the doping x. An incoherent band, which is the signature of large polarons in the material, is found to emerge as a function of doping and shows a satellite-like structure at 7 K. Adapted from [177]. **b** Temperature-dependent spectra of the dielectric function $\epsilon = \epsilon_1 + i\epsilon_2$ of $SrTiO_3$, in which the bandgap energy is found to blueshift for increasing temperature. This anomalous behaviour is a manifestation of the electron-phonon coupling in the material. Adapted from Ref. [178]

the long-wavelength limit. The emergence of a phonon mode in the infrared or in the Raman spectrum of a material relies solely on the symmetry of the mode according to group theory considerations. Typically, when the crystal possesses inversion symmetry, Raman-active modes are silent in infrared spectroscopy and infrared-active modes are silent in spontaneous Raman scattering. This concept is deeply rooted in the field of molecular spectroscopy, as the rule of mutual exclusion states that no normal modes can be both infrared and Raman-active in a molecule possessing a centre of symmetry. However, upon breaking spatial inversion symmetry, the same mode can simultaneously appear or be silent in both spectroscopies.

Another manifestation of phonons on the electrodynamics of a solid is represented by their effect on the high-energy excitations of the material. In the simple case of indirect bandgap semiconductors like Si or Ge, indirect absorption is only related to the mediation of phonons when impurities and defects are neglected [163]. In more complex scenarios of intermediate electron-phonon coupling, a series of sidebands due to coupling to several phonon modes are typically observed in correspondence of polaron absorption or interband particle-hole excitations. An example is offered in Fig. 1.10a, in which a large polaron band is shown to develop in the optical conductivity spectra of $SrTi_{1-x}Nb_xO_3$ as a function of doping x and at two different temperatures (adapted from Ref. [177]). The sidebands are smeared out in the presence of strong electron-phonon coupling, leading to broad Gaussian lineshapes manifesting even at the lowest temperature [17].

More subtle effects of the electron-phonon coupling emerge when temperature dependences are performed. Both the phonon modes detected in infrared spec-

troscopy/Raman scattering and the high-energy excitations of the solid are expected to soften with increasing temperature. This renormalization is accounted for by the thermal expansion of the lattice and, in the case of the high-energy interband transitions, it is well described by the empirical Varshni model [179]. However, anomalous situations have also been observed [178, 180, 181], in which the energy of an excitation hardens as the temperature is increased. An example is given in Fig. 1.10b, in which the temperature-dependent dielectric function of $SrTiO_3$ (adapted from Ref. [178]) is shown. An anomalous temperature dependence of the direct gap is found. The description of the microscopic processes behind these effects are a current topic of research and no conclusive explanation has been provided yet. In the framework of this Thesis, an anomalous temperature dependence has been revealed in the exciton spectrum of anatase TiO_2 and associated with the effect of the electron-phonon coupling at finite temperature.

1.3 Novel Frontiers in the Physics of Collective Excitations

In the previous Sections, we underlined how the study of collective excitations can decisively shape our comprehension of quantum many-body phenomena in complex matter. Nowadays, this task is being accomplished by two distinct, yet intimately related, areas of research, namely atomic physics and solid state physics. On the atomic physics side, tremendous developments in the field of trapped ultracold atomic gases in optical lattices has provided a physical realisation of a variety of quantum models, both for fermionic and bosonic particles [182]. The use of these *quantum simulators* provides a wealth of information concerning the emergence and the dynamics of several collective modes, which is important for unravelling the underlying symmetries of a system. In this regard, strong emphasis is being given to the search for those collective modes that play a fundamental role in elementary particle physics [183]. On the solid state physics side, the use of advanced spectroscopies has contributed to the discovery and assignments of novel collective excitations in quantum materials, whose properties shed light on the presence of interactions and correlations at the microscopic scale.

As already described above, one of the main frontiers in the latter field involves the study of the collective excitations under nonequilibrium conditions using ultrafast spectroscopies. Mapping the temporal evolution of these modes is highly desirable, as it bears the signature of the low-energy phenomena occurring in the system during its path to reach the thermodynamic equilibrium. This framework represents the main subject of this Thesis and, as such, it is applied to a number of materials characterized by a gradual degree of internal complexity beyond conventional band theory. The fingerprint of the collective excitations of interest is revealed either in the frequency or in the time domain, which is a powerful tool for accessing the dynamics of collective excitations lying at very different energy scales. The extension of this scheme to retrieve momentum-resolved information represents the future step in this field of research.

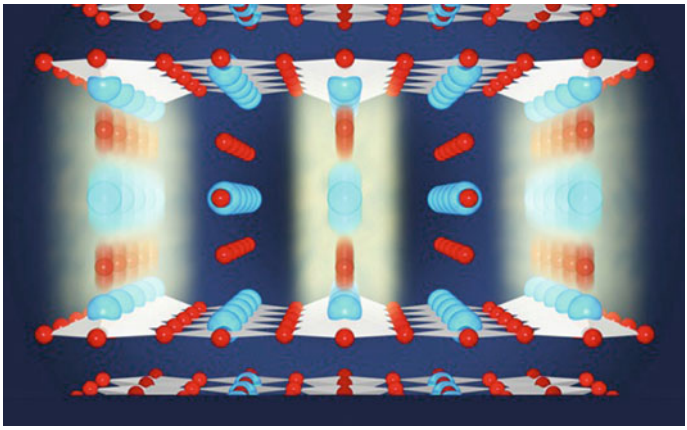

Fig. 1.11 Pictorial representation of the ultrafast control on a strongly correlated system via resonant excitation of an infrared-active phonon mode. The atoms associated with the eigenvector of the excited mode are strongly displaced from their equilibrium positions. The excitation of this infrared-active phonon can trigger additional lattice modes via a nonlinear coupling. A new nonequilibrium structure is developed and this can favor the emergence of novel quantum phenomena. Credits of Joerg M. Harms, Max Planck Institute for the Structure and Dynamics of Matter, Hamburg

A relatively new frontier in collective mode physics is strictly related to the concept of "control" under nonequilibrium conditions. This implies either the control *of* a specific collective excitation or the control of a material *through* a collective excitation. The former scenario holds special promise in magnonics and it relies on the use of coherent collective excitations in the time domain. These modes are coherent in the sense that two time-separated optical pulses can enhance or suppress the oscillation associated with the mode, depending on their mutual separation in time. As a result, a particular mode can be switched on and off by designing a suitably shaped train of laser pulses. In other words, this is a type of quantum control based on the interference between a collective mode and itself. This framework has been particularly studied in the case of phonons in band semiconductors and CDW materials [184, 185], but its extension to the characteristic modes of magnets and superconductors is attracting interest for engineering new protocols of coherent control that may have an impact on technology and applications. An alternative and very powerful approach is instead based on the control of a material properties through the excitation of a specific dipole-allowed (i.e. infrared-active) collective mode using high laser fluences (Fig. 1.11). As these modes lie typically in the THz or FIR spectral range, strong limitations in achieving their intense resonant excitation have been imposed by the scarcity of suitable laser sources. Recent progress in ultrafast laser physics and quantum electronics have opened the doors to the implementation of laser schemes that can selectively excite these infrared-active collective modes in the THz and FIR range. The impact of this method has been exceptional, particularly in the field of strongly correlated quantum systems. As these materials are very sensitive

to external stimuli, tailored photoexcitation of a collective mode can produce a variety of fascinating, yet still quite unpredictable, effects. The most impressive results have been achieved by resonant pumping infrared-active phonon modes in high-T_C cuprate superconductors and in manganites. In the cuprates, this has led to the establishment of a highly coherent state above T_C that resembles the properties of the SC phase [186, 187]. In underdoped (UD) monolayer cuprates of the $La_{2-x}Ba_xCuO_4$ family, the Josephson plasmon resonance has been shown to emerge above T_C upon suppression of the stripe order competing with superconductivity [186]. More surprisingly, in UD bilayer cuprates of the $YBa_2Cu_3O_{7-\delta}$ family, this nonequilibrium state has even been shown to persist up to room temperature (RT) and to involve a deformation of the crystal lattice which disrupts the competing CDW order [187, 188]. As a result, this ultrafast pathway is likely to stabilize superconductivity. In the manganites, pumping specific infrared-active modes has led to the creation of metastable electronic states or to the melting of the spin and orbital orders [149, 189, 190]. As the laser pump pulses used for these experiments are very intense and are believed to be absorbed selectively by the excited collective mode, the radiation-matter interaction is highly nonlinear and has paved the route to the development of the so-called "nonlinear phononics" scheme. The goal here is to reach the control of the lattice of a material within the framework of ionic Raman scattering [149, 191]. Motivated by these results, new advances in the field are exploring the resonant excitation of Josephson plasmons [192] and electromagnons [193], opening new intriguing perspectives for the future of this research area.

In conclusion, all these developments make the physics of collective excitations a fertile area of research, justifying the scope of their detailed analysis to gain insights into elusive low-energy phenomena in many-body systems. Before discussing the case studies of this Thesis, in the next Chapter we first introduce the spectroscopic methods aimed at the identification of the elementary excitations in condensed matter systems. We put special emphasis on the nonequilibrium techniques, as these will represent the main experimental tool for our investigation.

References

1. H. Bethe, Theorie der Beugung von Elektronen an Kristallen. Ann. Phys. **392**(17), 55–129 (1928)
2. A. Sommerfeld, I. Zusammenfassende Vorträge zum Hauptthema: Die Arten Chemischer Bindung und der Bau der Atome. Zur Frage nach der Bedeutung der Atommodelle. Z. Elktrochem. Angew. P, 34(9):426–430 (1928)
3. M.F. Bloch, Bemerkung zur Elektronentheorie des Ferromagnetismus und der Elektrischen Leitfähigkeit. Z. Phys. **57**(7–8), 545–555 (1929)
4. J.H. de Boer, E.J.W. Verwey, Semi-conductors with partially and with completely filled 3d-lattice bands. Proc. Phys. Soc. **49**(4S), 59 (1937)
5. N.F. Mott, R. Peierls, Discussion of the paper by de Boer and Verwey. Proc. Phys. Soc. **49**(4S), 72 (1937)
6. L.D. Landau, The theory of a Fermi liquid. Sov. Phys. JETP-USSR **3**(6), 920–925 (1957)

7. J. Bardeen, L.N. Cooper, J.R. Schrieffer, Theory of superconductivity. Phys. Rev. **108**(5), 1175 (1957)
8. G. M. Eliashberg, Interactions between electrons and lattice vibrations in a superconductor. Sov. Phys.-JETP Engl. Transl. 11(3) (1960). (United States)
9. J.G. Bednorz, K.A. Müller, Possible high T_C superconductivity in the Ba-La-Cu-O system. Z. Phys. B **64**, 189–193 (1986)
10. S. Jin, M. ThH Tiefel, R.A. McCormack, R. Fastnacht, L.H. Chen Ramesh, Thousandfold change in resistivity in magnetoresistive La-Ca-Mn-O films. Science **264**(5157), 413–414 (1994)
11. Z.X. Shen, A. Lanzara, S. Ishihara, N. Nagaosa, Role of the electron-phonon interaction in the strongly correlated cuprate superconductors. Phil. Mag. B **82**(13), 1349–1368 (2002)
12. D.N. Basov, R.D. Averitt, D. van der Marel, M. Dressel, K. Haule, Electrodynamics of correlated electron materials. Rev. Mod. Phys. **83**, 471–541 (2011)
13. A.J. Millis, Optical conductivity and correlated electron physics, in *Strong Interactions in Low Dimensions* (Springer, Dordrecht, 2004), pp. 195–235
14. A. Damascelli, Probing the electronic structure of complex systems by ARPES. Phys. Scr. **2004**(T109), 61 (2004)
15. L.J.P. Ament, M. Van Veenendaal, T.P. Devereaux, J.P. Hill, J. Van Den Brink, Resonant inelastic x-ray scattering studies of elementary excitations. Rev. Mod. Phys. **83**(2), 705 (2011)
16. P. Drude, Zur Elektronentheorie der Metalle. Ann. Phys. **306**(3), 566–613 (1900)
17. Y. Toyozawa, *Optical Processes in Solids* (Cambridge University Press, Cambridge, 2003)
18. G.D. Mahan, *Many-Particle Physics* (Springer Science & Business Media, 2013)
19. A.S. Alexandrov, *Polarons in Advanced Materials*, vol. 103 (Springer Science & Business Media, 2008)
20. D. Emin, *Polarons* (Cambridge University Press, 2013)
21. J.P. Carbotte, Properties of boson-exchange superconductors. Rev. Mod. Phys. **62**(4), 1027 (1990)
22. W.L. McMillan, Transition temperature of strong-coupled superconductors. Phys. Rev. **167**(2), 331 (1968)
23. Y. Kamihara, H. Hiramatsu, M. Hirano, R. Kawamura, H. Yanagi, T. Kamiya, H. Hosono, Iron-based layered superconductor: LaOFeP. J. Am. Chem. Soc. **128**(31), 10012–10013 (2006)
24. J. Nagamatsu, N. Nakagawa, T. Muranaka, Y. Zenitani, J. Akimitsu, Superconductivity at 39 K in magnesium diboride. Nature **410**(6824), 63–64 (2001)
25. A.P. Drozdov, M.I. Eremets, I.A. Troyan, V. Ksenofontov, S.I. Shylin, Conventional superconductivity at 203 Kelvin at high pressures in the sulfur hydride system. Nature **525**(7567), 73–76 (2015)
26. I. Errea, M. Calandra, C.J. Pickard, J. Nelson, R.J. Needs, Y. Li, H. Liu, Y. Zhang, Y. Ma, F. Mauri, High-pressure hydrogen sulfide from first principles: a strongly anharmonic phonon-mediated superconductor. Phys. Rev. Lett. **114**, 157004 (2015)
27. A. Bussmann-Holder, J. Köhler, M.H. Whangbo, A. Bianconi, A. Simon, High temperature superconductivity in sulfur hydride under ultrahigh pressure: a complex superconducting phase beyond conventional BCS. Novel Supercond. Mat. **2**(1), 37–42 (2016)
28. A.Y. Liu, I. Mazin, J. Kortus, Beyond Eliashberg superconductivity in MgB_2: anharmonicity, two-phonon scattering, and multiple gaps. Phys. Rev. Lett. **87**(8), 087005 (2001)
29. Y. Wang, T. Plackowski, A. Junod, Specific heat in the superconducting and normal state (2–300 K, 0–16 T), and magnetic susceptibility of the 38 K superconductor MgB_2: evidence for a multicomponent gap. Physica C **355**(3), 179–193 (2001)
30. S. Souma, Y. Machida, T. Sato, T. Takahashi, H. Matsui, S.C. Wang, H. Ding, A. Kaminski, J.C. Campuzano, S. Sasaki et al., The origin of multiple superconducting gaps in MgB_2. Nature **423**(6935), 65–67 (2003)
31. M. Iavarone, G. Karapetrov, A.E. Koshelev, W.K. Kwok, G.W. Crabtree, D.G. Hinks, W.N. Kang, E. Choi, Hyun J. Kim et al., Two-band superconductivity in MgB_2. Phys. Rev. Lett. **89**(18), 187002 (2002)

32. M.R. Eskildsen, M. Kugler, S. Tanaka, J. Jun, S.M. Kazakov, J. Karpinski, Ø. Fischer, Vortex imaging in the π band of magnesium diboride. Phys. Rev. Lett. **89**(18), 187003 (2002)
33. X.K. Chen, M.J. Konstantinović, J.C. Irwin, D.D. Lawrie, J.P. Franck, Evidence for two superconducting gaps in MgB_2. Phys. Rev. Lett. **87**(15), 157002 (2001)
34. A.F. Goncharov, V.V. Struzhkin, E. Gregoryanz, J. Hu, R.J. Hemley, H.-K. Mao, G. Lapertot, S.L. Budko, P.C. Canfield, Raman spectrum and lattice parameters of MgB_2 as a function of pressure. Phys. Rev. B **64**(10), 100509 (2001)
35. J.W. Quilty, S. Lee, A. Yamamoto, S. Tajima, Superconducting gap in MgB_2: electronic Raman scattering measurements of single crystals. Phys. Rev. Lett. **88**(8), 087001 (2002)
36. J.W. Quilty, S. Lee, S. Tajima, A. Yamanaka, c-Axis Raman scattering spectra of MgB_2: observation of a dirty-limit gap in the π bands. Phys. Rev. Lett. **90**(20), 207006 (2003)
37. G. Blumberg, A. Mialitsin, B.S. Dennis, N.D. Zhigadlo, J. Karpinski, Multi-gap superconductivity in MgB_2: magneto-Raman spectroscopy. Physica C **456**(1), 75–82 (2007)
38. V. Guritanu, A.B. Kuzmenko, D. van der Marel, S.M. Kazakov, N.D. Zhigadlo, J. Karpinski, Anisotropic optical conductivity and two colors of MgB_2. Phys. Rev. B **73**(10), 104509 (2006)
39. J. Kortus, I.I. Mazin, K.D. Belashchenko, V.P. Antropov, L.L. Boyer, Superconductivity of metallic boron in MgB_2. Phys. Rev. Lett. **86**(20), 4656 (2001)
40. K.P. Bohnen, R. Heid, B. Renker, Phonon dispersion and electron-phonon coupling in MgB_2 and AlB_2. Phys. Rev. Lett. **86**(25), 5771 (2001)
41. Y. Kong, O.V. Dolgov, O. Jepsen, O.K. Andersen, electron-phonon interaction in the normal and superconducting states of MgB_2. Phys. Rev. B **64**(2), 020501 (2001)
42. K. Kunc, I. Loa, K. Syassen, R.K. Kremer, K. Ahn, MgB_2 under pressure: phonon calculations, Raman spectroscopy, and optical reflectance. J. Phys. Cond. Matt. **13**(44), 9945 (2001)
43. H.J. Choi, D. Roundy, H. Sun, M.L. Cohen, S.G. Louie, The origin of the anomalous superconducting properties of MgB_2. Nature **418**(6899), 758–760 (2002)
44. T. Yildirim, O. Gülseren, J.W. Lynn, C.M. Brown, T.J. Udovic, Q. Huang, N. Rogado, K.A. Regan, M.A. Hayward, J.S. Slusky, T. He, M.K. Haas, P. Khalifah, K. Inumaru, R.J. Cava, Giant anharmonicity and nonlinear electron-phonon coupling in MgB_2: a combined first-principles calculation and neutron scattering study. Phys. Rev. Lett. **87**(3), 037001 (2001)
45. Y.Q. Cai, P. Chow, O.D. Restrepo, Y. Takano, K. Togano, H. Kito, H. Ishii, C.C. Chen, K.S. Liang, C.T. Chen et al., Low-energy charge-density excitations in MgB_2: striking interplay between single-particle and collective behavior for large momenta. Phys. Rev. Lett. **97**(17), 176402 (2006)
46. L.D. Landau, S.I. Pekar, Polaron effective mass. Zh. Eksp. Teor. Fiz. **18**(5), 419 (1948)
47. H. Fröhlich, Electrons in lattice fields. Adv. Phys. **3**(11), 325–361 (1954)
48. T. Holstein, Studies of polaron motion: part I the molecular-crystal model. Ann. Phys. **8**(3), 325–342 (1959)
49. T. Holstein, Studies of polaron motion: part II the small polaron. Ann. Phys. **8**(3), 343–389 (1959)
50. R.P. Feynman, Slow electrons in a polar crystal. Phys. Rev. **97**(3), 660 (1955)
51. A.M. Stoneham, J. Gavartin, A.L. Shluger, A.V. Kimmel, G. Aeppli, C. Renner et al., Trapping, self-trapping and the polaron family. J. Phys-Condens. Mat. **19**(25), 255208 (2007)
52. P.B. Allen, V. Perebeinos, Self-trapped exciton and Franck-Condon spectra predicted in $LaMnO_3$. Phys. Rev. Lett. **83**(23), 4828 (1999)
53. J. Callaway, D.P. Chen, D.G. Kanhere, Q. Li, Pairing in finite cluster models. Physica B **163**(1–3), 127–128 (1990)
54. C.J. Thompson, T. Matsubara, A unified statistical mechanical approach to high-temperature superconductivity, in *Studies of High Temperature Superconductors* (1991)
55. A. Macridin, G.A. Sawatzky, M. Jarrell, Two-dimensional Hubbard-Holstein bipolaron. Phys. Rev. B **69**(24), 245111 (2004)
56. A.S. Mishchenko, N. Nagaosa, Z.-X. Shen, G. De Filippis, V. Cataudella, T.P. Devereaux, C. Bernhard, K.W. Kim, J. Zaanen, Charge dynamics of doped holes in high T_c cuprate superconductors: a clue from optical conductivity. Phys. Rev. Lett. **100**(16), 166401 (2008)

57. G. De Filippis, V. Cataudella, E.A. Nowadnick, T.P. Devereaux, A.S. Mishchenko, N. Nagaosa, Quantum dynamics of the Hubbard-Holstein model in equilibrium and nonequilibrium: application to pump-probe phenomena. Phys. Rev. Lett. **109**(17), 176402 (2012)
58. J.P. Franck, D.M. Ginsberg, Physical properties of high temperature superconductors IV. World Sci, Singapore, p. 189 (1994)
59. H.J.A. Molegraaf, C. Presura, D. Van Der Marel, P.H. Kes, M. Li, Superconductivity-induced transfer of in-plane spectral weight in $Bi_2Sr_2CaCu_2O_{8+\delta}$. Science **295**(5563), 2239–2241 (2002)
60. J.M. Tranquada, B.J. Sternlieb, J.D. Axe, Y. Nakamura, S. Uchida, Evidence for stripe correlations of spins and holes in copper oxide superconductors. Nature **375**(6532), 561–563 (1995)
61. A. Bianconi, N.L. Saini, A. Lanzara, M. Missori, T. Rossetti, H. Oyanagi, H. Yamaguchi, K. Oka, T. Ito, Determination of the local lattice distortions in the CuO_2 plane of $La_{1.85}Sr_{0.15}CuO_4$. Phys. Rev. Lett. **76**(18), 3412 (1996)
62. V. Hinkov, D. Haug, B. Fauqué, P. Bourges, Y. Sidis, A. Ivanov, C. Bernhard, C.T. Lin, B. Keimer, Electronic liquid crystal state in the high-temperature superconductor $YBa_2Cu_3O_{6.45}$. Science **319**(5863), 597–600 (2008)
63. M. Vershinin, S. Misra, S. Ono, Y. Abe, Y. Ando, A. Yazdani, Local ordering in the pseudogap state of the high-T_c superconductor $Bi_2Sr_2CaCu_2O_{8+\delta}$. Science **303**(5666), 1995–1998 (2004)
64. G. Ghiringhelli, M. Le Tacon, M. Minola, S. Blanco-Canosa, C. Mazzoli, N.B. Brookes, G.M. De Luca, A. Frano, D.G. Hawthorn, F. He, Long-range incommensurate charge fluctuations in (Y, Nd)$Ba_2Cu_3O_{6+x}$. Science **303**(6096), 821–825 (2012)
65. M. Hashimoto, E.A. Nowadnick, R.-H. He, I.M. Vishik, B. Moritz, Y. He, K. Tanaka, R.G. Moore, D. Lu, Y. Yoshida, M. Ishikado, T. Sasagawa, K. Fujita, S. Ishida, S. Uchida, H. Eisaki, Z. Hussain, T.P. Devereaux, Z.-X. Shen, Direct spectroscopic evidence for phase competition between the pseudogap and superconductivity in $Bi_2Sr_2CaCu_2O_{8+\delta}$. Nat. Mat. **14**(1), 37–42 (2015)
66. J. Chang, E. Blackburn, A.T. Holmes, N.B. Christensen, J. Larsen, J. Mesot, R. Liang, D.A. Bonn, W.N. Hardy, A. Watenphul, Direct observation of competition between superconductivity and charge density wave order in $YBa_2Cu_3O_{6.67}$. Nat. Phys. **8**(12), 871–876 (2012)
67. W.W. Warren Jr., R.E. Walstedt, G.F. Brennert, R.J. Cava, R. Tycko, R.F. Bell, G. Dabbagh, Cu spin dynamics and superconducting precursor effects in planes above T_C in $YBa_2Cu_3O_{6.7}$. Phys. Rev. Lett. **62**(10), 1193 (1989)
68. H. Alloul, T. Ohno, P. Mendels, ^{89}Y NMR evidence for a Fermi-liquid behavior in $YBa_2Cu_3O_{6+x}$. Phys. Rev. Lett. **63**(16), 1700 (1989)
69. M. Takigawa, A.P. Reyes, P.C. Hammel, J.D. Thompson, R.H. Heffner, Z. Fisk, K.C. Ott, Cu and O NMR studies of the magnetic properties of $YBa_2Cu_3O_{6.63}$ (T_C = 62 K). Phys. Rev. B **43**(1), 247 (1991)
70. J.W. Loram, K.A. Mirza, J.R. Cooper, W.Y. Liang, Electronic specific heat of $YBa_2Cu_3O_{6+x}$ from 1.8 to 300 K. Phys. Rev. Lett. **71**(11), 1740 (1993)
71. K.K. Gomes, A.N. Pasupathy, A. Pushp, S. Ono, Y. Ando, A. Yazdani, Visualizing pair formation on the atomic scale in the high-T_C superconductor $Bi_2Sr_2CaCu_2O_{8+\delta}$. Nature **447**(7144), 569–572 (2007)
72. A. Yazdani, Visualizing pair formation on the atomic scale and the search for the mechanism of superconductivity in High-T_C cuprates. J. Phys. Cond. Matt. **21**(16), 164214 (2009)
73. M. Shi, A. Bendounan, E. Razzoli, S. Rosenkranz, M.R. Norman, J.C. Campuzano, J. Chang, M.Månsson, Y. Sassa, T. Claesson, O. Tjernberg, L. Patthey, N. Momono, M. Oda, M. Ido, S. Guerrero, C. Mudry, J. Mesot, Spectroscopic evidence for preformed Cooper pairs in the pseudogap phase of cuprates. EPL (Europhys. Lett.), 88(2):27008 (2009)
74. T. Kondo, Y. Hamaya, A.D. Palczewski, T. Takeuchi, J.S. Wen, Z.J. Xu, G. Gu, J. Schmalian, A. Kaminski, Disentangling Cooper-pair formation above the transition temperature from the pseudogap state in the cuprates. Nat. Phys. **7**(1), 21–25 (2011)

75. T. Kondo, W. Malaeb, Y. Ishida, T. Sasagawa, H. Sakamoto, T. Takeuchi, T. Tohyama, S. Shin, Point nodes persisting far beyond T_C in Bi2212. Nat. Comm. **6**, 7699 (2015)
76. N. Hussey, Phenomenology of the normal state in-plane transport properties of high-T_C cuprates. J. Phys. Cond. Matt. **20**(12), 123201 (2008)
77. J. Chang, M. Maansson, S. Pailhes, T. Claesson, O.J. Lipscombe, S.M. Hayden, L. Patthey, O. Tjernberg, J. Mesot. Anisotropic breakdown of Fermi liquid quasiparticle excitations in overdoped $La_{2-x}Sr_xCuO_4$. Nat. Comm. 4 (2013)
78. S. Uchida, T. Ido, H. Takagi, T. Arima, Y. Tokura, S. Tajima, Optical spectra of $La_{2-x}Sr_xCuO_4$: effect of carrier doping on the electronic structure of the CuO_2 plane. Phys. Rev. B **43**(10), 7942 (1991)
79. T. Valla, A.V. Fedorov, P.D. Johnson, B.O. Wells, S.L. Hulbert, Q. Li, G.D. Gu, N. Koshizuka, Evidence for quantum critical behavior in the optimally doped cuprate $Bi_2Sr_2CaCu_2O_{8+\delta}$. Science **285**(5436), 2110–2113 (1999)
80. S. Sachdev, Where is the quantum critical point in the cuprate superconductors? Phys. Stat. Sol. (b) **247**(3), 537–543 (2010)
81. J.P. Falck, A. Levy, M.A. Kastner, R.J. Birgeneau, Charge-transfer spectrum and its temperature dependence in La_2CuO_4. Phys. Rev. Lett. **69**(7), 1109 (1992)
82. A.J. Millis, A. Zimmers, R.P.S.M. Lobo, N. Bontemps, C.C. Homes, Mott physics and the optical conductivity of electron-doped cuprates. Phys. Rev. B **72**(22), 224517 (2005)
83. N. Hussey, High-temperature superconductivity: isolating the gap. Nat. Phys. **12**(4), 290–291 (2016)
84. C. Weber, K. Haule, G. Kotliar, Strength of correlations in electron-and hole-doped cuprates. Nat. Phys. **6**(8), 574–578 (2010)
85. C. Weber, K. Haule, G. Kotliar, Apical oxygens and correlation strength in electron-and hole-doped copper oxides. Phys. Rev. B **82**(12), 125107 (2010)
86. K. McElroy, J. Lee, J.A. Slezak, D.-H. Lee, H. Eisaki, S. Uchida, J.C. Davis, Atomic-scale sources and mechanism of nanoscale electronic disorder in $Bi_2Sr_2CaCu_2O_{8+\delta}$. Science **309**(5737), 1048–1052 (2005)
87. D.J. Scalapino, E. Loh, J.E. Hirsch, d-Wave pairing near a spin-density-wave instability. Phys. Rev. B **34**, 8190–8192 (1986)
88. R. Haslinger, A.V. Chubukov, A. Abanov, Spectral function and conductivity in the normal state of the cuprates: a spin fluctuation study. Phys. Rev. B **63**, 020503 (2000)
89. C.M. Varma, P.B. Littlewood, S. Schmitt-Rink, E. Abrahams, A.E. Ruckenstein, Phenomenology of the normal state of Cu-O high-temperature superconductors. Phys. Rev. Lett. **63**, 1996–1999 (1989)
90. J.P. Carbotte, E. Schachinger, D.N. Basov, Coupling strength of charge carriers to spin fluctuations in high-temperature superconductors. Nature **401**(6751), 354–356 (1999)
91. S.V. Dordevic, C.C. Homes, J.J. Tu, T. Valla, M. Strongin, P.D. Johnson, G.D. Gu, D.N. Basov, Extracting the electron-boson spectral function $\alpha^2 F(\omega)$ from infrared and photoemission data using inverse theory. Phys. Rev. B **71**, 104529 (2005)
92. P.V. Bogdanov, A. Lanzara, S.A. Kellar, X.J. Zhou, E.D. Lu, W.J. Zheng, G. Gu, J.I. Shimoyama, K. Kishio, H. Ikeda, R. Yoshizaki, Z. Hussain, Z.X. Shen, Evidence for an energy scale for quasiparticle dispersion in $Bi_2Sr_2CaCu_2O_8$. Phys. Rev. Lett. **85**, 2581–2584 (2000)
93. A. Lanzara, P.V. Bogdanov, X.J. Zhou, S.A. Kellar, D.L. Feng, E.D. Lu, T. Yoshida, H. Eisaki, A. Fujimori, K. Kishio et al., Evidence for ubiquitous strong electron-phonon coupling in high-temperature superconductors. Nature **412**(6846), 510–514 (2001)
94. M.R. Norman, A.V. Chubukov, High-frequency behavior of the infrared conductivity of cuprates. Phys. Rev. B **73**, 140501 (2006)
95. P.W. Anderson, Is there glue in cuprate superconductors? Science **316**(5832), 1705–1707 (2007)
96. P. Phillips, Mottness. Ann. Phys. **321**(7), 1634–1650 (2006)
97. A.V. Boris, N.N. Kovaleva, O.V. Dolgov, T. Holden, C.T. Lin, B. Keimer, C. Bernhard, In-plane spectral weight shift of charge carriers in $YBa_2Cu_3O_{6.9}$. Science **304**(5671), 708–710 (2004)

98. T.D. Stanescu, P. Phillips, Pseudogap in doped mott insulators is the near-neighbor analogue of the Mott gap. Phys. Rev. Lett. **91**(1), 017002 (2003)
99. F. Carbone, A.B. Kuzmenko, H.J. Molegraaf, E. Van Heumen, V. Lukovac, F. Marsiglio, D. van der Marel, K. Haule, G. Kotliar, H. Berger, Doping dependence of the redistribution of optical spectral weight in $Bi_2Sr_2CaCu_2O_{8+\delta}$. Phys. Rev. B **74**(6), 064510 (2006)
100. M. Rübhausen, A. Gozar, M.V. Klein, P. Guptasarma, D.G. Hinks, Superconductivity-induced optical changes for energies of 100δ in the cuprates. Phys. Rev. B **63**(22), 224514 (2001)
101. J. Bäckström, D. Budelmann, R. Rauer, M. Rübhausen, H. Rodriguez, H. Adrian, Optical properties of $YBa_2Cu_3O_{7-\delta}$ and $PrBa_2Cu_3O_{7-\delta}$ films: high-energy correlations and metallicity. Phys. Rev. B **70**(17), 174502 (2004)
102. M. Tinkham. *Introduction to Superconductivity: (Dover Books on Physics)*, vol. I (2004)
103. A.J. Leggett, Where is the energy saved in cuprate superconductivity? J. Phys. Chem. Solids **59**(10), 1729–1732 (1998)
104. A.J. Leggett, A midinfrared scenario for cuprate superconductivity. Proc. Natl. Acad. Sci. **96**(15), 8365–8372 (1999)
105. A.J. Leggett, Cuprate superconductivity: dependence of T_C on the c-axis layering structure. Phys. Rev. Lett. **83**(2), 392 (1999)
106. J. Levallois, M.K. Tran, D. Pouliot, C.N. Presura, L.H. Greene, J.N. Eckstein, J. Uccelli, E. Giannini, G.D. Gu, A.J. Leggett, D. van der Marel, Temperature-dependent ellipsometry measurements of partial Coulomb energy in superconducting cuprates. Phys. Rev. X **6**, 031027 (2016)
107. N.N. Bogoliubov, V.V. Tolmachev, D.V. Shirkov, A new method in the theory of superconductivity, in *Academy of Sciences of the USSR* (1958)
108. B. Mansart, J. Lorenzana, A. Mann, A. Odeh, M. Scarongella, M. Chergui, F. Carbone, Coupling of a high-energy excitation to superconducting quasiparticles in a cuprate from coherent charge fluctuation spectroscopy. Proc. Natl. Acad. Sci. **110**(12), 4539–4544 (2013)
109. J. Lorenzana, B. Mansart, A. Mann, A. Odeh, M. Chergui, F. Carbone, Investigating pairing interactions with coherent charge fluctuation spectroscopy. Eur. Phys. J. Spec. Top. **222**(5), 1223–1239 (2013)
110. R.A. Kaindl, M. Woerner, T. Elsaesser, D.C. Smith, J.F. Ryan, G.A. Farnan, M.P. McCurry, D.G. Walmsley, Ultrafast mid-infrared response of $YBa_2Cu_3O_{7-\delta}$. Science **287**(5452), 470–473 (2000)
111. A. Pashkin, M. Porer, M. Beyer, Kyung W. Kim, A. Dubroka, C. Bernhard, X. Yao, Y. Dagan, R. Hackl, A. Erb, J. Demsar, Femtosecond response of quasiparticles and phonons in superconducting $YBa_2Cu_3O_{7-\delta}$ studied by wideband terahertz spectroscopy. Phys. Rev. Lett. **105**(6), 067001 (2010)
112. D. Khomskii, *Transition Metal Compounds* (Cambridge University Press, 2014)
113. Y. Tokura, N. Nagaosa, Orbital physics in transition-metal oxides. Science **288**(5465), 462–468 (2000)
114. N.N. Kovaleva, A.V. Boris, C. Bernhard, A. Kulakov, A. Pimenov, A.M. Balbashov, G. Khaliullin, B. Keimer, Spin-controlled Mott-Hubbard bands in $LaMnO_3$ probed by optical ellipsometry. Phys. Rev. Lett. **93**(14), 147204 (2004)
115. A.S. Moskvin, A.A. Makhnev, L.V. Nomerovannaya, N.N. Loshkareva, A.M. Balbashov, Interplay of p-d and d-d charge transfer transitions in rare-earth perovskite manganites. Phys. Rev. B **82**(3), 035106 (2010)
116. J. Zaanen, G.A. Sawatzky, J.W. Allen, Band gaps and electronic structure of transition-metal compounds. Phys. Rev. Lett. **55**(4), 418 (1985)
117. J.F. Lawler, J.G. Lunney, J.M.D. Coey, Magneto-optic Faraday effect in $(La_{1-x}Ca_x)MnO_3$ films. Appl. Phys. Lett. **65**(23), 3017–3018 (1994)
118. N.N. Kovaleva, K.I. Kugel, Z. Potůček, O.E. Kusmartseva, N.S. Goryachev, Z. Bryknar, E.I. Demikhov, V.A. Trepakov, A. Dejneka, F.V. Kusmartsev, A.M. Stoneham, Optical evidence of quantum rotor orbital excitations in orthorhombic manganites. J. Exp. Theor. Phys. **122**(5), 890–901 (2016)

119. T. Kimura, S. Ishihara, H. Shintani, T. Arima, K.T. Takahashi, K. Ishizaka, Y. Tokura, Distorted perovskite with e_g^1 configuration as a frustrated spin system. Phys. Rev. B **68**(6), 060403 (2003)
120. T. Kimura, T. Goto, H. Shintani, K. Ishizaka, T. Arima, Y. Tokura, Magnetic control of ferroelectric polarization. Nature **426**(6962), 55–58 (2003)
121. T. Goto, T. Kimura, G. Lawes, A.P. Ramirez, Y. Tokura, Ferroelectricity and giant magnetocapacitance in perovskite rare-earth manganites. Phys. Rev. Lett. **92**(25), 257201 (2004)
122. M. Kenzelmann, A.B. Harris, S. Jonas, C. Broholm, J. Schefer, S.B. Kim, C.L. Zhang, S.-W. Cheong, O.P. Vajk, J.W. Lynn, Magnetic inversion symmetry breaking and ferroelectricity in $TbMnO_3$. Phys. Rev. Lett. **95**(8), 087206 (2005)
123. A.B. Sushkov, R. Valdés Aguilar, S. Park, S-W. Cheong, H.D. Drew. Electromagnons in multiferroic YMn_2O_5 and $TbMn_2O_5$. Phys. Rev. Lett. **98**, 027202 (2007)
124. Y. Takahashi, N. Kida, Y. Yamasaki, J. Fujioka, T. Arima, R. Shimano, S. Miyahara, M. Mochizuki, N. Furukawa, Y. Tokura, Evidence for an electric-dipole active continuum band of spin excitations in multiferroic $TbMnO_3$. Phys. Rev. Lett. **101**, 187201 (2008)
125. A. Pimenov, A.A. Mukhin, V.Y. Ivanov, V.D. Travkin, A.M. Balbashov, A. Loidl, Possible evidence for electromagnons in multiferroic manganites. Nat. Phys. **2**(2), 97–100 (2006)
126. P. Rovillain, M. Cazayous, Y. Gallais, A. Sacuto, M.-A. Measson, H. Sakata, Magnetoelectric excitations in multiferroic $TbMnO_3$ by Raman scattering. Phys. Rev. B **81**, 054428 (2010)
127. P. Rovillain, J. Liu, M. Cazayous, Y. Gallais, M.-A. Measson, H. Sakata, A. Sacuto, Electromagnon and phonon excitations in multiferroic $TbMnO_3$. Phys. Rev. B **86**, 014437 (2012)
128. D. Polli, M. Rini, S. Wall, R.W. Schoenlein, Y. Tomioka, Y. Tokura, G. Cerullo, A. Cavalleri, Coherent orbital waves in the photo-induced insulator-metal dynamics of a magnetoresistive manganite. Nat. Mat. **6**(9), 643–647 (2007)
129. S. Wall, D. Prabhakaran, A.T. Boothroyd, A. Cavalleri, Ultrafast coupling between light, coherent lattice vibrations, and the magnetic structure of semicovalent $LaMnO_3$. Phys. Rev. Lett. **103**(9), 097402 (2009)
130. I.P. Handayani, R.I. Tobey, J. Janusonis, D.A. Mazurenko, N. Mufti, A.A. Nugroho, M.O. Tjia, T.T.M. Palstra, P.H.M. van Loosdrecht, Dynamics of photo-excited electrons in magnetically ordered $TbMnO_3$. J. Phys-Condens. Mat. **25**(11), 116007 (2013)
131. P. Beaud, A. Caviezel, S.O. Mariager, L. Rettig, G. Ingold, C. Dornes, S.W. Huang, J.A. Johnson, M. Radovic, T. Huber et al., A time-dependent order parameter for ultrafast photoinduced phase transitions. Nat. Mat. **13**(10), 923–927 (2014)
132. J.A. Johnson, T. Kubacka, M.C. Hoffmann, C. Vicario, S. de Jong, P. Beaud, S. Grübel, S.-W. Huang, L. Huber, Y.W. Windsor, E.M. Bothschafter, L. Rettig, M. Ramakrishnan, A. Alberca, L. Patthey, Y.-D. Chuang, J.J. Turner, G.L. Dakovski, W.-S. Lee, M.P. Minitti, W. Schlotter, R.G. Moore, C.P. Hauri, S.M. Koohpayeh, V. Scagnoli, G. Ingold, S.L. Johnson, U. Staub, Magnetic order dynamics in optically excited multiferroic $TbMnO_3$. Phys. Rev. B **92**, 184429 (2015)
133. T. Ogasawara, T. Kimura, T. Ishikawa, M. Kuwata-Gonokami, Y. Tokura, Dynamics of photoinduced melting of charge/orbital order in a layered manganite $La_{0.5}Sr_{1.5}MnO_4$. Phys. Rev. B **63**(11), 113105 (2001)
134. M. Matsubara, Y. Okimoto, T. Ogasawara, Y. Tomioka, H. Okamoto, Y. Tokura, Ultrafast photoinduced insulator-ferromagnet transition in the perovskite manganite $Gd_{0.55}Sr_{0.45}MnO_3$. Phys. Rev. Lett. **99**, 207401 (2007)
135. P. Beaud, S.L. Johnson, E. Vorobeva, U. Staub, R.A. De Souza, C.J. Milne, Q.X. Jia, G. Ingold, Ultrafast structural phase transition driven by photoinduced melting of charge and orbital order. Phys. Rev. Lett. **103**(15), 155702 (2009)
136. K.B. Tolpygo, Physical properties of the salt lattice constructed from deforming ions. J. Exp. Theor. Phys. (USSR) **20**(6), 497–509 (1950)
137. S. Savasta, O. Di Stefano, V. Savona, W. Langbein, Quantum complementarity of microcavity polaritons. Phys. Rev. Lett. **94**(24), 246401 (2005)
138. T.C.H. Liew, V. Savona, Single photons from coupled quantum modes. Phys. Rev. Lett. **104**(18), 183601 (2010)

139. K.G. Lagoudakis, F. Manni, B. Pietka, M. Wouters, T.C.H. Liew, V. Savona, A.V. Kavokin, R. André, B. Deveaud-Plédran, Probing the dynamics of spontaneous quantum vortices in polariton superfluids. Phys. Rev. Lett. **106**(11), 115301 (2011)
140. P.W. Anderson, More is different. Science **177**(4047), 393–396 (1972)
141. Z. Fei, A.S. Rodin, G.O. Andreev, W. Bao, A.S. McLeod, M. Wagner, L.M. Zhang, Z. Zhao, M. Thiemens, G. Dominguez, M.M. Fogler, A.H. Castro Neto, C.N. Lau, F. Keilmann, D.N. Basov, D.N. Basov, Gate-tuning of graphene plasmons revealed by infrared nano-imaging. Nature **487**(7405), 82–85 (2012)
142. P. Abbamonte, T. Graber, J.P. Reed, S. Smadici, C.-L. Yeh, A. Shukla, J.-P. Rueff, W. Ku, Dynamical reconstruction of the exciton in LiF with inelastic x-ray scattering. Proc. Natl. Acad. Sci. **105**(34), 12159–12163 (2008)
143. M. Först, C. Manzoni, S. Kaiser, Y. Tomioka, Y. Tokura, R. Merlin, A. Cavalleri, Nonlinear phononics as an ultrafast route to lattice control. Nat. Phys. **7**(11), 854–856 (2011)
144. X. Zhang, T. Liu, M.E. Flatté, H.X. Tang, Electric-field coupling to spin waves in a centrosymmetric ferrite. Phys. Rev. Lett. **113**, 037202 (2014)
145. S.A. Maier. *Plasmonics: Fundamentals and Applications* (Springer Science & Business Media, 2007)
146. R.H. Ritchie, Plasma losses by fast electrons in thin films. Phys. Rev. **106**(5), 874 (1957)
147. B. Liedberg, C. Nylander, I. Lunström, Surface plasmon resonance for gas detection and biosensing. Sens. Act. **4**, 299–304 (1983)
148. S.K. Saikin, A. Eisfeld, S. Valleau, A. Aspuru-Guzik, Photonics meets excitonics: natural and artificial molecular aggregates. Nanophotonics **2**(1), 21–38 (2013)
149. M. Först, R.I. Tobey, S. Wall, H. Bromberger, V. Khanna, A.L. Cavalieri, Y.-D. Chuang, W.S. Lee, R. Moore, W.F. Schlotter, J.J. Turner, O. Krupin, M. Trigo, H. Zheng, J.F. Mitchell, S.S. Dhesi, J.P. Hill, A. Cavalleri, Driving magnetic order in a manganite by ultrafast lattice excitation. Phys. Rev. B **84**, 241104 (2011)
150. V.V. Kruglyak, S.O. Demokritov, D. Grundler, Magnonics. J. Phys. D Appl. Phys. **43**(26), 264001 (2010)
151. T. Feurer, N.S. Stoyanov, D.W. Ward, J.C. Vaughan, E.R. Statz, K.A. Nelson, Terahertz polaritonics. Annu. Rev. Mater. Res. **37**, 317–350 (2007)
152. E. Saitoh, S. Okamoto, K.T. Takahashi, K. Tobe, K. Yamamoto, T. Kimura, S. Ishihara, S. Maekawa, Y. Tokura, Observation of orbital waves as elementary excitations in a solid. Nature **410**(6825), 180–183 (2001)
153. Y. Nambu, G. Jona-Lasinio, Dynamical model of elementary particles based on an analogy with superconductivity. I. Phys. Rev. **122**(1), 345 (1961)
154. W.L. McMillan, Theory of discommensurations and the commensurate-incommensurate charge-density-wave phase transition. Phys. Rev. B **14**(4), 1496 (1976)
155. P.W. Anderson, Plasmons, gauge invariance, and mass. Phys. Rev. **130**, 439–442 (1963)
156. P.W. Higgs, Broken symmetries and the masses of gauge bosons. Phys. Rev. Lett. **13**(16), 508 (1964)
157. A.J. Leggett, Number-phase fluctuations in two-band superconductors. Prog. Theor. Phys. **36**(5), 901–930 (1966)
158. D. Pines, D. Bohm, A collective description of electron interactions: II. Collective vs individual particle aspects of the interactions. Phys. Rev. **85**(2), 338 (1952)
159. D. van der Marel, A. Tsvetkov, Transverse optical plasmons in layered superconductors. Czech J. Phys. **46**(6), 3165–3168 (1996)
160. W. Hayes, R. Loudon, *Scattering of Light by Crystals* (Courier Corporation, 2012)
161. S. Galambosi, J.A. Soininen, A. Mattila, S. Huotari, S. Manninen, G. Vankó, N.D. Zhigadlo, J. Karpinski, K. Hämäläinen, Inelastic x-ray scattering study of collective electron excitations in MgB_2. Phys. Rev. B **71**(6), 060504 (2005)
162. M. Dressel, G. Grüner, *Electrodynamics of Solids: Optical Properties of Electrons in Matter* (Cambridge University Press, 2002)
163. Y. U. Peter and M. Cardona. *Fundamentals of Semiconductors: Physics and Materials Properties* (Springer Science & Business Media, 2010)

164. L.D. Landau, On the vibrations of the electronic plasma. Zh. Eksp. Teor. Fiz. **10**, 25 (1946)
165. A. Toschi, M. Capone, M. Ortolani, P. Calvani, S. Lupi, C. Castellani, Temperature dependence of the optical spectral weight in the cuprates: role of electron correlations. Phys. Rev. Lett. **95**, 097002 (2005)
166. D. Nicoletti, O. Limaj, P. Calvani, G. Rohringer, A. Toschi, G. Sangiovanni, M. Capone, K. Held, S. Ono, Y. Ando, S. Lupi, High-temperature optical spectral weight and Fermi-liquid renormalization in bi-based cuprate superconductors. Phys. Rev. Lett. **105**, 077002 (2010)
167. E. van Heumen, R. Lortz, A.B. Kuzmenko, F. Carbone, D. van der Marel, X. Zhao, G. Yu, Y. Cho, N. Barisic, M. Greven, C.C. Homes, S.V. Dordevic, Optical and thermodynamic properties of the high-temperature superconductor $HgBa_2CuO_{4+\delta}$. Phys. Rev. B **75**, 054522 (2007)
168. L. Ortenzi, E. Cappelluti, L. Benfatto, L. Pietronero, Fermi-surface shrinking and interband coupling in iron-based pnictides. Phys. Rev. Lett. **103**, 046404 (2009)
169. L. Benfatto, E. Cappelluti, Effects of the Fermi-surface shrinking on the optical sum rule in pnictides. Phys. Rev. B **83**, 104516 (2011)
170. X.-Y. Zhu, Q. Yang, M. Muntwiler, Charge-transfer excitons at organic semiconductor surfaces and interfaces. Acc. Chem. Res. **42**(11), 1779–1787 (2009)
171. D.S. Ellis, J.P. Hill, S. Wakimoto, R.J. Birgeneau, D. Casa, T. Gog, Y.-J. Kim, Charge-transfer exciton in La_2CuO_4 probed with resonant inelastic x-ray scattering. Phys. Rev. B **77**(6), 060501 (2008)
172. E. Collart, A. Shukla, J.P. Rueff, P. Leininger, H. Ishii, I. Jarrige, Y.Q. Cai, S.-W. Cheong, G. Dhalenne, Localized and delocalized excitons: resonant inelastic x-ray scattering in $La_{2-x}Sr_xNiO_4$ and $La_{2-x}Sr_xCuO_4$. Phys. Rev. Lett. **96**(15), 157004 (2006)
173. E.E. Salpeter, H.A. Bethe, A relativistic equation for bound-state problems. Phys. Rev. **84**(6), 1232 (1951)
174. L.I. Bendavid, E.A. Carter, Status in calculating electronic excited states in transition metal oxides from first principles. in *First Principles Approaches to Spectroscopic Properties of Complex Materials* (Springer, 2014), pp. 47–98
175. H. Haug, S. Schmitt-Rink, Basic mechanisms of the optical nonlinearities of semiconductors near the band edge. JOSA B **2**(7), 1135–1142 (1985)
176. S. Schmitt-Rink, D.S. Chemla, D.A.B. Miller, Linear and nonlinear optical properties of semiconductor quantum wells. Adv. Phys. **38**(2), 89–188 (1989)
177. J.T. Devreese, S.N. Klimin, J.L.M. van Mechelen, D. van der Marel, Many-body large polaron optical conductivity in $SrTi_{1-x}Nb_xO_3$. Phys. Rev. B **81**(12), 125119 (2010)
178. M. Rössle, C.N. Wang, P. Marsik, M. Yazdi-Rizi, K.W. Kim, A. Dubroka, I. Marozau, C.W. Schneider, J. Humlíček, D. Baeriswyl, Optical probe of ferroelectric order in bulk and thin-film perovskite titanates. Phys. Rev. B **88**(10), 104110 (2013)
179. Y.P. Varshni, Temperature dependence of the energy gap in semiconductors. Physica **34**(1), 149–154 (1967)
180. C. Keffer, T.M. Hayes, A. Bienenstock, PbTe Debye-Waller factors and band-gap temperature dependence. Phys. Rev. Lett. **21**(25), 1676 (1968)
181. L. Yu, D. Munzar, A.V. Boris, P. Yordanov, J. Chaloupka, T. Wolf, C.T. Lin, B. Keimer, C. Bernhard, Evidence for two separate energy gaps in underdoped high-temperature cuprate superconductors from broadband infrared ellipsometry. Phys. Rev. Lett. **100**(17), 177004 (2008)
182. I. Bloch, J. Dalibard, W. Zwerger, Many-body physics with ultracold gases. Rev. Mod. Phys. **80**(3), 885 (2008)
183. M. Endres, T. Fukuhara, D. Pekker, M. Cheneau, P. Schauss, C. Gross, E. Demler, S. Kuhr, I. Bloch, The Higgs amplitude mode at the two-dimensional superfluid/Mott insulator transition. Nature **487**(7408), 454–458 (2012)
184. C.A.D. Roeser, M. Kandyla, A. Mendioroz, E. Mazur, Optical control of coherent lattice vibrations in tellurium. Phys. Rev. B **70**(21), 212302 (2004)
185. D. Mihailovic, D. Dvorsek, V.V. Kabanov, J. Demsar, L. Forró, H. Berger, Femtosecond data storage, processing, and search using collective excitations of a macroscopic quantum state. Appl. Phys. Lett. **80**(5), 871–873 (2002)

186. D. Fausti, R.I. Tobey, N. Dean, S. Kaiser, A. Dienst, M.C. Hoffmann, S. Pyon, T. Takayama, H. Takagi, A. Cavalleri, Light-induced superconductivity in a stripe-ordered cuprate. Science **331**(6014), 189–191 (2011)
187. W. Hu, S. Kaiser, D. Nicoletti, C.R Hunt, I.a Gierz, M.C. Hoffmann, M. Le Tacon, T. Loew, B. Keimer, A. Cavalleri. Optically enhanced coherent transport in $YBa_2Cu_3O_{6.5}$ by ultrafast redistribution of interlayer coupling. Nat. Mat., 13(7):705–711 (2014)
188. R. Mankowsky, A. Subedi, M. Först, S.O. Mariager, M. Chollet, H.T. Lemke, J.S. Robinson, J.M. Glownia, M.P. Minitti, A. Frano et al., Nonlinear lattice dynamics as a basis for enhanced superconductivity in $YBa_2Cu_3O_{6.5}$. Nature **516**(7529), 71–73 (2014)
189. M. Rini, N. Dean, J. Itatani, Y. Tomioka, Y. Tokura, R.W. Schoenlein, A. Cavalleri, Control of the electronic phase of a manganite by mode-selective vibrational excitation. Nature **449**(7158), 72–74 (2007)
190. R.I. Tobey, D. Prabhakaran, A.T. Boothroyd, A. Cavalleri, Ultrafast electronic phase transition in $La_{1/2}Sr_{3/2}MnO_4$ by coherent vibrational excitation: evidence for nonthermal melting of orbital order. Phys. Rev. Lett. **101**(19), 197404 (2008)
191. A. Subedi, A. Cavalleri, A. Georges, Theory of nonlinear phononics for coherent light control of solids. Phys. Rev. B **89**(22), 220301 (2014)
192. A. Dienst, E. Casandruc, D. Fausti, L. Zhang, M. Eckstein, M. Hoffmann, V. Khanna, N. Dean, M. Gensch, S. Winnerl et al., Optical excitation of Josephson plasma solitons in a cuprate superconductor. Nat. Mat. **12**(6), 535–541 (2013)
193. T. Kubacka, J.A. Johnson, M.C. Hoffmann, C. Vicario, S. De Jong, P. Beaud, S. Grübel, S.-W. Huang, L. Huber, L. Patthey et al., Large-amplitude spin dynamics driven by a THz pulse in resonance with an electromagnon. Science **343**(6177), 1333–1336 (2014)

Chapter 2
Equilibrium and Nonequilibrium Spectroscopy of Condensed Matter

In Chap. 1, we observed that understanding the excitation spectrum of a solid allows to reveal the elusive GS properties of the solid itself. Within this framework, the field of spectroscopy holds a huge promise for the future of condensed matter physics. Spectroscopy deals with the study of the interaction between matter and a specific source of radiative energy (e.g. the electromagnetic radiation, other particles like electrons and neutrons, acoustic vibrations, mechanical stress...). Over the last fifty years, the development of advanced spectroscopic techniques aimed at probing the excitation spectrum of solids has rapidly improved the approach of physicists to investigate the behaviour of condensed matter systems. Nowadays, it has become clear that there exists no unique method for unveiling the hidden physical properties of a complex solid. Only the combination of various techniques can indeed generate a detailed description of the quantum processes occurring in a material. The synergy among the different methods has become extremely beneficial also to theory, as the validity of the theoretical models can be tested by computing a broad class of observables that are accessible from a variety of experiments.

For these reasons, in Sect. 2.1, we provide a survey of the experimental techniques commonly used for probing the equilibrium (or steady-state) properties of condensed matter systems. The purpose of this survey is twofold: (i) Highlight that different probes access distinct observables and manifestations of the GS properties of the system; (ii) Set the basis for the extension of the steady-state techniques to their nonequilibrium counterparts. Indeed, one of the current frontiers of condensed matter research involves the development of novel spectroscopic techniques to reveal subtle details that have remained undetected from the application of previous experimental probes. In this regard, ultrafast spectroscopies hold great potential, due to their intrinsic ability of addressing the interplay between different electronic and structural excitations on the basis of their temporal response. While in Sect. 2.2 we offer a broad overview on the different classes of ultrafast techniques, in Sect. 2.3 we devote particular attention to the field of ultrafast optical spectroscopy, which is the main experimental method explored in the framework of this Thesis. After providing a complete description of the processes monitored by this technique, in Sects. 2.4

E. Baldini, *Nonequilibrium Dynamics of Collective Excitations in Quantum Materials*,
Springer Theses, https://doi.org/10.1007/978-3-319-77498-5_2

and 2.5 we describe the technical details of the two experimental setups that have been used for performing the measurements described in the following Chapters.

2.1 Experimental Probes of Elementary Excitations

The aim of equilibrium spectroscopies in solids is to explore, map and interpret the spectrum of the elementary excitations with high energy and momentum resolution. In this regard, it is instructive to illustrate the taxonomy of the main excitations characterizing a complex solid, which is indicated by the schematic cartoon of the energy- and momentum-dependent density of states (DOS) in Fig. 2.1. Besides the low-energy single-particle excitations in metals (not shown), which give rise to a well-defined Fermi surface and to low-energy fermionic bands, phonons and magnons dominate the excitation spectrum up to ∼250 meV and possess a characteristic dispersion that depends on their nature. At intermediate energies, one observes the emergence of on-site electronic transitions within the *d* orbitals of transition metal ions (*d d* transitions), CT excitations, and excitations across the Mott gap, which display reduced dispersions because of their localized nature. Finally, at higher energy (up to ∼1 keV), the characteristic excitations are the dispersionless core-valence transitions. Depending on its nature (fermionic vs. bosonic), symmetry and energy, a particular excitation in the solid can be mapped more precisely using a specific experimental technique. Moreover, not all experimental methods are capable of accessing the energy-momentum dispersion relation of the excitations, imposing a limitation in the amount of information that can be extracted.

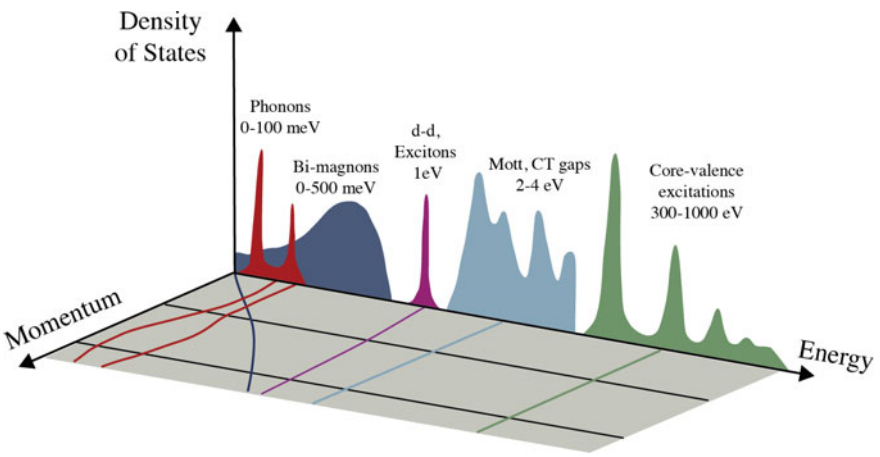

Fig. 2.1 Energy-momentum dispersion relation of the main elementary excitations in complex solids, which can be probed by spectroscopic methods

In this Section, we review the working principles behind some of the established spectroscopic probes of condensed matter systems under equilibrium conditions, putting emphasis on the observables that can be accessed and making a link with the taxonomy described in Fig. 2.1. In this survey, we do not include the experimental techniques aimed at the investigation of the structural and morphological properties of materials, as they are out of the scope of this Thesis.

The fundamental properties of a solid depend on its low-energy electronic structure, i.e. on the details of the energy-momentum dispersion relation of the fermionic particles. Key experimental tools for the study of the electronic structure are angle-resolved photoemission spectroscopy (ARPES) and acanning tunneling spectroscopy/microscopy (STS/STM). ARPES records the photoemission intensity of electrons residing in the filled states of the material at a specific energy and momentum, thus allowing for a detailed mapping of the band dispersion, the Fermi surface and many-body correlations [1]. In contrast, STS/STM measures the tunneling current, differential conductance, or the height at a specific position, providing information on both filled and empty states [2]. These two experimental techniques offer complementary information on the single-particle excitation spectrum of the material, i.e. the spectrum of the fundamental charged excitations. ARPES does not provide a high spatial resolution, since the beam illuminating the sample has a typical spot size ranging from tens to hundreds of micrometers, leading to spatially mixed and averaged values. In contrast, STS/STM possesses a spatial resolution on the sub-nm length-scale, thus offering local information and probing the real-space emergence of inhomogeneous electronic states. As a result, STM and ARPES provide high spatial and momentum resolution in the measurement of a material electronic structure, respectively. The main limitation of these techniques is related to their extreme surface sensitivity, which often prevents them from retrieving the electronic properties of the bulk. Despite this weakness, it is widely accepted that ARPES and STS/STM represent superior techniques for probing the "Fermiology" of quantum systems, which can be directly compared to the results of ab initio electronic structure calculations. On the contrary, these techniques are not suitable for accessing the bosonic excitations of a solid, as they manifest only indirectly via the renormalization of the electronic structure [3–5].

Another sensitive probe of the electronic structure is optical spectroscopy, which is performed in the energy region from 1 meV to 10 eV [6]. This method allows obtaining the two-particle excitation spectrum of the material, i.e. the spectrum of the neutral excitations of the solid, thus revealing the absorption/emission processes related to various excitations and collective modes. Indeed, besides measuring the intraband and interband transitions, optical spectroscopy also unveils the signature of dipole-allowed transverse collective excitations at $\mathbf{q} = 0$, like infrared-active phonons, plasmons, magnons and excitons. However, it probes only a limited subset of collective modes (depending on their symmetry) and cannot access their energy-momentum dispersion relation. The extension of absorption and emission spectroscopies to the soft- and hard x-ray regimes provides additional information on the unoccupied DOS and on the local structure of a material.

Complementary probes of collective modes are therefore needed. An alternative and very powerful approach to map the collective excitations relies on performing inelastic photon-, electron- or neutron-scattering experiments, like spontaneous Raman scattering, RIXS, EELS and inelastic neutron scattering (INS). Each one of these techniques possesses its own strengths and drawbacks. Spontaneous Raman scattering gives access to the Raman-active excitations of the solid, providing insights into their energy, lifetime and symmetry. As the scattered radiation lies in the visible/near-infrared range, in first order the excitations can be mapped only close to the Γ point of the BZ. Higher-order spontaneous Raman scattering processes extend this framework to all modes in the BZ, provided that the simultaneous creation of excitations is constrained by momentum conservation. Despite its limitations, spontaneous Raman scattering has established as one of the primary sources of characterization of solids, since it is relatively simple and can be performed under varying experimental conditions (temperature, pressure, magnetic field). Using this technique, Raman-active phonons, (bi)-magnons, orbitons, excitons and longitudinal plasmons have been widely studied [7]. IXS or its resonant version (RIXS) extends the class of observables probed by spontaneous Raman scattering by using a photon wavelength of the order of the material lattice constant. In this way, the dispersion of the elementary excitations can be accessed and the symmetry of such excitations evaluated by performing a detailed polarization dependence [8]. The cross-section of the IXS process is especially high at large momenta. Detailed knowledge on the intermediate $\mathbf{q}$'s regime is offered instead by EELS, which is a very sensitive probe of the momentum-dependent material loss function from low-energies up to the core-levels [9]. Its main drawback is associated with the sample preparation, as EELS requires a transmission electron microscope (TEM) to be implemented and can measure only carefully-prepared thin specimens. INS is a superior technique for mapping the energy-momentum dispersion relation of lattice- and magnetic collective modes over the whole BZ, but, contrary to the previous techniques, it typically requires the use of large single crystals, posing a limitation to the range of solids that can be probed.

From this survey, it becomes evident that the different strengths of the established spectroscopies can successfully provide a unified picture of the equilibrium microscopic properties of complex solids. Despite the wealth of information that can be extracted, these experiments offer only a time-averaged picture of the underlying mechanisms governing the physics of these materials. As a consequence, the separation of the contributions related to the different degrees of freedom is a challenge. This aspect becomes particularly limiting in the study of strong interactions and correlations, as the material properties often result from the coexistence or the competition between different exotic phases of matter. Even in the presence of a single electronic phase, the interplay between the charge, spin, orbital and lattice degrees of freedom gives rise to intricate excitation spectra. The same interplay also leads to the emergence of a number of collective bosonic modes, which play a crucial role in the charge transport by scattering or dressing the fermionic particles.

2.2 Ultrafast Techniques

In the previous Section, we concluded that the complexity behind strongly correlated electron systems calls for experimental methods that are able to disentangle the contributions of the different degrees of freedom. In the last decades, this task has been accomplished by the so-called ultrafast spectroscopies, which have become a reality thanks to recent advances in femtosecond laser technology. Nowadays, ultrafast spectroscopy serves as an effective tool for unravelling the many-body dynamics of atoms, molecules and solids, since the dynamical evolution of a system can be followed with a temporal resolution comparable to the timescale of relevant microscopic processes.

The main idea behind such a nonequilibrium approach is to excited a system using a pump pulse and subsequently monitor the coupling between different electronic and structural excitations with a variety of probes. The pump pulse is typically an ultrashort laser pulse, whose photon energy can be tuned either to optical frequencies or to the FIR/THz range. The probe can be either an ultrashort pulse of photons (covering a specific spectral region from the THz to the x-rays) or an ultrashort packet of electrons. This method allows one to track a variety of observables, like the single-particle spectral function (via time-resolved ARPES), the two-particle spectral function (via time-resolved optical spectroscopy), the diffraction pattern (via time-resolved x-ray or electron diffraction), the inelastic scattering of photons or electrons (via time-resolved Raman, RIXS or EELS) or the real-space image of a material (via time-resolved STM and TEM). In other words, depending on the specific phenomenon that has to be probed, direct insight into the chemistry and structure of materials can now be achieved via spectroscopy or diffraction with a sub-picosecond time resolution (Fig. 2.2).

From the discussion above, it becomes evident that ultrafast spectroscopy is able to capture the properties of a given system only in its nonequilibrium state. On one hand, this represents a strongly limiting factor when these techniques are applied on strongly correlated quantum systems, as a complete theoretical framework describing the material properties is already lacking at equilibrium. Hence, it becomes extremely challenging to predict the pathways followed by a complex material upon interaction with the pump pulse. On the other hand, ultrafast spectroscopy holds huge promise when the excitation is carefully prepared and a specific observable of the system is monitored with a suitable probe. Strongly correlated quantum systems are particularly sensitive to the application of external stimuli, making them the perfect candidates in which to discover hidden phases of matter or to implement exotic states. At the same time, the use of tailored pulses is being explored as a fertile route towards the light-induced control and manipulation of the order parameter in these materials. Among the most relevant results recently obtained within the context of light-induced phase transitions, we can cite the realization of the metal-insulator transition in Mott insulators [15, 16], the weakening [17] or the possible enhancement [18–20] of superconductivity in the cuprates or in organics and the melting of charge, orbital or spin order in the manganites [21–23]. The extension of these concepts to

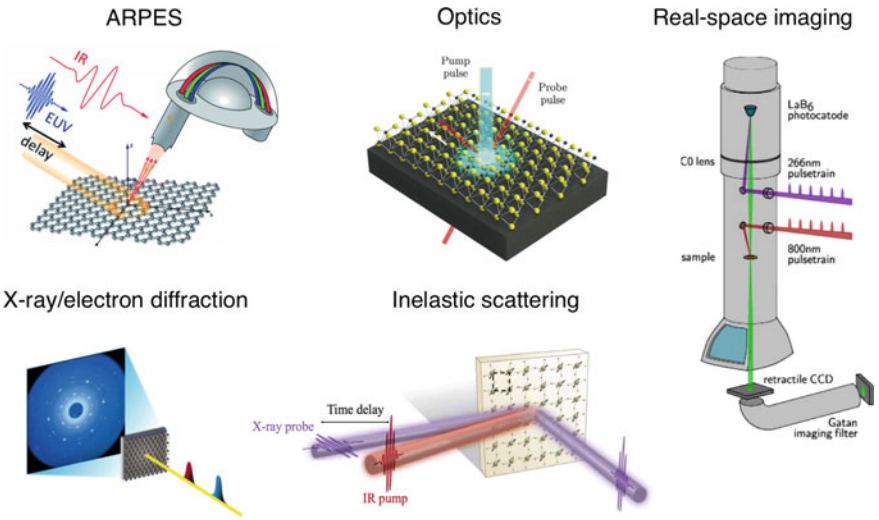

Fig. 2.2 Schematic representations of different ultrafast techniques. In all the figures the photoexcitation is provided by a near-infrared pump pulse. In trARPES, the probe is an extreme UV pulse that photo-ejects the electrons in the solid. In ultrafast optics the probe is an optical pulse that probes the variation in the dielectric properties of the material. In x-ray/electron diffraction, the probe is an ultrashort packet of electrons or x-ray photons that is elastically scattered by the material and records its diffraction pattern. In inelastic scattering, the probe is an ultrashort packet of electrons/visible/x-ray photons that is inelastically scattered by the material and records the spectrum of elementary excitations. In time-resolved TEM, the probe is an ultrashort packet of electrons travelling in the TEM column and producing real-space images of the sample. The figure has been adapted from [10–14]

the field of topological matter is also attracting increasing interest, due to its potential in the creation of novel topological phases under nonequilibrium conditions and in the manipulation of the material properties for opto-spintronic applications [24, 25].

2.3 Ultrafast Optical Spectroscopy

In Chap. 1, it was concluded that one of the distinctive characteristics of strongly interacting and correlated quantum systems is the non-trivial interplay between low- and high-energy degrees of freedom. The origin of this interplay lies in the electron-electron and electron-boson interactions, which spread the optical SW as a function of temperature over a wide energy range and create complex excitations and satellites extending up to a few eV. Prominent examples of high-energy excitations include excitons, *d*-*d* transitions, Mott and CT gaps or the characteristic spectral signatures of polaronic carriers. Addressing such a phenomenology is a challenge for experimental probes. Potentially, one needs a technique that can reveal the temporal hierarchy of

phenomena occurring in the material and simultaneously monitor the low- (meV) and high-energy (eV) scales with a temporal resolution of tens of femtoseconds.

A powerful method that fulfills the above-mentioned requirements is represented by ultrafast broadband optical spectroscopy. The underlying idea behind this technique is to illuminate a material with an ultrashort laser pulse and subsequently monitor the changes in the material optical properties with a delayed continuum probe, covering a broad spectral region in the visible or in the UV (Fig. 2.3). This approach possesses a number of advantages over other steady-state and ultrafast techniques. First, it allows monitoring the renormalization of the high-energy spectrum of the material under study, which depends on the dynamics of all the low-energy particle-hole excitations produced by the pump beam. In this regard, special attention must be reserved to high-energy bosonic collective modes as plasmons and excitons, since the dynamical evolution of their properties (peak energy, linewidth, lineshape...) sheds light on the complex many-body processes occurring in the material. Second, this technique gives access to the dynamics and intrinsic properties of low-energy bosonic collective modes that are coherently excited via the Impulsive Stimulated Raman Scattering (ISRS) process [26] or by a long-lived perturbation of the electronic ground state [27]. The combination of the ISRS framework and the use of a broad detection window in the optical range allows one to address one of the paradigms behind strongly correlated quantum systems [28–34]. When corroborated by theoretical calculations, this approach provides a very selective and quantitative estimate of the electron-boson coupling [29–31, 35, 36]. In addition, when some external parameter (e.g. temperature, pressure, magnetic field) is varied, the change of the electron-boson coupling can be followed across the phase diagram of the material [31].

In the description provided above, we have assumed that the pump photoexcitation occurs at a specific photon energy. However, tuning the pump photon energy,

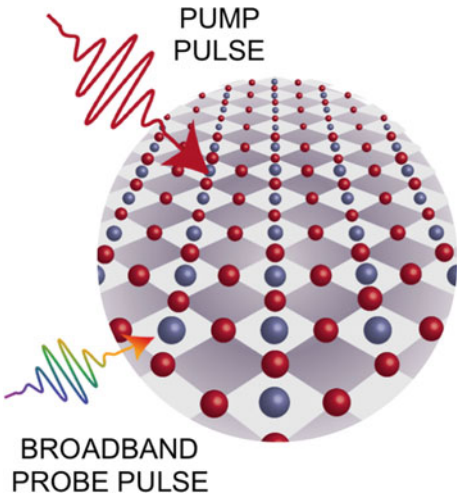

Fig. 2.3 Cartoon of an ultrafast broadband optical spectroscopy experiment. A solid is photoexcited with an ultrashort pump pulse and its optical properties are subsequently monitored in a broad energy range with a delayed continuum probe pulse

polarization, temporal duration and shape is highly desirable to prepare a correlated electron system in a well-defined excited state (ES). Several are the reasons behind the implementation of such an approach in this class of solids: (i) To unveil the detailed coupling between low- and high-energy excitations [34]; (ii) To investigate the carrier dynamics and many-body effects under different conditions of photoexcitation [37]; (iii) To hit specific resonances in the generation process of coherent collective modes; (iv) to achieve the light-induced control of the material properties [19, 20].

The concept of developing a nonequilibrium spectroscopy with a highly tunable pump pulse and a broad probing range is not a novel one, as it represents the cornerstone of the so-called "multidimensional" scheme of ultrafast optics. Multidimensional optical spectroscopies represent the optical analogues of multidimensional Nuclear Magnetic Resonance techniques and have been extensively used in the investigation of species of biological and chemical interest over the last decades. These methods were first developed in the infrared range [38] as a powerful tool to probe vibrational couplings, and subsequently implemented in the visible range for studying electronic/excitonic couplings [39, 40]. Finally, their extension into the deep-UV has given access to a very rich spectral region for the purposes of ultrafast biology [41]. In the language of physical chemistry, multidimensional spectroscopies are typically based on either a "transient absorption" or a "coherent photon-echo" approach. Since in solid-state physics the probed observable is typically the transient reflectivity of a material, in the following we will refer to the two schemes as the "frequency-domain" and the "time-domain" approach, respectively.

The "frequency-domain" technique follows the typical pump-probe scheme, in which the pump pulse is reduced in bandwidth before interacting with the sample. During the measurements, the pump photon energy is scanned and narrow band pump, broadband probe spectra are recorded for a given pump-probe time delay. The "time-domain" technique (photon-echo spectroscopy) is instead an interferometric approach that relies on the use of four different beams. The optical scheme is designed such that three beams form three corners of a square and are focused onto the sample. Here, phase-matching conditions give rise to an echo pulse, which is emitted towards the fourth corner (Fig. 2.4). This echo pulse is collinearly overlapped with a local oscillator pulse for heterodyne detection. Both the "frequency-domain" and the "time-domain" methods investigate the same third-order response function of the material, but differ in the way the response is read out, in the time resolution and in the internal complexity of the method. Pushing multidimensional spectroscopy to probe strong interactions and correlations in quantum solids is one of the frontiers of the field [42].

Irrespective of the complexity of the developed technique, the nonequilibrium evolution of the system can always be separated in terms of the so-called "incoherent" and "coherent" responses, which are direct manifestations of the type of interaction between the pump pulse and the material. The next Paragraphs of this Section are specifically aimed at providing a deeper comprehension of the temporal response emerging in a typical nonequilibrium experiment. We separately discuss the origin of the "incoherent" and the "coherent" response in Sects. 2.3.1 and 2.3.2, respectively.

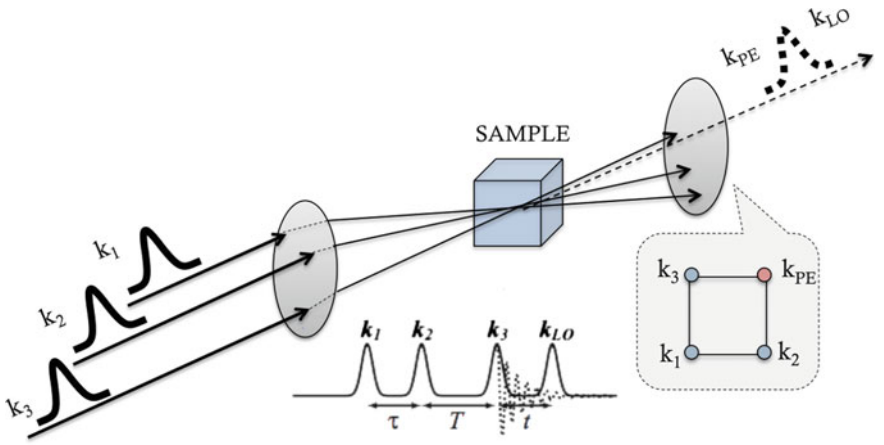

Fig. 2.4 Simplified scheme of a "time-domain" multidimensional spectroscopy, based on the photon-echo configuration. Three broadband ultrashort pulses form three corners of a square and are focused onto the sample. An echo pulse is emitted towards the fourth corner thanks to phase-matching conditions. This echo pulse is collinearly overlapped with a local oscillator for heterodyne detection

2.3.1 Incoherent Response

The simplest mechanism through which an ultrashort pump pulse can interact with a solid is via dipole-allowed processes. In this scenario, the corresponding matter-radiation interaction Hamiltonian is linear in the electric field and the dynamics are governed by the incoherent relaxation of the system. The photoexcited carriers cool down in femto- to picoseconds, first by distributing the excess energy among themselves and then by transferring the energy to other degrees of freedom (phonons, magnons...). To illustrate the details of the dynamics, here we make a distinction between the case of metals and that of band insulators.

Metals. In metals, the simplest phenomenological description of the ultrafast dynamics is offered by the so-called two-temperature model [43]. In this framework, the metal is divided into two subsystems, namely the conduction band (CB) electrons with a temperature T_e and the ionic lattice with a temperature T_L. The two-temperature model describes the flow of heat between the electrons and the lattice, which occurs upon photoexcitation as $T_e > T_L$. The first underlying assumption of this model is that the electron and phonon subsystems are each maintained in a thermalized state by Coulomb electron-electron and anharmonic phonon-phonon interaction, respectively. The time evolution of the energy (or temperature) of the electron gas and the lattice is given by two coupled equations

$$C_e \frac{dT_e}{dt} = \nabla \cdot (\kappa_e \nabla T_e) - H(T_e, T_L) + P(t), \tag{2.1}$$

$$C_L \frac{dT_L}{dt} = H(T_e, T_L), \tag{2.2}$$

where, P(t) is the amount of laser power that is dissipated in a unit volume of the electron gas and C_e and C_L are the specific heats of the electrons and lattice, respectively. H is the energy transfer rate between the electrons and the lattice. The term $\nabla \cdot (\kappa_e \nabla T_e)$ describes the diffusive electronic heat transport out of the excited region. Neglecting the heat transport and applying several approximations, these equations can be re-expressed as

$$C_e \frac{dT_e}{dt} = -g[T_e(t) - T_L(t)], \tag{2.3}$$

$$C_L \frac{dT_L}{dt} = g[T_e(t) - T_L(t)], \tag{2.4}$$

where g is the effective electron-phonon coupling constant, which is proportional to the square of the electron-phonon deformation potential. Assuming a weak perturbation regime ($T_e - T_0 \ll T_0$, with T_0 the initial equilibrium temperature), one can write $C_e(T_e) = \gamma T_e$, where γ is the electronic specific heat coefficient. This leads the electronic temperature dynamics to be governed by an exponential decay with a time constant $\tau_{e,ph} \approx \gamma T_0/g$. This situation is schematically illustrated in Fig. 2.5a, where the dynamics of the electronic and lattice temperatures are indicated in red and blue, respectively. For large perturbations, a nonexponential behaviour is instead predicted. At short time delays, a large slowing down of the T_e dynamics occurs, which is eventually followed by an exponential decay with time constant $\tau_{e,ph}$ as T_e approaches T_L.

The original two-temperature model and its extensions successfully reproduce the ultrafast dynamics of noble metals following femtosecond laser perturbation [44–46]. However, in more complex systems, the two-temperature model fails in describing the dynamics and alternative frameworks must be used. One common approach is to increase the number of interacting reservoirs that build up the system, thus generating a multi-temperature model. For example, a three-temperature model has been applied to reproduce the demagnetization dynamics in ferromagnetic (FM) metals (in which the three reservoirs are the electrons, the lattice and the spins, as schematically represented in Fig. 2.5b) [47], or to describe the anisotropic electron-phonon coupling of high-T_C cuprate superconductors (in which the three reservoirs are the electrons, the efficiently coupled phonons and the remaining lattice modes) [48, 49]. To capture the normal-state properties of cuprates, even four-temperature models have been applied [50].

Nevertheless, besides the case of simple metals, the validity of these models have often been doubted, as they imply that a certain degree of equilibrium is present within each reservoir. Given the short time scales, this assumption is not always valid and imposes a limit on the applicability of this description. Moreover, for systems with

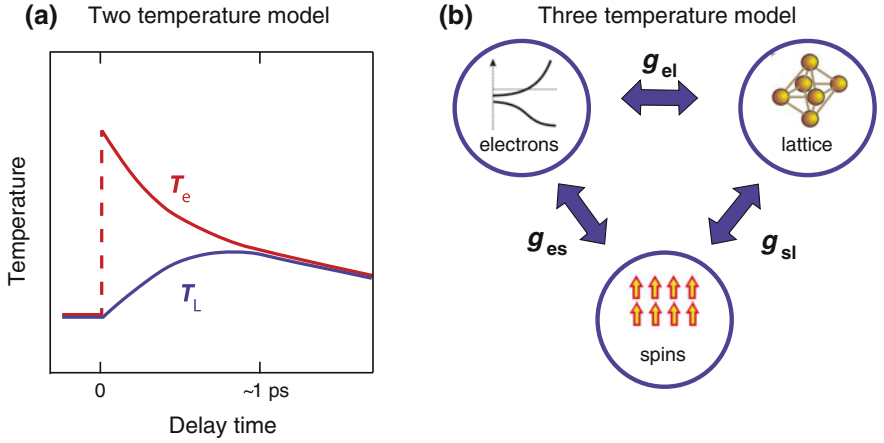

Fig. 2.5 **a** Schematic representation of the two-temperature model for reproducing the dynamics of noble metals. The electronic (T_e(t)) and lattice (T_L(t)) temperature dynamics are indicated in red and blue, respectively, and they equilibrate with a time constant $\tau_{e,ph} < 1$ ps. **b** Cartoon for a three-temperature model for materials with a spin degree of freedom. The three interacting reservoirs are the electrons, the lattice and the spins. Their effective interactions are expressed via the g parameters

a strong electron-boson coupling, the assumption that the electron-electron scattering is much faster than electron-phonon scattering is no longer valid [51, 52]. In this case, the initial relaxation of photoexcited electrons proceeds via the emission of high-energy bosons, which only subsequently release their energy to the electron system via boson-electron scattering, and to low-energy bosons via anharmonic decay. In the framework of this Thesis, the latter situation applies to MgB_2, which is a prototypical example of anisotropic Fermi liquid in the strong electron-phonon coupling regime. Understanding the details of the ultrafast dynamics in this class of materials represents a new challenge also for theoretical research.

Band insulators. We now briefly describe the incoherent response detected by ultrafast optical experiments in the case of band insulators, assuming for simplicity that no impurities and defects are present in the system. Under this condition, the incoherent response can only be generated by exciting interband transitions with the pump pulse. In a direct optical absorption process, this leads to the creation of electron-hole (e^--h^+) excitations across the energy gap of the insulator (Fig. 2.6). If the incident photon energy is larger than the gap, the nonequilibrium e^- and h^+ densities possess an excess energy and occupy different electronic states before relaxing to the bottom of the respective bands. This in turn influences the dielectric properties of the material, as the photoexcitation leads to a redistribution of SW in the solid. A delayed laser pulse centred around a specific photon energy can therefore reveal the microscopic processes affecting the ultrafast dynamics in a well-defined spectral range [53].

Typically, as the system evolves towards equilibrium, there is momentum and energy relaxation among the photoexcited particles [54]. Momentum relaxation

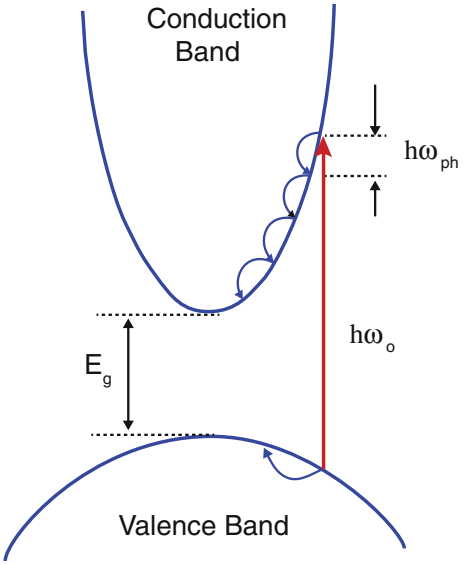

Fig. 2.6 Schematic representation of the e^{-}-h^{+} pair creation following illumination of a direct bandgap semiconductor with a photon energy $\hbar\omega_0$. The subsequent intraband energy relaxation is depicted via optical phonon emission with energies $\hbar\omega_{ph}$

occurs on a femtosecond time scale via elastic and inelastic scattering. On the same time scale, carrier-carrier scattering of the e^{-} (h^{+}) results in Coulomb thermalization and allows the e^{-} (h^{+}) system to be described by a Fermi-Dirac distribution with temperature T_e (T_h). Intraband energy relaxation of carriers proceeds mainly via the emission of optical phonons (as depicted in Fig. 2.6) and it is usually complete within several hundreds of femtoseconds. The emitted optical phonons undergo decay into two or more lower energy phonons via multiphonon mechanisms related to lattice anharmonicity.

Finally, recombination processes reduce the density of the nonequilibrium carriers via radiative or non-radiative relaxation channels. In the absence of defects and impurities, two-body radiative recombination processes and three-body non-radiative band-to-band (intrinsic) Auger processes are the primary sources of recombination [55]. Intrinsic Auger recombination refers to the mechanism occurring at sufficiently high excitation densities, in which an e^{-}-h^{+} pair across the bandgap recombines non-radiatively by transferring the energy to a third particle. The presence of impurities and defects in real materials alters and typically dominates the recombination dynamics, especially at low excitation densities. In simple semiconductors, the recombination dynamics can be unravelled by mapping the evolution of the decay time as a function of the absorbed laser fluence and fitting it with the solution of the following phenomenological rate equation [55]

$$\frac{dn}{dt} = -An - Bn^2 - Cn^3, \tag{2.5}$$

where n is the photocarrier density, and A, B and C are parameters determining the strengths of the different processes. The first term represents the single-carrier trapping, the second term consists of the radiative decay and trap-Auger mechanisms, the third term embodies the intrinsic Auger processes.

In more complex materials, the presence of strong interactions between the photoexcited carriers and bosonic degrees of freedom is also expected to modify the evolution of the system towards equilibrium. A first example is offered by the localization of carriers due to polaronic coupling, as this phenomenon shifts the optical SW to incoherent bands at low energies, whose dynamics can be detected directly with a MIR probe pulse or indirectly by following the photoinduced transparency of the above-gap region [56, 57]. A second example involves the presence of excitonic features at high energies, as the incoherent renormalization of these bosonic collective excitations is a very sensitive probe of the low-energy many-body processes occurring in the system [58, 59]. In this regard, Chap. 4 of this Thesis will shed light on the ultrafast carrier dynamics of anatase TiO_2 by monitoring the behaviour of its strongly bound excitons.

2.3.2 Coherent Response

In the previous Paragraph, we described a scenario in which the pump excitation occurs through dipole-allowed processes, in which the matter-radiation interaction Hamiltonian is linear in the electric field. Under these conditions, we observed that the dynamics of the system are governed by an incoherent evolution of the optical properties. In this Paragraph, we extend the class of phenomena that can be monitored using pump-probe spectroscopy, by including the second-order term of the matter-radiation interaction Hamiltonian (i.e. quadratic in the electric field). In this case, the interaction between the pump pulse and the sample can result in a coherent modulation of the optical properties in the time domain, due to the population of specific collective modes in the material. This scenario becomes effective when the time duration of the pump pulse is shorter than the period of the coherent oscillations. It is important to remark that such coherent modes are typically generated only during the excitation with ultrashort laser pulses, in contrast to hot incoherent collective modes that are created during the cooling process of hot carriers for several hundreds of femtoseconds. The term "coherent" indicates that two time-separated optical pulses can amplify or suppress the oscillating motion depending on their mutual separation.

The emergence of coherent collective modes in pump-probe spectroscopy was first reported in 1985 as a periodic modulation of the transient grating signal from organic materials [60] and subsequently observed in the transient reflectivity of semimetals [61] and semiconductors [62]. Since then, a body of work has been devoted to coherent optical phonon spectroscopy as a powerful route to probe lattice dynamics and to estimate the coupling between the electronic excitations and the vibrational degrees of freedom. More recently, the extension of the technique to strongly-correlated quan-

tum systems has paved the route to the observation of coherent collective modes of electronic origin (i.e. magnons, orbitons, charge-density fluctuations) [28, 63–67].

These studies have prompted the development of different theories to interpret the generation of the coherent collective modes in solids. While the description can vary from semiclassical to a quantum-field theory, the relevant normal mode's coherent amplitude Q is always expressed in terms of a driven harmonic oscillator. The equation of motion for the coordinate of a normal mode λ can be written as

$$\frac{d^2 Q_\lambda}{dt^2} + 2\beta \frac{dQ_\lambda}{dt} + \Omega_\lambda^2 Q_\lambda = F_\lambda(t), \tag{2.6}$$

where $\Omega_\lambda/2\pi$ is the natural frequency of the undamped oscillator and β is the damping parameter. By assuming for simplicity $\beta = 0$, we can solve the equation of motion, which yields

$$Q_\lambda(t) = \int_{-\infty}^{t} \mathrm{d}t' \frac{\sin[\Omega_\lambda(t-t')]}{\Omega_\lambda} F_\lambda(t'), \tag{2.7}$$

with the initial conditions $Q_\lambda(-\infty) = 0$ and $F_\lambda(-\infty) = 0$.

When Q_λ is considered as an operator, the quantum mechanical computation leads to the same result. Indeed, according to the Kubo formula

$$\begin{aligned} \langle Q_\lambda \rangle(t) &= \frac{i}{\hbar} \int_{-\infty}^{t} \mathrm{d}t' \langle [Q_\lambda(t),\, Q_\lambda(t')] \rangle F_\lambda(t') \\ &= -\int_{-\infty}^{\infty} \mathrm{d}t' \mathrm{D}^{\mathrm{ret}}_{\mathbf{q}\lambda}(t-t') F_\lambda(t'), \end{aligned} \tag{2.8}$$

where the retarded non-interacting phonon propagator is

$$\mathrm{D}^{\mathrm{ret}}_{\mathbf{q}\lambda}(t) = -\frac{i}{\hbar}\theta(t)\langle [Q_{\mathbf{q}\lambda}(t),\, Q_{-\mathbf{q}\lambda}(0)] \rangle = -\theta(t)\frac{\sin(\Omega_{\mathbf{q}\lambda} t)}{\Omega_{\mathbf{q}\lambda}}. \tag{2.9}$$

The function θ(t) denotes the Heaviside step function. While the theory up to this point is general, the classification of the generation processes arises from the temporal profile of the driving force F_λ(t), which can be impulsive or displacive.

Impulsive stimulated Raman scattering (ISRS). In the impulsive framework [26, 68], a broadband optical pulse offers multiple combinations of two photons whose energy difference matches the energy of a specific mode in the material (Fig. 2.7a). As a result, an impulsive (δ-like) driving force initiates the coherent motion on the electronic GS of the system. More precisely, a polarization in the solid is driven by the incident light field, which has a fast component corresponding to the laser central frequency ω_L and a "slow" modulation corresponding to the pump pulse shape

$$\mathbf{E}(t) = \mathscr{E}(t) e^{i\omega_L t}. \tag{2.10}$$

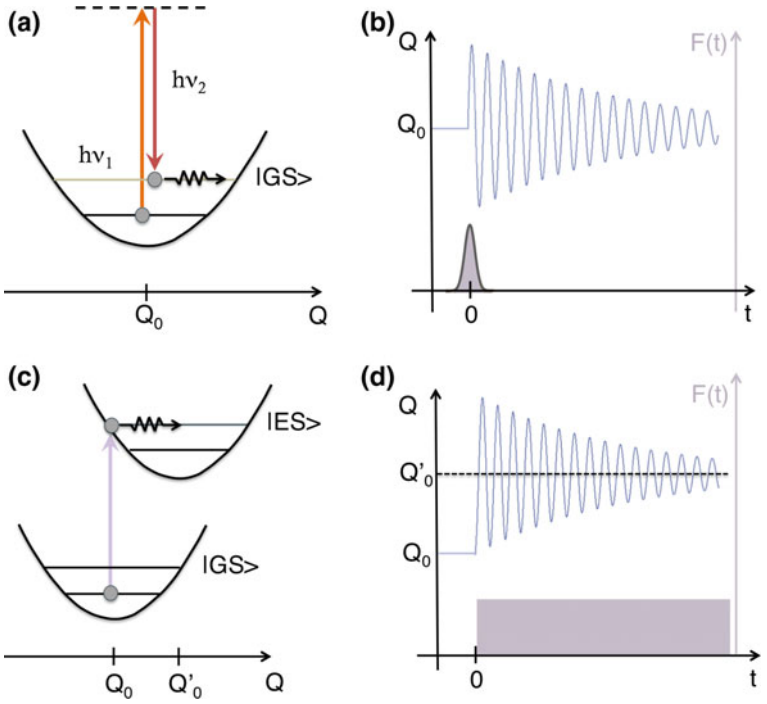

Fig. 2.7 Scheme for the generation mechanisms of coherent collective modes in condensed matter systems. **a**,**b** ISRS; **c**,**d** displacive excitation. For the two generation mechanisms, the potential energy surfaces of the electronic GS and ES of the systems are shown in (**a**) and (**c**), while the time-profile of the driving force and the resulting coherent response in (**b**) and (**d**)

The frequency ω_L is typically in the visible range and $\mathscr{E}(t)$ is the pulse shape with slow dynamics with respect to ω_L (typically on the order of 50 fs). The Raman Hamiltonian for one-phonon light scattering averaged over one cycle of period $T = 2\pi/\omega_L$ of the light wave reads

$$H_R = -\sum_{\lambda} F_\lambda Q_\lambda, \tag{2.11}$$

with the generalized time-dependent force acting on mode λ given by

$$F_\lambda(t) = \frac{V}{16\pi}\mathscr{E}(t)\frac{\partial \boldsymbol{\varepsilon}}{\partial Q_\lambda}(\omega_L)\mathscr{E}^*(t). \tag{2.12}$$

Here $\boldsymbol{\varepsilon}$ is the dielectric tensor of the material and its derivative $\partial\boldsymbol{\varepsilon}/\partial Q_\lambda$ represents the so-called Raman tensor. As a result, the quantity

$$\left|\mathbf{e}\cdot\frac{\partial \boldsymbol{\varepsilon}}{\partial Q_\lambda}\cdot\mathbf{e}\right|^2, \tag{2.13}$$

where **e** is a unit polarization vector, determines the cross-section for spontaneous Raman scattering. When this force field is substituted in Eq. 2.8, it leads to the same result as in the classical computation. Clearly, a necessary condition for the mode to be excited is that it is Raman active, i.e. $\partial \boldsymbol{\varepsilon} / \partial Q_\lambda \neq 0$. Assuming the presence of a single oscillator of mass M and frequency Ω_λ, the impulsive force in Eq. 2.12 produces an oscillation with maximum amplitude

$$Q_{\lambda,max} = \frac{V\mathscr{F}}{2\Omega_\lambda Mc} \left| \frac{\partial \boldsymbol{\varepsilon}_{\mathbf{pump}}}{\partial Q_\lambda}(\omega_L) \right|, \tag{2.14}$$

where the fluence $\mathscr{F}$ measures the energy per unit surface arriving at the sample per each pulse. The dielectric tensor $\boldsymbol{\varepsilon}_{\mathbf{pump}}$ is the one projected according to the polarization of the pump beam. This ISRS process can occur both under nonresonant and resonant conditions. Importantly, a resonant excitation leads to the enhancement of the Raman scattering cross-section, thus amplifying the amplitude of the coherent modes.

Displacive excitation. The displacive framework is instead achieved when a sudden shift of the potential starts the coherent oscillation on the electronic ES of the system (Fig. 2.7c). The potential shift in the ES is achieved by applying a step-function-like force during the pump excitation process (Fig. 2.7d). In this scenario, the ultrafast laser pulse creates a nonequilibrium carrier density in the material, which then couples to the bosonic collective mode in question and provides the force $F_\lambda(t)$ in Eq. 2.6. The shift in the equilibrium coordinate is assumed to be a linear function of the photoexcited electron density $n(t)$. The theory for displacive excitation was originally formulated to describe the generation of totally-symmetric modes [27], for which the force $F_\lambda(t)$ is proportional to the average value (i.e. isotropic component) of the excited charge density $n(t)$. However, this theory can also be extended to the excitation of lower-symmetry modes, provided that the appropriate component of the excited carrier density is used as the driving force. In this Thesis, we will analyse the emergence of coherent optical phonons generated via the displacive mechanism in Chap. 5–7.

A different context in which the displacive excitation also plays a central role concerns the excitation of coherent acoustic phonons (CAPs) in materials [69–71]. The generation of CAPs is based on the conversion of the optical energy of the pump beam into mechanical energy by a photoinduced stress $\sigma(z,t)$. The equation of elastic motion that is used to treat the phenomenology of CAPs is a semiclassical one, as it is based on the classical approach of wave physics, but includes the quantum mechanical source term $\sigma(z,t)$. The equation of motion reads

$$\frac{\partial^2 u}{\partial t^2} - C_a^2 \frac{\partial^2 u}{\partial z^2} = \frac{1}{\rho} \frac{\partial \sigma(z,t)}{\partial z}, \tag{2.15}$$

where u and ρ are respectively the displacement and the mass density in the material. Importantly, the source term $\sigma(z,t)$ is composed of different contributions,

embodying the microscopic processes that take place in the CAP generation. At the time of writing, five different mechanisms have been identified as possible sources of CAPs: Deformation potential (DP), thermoelasticity (TE), inverse piezoelectricity (PE) [72, 73], electrostriction and magnetostriction [74]. While DP, TE and PE are generally at play in a broad class of materials, the occurrence of electrostriction and magnetostriction is rather rare. For this reason, here we briefly discuss only the three main sources of the photoinduced stress. The DP mechanism is instantaneous and is based on the electronic pressure resulting from a spatial redistribution of photoexcited electrons after pump photon absorption. This redistribution induces a perturbation of the internal electric fields, forcing the ions to displace from their original positions. The TE mechanism is instead driven by the electron-phonon thermalization, as soon as the electronic subsystem transfers its energy to the phononic subsystem via phonon emission. An impulsive increase in phonon emission produces a rapid heating of the lattice and, because of lattice anharmonicity, the temperature increase produces a TE stress giving rise to the CAP. This process is also known as phononic pressure. PE is a phenomenon occurring in non-centro symmetric materials, in which there exists a mutual coupling between a macroscopic electric field ($\mathbf{E}$) inside the material and the lattice strain. In other words, the separation of the barycentre of positive and negative charges leads to a strain in the crystal structure. There are different situations where $\mathbf{E}$ exists in a material: external application of a bias, pre-existing built-in field in the vicinity of semiconductor surface or in a heterojunction, a dynamic separation of electrons and holes (Dember field) or the internal polarization of ferroelectric domains [71]. After the interaction between the pump and the system, the photoexcited carriers can screen $\mathbf{E}$, thus producing a transient time- and space-dependent $\mathbf{E}$ that induces a stress and launches CAPs. In the general case, the three effects of DP, TE and PE coupling take part simultaneously to the CAP generation. In practice, depending on the parameters of the pump photoexcitation and the material properties, one of them will dominate over the others. In Chap. 4, we will show how to estimate the relative magnitudes of the DP and TE couplings for the generation of CAPs in anatase TiO_2.

Comparison between ISRS and displacive excitation. In regard to the *generation* mechanism, as the bosonic modes interact with light only through the electrons, both ISRS and the displacive excitation give access to the electron boson coupling in the system. As a consequence, the two mechanisms differ solely in the nature of the electronic transition. Based on this argument, the displacive excitation was proposed to represent a resonant case of ISRS, in which the ES possesses an infinitely long lifetime [26, 68]. More recently, the model has been refined to account for finite electronic lifetime, providing more flexibility to reproduce the experimental findings [75]. One can verify the details of the generation mechanism by studying the phase of the coherent modes and performing a pump polarization dependence. In the pure ISRS framework, the coherent modes are expected to give rise to a sine wave as a function of time; in the language of molecular physics (where these effects have been extensively studied), this is consistent with a scenario of "wavepacket" dynamics in

the GS potential energy surface of the system. In contrast, in the purely displacive excitation regime, the coherent modes manifest in the time domain as a cosine wave; again, in the language of molecular physics, this corresponds to a framework of "wavepacket" dynamics in the ES potential energy surface of the system. The two frameworks of molecular physics and condensed matter physics reconcile in the picture shown in Fig. 2.7. Moreover, the coherent modes driven by ISRS (second order process) are expected to follow the symmetry of the Raman tensor, while those mediated by the displacive excitation should obey the polarization dependence of the optical absorption (first order process). In general, however, a single collective mode can be triggered via a combination of the ISRS and displacive excitation.

Detection mechanism of the coherent modes. We also discuss the details of the *detection* process of the coherently generated collective modes. In principle, a variety of experimental methods can resolve the coherent modes, provided that the coherent mode in question acts on the specific observable that is probed by the technique. Coherent oscillations have been revealed by trARPES [76–78], time-resolved x-ray [79–83] and electron [84] diffraction, trEELS [85], time-resolved TEM [86] and a variety of time-resolved optical techniques, including four-wave mixing [60], transient reflectivity [27, 32–34, 70, 75] and transmission [30, 69], transient magneto-optical Kerr effect [87, 88] and transient second harmonic generation (SHG) [89, 90]. Here, we concentrate only on the detection mechanism offered by the optical probes of reflectivity and transmission, since it is relevant to the purpose of this Thesis. Once a coherent collective excitation is generated, it induces a change in the dielectric function of the crystal. By treating, for simplicity, the collective coordinate as a time dependent classical variable Q(t) and assuming the elementary excitation is slow with respect to the frequency at which the optical properties are observed, then the Hamiltonian and all optical properties become functions of time. For coherent optical phonon modes, this leads to a modulation of the dielectric function $\boldsymbol{\varepsilon}$ that follows

$$\Delta\boldsymbol{\varepsilon}(\omega, t) = -4\pi \sum_X \frac{d\boldsymbol{\chi}}{dQ}(\omega) Q(t). \tag{2.16}$$

where $\boldsymbol{\chi}$ is the susceptivity tensor and the sum runs over all the modes excited in the system with a specific symmetry X. In the same way, for a coherent charge fluctuation, it leads to

$$\Delta\boldsymbol{\varepsilon}(\omega, t) = -4\pi \sum_X \frac{d\boldsymbol{\chi}}{dN_X}(\omega) \Delta N_X(t), \tag{2.17}$$

where the sum runs over all the density fluctuations present in the system, characterized by an operator N_X and a specific symmetry X.

As a result, when the transient reflectivity (ΔR/R) of the material is probed, the time-varying collective mode coordinate Q_λ induces oscillations in the material reflectance through the modulation of the dielectric tensor. This is expressed by

$$\left(\frac{\Delta R}{R}\right)^{\text{coh}} = \frac{\partial \ln R}{\partial \boldsymbol{\varepsilon}_{\mathbf{probe}}} \frac{\partial \boldsymbol{\varepsilon}_{\mathbf{probe}}}{\partial Q_\lambda} Q_\lambda(t), \tag{2.18}$$

where $\boldsymbol{\varepsilon}_{\mathbf{probe}}$ is the dielectric tensor projected according to the polarization of the probe beam and t is the time delay between the pump and the probe. The first factor on the right-hand side of Eq. 2.18 is known from Fresnel's equations. Taking the polarizations such as $\boldsymbol{\varepsilon}_{\mathbf{pump}} = \boldsymbol{\varepsilon}_{\mathbf{probe}}$ and evaluating Eq. 2.18 at the time of the maximum amplitude, one can obtain an equation for the squared magnitude of $\partial \boldsymbol{\varepsilon}_{\mathbf{probe}}/\partial Q_\lambda$ in terms of experimental quantities. Thus, Eq. 2.18 gives access to the full resonant Raman profile. Since this detection process is governed by the $\partial \boldsymbol{\varepsilon}_{\mathbf{probe}}/\partial Q_\lambda$ Raman tensor, linear optical detection can provide information only about the Raman-active modes.

Extension to broadband spectroscopy. The validity of the above discussion applies already at the single-wavelength pump-probe level, in which both the pump and probe pulses are characterized by the same photon energy. A powerful extension of this technique involves the use of a widely tunable pump pulse, in order to hit different resonances in the generation process of the coherent bosonic modes. At the same time, covering a broad detection range with a continuum probe in the vicinity of a specific high-energy charge excitation (e.g. a polaronic band, an exciton, the fundamental absorption gap in a semiconductor, the CT/Mott gap in a correlated insulator...) provides access to the energy-dependent Raman matrix element for the collective mode under study. This aspect will be deeply discussed in Chaps. 5, 6 and 7 in the case of La_2CuO_4, $NdBa_2Cu_3O_{6+x}$ and $TbMnO_3$ respectively. Remarkably, the determination of the Raman matrix elements is important from the fundamental point of view, as they carry microscopic information on the electron-boson matrix elements of a certain material [68]. Currently available methods for evaluating the electron-boson (e.g. electron-phonon) coupling allow one to obtain only averaged information over all modes (e.g. phonons). In contrast, when corroborated by theoretical calculations, ultrafast broadband optical spectroscopy provides a selective and quantitative estimate of the electron-boson coupling for specific collective modes [29–31]. From the experimental side, the Raman matrix elements reveal the selectivity of the pump photon energy and polarization in the excitation process of a specific collective mode, which opens intriguing scenarios towards the coherent control of collective modes in complex materials.

2.4 Ultrafast Broadband Visible Spectroscopy[1]

In the previous Section, we have highlighted how ultrafast optical spectroscopy has largely improved since its early implementation on molecules [91–94], noble metals [45, 46, 95, 96] and semiconductors [58, 97]. Nowadays, advanced techniques are even capable of reaching a time resolution of less than 10 femtoseconds and of capturing the ultrafast dynamics in previously unexplored spectral ranges [98–101]. Assessing the phenomenology of strongly correlated quantum systems requires one to modify the basic scheme of ultrafast optical spectroscopy in order to: (i) Achieve a high time resolution and detect possibly excited low-energy coherent bosonic modes of the material under study; (ii) Offer a broad detection window covering the region of the high-energy interband transitions of the solid, where the bosonic modes are likely to resonate; (iii) Provide a high versatility in the determination of the nonequilibrium optical properties under varying experimental conditions (temperature, magnetic field...); (iv) Obtain a high signal-to-noise ratio to clearly identify the spectro-temporal features characterizing the ultrafast optical response.

Practically, the extension of this framework to the study of complex solids requires the development of a suitable cryogenic environment for the sample and, in most situations, the implementation of a reflection geometry. In the last years, first important steps towards this goal have been made. A 250 kHz repetition-rate setup has been used for measuring the broadband transient reflectivity ($\Delta R/R$) of cuprates [31, 37, 50, 102, 103] and other transition metal oxides [104, 105], offering a high tunability in terms of pump photon energies and explored temperature range. However, due to limitations in the time resolution, coherent Raman-active bosonic modes were only observed up to a frequency of $\sim$19 meV [31]. More recently, a broadband (0.75–2.40 eV) and high time resolution (9–13 fs) instrument has been implemented with the same purpose [52]. Nevertheless, up to now, only operation down to 100 K has been demonstrated, due to the challenge of maintaining the same pulse compression inside a cryostat. This hinders the possibility to probe the strongly correlated quantum phases emerging at a lower temperature scale.

In the following, we present a versatile experimental setup for femtosecond broadband optical spectroscopy in the visible spectral range, which allows us to specifically address this problem [106]. The apparatus is based on a cryo-cooled amplified Ti:Sapphire laser and offers an overall time resolution of $\sim$45 fs. The pump beam can be tuned to different photon energies to explore several excitation conditions, while the probe is a broadband continuum covering the spectral region from 1.75 to 2.85 eV. The setup has been designed to allow systematic transient reflectivity ($\Delta R/R$) and transmissivity ($\Delta T/T$) studies for different temperatures (8–340 K) and applied magnetic fields (0–1 T). Section 2.4.1 describes the laser system and the optical design of the setup, Sect. 2.4.2 illustrates the design of the cryostat in which the experiments are performed, Sect. 2.4.3 highlights the operation of our instrument in terms of sig-

[1] The Sect. 2.4 is reprinted with permission from E. Baldini et al., Structural Dynamics 3, 064301. Copyright 2016 American Institute of Physics.

nal acquisition and processing. The basic scheme of this setup opens up intriguing possibilities for the future implementation of low-temperature time-resolved broadband magneto-optical measurements and time-resolved spectroscopic ellipsometry (SE) [107–109].

2.4.1 Laser System and Electronics

Our femtosecond broadband optical spectroscopy setup is laid out in a standard pump-probe configuration. An overview of the setup and its laser system is given in Fig. 2.8. A Ti:Sapphire oscillator (KM Labs, Griffin), pumped by a continuous-wave Nd:YVO_4 laser (Coherent, Verdi-V5), emits ∼45 fs pulses at 1.55 eV with a repetition rate of 80 MHz. The output of the oscillator seeds a cryo-cooled Ti:Sapphire amplifier (KM Labs, Wyvern-1000), which is pumped by a Q-switched Nd:YAG laser (Lee Laser, LDP-200MQG). This laser system provides ∼45 fs pulses at 1.55 eV with a repetition rate of 3–10 kHz at a pulse energy of up to 3 mJ [110].

In a basic configuration, a few μJ of the laser output are used for the pump beam when exciting a sample at 1.55 eV. Optionally, the pump output can be frequency-doubled to 3.10 eV using a β-barium borate (BBO) crystal, or can be tuned in the infrared between ∼60 meV (20 μm) and 1 eV (1.2 μm) using a commercial optical parametric amplifier (Light Conversion, TOPAS-C with NDFG stage). The white light pulse serving as the probe beam is generated by focusing pulses with an energy of about 1 μJ into a calcium fluoride (CaF_2) crystal of 3 mm thickness using a combination of a lens with short focal distance and an iris to limit the numerical aperture of the incoming beam. The generated continuum ranges from 1.72 to 2.92 eV and is peaked around 2.20 eV. The CaF_2 crystal is mechanically oscillated to slow down crystal degradation by spatial hole-burning caused by the high laser intensity.

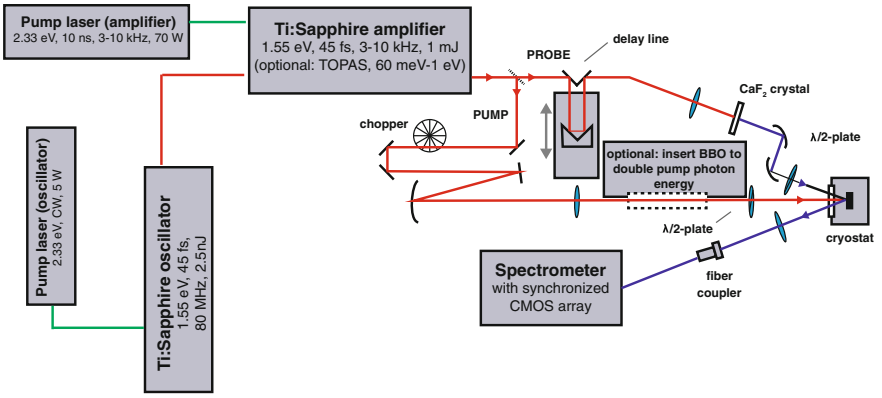

Fig. 2.8 A diagram of the ultrafast broadband visible spectroscopy setup, detailing the laser system and the broadband pump-probe experiment

The residual component of the generating beam at 1.55 eV is eliminated using a high-pass coloured glass filter, and the divergent white light beam is collimated and focused onto the sample in a dispersion-free manner using a pair of off-axis parabolic mirrors, impinging onto the sample surface at an angle of 15–20°. The spot sizes of the pump and probe beams at the sample surface are measured by a CCD-based beam profiler. Typical full width at half maximum dimensions of the near-Gaussian profiles are $150 \times 150\ \mu m^2$ for the pump beam and $50 \times 50\ \mu m^2$ for the probe beam. The polarizations of the pump and probe beams can be adjusted using half-wave retardation plates. The time-delay between pump and probe is adjusted via the use of a retroreflector mounted on a mechanical delay stage (Newport, M-UTM25PE-1), which is installed in the probe path prior reaching the CaF_2 crystal for white light generation.

The specular reflection of the probe beam is collimated into an optical fiber using an achromatic lens. The fiber couples the beam into a $f/4$-spectrometer, which uses a linear complementary metal oxide semiconductor (CMOS) array as a detector (Hamamatsu, S10453-1024Q). The electronic shutter of the CMOS detector is synchronized to the incoming laser pulses through a series of electronic circuits, sketched in Fig. 2.9. The core piece is a 16-bit analog-to-digital converter that produces a master clock pulse train at 11 MHz, fast enough to read out all 1024 detector pixels from pulse-to-pulse at the maximum laser repetition rate of 10 kHz. The signal derived from the amplifier pump laser trigger is synchronized to the master clock and ultimately paces the readout operations of the CMOS array. The same trigger signal is halved in frequency and sent to the chopper controller, which synchronizes the rotation of the mechanical chopper blade to the incoming laser pulses. The chopper runs at a quarter of the laser repetition rate, blocking and letting pass pulses in pairs of pump pulses. This is done to eliminate a particular intensity fluctuation that often occurs with continuously pumped Q-switched pump lasers that are operated at repe-

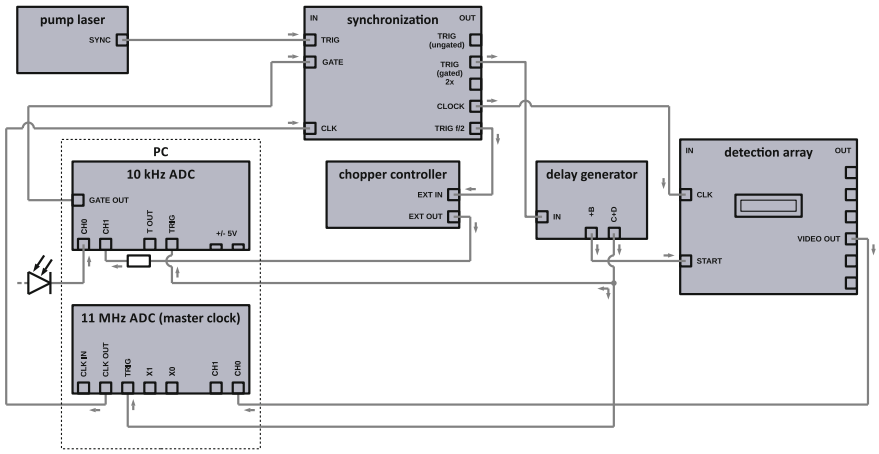

Fig. 2.9 Schematic representation of the synchronization electronics

tition rates around the inverse lifetime of the gain medium (in Nd:YAG, $T_f = 230\,\mu s$). In this regime, the "memory" of the gain medium extends over multiple pulses. Due to feedback between pulses (a relatively weak pulse leaves more residual gain for the next pulse, which will be stronger and leave less residual gain for its successor) repetitive intensity fluctuations are observed at half the repetition rate, often referred to as a "Ding-Dong" effect. Even when this modulation is very small ($\ll 1\%$), it can give rise to a strong artefact in the measured transient signal. By chopping pulse pairs (i.e. chopping at 1/4 of the repetition rate) this artefact is fully suppressed.

A gate signal is then created using the reference output of the chopper controller, and combined with the trigger signal. This gated trigger is finally used to start the data acquisition process of the CMOS array. Along the way, several extra delays are added to compensate for cable lengths, beam propagation, and positioning of the various elements along the beam path. Using this process, it is ensured that: (i) The electronic shutter of the CMOS array is opened in a time window around the arrival of the laser pulses; (ii) The shutter is closed between the arrival of pulses to reduce background noise; and (iii) All detector pixels are read out in the period between pulses. To compensate for the pump beam fluctuations, a photodiode is also connected to a channel of the analog-to-digital converter to monitor and eliminate the fluctuations of the pump beam intensity.

2.4.2 Sample Environment

The cryostat assembly used for optical experiments, shown in Fig. 2.10, is based on a closed-cycle liquid helium cold head (Advanced Research Systems Inc., DE-204) with a vibration-reducing gas interface. The cryostat expander is mounted to the laboratory ceiling, while the cold head and cryostat shroud are supported from the optical table, completely isolating the latter from the strong vibrations of the expander. The cold head allows for experiment temperatures between 8 and 340 K. Samples are mounted using fast-drying silver paint on a small copper plate attached to a copper wire of 2 mm thickness descended from the cold head.

The sample shroud is a custom design made of aluminium, allowing for the application of an external magnetic field, and is fitted to a standard ConFlat flange using a soft, annealed copper gasket. Optical access is provided via a 1-inch window port at the front. The window material is chosen according to the pump and probe energies of the experiment. For experiments in the visible/near-infrared range, CaF_2 is used. A turbo pump, backed up by an oil pump, is attached to the back of the shroud, the proximity to the sample significantly improving the vacuum. The vacuum pressure is measured by a sensor attached to the cold head shroud. Achievable minimum pressures range from 10^{-8} mbar at R to 10^{-9} mbar at 10 K. The vacuum is improved after closing the cryostat by heating up to the maximum temperature over $\sim$10 h.

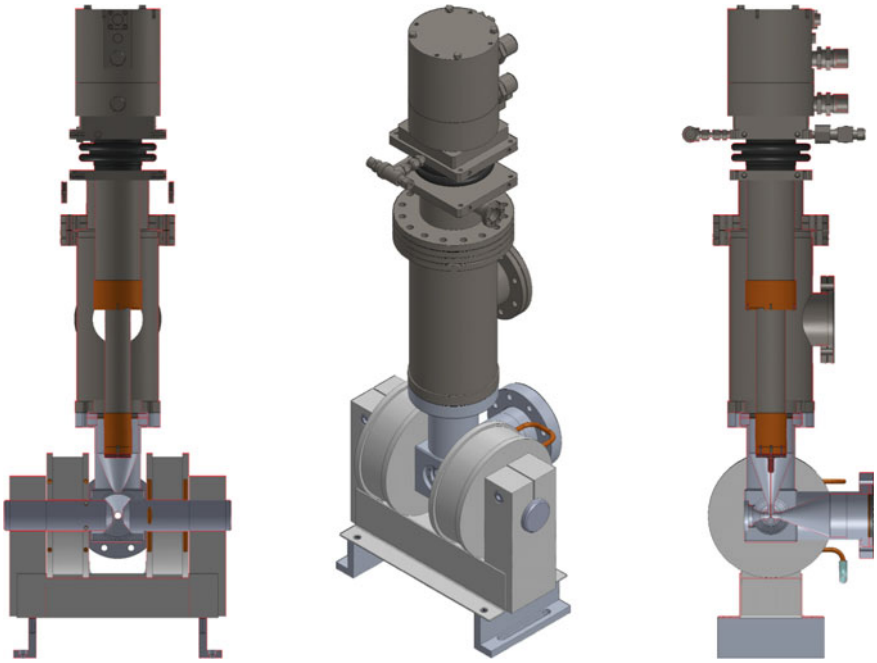

Fig. 2.10 The cryostat assembly with the magnet in position. From top to bottom, the assembly comprises the expander (dark gray), the gas interface (black), the cold head shroud (dark gray), and the aluminium sample shroud (light gray)

The sample shroud depicted in Fig. 2.3 is optimized for transient reflectivity and ultrafast magneto-optical Kerr effect measurements. The small cubic sample space of about 1 cm edge length allows bringing the poles of an electromagnet (GMW Associates, 3470) close enough to the sample to achieve in-plane fields ranging from 0 to 1 T. For transmission and ellipsometric measurements, different aluminium shrouds were designed. In particular, for transient SE, the shroud features probe entrance and exit windows under 70° with respect to the pump entrance window (which allows the pump to illuminate the sample under normal incidence).

2.4.3 Signal Acquisition and Processing

In the previous Paragraph, we described the possibility of performing measurements both in reflection ($\Delta R/R$) and transmission ($\Delta T/T$) geometry, depending on the specific sample (bulk crystal, thin-film...) that is measured. In this Paragraph, we focus on the acquisition and preliminary processing of the data. For simplicity, we restrict our discussion to transient reflectivity measurements on bulk crystals.

The differential reflectivity change ΔR/R is extracted from the data by calculating the quantity ΔR (ω, t)

$$\frac{\Delta R}{R}(\omega, t) = \frac{\mathrm{R_{pumped}}(\omega, t) - \mathrm{R_{unpumped}}(\omega, t)}{\mathrm{R_{unpumped}}(\omega, t)}, \tag{2.19}$$

where $\mathrm{R_{pumped}}$ and $\mathrm{R_{unpumped}}$ are the two arrays containing the sums over the spectra received from the analog-to-digital converter. Every individual curve is corrected for the offset spectrum $\mathrm{R_{dark}}(\omega)$, which is acquired before every scan by measuring the light entering the fiber when the probe beam is blocked and the pump beam is open, eliminating the scattered pump light as well as any ambient light from the acquired spectra. It is important to note that the sign of the right-hand side of Eq. 2.19 depends on the electronic phase offset of the chopper as well as its position along the beam path, which have to be adjusted properly to obtain the physical sign of the reflectivity change. Finally, the dataset ΔR/R(ω,t) containing the reflectivity change at every time delay for every probe energy is retrieved in the form of a rectangular matrix. In a typical experiment, the acquisition of each matrix is repeated multiple times to improve the statistics of the measurement. Hence, the experiment strongly relies on the repeatability of scans, implying the stability of the sample under laser light illumination for hours.

Acquiring a dataset for one set of experimental parameters (fluence, polarization, sample temperature) typically requires from few hours to a whole day, depending on the signal level and the desired signal-to-noise ratio. Before the data are analysed, the ΔR/R matrix has to be corrected for the Group Velocity Dispersion (GVD) of the probe beam. Since the probe beam is not dispersion-compensated after generation of the white light continuum, the probe pulses arrive at the sample stretched to a duration of few picoseconds. This is beneficial for the experiment, because it significantly reduces the momentary probe light intensity in the sample. It is noteworthy that the probe beam dispersion is not a limiting factor for the time resolution of the setup, which is given on the detection side by the much smaller effective pulse duration per detector pixel. The correction of the GVD is done numerically by defining values for time-zero (i.e. pump-probe overlap) for a number of probe photon energies across the spectrum by looking at the time traces ΔR/R(t). Typically, the onset of the signal can be used as point of overlap. The final result depends on the exact method used to define time-zero given a certain slope, but consistent results can easily be achieved due to the fact that the GVD can be represented as a Taylor series with sizeable contributions only up to third order. While the time traces can be understood in terms of the sample response to a δ-like excitation convolved with the Gaussian shape of the pump pulse, it is in general not necessary to deconvolve the traces to obtain the true pump-probe overlap in time. It should be noted, however, that the GVD correction has an intrinsic uncertainty that cannot be pushed very far below half the pump pulse duration. The raw data are corrected for GVD by shifting each time trace by its assigned time-zero value, as well as subtracting any possible offsets caused by noise in the offset spectrum from Eq. 2.19. The matrix is then trimmed around the edges to eliminate missing data points.

Integrating over a typical value of 1000 laser shots per acquisition, the setup has an intrinsic noise level of about 0.1% rms. The main noise sources are given by the amplifier output noise, which is strongly increased by the nonlinear white light generation process, the electronic noise of the CMOS array and the noise due to AD conversion. The signal-to-noise ratio is improved statistically by repeating each measurement many times, typically up to 100 scans per matrix. In addition, the output of several detector pixels is binned, averaging in energy. In this way, relative reflectivity changes down to the order of 10^{-4} can be observed. Although the measurable signal variation is several orders of magnitude higher than the one detected in single-wavelength (i.e. oscillator based) pump-probe experiments, we remark that the advantage of our broadband probe is to provide a spectrally-resolved picture of the nonequilibrium optical response, revealing valuable information on the electronic structure of the material under study. This aspect is particularly crucial when one aims at unveiling SW transfers occurring on ultrafast timescale in strongly correlated quantum systems. In addition, for most systems, the pump fluences required for producing a reflectivity change of 10^{-4} in the optical range are still within the linear regime of the sample response [17]. Finally, the use of an amplified laser system is ideal for the study of photoinduced phase transitions in complex materials, where fluences on the order of $\sim$ mJ/cm^2 are typically required [15, 16, 22, 111, 112].

2.5 Ultrafast Two-Dimensional Deep-UV Spectroscopy

In the previous Sections, we described how the combination of a highly tunable pump pulse and a broad detection scheme can offer new perspectives in the field of ultrafast optical spectroscopy of strongly correlated quantum system. The main goal of this Thesis is to reveal the low-energy nonequilibrium dynamics of strongly interacting and correlated many-body systems by tracking the signature of specific collective modes either in the time- or energy domain. In the latter case, it is important to observe that many collective modes of interest (i.e. excitons and plasmons) lie in the in the deep-UV spectral range. This calls for the extension of broadband optical spectroscopy to the spectral region between 3.10 and 4.80 eV. A further development of this technique towards the multidimensional scheme would help clarifying the carrier dynamics and many-body effects under different conditions of photoexcitation. Only a few broadband pump-probe setups have been reported so far in the UV range and all of them implement a multidimensional scheme based on a photon-echo configuration [113–115]. In this regard, the covered spectral bandwidth extends over less than 0.2 eV in the UV. This limitation is imposed by the stringent requirements on phase stability and temporal, as well as spatial, chirp control within this scheme. A different approach relies on the implementation of a transient absorption multidimensional spectroscopy in the UV, that enables measurements with photon energy windows of 1.3 and 0.9 eV along the probe and pump axis, respectively. This method is essentially a pump-probe scheme where two pulses are sent to the sample. The pumping process exploits a small bandwidth tunable pulse, while the probe is a broad

UV pulse. The scan along different time-delays is repeated while changing the pump photon energy, leading to the construction of a two-dimensional (2D) spectrum line by line. The energy resolution is limited by the step in the pump photon energy, while the time resolution by the duration of the pump pulse.

In the literature, pioneering multidimensional spectroscopy experiments on condensed matter systems have been performed either in the visible range [34, 116–118] or in the THz regime [119, 120]. Thus, our approach opens the doors to the study of high-energy excitations in wide band-gap insulators with strong interactions and correlations. In Chap. 4, we make use of this technique to investigate the excitonic spectral features of anatase TiO_2, which is a prototypical example of strongly interacting band insulator. Future extensions of this technique to more complex correlated solids could involve the study of the CT gap in NiO [121] and of the spin-polaron spectral features of $LaSrMnO_4$ [122]. In the following Paragraphs we present the details of the setup used for the experiments of Chap. 4.

2.5.1 Laser System

The ultrafast broadband UV experiments have been performed using a novel setup of tunable UV pump and broadband UV probe [93, 94, 123]. An overview of the setup and its laser system is given in Fig. 2.11. A 20 kHz Ti:Sapphire regenerative amplifier (KMLabs, Halcyon + Wyvern500), providing pulses at 1.55 eV, with typically 0.6 mJ energy and around 50 fs duration, pumps a noncollinear optical parametric amplifier (NOPA) (TOPAS white-Light Conversion) to generate sub-90 fs visible pulses (1.77–2.30 eV range). The typical output energy per pulse is 13 mJ. Around 60% of the output of the NOPA is used to generate the narrowband pump pulses. The visible beam, after passing through a chopper, operating at 10 kHz and phase-locked to the laser system, is focused onto a 2 mm thick BBO crystal for performing SHG and obtaining the UV pump pulse. The pump photon energy is controlled by the rotation of the crystal around the ordinary axis and can be tuned in a wide spectral range up to ∼0.9 eV. The typical pump bandwidth is 20 meV and the maximum excitation energy is about 120 nJ. The pump power is recorded on a shot-to-shot basis by a calibrated photodiode for each pump photon energy, allowing for the normalization of the data for the pump power.

The remaining NOPA output is used to generate the broadband UV probe pulses with ∼1.3 eV bandwidth through an achromatic frequency doubling scheme. A simple picture for the achromatic frequency doubling scheme is shown in Fig. 2.12. It comprises two fused silica prisms that spatially disperse and recollimate the visible beam coming from the NOPA. The resulting spatially chirped beam is focused with a 90° off-axis parabolic mirror on a 200 μm thick BBO crystal. The goal is to match the angular chirp with the (external) phase matching angle for SHG of all probe photon energies. The frequency-doubled beam is subsequently recollimated with another 90° off-axis parabola and recombined with two additional CaF_2 prisms.

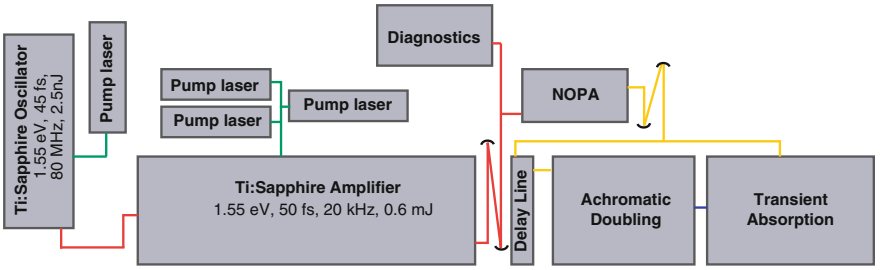

Fig. 2.11 A diagram of the ultrafast 2D deep-UV spectroscopy setup, detailing the laser system and the broadband pump-probe experiment

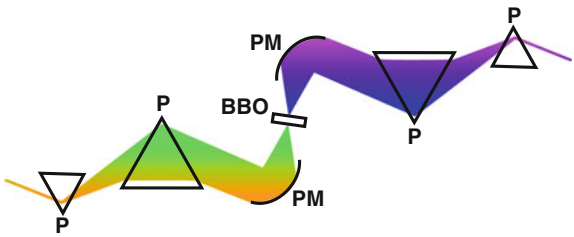

Fig. 2.12 Schematic of the achromatic doubling, adapted from Ref. [93]. P: Prism, PM: Off-axis parabolic mirror

The pump and probe pulses, which have the same polarization, are finally focused onto the sample, where they are spatially and temporally overlapped. The full width at half maximum of the pump and the probe spot size is 100 mm and 40 mm, respectively, resulting in a homogeneous illumination of the probed region. This setup can be used either in transmission or in reflection configuration.

2.5.2 Sample Environment

When the femtosecond 2D UV spectroscopy setup is used in the reflection configuration, the investigated single crystals are mounted on a rotating sample holder, in order to explore the $\Delta R/R$ response along the desired crystallographic axis. The portion of the probe beam reflected by the polished surface of the crystal is subsequently detected and the time evolution of the difference in the UV probe reflection with and without the pump pulse reconstructed. At the time of writing, the setup allows for measurements only at RT.

In the case of transmission measurements, the sample typically consists of a thin-film or of a colloidal solution of NPs. In the latter case, the colloidal solution is circulated into a 0.2 mm thick quartz flow-cell to prevent photodamage of the NPs and its concentration is adjusted to reach the desired optical density. Alternatively, for limiting the issues of cross-phase modulation (CPM) in the sample and achieving a higher time resolution, the colloidal solution can be made flowing in the form of

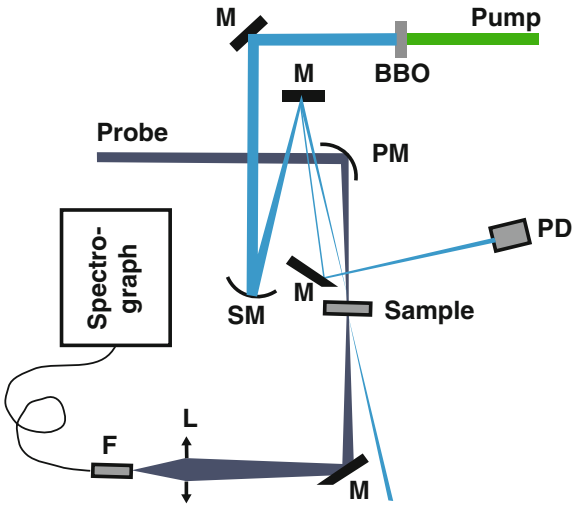

Fig. 2.13 Ultrafast broadband UV spectroscopy setup in the transmission geometry. PM: Off-axis parabolic mirror, M: Mirror, SM: Spherical mirror, PD: Photodiode, L: Lens, F: Multi-mode fiber

0.2 mm thick jet. The probe is measured after its transmission through the sample and its detection synchronized with the laser repetition rate. The difference of the probe absorption with and without the pump pulse is measured at different time delays between the pump and the probe, thanks to a motorized delay line in the probe path. A schematic representation of the transmission configuration is provided in Fig. 2.13.

After the sample, the reflected/transmitted broadband probe beam is focused in a multi-mode optical fiber (100 μm), which is coupled to the entrance slit of a 0.25 m imaging spectrograph (Chromex 250is). The beam is dispersed by a 150 gr/mm holographic grating and imaged onto a multichannel detector consisting of a 512 pixel CMOS linear sensor (Hamamatsu S11105, 12.5×250 mm pixel size) with up to 50 MHz pixel readout, so the maximum read-out rate per spectrum (almost 100 kHz) allows us to perform shot to-shot detection easily. The described experimental setup typically offers a time resolution of 150 fs, but can be improved to 80 fs with the adoption of a prism compressor on the pump pulses, at the expenses of a reduction of the probe bandwidth in the achromatic frequency doubling scheme.

References

1. A. Damascelli, Probing the electronic structure of complex systems by ARPES. Phys. Scr. **2004**(T109), 61 (2004)
2. C.J. Chen, *Introduction to Scanning Tunneling Microscopy*, vol. 2 (Oxford University Press, New York, 1993)
3. J.C. Campuzano, H. Ding, M.R. Norman, H.M. Fretwell, M. Randeria, A. Kaminski, J. Mesot, T. Takeuchi, T. Sato, T. Yokoya et al., Electronic spectra and their relation to the (π, π) collective mode in high-T_C superconductors. Phys. Rev. Lett. **83**(18), 3709 (1999)

4. A. Lanzara, P.V. Bogdanov, X.J. Zhou, S.A. Kellar, D.L. Feng, E.D. Lu, T. Yoshida, H. Eisaki, A. Fujimori, K. Kishio et al., Evidence for ubiquitous strong electron-phonon coupling in high-temperature superconductors. Nature **412**(6846), 510–514 (2001)
5. D. Mou, R. Jiang, V. Taufour, R. Flint, S.L. Bud'ko, P.C. Canfield, J.S. Wen, Z.J. Xu, Ge. Gu, A. Kaminski, Strong interaction between electrons and collective excitations in the multiband superconductor MgB_2. Phys. Rev. B **91**(14), 140502 (2015)
6. D.N. Basov, R.D. Averitt, D. van der Marel, M. Dressel, K. Haule, Electrodynamics of correlated electron materials. Rev. Mod. Phys. **83**, 471–541 (2011)
7. W. Hayes, R. Loudon, *Scattering of Light by Crystals*. (Courier Corporation, 2012)
8. L.J.P. Ament, M. Van Veenendaal, T.P. Devereaux, J.P. Hill, J. Van Den Brink, Resonant inelastic x-ray scattering studies of elementary excitations. Rev. Mod. Phys. **83**(2), 705 (2011)
9. R.F. Egerton, *Electron Energy-Loss Spectroscopy in the Electron Microscope*. (Springer Science & Business Media, 2011)
10. I. Gierz, J.C. Petersen, M. Mitrano, C. Cacho, I.C.E. Turcu, E. Springate, A. Stöhr, A. Köhler, U. Starke, A. Cavalleri, Snapshots of non-equilibrium Dirac carrier distributions in graphene. Nat. Mat. **12**(12), 1119–1124 (2013)
11. E.J. Sie, A.J. Frenzel, Y.H. Lee, J. Kong, N. Gedik, Intervalley biexcitons and many-body effects in monolayer MoS_2. Phys. Rev. B **92**(12), 125417 (2015)
12. E.M. Mannebach, R. Li, K.-A. Duerloo, C. Nyby, P. Zalden, T. Vecchione, F. Ernst, A.H. Reid, T. Chase, X. Shen et al., Dynamic structural response and deformations of monolayer MoS_2 visualized by femtosecond electron diffraction. Nano Lett. **15**(10), 6889–6895 (2015)
13. M.P.M. Dean, G. Dellea, R.S. Springell, F. Yakhou-Harris, K. Kummer, N.B. Brookes, X. Liu, Y.J. Sun, J. Strle, T. Schmitt et al., Persistence of magnetic excitations in $La_{2-x}Sr_xCuO_4$ from the undoped insulator to the heavily overdoped non-superconducting metal. Nat. Mat. **12**(11), 1019–1023 (2013)
14. L. Piazza, D.J. Masiel, T. LaGrange, B.W. Reed, B. Barwick, F. Carbone, Design and implementation of a fs-resolved transmission electron microscope based on thermionic gun technology. Chem. Phys. **423**, 79–84 (2013)
15. A. Cavalleri, C. Tóth, C.W. Siders, J.A. Squier, F. Ráksi, P. Forget, J.C. Kieffer, Femtosecond structural dynamics in VO_2 during an ultrafast solid-solid phase transition. Phys. Rev. Lett. **87**(23), 237401 (2001)
16. D.J. Hilton, R.P. Prasankumar, S. Fourmaux, A. Cavalleri, D. Brassard, M.A. El Khakani, J.C. Kieffer, A.J. Taylor, R.D. Averitt, Enhanced photosusceptibility near T_c for the light-induced insulator-to-metal phase transition in vanadium dioxide. Phys. Rev. Lett. **99**(22), 226401 (2007)
17. C. Giannetti, G. Coslovich, F. Cilento, G. Ferrini, H. Eisaki, N. Kaneko, M. Greven, F. Parmigiani, Discontinuity of the ultrafast electronic response of underdoped superconducting $Bi_2Sr_2CaCu_2O_{8+\delta}$ strongly excited by ultrashort light pulses. Phys. Rev. B **79**(22), 224502 (2009)
18. D. Fausti, R.I. Tobey, N. Dean, S. Kaiser, A. Dienst, M.C. Hoffmann, S. Pyon, T. Takayama, H. Takagi, A. Cavalleri, Light-induced superconductivity in a stripe-ordered cuprate. Science **331**(6014), 189–191 (2011)
19. W. Hu, S. Kaiser, D. Nicoletti, C.R. Hunt, I.A. Gierz, M.C. Hoffmann, M. Le Tacon, T. Loew, B. Keimer, A. Cavalleri, Optically enhanced coherent transport in $YBa_2Cu_3O_{6.5}$ by ultrafast redistribution of interlayer coupling. Nat. Mat. **13**(7), 705–711 (2014)
20. M. Mitrano, A. Cantaluppi, D. Nicoletti, S. Kaiser, A. Perucchi, S. Lupi, P. Di Pietro, D. Pontiroli, M. Riccò, S.R. Clark et al., Possible light-induced superconductivity in K_3C_{60} at high temperature. Nature **530**(7591), 461–464 (2016)
21. R.I. Tobey, D. Prabhakaran, A.T. Boothroyd, A. Cavalleri, Ultrafast electronic phase transition in $La_{1/2}Sr_{3/2}MnO_4$ by coherent vibrational excitation: evidence for nonthermal melting of orbital order. Phys. Rev. Lett. **101**(19), 197404 (2008)
22. P. Beaud, S.L. Johnson, E. Vorobeva, U. Staub, R.A. De Souza, C.J. Milne, Q.X. Jia, G. Ingold, Ultrafast structural phase transition driven by photoinduced melting of charge and orbital order. Phys. Rev. Lett. **103**(15), 155702 (2009)

23. J.A. Johnson, T. Kubacka, M.C. Hoffmann, C. Vicario, S. de Jong, P. Beaud, S. Grübel, S.-W. Huang, L. Huber, Y.W. Windsor, E.M. Bothschafter, L. Rettig, M. Ramakrishnan, A. Alberca, L. Patthey, Y.-D. Chuang, J.J. Turner, G.L. Dakovski, W.-S. Lee, M.P. Minitti, W. Schlotter, R.G. Moore, C.P. Hauri, S.M. Koohpayeh, V. Scagnoli, G. Ingold, S.L. Johnson, U. Staub, Magnetic order dynamics in optically excited multiferroic $TbMnO_3$. Phys. Rev. B **92**, 184429 (2015)
24. Y.H. Wang, H. Steinberg, P. Jarillo-Herrero, N. Gedik, Observation of Floquet-Bloch states on the surface of a topological insulator. Science **342**(6157), 453–457 (2013)
25. F. Mahmood, C.K. Chan, Z. Alpichshev, D. Gardner, Y. Lee, P.A. Lee, N. Gedik, Selective scattering between Floquet-Bloch and Volkov states in a topological insulator (2015)
26. R. Merlin, Generating coherent THz phonons with light pulses. Sol. State Comm. **102**(2), 207–220 (1997)
27. H.J. Zeiger, J. Vidal, T.K. Cheng, E.P. Ippen, G. Dresselhaus, M.S. Dresselhaus, Theory for displacive excitation of coherent phonons. Phys. Rev. B **45**(2), 768 (1992)
28. B. Mansart, J. Lorenzana, A. Mann, A. Odeh, M. Scarongella, M. Chergui, F. Carbone, Coupling of a high-energy excitation to superconducting quasiparticles in a cuprate from coherent charge fluctuation spectroscopy. Proc. Natl. Acad. Sci. **110**(12), 4539–4544 (2013)
29. A. Mann, E. Baldini, A. Tramontana, E. Pomjakushina, K. Conder, C. Arrell, F. van Mourik, J. Lorenzana, F. Carbone, Probing the electron-phonon interaction in correlated systems with coherent lattice fluctuation spectroscopy. Phys. Rev. B **92**(3), 035147 (2015)
30. D. Rossi, L.E. Camacho-Forero, G. Ramos-Sánchez, J.H. Han, J. Cheon, P. Balbuena, D.H. Son, Anisotropic electron-phonon coupling in colloidal layered TiS_2 nanodiscs observed via coherent acoustic phonons. J. Phys. Chem. C **119**(13), 7436–7442 (2015)
31. F. Novelli, G. Giovannetti, A. Avella, F. Cilento, L. Patthey, M. Radovic, M. Capone, F. Parmigiani, D. Fausti, Localized vibrations in superconducting $YBa_2Cu_3O_7$ revealed by ultrafast optical coherent spectroscopy. Phys. Rev. B **95**(17), 174524 (2017)
32. S. Borroni, E. Baldini, V.M. Katukuri, A. Mann, K. Parlinski, D. Legut, C. Arrell, F. van Mourik, J. Teyssier, A. Kozlowski, P. Piekarz, O.V. Yazyev, A.M. Oleś, J. Lorenzana, F. Carbone, Coherent generation of symmetry-forbidden phonons by light-induced electron-phonon interactions in magnetite. Phys. Rev. B **96**(10), 104308 (2017)
33. E. Baldini, A. Mann, B.P.P. Mallett, C. Arrell, F. Van Mourik, T. Wolf, D. Mihailovic, J.L. Tallon, C. Bernhard, J. Lorenzana, F. Carbone, Clocking the onset of bilayer coherence in a high-T_c cuprate. Phys. Rev. B **95**(2), 024501 (2017)
34. A. Mann, E. Baldini, A. Odeh, A. Magrez, H. Berger, F. Carbone, Probing the coupling between a doublon excitation and the charge-density wave in TaS_2 by ultrafast optical spectroscopy. Phys. Rev. B **94**, 115122 (2016)
35. C.A.D. Roeser, M. Kandyla, A. Mendioroz, E. Mazur, Optical control of coherent lattice vibrations in tellurium. Phys. Rev. B **70**(21), 212302 (2004)
36. S.I. Kudryashov, M. Kandyla, C.A.D. Roeser, E. Mazur, Intraband and interband optical deformation potentials in femtosecond-laser-excited α-Te. Phys. Rev. B **75**(8), 085207 (2007)
37. F. Novelli, G. De Filippis, V. Cataudella, M. Esposito, I. Vergara, F. Cilento, E. Sindici, A. Amaricci, C. Giannetti, D. Prabhakaran et al. Witnessing the formation and relaxation of dressed quasi-particles in a strongly correlated electron system. Nat. Comm., **5** (2014)
38. P. Hamm, M. Lim, R.M. Hochstrasser, Structure of the amide I band of peptides measured by femtosecond nonlinear-infrared spectroscopy. J. Phys. Chem. B **102**(31), 6123–6138 (1998)
39. J.D. Hybl, A.W. Albrecht, S.M.G. Faeder, D.M. Jonas, Two-dimensional electronic spectroscopy. Chem. Phys. Lett. **297**(3), 307–313 (1998)
40. T. Brixner, I.V. Stiopkin, G.R. Fleming, Tunable two-dimensional femtosecond spectroscopy. Opt. Lett. **29**(8), 884–886 (2004)
41. C. Consani, G. Auböck, F. van Mourik, M. Chergui, Ultrafast tryptophan-to-heme electron transfer in myoglobins revealed by UV 2D spectroscopy. Science **339**(6127), 1586–1589 (2013)
42. C Giannetti, New perspectives in the ultrafast spectroscopy of many-body excitations in correlated materials. Nuovo Cimento C Geophys. Space Phys. C, **39** (2016)

43. S.I. Anisimov, B.L. Kapeliovich, T.L. Perel'man, Electron emission from the metal surfaces induced by ultrashort lasers pulses. Zhurnal Ehksperimental'noj i Teoreticheskoj Fiziki **66**(2), 776–781 (1974)
44. S.D. Brorson, A. Kazeroonian, J.S. Moodera, D.W. Face, T.K. Cheng, E.P. Ippen, M.S. Dresselhaus, G. Dresselhaus, Femtosecond room-temperature measurement of the electron-phonon coupling constant γ in metallic superconductors. Phys. Rev. Lett. **64**(18), 2172 (1990)
45. C.-K. Sun, F. Vallée, L.H. Acioli, E.P. Ippen, J.G. Fujimoto, Femtosecond-tunable measurement of electron thermalization in gold. Phys. Rev. B **50**(20), 15337 (1994)
46. N. Del Fatti, C. Voisin, M. Achermann, S. Tzortzakis, D. Christofilos, F. Vallée, Nonequilibrium electron dynamics in noble metals. Phys. Rev. B **61**(24), 16956 (2000)
47. A. Kirilyuk, A.V. Kimel, T. Rasing, Ultrafast optical manipulation of magnetic order. Rev. Mod. Phys. **82**(3), 2731 (2010)
48. B. Mansart, D. Boschetto, A. Savoia, F. Rullier-Albenque, F. Bouquet, E. Papalazarou, A. Forget, D. Colson, A. Rousse, M. Marsi, Ultrafast transient response and electron-phonon coupling in the iron-pnictide superconductor $Ba(Fe_{(1-x)}Co(x))_2As_2$. Phys. Rev. B **82**, 024513 (2010)
49. B. Mansart, M.J.G. Cottet, G.F. Mancini, T. Jarlborg, S.B. Dugdale, S.L. Johnson, S.O. Mariager, C.J. Milne, P. Beaud, S. Grübel et al., Temperature-dependent electron-phonon coupling in $La_{2-x}Sr_xCuO_4$ probed by femtosecond x-ray diffraction. Phys. Rev. B **88**(5), 054507 (2013)
50. S. Dal Conte, C. Giannetti, G. Coslovich, F. Cilento, D. Bossini, T. Abebaw, F. Banfi, G. Ferrini, H. Eisaki, M. Greven et al., Disentangling the electronic and phononic glue in a high-T_c superconductor. Science **335**(6076), 1600–1603 (2012)
51. J. Demsar, R.D. Averitt, A.J. Taylor, V.V. Kabanov, W.N. Kang, H.J. Kim, E.M. Choi, S.I. Lee, Pair-breaking and superconducting state recovery dynamics in MgB_2. Phys. Rev. Lett. **91**(26), 267002 (2003)
52. S. Dal Conte, L. Vidmar, D. Golež, M. Mierzejewski, G.O. Soavi, S. Peli, F. Banfi, G. Ferrini, R. Comin, B.M. Ludbrook et al. Snapshots of the retarded interaction of charge carriers with ultrafast fluctuations in cuprates. Nat. Phys. **11**(5), 421–426 (2015)
53. S.K. Sundaram, E. Mazur, Inducing and probing non-thermal transitions in semiconductors using femtosecond laser pulses. Nat. Mat. **1**(4), 217–224 (2002)
54. A. Othonos, Probing ultrafast carrier and phonon dynamics in semiconductors. Jpn. J. Appl. Phys. **83**(4), 1789–1830 (1998)
55. P.T. Landsberg, *Recombination in Semiconductors*. (Cambridge University Press, 2003)
56. H. Okamoto, T. Miyagoe, K. Kobayashi, H. Uemura, H. Nishioka, H. Matsuzaki, A. Sawa, Y. Tokura, Ultrafast charge dynamics in photoexcited Nd_2CuO_4 and La_2CuO_4 cuprate compounds investigated by femtosecond absorption spectroscopy. Phys. Rev. B **82**(6), 060513 (2010)
57. H. Okamoto, T. Miyagoe, K. Kobayashi, H. Uemura, H. Nishioka, H. Matsuzaki, A. Sawa, Y. Tokura, Photoinduced transition from Mott insulator to metal in the undoped cuprates Nd_2CuO_4 and La_2CuO_4. Phys. Rev. B **83**(12), 125102 (2011)
58. N. Peyghambarian, H.M. Gibbs, J.L. Jewell, A. Antonetti, A. Migus, D. Hulin, A. Mysyrowicz, Blue shift of the exciton resonance due to exciton-exciton interactions in a multiple-quantum-well structure. Phys. Rev. Lett. **53**, 2433–2436 (1984)
59. S. Hunsche, K. Leo, H. Kurz, K. Köhler, Exciton absorption saturation by phase-space filling: influence of carrier temperature and density. Phys. Rev. B **49**(23), 16565 (1994)
60. S. De Silvestri, J.G. Fujimoto, E.P. Ippen, E.B. Gamble, L.R. Williams, K.A. Nelson, Femtosecond time-resolved measurements of optic phonon dephasing by impulsive stimulated raman scattering in α-perylene crystal from 20 to 300 K. Chem. Phys. Lett. **116**(2–3), 146–152 (1985)
61. T.K. Cheng, S.D. Brorson, A.S. Kazeroonian, J.S. Moodera, G.D.M.S. Dresselhaus, M.S. Dresselhaus, E.P. Ippen, Impulsive excitation of coherent phonons observed in reflection in bismuth and antimony. Appl. Phys. Lett. **57**(10), 1004–1006 (1990)

62. G.C. Cho, W. Kütt, H. Kurz, Subpicosecond time-resolved coherent-phonon oscillations in GaAs. Phys. Rev. Lett. **65**(6), 764 (1990)
63. J. Zhao, A.V. Bragas, D.J. Lockwood, R. Merlin, Magnon squeezing in an antiferromagnet: reducing the spin noise below the standard quantum limit. Phys. Rev. Lett. **93**(10), 107203 (2004)
64. D. Polli, M. Rini, S. Wall, R.W. Schoenlein, Y. Tomioka, Y. Tokura, G. Cerullo, A. Cavalleri, Coherent orbital waves in the photo-induced insulator-metal dynamics of a magnetoresistive manganite. Nat. Mat. **6**(9), 643–647 (2007)
65. D.H. Torchinsky, F. Mahmood, A.T. Bollinger, I. Boovi, N. Gedik, Fluctuating charge-density waves in a cuprate superconductor. Nat. Mat. **12**(5), 387–391 (2013)
66. R. Matsunaga, Y.I. Hamada, K. Makise, Y. Uzawa, H. Terai, Z. Wang, R. Shimano, Higgs amplitude mode in the BCS superconductors $Nb_{1-x}Ti_xN$ induced by terahertz pulse excitation. Phys. Rev. Lett. **111**(5), 057002 (2013)
67. R. Matsunaga, N. Tsuji, H. Fujita, A. Sugioka, K. Makise, Y. Uzawa, H. Terai, Z. Wang, H. Aoki, R. Shimano, Light-induced collective pseudospin precession resonating with Higgs mode in a superconductor. Science **345**(6201), 1145–1149 (2014)
68. T.E. Stevens, J. Kuhl, R. Merlin, Coherent phonon generation and the two stimulated Raman tensors. Phys. Rev. B **65**(14), 144304 (2002)
69. C. Thomsen, J. Strait, Z. Vardeny, H.J. Maris, J. Tauc, J.J. Hauser, Coherent phonon generation and detection by picosecond light pulses. Phys. Rev. Lett. **53**(10), 989 (1984)
70. C. Thomsen, H.T. Grahn, H.J. Maris, J. Tauc, Surface generation and detection of phonons by picosecond light pulses. Phys. Rev. B **34**(6), 4129 (1986)
71. P. Ruello, V.E. Gusev, Physical mechanisms of coherent acoustic phonons generation by ultrafast laser action. Ultrasonics **56**, 21–35 (2015)
72. Y.-C. Wen, T.-S. Ko, T.-H. Lu, H.-C. Kuo, J.-I. Chyi, C.-K. Sun, Photogeneration of coherent shear phonons in orientated wurtzite semiconductors by piezoelectric coupling. Phys. Rev. B **80**(19), 195201 (2009)
73. O. Matsuda, O.B. Wright, D.H. Hurley, V.E. Gusev, K. Shimizu, Coherent shear phonon generation and detection with ultrashort optical pulses. Phys. Rev. Lett. **93**(9), 095501 (2004)
74. C.V. Korff Schmising, A. Harpoeth, N. Zhavoronkov, Z. Ansari, C. Aku-Leh, M. Woerner, T. Elsaesser, M. Bargheer, M. Schmidbauer, I. Vrejoiu et al. Ultrafast magnetostriction and phonon-mediated stress in a photoexcited ferromagnet. Phys. Rev. B **78**(6), 060404 (2008)
75. J.J. Li, J. Chen, D.A. Reis, S. Fahy, R. Merlin, Optical probing of ultrafast electronic decay in Bi and Sb with slow phonons. Phys. Rev. Lett. **110**(4), 047401 (2013)
76. F. Schmitt, P.S. Kirchmann, U. Bovensiepen, R.G. Moore, L. Rettig, M. Krenz, J.H. Chu, N. Ru, L. Perfetti, D.H. Lu et al., Transient electronic structure and melting of a charge density wave in $TbTe_3$. Science **321**(5896), 1649–1652 (2008)
77. J.C. Petersen, S. Kaiser, N. Dean, A. Simoncig, H.Y. Liu, A.L. Cavalieri, C. Cacho, I.C.E. Turcu, E. Springate, F. Frassetto et al., Clocking the melting transition of charge and lattice order in 1T-TaS_2 with ultrafast extreme-ultraviolet angle-resolved photoemission spectroscopy. Phys. Rev. Lett. **107**(17), 177402 (2011)
78. L.X. Yang, G. Rohde, T. Rohwer, A. Stange, K. Hanff, C. Sohrt, L. Rettig, R. Cortés, F. Chen, D.L. Feng et al., Ultrafast modulation of the chemical potential in $BaFe_2As_2$ by coherent phonons. Phys. Rev. Lett. **112**(20), 207001 (2014)
79. A.M. Lindenberg, I. Kang, S.L. Johnson, T. Missalla, P.A. Heimann, Z. Chang, J. Larsson, P.H. Bucksbaum, H.C. Kapteyn, H.A. Padmore et al., Time-resolved x-ray diffraction from coherent phonons during a laser-induced phase transition. Phys. Rev. Lett. **84**(1), 111 (2000)
80. K. Sokolowski-Tinten, C. Blome, J. Blums, A. Cavalleri, C. Dietrich, A. Tarasevitch, I. Uschmann, E. Förster, M. Kammler, M. Horn-von Hoegen, D. von der Linde, Femtosecond x-ray measurement of coherent lattice vibrations near the lindemann stability limit. Nature **422**(6929), 287–289 (2003)
81. M. Bargheer, N. Zhavoronkov, Y. Gritsai, J.C. Woo, D.S. Kim, M. Wörner, T. Elsässer, Coherent atomic motions in a nanostructure studied by femtosecond x-ray diffraction. Science **306**(5702), 1771–1773 (2004)

82. S.L. Johnson, P. Beaud, E. Vorobeva, C.J. Milne, E.D. Murray, S. Fahy, G. Ingold, Directly observing squeezed phonon states with femtosecond x-ray diffraction. Phys. Rev. Lett. **102**(17), 175503 (2009)
83. P. Beaud, A. Caviezel, S.O. Mariager, L. Rettig, G. Ingold, C. Dornes, S.W. Huang, J.A. Johnson, M. Radovic, T. Huber et al., A time-dependent order parameter for ultrafast photoinduced phase transitions. Nat. Mat. **13**(10), 923–927 (2014)
84. H. Park, X. Wang, S. Nie, R. Clinite, J. Cao, Mechanism of coherent acoustic phonon generation under nonequilibrium conditions. Phys. Rev. B **72**(10), 100301 (2005)
85. L. Piazza, C. Ma, H.X. Yang, A. Mann, Y. Zhu, J.Q. Li, F. Carbone, Ultrafast structural and electronic dynamics of the metallic phase in a layered manganite. Structural Dynamics **1**(1), 014501 (2014)
86. D.R. Cremons, D.A. Plemmons, D.J. Flannigan, Femtosecond electron imaging of defect-modulated phonon dynamics. Nat. Comm., 7 (2016)
87. G. Ju, A.V. Nurmikko, R.F.C. Farrow, R.F. Marks, M.J. Carey, B.A. Gurney, Ultrafast time resolved photoinduced magnetization rotation in a ferromagnetic/antiferromagnetic exchange coupled system. Phys. Rev. Lett. **82**(18), 3705 (1999)
88. J. Qi, Y. Xu, N.H. Tolk, X. Liu, J.K. Furdyna, I.E. Perakis, Coherent magnetization precession in GaMnAs induced by ultrafast optical excitation. Appl. Phys. Lett. **91**(11), 2506 (2007)
89. N.P. Duong, T. Satoh, M. Fiebig, Ultrafast manipulation of antiferromagnetism of NiO. Phys. Rev. Lett. **93**(11), 117402 (2004)
90. M. Lisowski, P.A. Loukakos, A. Melnikov, I. Radu, L. Ungureanu, M. Wolf, U. Bovensiepen, Femtosecond electron and spin dynamics in Gd (0001) studied by time-resolved photoemission and magneto-optics. Phys. Rev. Lett. **95**(13), 137402 (2005)
91. D. Polli, L. Lüer, G. Cerullo, High-time-resolution pump-probe system with broadband detection for the study of time-domain vibrational dynamics. Rev. Sci. Instrum. **78**(10), 103108–103108 (2007)
92. U. Megerle, I. Pugliesi, C. Schriever, C.F. Sailer, E. Riedle, Sub-50 fs broadband absorption spectroscopy with tunable excitation: putting the analysis of ultrafast molecular dynamics on solid ground. Appl. Phys. B **96**(2–3), 215–231 (2009)
93. G. Auböck, C. Consani, F. van Mourik, M. Chergui, Ultrabroadband femtosecond two-dimensional ultraviolet transient absorption. Opt. Lett. **37**(12), 2337–2339 (2012)
94. G. Auböck, C. Consani, R. Monni, A. Cannizzo, F. van Mourik, M. Chergui, Femtosecond pump/supercontinuum-probe setup with 20 kHz repetition rate. Rev. Sci. Instrum. **83**(9), 093105 (2012)
95. R.W. Schoenlein, W.Z. Lin, J.G. Fujimoto, G.L. Eesley, Femtosecond studies of nonequilibrium electronic processes in metals. Phys. Rev. Lett. **58**(16), 1680 (1987)
96. V.V. Kruglyak, R.J. Hicken, P. Matousek, M. Towrie, Spectroscopic study of optically induced ultrafast electron dynamics in gold. Phys. Rev. B **75**(3), 035410 (2007)
97. C.V. Shank, R.L. Fork, R.F. Leheny, J. Shah, Dynamics of photoexcited GaAs band-edge absorption with subpicosecond resolution. Phys. Rev. Lett. **42**, 112–115 (1979)
98. R.A. Kaindl, M. Woerner, T. Elsaesser, D.C. Smith, J.F. Ryan, G.A. Farnan, M.P. McCurry, D.G. Walmsley, Ultrafast mid-infrared response of $YBa_2Cu_3O_{7-\delta}$. Science **287**(5452), 470–473 (2000)
99. S. Wall, D. Brida, S.R. Clark, H.P. Ehrke, D. Jaksch, A. Ardavan, S. Bonora, H. Uemura, Y. Takahashi, T. Hasegawa et al., Quantum interference between charge excitation paths in a solid-state Mott insulator. Nat. Phys. **7**(2), 114–118 (2011)
100. A. Pashkin, M. Porer, M. Beyer, K.W. Kim, A. Dubroka, C. Bernhard, X. Yao, Y. Dagan, R. Hackl, A. Erb, A. Erb, Femtosecond response of quasiparticles and phonons in superconducting $YBa_2Cu_3O_{7-\delta}$ studied by wideband terahertz spectroscopy. Phys. Rev. Lett. **105**(6), 067001 (2010)
101. E. Baldini, L. Chiodo, A. Dominguez, M. Palummo, S. Moser, M. Yazdi-Rizi, G. Auböck, B.P.P. Mallett, H. Berger, A. Magrez, C. Bernhard, M. Grioni, A. Rubio, M. Chergui, Strongly bound excitons in anatase TiO_2 single crystals and nanoparticles. Nat. Comm., 8, 13 (2017)

102. C. Giannetti, F. Cilento, S. Dal Conte, G. Coslovich, G. Ferrini, H. Molegraaf, M. Raichle, R. Liang, H. Eisaki, M. Greven et al., Revealing the high-energy electronic excitations underlying the onset of high-temperature superconductivity in cuprates. Nat. Comm. **2**, 353 (2011)
103. F. Cilento, S. Dal Conte, G. Coslovich, S. Peli, N. Nembrini, S. Mor, F. Banfi, G. Ferrini, H. Eisaki, M.K. Chan et al., Photo-enhanced antinodal conductivity in the pseudogap state of high-T_c cuprates. Nat. Comm., 5 (2014)
104. F. Novelli, D. Fausti, J. Reul, F. Cilento, P.H.M. van Loosdrecht, A.A. Nugroho, T.T.M. Palstra, M. Grüninger, F. Parmigiani, Ultrafast optical spectroscopy of the lowest energy excitations in the Mott insulator compound YVO_3: evidence for Hubbard-type excitons. Phys. Rev. B **86**(16), 165135 (2012)
105. F. Randi, I. Vergara, F. Novelli, M. Esposito, M. Dell'Angela, V. Brabers, P. Metcalf, R. Kukreja, H.A. Dürr, D. Fausti et al. Phase separation in the nonequilibrium Verwey transition in magnetite
106. E. Baldini, A. Mann, S. Borroni, C. Arrell, F. van Mourik, F. Carbone, A versatile setup for ultrafast broadband optical spectroscopy of coherent collective modes in strongly correlated quantum systems. Struc. Dyn. **3**(6), 064301 (2016)
107. L. Huang, J.P. Callan, E.N. Glezer, E. Mazur, GaAs under intense ultrafast excitation: response of the dielectric function. Phys. Rev. Lett. **80**, 185–188 (1998)
108. C.A.D. Roeser, A.M.-T. Kim, J.P. Callan, L. Huang, E.N. Glezer, Y. Siegal, E. Mazur, Femtosecond time-resolved dielectric function measurements by dual-angle reflectometry. Rev. Sci. Instr. **74**(7), 3413–3422 (2003)
109. F. Boschini, H. Hedayat, C. Piovera, C. Dallera, A. Gupta, E. Carpene, A flexible experimental setup for femtosecond time-resolved broad-band ellipsometry and magneto-optics. Rev. Sci. Instrum. **86**(1), 013909 (2015)
110. J. Ojeda, C.A. Arrell, J. Grilj, F. Frassetto, L. Mewes, H. Zhang, F. van Mourik, L. Poletto, M. Chergui, Harmonium: a pulse preserving source of monochromatic extreme ultraviolet (30–110 eV) radiation for ultrafast photoelectron spectroscopy of liquids. Struct. Dyn. **3**(2), 023602 (2016)
111. N. Gedik, D. Yang, G. Logvenov, I. Bozovic, A.H. Zewail, Nonequilibrium phase transitions in cuprates observed by ultrafast electron crystallography. Science **316**(5823), 425–429 (2007)
112. M. Eichberger, H. Schäfer, M. Krumova, M. Beyer, J. Demsar, H. Berger, G. Moriena, G. Sciaini, R.J.D. Miller, Snapshots of cooperative atomic motions in the optical suppression of charge density waves. Nature **468**(7325), 799–802 (2010)
113. C. Tseng, S. Matsika, T.C. Weinacht, Two-dimensional ultrafast Fourier transform spectroscopy in the deep ultraviolet. Opt. Express **17**(21), 18788–18793 (2009)
114. U. Selig, C.F. Schleussner, M. Foerster, F. Langhojer, P. Nuernberger, T. Brixner, Coherent two-dimensional ultraviolet spectroscopy in fully noncollinear geometry. Opt. Lett. **35**(24), 4178–4180 (2010)
115. B.A. West, J.M. Womick, A.M. Moran, Probing ultrafast dynamics in adenine with mid-UV four-wave mixing spectroscopies. J. Phys. Chem. A **115**(31), 8630–8637 (2011)
116. X. Li, T. Zhang, C.N. Borca, S.T. Cundiff, Many-body interactions in semiconductors probed by optical two-dimensional Fourier transform spectroscopy. Phys. Rev. Lett. **96**(5), 057406 (2006)
117. T. Zhang, I. Kuznetsova, T. Meier, X. Li, R.P. Mirin, P. Thomas, S.T. Cundiff, Polarization-dependent optical 2D Fourier transform spectroscopy of semiconductors. Proc. Natl. Acad. Sci. **104**(36), 14227–14232 (2007)
118. K.W. Stone, K. Gundogdu, D.B. Turner, X. Li, S.T. Cundiff, K.A. Nelson, Two-quantum 2D FT electronic spectroscopy of biexcitons in GaAs quantum wells. Science **324**(5931), 1169–1173 (2009)
119. W. Kuehn, K. Reimann, M. Woerner, T. Elsaesser, R. Hey, U. Schade, Strong correlation of electronic and lattice excitations in GaAs/AlGaAs semiconductor quantum wells revealed by two-dimensional terahertz spectroscopy. Phys. Rev. Lett. **107**(6), 067401 (2011)
120. P. Bowlan, E.M. Moreno, K. Reimann, M. Woerner, T. Elsaesser, Ultrafast two-dimensional THz spectroscopy of graphene, in *EPJ Web of Conferences*, vol. 41 (EDP Sciences, 2013), p. 04024

121. R. Newman, R.M. Chrenko, Optical properties of nickel oxide. Phys. Rev. **114**(6), 1507 (1959)
122. C. Taranto, G. Sangiovanni, K. Held, M. Capone, A. Georges, A. Toschi, Signature of antiferromagnetic long-range order in the optical spectrum of strongly correlated electron systems. Phys. Rev. B **85**(8), 085124 (2012)
123. M. Oppermann, N.S. Nagornova, A. Oriana, E. Baldini, L. Mewes, B. Bauer, T. Palmieri, T. Rossi, F. van Mourik, M. Chergui, The LOUVRE laboratory: state-of-the-art ultrafast ultraviolet spectroscopies for molecular and materials science. CHIMIA Int. J. Chem. **71**(5), 288–294 (2017)

Chapter 3
Clocking the Interband Scattering in Strongly Interacting Multiband Metals

One of the cornerstones of ultrafast spectroscopy is the ability to disentangle the carrier dynamics from the response of other degrees of freedom. The origin of this concept is intimately related to the so-called two-temperature model, the earliest and simplest phenomenological model describing the nonequilibrium response of conventional Fermi liquids [1]. According to this scenario, the interaction between an optical pump pulse and the solid solely involves the electronic degrees of freedom, raising their temperature T_e while leaving the lattice temperature T_L unchanged. As the system evolves, energy exchange among the hot electrons and the lattice occurs until $T_e = T_L$. After that, the system eventually relaxes on longer timescales to reach the thermodynamic equilibrium. The first strong assumption behind this model is that the electron and phonon subsystems are each maintained in a thermalized state by Coulomb electron-electron and anharmonic phonon-phonon interaction, respectively. Moreover, the electron-electron scattering rate is considered to be much larger than the electron-phonon scattering rate. This, in turn, leads to the description of the system via two coupled differential equations, whose dynamics is governed by the electron-phonon coupling constant. Besides requiring small corrections to its original formulation, the two-temperature model still provides a robust starting point to interpret the ultrafast dynamics of weakly interacting and correlated metals [2–4].

Going beyond conventional band theory, the two-temperature model is seriously invalidated when strong electron-boson interaction plays a central role in the physics of metals and semimetals. Whenever a preferential electron-boson interaction channel exists, it dominates the carrier thermalization via simultaneous heating of the bosonic mode. In the last years, a body of work has demonstrated the emergence of hot optical phonon effects in graphite [5–8] and graphene [9], leading to the failure of the two-temperature model. Key ingredient to this scenario is the fall of

Parts of this chapter are reprinted with permission from E. Baldini et al., Physical Review Letters 119, 097002. Copyright 2017 American Physical Society.

E. Baldini, *Nonequilibrium Dynamics of Collective Excitations in Quantum Materials*, Springer Theses, https://doi.org/10.1007/978-3-319-77498-5_3

the assumption that the electron-electron scattering proceeds much faster than the electron-phonon scattering. This is particularly true in semimetals, where strong electron-phonon coupling arises due to the ineffective screening of the Coulomb interaction [10, 11]. Clear manifestations of such a strong coupling involve the presence of Kohn anomalies [12] and the shift of the phonon frequencies upon carrier doping [13]. In this strong coupling regime, the photoexcited *nonthermal* electron distribution has an increased probability to generate hot optical phonon modes before degrading into a lower energy quasiequilibrium electron distribution. In carbon-based materials, the formation of such a quasi-Fermi carrier distribution by the combined action of electron-electron and electron-phonon interaction is found to occur within 250 fs [7, 9]. This suggests that the duration of the nonthermal electron distribution concurs with the strong electron-phonon coupling to efficiently generate hot phonons within this first stage of "*coupled*" dynamics [7, 8].

Differently from cold phonons, hot phonons can be reabsorbed by the carriers, resulting in a slower electron cooling that persist for several picoseconds [9]. The strongly coupled lattice modes in graphite are represented by the E_{2g1} interlayer shear mode and the E_{2g2} carbon stretching mode [6]. Importantly, due to their high quantum energies up to 200 meV, these modes can be effectively become hot only in the presence of high-energy electrons, as those photoexcited by an ultrashort laser pulse in the optical range. Once set out of equilibrium, hot phonons cool down within a timescale of tens of picoseconds [5], i.e. the time required by lattice anharmonicity to dissipate their excess energy via phonon-phonon scattering.

From this discussion, it emerges that photoexciting a strongly interacting semimetal typically leads to an ultrafast and efficient hot phonon generation. Nowadays, this picture is well accepted in a large part of the ultrafast spectroscopy community and is raising interest in the fields of condensed matter theory and material science. On the theory side, these phenomena are still lacking a complete and detailed many-body framework, especially due to the difficulty of developing a nonequilibrium approach. On the application side, strongly coupled optical phonons are believed to hinder the dc transport and cause the energy relaxation of electrons subjected to high electric fields in carbon-based materials [14]. With this respect, it is important to underline that in these compounds the hot phonon generation proceeds dramatically faster than in doped semiconductors, in which such phenomenon has been first explored [15, 16]. This is due to the strong electron-phonon coupling present in these semimetals and the large phonon quantum energies involved.

A step further in hot phonon research involves the observation of an anisotropic coupling between different subsets of carriers and a specific phonon. An intriguing system that can serve as a benchmark for this purpose is represented by the anisotropic Fermi liquid MgB_2. The crystal structure of this material consists of graphite-type layers of B atoms, separated by hexagonal close-packed layers of Mg. As such, it shares a similar crystal structure to graphite. More interestingly, this anisotropic compound provides a rare example of two-band phonon-mediated superconductor in the strong coupling regime below $T_C = 39$ K [17]. Thus, in its normal state, MgB_2 is characterized by the simultaneous presence of two electronic subsystems, known as the σ and π carriers, governing the low-energy transport and electrodynamic

properties [18]. The electron-phonon coupling is very asymmetric between the two electronic subsets, as the σ holes display a coupling three times larger than the π carriers [19–23]. So far, the existence of a highly anisotropic electron-phonon coupling in the σ- and π-bands has been accessed experimentally only in an indirect way, via quantum oscillations [24] or as a signature of the two superconducting gaps [25, 26]. The optical phonon branch of interest is the one of the E_{2g} mode, involving the in-plane stretching of the B-B bonds and giving rise to a strong peak in the Eliashberg function $\alpha^2F(\omega)$ around 70 meV [19, 20, 23, 27, 28]. The combination of multiband behaviour and strong electron-phonon coupling with *only one* high-energy mode makes MgB_2 a fascinating candidate in which to observe novel effects related to hot phonon generation and dissipation. Preliminary evidence for the presence of hot phonon effects in MgB_2 has been provided by a recent broadband pump-probe study in the near-infrared [29], but could not be interpreted in relation to the multiband framework due to the absence of a clear observable. To overcome these limitations and disentangle the dynamics of both types of carriers, one needs to selectively monitor suitable observables under nonequilibrium conditions. In MgB_2, the large disparity of electron-phonon coupling between the two electronic subsystems allows one to exploit hot phonon effects as a platform for highlighting the dynamics of the σ holes and disentangling it from the response of the π carriers. By combining this observable in the time domain with a spectral feature associated solely with the π carriers, a complete mapping of the charge dynamics within the two bands can be achieved. This aspect is of pivotal interest in MgB_2, as it sheds light on a fascinating topic that has remained elusive over the years, namely the mechanism responsible for connecting the two bands in the normal state. Depending on its origin (electron- or phonon-mediated), such interband scattering is expected to take place on a sub-picosecond or picosecond timescale, which requires the intrinsic time-resolution of ultrafast spectroscopies to be unravelled.

In this Chapter, we reveal the presence of hot phonon effects and elucidate the off-diagonal scattering mechanism connecting the two different bands in MgB_2 [30]. To this aim, we photoexcite both the σ and π carriers with an ultrashort laser pulse and we subsequently monitor the change of reflectivity in a broad spectral range covering the plasma edges of the *a*- and *c*-axis. While the dynamics of the σ carriers is entangled with the ultrafast response of the hot phonon modes to which they are strongly coupled, the signature of the π carriers is uniquely encoded in the renormalization of the *c*-axis plasmon in the material. Thus, the combination of high temporal resolution and broad probing range allows us to separate the contributions of the σ and π carriers, leading to the observation of a phonon-mediated interband scattering mechanism. Furthermore, this work shows that the photoinduced creation of a hot phonon bath in a multiband system can be used to selectively trigger a transient increase of the number of carriers in a given band, opening new perspectives for the selective carrier-density manipulation via near-infrared light. Section 3.1 is devoted to the description of the intrinsic properties of MgB_2, focusing on its peculiar band structure. This naturally leads to the discussion of the electrodynamic properties of the material under equilibrium conditions, which are presented in Sect. 3.2. Section 3.3 illustrates the spontaneous Raman scattering response of the material, putting special emphasis

on the role played by the E_{2g} mode at $\mathbf{q} = 0$. Section 3.4 focuses on our nonequilibrium study, which leads to the identification of hot phonon effects and the observation of the σ-π interband scattering process. Section 3.5 shows the results of the theoretical calculations that rationalise our findings. Conclusions are given in Sect. 3.7.

3.1 MgB_2

A prototypical multiband system with strong electron-phonon interaction is MgB_2, which crystallises with alternating hexagonal layers of Mg atoms and graphite-like honeycomb layers of B atoms (Fig. 3.1a). Despite having been synthesised for the first time in the 1950s [32], this material had not received particular attention for almost fifty years. The scenario changed tremendously in 2001, following the discovery of high-T_C superconductivity at temperatures as high as 39 K [17]. At the beginning, the high-T_C was erroneously considered as the signature of an unconventional (i.e. non-BCS) type of pairing in this material. Soon after, studies of the B isotope effect on T_C [33] and experiments on the ^{11}B nuclear spin-lattice relaxation rate [34] indicated that an s-wave phonon-mediated mechanism of superconductivity is instead at play in MgB_2. To correctly describe the BCS-like superconductivity at 39 K in MgB_2, the crucial elements to evaluate were represented by the electronic structure, the phonon dispersion and the electron-phonon coupling.

The calculation of the electronic structure and Fermi surface of MgB_2 led to a first intriguing result [18]. The band structure is shown in Fig. 3.1b, as calculated

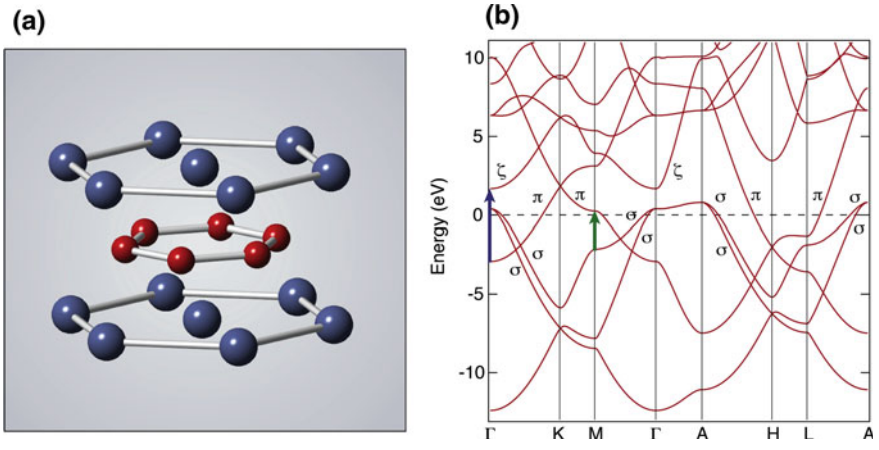

Fig. 3.1 **a** Crystallographic structure of MgB_2 with highlighted Mg and B hexagons. Blue atoms represent Mg, red atoms represent B. **b** Band structure of MgB_2 adapted from Ref. [31]. The Fermi level E_F is at zero energy and the σ, π and ζ bands are indicated. The green arrow represents the σ-π interband transition, while the blue arrow the π-ζ transitions that define the c-axis plasmon energy

in Ref. [31]. Two distinct electronic bands are observed to cross the Fermi energy (E_F), namely the quasi-2D hole-like σ bands, formed by hybridized s-$p_{x,y}$ orbitals of the B atoms, and the three-dimensional (3D) hole- and electron-like π bands with B p_z symmetry. This peculiar electronic structure is at the origin of an exotic phenomenon emerging in MgB_2, namely the appearance of multiple SC gaps. This two-band superconductivity scenario was first proposed theoretically [35] and soon confirmed experimentally by a number of studies, including heat capacity experiments [36], ARPES [25], STS [37, 38] and spontaneous Raman scattering [26, 39–42]. The calculation of the phonon dispersion and related electron-phonon coupling led to identify the doubly degenerate mode with E_{2g} symmetry at Γ as the phonon responsible for the high-T_C behaviour of MgB_2 [19, 20, 23, 27, 28]. This optical phonon involves the in-plane (hexagon distorting) movement of B atoms and displays a high degree of anharmonicity. The eigenvector associated with this mode causes a large modification in the orbital overlap between neighbouring B atoms, thus modulating in particular the energies of the σ bonds. As a result, the holes residing in the σ bands along the Γ-A direction of the BZ interact very strongly with this optical phonon branch and display a three-times larger coupling than the carriers at the top of the π bands [19–23]. The coupling was also predicted to possess a nonlinear character [27]. The two SC gaps in MgB_2 arise naturally from the different strengths of the electron-phonon coupling in the σ and π bands, which have been successfully modelled via Eliashberg theory [22, 23]. The value of T_C can be considered as the result of competing effects of small carrier density in the σ bands, large and nonlinear electron-phonon coupling, and phonon anharmonicity. In this respect, MgB_2 represents a very rare system, where multiband physics and strong electron-phonon coupling coexist and concur in providing peculiarity to the properties of an otherwise conventional superconductor. For example, if the two electronic bands were independent, two non-interacting SC condensates would share the same lattice but display different T_C's and distinct SC properties. In contrast, in the presence of a large interaction, the two bands would become mixed and the distinction of their energy gaps would be removed. In MgB_2, the two electronic subsystems weakly interact through scattering from states in one band to states in the other and through Coulomb repulsion. This small interaction is responsible for many properties of MgB_2, causing for instance both bands to become SC at the same T_C but with different gap energies. One of the main goals of our study is to observe the real-time crosstalk between the σ and π bands and to identify the mechanism lying at the origin of this interband scattering on the basis of its timescale.

3.2 Steady-State Optical Properties

The starting point of our study naturally follows the characterization of the single-particle electronic structure of MgB_2 and deals with the electrodynamic properties of the material. Indeed, optical experiments have provided key insights into the multiband structure of MgB_2 and the strength of the electron-phonon interaction.

Figure 3.2a shows the real part of the optical conductivity $\sigma_1(\omega)$ at RT, in response to an in-plane (blue curve) or c-axis (pink curve) polarized electric field. The spectra have been adapted from the SE measurements of Ref. [43]. The in-plane and c-axis response exhibit a strongly anisotropic character but share a similar metallic behaviour, characterized by a Drude peak at low energies. In the in-plane response an intense interband transition also emerges at 2.60 eV. Such interband transition occurs at the M point of the BZ [44], where a Van Hove singularity strongly enhances the DOS [18]. As this excitation involves occupied states in the σ band below E_F and unoccupied states in the π band above E_F, it is typically referred to as the σ-π interband transition (indicated as a green arrow in Fig. 3.1b).

The metallic nature of the system and the emergence of the σ-π interband transition become also evident in the steady-state reflectivity $R(\omega)$, which is displayed in Fig. 3.2b as calculated from SE measurements. Consistent with the data of Fig. 3.2a, we observe the presence of a reflectivity plasma edge that extends up to 2.00 eV in the in-plane response and to 2.60 eV in the c-axis response. While the in-plane plasma edge is significantly broadened by the presence of the intense interband transition at 2.60 eV, the c-axis plasma edge is very sharp.

In the electrodynamics of the material, the contrast between the two subsets of carriers emerges from the different anisotropies of the plasma frequencies $\omega_{p,\sigma}$ and $\omega_{p,\pi}$ contributing to the in-plane- and c-axis responses. Indeed, from previous optical studies, it was concluded that the cylinder-like 2D σ bands possess a negligible electromagnetic response along the c-axis and play a relevant role only in the in-plane conduction [43–45], in agreement with measurements of the Hall coefficient [46]. As a consequence, the c-axis optical response of MgB_2 is totally dominated by

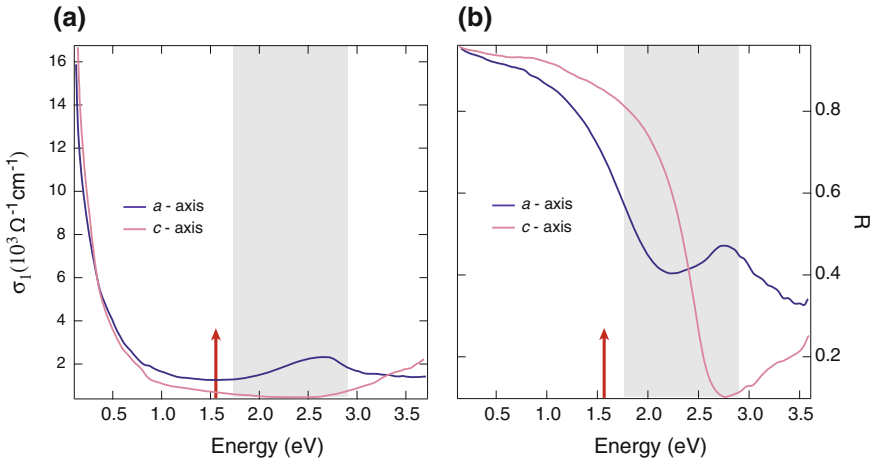

Fig. 3.2 **a** Real part of the optical conductivity and **b** reflectivity of MgB_2 measured via SE at RT along the a-(blue curves) and c-axis (pink curves). The data have been adapted from Ref. [43]. The red arrow indicates the pump photon energy and the grey shaded area the probing range of the nonequilibrium experiment

the contribution of the more 3D π bands. This scenario has been further refined by theoretical calculations of the σ and π contributions to the plasma-edges [47]. Hence, the in-plane bare plasma frequency reflects a mixed response between the σ holes and π carriers, while the c-axis bare plasma frequency is an extremely sensitive probe of the π carrier density.

The importance of the plasma frequency calls for a deeper investigation of the real part of the dielectric function ϵ_1, as it can reveal insightful information on the existence of collective plasmon modes in correspondence to the drop in reflectivity. The real part of the dielectric function ϵ_1 is shown in Fig. 3.3a. While the in-plane response maintains a negative sign over the whole spectral range, the c-axis response changes sign in correspondence to 2.65 eV. This zero-crossing in ϵ_1 is the signature of a longitudinal plasmon mode appearing at the screened plasma frequency $\omega^*_{p,c}$ = 2.65 eV. Correspondingly, a peak is expected to take place at the same energy in the loss function of the system.

This plasmon has been subject of intensive theoretical and experimental study in the past [31, 48–51]. Although this bosonic mode has no relevance to superconductivity [50], from the previous discussion it is evident that such a plasmon has a strong impact on the dielectric and electrodynamic properties of the material [43, 48], leading to the two-colour nature of MgB_2 depending on the incident light polarization [43]. Ab initio calculations highlighted that the energy of this collective mode is mainly determined by the interband transitions from the B π to the Mg ζ bands, which possess an almost parallel dispersion in the Γ-K-M plane of the BZ (indicated with the blue arrow in Fig. 3.1b) [49]. Correspondingly, its real-space charge distribution involves coherent charge fluctuations between parallel sheets of B and Mg

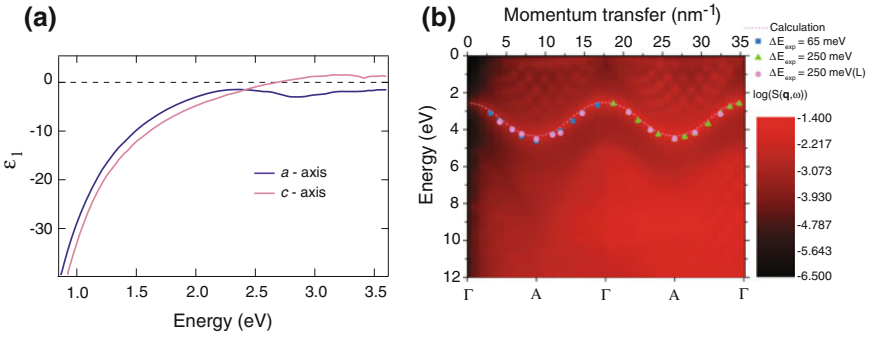

Fig. 3.3 **a** Real part of the dielectric function of MgB_2 measured via SE at RT along the a-(blue curves) and c-axis (pink curves). The c-axis response changes sign around 2.65 eV, indicating the emergence of a plasmon mode. The data have been adapted from Ref. [43]. **b** Calculated and measured energy-momentum dispersion relation of the c-axis plasmon. The experimental data are indicated as symbols on top of the calculated cosinusoidal dispersion and have been obtained using different experimental energy resolution conditions. The figure has been reprinted with permission from Y. Q. Cai et al., Physical Review Letters 97, 176402. Copyright 2006 American Physical Society [48]

atoms. Finally, the dispersion of this collective mode far from $\mathbf{q} = 0$ has been investigated by EELS and IXS measurements [48, 51]. Remarkably, it was found that due to the strong coupling between single-particle and collective excitation channels in MgB_2, the conventional Landau-damping mechanism does not restrict this mode to a small fraction of the momentum space [52], leading to the extension of its sinusoidal dispersion to higher BZs along the c^* axis [48]. The energy-momentum dispersion relation of the *c*-axis plasmon is shown in Fig. 3.3b, which has been adapted from Ref. [48].

Despite the wealth of information that can be extracted by steady-state electrodynamic measurements like optics, IXS and EELS, these experiments provide only a time-averaged picture of the underlying charge dynamics. This hinders the possibility to directly observe dynamical phenomena as the interband scattering between the two different bands. To this aim, in Sect. 3.4, we apply ultrafast broadband optical spectroscopy on MgB_2 to unravel the details of the charge dynamics occurring upon photoexcitation.

3.3 Spontaneous Raman Scattering

In Sect. 3.1, we discussed the crucial role played in MgB_2 by the E_{2g} bond-stretching phonon branch in providing the glue that binds the carriers into pairs. In this Section, we describe the emergence of this mode and of other peculiar collective excitations, as detected by spontaneous Raman scattering. The purpose of this discussion is twofold: (i) To introduce the underlying properties of the "glue boson" of MgB_2 in the long-wavelength limit $\mathbf{q} = 0$; (ii) To illustrate how MgB_2 can be considered as a prototypical system where to study exotic Raman-active low-energy collective modes that may emerge also under nonequilibrium conditions within the ISRS framework. All these features make MgB_2 a natural playground for the study of many-body effects even in the absence of strong electron-electron correlations.

Figures 3.4a and 3.4b show the resonant Raman response of MgB_2 in the E_{2g} and A_{1g} scattering channels, respectively. The data, adapted from Ref. [42], have all been measured at 8 K, and the normal state response has been obtained by applying a static magnetic field of 5 T along the material *c*-axis direction. To provide resonant enhancement to the measured excitations, the E_{2g} signal has been measured using an incident photon energy of 2.57 eV, while the A_{1g} response using a photon energy tuned at 1.65 eV.

We observe that in both scattering configurations the response involves electronic and phononic contributions. The E_{2g} symmetry channel comprises a threshold of Raman intensity at 3–5 meV and a sharper peak at 13 meV. These low-energy features are suppressed once the material is driven in the normal state. These are the signatures of elementary excitations of electronic origin, associated with Bogoliubov quasiparticles in the system. This pair-breaking peak (typically referred to as coherent SC peak) is a representative feature characterizing all superconductors, since it arises from the breaking of the Cooper pairs in the SC state [53]. More precisely,

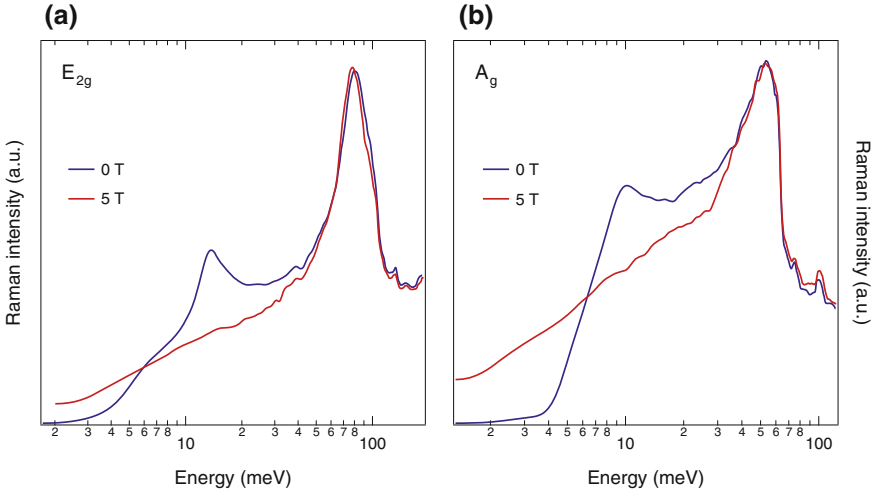

Fig. 3.4 Spontaneous Raman scattering spectra of an MgB_2 single crystal in the normal (red) and SC (blue) states for the (**a**) E_{2g} and (**b**) A_{1g} scattering channels. The data are adapted from Ref. [42]. All measurements are performed at 8 K and the normal state has been achieved by applying a 5 T magnetic field parallel to the *c*-axis

during the Raman process, the incoming photon breaks a Cooper pair of energy $2\Delta_k$ on the Fermi surface and the photon that is scattered retains a signature of this excitation showing a decreased photon energy of $2\Delta_k$. Concerning MgB_2, we observe that the threshold at 3–5 meV does not evolve into a clear pair-breaking peak because the probed material was in the dirty limit. However, being a (charged) reflection of the SC gap, this pair-breaking peak allows gaining insightful information on the symmetry of the SC gap and on the possible coupling of superconductivity with other elementary excitations. The presence of two superconductivity-related peaks in the Raman spectra of MgB_2 has always been considered as a strong evidence in favour of the multi-gap SC nature of this material, in which the two gaps are $2\Delta_\pi$ and $2\Delta_\sigma$. Hence, it is not surprising that, after the discovery of MgB_2, spontaneous Raman scattering has played a crucial role in confirming experimentally the coexistence of two distinct gaps [26, 39–42]. As demonstrated also by other techniques, the symmetry of the SC gap in MgB_2 is s-wave (with a slight anisotropy), leading to the invariance of the pair-breaking peaks' energy under different Raman scattering geometries.

The high-energy part of the E_{2g} spectrum is instead dominated by a broad band centred around 80 meV. This is the only Raman-active phonon allowed in this symmetry channel from group theory considerations and corresponds to the above described E_{2g} bond-stretching mode. As already observed, this mode strongly couples to the σ holes, thus making MgB_2 an anisotropic Fermi liquid in a strong electron-boson coupling regime. The unusual broad linewidth of this mode in the Raman spectra has been subject of extensive debate [26, 28, 40, 42, 54]. As the role of impurity

scattering can be excluded, the two remaining contributions are: (i) Strong phonon-electron coupling; and (ii) Anharmonic decay into lower energy phonons. While Density Functional Theory (DFT) calculations point towards a negligible effect of phonon anharmonicity [28], the analysis of the phonon self-energy at $\mathbf{q} = 0$ suggests that σ carriers cannot represent a scattering channel [54]. Nowadays, a consensus has been reached in that the main origin of the E_{2g} phonon linewidth is represented by its giant anharmonicity [42].

In the A_{1g} scattering geometry, different structures become evident. For our purposes, we do not discuss the details of all the other features above 20 meV in Fig. 3.4b, since they are due to two-phonon modes arising from flat portions in the phonon dispersion as measured via IXS [28]. Here, we restrict our discussion to the origin of the broad feature emerging around 10 meV. Remarkably, this feature is related to the SC state but it is active only in the A_{1g} scattering channel. Tuning the excitation photon energy towards the σ-π interband transition (i.e. performing a resonant Raman experiment as in Ref. [42]) results in the suppression of this mode, thus suggesting that the mode acquires more contrast when the electronic continuum above the fundamental threshold of the SC gap is weaker. This feature has been assigned to the spectral fingerprint of the Leggett collective mode, which arises in multiband superconductors containing two coupled superfluids due to a simultaneous cross-tunneling of a pair of electrons [55]. As observed above, the two superfluids in MgB_2 are represented by the σ and π condensates, which are neither strongly interacting nor totally independent. The weak coupling between the two condensates allows a mutual crosstalk via dynamical oscillations of Cooper pairs. These in turn produce small fluctuations of the relative phases between the two superfluids, but the total electron density is maintained constant at every spatial point of the material. In a multiband superconductor where the Leggett mode is below the pair-breaking peaks, it is long-lived due to the absence of scattering channels. In MgB_2, as the Leggett mode lies between Δ_π and Δ_σ, it is expected to rapidly relax into π-band quasiparticles within a couple of tunneling oscillations [55]. A complete theoretical treatment of the emergence of the Leggett mode in the A_{1g} Raman response of multiband superconductors is provided in Ref. [56]. Recently, from the analysis of ARPES data, it was suggested that not only the E_{2g} bond-stretching mode but also the Leggett mode strongly interact with the quasiparticles, leading to a pronounced renormalization of the Fermi velocity in the energy-momentum dispersion relation close to the Fermi surface [57].

After presenting the possible collective modes that can play a fundamental role in our nonequilibrium dynamics of MgB_2, in the following we describe the results of our pump-probe study where we elucidate the scattering mechanism between the σ and π bands.

3.4 Ultrafast Broadband Optical Spectroscopy

In our experiments, we use an ultrashort 1.55 eV laser pulse to set the σ and π electronic subsystems of MgB_2 out of equilibrium and follow the σ-π interband scattering by probing the variation of the sample reflectivity ($\Delta R/R$) with a broadband

pulse covering the plasma edges of both axes. In Fig. 3.2a, b, the pump photon energy is represented by a red arrow and the probed spectral region is highlighted with a grey shaded area. We use a high-quality (0001)-oriented MgB_2 thin-film, which has been carefully handled to prevent its oxidation upon exposure to air (more details are given in Appendix A.1). In our geometry, the in-plane polarized pump beam hits the sample surface at normal incidence and it is in-plane polarized; the probe beam is directed towards the sample under an angle of 15°, primarily detecting the in-plane plasma edge but also exploring the *c*-axis response.

Figure 3.5 shows the colour-coded map of $\Delta R/R$ at 10 K as a function of the probe photon energy and time delay between pump and probe. Direct inspection of the map reveals three features evolving in time: (i) A broad positive contribution centered around 2.15 eV (labelled P_a), which has a straightforward correspondence with the in-plane plasma edge (see Fig. 3.2b); (ii) A broad negative background covering the 2.55–2.90 eV spectral region, which mirrors the σ-π interband transition centered around 2.78 eV; and (iii) A narrow feature around 2.67 eV (P_c), which overlaps with the broad interband transition and becomes stronger with increasing time delay. This feature is assigned to the *c*-axis plasmon of MgB_2, as discussed below.

All features become more evident in the transient spectra at selected time delays. Figure 3.6a, b collect the $\Delta R/R$ spectra during the rise and the decay of the response, respectively. During the rise (Fig. 3.6a), the positive feature P_a undergoes a slight redshift of its maximum, while the barely observable peak of feature P_c does not evolve in energy. In the relaxation (Fig. 3.6b), three salient effects take place: (i) Both the low-energy zero-crossing point around 1.80 eV and the peak of the feature P_a shift to higher energies as a function of time; (ii) An isosbestic point in $\Delta R/R$ develops around 2.50 eV; (iii) The feature P_c reinforces its weight over time and undergoes a pronounced blueshift. The detailed temporal evolution of the P_c peak is mapped in Fig. 3.7.

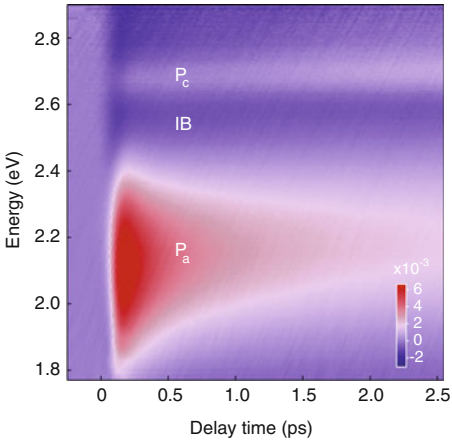

Fig. 3.5 Colour-coded map of $\Delta R/R$ at 10 K as a function of probe photon energy and time delay between pump and probe. The pump photon energy is set at 1.55 eV and the absorbed fluence is 1.2 mJ/cm^2

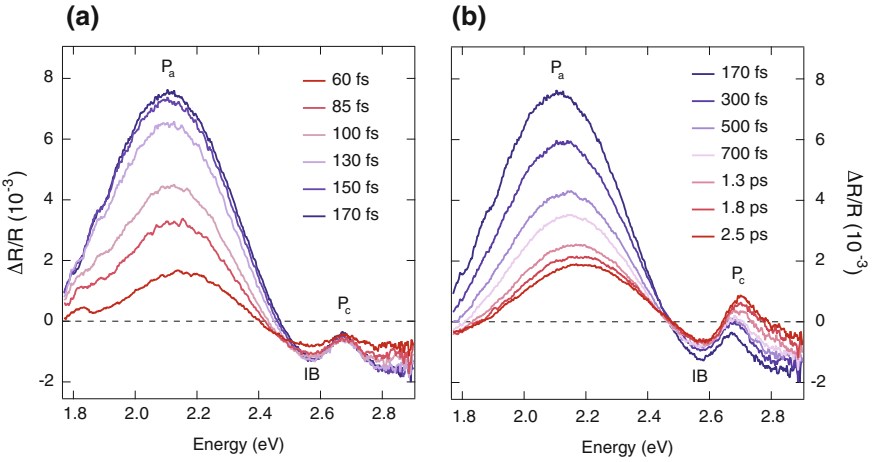

Fig. 3.6 **a**, **b** Transient spectra of ΔR/R for different time delays during (**a**) the rise (**b**) the decay of the response

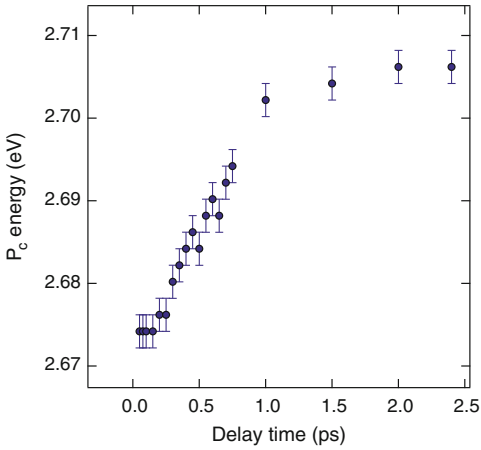

Fig. 3.7 Evolution of the P_c peak energy as a function of time

Complementary information is provided by the ΔR/R temporal dynamics. Several time traces are shown in Fig. 3.8a, b at representative probe photon energies. We observe that the signal displays a much longer rise time than the response function of our set-up (45 fs), reaching its maximum absolute amplitude at 170 fs. More remarkably, the ΔR/R decay depends on the probe photon energy, as the relaxation dynamics in correspondence to the feature P_c (2.67 eV) differs from the one governing the rest of the spectrum. As expected from Fig. 3.6b, on the low-energy side (red trace at 1.80 eV in Fig. 3.8a) the signal undergoes a sign change over time, consistent with previous single-wavelength pump-probe experiments in the normal state [58, 59]. These results are rather independent of the sample temperature, except that the feature P_c becomes sharper for decreasing temperatures.

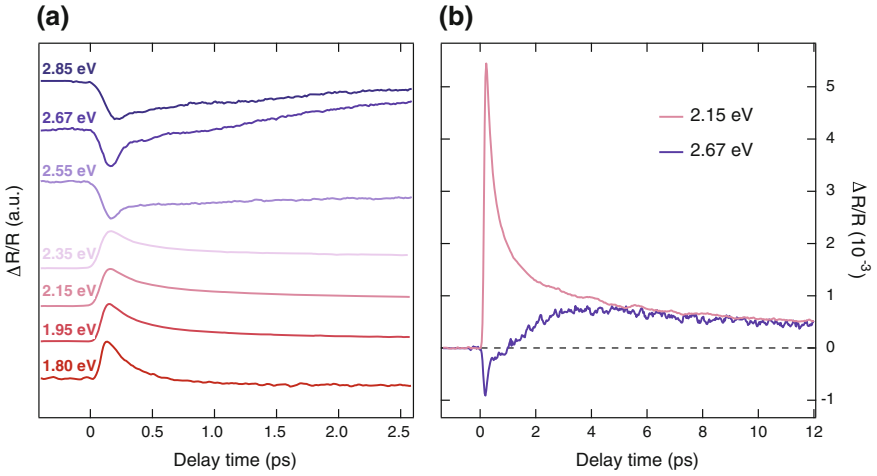

Fig. 3.8 **a** Normalized ΔR/R temporal traces up to 2.5 ps at 10 K for different probe photon energies, indicated in the labels. **b** ΔR/R temporal traces up to 12 ps in correspondence of the P_a and P_c spectral features

We first consider the evolution of P_a and of the interband transition features. Recent broadband pump-probe experiments covering the 0.75–1.40 eV spectral range of MgB_2 have revealed a negative sign in the ΔR/R response [29]. Thus, the positive sign of P_a in our spectra is compatible with an instantaneous broadening of the *a*-axis plasma edge in the rise of the response. Moreover, during the same rise time, the *a*-axis plasma edge blueshifts significantly, which is evidenced by the ΔR/R zero-crossing evolution. Similarly, during the relaxation, the *a*-axis plasma edge narrows and redshifts over time, which is evidenced by the ΔR/R zero-crossing evolution. The negative background in the 2.50–2.85 eV region suggests that an ultrafast change of the σ-π interband transition has also occurred after the photoexcitation, involving a broadening of its shape.

We now focus on the assignment of the feature P_c, which comprises a very narrow peak in correspondence to the *c*-axis plasma edge. A simple phenomenological explanation for the presence of a sharp peak in the ΔR/R spectrum of an ideal metal can be provided by recalling that, at high frequencies, the dielectric function $\epsilon_1(\omega)$ can be written as

$$\epsilon_1(\omega) = \epsilon_\infty - \frac{\omega_p^{*2}}{\omega^2}, \tag{3.1}$$

where ϵ_∞ is the high-frequency dielectric constant, $\omega_p^{*2} = 4\pi\tilde{n}e^2/m$ and m is the electron mass. By assuming that the main effect of the pump pulse is to change the effective carrier concentration $\tilde{n}$, it results that

$$\frac{\Delta R}{R} \approx \frac{8\pi e^2 \Delta\tilde{n}}{m\omega^2\sqrt{\epsilon_1}}. \tag{3.2}$$

Hence, $\Delta R/R$ displays a peak at ω_p^*, i.e. the energy at which $\epsilon_1 = 0$. The same argument applies to the loss function $L(\mathbf{q}, \omega) = \mathrm{Im}[\epsilon^{-1}(\mathbf{q}, \omega)]$, where $\mathbf{q}$ is the momentum transfer. Therefore, the increase of $\widetilde{n}$ implies a rigid shift of the plasma edge towards higher energies. Following these considerations, we naturally assign P_c to the c-axis longitudinal plasmon mode, which consistently lies at ∼2.65 eV in the equilibrium optical spectra (i.e. in correspondence to the zero-crossing of ϵ_1 at $\mathbf{q} = 0$).

3.4.1 Fluence Dependence

We now investigate how the feature P_c is renormalized as a function of the incoming pump fluence. In this regard, we perform a fluence dependence at RT by varying the absorbed fluence of one order of magnitude in the range 0.24–2.4 mJ/cm^2. Figure 3.9a, b show the $\Delta R/R$ spectra at different absorbed pump fluences and for a time delay of 170 fs and 2.4 ps, respectively. The values of the corresponding absorbed pump fluence are given in the labels. The wiggles that emerge in the spectral range 1.80–2.40 eV are artifacts due to an interference pattern affecting our probe pulse during the fluence dependence.

In correspondence to the maximum of the response (170 fs, Fig. 3.9a), the c-axis plasmon peak is barely visible and becomes more apparent only for increased pump fluence. In addition, a redshift of ∼20 meV manifests when the absorbed pump fluence is increased from 0.24 mJ/cm^2 to 2.40 mJ/cm^2. At long time delays (2.4 ps, Fig. 3.9b), the c-axis plasmon is more evident and a similar redshift of ∼20 meV is retrieved in the peak position when the absorbed pump fluence is increased

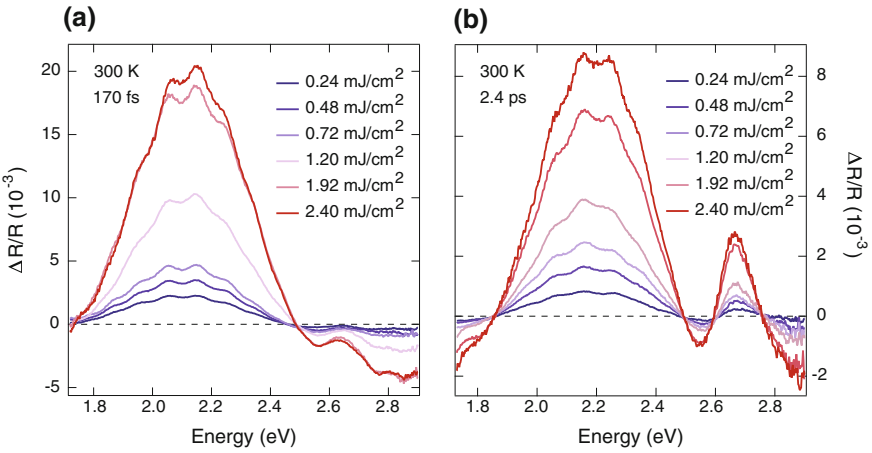

Fig. 3.9 Transient spectra of $\Delta R/R$ at RT for different absorbed fluences for a delay time of (**a**) 170 fs (**b**) 2.4 ps

from 0.24 mJ/cm^2 to 2.40 mJ/cm^2. These shift can be interpreted as plasmon optical nonlinearities induced by the effect of the pump pulse and will be addressed in detail in Sect. 3.5.4.

3.4.2 Photoexcitation Mechanism

To correctly interpret the observed ultrafast dynamics, it is crucial to clarify how the electrons of MgB_2 are affected by the interaction with the near-infrared pump pulse at 1.55 eV. Since the pump photon energy lies below 2.40 eV, it is not sufficient to efficiently induce the in-plane σ-π interband transition. On one hand, we can expect that the tails of both oscillators associated with the σ-σ and the σ-π interband transitions can provide a contribution to the excitation process [43]. On the other hand, energy transfer from the laser to the electron system is expected to occur mainly via free-carrier absorption processes. This idea is confirmed by observing that the laser pulse at 1.55 eV lies also on the tail of the Drude response in the a-axis optical conductivity shown in Fig. 3.2a. However, it is well established that the a-axis optical conductivity of MgB_2 can be described only by assuming a two-component Drude response, due to the contributions of both σ and π carriers [43, 45]. Thus, it becomes crucial to establish whether our laser pulse at 1.55 eV selectively excites one type of carriers or if it exchanges energy with both electronic subsystems.

To clarify this point, we quantified the relative contribution of the σ and π carriers to the equilibrium Drude response at 1.55 eV by performing an ab initio simulation of the optical properties of MgB_2 including one type of electronic subsystem at a time. The two contributions to the optical conductivity are evaluated on the basis of the calculations reported in Ref. [43]. The results are shown in Fig. 3.10a, b and show that both electronic subsystems provide a sizeable response to the electromagnetic field at 1.55 eV.

As a result, we conclude that our pump pulse is not able to selectively excite the carriers residing in either the σ or the π band and that both electronic subsystems undergo an increase of their temperature $T_{e,\sigma}$ and $T_{e,\pi}$ upon interaction with the pump pulse. Irrespective of the details of the photoexcited carrier density, it is important to observe that our pump pulse lies in the near-infrared spectral range, thus enabling the photoexcited carriers to generate high-energy phonons. This argument will play a crucial role in the interpretation of the data, as will be explained in the following Sections.

Finally, we observe that our results are rather independent of the sample temperature, except that the feature P_c becomes sharper for decreasing temperature. The insensitivity of the transient response to temperature is due to the large absorbed fluence regime (0.2–3 mJ/cm^2) of our experiment, which exceeds the threshold for the complete vaporization of the SC condensate by two orders of magnitude [58, 59]. At 10 K, we can safely assume that the pump pulse suddenly melts the SC order parameter and drives MgB_2 into its normal phase. The recombination dynamics of

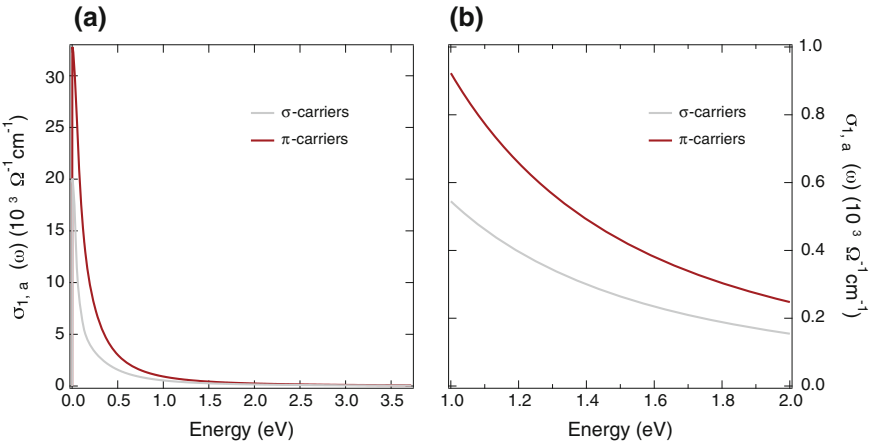

Fig. 3.10 **a** Relative contribution of the σ and π carriers to the equilibrium Drude response, on the basis of the calculations reported in Ref. [43]. **b** Zoom of the calculations shown in (**a**) in the vicinity of the pump photon energy at 1.55 eV

the quasiparticles into Cooper pairs occurs within hundreds of picoseconds [58, 59], i.e. outside our temporal window. Therefore, in the following, we will neglect the presence of effects associated with superconductivity.

3.4.3 Anisotropic Drude-Lorentz Model

After establishing the effect produced by the pump pulse upon interaction with MgB_2, it is crucial to obtain more quantitative insights into the carrier dynamics along the *a*- and *c*-axis. To this aim, we fit an anisotropic Drude-Lorentz model to the static data of Ref. [43] and to our time-resolved data at RT. This allows us to disentangle the *a*- and *c*-axis contributions to the $\Delta R/R$ caused by the 15° angle of incidence of our probe beam.

Due to the higher quality of our sample compared to the one used in Ref. [43], we increased by $\sim$8% the *c*-axis bare plasma frequency to achieve a better fit. The spectral features covered by our probe range are the *a*-axis plasma edge, the *a*-axis σ-π interband transition transition and the *c*-axis plasma edge. For what concerns the boundary conditions in the Drude-Lorentz model, we fixed the parameters that did not influence the ultrafast dynamics. This was done by first letting all parameters free and monitoring which of them gave rise to a flat evolution as a function of time. One example is represented by the energy of the σ-π interband transition oscillator, which was found not to vary with time. Fixing the irrelevant parameters also allowed us to reduce the overall noise on the final results. Following this procedure, we could limit the fit of our model to six free parameters: The bare plasma frequencies $\omega_{p,a}$

and $\omega_{p,c}$ along the a- and c-axis, the corresponding dampings Γ_a and Γ_c, and the plasma frequency and optical scattering rates of the a-axis σ-π interband transition. This provided a reliable fit of the ΔR/R data while enabling us to identify the physical origin of its features. The fit was performed separately for the spectra at RT (to match the temperature of the steady-state data) at each time delay, covering a temporal window up to 2.4 ps. The robustness of the fit is evidenced by Fig. 3.11a, b, where we show the results in correspondence to the rise (170 fs) and decay (2.2 ps) of the response. We observe that the fit is an excellent match to the experimental data. We note that the fit does not converge if $\omega_{p,a/c}$ are not left free but are forced to redshift after the interaction with the pump pulse. This also confirms the reliability and the analysis of the presented results.

By iterating this procedure over the probed time window, we can map the temporal evolution of the bare plasma frequencies ($\omega_{p,a-c}$ in Fig. 3.12a) and optical scattering rates ($\Gamma_{p,a-c}$ in Fig. 3.12b), which respectively control the position and damping of the plasma edge. We obtain an ultrafast blueshift of the a-axis plasma frequency $\omega_{p,a}$ (violet dots, Fig. 3.12a), accompanied by a simultaneous increase of the a-axis scattering rate Γ_a (violet dots, Fig. 3.12b). After 170 fs, $\omega_{p,a}$ redshifts with a timescale of several picoseconds, while Γ_a relaxes to its equilibrium value within $\sim$1 ps. Remarkably, we observe that the temporal evolution of Γ_a agrees with the results of the broadband pump-probe measurements of Ref. [29]. However, in contrast with previous results, the dynamics of $\omega_{p,a}$ is a completely new observable that becomes apparent only when the broadband probe is tuned in our spectral region. Signatures of this behaviour were already evident in Ref. [60], but never discussed. Of particular importance is also the temporal evolution shown the c-axis Drude contribution (blue

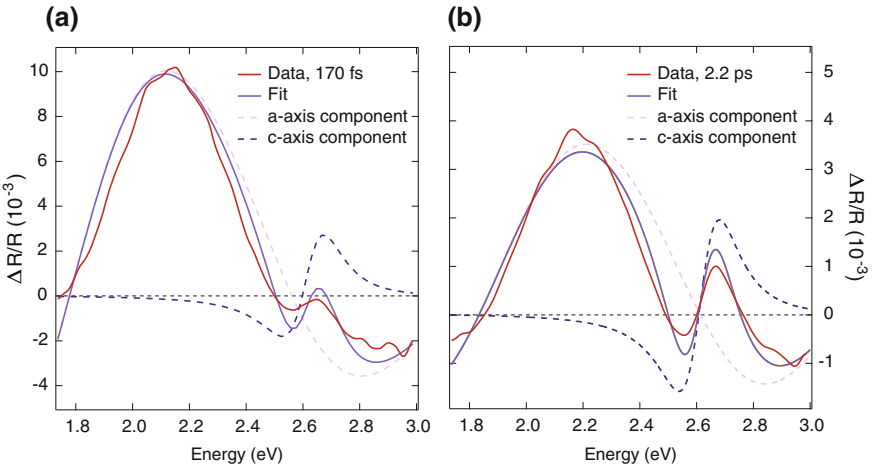

Fig. 3.11 Results of the anisotropic differential Drude-Lorentz model on the ΔR/R spectrum at RT for a delay time of (**a**) 170 fs and (b) 2.2 ps. The original data are shown as solid red lines, the resulting fit as solid violet lines, the a- and c-axis contributions in dashed pink and blue lines, respectively

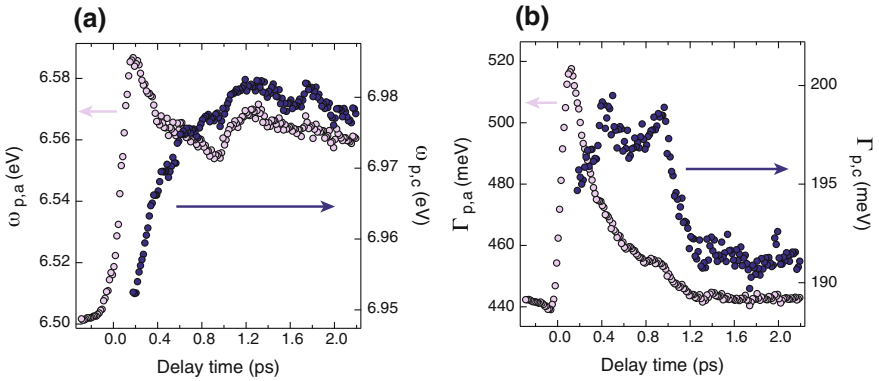

Fig. 3.12 Temporal evolution of **a** the bare plasma frequency $\omega_{p,a-c}$ and **b** the optical scattering rate Γ_{a-c} along the a- (pink dots) and c-axis (blue dots)

dots, Fig. 3.12a, b). The $\omega_{p,c}$ undergoes a slow blueshift within 1 ps (anticipated in Fig. 3.6c), followed by its stabilization around a constant value. Instead, Γ_c slowly rises with a timescale of ∼300 fs, before decreasing again after 1 ps.

3.5 Theoretical Calculations

In the previous Section, our quantitative model has shown that both the a- and c-axis bare plasma frequencies increase after the arrival of the pump pulse, albeit with different timescales. While $\omega_{p,a}$ increases within the first 170 fs and decays on the order of tens of picoseconds, $\omega_{p,c}$ displays a delayed blueshift within 1 ps and stabilize around an increased constant value. This behaviour is very anomalous, especially in relation to the increased temperature that the electrons reach out-of-equilibrium after the interaction with a pump pulse. Indeed, it is well established that conventional Fermi liquids show a decrease of the bare plasma frequencies as T_e increases. An opposite behaviour is instead observed in semimetals, which are characterized by a strongly varying electronic DOS near E_F. Our data support a scenario that is very similar to the physics of a semimetal. In this regard, we need to recall that MgB_2 is a multiband and anisotropic Fermi liquid in the strong coupling regime and, as such, its plasma frequencies may undergo a more complex temperature dependence. Thus, in order to assess in a compelling way the origin of the unconventional increase displayed by the a- and c-axis plasma edges, the different physical processes operative during the pump-probe experiment need to be examined and evaluated. In the following, we discuss in detail different relevant physical effects that need to be taken into account. On the base of this analysis, we conclude that the presence of strong multiband many-body effects mediated by the electron-phonon interaction is the most likely scenario to account for the anomalous blueshift.

3.5.1 Electronic Heating

The transient optical data was analyzed by means of an anisotropic Drude-Lorentz model, where the plasma frequency $\omega_{p,i}$ represents the total SW of the electronic intraband optical excitations with polarization along the corresponding ($i = a, c$) directions. Within this context, however, one should keep in mind that the SW do not need to obey the f-sum rule, as discussed in detail below. As a result, the plasma frequencies can acquire a finite dependence on the effective electronic temperature. This scenario was extensively analyzed in Ref. [61], and the relevance of these effects on the analysis of the present pump-probe experiments is here presented.

As a starting point, it is useful to recall the restricted optical sum rule that applies to an electronic system with band dispersion $\epsilon_{\mathbf{k}}$ [61]

$$\int_{-\omega_M}^{\omega_M} \mathrm{Re}\,\sigma_{ii}(\omega, T)d\omega \equiv \frac{\omega_{p,i}^2}{4} = \pi e^2 \int \frac{d^3\mathbf{k}}{(2\pi)^3} \sum_{\mathbf{k},\sigma} \frac{\partial^2 \epsilon_{\mathbf{k}}}{\partial k_i^2} n_{\mathbf{k},\sigma}. \tag{3.3}$$

Here $n_{\mathbf{k},\sigma}$ is the occupation number of the states with momentum $\mathbf{k}$ and spin σ, and ω_M is a frequency cut-off implemented to include only intraband transitions. In the textbook limit of parabolic and isotropic band dispersion, $\epsilon_{\mathbf{k}} = k^2/2m$, the above equation reduces to the familiar expression relating the plasma frequency to the density of carriers, $\omega_p^2 = 4\pi e^2 \tilde{n}/m$ which is a conserved quantity for any temperature. Correspondingly, no dependence of the plasma frequency on the electronic temperature is expected in this simplified case.

For more realistic materials, however, a finite temperature dependence of the plasma frequency can be expected [61]. This is essentially due to the thermal smearing of the electronic excitations and it is predicted to give rise to a *redshift*, which is at odds with our experimental observation.

In order to understand the origin of this redshift, consider the paradigmatic case of a single-band three-dimensional electronic system with square nearest neighbor tight-binding dispersion, $\epsilon_{\mathbf{k}} = t \sum_{i=x,y,z} \cos(k_i a)$, a being the lattice spacing and t the hopping energy. The lattice structure induces a relevant deviation of the electronic dispersion $\epsilon_{\mathbf{k}}$ from a simple parabolic behaviour. Thus, we get $\partial^2 \epsilon_{\mathbf{k}}/\partial k_i^2 = -\epsilon_{\mathbf{k}}/3$, and $\omega_p^2 = 4\pi e^2 \langle K \rangle/(3a)$, where $\langle K \rangle$ is the electronic kinetic energy. A finite temperature dependence of the plasma frequency thus stems from thermal smearing of the Fermi function, and it can be captured by the usual Sommerfeld expansion

$$\langle K \rangle = \int \frac{d^3\mathbf{k}}{(2\pi)^3} \epsilon_{\mathbf{k}} f(\xi_{\mathbf{k}}) = -\int d\epsilon N(\epsilon) \epsilon f(\epsilon - \mu) = \langle K \rangle_{T=0} - c(\mu) T^2, \tag{3.4}$$

where $c(\epsilon) = (\pi^2/6)[\epsilon N'(\epsilon) + N(\epsilon)]$, and $N(\epsilon)$ and $N'(\epsilon)$ are the DOS (per spin) and its derivative, respectively. Note that $c(\mu) \sim 1/W$, where W is the electronic bandwidth. This analysis shows that the thermal smearing driven by an increase of the electronic temperature leads to a *redshift* of the plasma edge, on the order of $\sim [1 - (T/W)^2]$. In normal metals, this corresponds to a reduction of the plasma

frequency of a few percent when warming the sample from zero temperature to RT [62]. A stronger redshift has been observed in correlated metals [62], in agreement with the effective reduction of the quasiparticle bandwidth W in the presence of strong correlations [63].

In conclusion, even accounting for the small deviations from parabolicity of the band dispersion of the σ and π carriers in MgB_2, the electron heating could only account for a negligible redshift of the plasma frequency, instead of the observed relatively large blueshift of $\omega_{p,a/c}$.

3.5.2 σ-π Interband Transitions

Here, we consider the possibility that the renormalization of interband transitions could lead to the appearance of the very sharp feature P_c observed in the $\Delta R/R$ response and to its blueshift as a function of time. This scenario has to be considered because interband transitions have been found to play an essential role in the pump-probe spectrum of noble metals such as Au, where the interband transition couples filled states in the d-band below E_F with states near E_F [3, 4, 64, 65]. As described in Sect. 3.2, the equilibrium in-plane reflectivity spectrum of MgB_2 in the visible range exhibits a structure peaking at 2.78 eV [43, 45]. Around this value, DFT calculations show a feature due to interband transitions involving occupied σ and unoccupied π states over a wide portion of the BZ [43], with a contribution from direct transitions in the proximity of the M point (green arrow in Fig. 3.1b). This feature is strongly broadened by electron-electron and electron-phonon interaction processes, to the extent that its linewidth is $\sim$1 eV. As such, this structure cannot account for the extremely sharp peak observed in our $\Delta R/R$ data.

To produce such a sharp peak, one would have to assume that only a small subset of transitions changes within the manifold after 170 fs, while all others do not renormalize. This scenario is unphysical in a metallic system such as MgB_2, since the fast electronic degrees of freedom thermalize within 170 fs. This proves that P_c does not originate from σ-π interband transitions, supporting our contention that P_c is due to the excitation of plasmons. Recalling results on noble metals [3, 4, 64, 65], we further note that the renormalization due to the excitation of particles close to E_F would produce a similar $\Delta R/R$ shape (although broader) but the dynamics would display the opposite sign from what is observed (i.e. a redshift), regardless of whether the states near E_F are the initial or the final states. Our arguments are reinforced by two additional points: (i) Theoretical calculations [31, 48, 49] and experimental observations [43, 45, 48] identify the presence of the c-axis plasmon mode at the energy of P_c; (ii) The temporal behavior observed in the proximity of P_c differs from that characterizing other features in the interband region. This cannot be explained either by a different dynamical response of the photogenerated electron-hole pairs, or by a photoinduced change of the interband transitions because the pump is at a far lower energy (1.55 eV). Thus, such a distinct temporal dynamics must be caused by channels that differ from the photogenerated electron-hole pairs, as discussed below.

3.5.3 Electron-Phonon Interaction in a Multiband Systems

Here, we analyze the effects arising from strong electron-phonon interaction in MgB_2. We show that these effects, specifically the strong coupling of σ carriers to hot E_{2g} phonons lead to a sizeable blueshift of the in-plane plasma frequency $\omega_{p,\sigma}$ after photoexcitation. During the subsequent relaxation, the exchange processes between σ and π carriers lead to an additional increase of $\omega_{p,\pi}$, in qualitative and quantitative agreement with the experimental observations. These findings suggest that the hot phonon generation is the most likely candidate to explain the observed blueshift.

Let us consider the processes that can occur in a multiband system with highly asymmetric particle-hole bands and strong electron-boson coupling. Similar to the case of pnictides [66, 67], these conditions can make the effect of the electron-phonon coupling visible in an interaction-dependent change of size of the Fermi surface with respect to Local Density Approximation (LDA) calculations. For a purely parabolic two-dimensional band, one can relate [66, 67] the density of carriers $\tilde{n}$ to the top/bottom E_M of the band as

$$\tilde{n} = \frac{k_F^2}{2\pi} = \frac{2m(E_M + \chi)}{2\pi}, \tag{3.5}$$

where χ denotes the real part of the electron-phonon self-energy at zero energy. While the Eliashberg calculation of the self-energy gives $\chi = 0$ for half-filled bands, at low carrier density χ becomes in general different from zero, and can lead to an observable shrinking or expansion of the Fermi surface area as a function of the electron-phonon interaction. By computing χ for an Einstein phonon and making the analytical continuation with the Marsiglio-Schlossmann-Carbotte method [68], one can show that the electronic χ_{el} and bosonic χ_{bos} contributions to χ can be written as

$$\chi_{\text{el}}(T = 0) = -\lambda \frac{\omega_0}{2} \ln \left| \frac{E_B - \omega_0}{E_B + \omega_0} \right|, \tag{3.6}$$

$$\chi_{\text{ph}}(T = 0) = -\lambda \frac{\omega_0}{2} \ln \left| \frac{E_T + \omega_0}{E_B - \omega_0} \right|, \tag{3.7}$$

so that

$$\chi_{\text{tot}}(T = 0) = \chi_{\text{el}}(T = 0) + \chi_{\text{ph}}(T = 0) = -\lambda \frac{\omega_0}{2} \ln \left| \frac{E_T + \omega_0}{E_B + \omega_0} \right|, \tag{3.8}$$

in agreement with previous estimates [67]. Here ω_0 is the phonon energy, λ is the dimensionless electron-phonon coupling and $E_{T/B}$ represent the band top/bottom, respectively. In a multiband system the previous Eq. (3.8) must be generalized to account for both the interband and intraband contributions, mediated in general by phonons or other collective modes, so that $\chi_\alpha = \sum_\beta \lambda_{\alpha\beta} R_\beta$ where $R_\beta =$

$\frac{\omega_0}{2} \ln \left| \frac{E_T^\beta + \omega_0}{E_B^\beta + \omega_0} \right|$. Since $R_\beta > 0$ for a band having electron character (so that $E_T^\beta \gg E_B^\beta$) while $R_\beta < 0$ for a band having hole character the final sign of χ_α depends on the intraband *versus* interband nature of the dominant interaction. For example, in the case of pnictides, the dominant channel is provided by spin-fluctuations interband interactions between hole and electron bands, leading to a shrinking of all the Fermi pockets with respect to LDA [66, 67]. In the case of MgB_2, we expect that the largest channel of interaction is the intraband coupling between the σ electrons and the E_{2g} phonon. In this situation, we expect that $\chi_\sigma(T = 0) > 0$, but since the unperturbed Fermi area of the σ pocket is much larger than in the pnictides, this effect is quantitatively much smaller at equilibrium, explaining why ARPES measurements on MgB_2 are overall in good agreement with LDA predictions [69]. Nonetheless, as we argued in the main text, this scenario can explain the small variations of the plasma frequency observed by heating the system with an intense laser pulse.

To address thermal effects, we consider the possibility that the electronic temperature T_e does not necessarely coincide with the bosonic one T_{ph}. We then identify in the expression for $\chi(T)$ two separate terms, one depending on the Fermi function $f(\omega_0, T_e)$, controlled by T_e, and one depending on the Bose function $b(\omega_0, T_{ph})$, controlled by T_{ph}. This distinction can be achieved by performing the analytical continuation of the Matsubara self-energy $\Sigma(i\omega_n)$ without leaving the ambiguity in the use of the Fermi and Bose factors. One can show that the final result at the lowest order of the perturbation theory is

$$\begin{aligned}\Delta\chi_{el}(T) = &-\lambda \frac{T}{2} \sum_m \frac{\omega_0^2}{\omega_m^2 + \omega_0^2} \ln \left| \frac{E_T^2 + \omega_m^2}{E_B^2 + \omega_m^2} \right| \\ &-\lambda \frac{\omega_0}{2} f(\omega_0) \ln \left| \frac{E_T^2 - \omega_0^2}{E_B^2 - \omega_0^2} \right| \\ &+\lambda \frac{\omega_0}{2} \ln \left| \frac{E_T + \omega_0}{E_B - \omega_0} \right|, \end{aligned} \tag{3.9}$$

$$\Delta\chi_{ph}(T) = -\lambda \frac{\omega_0}{2} b(\omega_0) \ln \left| \frac{E_T^2 - \omega_0^2}{E_B^2 - \omega_0^2} \right|. \tag{3.10}$$

The two separate contributions (3.9)–(3.10) were computed for realistic parameter values appropriate for the σ band. In particular, the phonon energy ω_0 is set at 70 meV to account for the strong peak found at this energy in the Eliashberg function $\alpha^2 F(\omega)$ (which integrates over all momenta) [20]. This is mainly governed by the contribution of the strongly softened in-plane vibrations of the boron atoms. The result is shown in Fig. 3.13, where one clearly sees the predominance of the thermal effects due to heating of the phonon bath. This has a direct impact on the evolution of the plasma frequencies of the σ and π bands after the pump. Indeed, the initial heating of the electronic bath due to the pump is also effective on the E_{2g} phonon, which is strongly coupled to the σ electrons. This, in turn, implies an *increase* of the Fermi area of the σ pocket that is coupled to the E_{2g} hot phonon at a large temperature

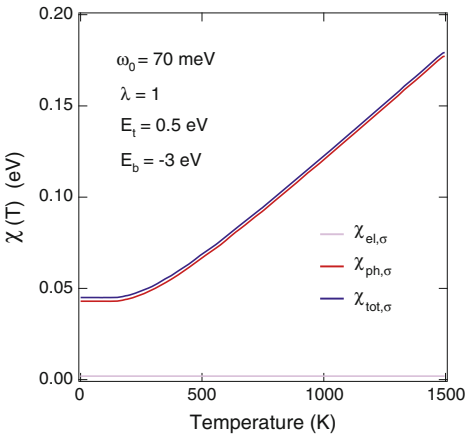

Fig. 3.13 Temperature dependence for the bosonic and electronic contributions to the shift of the σ bands in temperature

$T_{ph}^{E_{2g}}$. The π band is instead unaffected, since it is weakly coupled to the remaining cold phononic bath. We emphasize the fact that the initial increase of the plasma frequency in the σ band is in striking contrast with the usual findings in single-band systems, where heating the electronic bath results in a suppression of the plasma edge (see Sect. 3.5.1) [61, 63].

After the first 170 fs, the system equilibrates to a state with hot σ/π carriers and E_{2g} branch phonons, and then starts to equilibrate with the remaining phononic bath with the less efficient electron-phonon scattering channels and the phonon-phonon anharmonic processes. This relaxation process activates the interband σ-π scattering mechanisms which leads to an increase of the π Fermi surface, needed to preserve the total number of carriers in the system. After about 2 ps, the system is then overall at equilibrium with a larger effective number of carriers in all bands, consistent with our pump-probe optical measurements. The above scheme can be used to indirectly estimate the temperature $T_{ph}^{E_{2g}}$ of the hot phononic bath via its effect on the plasma frequency of the σ band, given by

$$\omega_{p,\sigma} = \sqrt{\frac{4\pi e^2 \tilde{n}_\sigma}{m}}. \tag{3.11}$$

From Eq. 3.11 we can estimate the change of $\tilde{n}_\sigma$ due to the measured change in $\omega_{p,\sigma}$

$$\delta_\sigma \equiv \frac{\Delta\omega_{p,\sigma}}{\omega_{p,\sigma}} = \frac{1}{2}\frac{\Delta\tilde{n}_\sigma}{\tilde{n}_\sigma} \simeq 1.23 \times 10^{-2}. \tag{3.12}$$

Since $\Delta\tilde{n}_\sigma$ depends on the $\Delta\chi_\sigma$ computed above, we then conclude that the hot phonons reach a temperature $T_{ph}^{E_{2g}}$ around 450 K.

3.5.4 Photoinduced Renormalization of the Electronic Structure

We also consider the possibility that nonlinear effects caused by the interaction with the pump pulse may act as a source of renormalization for the electronic structure of MgB_2 and thereby lead to the anomalous behaviour of the plasma edge. To this end, we perform frozen-phonon ab initio calculations of the coherent electron dynamics triggered by an ultrashort laser pulse, and study how the electronic structure of MgB_2 is modified after the photoexcitation. This method can provide insightful information on the coherent electron dynamics generated by intense short laser pulses and give a microscopic description of the fast electronic response in photoexcited systems with attosecond resolution [70–76]. We find that these modifications cannot account for our results.

The effect of an in-plane polarized laser beam has been investigated on the fast time scale (∼80 fs) at the Γ, A, K and M points of the BZ. The field-induced changes of the electronic structure are calculated using a pump photon energy at 1.55 eV or tuned to resonate with selected k points. Moreover, in order to investigate the dependence of the electronic response on the pump fluence, different field strengths are applied during the dynamics, corresponding to fluences of 0.10, 0.42, 1.68, 3.77, 6.72 and 10.51 mJ/cm^2. The details of the calculations are provided in Appendix C.1.1. Tables 3.1 and 3.2 show, respectively, the net bandgap calculated as the difference between initial (at 0 time) and final (after 40 fs) gap for Γ, A, M and K points for a pump photon energy at 1.55 eV or in resonance with the different k points. Notice that a negative value in the tables indicates a decrease in the single-particle band energies, while a positive value corresponds to their increase.

Remarkably, we find that the pump pulse at 1.55 eV cannot cause substantial renormalization of the electronic structure at the A, K and M points but affects the Γ point, in that the single-particle energies significantly depend on the absorbed pump fluence. In this regard, the renormalization of the Mg ζ band has an impact on the interband transition at Γ that determines the c-axis plasmon energy, leading to its *redshift*. The time-evolution of the B π—Mg ζ interband transition energy at the Γ point of the BZ is shown in Fig. 3.14a for different field strengths. We observe that the single-particle energies undergo a shrinkage of 40 meV upon increasing the absorbed fluence from 0.10 mJ/cm^2 to 1.68 mJ/cm^2. This effect is consistently observed at early time-delays (i.e. the maximum of the response at 170 fs) in our $\Delta R/R$ as a function of fluence (Fig. 3.14b). The plasmon blueshift decreases by 20 meV when the absorbed pump fluence changes from 0.24 mJ/cm^2 to 2.40 mJ/cm^2, in striking quantitative agreement with the shift predicted by our ab initio calculations. The shift observed in the experimental spectra has to be interpreted as a net variation of the plasmon energy that results from the combination of two effects: The blueshift induced by the increased carrier density $\widetilde{n}$ and the redshift caused by the photoinduced renormalization of the electronic structure. In conclusion, the present calculations rule out the possibility that the nonlinear interaction with the ultrashort laser pulse is responsible for the plasmon blueshift.

Table 3.1 Gap renormalization calculated upon excitation with a 1.55 eV pump pulse at different points (Γ, A, M, K) of the BZ and for different absorbed pump fluences

Fluence (mJ/cm^2)	Γ (eV)	A (eV)	M (eV)	K (eV)
0.10	−0.009	0	0	0
0.42	−0.036	0	0	0
1.68	−0.141	0	0	0
3.77	−0.310	0	0	0
6.72	−0.532	0	0	0
10.51	−0.794	0	0	0

Table 3.2 Gap renormalization calculated upon excitation with a resonant pump pulse at different points (Γ, A, M, K) of the BZ and for different absorbed pump fluences

Fluence (mJ/cm^2)	Γ (eV)	A (eV)	M (eV)	K (eV)
0.10	−0.12	−0.329	−0.005	−0.003
0.42	−0.046	−1.265	−0.020	−0.013
1.68	−0.178	−4.323	−0.080	−0.033
3.77	−0.392	−4.065	−0.179	−0.020
6.72	−0.676	−3.120	−0.317	−0.002
10.51	−1.011	−3.858	−0.494	−0.006

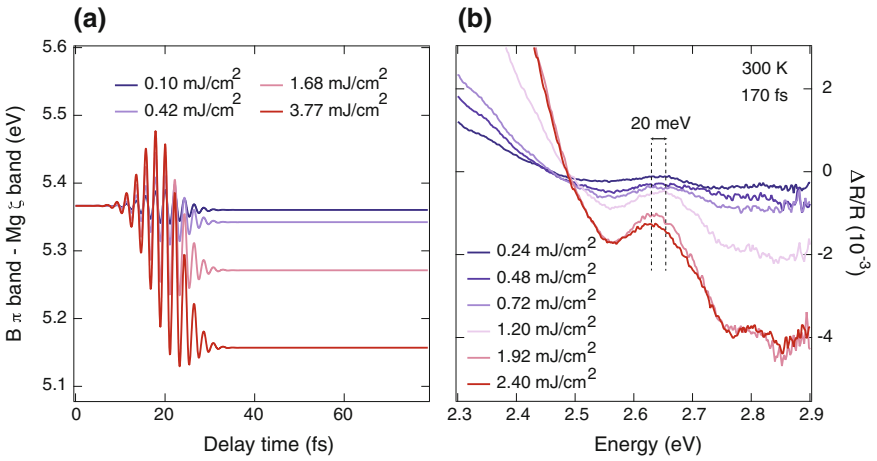

Fig. 3.14 **a** Calculated ultrafast renormalization of the B π - Mg ζ interband transition energy at the Γ point of the BZ. The results are shown for different field strengths (indicated in the label), which are comparable to the experimental conditions. **b** Transient spectra of ΔR/R in the vicinity of the *c*-axis plasmon peak at 300 K for different absorbed fluences and at a delay time of 170 fs

3.6 Anharmonic Decay of the Hot Phonons

Having established the crucial role of hot phonons in the observed plasmon blueshift, we finally consider the effects of lattice anharmonicity and thermal expansion on the c-axis plasmon energy. Indeed, as discussed above, lattice expansion is expected to result from hot phonon energy dissipation via anharmonic coupling with low-energy acoustic modes. To study these effects, we perform ab initio calculations of the dynamical electronic properties of MgB_2 for different lattice parameters in the case of uniaxial (c-axis) and of 3D lattice expansion. Specifically, we simulate the effect of the lattice expansion on the c-axis plasmon of MgB_2 by calculating the loss function $L(\mathbf{q}, \omega)$ in the long-wavelength limit ($\mathbf{q} = 0$) and at different lattice parameters. Indeed, the collective electronic excitations of a bulk solid can be obtained from to the peaks in the loss function $L(\mathbf{q}, \omega)$ [77, 78], defined as the imaginary part of the inverse dielectric function

$$L(\mathbf{q}, \omega) = \mathrm{Im}[\epsilon^{-1}(\mathbf{q}, \omega)], \tag{3.13}$$

where $\mathbf{q}$ and ω are momentum and energy, respectively, transferred to the system. The inverse dielectric function ϵ^{-1} is related to the density-response function of interacting electrons χ through the integral equation $\epsilon^{-1} = 1 + \upsilon\chi$, where υ is the Coulomb potential. In the framework of the Time-Dependent DFT [79, 80], χ obeys the integral equation $\chi = \chi^o + \chi^o(\upsilon + \mathrm{K_{xc}})\chi$, where χ^o is the response function for a non-interacting electron system and $\mathrm{K_{xc}}$ accounts for dynamical exchange-

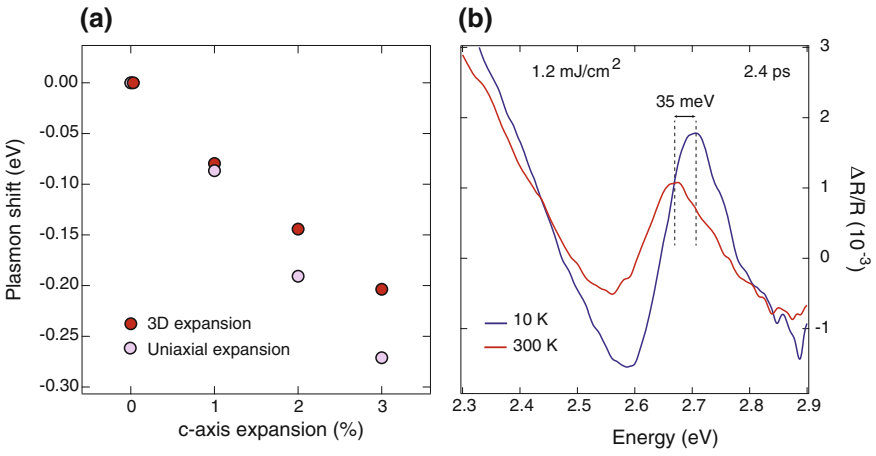

Fig. 3.15 **a** Calculated plasmon shift as a function of the crystal expansion along the c-axis, which mimics the effect of thermal heating on the plasmon energy. The values are shown in two different cases: Three-dimensional expansion (red dots) and uniaxial expansion (violet dots). **b** Transient spectra of ΔR/R in the vicinity of the c-axis plasmon peak at 10 and RT, for an absorbed fluence of 1.2 mJ/cm^2 and at a delay time of 2.4 ps

correlation effects. The imaginary part of χ^o, which takes a matrix form for a three-dimensional solid, is calculated according to

$$\mathrm{Im}[\chi^o_{\mathbf{G}\mathbf{G}'}(\mathbf{q},\omega)] = \frac{2}{\Omega}\sum_{\mathbf{k}}^{\mathrm{BZ}}\sum_{nn'}(f_{n\mathbf{k}} - f_{n'\mathbf{k}+\mathbf{q}})\langle\psi_{n\mathbf{k}}|e^{-\mathrm{i}(\mathbf{q}+\mathbf{G})\cdot\mathbf{r}}|\psi_{n'\mathbf{k}+\mathbf{q}}\rangle \\ \langle\psi_{n'\mathbf{k}+\mathbf{q}}|e^{\mathrm{i}(\mathbf{q}+\mathbf{G}')\cdot\mathbf{r}}|\psi_{n\mathbf{k}}\rangle\delta(\varepsilon_{n\mathbf{k}} - \varepsilon_{n'\mathbf{k}+\mathbf{q}} + \omega), \tag{3.14}$$

where the factor 2 accounts for spin, Ω is the normalization volume, n and n' are the energy band indices, vector $\mathbf{k}$ is in the first BZ, $f_{n\mathbf{k}}$ is the Fermi distribution function, $\varepsilon_{n\mathbf{k}}$ and $\psi_{n\mathbf{k}}$ are Bloch eigenvalues and eigenfunctions, respectively, of the Kohn-Sham Hamiltonian. The details of the calculations are provided in Appendix C.1.2.

In both analyzed cases, we find that the c-axis plasmon peak energy redshifts by 37 meV/P, where P is rate of the volume expansion in percent. The results of the calculations are shown in Fig. 3.15a. The origin of such a behaviour resides again in the fact that the plasmon energy is mainly determined by the transitions from

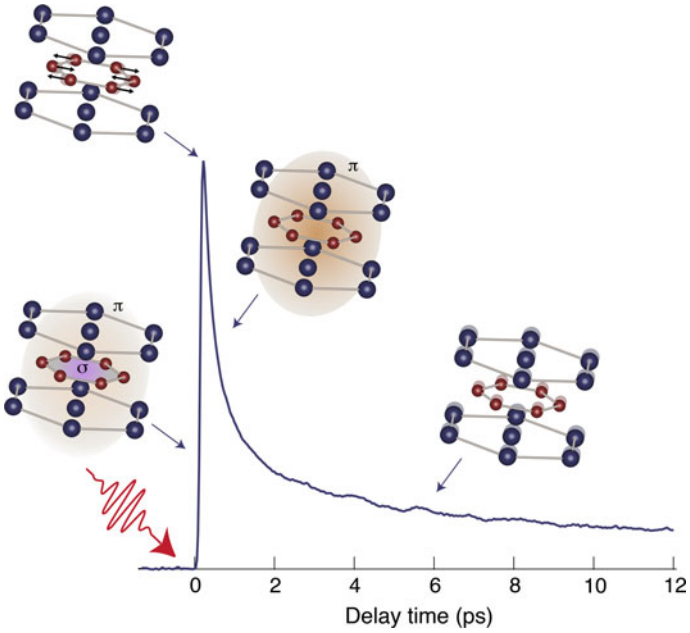

Fig. 3.16 Cartoon of the ultrafast dynamics in MgB_2 following photoexcitation with 1.55 eV laser pulses. After the interaction with the solid, the ultrashort laser pulse leads to the excitation of both σ and π carriers. The nonthermal σ carriers are strongly coupled to the branch of the E_{2g} phonon mode and efficiently generate hot phonons during the first 170 fs. Subsequently, the energy stored in the hot-phonon subsystem is released to the π carrier density via interband scattering and to low-energy phonons via anharmonic decay

the B π band to the Mg ζ band at the Γ point of the BZ. As the distance between atomic planes increases, the energy separation between these two bands diminishes, which results in the plasmon *redshift*. This scenario is confirmed by our ΔR/R data at 10 K and 300 K (Fig. 3.15b) at a time delay of 2.4 ps, i.e. well after the extinction of hot phonon effects. At this time delay, we observe a redshift of $\sim$35 meV in the *c*-axis plasmon peak when the temperature is raised from 10 K to 300 K, due to the increased lattice constants in the crystal. This result rationalizes the last step of the dynamics probed within our temporal window and offers a complete explanation of the ultrafast optical response of MgB_2.

3.7 Conclusions

In the previous Sections, we demonstrated the capability of ultrafast broadband optical spectroscopy to shed new light on the physics of multiband systems in the strong electron-boson coupling regime. Disentangling the contributions of different subsets of carriers within the same measurement is a rare event in ultrafast spectroscopy, as the pump-probe signal is typically blind to the details of the photoexcited electronic density. Here, instead, the combination of high temporal resolution and wide probing range in the visible allows us to monitor two specific observables related to the σ and π carriers, providing direct access into their dynamics.

On one hand, high time resolution is necessary to reveal hot phonon effects associated with the σ carriers, as the rise-time in the *a*-axis response indicates the build-up of the effective interaction between the σ holes and the strongly coupled optical phonons of the E_{2g} branch. This, in turn, causes a blueshift of $\omega_{p,a}$ within 170 fs and explains the prompt increase of the optical scattering rate Γ_a [5]. On the other hand, the broad spectral range monitored by the probe is crucial to reveal the renormalization of the *c*-axis plasmon, which is a very sensitive observable to the π carrier dynamics. The delayed blueshift of $\omega_{p,c}$ is the signature of a crosstalk between the σ and π bands, regulated by the emission and re-absorption of the high-energy optical phonons associated with the branch of the E_{2g} mode. Consistent with this scenario, the optical scattering rate Γ_c displays a slow rise, as the increased density of π carriers undergo scattering events with the nonequilibrium phonon population. As the system evolves towards equilibrium, the decay of the *a*-axis signal is governed by the release of the energy stored in the hot-phonon subsystem to the electronic degrees of freedom via phonon-electron scattering, and to low-energy phonons via anharmonic decay [60]. This explanation implies that the picosecond dynamics of the *a*-axis plasma edge is due to the energy relaxation of the optical phonon population, rather than the electron-phonon thermalization observed in conventional noble metals [81]. The increased phonon re-absorption by the σ and π carriers in turn reduces their net thermalization (i.e. phonon emission) rate, resulting in a hot-phonon bottleneck mechanism lasting tens of picoseconds. A representative cartoon of the emerging ultrafast dynamics is shown in Fig. 3.16.

The different stages of the ultrafast dynamics in MgB_2 are modelled by theoretical calculations, which reveal the impact of the pump pulse on the electronic structure, explain the anomalous blueshift of the plasma frequencies and highlight the modification of the electrodynamic properties upon anharmonic phonon decay. In particular, it is intriguing to notice how the temperature dependence of the bare plasma frequencies in MgB_2 does not follow the typical behaviour of weakly-interacting single-band Fermi liquids. Indeed, it is the presence of the strong electron-boson interaction that affects the carrier density in each band of the material, regulating the size of the Fermi surface through the the boson thermal activation. With this respect, the physics of MgB_2 is closer to that of strongly interacting semimetals with hole and electron bands, which is a very curious aspect deserving future attention. More interestingly, photoexciting the system using optical photons changes the balance of the electronic and bosonic temperature and leads to an effective increase of the Fermi surface area of the σ band. Thus, the effective carrier density can be controlled by the photoexcitation in an ultrafast fashion, which possesses a number of advantages over conventional chemical doping. In MgB_2, doping carriers by atomic substitution has always led to a decrease of T_C [82], since hole doping cannot be achieved and doped carriers produce band filling (i.e. decrease of the hole density) and disorder in the system. In contrast, under nonequilibrium conditions, the hot phonon platform allows increasing the Fermi surface size without introducing additional disorder, and the strong coupling of the σ holes with *one* specific phonon enables a selective transfer of energy towards that mode. These concepts might be used to engineer future devices for concentrating and temporarily storing the energy into a single lattice mode of interest. A promising frontier would involve the coherent generation and detection of the E_{2g} phonon mode, similarly to previous experiments on graphite with its high-energy E_{2g2} phonon mode [6]. Although our pump pulse duration is sufficiently short to coherently excite this mode, in our $\Delta R/R$ maps we did not find any evidence for fast coherent oscillations. Future experiments with tunable pump and probe photon energy and polarization are therefore required to elucidate the coherent transfer of energy from the σ hole subsystem to the E_{2g} phonon mode and to identify the subsequent influence of the relaxing carriers on the lattice properties [6].

To conclude this Chapter, our results rationalise the emergence of hot phonon effects in MgB_2 and provide the first dynamical observation of the interband scattering process in a multiband system. With respect to the latter point, our experiment confirms the hypothesis of early nanosecond infrared reflectivity and electron spin resonance studies [83, 84] and goes beyond that interpretation by clocking the timescale at which the interband scattering process takes place. In addition, our measurement highlights how ultrafast broadband optical spectroscopy can investigate the interplay between single-particle and collective structural (phonon) and charge (plasmon) excitations in strongly interacting multiband systems, which is a previously unexplored topic. Finally, we believe that our approach paves the route to the observation of exotic collective modes of electronic origin via the ISRS mechanism. In the normal state, by tailoring the parameters of the photoexcitation to hit resonance conditions, one can possibly access the dynamics of the theoretically predicted acoustic plasmons [50, 85]. In the SC state, by decreasing the fluence of the

pump pulse and selecting the A_{1g} symmetry channel, one can reveal the emergence of the Leggett mode and gain novel insights into interband *pairing* mechanisms in multiband superconductors [42, 55, 56].

References

1. S.I. Anisimov, B.L. Kapeliovich, T.L. Perel'man, Electron emission from the metal surfaces induced by ultrashort lasers pulses. Zhurnal Ehksperimental'noj i Teoreticheskoj Fiziki **66**(2), 776–781 (1974)
2. S.D. Brorson, A. Kazeroonian, J.S. Moodera, D.W. Face, T.K. Cheng, E.P. Ippen, M.S. Dresselhaus, G. Dresselhaus, Femtosecond room-temperature measurement of the electron-phonon coupling constant γ in metallic superconductors. Phys. Rev. Lett. **64**(18), 2172 (1990)
3. C.-K. Sun, F. Vallée, L.H. Acioli, E.P. Ippen, J.G. Fujimoto, Femtosecond-tunable measurement of electron thermalization in gold. Phys. Rev. B **50**(20), 15337 (1994)
4. N. Del Fatti, C. Voisin, M. Achermann, S. Tzortzakis, D. Christofilos, F. Vallée, Nonequilibrium electron dynamics in noble metals. Phys. Rev. B **61**(24), 16956 (2000)
5. T. Kampfrath, L. Perfetti, F. Schapper, C. Frischkorn, M. Wolf, Strongly coupled optical phonons in the ultrafast dynamics of the electronic energy and current relaxation in graphite. Phys. Rev. Lett. **95**(18), 187403 (2005)
6. K. Ishioka, M. Hase, M. Kitajima, L. Wirtz, A. Rubio, H. Petek, Ultrafast electron-phonon decoupling in graphite. Phys. Rev. B **77**(12), 121402 (2008)
7. M. Breusing, C. Ropers, T. Elsaesser, Ultrafast carrier dynamics in graphite. Phys. Rev. Lett. **102**(8), 086809 (2009)
8. Y. Ishida, T. Togashi, K. Yamamoto, M. Tanaka, T. Taniuchi, T. Kiss, M. Nakajima, T. Suemoto, S. Shin, Non-thermal hot electrons ultrafastly generating hot optical phonons in graphite. Sci. Rep. **1**, 64 (2011)
9. M. Breusing, S. Kuehn, T. Winzer, E. Malić, F. Milde, N. Severin, J.P. Rabe, C. Ropers, A. Knorr, T. Elsaesser, Ultrafast nonequilibrium carrier dynamics in a single graphene layer. Phys. Rev. B **83**(15), 153410 (2011)
10. D.P. Di Vincenzo, E.J. Mele, Self-consistent effective-mass theory for intralayer screening in graphite intercalation compounds. Phys. Rev. B **29**(4), 1685 (1984)
11. C.D. Spataru, M.A. Cazalilla, A. Rubio, L.X. Benedict, P.M. Echenique, S.G. Louie, Anomalous quasiparticle lifetime in graphite: band structure effects. Phys. Rev. Lett. **87**(24), 246405 (2001)
12. S. Piscanec, M. Lazzeri, F. Mauri, A.C. Ferrari, J. Robertson, Kohn anomalies and electron-phonon interactions in graphite. Phys. Rev. Lett. **93**(18), 185503 (2004)
13. M.S. Dresselhaus, G. Dresselhaus, Light scattering in graphite intercalation compounds, in Light Scattering in Solids III, (Springer, Berlin, 1982), pp. 3–57
14. A. Javey, J. Guo, M. Paulsson, Q. Wang, D. Mann, M. Lundstrom, H. Dai, High-field quasi-ballistic transport in short carbon nanotubes. Phys. Rev. Lett. **92**(10), 106804 (2004)
15. T. Elsaesser, R.J. Bäuerle, W. Kaiser, Hot phonons in InAs observed via picosecond free-carrier absorption. Phys. Rev. B **40**(5), 2976 (1989)
16. H.P.M. Pellemans, P.C.M. Planken, Effect of nonequilibrium LO phonons and hot electrons on far-infrared intraband absorption in n-type GaAs. Phys. Rev. B **57**(8), R4222 (1998)
17. J. Nagamatsu, N. Nakagawa, T. Muranaka, Y. Zenitani, J. Akimitsu, Superconductivity at 39 K in magnesium diboride. Nature **410**(6824), 63–64 (2001)
18. J. Kortus, I.I. Mazin, K.D. Belashchenko, V.P. Antropov, L.L. Boyer, Superconductivity of metallic boron in MgB_2. Phys. Rev. Lett. **86**(20), 4656 (2001)
19. Y. Kong, O.V. Dolgov, O. Jepsen, O.K. Andersen, Electron-phonon interaction in the normal and superconducting states of MgB_2. Phys. Rev. B **64**(2), 020501 (2001)

20. K.P. Bohnen, R. Heid, B. Renker, Phonon dispersion and electron-phonon coupling in MgB_2 and AlB_2. Phys. Rev. Lett. **86**(25), 5771 (2001)
21. K. Kunc, I. Loa, K. Syassen, R.K. Kremer, K. Ahn, MgB_2 Under pressure: phonon calculations, raman spectroscopy, and optical reflectance. J. Phys. Cond. Matt. **13**(44), 9945 (2001)
22. A.A. Golubov, J. Kortus, O.V. Dolgov, O. Jepsen, Y. Kong, O.K. Andersen, B.J. Gibson, K. Ahn, R.K. Kremer, Specific heat of MgB_2 in a one- and a two-band model from first-principles calculations. J. Phys. Cond. Matt. **14**(6), 1353 (2002)
23. H.J. Choi, D. Roundy, H. Sun, M.L. Cohen, S.G. Louie, The origin of the anomalous superconducting properties of MgB_2. Nature **418**(6899), 758–760 (2002)
24. E.A. Yelland, J.R. Cooper, A. Carrington, N.E. Hussey, P.J. Meeson, S. Lee, A. Yamamoto, S. Tajima, de haas-van alphen effect in single crystal mgb_2. Phys. Rev. Lett. **88**, 217002 (2002)
25. S. Souma, Y. Machida, T. Sato, T. Takahashi, H. Matsui, S.C. Wang, H. Ding, A. Kaminski, J.C. Campuzano, S. Sasaki et al., The origin of multiple superconducting gaps in MgB_2. Nature **423**(6935), 65–67 (2003)
26. J.W. Quilty, S. Lee, A. Yamamoto, S. Tajima, Superconducting gap in MgB_2: electronic Raman scattering measurements of single crystals. Phys. Rev. Lett. **88**(8), 087001 (2002)
27. T. Yildirim, O. Gülseren, J.W. Lynn, C.M. Brown, T.J. Udovic, Q. Huang, N. Rogado, K.A. Regan, M.A. Hayward, J.S. Slusky, T. He, M.K. Haas, P. Khalifah, K. Inumaru, R.J. Cava, Giant anharmonicity and nonlinear electron-phonon coupling in MgB_2: a combined first-principles calculation and neutron scattering study. Phys. Rev. Lett. **87**(3), 037001 (2001)
28. A. Shukla, M. Calandra, M. d'Astuto, M. Lazzeri, F. Mauri, C. Bellin, M. Krisch, J. Karpinski, S.M. Kazakov, J. Jun et al., Phonon dispersion and lifetimes in MgB_2. Phys. Rev. Lett. **90**(9), 095506 (2003)
29. S. Dal Conte, L. Vidmar, D. Golež, M. Mierzejewski, G. Soavi, S. Peli, F. Banfi, G. Ferrini, R. Comin, B.M. Ludbrook et al., Snapshots of the retarded interaction of charge carriers with ultrafast fluctuations in cuprates. Nat. Phys. **11**(5), 421–426 (2015)
30. E. Baldini, A. Mann, L. Benfatto, E. Cappelluti, A. Acocella, V.M. Silkin, S.V. Eremeev, A.B. Kuzmenko, S. Borroni, T. Tan, X.X. Xi, F. Zerbetto, R. Merlin, F. Carbone, Real-time observation of phonon-mediated σ-π interband scattering in MgB_2. Phys. Rev. Lett. **119**, 097002 (2017)
31. A. Balassis, E.V. Chulkov, P.M. Echenique, V.M. Silkin, First-principles calculations of dielectric and optical properties of MgB_2. Phys. Rev. B **78**(22), 224502 (2008)
32. V. Russell, R. Hirst, F.A. Kanda, A.J. King, An x-ray study of the magnesium borides. Acta Crystallogr. **6**(11–12), 870–870 (1953)
33. S.L. Bud'ko, G. Lapertot, C. Petrovic, C.E. Cunningham, N. Anderson, P.C. Canfield, Boron isotope effect in superconducting MgB_2. Phys. Rev. Lett. **86**(9), 1877 (2001)
34. H. Kotegawa, K. Ishida, Y. Kitaoka, T. Muranaka, J. Akimitsu, Evidence for strong-coupling s-wave superconductivity in MgB_2: ^{11}B NMR study. Phys. Rev. Lett. **87**(12), 127001 (2001)
35. A.Y. Liu, I. Mazin, J. Kortus, Beyond Eliashberg superconductivity in MgB_2: anharmonicity, two-phonon scattering, and multiple gaps. Phys. Rev. Lett. **87**(8), 087005 (2001)
36. Y. Wang, T. Plackowski, A. Junod, Specific heat in the superconducting and normal state (2–300 K, 0–16 T), and magnetic susceptibility of the 38 K superconductor MgB_2: evidence for a multicomponent gap. Physica C **355**(3), 179–193 (2001)
37. M. Iavarone, G. Karapetrov, A.E. Koshelev, W.K. Kwok, G.W. Crabtree, D.G. Hinks, W.N. Kang, E. Choi, H.J. Kim, H. Kim et al., Two-band superconductivity in MgB_2. Phys. Rev. Lett. **89**(18), 187002 (2002)
38. M.R. Eskildsen, M. Kugler, S. Tanaka, J. Jun, S.M. Kazakov, J. Karpinski, Ø. Fischer, Vortex imaging in the π band of magnesium diboride. Phys. Rev. Lett. **89**(18), 187003 (2002)
39. X.K. Chen, M.J. Konstantinović, J.C. Irwin, D.D. Lawrie, J.P. Franck, Evidence for two superconducting gaps in MgB_2. Phys. Rev. Lett. **87**(15), 157002 (2001)
40. A.F. Goncharov, V.V. Struzhkin, E. Gregoryanz, J. Hu, R.J. Hemley, H.-K. Mao, G. Lapertot, S.L. Bud'ko, P.C. Canfield, Raman spectrum and lattice parameters of MgB_2 as a function of pressure. Phys. Rev. B **64**(10), 100509 (2001)

41. J.W. Quilty, S. Lee, S. Tajima, A. Yamanaka, c-axis Raman scattering spectra of MgB_2: observation of a dirty-limit gap in the π bands. Phys. Rev. Lett. **90**(20), 207006 (2003)
42. G. Blumberg, A. Mialitsin, B.S. Dennis, N.D. Zhigadlo, J. Karpinski, Multi-gap superconductivity in MgB_2: magneto-Raman spectroscopy. Physica C **456**(1), 75–82 (2007)
43. V. Guritanu, A.B. Kuzmenko, D. van der Marel, S.M. Kazakov, N.D. Zhigadlo, J. Karpinski, Anisotropic optical conductivity and two colors of MgB_2. Phys. Rev. B **73**(10), 104509 (2006)
44. A.B. Kuzmenko, Multiband and impurity effects in infrared and optical spectra of MgB_2. Physica C **456**(1), 63–74 (2007)
45. T. Kakeshita, S. Lee, S. Tajima, Anisotropic Drude response and the effect of anisotropic C substitution in $Mg(B_{1-x}C_x)_2$. Phys. Rev. Lett. **97**(3), 037002 (2006)
46. T. Masui, S. Lee, S. Tajima, Carbon-substitution effect on the electronic properties of MgB_2 single crystals. Phys. Rev. B **70**(2), 024504 (2004)
47. I.I. Mazin, V.P. Antropov, Electronic structure, electron-phonon coupling, and multiband effects in MgB_2. Physica C **385**(1), 49–65 (2003)
48. Y.Q. Cai, P. Chow, O.D. Restrepo, Y. Takano, K. Togano, H. Kito, H. Ishii, C.C. Chen, K.S. Liang, C.T. Chen et al., Low-energy charge-density excitations in MgB_2: striking interplay between single-particle and collective behavior for large momenta. Phys. Rev. Lett. **97**(17), 176402 (2006)
49. W. Ku, W.E. Pickett, R.T. Scalettar, A.G. Eguiluz, Ab initio investigation of collective charge excitations in MgB_2. Phys. Rev. Lett. **88**(5), 057001 (2002)
50. V.M. Silkin, A. Balassis, P.M. Echenique, E.V. Chulkov, Ab initio calculation of low-energy collective charge-density excitations in MgB_2. Phys. Rev. B **80**(5), 054521 (2009)
51. S. Galambosi, J.A. Soininen, A. Mattila, S. Huotari, S. Manninen, G. Vankó, N.D. Zhigadlo, J. Karpinski, K. Hämäläinen, Inelastic x-ray scattering study of collective electron excitations in MgB_2. Phys. Rev. B **71**(6), 060504 (2005)
52. L.D. Landau, On the vibrations of the electronic plasma. Zh. Eksp. Teor. Fiz. **10**, 25 (1946)
53. N.N. Bogoliubov, V.V. Tolmachev, D.V. Shirkov, A new method in the theory of superconductivity, in *Academy of Sciences of the USSR*, (1958)
54. M. Calandra, F. Mauri, Electron-phonon coupling and phonon self-energy in MgB_2: interpretation of MgB_2 Raman spectra. Phys. Rev. B **71**(6), 064501 (2005)
55. A.J. Leggett, Number-phase fluctuations in two-band superconductors. Prog. Theor. Phys. **36**(5), 901–930 (1966)
56. T. Cea, L. Benfatto, Signature of the Leggett mode in the A_{1g} Raman response: from MgB_2 to iron-based superconductors. Phys. Rev. B **94**(6), 064512 (2016)
57. D. Mou, R. Jiang, V. Taufour, R. Flint, S.L. Bud'ko, P.C. Canfield, J.S. Wen, Z.J. Xu, Ge. Gu, A. Kaminski, Strong interaction between electrons and collective excitations in the multiband superconductor MgB2. Phys. Rev. B **91**(14), 140502 (2015)
58. Y. Xu, M. Khafizov, L. Satrapinsky, P. Kúš, A. Plecenik, R. Sobolewski, Time-resolved photoexcitation of the superconducting two-gap state in MgB_2 thin films. *Phys. Rev. B***91**(19) (2003)
59. J. Demsar, B. Podobnik, V.V. Kabanov, Th Wolf, D. Mihailovic, Superconducting gap Δ_C, the pseudogap Δ_P, and pair fluctuations above T_C in overdoped $Y_{1-x}Ca_xBa_2Cu_3O_{7-\delta}$ from femtosecond time-domain spectroscopy. Phys. Rev. Lett. **82**(24), 4918 (1999)
60. J. Demsar, R.D. Averitt, A.J. Taylor, V.V. Kabanov, W.N. Kang, H.J. Kim, E.M. Choi, S.I. Lee, Pair-breaking and superconducting state recovery dynamics in MgB_2. Phys. Rev. Lett. **91**(26), 267002 (2003)
61. L. Benfatto, S.G. Sharapov, Optical-conductivity sum rule in cuprates and unconventional charge density waves: a short review. Low Temp. Phys. **32**(6), 533–545 (2006)
62. M. Ortolani, P. Calvani, S. Lupi, Frequency-dependent thermal response of the charge system and the restricted sum rules of $La_{2-x}S\ r_xCuO_4$. Phys. Rev. Lett. **94**(6), 067002 (2005)
63. A. Toschi, M. Capone, M. Ortolani, P. Calvani, S. Lupi, C. Castellani, Temperature dependence of the optical spectral weight in the cuprates: role of electron correlations. Phys. Rev. Lett. **95**, 097002 (2005)

64. R.W. Schoenlein, W.Z. Lin, J.G. Fujimoto, G.L. Eesley, Femtosecond studies of nonequilibrium electronic processes in metals. Phys. Rev. Lett. **58**(16), 1680 (1987)
65. V.V. Kruglyak, R.J. Hicken, P. Matousek, M. Towrie, Spectroscopic study of optically induced ultrafast electron dynamics in gold. Phys. Rev. B **75**(3), 035410 (2007)
66. L. Ortenzi, E. Cappelluti, L. Benfatto, L. Pietronero, Fermi-surface shrinking and interband coupling in iron-based pnictides. Phys. Rev. Lett. **103**, 046404 (2009)
67. L. Benfatto, E. Cappelluti, Effects of the Fermi-surface shrinking on the optical sum rule in pnictides. Phys. Rev. B **83**, 104516 (2011)
68. F. Marsiglio, M. Schossmann, J.P. Carbotte, Iterative analytic continuation of the electron self-energy to the real axis. Phys. Rev. B **37**(10), 4965 (1988)
69. H. Uchiyama, K.M. Shen, S. Lee, A. Damascelli, D.H. Lu, D.L. Feng, Z.-X. Shen, S. Tajima, Electronic structure of MgB_2 from angle-resolved photoemission spectroscopy. Phys. Rev. Lett. **88**(15), 157002 (2002)
70. A. Acocella, G.A. Jones, F. Zerbetto, Excitation energy transfer and low-efficiency photolytic splitting of water ice by vacuum UV light. J. Phys. Chem. Lett. **3**(23), 3610–3615 (2012)
71. A. Acocella, F. Carbone, F. Zerbetto, Quantum study of laser-induced initial activation of graphite-to-diamond conversion. J. Am. Chem. Soc. **132**(35), 12166–12167 (2010)
72. A. Acocella, G.A. Jones, F. Zerbetto, What is adenine doing in photolyase? The Journal of Phys. Chem. B **114**(11), 4101–4106 (2010)
73. G.A. Jones, A. Acocella, F. Zerbetto, On-the-fly, electric-field-driven, coupled electron–nuclear dynamics. J. Phys. Chem. A **112**(40), 9650–9656 (2008)
74. G.A. Jones, A. Acocella, F. Zerbetto, Nonlinear optical properties of C_{60} with explicit time-dependent electron dynamics. Theor. Chem. Acc. **118**(1), 99–106 (2007)
75. A. Acocella, G.A. Jones, F. Zerbetto, Mono-and bichromatic electron dynamics: LiH, a test case. J. Phys. Chem. A **110**(15), 5164–5172 (2006)
76. A. Acocella, M. de Simone, F. Evangelista, M. Coreno, P. Rudolf, F. Zerbetto, Time-dependent quantum simulation of coronene photoemission spectra. Phys. Chem. Chem. Phys **18**, 13604 (2016)
77. D. Pines, P. Nozières, *The Theory of Quantum Liquids: Normal Fermi Liquids*, vol. 1 (WA Benjamin, San Francisco, 1966)
78. G. Giuliani, G. Vignale, *Quantum Theory of the Electron Liquid* (Cambridge University Press, Cambridge, 2005)
79. E. Runge, E.K. Gross, Density-functional theory for time-dependent systems. Phys. Rev. Lett. **52**(12), 997 (1984)
80. M. Petersilka, U. Gossmann, E. Gross, Excitation energies from time-dependent density-functional theory. Phys. Rev. Lett. **76**(8), 1212 (1996)
81. H.E. Elsayed-Ali, T.B. Norris, M.A. Pessot, G.A. Mourou, Time-resolved observation of electron-phonon relaxation in copper. Phys. Rev. Lett. **58**(12), 1212 (1987)
82. J. Kortus, O.V. Dolgov, R.K. Kremer, A.A. Golubov, Band filling and interband scattering effects in MgB_2: carbon versus aluminum doping. Phys. Rev. Lett. **94**(2), 027002 (2005)
83. R.P.S.M. Lobo, J. Tu, E. Choi, H. Kim, W.N. Kang, S. Lee, G.L. Carr. Transient infrared photoreflectance study of superconducting MgB_2: evidence for multiple gaps and interband scattering. arXiv preprint cond-mat/0404708. (2004)
84. R.P.S.M. Lobo, M. Elsen, P. Monod, J.J. Tu, E. Choi, H. Kim, W.N. Kang, S. Lee, R.J. Cava, G.L. Carr, *Interband scattering in* MgB_2, *in New Challenges in Superconductivity: Experimental Advances and Emerging Theories* (Springer, Berlin, 2005), pp. 243–248
85. K. Voelker, V.I. Anisimov, T.M. Rice, Acoustic plasmons in MgB_2. arXiv preprint cond-mat/0103082 (2001)

Chapter 4
Revealing Bound Exciton Physics in Strongly Interacting Band Insulators

The field of excitonics has gained increased attention in the last years, due to the unique properties that excitons manifest in the conversion and transport of energy.[1] Key to these developments is the ability to exploit the physics of these collective charge excitations in materials that are easily fabricated and widely available. Particular interest is being devoted to organic semiconductors, transition metal dichalcogenides and wide-bandgap oxides, following the discovery of bound and resonant excitons in these classes of materials. In organic semiconductors (like pentacene), a variety of excitons arise because the electronic properties are governed by those of the individual molecular building blocks, which are only slightly altered by the weak intermolecular interactions of the solid phase [1]. In layered transition metal dichalcogenides (like MoS_2), exciton physics emerges due to the low-dimensionality of the electronic structure, which is well-known to provide a strong enhancement of the electron-hole interaction energy. Finally, in wide-bandgap oxides (like ZnO), the strength of the Coulomb forces undergoes a remarkable increase because of the reduced screening [2]. The existence of these bosonic excitations has been predicted by many-body perturbation theory [3–5] and confirmed experimentally via the estimate of the fundamental parameter characterizing an exciton, namely its binding energy E_B [6, 7].

A prototypical system in which these collective excitations have been theoretically predicted [8, 9] but never experimentally confirmed is the anatase polymorph of TiO_2, which belongs to a class of solids with superior functionalities for the conversion of light into other forms of energy [10–12]. Indeed, despite decades of extensive studies, the nature of its fundamental optical excitations remains unknown.

[1] Parts of this Chapter are reprinted with permission from E. Baldini et al., Nature Communications 8, 13. Copyright 2017 Springer Nature; E. Baldini et al., Physical Review B 96, 041204(R). Copyright 2017 American Physical Society; E. Baldini et al., J. Am. Chem. Soc. 139 (33), 11584–11589. Copyright 2017 American Chemical Society. E. Baldini et al., ACS Photonics DOI: 10.1021/acsphotonics.7b00945. Copyright 2018 American Chemical Society.

E. Baldini, *Nonequilibrium Dynamics of Collective Excitations in Quantum Materials*, Springer Theses, https://doi.org/10.1007/978-3-319-77498-5_4

The main source of uncertainty is the electronic structure of this material and its relationship to the optical spectra. As anatase TiO_2 is a d^0 TMO, strong electron-electron correlations are not expected to play a fundamental role in the renormalization of the electronic structure. Therefore, this solid can be classified within the simple band insulator scheme, in which the forbidden energy gap arises as a result of band theory and it is not a consequence of the strong on-site Coulomb interaction. However, differently from other conventional band insulators, anatase TiO_2 represents a peculiar example in which electron-phonon interaction becomes relatively strong and act as a source of renormalization for the electronic and optical spectra. The presence of an intermediate-to-strong electron-phonon coupling in anatase TiO_2 has already been invoked to explain experimental results naturally pointing to the polaron concept [13, 14]. Recent transport [15], ARPES [16] and STM [17] data detected signatures of dressed electrons in the CB behaving like large polarons, while earlier threshold absorption [18] and photoluminescence [19] data provided clear evidence for Toyozawa's theory of the Urbach tail and radiative recombination of self-trapped excitons [20].

It is therefore pivotal to clarify the single- and two-particle excitation spectra of anatase TiO_2 and to establish the possible existence of strongly bound excitons among the fundamental charge excitations produced upon photon absorption. In such a scenario, studying exciton physics in a strongly interacting band insulator opens intriguing perspectives from a fundamental point of view, as it can shed light on the subtle details of the *exciton-phonon* coupling. This interaction is a topic of pivotal importance in solid-state physics, lying at the heart of a variety of phenomena like exciton self-trapping, SW transfers to phonon sidebands and Stokes-shifted emissions [20]. Historically, the microscopic details of this interaction have been addressed via absorption spectroscopy and photoluminescence in bulk materials at low temperatures [21–23]. The possibility to extend these concepts at RT in bulk materials paves the route to the development of novel devices where the optical properties can be tailored by tuning the exciton-phonon coupling, e.g. through the applications of mechanical strain, via isotope substitution or dielectric screening.

To address the physics of strong interactions in band insulators and to bridge the gap between fundamental research and future applications, in this Chapter we provide an extensive study of anatase TiO_2. After introducing the main properties of the material in Sect. 4.1, we apply advanced steady-state spectroscopies in Sects. 4.2 and 4.3 to demonstrate that the direct optical gap of anatase TiO_2 single crystals is dominated by a strongly bound exciton rising over the continuum of indirect interband transitions. Our results are rationalized by the use of state-of-the-art many-body perturbation theory calculations in Sect. 4.4, which unveil the character of the excitonic species. We finally demonstrate the universality of our results in the typical defect-rich samples (e.g. NPs) used in light-energy conversion applications. To reveal the spectroscopic signatures of the excitons in anatase TiO_2 NPs, in Sect. 4.5 we adopt a nonequilibrium approach and apply for the first time femtosecond 2D spectroscopy covering the spectral range of the exciton features in the deep-UV. This finding opens the doors to a detailed investigation of the low-energy single-particle and many-body dynamics of the system from the inspection of the exciton

renormalization. A step further consists of mapping the exciton-phonon coupling under nonequilibrium conditions, as this involves the interaction between two distinct types of collective excitations, i.e. excitons and phonons. We conclude the Chapter by proposing a possible application based on the optical properties of the excitons under nonequilibrium conditions, namely a methodology for probing the interfacial electron transfer (ET) between an adsorbed dye molecule and anatase TiO_2 NPs for the fields of photocatalysis and dye-sensitized solar cells.

4.1 Anatase TiO_2

Anatase TiO_2 crystallises in a tetragonal unit cell, built on a network of corner- or edge- sharing TiO_6 octahedra (Fig. 4.1a). The substantial difference between the lattice constants a = 3.78 Å and c = 9.51 Å results in a pronounced anisotropy of the electronic and optical properties. First significant steps towards understanding the electronic structure of this material were achieved by experimental probes such as ARPES [16, 24] and optical spectroscopies [18, 25, 26]. Recent ARPES studies revealed that anatase TiO_2 has an indirect bandgap, since the VB maximum lies close to the X point of the BZ and the CB minimum is at the Γ point [16, 24]; consequently, the lowest optical absorption edge can be described in terms of an Urbach tail caused by the phonon-induced localization of excitons [18]. This Urbach tail displays two independent responses for light polarized perpendicular or parallel to the *c*-axis, as expected from the intrinsic structural anisotropy of the system. Less attention, however, has been paid to the detailed characterization of the optical response above the absorption threshold, where anisotropy effects become more pronounced [25, 26]. In particular, the role played by many-body correlations in the optical properties has remained elusive to experimental probes, leading to a lack of knowledge about the nature of the elementary direct charge excitations in this material.

On the theory side, DFT with many-body perturbation-theory corrections at the GW level (where the name GW derives from the expression used for treating the self-energy, with G denoting the Green's function and W the screened Coulomb interaction) provided a preliminary description of the material's dielectric function [8, 9, 27, 28]. The diagonalization of the Bethe-Salpeter Hamiltonian predicted several direct optical transitions at energies well below the direct electronic gap computed at the GW level. The existence of bound excitons in anatase TiO_2 is, however, still awaiting experimental verification, due to the difficulty of measuring E_B. Indeed, conventional experimental methods like optical absorption [29], photoluminescence [30, 31] and magneto-optics [32] are not suitable for an indirect gap material, as the onset of direct band-to-band transitions cannot be identified; moreover, to derive E_B, these methods often rely on approximate models valid only for hydrogenic Wannier-Mott excitons [33].

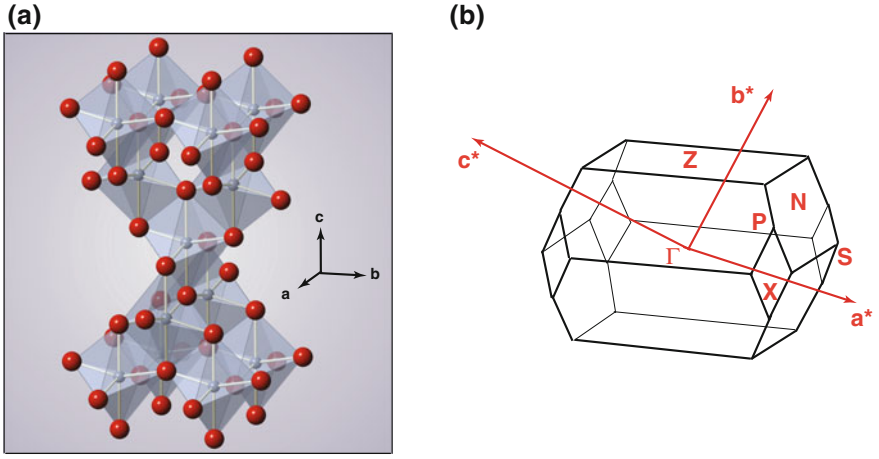

Fig. 4.1 **a** Crystallographic structure of anatase TiO_2 with highlighted TiO_6 polyhedra. Blue atoms represent Ti, red atoms represent O. **b** Representation of the 3D BZ of anatase TiO_2

In the next Sections, we first demonstrate the importance of many-body correlations in anatase TiO_2 by a combination of ARPES and SE, which allows us to provide very accurate values of the direct gap for both charged and neutral excitations. Their difference quantifies the interaction energy between the electron and hole generated by photon absorption. Importantly, we demonstrate the existence of strongly bound excitons in anatase TiO_2 and offer a rigorous estimate of E_B for a direct exciton rising over the continuum of indirect (phonon-mediated) interband transitions, free from assumptions on the nature of the excitonic species under study. Our results are corroborated by many-body perturbation-theory using the GW self-energy [34], unveiling the 2D spatial distribution of the excitonic states on the (001) plane and the localized nature of the excitonic states for light polarized along the *c*-axis.

4.2 Electronic Band Structure

To reveal the possible existence of a direct exciton, an accurate determination of the direct electronic bandgap is needed. To experimentally estimate the direct bandgap for this material, we perform ARPES measurements on anatase TiO_2 single crystals at low temperature. In particular, we introduce an excess electron density (n) in the CB of anatase TiO_2 by inducing oxygen vacancies in a (001)-oriented single crystal, similarly to the experiments reported in Ref. [16]. As a consequence, the Fermi level (E_F) pins slightly above the CB edge, providing a robust reference to measure the quasiparticle gap at the Γ point. To evaluate the shift of E_F above the CB edge, in Fig. 4.2 we show the energy distribution curves at the X (blue curve) and Γ (violet curve) points of the 3D BZ for a crystal that is doped with an excess electron density

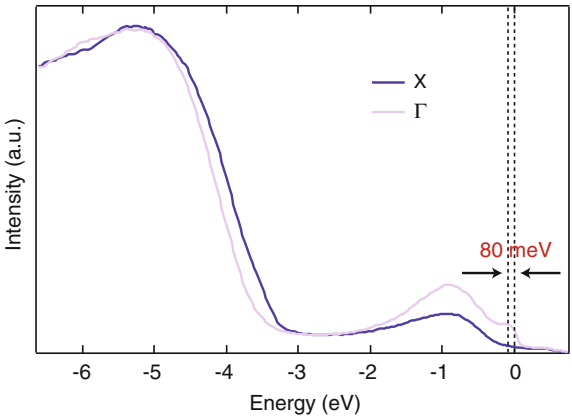

Fig. 4.2 Energy distribution curves at the X (blue curve) and Γ (violet curve) points of the BZ for a crystal that is doped with an excess electron density $n = 2 \times 10^{19}\,\mathrm{cm}^{-3}$. The temperature is 20 K. The spectra exhibit a feature at −1 eV, corresponding to the in-gap oxygen defect state. The curve at Γ exhibits SW at E_F, which lies 80 meV above the conduction quasiparticle band

$n = 2 \times 10^{19}\,\mathrm{cm}^{-3}$. The temperature of the sample is maintained at 20 K. In both spectra, the structure arising at -1 eV corresponds to the well-established in-gap oxygen defect states [35]. The curve at Γ exhibits SW at E_F, which lies 80 meV above the conduction quasiparticle band.

The valence states at 20 K between the Γ and X points are displayed in Fig. 4.3a and referenced to the bottom of the CB. To resolve the dispersive features present in the ARPES maps and evaluate the energy of the quasiparticle in the VB, we make use of a well-established methodology for ARPES data analysis, which relies on computing the second-derivative of the ARPES data along the energy direction [36]. Figure 4.3b shows the second derivative of the ARPES data. The dashed blue line, highlighting the top of the VB, has been drawn as a guide to the eye. As expected, the VB onset occurs close to the X point, and precedes the rise at Γ by ∼0.5 eV. Direct inspection of the band structure yields a first highly dispersing band close to the VB upper edges, whose maxima in the vicinity of the X and Γ points sit at -3.47 ± 0.05 eV and -3.97 ± 0.05 eV, respectively. These maxima represent a valuable estimate of the quasiparticle energies. Our primary interest here is the value of the direct gap at the Γ point, which can now be estimated to be ∼3.97 eV in a doped single crystal with $n = 2 \times 10^{19}\,\mathrm{cm}^{-3}$.

To monitor the evolution of the quasiparticle gap at the Γ point as a function of doping, we perform additional ARPES experiments with a variable excess electron density ($5 \times 10^{17}\,\mathrm{cm}^{-3} \leq n \leq 5 \times 10^{20}\,\mathrm{cm}^{-3}$) in the CB. The energy-momentum dispersion relations for the bottom of the CB in the two extreme n-doping levels considered in our experiment are displayed in Fig. 4.4a, b; the second-derivative of these maps with respect to the energy axis are instead shown in Fig. 4.4c, d. The second-derivative analysis allows us to identify the position of the quasiparticle energy at the bottom of the CB.

Figure 4.4e compares the energy distribution curves at the Γ point of the BZ at the two considered doping levels. Relying on the second-derivative analysis also for the VB, we can estimate the quasiparticle gap at Γ for the two dopings at ∼3.98

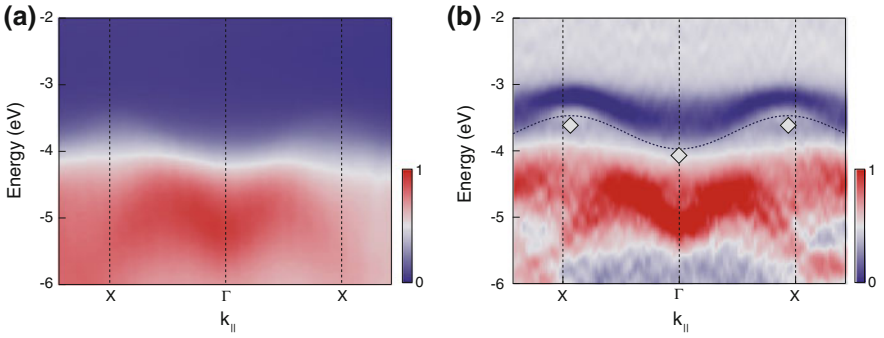

Fig. 4.3 **a** ARPES data and **b** second derivative ARPES data of the electronic structure of n-doped anatase TiO_2 ($n = 2 \times 10^{19}\,cm^{-3}$) at the top of the VB between Γ and X. Dashed blue lines are drawn as a guide to the eye. The spectrum is referenced to the bottom of the CB at Γ. The intensity is indicated by a linear colour scale, as shown in the colour bar

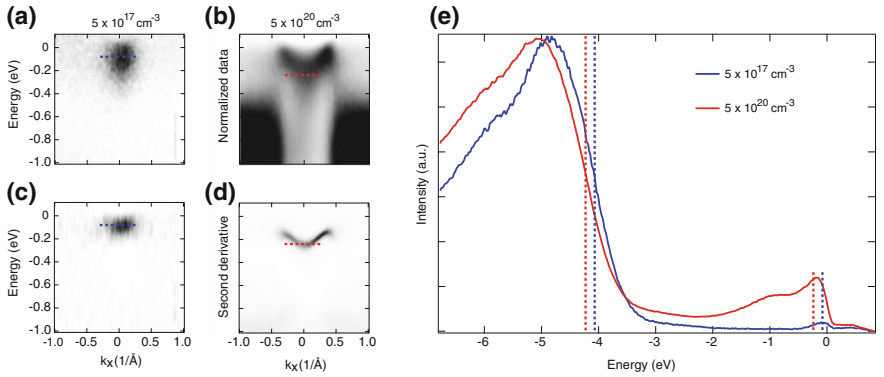

Fig. 4.4 **a**, **b** Energy-momentum dispersion relations of the bottom of the CB for n-doped samples with $n = 5 \times 10^{17}\,cm^{-3}$ and $n = 5 \times 10^{20}\,cm^{-3}$. **c**, **d** Second-derivative maps of the energy vs. momentum dispersion obtained from panels (**a**, **b**) respectively. **e** Energy distribution curves at the Γ point of the BZ for the two considered doping levels. The dashed vertical lines identify the positions of the quasiparticle energies for the VB and CB in the two different samples

eV. Remarkably, this implies that we do not observe any significant shrinkage of the quasiparticle gap at Γ upon increased electron concentration within our experimental resolution. The stability of the quasiparticle gap with respect to the excess carrier density (over the three order of magnitudes explored in our experimental conditions) excludes that strong band gap renormalization (BGR) plays a dominant role in anatase TiO_2. Later, we will show that this experimental finding agrees well with predictions by many-body perturbation theory (Sect. 4.4.1).

4.3 Steady-State Optical Properties

The second step of our investigation at equilibrium involves the measurement of the direct gap of the two-particle excitation spectrum of the material (i.e. the optical spectrum). A very reliable experimental technique for measuring the dielectric function $\epsilon(\omega) = \epsilon_1(\omega) + i\epsilon_2(\omega)$ of a material is SE. Here, temperature-dependent SE measurements are performed on two classes of (010)-oriented anatase TiO_2 single crystals, namely pristine anatase ($n \sim 0\,\mathrm{cm}^{-3}$) and the same n-doped ($n = 2 \times 10^{19}\,\mathrm{cm}^{-3}$) anatase crystal used for the ARPES measurement of Fig. 4.3.

Figures 4.5a, b show the imaginary part of the dielectric function, $\epsilon_2(\omega)$, measured at 20 K in (010)-oriented single crystals, with light polarized perpendicular ($\mathbf{E} \perp c$) and parallel ($\mathbf{E} \parallel c$) to the c-axis, respectively. The spectra obtained on the pristine crystal are shown in blue lines, while those measured on the n-doped sample in green lines. In the pristine crystal, the direct absorption for $\mathbf{E} \perp c$ (Fig. 4.5a) is characterized by the presence of a sharp peak at 3.79 eV (I), preceded by a long Urbach tail at lower energies [18]. A second, broader charge excitation (II) lies at 4.61 eV and extends up to 5.00 eV. The c-axis response (Fig. 4.5b) is instead characterized by a feature peaking at 4.13 eV (III) with a shoulder at 5.00 eV. Remarkably, all these excitations are still well defined in the n-doped sample, where we observe: (i) No apparent shift in the peak energy of features I and III and an 80 meV redshift in the peak energy of feature II; (ii) A reduction of the oscillator strength of all peaks, evidenced by a SW transfer from the above-gap to the below-gap region; and (iii) A pronounced broadening of the spectral features.

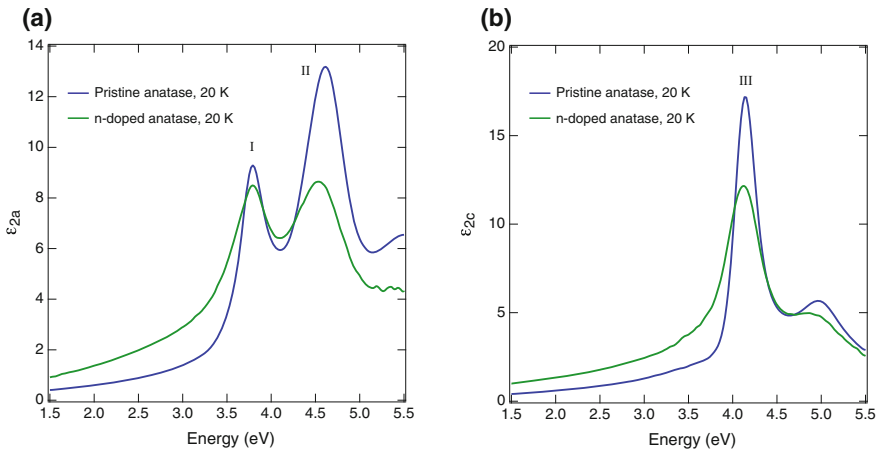

Fig. 4.5 **a**, **b** Imaginary part of the dielectric function at 20 K with the electric field polarized along (**a**) the a-axis ($\mathbf{E} \perp$ c) and **b** the c-axis ($\mathbf{E} \parallel$ c). The experimental data measured by SE on a pristine anatase TiO_2 single crystal are shown in blue, while those obtained on a highly n-doped single crystal ($n = 2 \times 10^{19}\,\mathrm{cm}^{-3}$) in green

The inspection of the optical spectra leads to the first important conclusion of our investigation under equilibrium conditions. The lowest direct optical excitation, corresponding to the direct optical gap of the material, can be identified with the feature at 3.79 eV for both the pristine and the n-doped ($n = 2 \times 10^{19}\,\mathrm{cm}^{-3}$) anatase TiO_2. When this observation is combined with the information extracted from the ARPES spectra, it allows to establish a bound exciton scenario for peak I of the n-doped single crystal, and to provide the first experimental estimate of $E_B = 180$ meV in anatase TiO_2. By performing temperature-dependent SE measurements in a wide temperature range from 10 to 300 K, the stability of all the charge excitations up to 300 K can be also confirmed. The detailed analysis of the temperature-dependent dielectric function is provided in Sect. 4.3.2.

4.3.1 Comparison with Previous Experiments

In this Paragraph, we establish a direct comparison between our optical spectra and previous data available in literature, which consist of normal-incidence reflectivity measurements at 100 K. To this aim, using the Fresnel formulas, we calculate the reflectivity response of our pristine (violet lines) and n-doped (blue lines) single crystals from the SE data at 100 K. These reflectivity responses are plotted in Fig. 4.6a, b together with the data of Ref. [25] (red lines), for light polarized along the a- (Fig. 4.6a) and c-axis of the crystals (Fig. 4.6b). We observe the overall agreement of our results with the ones reported in literature,[2] with slight shifts in the reflectivity peak energies. However, given the sharpness of the reflectivity lineshapes, we can also deduce that the quality of our pristine crystal is much higher than the one employed in Ref. [25]. Indeed, the reflectivity spectrum of the latter is closer to the response measured on our n-doped crystal, which has a large percentage of oxygen vacancies.

Finally, we proceed to check whether the Kramers-Kronig (KK) analysis of the reflectivity data is a reliable method to extract $\epsilon_1(\omega)$ and $\epsilon_2(\omega)$. Indeed, this approach has been widely used in the past on anatase TiO_2 [25]. Figures 4.7a and b display $\epsilon_1(\omega)$ and $\epsilon_2(\omega)$ calculated by applying the KK analysis on the reflectivity spectrum at RT. By comparing them with our original $\epsilon_1(\omega)$ and $\epsilon_2(\omega)$ values, we observe that the effect of the KK transformation is to modify the lineshape and the intensity of the peaks and to change the SW in the Urbach tail. This behaviour shows that the KK analysis, even performed on a broad spectral range, is not a precise approach to evaluate the dielectric function of the material.

[2] We note that the two different energy scales used in Ref. [25] to display the data of the dielectric function for $\mathbf{E} \perp c$ and $\mathbf{E} \parallel c$ has led to an error of digitalization by early computational works, which has propagated in the literature of anatase TiO_2 [8, 9, 27, 28].

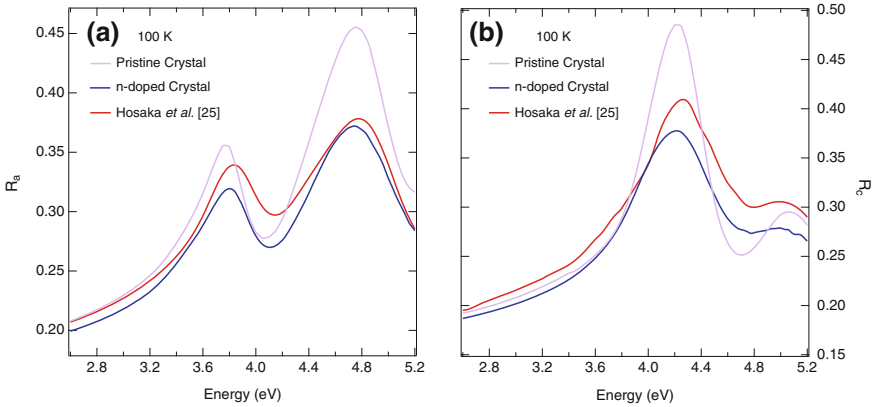

Fig. 4.6 **a**, **b** Static reflectivity spectra of (010)-oriented anatase TiO_2 single crystals at 100 K. The electric field is polarized along (**a**) the *a*-axis; **b** the *c*-axis of the crystals. The data derived from our SE measurements are depicted in violet for the pristine ($n \sim 0\,\mathrm{cm}^{-3}$) crystal and in blue for the *n*-doped ($n = 2 \times 10^{19}\,\mathrm{cm}^{-3}$) crystal, while the reflectivity measured in Ref. [25] is shown in red lines

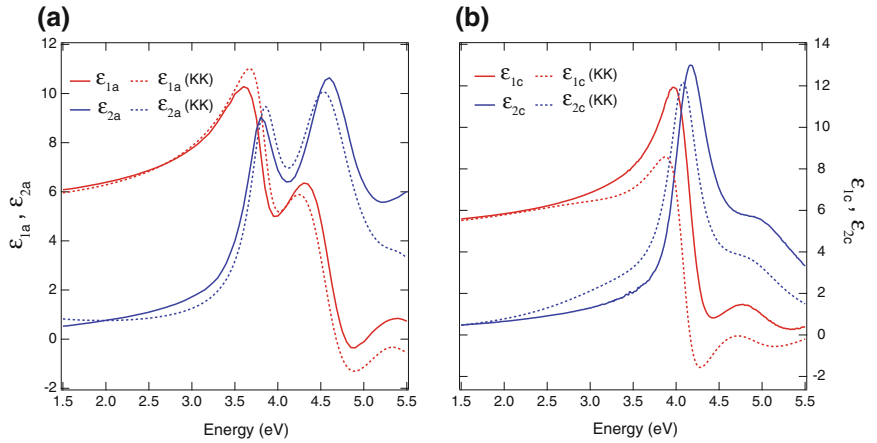

Fig. 4.7 Complex dielectric function of the (010)-oriented anatase TiO_2 single crystal at RT. The electric field is polarized along **a** the *a*-axis and **b** the *c*-axis. The real part, $\epsilon_1(\omega)$, is plotted in red, while the imaginary part, $\epsilon_2(\omega)$, in blue. The solid-line curves depict the data directly measured by SE, while the dashed lines are calculated by a KK analysis of reflectivity

4.3.2 Temperature Dependence of the Dielectric Function

Having confirmed the bound exciton scenario for peak I, here we investigate how the peak energy of all fundamental charge excitations in anatase TiO_2 is renormalized as a function of temperature. Studying the temperature dependence of elementary

excitations is of pivotal importance, as it provides insightful information on the microscopic details of quantum many-body interactions and correlations. In particular, the temperature dependence of interband transitions and excitons in semiconductors and insulators has been subject of extensive studies. The energy of these excitations typically undergoes a sizeable softening with increasing temperature, which has been first described within the empirical Varshni model [37]. However, in few exceptional cases, including PbTe [38], chalcopyrites [39] and perovskite titanates [40], the opposite effect or more complex temperature dependences have been observed. Part of this renormalization is accounted for by the thermal expansion of the lattice, but an important contribution arises from the electron-phonon interaction [41]. Thus, measuring the temperature dependent dielectric function of anatase TiO_2 can shed light on subtle effects associated with the electron-phonon coupling.

Figures 4.8a, b and c, d show the temperature dependent spectra of the real and imaginary parts of the dielectric function, $\epsilon_1(\omega)$ and $\epsilon_2(\omega)$, along the a- and c-axis, respectively. The temperature dependence of the peak energies I and II is presented in Fig. 4.9a, while the one of peak III in Fig. 4.9b. We observe a remarkable qualitative difference in the temperature behaviour of such charge excitations. As the temperature increases from 10 to 300 K, the peak energy of exciton I displays a sizeable blueshift of 40 meV, while the peak energy of feature II undergoes an opposite redshift. Along the c-axis, the peak energy of excitation III remains constant as a function of temperature. In anatase TiO_2, the thermal expansion of the lattice has a regular temperature dependence and thus should contribute to a decrease of the exciton I peak energy as the lattice expands with increasing temperature [42, 43]. As a result, the behaviour shown by features I and III is rather anomalous. In the next Sections, our primary interest is to elucidate the origin of the temperature evolution characterizing exciton I, as it may represent the signature of strong exciton-phonon interaction at finite temperature.

4.3.3 Many-Body Effects

In the case of the n-doped anatase TiO_2 crystals, the presence of an excess electron density at the Γ point of the CB may give rise to a variety of effects having a profound impact on both the single-particle and the two-particle excitation spectra. According to their origin, these effects can be distinguished between those involving single-particle states (phase-space filling) and those that can be attributed to many-body interactions among the doped carriers (long-range Coulomb screening and BGR). Phase-space filling arises because of the Pauli exclusion principle, which applies to the electrons and holes constituting the excitons. This produces a finite exclusion volume in phase-space for each exciton. As a consequence, the VB to CB transition probability is reduced, which is evidenced by a reduction of the oscillator strength of the excitonic transition in the optical spectra.

On the other hand, many-body interactions alter the exciton energy and composition by affecting the underlying electronic states. This occurs via the direct and

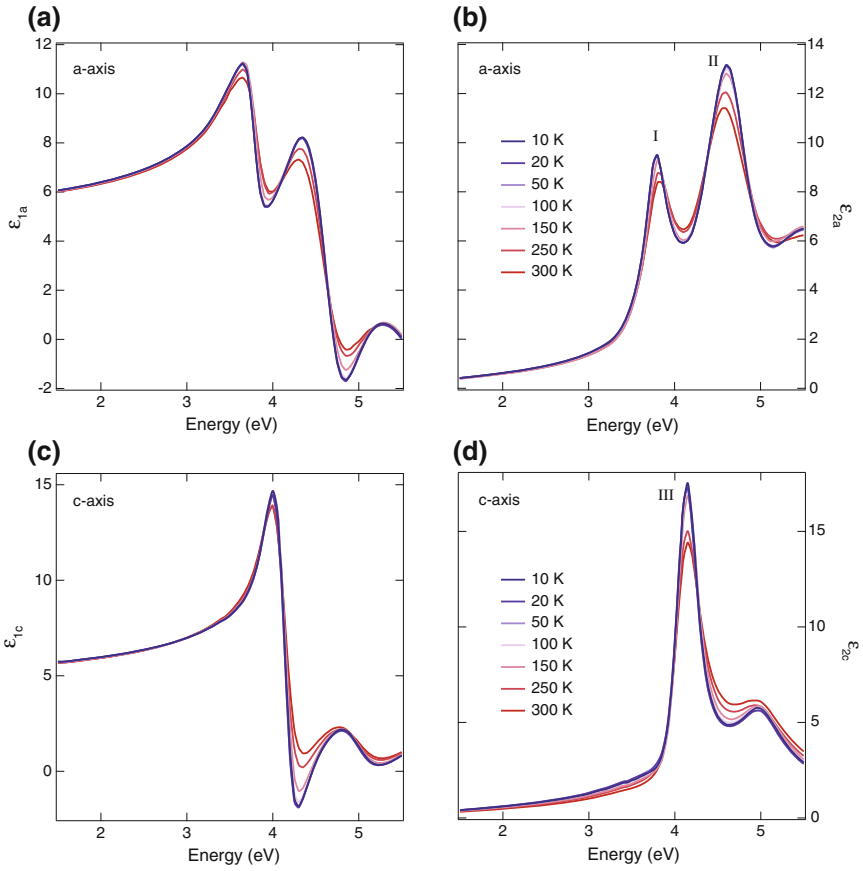

Fig. 4.8 Temperature dependence of the dielectric function of pristine anatase TiO_2 single crystal in **a**, **b** *a*-axis and **c**, **d** *c*-axis polarization

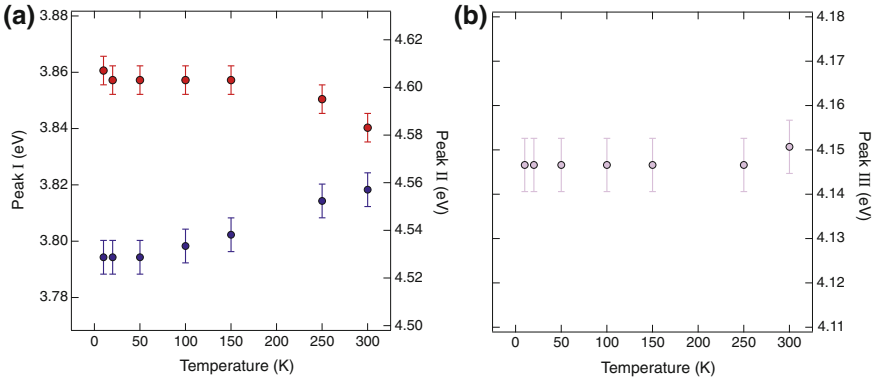

Fig. 4.9 Temperature behaviour of the peak energy for the charge excitations **a** I and II and **b** III

exchange Coulomb interactions of electrons and holes, which at high plasma density provide additional screening channels. First, long-range free-carrier screening modifies the exciton Coulomb potential $\phi \sim e/4\pi\epsilon r$ through a multiplicative factor $e^{-r/\lambda}$, where λ is the Debye length. Substantial screening occurs when the Debye length and the exciton radius become comparable. Second, the excess electrons also lead to BGR, i.e. a density-dependent shrinkage of the quasiparticle gap due to electron and hole self-energy corrections. As a result, the enhancement of the electronic screening leads to the simultaneous renormalization of both the exciton E_B and the electronic gap. In this scenario, the exciton absorption energy in the SE data is determined by the combination of the weakened Coulomb interaction and the BGR, the former inducing a blueshift and the latter a redshift of the exciton peak. The quantitative details of this compensation depend on both material and dimensionality but this arises as a general effect in many standard bulk semiconductors [44] and nanostructures [45, 46]. In the low-density limit, they have been shown to cancel to first order [47]. Relying on this argument, we can provide a deeper interpretation of the changes in the low-temperature dielectric function of anatase TiO_2 upon electron doping (Fig. 4.5a, b). The redistribution of SW can be attributed to the combination of phase-space filling and defect-induced in-gap absorption. The enhanced broadening of the exciton lineshapes can be directly associated with a modification of the exciton lifetime, due to the combination of long-range Coulomb screening and exciton-defect scattering. Finally, the insensitivity of the exciton energies to the effective doping level suggests that the long-range Coulomb screening and the BGR perfectly compensate each other even at high doping levels. This idea is reinforced by our ab initio calculations (Sect. 4.4.2), which reveal that doping-induced many-body effects in anatase TiO_2 play a marginal role even at high carrier densities.

4.4 Many-Body Perturbation Theory Calculations

To rationalise our experimental data at equilibrium, we calculate band structure and optical spectra of pristine and *n*-doped anatase TiO_2 within the frozen lattice approximation and including many-body effects.

4.4.1 Single-Particle Excitation Spectrum

Figure 4.10 shows the complete band structure of pristine anatase TiO_2. Grey diamonds denote the values obtained within GW for VB and CB at the Γ and X points. These are also displayed in Fig. 4.3b for a direct comparison with the ARPES data. The overall agreement is good, but the theoretical values are higher by $\sim$100 meV. This discrepancy can be caused by the combined effects of the doped electron density and strong electron-phonon interaction in the experimental data. In the following, we separately address the relevance of these effects.

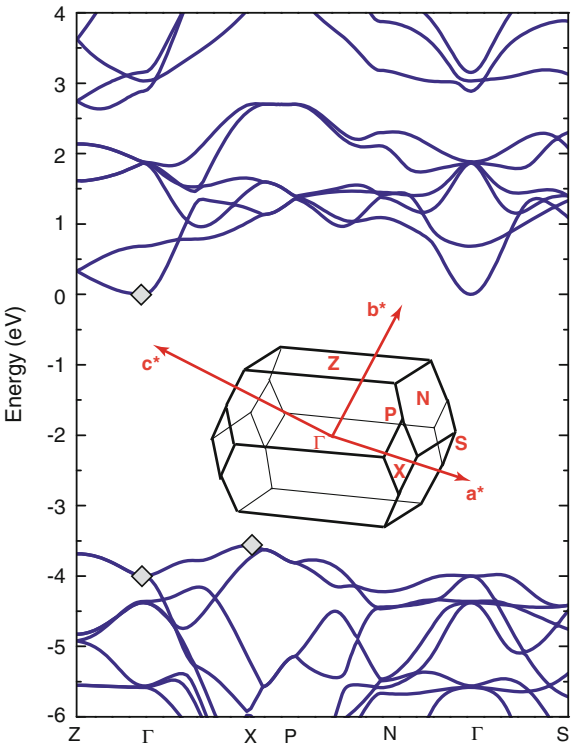

Fig. 4.10 Complete GW electronic band structure of bulk anatase TiO_2. The zero of the energy is set at the minimum of the CB at the Γ point. The direct gap at Γ sets a reference for defining the bound character of the excitons. The inset shows the 3D BZ of anatase TiO_2

In general, in the presence of doping, two competing effects contribute to changing the electronic gap of an insulator, with either a redshift or blueshift depending on which effect dominates. The CB filling gives rise to a blueshift, while the modification of the exchange-correlation potential (with the system becoming slightly metallic) is responsible for a redshift. From the experimental ARPES data of Fig. 4.4, we observe the insensitivity of the quasiparticle gap at Γ on the doped electron density, which suggests a negligible effect of BGR in this material.

To address the impact of the doped carrier density on the electronic band structure, the GW theoretical framework has been extended to the case of uniformly doped anatase TiO_2, verifying the influence of doping on the electronic gap. Here, we show the results for two cases of uniform excess electron density $n = 10^{19}\,\mathrm{cm}^{-3}$ and $n = 10^{20}\,\mathrm{cm}^{-3}$. It is observed that the change in the electronic direct gap at Γ is marginally affected by doping for $n \leq 10^{19}\,\mathrm{cm}^{-3}$. The calculated GW gap (both direct and indirect gap) are similar to the pristine anatase TiO_2 case, with an increase of 1 meV for the doping of $n = 10^{19}\,\mathrm{cm}^{-3}$ and of 17 meV for $n = 10^{20}\,\mathrm{cm}^{-3}$. These results complement the experimental ARPES data of Fig. 4.4, demonstrating that the electronic gap from doped samples is a suitable value to describe also the gap of pristine anatase TiO_2. It results that, in this material, the dominant effect for the considered doping ranges is the CB filling. For the doping values relevant in our

measurements, the correction is well below the computational error. Therefore, there is no detectable effect of doping in the electronic bandgap. In Sect. 4.4.2 the same argument holds for the calculation of the optical response, as the position and shape of peak I in ϵ_{2a} do not change for $n = 10^{19}$ cm^{-3}. For this reason, hereafter we refer only to the results of the GW calculations in the pristine sample.

The arguments above rule out the involvement of the doped electron density in generating the discrepancy between the experimental ARPES data and the theoretical calculations at the GW level. Thus, it is crucial to estimate the role of the electron-phonon interaction. To this aim, we consider both the zero-point renormalization (ZPR) at zero temperature and the electron-phonon coupling at finite temperature. We evaluate the effect of the ZPR by relying on recent theoretical data for rutile TiO_2 [48], where a redshift of 150 meV was estimated for the electronic gap. Assuming a similar correction for anatase TiO_2, we can estimate a theoretical gap of 3.92 eV at zero temperature with ZPR effects. To account for the electron-phonon coupling at finite temperature, frozen phonon calculations for 20 and 300 K have been performed. We additionally consider the effect of the thermal expansion of the lattice with temperature, which also acts as a source of renormalization for the quasiparticle gap. We find that the combined effect of the lattice expansion and electron-phonon coupling leads to a net blueshift of 30 to 50 meV at 300 K and a negligible shift at 20 K. Hence, at low temperature, the BGR of anatase TiO_2 is only due to the ZPR effect. This leads to a theoretical value of the direct bandgap of 3.92 eV, which is in excellent agreement with the experimental value of 3.97 ± 0.05 eV.

Finally, we underline that the GW band structure in Fig. 4.10 yields important information about the Γ-Z direction, which is crucial for understanding the optical transitions of the material. The CB and VB dispersions between Γ and Z are nearly parallel, providing a large joint DOS for the occurrence of optical transitions. Below, we show that this peculiar dispersion leads to the intense excitonic transitions observed in the optical absorption spectrum.

4.4.2 Two-Particle Excitation Spectrum

To identify the microscopic nature of the optical excitations, we rely on the calculated $\epsilon_2(\omega)$ of the pristine anatase TiO_2 at zero temperature with and without many-body electron-hole correlations and electron-phonon interactions. The optical spectra in the uncorrelated-particle picture (Fig. 4.11a, b, red lines) are obtained within the random-phase approximation (RPA) on top of GW, while the many-body absorption spectra (violet lines) are calculated by solving the BSE. The details of the calculations are reported in Appendix C.2.1, while the results in Appendix C.2.2. By including many-body effects [8, 9, 27, 28], we obtain an excellent agreement with the SE spectra. For $\mathbf{E} \perp c$, the sharp absorption maximum at 3.76 eV is very close to feature I (3.79 eV) and well below the direct VB-to-CB optical transition evaluated at the independent particles level (3.92 eV) (see the red trace). A second peak at 4.81 eV clearly corresponds to the experimental peak II (4.61 eV). For $\mathbf{E} \parallel c$ the intense optical

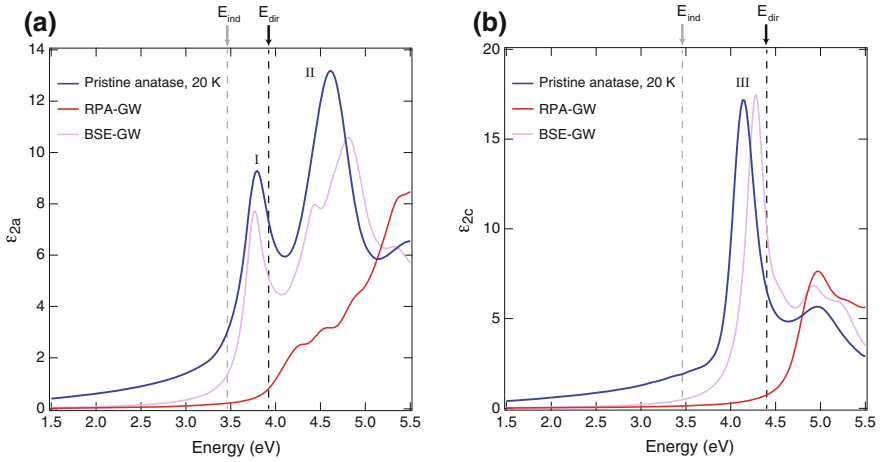

Fig. 4.11 **a**, **b** Comparison between the spectra measured at 20 K on the pristine anatase TiO_2 single crystal and those obtained from frozen-lattice ab initio calculations for pristine anatase TiO_2. The experimental data are shown in blue, the calculated spectra in the RPA-GW scheme in red and the calculated spectra in the BSE-GW scheme in violet. The quasiparticle indirect gap $E_{ind} = 3.46$ eV is indicated by a dashed grey vertical line; the direct gaps $E_{dir} = 3.92$ eV (at the Γ point) for $\mathbf{E} \perp c$ and $E_{dir} = 4.40$ eV (coincident with the onset of the RPA-GW) for $\mathbf{E} \parallel c$ are indicated by dashed black vertical lines in Fig. (a) and (b) respectively

peak at 4.28 eV is easily associated with the experimental peak III (4.13 eV). The BSE calculations performed for doped anatase TiO_2 at concentrations of $n = 10^{19}\,\mathrm{cm}^{-3}$ and $n = 10^{20}\,\mathrm{cm}^{-3}$ (Fig. 4.12) show a negligible effect on the considered optical peaks, supporting our SE data of Fig. 4.5. The insensitivity of peak I for the different doping levels suggests that the (weak) effects of phase-space filling and long-range Coulomb screening perfectly compensate the (small) shift induced by BGR for this transition even at high doping levels.

We also investigate the role of thermal expansion of the lattice and the electron-phonon interaction in the absorption spectra, by carrying out frozen-phonon BSE simulations, described in Appendix C.2.3. We find that the position of the excitonic peak I at 20 K shows a negligible shift with respect to the zero temperature value and moves to higher energies by 70–80 meV when the temperature is increased from 20 to 300 K. This behaviour well explains the temperature dependence shown by peak I in our SE data (Fig. 4.8e).

Although exciton I is bound with respect to the direct electronic gap, it may be considered as resonant with respect to all phonon-mediated indirect transitions of the material. Hence, to account for possible effects originating from the indirect nature of the anatase TiO_2 gap, the BSE has been solved for a supercell, thus allowing for the coupling of electron and hole states with different momenta via phonons with non-zero $\mathbf{q}$-vectors. We find a negligible role of the indirect gap in the exciton properties of anatase TiO_2, besides adding an Urbach tail at the lower energy side of the exciton peak I (see Appendix C.2.4 for details).

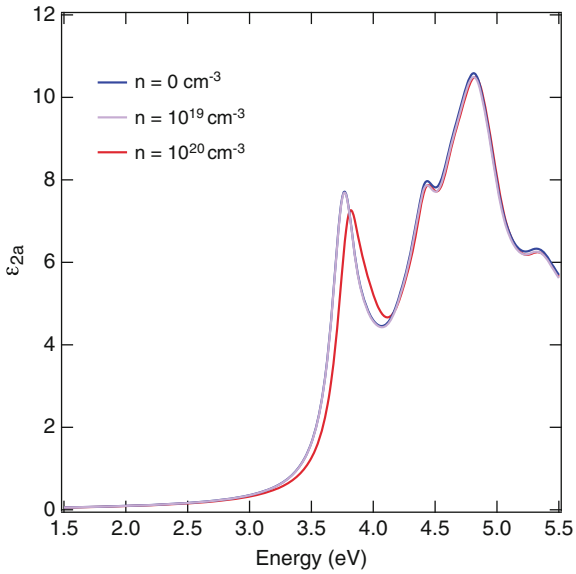

Fig. 4.12 Comparison between the calculated ϵ_{2a} for pristine and n-doped anatase TiO_2. The optical response of the n-doped TiO_2 with $n = 10^{19}\,cm^{-3}$ (violet curve) overlaps almost completely to the pristine case (blue curve), showing that this doping level does not produce a significant effect the peak energy of feature I. Only when n is increased to $10^{20}\,cm^{-3}$ (red curve), the peak energy of feature I is found to blueshift of ∼50 meV

4.4.3 Exciton Isosurfaces

The analysis of the optical charge excitations both in real and reciprocal space reveals very insightful information about their microscopic nature. As far as exciton I is concerned, it extends two-dimensionally on the (001) plane with a radius of 15 Å, being almost confined to a single atomic plane along the c-axis (Fig. 4.13a and d). In addition, a reciprocal space analysis shows that the excitonic wavefunction is formed mainly by mixing of single-particle vertical transitions along the Γ-Z direction (Fig. 4.10). Due to the almost parallel CB and VB dispersion along Γ-Z, the electronic gap at Γ (coincident with the continuum absorption rise) is used as a reference to evaluate E_B. Considering the renormalization of the electronic bandgap discussed above, we estimate a theoretical value of $E_B = 160$ meV at 20 K, in line with our measurements.

The energy, shape and reciprocal space contributions of the charge excitation II highlight its bulk-resonance character, most evident as its offset coincides with the independent particle-GW absorption rise. Figure 4.13b depicts the spatial distribution of the charge excitations associated with peak II, showing significant contributions from extended bulk states. Its electron wavefunction appears completely delocalized over many lattice constants around the hole. Hence, this peak is ascribed to a resonant excitation that does not form a bound state. Carrying out a similar analysis for the excitation III, we conclude that it presents a mix of localized and bulk-resonant contributions, as the continuum onset in independent particle-GW undergoes an intensity enhancement. Different from peak I, the k-points contributing to this charge excitation are both localized along the Γ-Z line and distributed over the whole BZ.

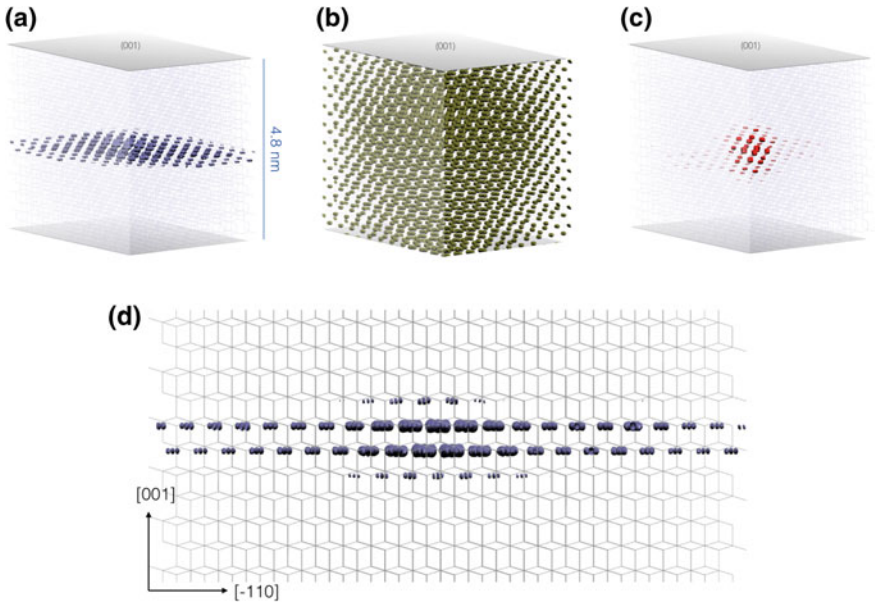

Fig. 4.13 Each isosurface representation displays the electronic configuration when the hole of the considered excitonic pair is localized close to one O atom. **a** Bound exciton I at 3.76 eV. **b** Resonance II at 4.37 eV. **c** Bound exciton III at 4.28 eV. **d** Side-view of the bound exciton I at 3.76 eV

Due to the mixed nature of exciton III, it is less straightforward to define and estimate its E_B. Assuming the GW onset at 4.40 eV for $\mathbf{E} \parallel c$ as the reference energy (marked as E_{dir} in Fig. 4.11b), we obtain $E_B \sim 150$ meV (in the frozen lattice scheme), which is still well above the standard E_B observed in bulk semiconductors. Indeed, as shown in Fig. 4.13c, the linear combination of excitonic wavefunctions (with eigenvalues in the range 4.18–4.38 eV for $\mathbf{E} \parallel c$) contributing to peak III leads to a fairly localized exciton in all three directions, with an average radius of 20 Å.

Thus, our extensive study allows us to demonstrate the stability of bound excitons in anatase TiO_2. In the following, we clarify the origin of these peculiar excitonic effects in this system by setting a comparison with other prototypical titanates (rutile TiO_2 and $SrTiO_3$). Importantly, before our study, excitonic effects have been thought to be weak in anatase TiO_2, due to its large static dielectric constant ($\epsilon_S \sim 22/45$) [49, 50]. Moreover, due to a smaller effective mass [51], one would expect the electron-hole interaction to be even weaker than that in rutile TiO_2, in which E_B has been estimated ∼4 meV [52, 53]. However, the presence of a large ϵ_S is not a sufficient condition to prevent the formation of excitons in materials, as the screening of the electron-hole interaction should rigorously take into account the momentum- and energy-dependence of the dielectric constant [20]. Therefore, it is the combination of the electronic structure and the nature of the screening that determines the existence of bound excitons in materials. The degree of excitonic spatial delocalization is

instead influenced by the crystal structure, as the packing of the polyhedra containing the atoms involved in the excitonic transitions is related to the details of the band structure. These observations rationalize well the exciton physics in titanates.

A necessary condition for a many-state transition to occur and for a bound collective excitonic state to form is that the electron and hole group velocities are the same, i.e. that the gradients of the lowest CB and the highest VB are identical in a specific portion of the BZ [20]. As a matter of fact, the band edge states of anatase TiO_2 (Fig. 4.10) and $SrTiO_3$ [54, 55] are parallel in extended portions of the BZ, which contribute DOS to the collective transition associated with bound excitonic species ($E_B \sim 180/220$ meV) [8, 56]. In contrast, the band structure of rutile TiO_2 is not characterized by such extended portions with similar electron and hole group velocities [8], thus resulting in $E_B \sim 4$ meV [52, 53].

Concerning the spatial distribution of the excitons in $SrTiO_3$ and TiO_2, since all the bound excitonic transitions are predicted to involve O $2p$ and Ti $3d$ (t_{2g}) states [8, 9, 56], one should consider the role of different TiO_6 octahedra packing. In $SrTiO_3$, the unit cell is built on a distorted perovskite structure, thus providing a high degree of coordination among neighbouring TiO_6 octahedra. As a consequence, the single-particle band states involved in the excitonic transition undergo pronounced dispersion and the strongly bound exciton predicted in $SrTiO_3$ retains a highly delocalized nature similarly to a Wannier-Mott exciton [56]. In TiO_2, both the anatase and rutile polymorphs are also built on a network of coordinated TiO_6 octahedra, but they significantly differ in their structural properties. In rutile, each distorted TiO_6 octahedron is connected to ten neighbouring ones, sharing a corner or an edge. In anatase, the coordination of the TiO_6 octahedra is less compact and each octahedron is coordinated only with eight neighboring ones. This seemingly tiny difference has in turn profound effects on the spatial properties of the elementary charge excitations: While in rutile the weakly-bound excitons are Wannier-Mott-like, in anatase the bound exciton is confined to the (001) plane [8]. More specifically, it is the chain-like structure of anatase TiO_2 that leads to unique characteristics of the band structure and hinders the delocalization in 3D of the bound exciton over many unit cells. Indeed, the band dispersion along the Γ-Z direction is rather flat, thus implying a high degree of localization for the excitonic state along the c-axis. This almost 2D wavefunction also contributes to enhance the exciton E_B, in a way similar to the low-dimensional effect in semiconductor quantum structures [57]. Under these conditions, according to the 2D hydrogen model, E_B is 4 times larger than for a 3D exciton. With E_B exceeding the highest energy of the infrared-active longitudinal optical phonons (i.e. 108 meV in anatase TiO_2) [49], the ionic (polaronic) contribution to the screening of the Coulomb interaction is strongly suppressed [20]. As a consequence, the total screening reduces to the pure contribution of the background valence electrons, embodied by the rather small dielectric constant at optical frequencies $\epsilon_{opt} \sim 6/8$. This weak screening in turn reduces the exciton Bohr radius on the (001) plane (∼3.2 nm).

Following these arguments, the 2D wavefunction of exciton I in anatase TiO_2 represents a peculiar and fascinating object. Indeed, in recent years, several 2D excitons were reported in materials such as hexagonal boron nitride [58] and transition metal

dichalcogenides [4, 6, 7], which are layered 2D systems held together by van der Waals forces to form a 3D lattice. The situation of anatase TiO_2 is radically different in that a genuine 3D material exhibits a 2D exciton wavefunction on a specific lattice plane.

4.5 Exciton Physics Under Nonequilibrium Conditions

The above description dealt with bulk single crystals of anatase TiO_2, but in most applications [10–12], highly-defective samples are used at RT and ambient pressure (e.g. NPs or mesoporous films). One may therefore question the relevance of the above conclusions for the actual systems used in technology. The possible extension of our findings to such samples would have a strong impact on the common understanding of charge interaction and energy transport in applications involving anatase TiO_2. One could expect that the carriers released at defects and the local electric fields generated by charged impurities would screen the Coulomb interaction in the exciton, leading to the cancellation of the binding forces. Moreover, strong exciton-defect and exciton-impurity scattering can also cause an extreme broadening of the exciton linewidth, hiding the characteristic exciton feature into the continuum of indirect interband excitations. These ideas are reinforced by the inspection of the RT equilibrium absorption spectrum of colloidal anatase TiO_2 NPs (Fig. 4.14), which does not show obvious signatures of excitonic transitions [59, 60]. However, it is important to remark that this spectrum is strongly affected by the scattering of the incident light.

Therefore, it becomes crucial to find a route for confirming if the bound excitons of bulk single crystals emerge with the same phenomenology in anatase TiO_2 NPs at RT. A powerful approach to address this open question is to photoexcite the anatase

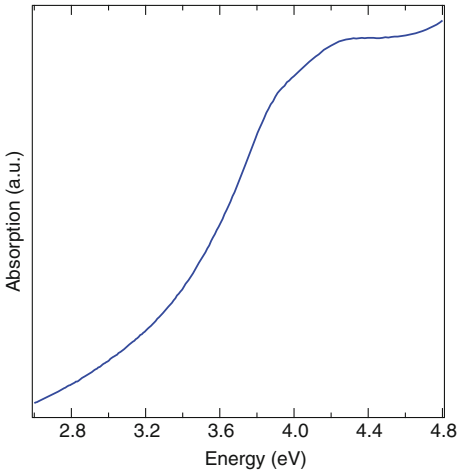

Fig. 4.14 Steady-state absorption spectrum of anatase TiO_2 NPs dispersed in aqueous solution at RT

TiO_2 NPs with a deep-UV pump pulse and monitor their nonequilibrium optical response with a delayed broadband probe covering the spectral region where the excitonic resonances are expected to appear. The unique strength of this technique relies on the subtraction of the probe scattered light, thus providing a better contrast for resolving features that are hidden in the equilibrium spectrum. In this way, the exciton lineshapes can be identified through the pump-induced transparency of the excitonic peak, typically referred to as "exciton bleaching". This is a nonlinear optical process that is intrinsically related to a many-body phenomenon. Its manifestation depends not only on the final-state interactions of electron and hole involved in the excitonic state but also on the interaction with all other particles in the material, that can contribute to screening or blocking the excitonic transition [61].

In the following Paragraphs, we perform a complete study of the excitonic collective excitations under nonequilibrium conditions, confirming their existence in anatase TiO_2 NPs at RT, tracking their renormalization for revealing the material many-body dynamics and demonstrating a possible application of their spectroscopic signature. To this end, in Sect. 4.5.1, we first perform deep-UV broadband transient reflectivity ($\Delta R/R$) on oriented anatase TiO_2 single crystals and extract the temporal evolution of the transient absorption (ΔA). In Sect. 4.5.2, we apply femtosecond 2D deep-UV spectroscopy on a colloidal solution of anatase TiO_2 NPs to directly reveal the presence of the excitonic features in the ΔA signal. In Sect. 4.5.3, we make use of the renormalization of the high-energy exciton feature to unravel the low-energy carrier dynamics in the material. Finally, in Sect. 4.5.4, we further extend the class of phenomena that can be observed via our nonequilibrium technique, revealing the interplay between low-energy CAPs and high-energy excitons.

4.5.1 Ultrafast Transient Reflectivity of Single Crystals

We start our investigation by performing femtosecond broadband transient reflectivity experiments on three different types of (001)-oriented single crystals, namely pristine anatase ($n \sim 0\,\mathrm{cm}^{-3}$), Cu-doped anatase ($n = 2 \times 10^{17}\,\mathrm{cm}^{-3}$) and raw anatase ($n = 2 \times 10^{19}\,\mathrm{cm}^{-3}$), and on a (010)-oriented raw anatase single crystal. In the first experiment, we monitor the $\Delta R/R$ signal in a broadband deep-UV range (3.75–4.35 eV) for the three classes of (001)-oriented samples. Both pump and probe polarizations are set along the *a*-axis. An isotropic optical response is found when the (001)-oriented crystals are rotated about the *c* axis. The pump energy was set at 4.10 eV, in order to selectively perturb the spectral region above the first excitonic peak.

Figure 4.15a compares the $\Delta R/R$ spectrum obtained from the three specimens at a fixed time-delay of 6 ps. This spectrum shows a sign inversion around 3.96 eV. The inflection that is present in the signal obtained from the Cu-doped sample around 4.10 eV is an artefact produced by the scattering of the pump beam. A similar response can be found for all the temporal delays between pump and probe up to 1 ns. The main difference is displayed by the intensity of the signal at long time delays, since it depends on the rate of the carrier recombination process. Figure 4.15b shows three

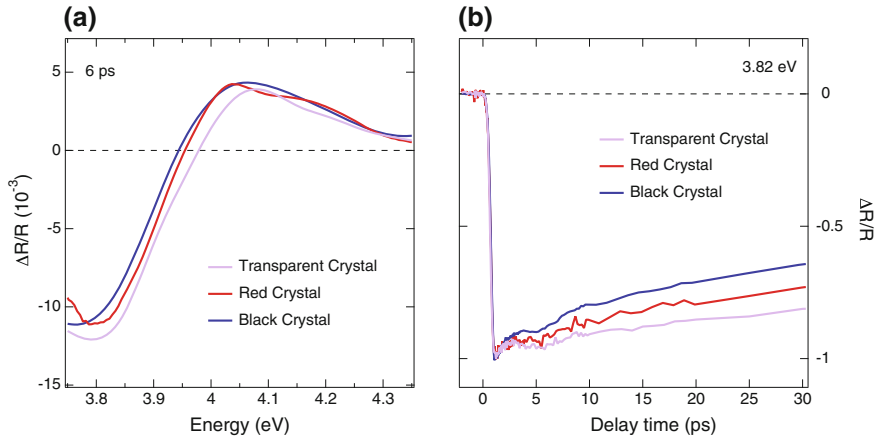

Fig. 4.15 Ultrafast broadband $\Delta R/R$ of different classes of (001)-oriented anatase TiO_2 single crystals at RT. The signals measured from raw crystals are shown in blue, from Cu-doped crystals in red and from pristine crystals in violet. Both pump and probe polarizations lie along the *a*-axis and the pump energy is set at 4.10 eV: **a** $\Delta R/R$ spectrum at the fixed time delay of 6 ps; **b** normalized temporal traces at a fixed probe photon energy of 3.82 eV

temporal traces up to 100 ps probed around 3.82 eV, in which this effect is clearly visible. The decay of the nonequilibrium signal in the strongly *n*-doped crystal is faster than the other responses, since the increased density of in-gap states facilitates charge carrier recombination across the indirect bandgap.

Next, we perform a second set of experiments on a (010)-oriented *n*-doped ($n = 2 \times 10^{19}\,\mathrm{cm}^{-3}$) single crystal of anatase TiO_2, in order to access the anisotropic dynamics along *a*- and *c*-axis. Figure 4.16a and c display the $\Delta R/R$ maps of the *a*- and *c*-axis response as a function of the probe photon energy and of the time delay between pump and probe. Although the temporal evolution has been measured up to 1 ns, the two maps are displayed up to 10 ps. The *a*-axis response has been measured upon photoexcitation at 4.40 eV, with the broadband probe covering the range 3.70–4.65 eV. These results are consistent with those obtained by polarizing the beams along the *a*-axis of the (001)-oriented samples. The higher-energy region of the spectrum does not evolve in time, remaining unaffected by the photoexcitation process. The *c*-axis response (Fig. 4.16c) is obtained through the measurement of the (010)-oriented single crystal with a pump and probe polarizations set along the *c*-axis. Also in this case, the pump photon energy is at 4.40 eV, but the probed range is shifted to 4.05–4.80 eV. As expected from the strong optical anisotropy of anatase TiO_2, the $\Delta R/R$ spectrum of Fig. 4.16d strongly differs from one of the *a*-axis, consisting of a negative contribution set around 4.28 eV and a tail extending to 4.60 eV in the high-energy range.

A final $\Delta R/R$ map with both pump (at 4.40 eV) and probe (between 3.70 and 4.60 eV) polarized along the *c*-axis of the (010)-oriented single crystal is shown in Fig. 4.17. This demonstrates the absence of *c*-axis spectral features at low energies

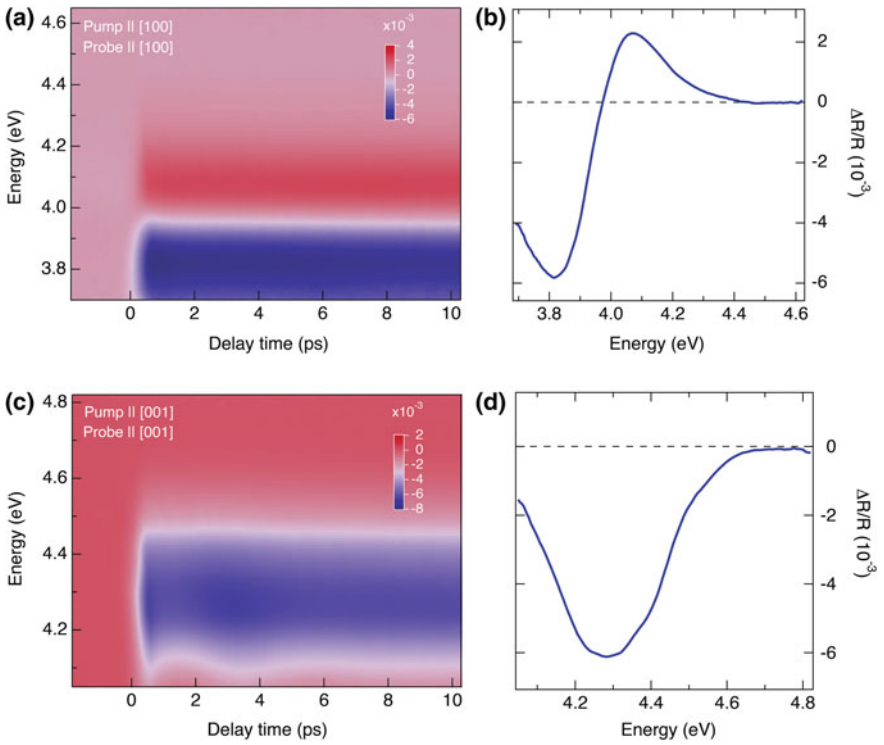

Fig. 4.16 Ultrafast broadband ΔR/R on (010)-oriented anatase TiO_2 single crystals at RT. **a**, **b** Colour-coded maps of ΔR/R measured upon photoexcitation at 4.40 eV. **c**, **d** Transient spectra, obtained from a cut at 1 ps in the experimental conditions reported for (**a**) and (**b**), respectively

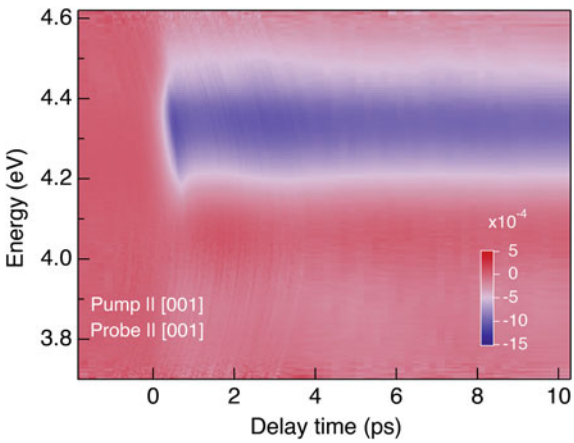

Fig. 4.17 Colour-coded map of ΔR/R from the (010)-oriented single crystal measured at RT upon photoexcitation at 4.40 eV and with pump and probe beams polarized along the *c*-axis. The probe photon energy covers the spectral range 3.70–4.60 eV, which demonstrates the absence of emerging features at low energies

and confirms the finding of the pump-probe experiment along the *c*-axis presented in Fig. 4.16c. The difference in terms of intensity with respect to Fig. 4.16c has to be attributed to the reduced pump intensity (of $\sim 1/3$) that the experimental setup can achieve when a broadband probe beam covering the 3.70–4.60 eV spectral region is simultaneously generated.

The main goal of our ultrafast measurements is to probe the ΔA of a colloidal solution of NPs. Thus, it is useful to analyse the time-resolved dynamics of the single crystals in terms of their ΔA, in order to establish a link with the data on NPs. However, while ΔA is directly proportional to $\Delta\epsilon_2$, ΔR/R has a complex relationship with both $\Delta\epsilon_1$ and $\Delta\epsilon_2$ in the probed spectral range. Indeed, in the UV, the real and imaginary part of the dielectric constant have rather similar absolute values. For this reason, the optical reflectivity is equally sensitive to the reactive and the absorptive components of the dielectric function.

Hence, in order to calculate the pump-induced evolution of the ΔA from the ΔR/R data, we proceed as follows. We model the SE data using a set of Lorentz oscillators, we calculate the equilibrium reflectivity (R_0), and we fit the measured transient reflectivity $R_{exp}(t)/R_{exp}$ with a differential model $(R(t) - R_0)/R_0$, where $R(\tau)$ is a model for the perturbed reflectivity obtained by variation of the parameters used to fit the equilibrium data as a function of the pump-probe delay t. We adopt this approach to treat our ΔR/R data in order to avoid possible systematic errors that can be produced by the typical analysis through KK transformations. The SE spectra are fitted using a dielectric function of the form

$$\epsilon(\omega) = \epsilon_\infty + \sum_i \frac{\omega_{pi}^2}{\omega_{0i}^2 - \omega^2 - i\Gamma_i\omega}, \tag{4.1}$$

where ϵ_∞ is the high-frequency dielectric constant, and ω_{pi}^2, ω_{0i}^2, Γ_i are, respectively, the plasma frequency, the transverse frequency and the scattering rate of the *i*-th

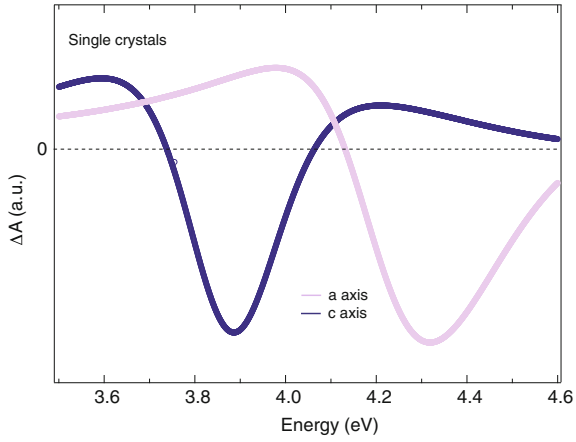

Fig. 4.18 ΔA spectrum of anatase TiO_2 single crystals at RT along the *a*- and *c*-axis at a fixed time delay of 1 ps. The pump photon energy is 4.40 eV

Lorentz oscillator. The absorbance is then given by $A(\omega) = \omega \, \mathrm{Im} \sqrt{\epsilon}$. For the fitting of the transient data, the Lorentz oscillators in our experimental range are allowed to change in order to reproduce the dynamical reflectivity. This procedure enables to extract the transient dielectric function $\Delta\epsilon(\omega, t) = \Delta\epsilon_1(\omega, t) + i\Delta\epsilon_2(\omega, t)$ and finally leads to the evaluation of the ΔA for the single crystals. The results along the *a*- and *c*-axis are presented in Fig. 4.18.

4.5.2 *Ultrafast Two-Dimensional Deep-UV Spectroscopy of Nanoparticles*

To verify the universality of our findings in the typical anatase TiO_2 samples used for applications, we perform ultrafast 2D deep-UV spectroscopy on a colloidal solution of anatase TiO_2. In our experiment, we vary the pump photoexcitation between 4.00 eV and 4.60 eV and simultaneously monitor the ΔA in a broad spectral range between 3.50 and 4.60 eV. The time resolution is estimated 150 fs and the photoexcited carrier density is $n = 5.7 \times 10^{19}\,\mathrm{cm}^{-3}$. Figure 4.19 shows typical ultrafast 2D UV spectroscopy maps at different time delays (1, 100 and 500 ps). The straight line in each map indicates the region in which the pump and the probe have the same photon energy. This spectral range is affected by artefacts caused by the scattering of the pump beam into the spectrometer. It can be observed that all the transients in the 2D map are characterized by a negative signal, in which two long-lived features are clearly distinguished even at short time scales. All the transients exhibit a negative (bleach) signal, and display two prominent features at a probe photon energy of 3.88 and 4.35 eV. While the former excitation is present at all pump photon energies, the latter becomes more prominent when the pump is tuned beyond 4.10 eV.

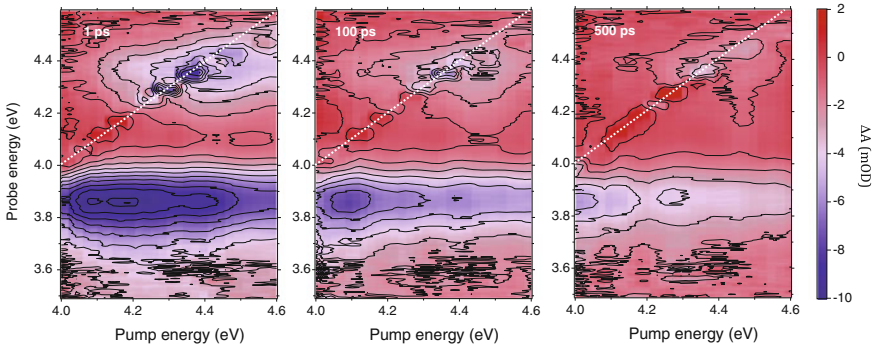

Fig. 4.19 Colour-coded maps of ΔA measured via ultrafast 2D deep-UV spectroscopy on a colloidal solution of anatase TiO_2 NPs at RT as a function of pump- and probe photon energy. The spectral response is displayed at three different time delays between pump and probe: 1 ps, 100 ps, 500 ps. The time resolution is estimated 150 fs and the photoexcited carrier density is $n = 5.7 \times 10^{19}\,\mathrm{cm}^{-3}$

Further insights into the evolution of the ΔA spectrum for different pump photon energies can be obtained by cutting the map of Fig. 4.19 at 1 ps along the probe photon energy axis. The selected spectra are shown in Fig. 4.20a and normalized with respect to the absolute maximum of the feature peaking at 3.88 eV. For comparison, also the inverted steady-state spectrum of the same colloidal solution of anatase TiO_2 NPs is displayed. Remarkably, we observe that both features appearing in the ΔA spectra retain a well-defined Lorentzian lineshape with a width of ∼250 meV, in contrast with the featureless steady-state absorption spectrum. To assign these features, we rely on a direct comparison with the ΔA spectra obtained from the single crystals. The spectra are shown for clarity in Fig. 4.20b along the *a*- and *c*-axis, for a 4.40 eV pump photon energy and a time delay of 1 ps. As already observed above, in these separate polarization channels, two negative features appear at 3.88 and 4.32 eV, similarly to the ΔA spectra of NPs. These energies match those of the excitonic peaks I and III in the equilibrium absorption spectrum along the *a*- and *c*-axis (note that the values of the absorption peaks slightly differ from the peaks in the dielectric function). As a result, the combined measurements on the single crystals and the NPs

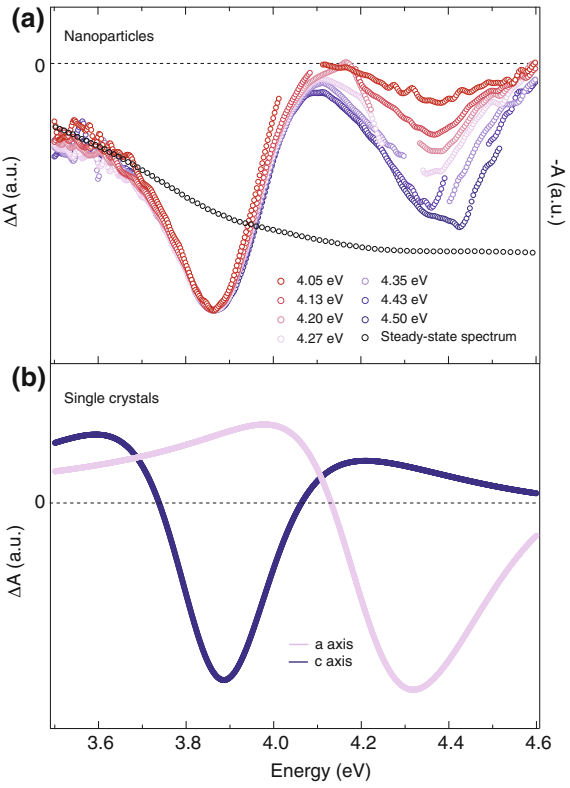

Fig. 4.20 **a** Normalized ΔA spectra of RT colloidal solution of anatase TiO_2 NPs at a fixed time-delay of 1 ps and for different pump photon energies (indicated in the figure). Each trace is normalized with respect to the minimum of the main feature at 3.88 eV. For comparison, the black trace shows the inverted steady-state absorption spectrum. **b** ΔA spectrum of RT anatase TiO_2 single crystals along the *a*- and *c*-axis at a fixed time delay of 1 ps. The pump photon energy is 4.40 eV

allow us to disentangle the *a*-axis and *c*-axis contributions in the ΔA response of the NPs. Both excitons are found to appear in the latter response due to the random orientation of NPs in solution.

This leads us to conclude that the excitonic features are also present in the equilibrium absorption spectrum of anatase TiO_2 NPs, but they are shadowed by the strong scattering experienced by light through the colloidal solution during the measurement in a conventional spectrometer. It is important to remark that this result has been made possible by the detection of the ultrafast spectral response in the deep-UV range, which has always been inaccessible to previous ultrafast broadband optical experiments.

4.5.3 Origin of the Exciton Bleaching

The demonstration of the RT-stability of the bound excitons in anatase TiO_2 NPs opens novel scenarios towards the understanding of the nonequilibrium dynamics occurring in this material after photoexcitation. Indeed, given the importance of interactions and correlations in anatase TiO_2, one expects them to have a pronounced influence on the carrier dynamics. In particular, these phenomena are predicted to govern the timescales for intraband carrier cooling via phonon emission [62] and they can also influence the optical properties of the material via strong optical nonlinearities. As such, their comprehension is of pivotal importance for the design of novel devices and the optimization of existing ones [63].

So far, the charge carrier dynamics in TiO_2 has intensely been studied by ultrafast broadband transient absorption spectroscopy from the THz to the visible [64–70]. In these studies, the photoexcited electrons and holes in the system were treated as uncorrelated, an approximation that is valid only when the pump photons are non-resonant with the excitons. Under these conditions, the material response is dominated by a free-carrier Drude response and by absorption features attributed to localized charges trapped at impurity and/or defect centres [64–69]. Although these studies shed light on the electron-hole recombination pathways, they were biased towards surface effects, probed only intraband transitions, ignored the material electronic structure, while the identification of impurity/defect bands is still debated [71, 72]. More insightful information was provided by time-resolved photoluminescence, which revealed a strongly Stokes-shifted emission in the visible range assigned to self-trapped excitons and/or charges trapped at defects [73–78]. However, these processes were found to emerge only at low temperatures and to disappear at RT. Furthermore, only long timescales (>20 ps) were investigated.

Here, to reveal the hierarchy of interactions and correlations in the dynamical response of anatase TiO_2, we focus more closely on our ultrafast 2D deep-UV spectroscopy results of Fig. 4.19. When dealing with excitonic optical nonlinearities in semiconductors, the most prominent effects are: (i) Phase-space filling, which causes a reduced oscillator strength by decreasing the number of single-particle states contributing to the exciton; (ii) Long-range Coulomb screening, which broadens the

exciton band and shifts it to the blue, as the photoexcited carrier density screens the electron-hole interaction and reduces E_B; (iii) BGR, which leads to a density-dependent shrinkage of the single-particle states (and consequently of the exciton states), and may reduce the exciton oscillator strength. These processes act simultaneously on the exciton lineshapes, their relative weights being governed by the material parameters and dimensionality [57, 61].

To this purpose, we select a data set from Fig. 4.19, namely the one at the pump photon energy of 4.05 eV, since it lies below the *c*-axis exciton peak and is expected to minimize its contribution. This, in turn, allows us to link more accurately the resulting ultrafast dynamics to the details of the electronic structure. The data are displayed in Fig. 4.21a as a colour-coded map of ΔA as a function of probe photon energy and time delay between pump and probe. As expected, the spectral response features the long-lived *a*-axis exciton band at 3.88 eV, followed by the weaker shoulder of the *c*-axis exciton around 4.35 eV. The transient spectra at different time delays of Fig. 4.21b show that the 3.88 eV peak position does not change with time. Figure 4.21c displays the kinetic traces at three specific probe photon energies: below (3.77 eV), at (3.90 eV) and above (4.10 eV) the *a*-axis exciton peak. All temporal traces exhibit a

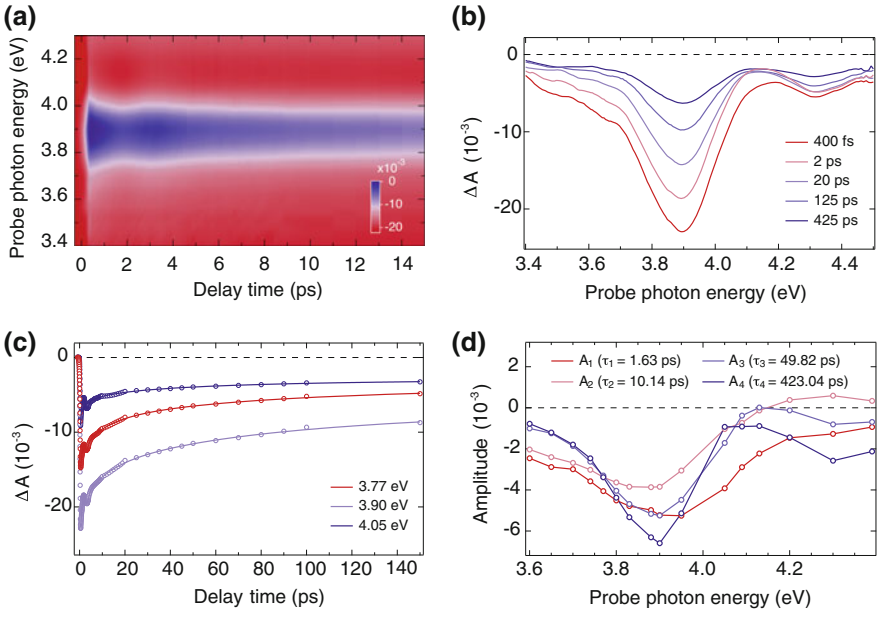

Fig. 4.21 **a** Colour-coded map of ΔA measured on a colloidal solution of anatase TiO_2 NPs as a function of probe photon energy and time delay between pump and probe. The time resolution is estimated to be 150 fs, the pump photon energy is set at 4.05 eV and the photoexcited carrier density is $n = 5.7 \times 10^{19}\,\mathrm{cm}^{-3}$. **b** ΔA spectra as a function of probe photon energy at representative delay times between pump and probe. **c** Experimental temporal traces of ΔA for different probe photon energies (dotted lines) and results of the global fit analysis (solid lines). **d** Contribution to the ΔA response of the four relaxation components obtained from the global fit analysis

resolution-limited rise of 150 fs, followed by a long-lived decay persisting beyond 1 ns. In addition, a low-frequency oscillation modulates the whole spectrum during the first 5 ps, which is fully damped within one oscillation period. This feature is due to coherent acoustic phonons confined within the spherical TiO_2 NPs, and it will be discussed in the following Paragraph. Here, we retrieve the significant parameters of the incoherent response, by performing a global fit of sixteen selected temporal traces in the 3.60–4.40 eV probe range of the ΔA map. A satisfactory global fit up to 1 ns (solid line in Fig. 4.21c) is optimal using a multiexponential function with four time constants (τ) convoluted with a Gaussian accounting for the instrument response function of ~150 fs: $\tau_1 = 1.60 \pm 0.12$ ps, $\tau_2 = 10 \pm 0.40$ ps, $\tau_3 = 50 \pm 1.70$ ps, $\tau_4 = 423 \pm 14.70$ ps. The global fit enables us to disentangle the spectral dependence of the decay processes contributing to the recovery of the exciton bleach. To this aim, in Fig. 4.21d, we plot the pre-exponential factors associated with a given time constant as a function of the probe photon energy. The spectral dependence of the τ_1 and τ_2 components show a negative amplitude broader than the exciton lineshapes, while the contributions of the τ_3 and τ_4 components mainly reproduce the contours of both exciton bands, suggestive of a different nature for the two sets of components. All decay processes are strictly related to the electron-hole recombination mechanisms, which reduce the density of delocalized carriers via radiative or non-radiative relaxation channels.

In order to identify the phenomena behind the different time constants, one first needs to assess the relative weights of the optical nonlinearities contributing to the transient signal. Central for this is to clarify the electron-hole populations giving rise to the exciton collective state. Based on the band structure of anatase TiO_2 [8], the single-particle states contributing to the *a*-axis exciton lie along the Γ-Z direction of the BZ (Fig. 4.22). Due to the symmetry of the *p-d* wavefunctions, however, the states exactly at the Γ point are symmetry forbidden and do not contribute to the exciton

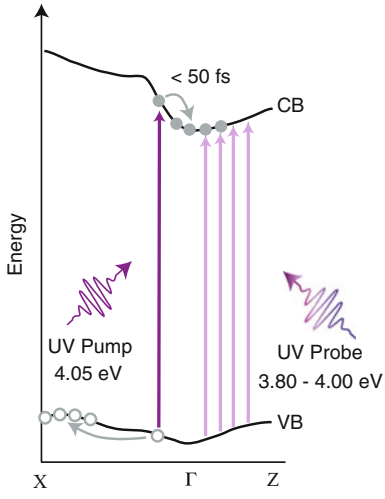

Fig. 4.22 Schematic representation of the deep-UV based detection of the ultrafast carrier dynamics in anatase TiO_2 NPs. The pump photon at 4.05 eV (purple arrow) excites electron-hole pairs through direct transitions. The broadband UV pulse (violet arrows) probes the exciton feature at 3.88 eV. The direct transitions contributing to this collective state lie along the Γ-Z region of the BZ. The band structure of anatase TiO_2 has been taken from our ab initio calculations

state [8]. Once a nonequilibrium distribution of uncorrelated electron-hole pairs is created, the electrons are expected to thermalize to the bottom of the CB at Γ and the holes to the top of the VB close to X. Since the deep-UV probe is sensitive to the joint DOS in the material, an induced transparency ($\Delta A < 0$) can arise from a density of electrons (holes) accumulated in the CB (VB) alone. In anatase TiO_2, the phase-space filling contribution to the exciton bleaching is expected to arise exclusively due an electron population close to the bottom of the CB. The hole contribution is absent, due to their ultimate relaxation to the top of the VB close at the X point. This consideration implies that phase-space filling, long-range Coulomb screening and BGR may all contribute to the observed optical nonlinearities. This requires addressing the effects related to the enhancement of the electronic screening upon pump photoexcitation.

To this aim, we study how the exciton spectrum is renormalized as a function of the pump fluence at 4.05 eV, narrowing our detection range to cover only the spectral region of the *a*-axis exciton. This allows a higher stability of our setup, maintaining the same experimental conditions over the time required for the fluence dependence study. Within the explored range, the maximum intensity of the signal scales linearly with the absorbed fluence, which excludes multiphoton absorption processes from the pump beam. The normalized spectra are shown in Fig. 4.23a, b for delay times of 400 fs and 10 ps, respectively. We observe that the exciton lineshape slightly broadens with increasing carrier density. We assign this behaviour to the presence of long-range CS. Indeed, under our experimental conditions, we can exclude that the broadening originates from other exciton decay channels opened by the photoexcitation process. Radiative or non-radiative exciton decay processes are found in direct bandgap semiconductors in the presence of low-dimensionality and reduced dielectric screening [79–82], since non-resonant photoexcitation can spontaneously evolve into exciton formation via the single-particle states at the band edges. In contrast, in indirect bandgap semiconductors, photoexcited uncorrelated

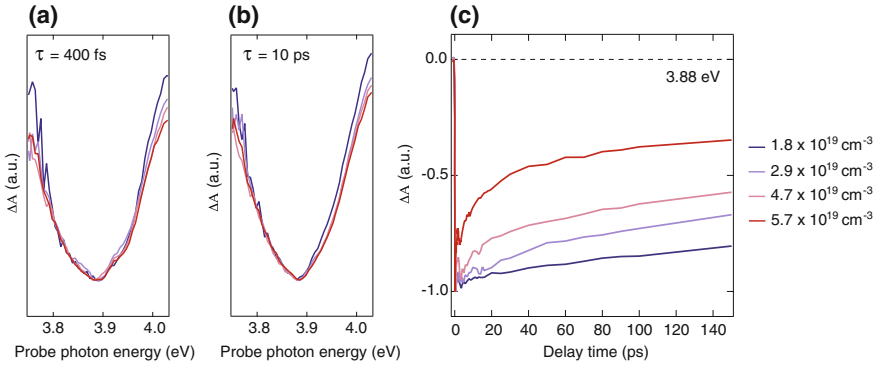

Fig. 4.23 **a**, **b** Normalized ΔA spectra as a function of probe photon energy for different photoexcited carrier densities. Spectra in (**a**) are cut at a delay time of 400 fs, spectra in (**b**) at 10 ps. **c** Normalized temporal traces at 3.88 eV for different photoexcited carrier densities

electrons and holes quickly relax towards the bottom of their respective bands and no direct excitons are energetically favoured [83]. In principle, indirect excitons would be allowed to form through the mediation of phonon modes. However, in the case of anatase TiO_2 nanosystems, their existence at RT has been disproven by extensive measurements [76, 84–86] and by the results we present in the following. As such, many-body processes such as exciton-exciton annihilation can be excluded. Consistent with the idea that long-range Coulomb screening from free carriers is the optical nonlinearity governing the exciton broadening, in Sect. 4.6 we will show that the excitonic band of anatase TiO_2 is broadened upon charge injection from an external dye adsorbed on the surface of NPs (i.e. in the absence of holes in the VB of TiO_2). Long-range Coulomb screening is also expected to lead to a blueshift of the exciton peak. However, within our experimental accuracy, here we observe no shifts in the peak energy position, nor derivative-like shapes. This apparent insensitivity of the exciton peak energy to the photoinduced carrier density even in the presence of CS-induced broadening has been rationalized in the literature by invoking an exact cancellation of the effects of CS and BGR on the excitonic resonances [44]. In general, the quantitative details of this compensation depend on both material and dimensionality [47]. From these measurements, we can conclude that the carrier density which is required to induce such dramatic changes of the exciton peak is higher than those produced by our photoexcitation. As a consequence, at sufficiently low electron-hole pair densities, when the continuum is still far from the resonances, only the loss of oscillator strength due to phase-space filling and the broadening due to Coulomb screening are apparent.

These results further confirm the strongly bound exciton scenario deduced above for the *a*-axis exciton, in which we demonstrated the ineffectiveness of BGR even for extremely high carrier densities ($n \sim 10^{20}\,\mathrm{cm}^{-3}$). Thus, we conclude that phase-space filling is the dominant effect contributing to the excitonic optical nonlinearities at our carrier densities. Consistent with this scenario, the exciton bleach is found to persist even when the pump photon energy is tuned to 3.54 eV, thus promoting indirect (phonon-assisted) interband transitions (Fig. 4.24). On the contrary, upon 3.10 eV excitation, no signal is detected even up to incident fluences of 34 $\mathrm{mJ/cm}^2$.

Having established the dominant role played by CB electrons in blocking the excitonic transitions allows one to retrieve valuable information on the electron recombination dynamics. Indeed, the ΔA signal at the excitonic resonance can be used as a measure of the photoexcited electron concentration changing with time. Representative temporal traces at a probe photon energy of 3.88 eV and for different excitation densities are shown in Fig. 4.23c and normalized with respect to their maximum. We observe that below 40 ps the bleach recovery accelerates with fluence, which is indicative of higher-order recombination processes for the charge carriers, such as bimolecular and Auger recombination. Indeed, the recombination dynamics in semiconductors and insulators proceeds via single-carrier nonradiative processes (trapping at impurity states), two-body radiative (bimolecular) mechanisms and non-radiative trap-Auger recombination processes and three-body band-to-band Auger processes [87]. Since anatase TiO_2 is an indirect bandgap insulator, band-to-band radiative recombination is known to be extremely inefficient. Thus, the only radiative

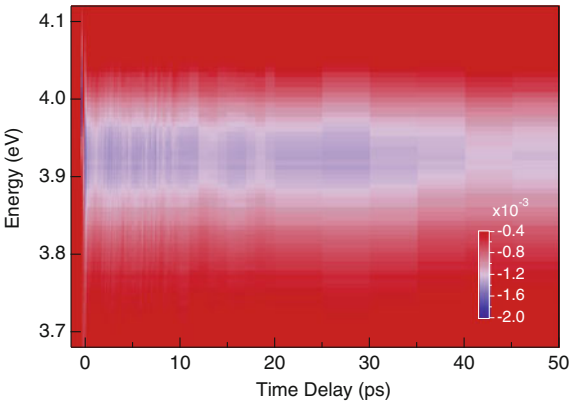

Fig. 4.24 Colour-coded map of ΔA measured on a colloidal solution of anatase TiO_2 NPs at RT as a function of probe photon energy and time delay between pump and probe. The time resolution is estimated 150 fs, the pump photon energy is set at 3.54 eV and the delivered pump fluence is 100 $\mu J/cm^2$

recombination pathways that can take place at RT are those involving a delocalized carrier in a band and a localized carrier trapped at a defect state. To verify the efficiency of the radiative recombination processes, we measured the photoluminescence obtained in colloidal anatase TiO_2 NPs by femtosecond fluorescence up-conversion. As it is well established that the spectral content of the photoluminescence does not depend on the pump photon energy for above-gap excitation, we illuminate the NPs with a pump pulse centered around 4.66 eV. The broad photoluminescence spectrum at a time delay of 1 ps is shown in Fig. 4.25a. The photoluminescence appears only in the visible regime and is completely absent in the spectral region >3.00 eV. It retains the form of a broad band centered around 2.24 eV, which is characterized by an extremely weak intensity. Figure 4.25b displays the temporal traces at 1.91, 2.18 and 2.58 eV. The photoluminescence signal rises within our experimental temporal resolution (200 fs) and decays bi-exponentially with time constants of 2 ps and 30–40 ps. Since the PL band is centered around 2.24 eV, it can be readily assigned to an extrinsic radiative recombination channel that involves carriers trapped at defect states, ruling out the involvement of any self-trapped exciton recombination process. By evaluating the photoluminescence quantum yield for time delays below 500 ps, we find it to be of the order of $\sim 1.3 \times 10^{-6}$, i.e. extremely weak. As a consequence, it is straightforward to assume that the recombination dynamics at early time delays in anatase TiO_2 is entirely governed by Auger mechanisms, as already inferred from transient absorption spectroscopy studies in the infrared and visibile for highly-excited anatase TiO_2 NPs and thin films [64, 70]. It is also consistent with the spectral dependence of the τ_1 and τ_2 relaxation components (Fig. 4.21d), whose broad shape hints to energetically redistributed carriers over a wider phase space during the Auger processes. In contrast, the longer τ_3 and τ_4 relaxation components can be assigned to electron trapping processes at defect states, which lead to bleach recovery by emptying the phase space involved in the exciton state.

More interestingly, having established phase-space filling as the main mechanism behind exciton bleaching allows us to address the long elusive issue of the timescale of electron cooling to the CB minimum in anatase TiO_2. A recent single-wavelength

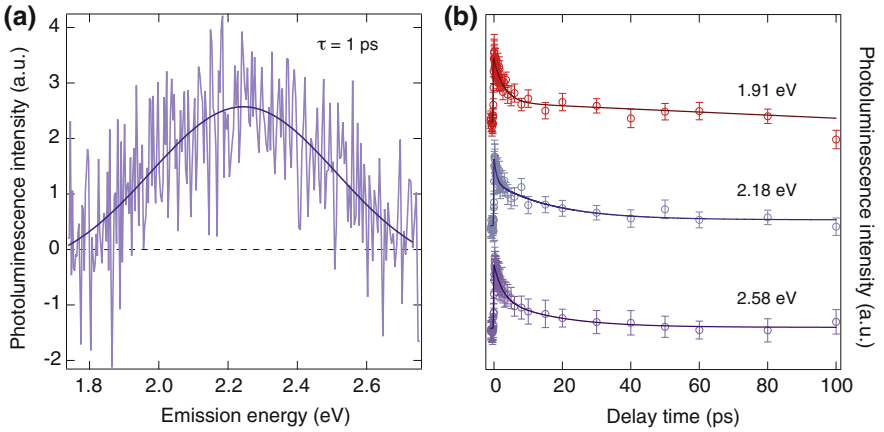

Fig. 4.25 **a** Experimental spectrum of the ultrafast PL at a time delay of 1 ps (violet curve) and gaussian fit of the response (blue curve). **b** Temporal evolution of the ultrafast PL at 1.91 eV (red dots), 2.18 eV (blue dots) and 2.58 eV (violet dots). The solid lines are fit to the experimental curves

transient reflectivity experiment on rutile TiO_2 single crystals tracked the influence of carrier cooling onto the phase of the coherent A_g phonon mode at 74.4 meV, offering valuable information on the electron-phonon coupling dynamics [88]. Nevertheless, this approach is blind to the details of the electronic structure and relies on the analysis of coherent optical phonons, whose observation is not always straightforward.

Here, we circumvent these limitations by demonstrating the effectiveness of exciton bleaching as a probe of the intraband electron thermalization. To this aim, we focus on the rise of the exciton bleach signal by reducing the instrument response function of our setup to 80 fs. Given the high intensity of the pump pulses, effects of CPM around zero time delay (where pump and probe pulses overlap spatially) are present in the measured signal in the form of interference-induced amplitude modulation. The use of a liquid jet allows us to avoid the CPM provided by the flow cell in which the solution flows and limits it only to the CPM provided by the solvent. In Fig. 4.26a, we compare the signal at 3.88 eV and an excitation density $n \sim 2.1 \times 10^{19}\,\mathrm{cm}^{-3}$ (violet curve) with that of the pure solvent (pink curve). In both traces, artefacts due to the residual CPM after t = 0 can be identified. Moreover, while the signal from the solvent dies immediately after the CPM, the one from anatase TiO_2 persists over time and comprises a relaxation component that starts around 200 fs. However, to isolate the anatase TiO_2 signal, the two traces cannot be directly subtracted due to slightly different experimental conditions in the measurements. Therefore, we adopt a common procedure in ultrafast spectroscopy, in which the instrument response function is assumed to coincide with the duration of the CPM signal and is represented by a Gaussian function (with a full-width at half-maximum of 80 fs) folding in the CPM modulations (blue curve in Fig. 4.26a). The isolated TiO_2 signal is shown as red dots superimposed to the original trace. To provide an upper limit to the rise time of the bleach signal, in Fig. 4.26b the isolated

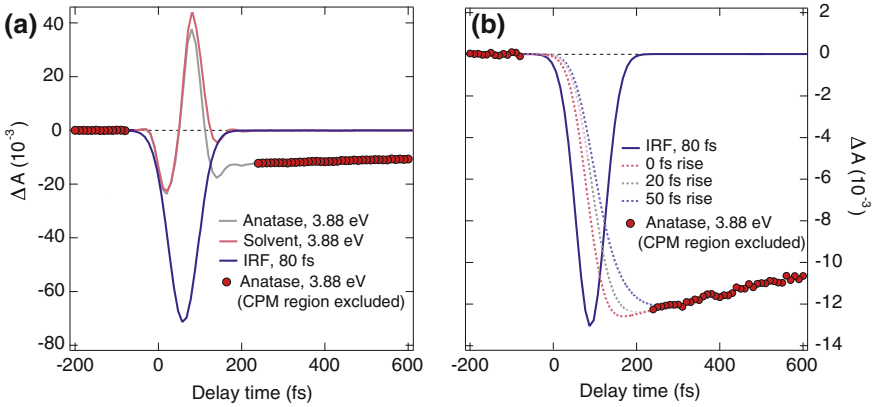

Fig. 4.26 **a** Comparison of the kinetic trace of the ΔA signal at 3.88 eV from the colloidal solution of anatase TiO_2 (grey trace, red dots) with that of the solvent alone (pink trace). The sample response with the CPM region excluded is represented by the red dots. The Gaussian instrument response function of 80 fs is also shown. **b** Evaluation of the rise-time of the ΔA signal by interpolating the ΔA response of anatase TiO_2 in the region where CPM is excluded, using a rising function (convoluted with a Gaussian instrument response function of 80 fs) at three different times

TiO_2 signal (red dots) is compared to three computed time traces convoluted with the Gaussian instrument response function of 80 fs. They consist of different rise times and an exponential recovery time of 200 fs. Here, the time t = 0 is consistently defined with respect to the subtracted CPM. It can be seen that the 20 fs rise time interpolates nicely between the $t < 0$ points and the $t > 200$ fs ones. In any case, the upper limit cannot exceed 50 fs. Thus, the rise of the exciton bleach is <50 fs, which is the timescale for the intraband electron cooling.

We now discuss the origin of this ultrafast electron cooling. Upon photoexcitation, momentum conservation results in the partition of the excess energy provided by the pump pulse into kinetic energy of the electrons and holes according to the reciprocal ratio of their effective mass m_e^*/m_h^*, with the carrier having lower effective mass receiving more of excess energy

$$E_{\mathrm{exc}}^{\mathrm{e}}(\hbar\omega) = \frac{\hbar^2 k^2}{2m_e^*} = \frac{m_h^*}{m_e^* + m_h^*}\left(\hbar\omega - E_{\mathrm{gap}}\right), \tag{4.2}$$

$$E_{\mathrm{exc}}^{\mathrm{h}}(\hbar\omega) = \frac{\hbar^2 k^2}{2m_h^*} = \frac{m_e^*}{m_e^* + m_h^*}\left(\hbar\omega - E_{\mathrm{gap}}\right). \tag{4.3}$$

In our experiment, $\hbar\omega = 4.05$ eV and $E_{\mathrm{gap}} = 3.20$ eV. Rigorously, the electron and hole effective masses vary as a function of momentum k. These masses are well-defined concepts only within the parabolic approximation for the band structure. From the latter, we expect our pump photons to promote uncorrelated electron-hole pairs in the vicinity of the Γ point along the Γ-X direction (purple arrow in

Fig. 4.22). The electron effective mass was recently measured via ARPES to be around $m_e^* = 0.7\, m_e$ (where m_e is the bare electron mass) for excess carrier densities $n \sim 10^{18} \div 10^{19}\,\mathrm{cm}^{-3}$ [16], which is larger than the one predicted by band structure calculations ($m_e^* = 0.42\, m_e$ [89]) due to the polaronic dressing of the electrons. For higher carrier density regimes, m_e^* is expected to decrease towards the values predicted by band structure calculations due to an effective screening of the electron-phonon interaction [16]. Thus, in Eqs. (4.2)–(4.2), we make use of the value reported by band theory. On the other hand, to provide an estimate of m_h^* from the details of the measured electronic structure, we rely on our ARPES data for the top of the VB along the Γ-X direction in the case of an excess carrier density $n \sim 10^{19}\,\mathrm{cm}^{-3}$ (Fig. 4.3). Performing a parabolic fit yields $m_h^* = (2.78 \pm 0.5) m_e$, which also accounts for the polaronic contribution to the mass renormalization. The values of m_e^* and m_h^* lead to an excess energy repartition $E_{exc}^e \sim 0.74$ eV and $E_{exc}^h \sim 0.11$ eV.

Once the carriers have received this excess energy in their respective bands, they start interacting with the phonon modes of the lattice. When the timescale obtained for the electron cooling in anatase TiO_2 is compared with the slower (>250 fs) electron relaxation timescales retrieved in nonpolar indirect gap semiconductors, some conclusions can be drawn concerning the role of electron-phonon scattering in different materials. In nonpolar semiconductors (such as Ge and Si) phonon scattering occurs through the optical phonon DP interaction, while in partially-ionic polar systems (such as anatase TiO_2) the most effective coupling mechanism is represented by the electron-longitudinal optical phonon scattering described by the Fröhlich interaction [90]. In TiO_2, the optical phonons that are most strongly coupled to the electronic degrees of freedom are those belonging to the branches of the E_u and A_{2u} modes [13, 16, 91]. Due to this coupling, in the low carrier density limit, the CB electrons form well-defined large polaron quasiparticles, characterized by a dimensionless polaron coupling constant $\alpha \sim 2$ [16]. This constant determines the ratio between the polaron self-energy and the longitudinal optical phonon energy, thus defining an intermediate-to-strong electron-phonon coupling regime for the electrons in anatase TiO_2. At high density, the polaronic quasiparticle are observed to collapse into an electron liquid coupled to the phonon modes. Within the single-particle limit probed by ARPES, the crossover takes place around $n = 10^{19}\,\mathrm{cm}^{-3}$ [16]. In the two-particle limit of optical absorption, this threshold may be even lower, leading to the emergence of a well-defined Drude response for the photocarriers [70] instead of the characteristic absorption features of large polarons [92]. Even in this diffusive regime, the electron-phonon coupling can lead to an efficient and fast transfer of electron excess energies to the phonon bath within a few tens of fs.

To theoretically interpret the relaxation times observed in our experiment, we first rely on a simple estimate of the scattering rate as expected from first order perturbation theory. In the case of electrons in a parabolic CB, the scattering rate can be calculated via Fermi's golden rule as [93]

$$\Gamma = \Gamma_0 \left(\frac{1}{\epsilon_\infty} - \frac{1}{\epsilon_s} \right) \mathrm{arcsinh}\left(\sqrt{\frac{E_{exc}^e}{\hbar\omega_{LO}} - 1} \right) (1 + 2n_{BE}), \tag{4.4}$$

where ϵ_∞ and ϵ_s are the dielectric constants at energies well above and below the phonon energy ω_{LO}, respectively, and n_{BE} is the Bose-Einstein statistical factor. Γ_0 is a nearly temperature-independent prefactor that reads

$$\Gamma_0 = \sqrt{\frac{m_e^*}{2E_{exc}^e}} \frac{e^2 \omega_{LO}}{2\pi\hbar\epsilon_0}. \tag{4.5}$$

Substituting the relevant parameters for anatase TiO_2 [49] yields ∼4 fs for the electron cooling time, which could be compatible with our experimental observation. However, we point out that Eq. 4.4 is valid under the conditions that a single phonon mode is interacting with the electrons and that $\alpha < 1$. Since α represents a measure for the relative importance of higher-order processes, Eq. 4.4 may not provide an accurate estimate of the actual electron cooling rate. A more reliable estimate relies on density-functional perturbation theory accounting for the phonon DOS of the material, as computed in Ref. [62]. According to this ab initio approach, under our experimental conditions we expect the timescale for emission of a single phonon by an excited electron to be ∼2 fs and the total thermalization time to the CB edge ∼40 fs, in very good agreement with the present upper limit of 50 fs. On the other hand, the holes can undergo rapid intervalley scattering to the X and Z points via emission of high-wavevector phonons.

Within the semiclassical limit, for excess energies less than the minimum polar longitudinal optical phonon energy (∼45 meV in TiO_2 [49]), severe constraints in the phonon phase space are expected to result in a dramatic decrease of the intraband cooling rate [62]. However, for polaronic materials governed by the Fröhlich interaction, purely quantum kinetic relaxation channels can open also in the case of small excess energies, leading to an efficient redistribution of the electronic energy into the strongly coupled phonons [94, 95]. This effect can be viewed as the buildup of the polaronic dressing in the low-density limit. Future quantum kinetic calculations involving the solution of the Dyson equation will shed light on these phenomena. At this stage, irrespective of the mechanism at play, the net result is that no effective energy will be stored in the electronic degrees of freedom for sufficiently long timescales.

These arguments lead us to conclude that, in anatase TiO_2, fast relaxation processes impose serious limitations to the practical use of the full photon energy in applications. This scenario is radically different from the physics of semiconductor quantum dots, in which the spacing between the discrete electronic levels is large enough to prevent fast phonon-mediated carrier cooling processes [96]. For photocalaysis, fast thermalization is a favourable process, since the lower energy states are important. This issue is also of importance in photovoltaics since a large driving force is often sought after for efficient injection, especially when the coupling between the sensitizer to the TiO_2 substrate is weak. However, the present study shows that the large excess energy is lost to phonons. Therefore, alternative excitation schemes, such as resonant excitation of the strongly bound exciton species, are preferable in which the energy can be temporarily harvested. Furthermore, as we showed that the

a-axis excitons are 2D and robust against temperature and defects, they are expected to move freely on the (001) plane [8, 97]. As such, they may offer an efficient source to mediate the flow of energy at the nanoscale in engineered devices based on anatase TiO_2.

4.5.4 Interplay Between Excitons and Coherent Acoustic Phonons

In the previous Paragraph, we addressed the microscopic details of the electron intraband relaxation in anatase TiO_2, rationalising it in terms of the Fröhlich interaction between the photoexcited carriers and polar longitudinal optical phonons [90]. However, there is a plethora of ways the carriers can interact with the lattice degrees of freedom in a complex material [98, 99], the Fröhlich interaction being only one of the different terms contributing to the first-order electron-phonon interaction Hamiltonian at $\mathbf{q} \sim 0$. Indeed, depending on the details of the electron-phonon matrix element, several other mechanisms can arise [98]. In the long-wavelength limit, transverse acoustic and longitudinal acoustic phonons typically couple to the electrons via the DP and the piezoelectric interactions, while transverse optical and longitudinal optical modes couple via the DP interaction. Beyond these first-order electron-phonon interaction terms (also known as Fan-Migdal terms), the effect of second-order electron-phonon interaction in first-order perturbation theory (the so-called Debye-Waller or Yu-Brooks terms) can provide a non-negligible contribution [100]. More complex phenomena can be expected in the case of exciton-phonon coupling, which represents an intriguing example of boson-boson interaction. Excitons can be viewed as quanta of electronic excitation energy travelling in the periodic crystal lattice, and their motion is influenced by the fluctuating potential field due to lattice vibrations. This coupling between excitons and phonon modes of the crystal lattice results in effects such as exciton self-trapping, spectral-weight transfers to phonon sidebands and Stokes-shifted emissions [20].

Experimentally, the microscopic details of the exciton in the phonon field can be addressed via absorption and photoluminescence spectroscopy, since the shape and width of the optical spectra directly reflect the scattering of the exciton by the lattice vibrations. However, these methods offer only averaged information on the exciton-phonon interaction, i.e. mediated over all the coupled phonon modes. This calls for the development of alternative approaches to extract quantitative information on the exciton-phonon coupling matrix elements for specific lattice modes of interest. As anticipated in Chap. 2, a powerful tool relies on setting a particular phonon mode out of equilibrium and monitor the impact of the ionic motion on the exciton feature [101, 102] via ultrafast broadband optical spectroscopy.

Here we explore this phenomenology by focusing more closely to the first steps of the dynamics of our photoexcited anatase TiO_2 NPs. Direct inspection of the data of Fig. 4.21a shows the emergence of a low-frequency oscillation that modulates the

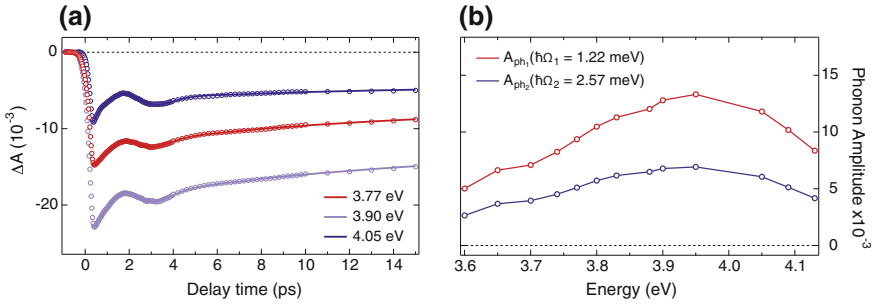

Fig. 4.27 **a** Experimental temporal traces of ΔA for different probe photon energies (dotted lines) and results of the global fit analysis (solid lines). The dynamics are shown up to 15 ps. The time resolution is estimated to be 150 fs, the pump photon energy is set at 4.05 eV and the photoexcited carrier density is $n = 5.7 \times 10^{19}$ cm^{-3}. **b** Contribution to ΔA response of the two CAPs amplitudes

exciton I feature at 3.88 eV during the first 5 ps. In Fig. 4.27a we present the temporal evolution of the ΔA response by cutting three temporal traces at specific probe photon energies below (3.77 eV), in correspondence to (3.90 eV) and above (4.05 eV) the peak of exciton I. All the temporal traces exhibit a resolution-limited rise of the negative signal, consistent with the findings reported in Sect. 4.5.3). On top of this incoherent response, the low-frequency modulation undergoes a dramatic damping after one oscillation period. To retrieve the significant parameters of the response in the probed spectral range and assign the coherent oscillations, we perform a global fit analysis of ΔA as a function of time. Thirteen temporal traces are selected from the 3.60–4.15 eV range of the ΔA map and fitted simultaneously by imposing the same time constants. A satisfactory fit up to 1 ns can only be obtained by using four exponential functions (with relaxation time τ) and two damped sinusoidal terms (with frequency Ω and damping τ_D) convolved with a Gaussian response accounting for the temporal shape of the pump pulse

$$f(t) = I(t) * \sum_{i=1}^{4} A_i e^{-t/\tau_i} + \sum_{j=1}^{2} C_j \sin(\Omega_j t + \phi_j) e^{-t/\tau_{Dj}}. \tag{4.6}$$

We remark that two damped sinusoidal terms are necessary to correctly reproduce the dynamics instead of one. While the first damped sinusoidal function is related to the large-amplitude oscillation that emerges in the slow recovery of the bleach signal, the second one accounts for an additional modulation (with smaller amplitude) that becomes apparent in the residuals of the fit when this term is not included. The frequencies of the two oscillations are imposed to be the same for all probe photon energies, since they do not display significant variations across the whole spectral range. From the global fit analysis, we obtain the four time constants $\tau_1 ... \tau_4$ indicated in the previous Paragraph (characterizing the recovery of the bleach) and two frequencies $\hbar\Omega_1 = 1.22$ meV, $\hbar\Omega_2 = 2.57$ meV, accounting for the oscillatory

response. Within our accuracy, the phases of the two sinusoidal terms are found to be constant across the probed spectral range, being typical of a cosinusoidal response. The results of the global fit are indicated as solid lines in Fig. 4.27a, overlapped to the experimental data (displayed as dots). The use of a global fit analysis enables us to disentangle the spectral dependence of the relaxation processes contributing to the recovery of the exciton bleach. Figure 4.27b shows the spectral response associated with the two coherent excitations. We observe that both collective modes possess the largest amplitude in correspondence to the probe photon energy of 3.95 eV. In other words, the effect produced by the excitation of these collective modes is represented by a strong renormalization of the spectrum peaked around 3.95 eV.

The quantum energies of the oscillatory components extracted from the global fit analysis are very low and can be ascribed to the excitation of CAPs within the anatase TiO_2 NPs. Due to their acoustic energy-momentum dispersion relation in the long-wavelength limit, in bulk single crystals the frequency of these coherent lattice modes is expected to vary with the probe photon energy. The change in frequency of the CAPs in bulk insulators is related to the particular detection mechanism offered by the probe pulse. In the simple case of transparent media, this can be interpreted in terms of Brillouin scattering [103], in which only the real part of the refractive index undergoes a modulation. In the more complex scenario of absorbing media, one should generalise the Brillouin scattering formula to include the change in the imaginary part of the refractive index [104]. In our experiment of the anatase TiO_2 NPs, the frequency of the acoustic oscillations is found instead not vary with the probe photon energy. This observation finds a natural explanation in the breakdown of the generalised Brillouin scattering condition when the size of the crystal becomes smaller than the coherence length of the acoustic mode. Hence, the acoustic mode results confined within the anatase TiO_2 NPs. Confined CAPs have already been observed in numerous experiments on metallic nanocrystallites [105, 106], semiconducting quantum dots [107, 108], semiconducting heterostructures [109] and other types of nano-objects [110].

The confinement condition enables to identify the CAPs by calculating the eigenfrequencies of the modes supported by a spherical anatase TiO_2 NP through Lamb's theory of vibrations [111]. This theory relies on the treatment of the NP as a homogeneous elastic sphere embedded in an infinite elastic medium, neglecting the anisotropy of the elastic constants of the crystal and the presence of the surrounding environment. Therefore, Lamb's classical description can be exploited just to compute the approximate eigenfrequencies of the modes and it is not effective in the estimation of the damping associated to the oscillations. The solution of the Navier's equation for the displacement field with proper boundary conditions at the surface of the particle gives rise to two classes of eigenmodes, the spheroidal and the torsional ones. A general spheroidal oscillation involves both longitudinal and transverse character, corresponding to a movement accompanied by a volume change of the particle. On the contrary, torsional modes are completely transverse and do not influence the volume of the sphere. In low-frequency spontaneous Raman scattering both types of modes can be monitored, while in femtosecond pump-probe experiments only the spheroidal family has been observed. The symmetry group of the sphere allows the

characterization of each mode in terms of an angular momentum number l, which gives an estimation of the number of wavelengths along a circle on the surface of the particle. There is a general agreement in considering modes with even-valued l (l = 0, 2, ...) as Raman-active, while those with odd-valued l (l = 1, 3, ...) as infrared-active. The oscillation with l = 0 can be regarded as a special type of spheroidal mode, since it is associated only with a radial displacement. Another index, n, is used to determine the order of the mode, defining the fundamental oscillation (n = 0) and its overtones (n > 1).

According to Lamb's theory and its extension for large-enough NPs [112, 113], the eigenfrequencies of the spheroidal modes can be derived as

$$\Omega_{l,n} = \xi_{l,n} \frac{v_{Lp}}{R}, \tag{4.7}$$

where v_{Lp} is the longitudinal sound velocity in the NP, R is the radius of the sphere and $\xi_{l,n}$ are the normalized eigenfrequencies that can be found as a solution of the equation

$$\tan(\xi_{0,n}) = \frac{\xi_{0,n}}{1 - \frac{1}{4}\xi_{0,n}^2 \left(\frac{v_{Lp}}{v_{Tp}}\right)^2}. \tag{4.8}$$

To assign the mode associated with the oscillation observed in our data, we numerically solve Eq. 4.8. We use the values of v_{Lp} = 8880 m/s and v_{Tp} = 3900 m/s for the sound velocities, which refer to the case of anatase TiO_2 NPs embedded in a glass matrix [114], and R = 14 nm, which is evaluated by TEM measurements [115]. As a result, for n = 0 and n = 1, we find the eigenvalue $\xi_{0,0} = 2.85$ and $\xi_{0,1} = 6.16$ respectively. The substitution of this parameter into Eq. 4.7 leads to the calculation of the frequencies $\hbar\Omega_{0,0} = 1.20$ meV and $\hbar\Omega_{0,1} = 2.56$ meV, which are in excellent agreement with our experimental data. This allows the assignment of the two CAPs as the fundamental spheroidal radial mode and its first overtone. The fundamental spheroidal radial mode is typically known as "breathing mode", since it involves a surface-localized change of volume of the NP, leading to its contraction and expansion. Further corrections should consider the size-distribution of the NPs around the central radius R, as well as the contribution given by their elliptical shape. The rapid dephasing of the oscillation can be further ascribed to the combination of the particle size distribution and the damping produced by the surrounding environment.

One interesting aspect related to the observation of coherent collective modes in materials under nonequilibrium conditions is represented by the comprehension of their generation and detection mechanisms. In the case of CAPs, the generation process provides insight into the coupling between the photoexcited carriers and the acoustic lattice modes, while the detection mechanism offers insightful information on the renormalization of the electronic structure under the influence of the coherent acoustic field.

Generation mechanism. As already observed in Chap. 2, the generation mechanism of CAPs in opaque materials upon photoexcitation has been historically described

in the phenomenological theory by Thomsen [104, 116]. Two processes are commonly involved, namely a non-thermal DP mechanism (electronic pressure) and a TE coupling mechanism (phononic pressure). In the last decade, several alternative non-thermal effects have been identified at the origin of CAP generation, such as piezoelectric coupling [117, 118], electrostriction [119, 120] and magnetostriction [121]. Depending on the characteristics of the material under study and of the parameters of the pump pulse, one mechanism can dominate over the others. Anatase TiO_2 is a non-magnetic and non-piezoelectric TMO and therefore the CAP generation can proceed only via the influence of the electronic or the phononic pressure. Whether the generation mechanism is governed by the electronic or the phononic pressure depends on a critical parameter, which is the ratio between the DP- and TE coupling contributions to the photoinduced stress (σ_{DP}/σ_{TE}). If this parameter is $\ll 1$, the lattice contribution takes control of the coherent motion. In band insulators and semiconductors, the DP mechanism typically provides the main contribution [102]. However, as discussed above, the photocarriers in anatase TiO_2 undergo an extremely fast intraband relaxation of less than 50 fs towards the edges of the respective bands, suggesting that the electronic pressure can in reality compete with the phononic pressure for the CAP excitation process. To quantify the separate electronic and phononic contributions to the generation mechanism, we rely on the following expressions for the photoinduced stress

$$\sigma_{DP} = \sum_k \delta n(k) \frac{dE_k}{d\eta}, \tag{4.9}$$

where $\delta n(k)$ is the change of the electronic concentration at level k and $\mathrm{d}E_k/\mathrm{d}\eta$ is the DP parameter. Given that after 50 fs the carriers have thermalized to the bottom of the respective bands at Γ and $\sim$ X, the expression can be simplified as

$$\sigma_{DP} = -nB\left[\left.\frac{dE_e}{dP}\right|_\Gamma + \left.\frac{dE_h}{dP}\right|_X\right] = -nB(d_e + d_h), \tag{4.10}$$

where n is the photoinduced carrier concentration, B is the bulk modulus and $d_{e,h}$ are the electron (hole) DPs.

On the other side, the photoinduced stress related to the TE coupling can be expressed as

$$\sigma_{TE} = -\alpha_V B \Delta T_L = -\alpha_V B \frac{nE_{exc}}{C_L}, \tag{4.11}$$

where α_V is the volumetric expansion coefficient, which can be written for a tetragonal crystal as $\alpha_V = 2\alpha_\perp + \alpha_\parallel$. ΔT_L is the lattice temperature, C_L is the lattice heat capacity per unit volume and E_{exc} is the excess energy with respect to the optical bandgap energy. The ratio between the two contributions is given by

$$\frac{\sigma_{DP}}{\sigma_{TE}} = \frac{C_L}{\alpha_V E_{exc}}\left[\left.\frac{dE_e}{dP}\right|_\Gamma + \left.\frac{dE_h}{dP}\right|_X\right]. \tag{4.12}$$

For evaluating this ratio, we compute the electron and hole DPs from ab initio calculations. In particular, the single-particle excitation spectrum of anatase TiO_2 is calculated at the GW level for different strengths of isotropic deformation of the unit cell along the three crystal axes. This isotropic deformation is artificially introduced to mimic the displacement that the unit cell undergoes during the occurrence of the fundamental breathing mode. The GW treatment of the DPs refines the GGA values reported in literature, yielding $d_e = -0.089$ eV/GPa and $d_h = -0.065$ eV/GPa. The negative sign of the DPs suggests that the photoinduced stress is compressive in nature. It is worth to note that the DPs are as large as the ones at Γ point of the Brillouin zone in GaAs [98], but retain an opposite sign. Table 4.1 summarises all parameters used in the calculations. Substituting these values in Eq. 4.12, we obtain $\sigma_{DP}/\sigma_{TE} = -27.47$. Thus, we conclude that the DP mechanism provides the dominant contribution to the generation of the confined CAPs in anatase TiO_2 NPs. As highlighted in Chap. 2, this is the common mechanism expected for CAP generation in semiconductors and insulators. However, we underline that this result can be obtained only with a reliable estimate of the DPs, as the one provided at the GW level. In contrast, by relying on the simple DFT-GGA level of theory [122], the value $\sigma_{DP}/\sigma_{TE} = -0.84$ is obtained. This in turn implies a larger contribution of the TE coupling to the photoinduced stress, which is an unlikely scenario for a wide-bandgap insulator. In conclusion, our analysis demonstrates the crucial role played by many-body perturbation theory in providing the correct interpretation of the CAP generation mechanism in a wide-bandgap insulator.

Detection mechanism. We now turn our attention to the detection process of the CAPs, which offers unexpected and surprising results. The use of a broadband deep-UV probe pulse reveals novel information on the response of the anatase TiO_2 electronic structure during the establishment of a *radial* acoustic strain. In general, all the parameters of the electronic Hamiltonian depend on the nuclear coordinates and, as a consequence, the electronic structure of a material varies in a complex way upon

Table 4.1 Parameters used for evaluating the DP and TE coupling contributions to the photoinduced stress in anatase TiO_2 NPs

Parameter	Value
Thermal expansion coefficients (K^{-1})	
α_a	7.57×10^{-6} [42]
α_c	3.66×10^{-6} [42]
Deformation potentials (eV/GPa)	
d_e	−0.089
d_h	−0.065
Excess energy E_{exc} (eV)	0.80
Heat capacity per mole C_m (J mol^{-1} K^{-1})	55.100 [123]
Mass density ρ (m^{-3})	3.89×10^6
Molar mass M (g mol^{-1})	79.9

lattice motion. Typically, a coherent lattice strain modulates the band structure via a DP mechanism, which results in a periodic energy renormalization of the excitonic and the interband charge excitations. In this case, the intensity of the coherent oscillation detected in the pump-probe signal is roughly proportional to the square of the derivative of the absorption spectrum, while the phase displays an inversion of π below and above the resonance [110]. In less conventional situations, the ion motion can influence the hopping integral t of an electron from site to site, modifying the electron bandwidth and therefore the DOS, or the transition dipole moment μ of an interband transition (similarly to the Herzberg-Teller wavepackets in the language of molecular physics) [124, 125]. As a result, the intensity of the resonance in the absorption spectrum varies with time, maintaining a fixed peak energy. In such an amplitude modulation scenario, the phase of the phonon field detected in a broadband optical pump-probe experiment remains constant across the resonance. In our ΔA temporal traces we observe no change of the phase across the excitonic feature, which is indicative of an amplitude modulation of the resonance. The experimental data cannot distinguish whether the amplitude modulation is produced by a variation of DOS or μ of the excitonic transition. In this regard, only the extension of the BSE many-body theoretical framework to the presence of acoustic fields can shed light on the detailed phonon-induced renormalization of the excitonic feature. This would also pave the route to the precise estimate of the exciton-phonon coupling matrix elements.

4.6 Exciton Bleaching as a Probe of Ultrafast Interfacial Electron Injection

In the previous Sections, we demonstrated the existence of strongly bound excitons in anatase TiO_2 single crystals and NPs, and we clarified the details of the nonequilibrium dynamics resulting upon photoexcitation. In other words, this study has retained a fundamental character up to this point. In this Paragraph, we focus instead on a possible application involving the newly discovered spectroscopic feature of the strongly bound excitons in anatase TiO_2. This step is particularly important in the perspective of providing a technological relevance to the physics of collective excitations, as explained in Chap. 1.

Here, the technological problem that we address concerns the detection of the interfacial ET between molecular adsorbates and semiconductor transition metal oxide substrates, which has been subject of huge interest for several years in the fields of solar energy conversion [126–129] and photocatalysis [130–132]. In the former case, dye-sensitized solar cells, consisting of a dye molecule adsorbed onto the surface of a mesoporous TiO_2 film have been the most explored systems; the recently-developed perovskite-sensitized-solar cells, which use hybrid organic-inorganic perovskites as sensitizers of the transition metal oxide [133–137], are also being intensely investigated. Furthermore, alternative schemes for charge injection,

using metallic (e.g. gold) NPs, are being considered [138, 139]. In all these schemes, the mechanism and timescale for charge injection into the CB of the semiconductor substrate are crucial for optimizing photovoltaic efficiency. Ultrafast interfacial ET has been studied using various optical probes. Measuring the time-resolved fluorescence of the sensitizer and associating its quenching with the injection rate has been commonly used [140–144]; however, this method can be ambiguous, as other quenching mechanisms may be operative, especially at long timescales. Transient absorption spectroscopy from the visible to the THz range is the most common approach for studying interfacial ET [145–158], as it probes the absorption by the CB electrons of the transition metal oxide, resulting from free-carrier intraband and trapped-state absorption [159]. However, the featureless nature of the latter and the spectral overlap between absorption bands of different states of the adsorbate (ground, singlet, triplet and oxidized form) are the main weaknesses of this approach. In particular, the free-carrier absorption is problematic when dealing with solid-state sensitizers, such as perovskites, due to their significant free-carrier absorption. Recently, time-resolved x-ray absorption spectroscopy was implemented to probe the transition metal oxide [160–163]. Although an unambiguous tool of charge injection, time-resolved x-ray absorption spectroscopy is mostly sensitive to trapped charges in the transition metal oxide. In addition, it can only be implemented at large-scale facilities such as synchrotrons or free electron lasers.

An unambiguous, universal and laboratory-based probe of charge injection is therefore needed. In this regard, a simple and novel methodology can be based on the detection of specific spectroscopic signatures of the transition metal oxide of interest, as opposed to the rather featureless and non-specific intraband absorption of free carriers in the CB. Natural candidates for such signatures are the high-energy excitons and interband transitions of the substrate, which in transition metal oxides typically lie in the deep-UV above 3.10 eV. A similar approach has been recently implemented in the visible range by Wachtveitl and co-workers [164], who detected the excitonic transitions of CdSe quantum dots after selective photoexcitation of a surface-bound alizarin dye injecting an electron. Demonstrating this methodology in the deep-UV has two main advantages: (i) In transition metal oxides, upon electron injection into the CB, specific excitons and interband transitions can undergo pronounced changes through various mechanisms, e.g. phase-space filling, Coulomb screening, etc. Thus, appearance of these features in a visible pump/deep-UV continuum probe experiment provides a distinct signature of ET from the sensitizer, allowing one to monitor the evolution of the electrons in the CB; (ii) The deep-UV region is weakly affected by the free-carrier absorption signal, which scales as λ^p within the extended Drude model (where $p > 1$ accounts for the scattering mechanisms that dominate in the material) [98].

In this Paragraph, we show that a pronounced bleaching of the exciton feature is retrieved in anatase TiO_2 NPs following the injection from the external dye cis-di(thiocyanato)bis(2,2'-bipyridyl-4,4'-dicarboxylate)ruthenium(II), referred to as N719. These results offer a new methodology that can be applied on different samples, like other transition metal oxides and/or different sensitizers [165]. In particular, we use our versatile femtosecond broadband pump-probe setup to compare

the nonequilibrium dynamics in three different samples: The N719 dye alone, bare anatase TiO_2 NPs, and dye-sensitized anatase TiO_2 NPs. The description of the sample preparation is given in Appendix A.2.2.

We first measure the RT steady-state absorption spectrum of the different samples. Figure 4.28a shows the absorption spectra of the N719 dye (pink curve), of the colloidal solution of bare anatase TiO_2 NPs (blue curve) and of the colloidal solution of dye-sensitized anatase TiO_2 NPs (red curve) in a range between 1.70 and 4.60 eV. These spectra have been obtained accounting for the reference spectrum of the pure solvent. The absorption spectrum of the N719 dye agrees with the literature [166]. In the measured spectral range, it comprises distinct absorption bands: The broad Metal-to-Ligand Charge Transfer (MLCT) bands around 2.30 and 3.18 eV and the prominent Ligand-Centred (LC) band around 4.00 eV. Also the absorption spectrum of bare anatase TiO_2 NPs is comparable to the one reported in previous works [59, 60], with the main absorption onset around 3.26 eV and a long tail extending within the bandgap. This tail can be associated with scattering of light and with impurity- and defect-assisted transitions. Finally, the absorption spectrum of dye-sensitized anatase TiO_2 NPs at low concentrations does not show significant differences with respect to the one of bare anatase TiO_2 NPs. When the concentration is increased (Fig. 4.28b), we observe the emergence of the MLCT excitation around 2.30 eV.

We now focus on the nonequilibrium response of the three samples. We start with the transient deep-UV response of N719 molecules in solution upon photoexcitation of the MLCT state at 2.25 eV, green arrow in Fig. 4.28). The probe covers the region

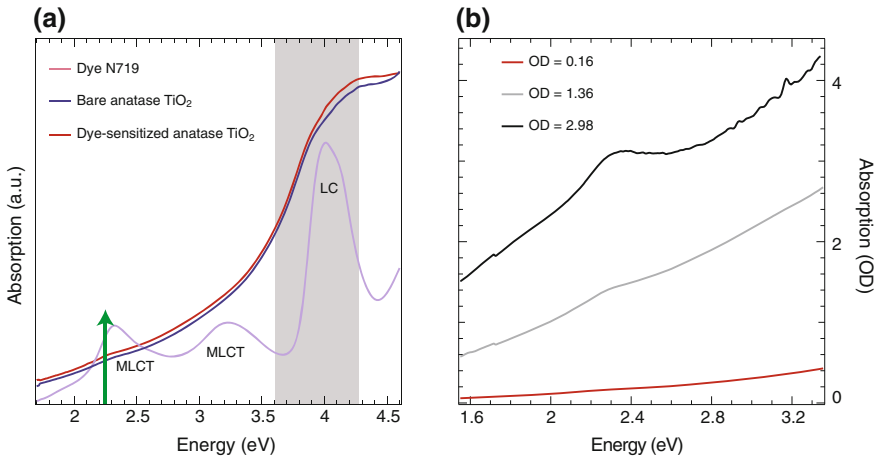

Fig. 4.28 **a** Steady-state absorption spectra of the N719 dye (pink curve) in dimethylformamide, the colloidal solution of bare anatase TiO_2 NPs (blue curve) in acidic water and the colloidal solution of dye-sensitized anatase TiO_2 NPs (red curve) in dimethylformamide. The pump photon energy of 2.25 eV used for the pump-probe experiment is indicated as a green arrow and the probed broadband UV region is highlighted as a grey shaded area. The assignments of the MLCT bands and the LC band are also highlighted. **b** Steady-state absorption spectra of the colloidal solution of dye-sensitized anatase TiO_2 NPs in dimethylformamide as a function of concentration

from 3.59 to 4.28 eV (shaded area in Fig. 4.28a). Figure 4.29a displays the resulting colour-coded map of ΔA as a function of probe photon energy and time delay between the visible pump and the UV probe. A prominent negative feature appears between 3.81 and 4.20 eV, which corresponds to the bleach of the ligand-centred (LC, Fig. 4.28) band due to depopulation of the GS by the pump pulse. The regions to the blue and the red side of this bleach band are positive. All features (positive or negative) exhibit a long temporal behaviour, characteristic of the promptly populated ($\leq$ 30–40 fs [167, 168]) ^{3}MLCT state [169]. This implies that the positive features in Fig. 4.29b are due to an ES absorption of the ^{3}MLCT state. The weak evolution at early times of all features in Fig. 4.29a is due to vibrational cooling processes [170].

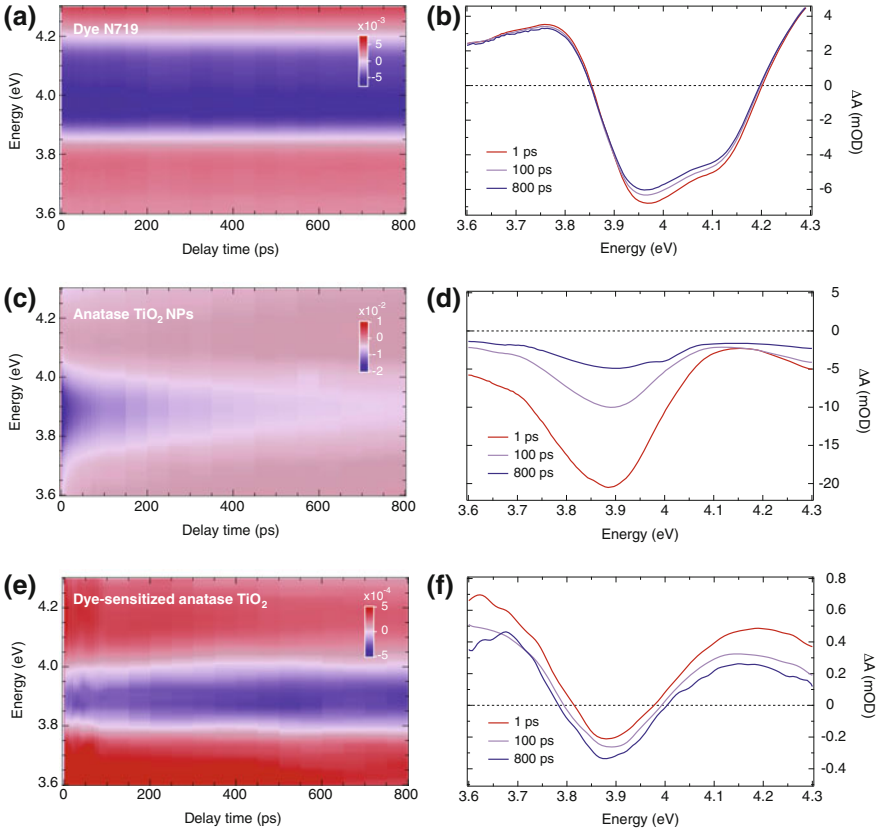

Fig. 4.29 **a**, **c**, **e** Colour-coded maps of ΔA as a function of probe photon energy and time delay between pump and probe. **b**, **d**, **f** ΔA spectra at selected delays of 1 ps (red curves), 100 ps (violet curves) and 800 ps (blue curves). **a**, **b** Visible pump/UV-probe ΔA on the dye N719 in solution excited at 2.25 eV, with a fluence of 40 μJ/cm^2. **c**, **d** UV pump/UV probe ΔA of a colloidal solution of bare anatase TiO_2 NPs, excited at 4.00 eV with a fluence of 176 μJ/cm^2. **e**, **f** Visible pump/UV probe experiment on a colloidal solution of N719 dye-sensitized anatase TiO_2 NPs, excited at 2.25 eV with a fluence of 168 μJ/cm^2

We now turn to the case of bare anatase TiO_2 NPs in an acidic aqueous solution. As the indirect optical bandgap of the material lies at 3.20 eV, the pump photoexcitation is tuned to 4.05 eV to excite uncorrelated electron-hole pairs via direct interband transitions. Figure 4.29c shows ΔA as a function of probe photon energy and time delay between the UV pump and the UV probe. A strong (10^{-2} variation of ΔA) bleach signal appears over the entire probe range, with a pronounced band around 3.88 eV, which undergoes a clear recovery over the measured 800 ps. Figure 4.29d shows the ΔA spectra at different time delays, in agreement with those presented in Sect. 4.5.3. The 3.88 eV feature is due to the strongly bound direct exciton of anatase TiO_2. The strong bleach dominates over the positive signal due to free-carrier absorption, which is expected to be weak in the deep-UV [98].

Finally, we investigate the N719 dye-sensitized anatase TiO_2 NPs dispersed in aqueous solution by setting the photoexcitation at 2.25 eV. Thus, the pump photon energy is tuned to the MLCT band of the dye and is not sufficient to excite anatase TiO_2. The resulting ΔA signal, shown in Fig. 4.29e, f, is similar to the one in Fig. 4.29c, d. Of importance here is that the signal is about two orders of magnitude smaller (10^{-4} variation of ΔA) than the one retrieved upon above-gap excitation. Figure 4.29f shows the ΔA at different time delays. A region of decreased absorption appears between 3.81 and 3.97 eV and two positive features at the edges of the probed region.

To avoid the possibility that multiphoton absorption plays a role in our nonequilibrium experiment on the dye-sensitized anatase TiO_2 NPs, we perform a number of additional experiments. We measure the broadband deep-UV ΔA of dye-sensitized anatase TiO_2 NPs by varying the fluence of the pump excitation at 2.25 eV between 84 and 336 $\mu J/cm^2$. The colour-coded maps of the ΔA for different pump fluences are shown in Fig. 4.30a, c, e, while the corresponding transient spectra at 1, 100 and 800 ps in Fig. 4.30b, d, f. We observe a similar response in the probed spectral range, with the bleach of the exciton band emerging around 3.88 eV.

Figure 4.31a compares the transient spectra at 1 ps at the three different fluences. The response can be described by assuming a simple broadening of the exciton lineshape due to the screening produced by the free electrons injected in the anatase TiO_2 NPs. The signal scales linearly in the explored fluence regime and no relevant differences are evidenced after the normalization of the spectra with respect to the minimum (Fig. 4.31b). Only the broadening becomes more pronounced when the pump fluence is increased. The linearity of the signal allows us to exclude the occurrence of multiphoton absorption from the anatase TiO_2 NPs. Furthermore, we also investigate the response of a colloidal solution of bare anatase TiO_2 NPs when the pump photon energy is tuned to 2.25 eV or 3.10 eV, i.e. below the absorption threshold of the system. No sizeable signal is observed even by increasing the pump fluence up to the value of 34 mJ/cm^2, which is much larger than the fluence used in the experiments on dye-sensitized anatase TiO_2 NPs. We remark that a similar conclusion was drawn from a previous ps x-ray absorption spectroscopy experiment on the same sample of anatase TiO_2 NPs where even in the presence of delivered pump fluences exceeding 150 mJ/cm^2 at 2.25 eV, no sizeable x-ray absorption signal from anatase TiO_2 NPs could be detected [115]. Thus, we can conclude that in

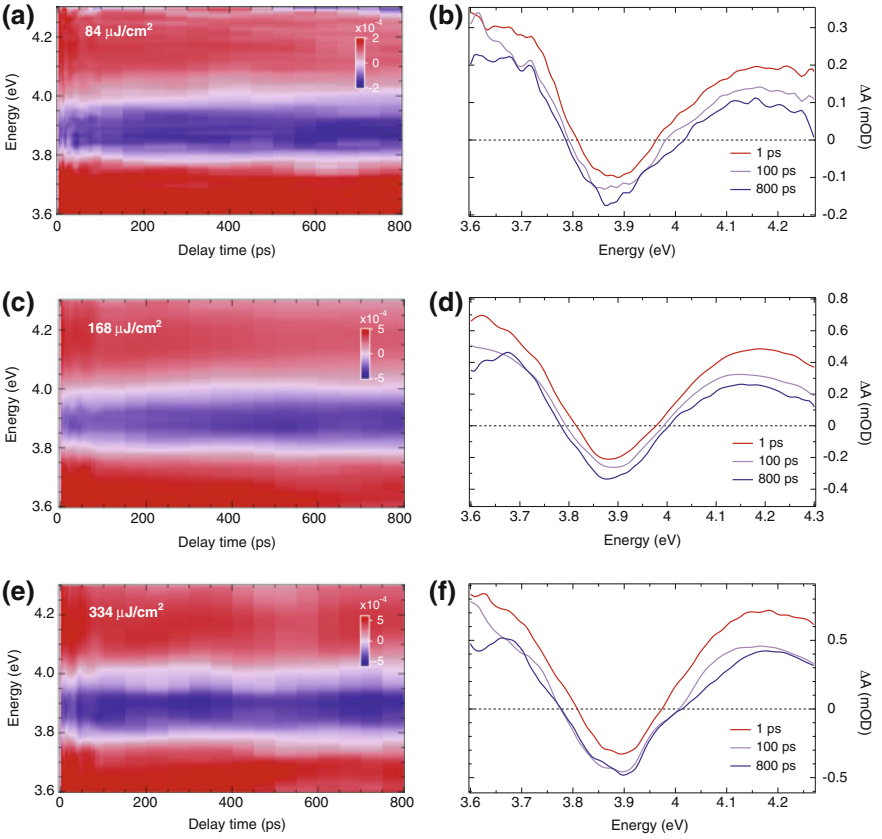

Fig. 4.30 **a**, **c**, **b** Colour-coded maps of ΔA of dye-sensitized TiO_2 NPs, as a function of probe photon energy and time delay between pump and probe, for different pump fluences. **b**, **d**, **f** Correspondent ΔA spectra at selected time delays of 1 ps (red curves), 100 ps (violet curves) and 800 ps (blue curves)

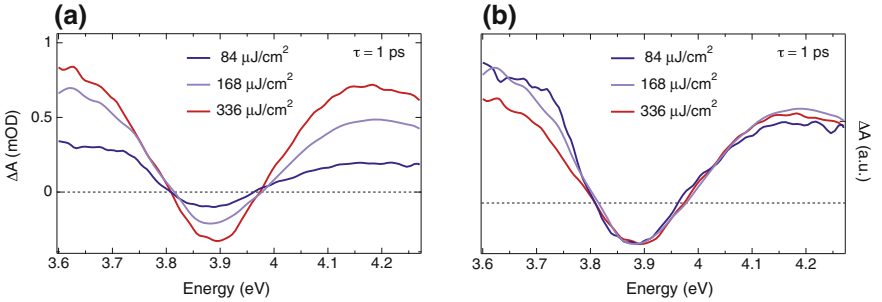

Fig. 4.31 Comparison among the ΔA spectra of the dye-sensitized TiO_2 NPs at the time delay of 1 ps and for different pump fluences at 2.25 eV (indicated in the labels). **a** As measured spectra. **b** Normalized spectra

the dye-sensitized TiO_2 NPs, defect-assisted transitions are not sufficient to induce a detectable bleach of the excitonic transition and multiphoton absorption can be safely excluded.

By comparing the transient spectra at 1 ps (rescaled for clarity) obtained from the three separate experiments in Fig. 4.32, we confirm the almost analogous spectral response of bare and sensitized anatase NPs, except for a vertical shift and the above-mentioned orders of magnitude difference in signal amplitude. In constrast, no common features are shared with the spectral response of the N719 dye under identical excitation conditions. This clearly points to charge injection from the dye into the anatase TiO_2 NPs, leading to the bleach of the excitonic feature.

The occurrence of charge injection is further confirmed by Fig. 4.33a, which shows the time evolution of the signals at 3.88 eV for both bare and dye-sensitized NPs. The exciton signal of the bare NPs appears promptly near t=0 and then decays on the ns time scale, due to recombination dynamics of uncorrelated e^- - h^+ pairs across the bandgap of the material. Fits with four exponential functions provide time constants of $\tau_{NP2} = 1.6 \pm 0.12$ ps, $\tau_{NP3} = 10 \pm 1.4$ ps, $\tau_{NP4} = 50 \pm 1.7$ ps and $\tau_{NP5} = 423 \pm 15$ ps. Because anatase TiO_2 is an indirect bandgap insulator, the recombination proceeds slowly and can be accelerated only through the assistance of defect and impurity states.

In the case of dye-sensitized NPs, the signal (Fig. 4.33b) in the central (negative) part of the spectrum also appears promptly, which indicates the presence of a dominating sub-picosecond component in the charge injection from the external dye. Thereafter, the response undergoes a further growth. The kinetic traces of the positive and negative regions of the transient spectra can be globally fit using the same set of time constants: a resolution-limited rise, $\tau_{D1} \sim 150$ fs, and decay/rise (positive/negative parts, respectively) components, $\tau_{D2} = 22$ ps and $\tau_{D3} = 1.1$ ns. This suggests a common origin for the growth and decays of the various parts of the signal.

From the above discussion and the results obtained in Sect. 4.5.3, it emerges that the spectral response of the anatase TiO_2 NPs upon electron delivery to the CB (via bandgap excitation or injection) can be understood as the combination of two

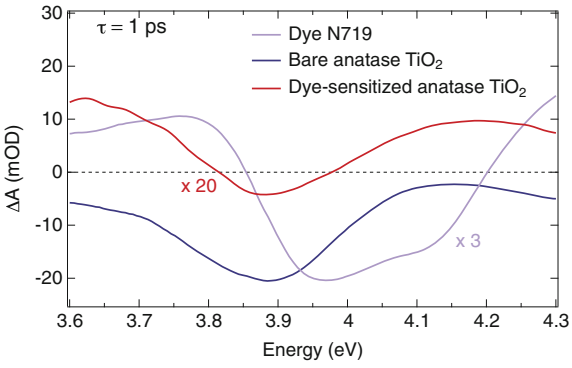

Fig. 4.32 Comparison of the ΔA spectra measured in the three separate experiments at a time delay of 1 ps. The transient spectrum of the dye N719 is shown in violet, the one of the bare anatase TiO_2 in blue, and the one of the dye-sensitized anatase TiO_2 in red

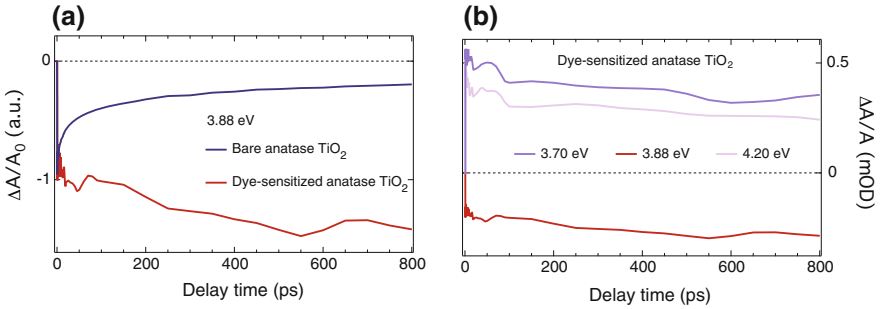

Fig. 4.33 **a** Comparison between the temporal traces of the bare (blue curve) and dye-sensitized (red curve) anatase TiO_2, cut at the probe photon energy of 3.88 eV. **b** Time traces of the dye-sensitized anatase TiO_2, cut at the probe photon energy of 3.70 eV (purple curve), 3.88 eV (red curve) and 4.20 eV (violet curve)

effects: Phase-space filling and long-range Coulomb screening. In the case of above bandgap excitation of bare anatase TiO_2, the density of e^- in the CB is high enough to fill the single-particle states involved in the exciton collective charge excitations, and the signal is dominated by phase-space filling. This overwhelms any positive signal associated with the exciton broadening and results in a negative signal over the entire spectral range (Fig. 4.29c–d). In contrast, upon injection, the phase-space filling contribution becomes extremely weak, as the e^- density transferred from the dye into the CB is two orders of magnitude less than in the case of bandgap excitation. In addition, the e^- density is expected to be located just at the bottom of the CB at Γ, whose states are predicted not to participate to the exciton transition from symmetry arguments [8]. In these conditions, the positive contribution due to the broadening of the exciton linewidth arises clearly and the sign of the resulting signal reflects solely the presence of long-range Coulomb screening. The signal of the dye-sensitized anatase TiO_2 NPs is not affected by the spectral features associated with the dye alone (Fig. 4.29a–b). The lack of an LC bleach can be explained by the fact that the LC transition is not sensitive to a change of the Ru oxidation state [171], so that the LC band of the cation and the bleached one cancel each other after interfacial ET has occurred. In addition, the dye coverage of the NPs is such that their concentration is very low and their signal would hardly be detected. The two ES absorption features have instead disappeared because the excited molecule becomes a cation after injection. Previous visible, [150, 154, 172, 173] and THz [156] TA studies on N719- or N3-sensitized TiO_2 reported a bimodal electron injection: A prompt one at very short times (<10 fs) from the initially accessed Franck-Condon ^{1}MLCT state, followed by injection from the rapidly populated [146] long-lived ^{3}MLCT state, over tens to hundreds of picoseconds. The behaviour we observe in Fig. 4.33 for the dye-sensitized NPs reflects precisely this bimodal injection regime.

The above results unambiguously demonstrate the deep-UV probing of interfacial ET from the N719 dye to the anatase TiO_2 NPs. Although this aspect is of major interest for the field of applications, we point out the relevance of these results for

the comprehension of charge dynamics in dye-sensitized anatase TiO_2. Indeed, as shown in Sect. 4.4, the strongly bound exciton retains a highly localized nature, extending two-dimensionally over five unit cells on the (001) plane of the crystal. The small size of the exciton (compared to Wannier-Mott excitons) implies that the electronic structure of the anatase TiO_2 NPs typically used for applications (with a diameter between 10 and 30 nm) can be safely described by the bulk electronic structure of single crystals. As discussed in Sect. 4.4, the exciton state at 3.88 eV arises from a manifold of direct interband transitions along the Γ-Z points of the BZ, in which the CB and VB dispersions are almost parallel (Fig. 4.34). Hence, the injected electron density at the bottom of the CB is sufficient to block the final states involved in the excitonic transition. This is again consistent with a phase-space filling mechanism at play [61], which gives rise to the exciton bleaching as presented in Sect. 4.5.3. This phenomenon causes a reduction of the exciton oscillator strength by reducing the number of single-particle states contributing to the bound state. A pictorial representation of the deep-UV based detection of the ultrafast ET dynamics in sensitized TiO_2 NPs is provided in Fig. 4.34. Our measurement also suggests that long-range Coulomb screening is acting simultaneously to bleaching the excitonic species, as most single-particle states contributing to the exciton are situated along the Γ-Z points of the BZ, i.e. far from the bottom of the CB. Long-range Coulomb screening causes a broadening of the exciton linewidth, as shown by the dependence of the exciton linewidth with pump fluence.

In conclusion, we establish an elegant methodology for probing interfacial charge dynamics in sensitized transition metal oxides by exploiting the spectroscopic feature of a collective charge excitation. This approach is ideal in the case of solid-state sen-

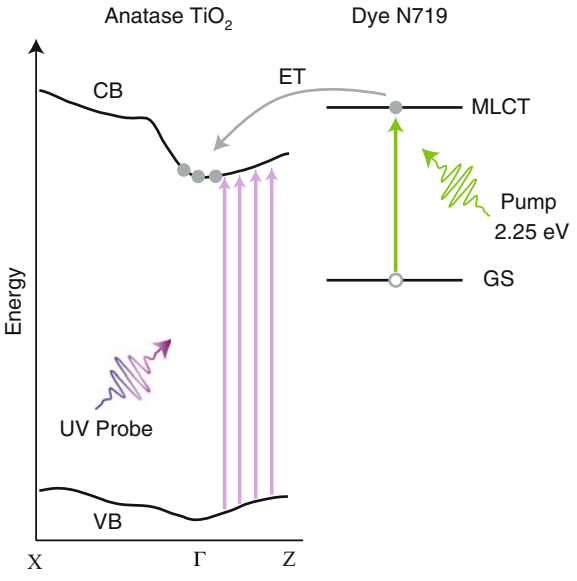

Fig. 4.34 Schematic representation of the deep-UV based detection of the ultrafast ET dynamics in sensitized TiO_2 NPs. The pump photon at 2.25 eV (green arrow) excites the MLCT state of the N719 dye, which then injects an electron into the CB of anatase TiO_2. The broadband UV pulse (violet arrows) probes the bleach of the exciton I band at 3.88 eV. The direct transitions contributing to this exciton state lie along the Γ-Z region of the BZ. The band structure of anatase TiO_2 has been taken from our ab initio calculations

sitizers, such as hybrid organic-inorganic perovskites or gold NPs, as the absorption of the CB electrons is expected to be weak in the deep-UV. It can also be extended to other transition metal oxides, e.g. ZnO, which is well known to display a strongly bound exciton state around 3.31 eV at RTg [2].

4.7 Conclusions

In this Chapter, the use of advanced steady-state spectroscopies, along with state-of-the-art theoretical calculations, allowed us to demonstrate that the direct optical gap of anatase TiO_2 is dominated by a strongly bound exciton rising over the continuum of indirect interband transitions. Remarkably, this exciton possesses an intermediate nature between Wannier-Mott and Frenkel regimes and displays a unique 2D character in the 3D lattice.

These findings also apply to the defect-rich samples (e.g. NPs) used in light-energy conversion applications, which lack a clear fingerprint of the exciton feature under equilibrium conditions. Only the powerful tool of ultrafast broadband optical spectroscopy, performed in the unexplored deep-UV spectral range, paves the route to the identification of the excitonic collective excitations in these samples. The importance of this observation is twofold: (i) to reveal a prototypical high-energy spectroscopic feature whose renormalization provides insights into the low-energy single-particle and many-body processes occurring in the material; (ii) to make use of the excitonic feature as a sensitive observable that reacts to external stimuli. In our nonequilibrium investigation, we address both aspects, first unraveling how the excitonic feature is affected by the carrier dynamics and the emergence of coherent lattice modes, and finally using such exciton as a sensitive probe of the ultrafast ET from an external dye into the anatase TiO_2 NPs.

In conclusion, all these elements concur to provide a novel and complete description of the equilibrium and nonequilibrium electrodynamics of this widely studied material. Besides the fundamental impact on the field of condensed matter physics with the discovery of these exotic collective excitation, our study can have relevant consequences for the comprehension of the photocatalytic activity of anatase TiO_2. To this purpose, in the future it will crucial to investigate how molecules adsorbed to specific TiO_2 surfaces react to tailored charge excitations (excitons versus uncorrelated particle-hole pairs) generated by tunable incident light. From the point of view of devices, the newly discovered bound excitons may also provide a significant source of optical nonlinearity, opening the doors to the development of electro-optical or all-optical switches in the UV. In this regard, high optical nonlinearities have already been demonstrated in TiO_2 for off-resonant excitation [174, 175], leading to efficient third-harmonic generation [176]. Also engineered nanostructures exposing a large percentage of (001) facets can be useful in guiding the energy at the nanoscale in a selective way [177–179]. Finally, due to the important contribution that phonons play in the exciton linewidth and lineshape, we expect that the optical properties of anatase TiO_2 can be effectively altered by tuning the exciton-phonon coupling,

e.g. through the applications of mechanical strain or via dielectric screening. In this regard, new insights from many-body theory will be crucial for evaluating the transport of these excitonic species, their coupling to the vibrational degrees of freedom and their reaction to various external stimuli.

References

1. R. Schuster, M. Knupfer, H. Berger, Exciton band structure of pentacene molecular solids: breakdown of the Frenkel exciton model. Phys. Rev. Lett. **98**(3), 037402 (2007)
2. P. Zu, Z.K. Tang, G.K. Wong, M. Kawasaki, A. Ohtomo, H. Koinuma, Y. Segawa, Ultraviolet spontaneous and stimulated emissions from ZnO microcrystallite thin films at room temperature. Solid State Commun. **103**(8), 459–463 (1997)
3. M.L. Tiago, J.E. Northrup, S.G. Louie, Ab initio calculation of the electronic and optical properties of solid pentacene. Phys. Rev. B **67**(11), 115212 (2003)
4. D.Y. Qiu, H. Felipe, S.G. Louie, Optical spectrum of MoS_2: many-body effects and diversity of exciton states. Phys. Rev. Lett. **111**(21), 216805 (2013)
5. L.I. Bendavid, E.A. Carter, Status in calculating electronic excited states in transition metal oxides from first principles, in *First Principles Approaches to Spectroscopic Properties of Complex Materials* (Springer, 2014), pp. 47–98
6. K. He, N. Kumar, L. Zhao, Z. Wang, K.F. Mak, H. Zhao, J. Shan, Tightly bound excitons in monolayer WSe_2. Phys. Rev. Lett. **113**(2), 026803 (2014)
7. M.M. Ugeda, A.J. Bradley, S. Shi, H. Felipe, Y. Zhang, Diana Y. Qiu, W. Ruan, S. Mo, Z. Hussain and Z. Shen, Z. Shen., Giant bandgap renormalization and excitonic effects in a monolayer transition metal dichalcogenide semiconductor. Nat. Mater. **13**(12), 1091–1095 (2014)
8. L. Chiodo, J.M. García-Lastra, A. Iacomino, S. Ossicini, J. Zhao, H. Petek, A. Rubio, Self-energy and excitonic effects in the electronic and optical properties of TiO_2 crystalline phases. Phys. Rev. B **82**(4), 045207 (2010)
9. W. Kang, M.S. Hybertsen, Quasiparticle and optical properties of rutile and anatase TiO_2. Phys. Rev. B **82**(8), 085203 (2010)
10. A. Fujishima, K. Honda, Electrochemical photolysis of water at a semiconductor electrode. Nature **238**, 37–38 (1972)
11. B.O. Reagen, M. Grätzel, A low-cost, high-efficiency solar cell based on dye-sensitized colloidal TiO_2 films. Nature **353**(6346), 737 (1991)
12. E. Pelizzetti, C. Minero, Mechanism of the photo-oxidative degradation of organic pollutants over TiO_2 particles. Electrochimica Acta **38**(1), 47–55 (1993)
13. N.A. Deskins, M. Dupuis, Electron transport via polaron hopping in bulk TiO_2: a density functional theory characterization. Phys. Rev. B **75**(19), 195212 (2007)
14. C. Di Valentin, A. Selloni, Bulk and surface polarons in photoexcited anatase TiO_2. J. Phys. Chem. Lett. **2**(17), 2223–2228 (2011)
15. J. Jaćimović, C. Vaju, A. Magrez, H. Berger, L. Forró, R. Gaal, V. Cerovski, R. Žikić, Pressure dependence of the large-polaron transport in anatase TiO_2 single crystals. EPL Europhys. Lett. **99**(5), 57005 (2012)
16. S. Moser, L. Moreschini, J. Jaćimović, O.S. Barišić, H. Berger, A. Magrez, Y.J. Chang, K.S. Kim, A. Bostwick, E. Rotenberg, Tunable polaronic conduction in anatase TiO_2. Phys. Rev. Lett. **110**(19), 196403 (2013)
17. M. Setvin, C. Franchini, X. Hao, M. Schmid, A. Janotti, M. Kaltak, C.G. van de Walle, G. Kresse, U. Diebold, Direct view at excess electrons in TiO_2 rutile and anatase. Phys. Rev. Lett. **113**(8), 086402 (2014)
18. H. Tang, F. Levy, H. Berger, P.E. Schmid, Urbach tail of anatase TiO_2. Phys. Rev. B **52**(11), 7771 (1995)

19. H. Tang, H. Berger, P.E. Schmid, F. Levy, G. Burri, Photoluminescence in TiO_2 anatase single crystals. Solid State Commun. **87**(9), 847–850 (1993)
20. Y. Toyozawa. *Optical Processes in Solids* (Cambridge University Press, 2003)
21. T. Miyata, Line shape analysis of the Γ-exciton spectra of NaCl, NaBr and NaI single crystals. J. Phys. Soc. Jpn. **31**(2), 529–551 (1971)
22. G. Baldini, A. Bosacchi, B. Bosacchi, Exciton-phonon interaction in alkali halides. Phys. Rev. Lett. **23**(15), 846 (1969)
23. M. Kamada, M. Yoshikawa, R. Kato, Phonon side bands of UV absorption in $NaNO_2$. J. Phys. Soc. Jpn. **39**(4), 1004–1012 (1975)
24. M. Emori, M. Sugita, K. Ozawa, H. Sakama, Electronic structure of epitaxial anatase TiO_2 films: angle-resolved photoelectron spectroscopy study. Phys. Rev. B **85**(3), 035129 (2012)
25. N. Hosaka, T. Sekiya, C. Satoko, S. Kurita, Optical properties of single-crystal anatase TiO_2. J. Phys. Soc. Jpn. **66**(3), 877–880 (1997)
26. T. Sekiya, M. Igarashi, S. Kurita, S. Takekawa, M. Fujisawa, Structure dependence of reflection spectra of TiO_2 single crystals. J. Electron Spectrosc. Relat. Phenom. **92**(1), 247–250 (1998)
27. H.M. Lawler, J.J. Rehr, F. Vila, S.D. Dalosto, E.L. Shirley, Z.H. Levine, Optical to UV spectra and birefringence of SiO_2 and TiO_2: first-principles calculations with excitonic effects. Phys. Rev. B **78**(20), 205108 (2008)
28. M. Landmann, E. Rauls, W.G. Schmidt, The electronic structure and optical response of rutile, anatase and brookite TiO_2. J. Phys. Condens. Matter **24**(19), 195503 (2012)
29. J.F. Muth, J.H. Lee, I.K. Shmagin, R.M. Kolbas, H.C. Casey Jr., B.P. Keller, U.K. Mishra, S.P. DenBaars, Absorption coefficient, energy gap, exciton binding energy, and recombination lifetime of GaN obtained from transmission measurements. Appl. Phys. Lett. **71**(18), 2572–2574 (1997)
30. D.D. Sell, Resolved free-exciton transitions in the optical-absorption spectrum of GaAs. Phys. Rev. B **6**(10), 3750 (1972)
31. R. Rinaldi, R. Cingolani, M. Lepore, M. Ferrara, I.M. Catalano, F. Rossi, L. Rota, E. Molinari, P. Lugli, U. Marti, Exciton binding energy in GaAs V-shaped quantum wires. Phys. Rev. Lett. **73**(21), 2899 (1994)
32. J.C. Maan, G. Belle, A. Fasolino, M. Altarelli, K. Ploog, Magneto-optical determination of exciton binding energy in GaAs-$Ga_{1-x}Al_xAs$ quantum wells. Phys. Rev. B **30**(4), 2253 (1984)
33. R.J. Elliott, Intensity of optical absorption by excitons. Phys. Rev. **108**(6), 1384 (1957)
34. L. Hedin, New method for calculating the one-particle Green's function with application to the electron-gas problem. Phys. Rev. **139**(3A), A796 (1965)
35. A.G. Thomas, W.R. Flavell, A.K. Mallick, A.R. Kumarasinghe, D. Tsoutsou, N. Khan, C. Chatwin, S. Rayner, G.C. Smith, R.L. Stockbauer, Comparison of the electronic structure of anatase and rutile TiO_2 single-crystal surfaces using resonant photoemission and x-ray absorption spectroscopy. Phys. Rev. B **75**(3), 035105 (2007)
36. P. Zhang, P. Richard, T. Qian, Y.-M. Xu, X. Dai, H. Ding, A precise method for visualizing dispersive features in image plots. Rev. Sci. Instrum. **82**(4), 043712 (2011)
37. Y.P. Varshni, Temperature dependence of the energy gap in semiconductors. Physica **34**(1), 149–154 (1967)
38. C. Keffer, T.M. Hayes, A. Bienenstock, PbTe Debye-Waller factors and band-gap temperature dependence. Phys. Rev. Lett. **21**(25), 1676 (1968)
39. P.W. Yu, W.J. Anderson, Y.S. Park, Anomalous temperature dependence of the energy gap of $AgGaS_2$. Solid State Commun. **13**(11), 1883–1887 (1973)
40. M. Rössle, C.N. Wang, P. Marsik, M. Yazdi-Rizi, K.W. Kim, A. Dubroka, I. Marozau, C.W. Schneider, J. Humlíček, D. Baeriswyl, Optical probe of ferroelectric order in bulk and thin-film perovskite titanates. Phys. Rev. B **88**(10), 104110 (2013)
41. M. Cardona. Renormalization of the optical response of semiconductors by electron-phonon interaction. Cond-Mat0108160 (2001) https://doi.org/10.1002/1521-396X(200112)188:4%3C1209::AID-PSSA1209%3E3.0.CO;2-2/full (ArXiv Prepr.)
42. K.K. Rao, S.N. Naidu, L. Iyengar, Thermal expansion of rutile and anatase. J. Am. Ceram. Soc. **53**(3), 124–126 (1970)

43. J.K. Burdett, T. Hughbanks, G.J. Miller, J.W. Richardson Jr, J.V. Smith, Structural-electronic relationships in inorganic solids: powder neutron diffraction studies of the rutile and anatase polymorphs of titanium dioxide at 15 and 295 K. J. Am. Chem. Soc. **109**(12), 3639–3646 (1987)
44. D.C. Reynolds, D.C. Look, B. Jogai, B. Jogai, Combined effects of screening and band gap renormalization on the energy of optical transitions in ZnO and GaN. J. Appl. Phys. **88**(10), 5760 (2000)
45. W. Wegscheider, L.N. Pfeiffer, M.M. Dignam, A. Pinczuk, K.W. West, S.L. McCall, R. Hull, Lasing from excitons in quantum wires. Phys. Rev. Lett. **71**(24), 4071 (1993)
46. R. Ambigapathy, I. Bar-Joseph, D.Y. Oberli, S. Haacke, M.J. Brasil, F. Reinhardt, E. Kapon, B. Deveaud, Coulomb correlation and band gap renormalization at high carrier densities in quantum wires. Phys. Rev. Lett. **78**(18), 3579 (1997)
47. S.D. Sarma, D.W. Wang, Many-body renormalization of semiconductor quantum wire excitons: absorption, gain, binding, and unbinding. Phys. Rev. Lett. **84**(9), 2010 (2000)
48. B. Monserrat, Correlation effects on electron-phonon coupling in semiconductors: many-body theory along thermal lines. Phys. Rev. B **93**(10), 100301 (2016)
49. R.J. Gonzalez, R. Zallen, H. Berger, Infrared reflectivity and lattice fundamentals in anatase TiO_2. Phys. Rev. B **55**(11), 7014 (1997)
50. R. Shepard, Dielectric constants and polarizabilities of ions in simple crystals and barium titanate. Phys. Rev. **76**(8), 1215 (1949)
51. H. Tang, K. Prasad, R. Sanjines, P.E. Schmid, F. Levy, Electrical and optical properties of TiO_2 anatase thin films. J. App. Phys. **75**(4), 2042–2047 (1994)
52. J. Pascual, J. Camassel, H. Mathieu, Fine structure in the intrinsic absorption edge of TiO_2. Phys. Rev. B **18**(10), 5606 (1978)
53. A. Amtout, R. Leonelli, Optical properties of rutile near its fundamental band gap. Phys. Rev. B **51**(11), 6842 (1995)
54. A.R. Benrekia, N. Benkhettou, A. Nassour, M. Driz, M. Sahnoun, S. Lebègue, Structural, electronic and optical properties of cubic $SrTiO_3$ and $KTaO_3$: ab initio and GW calculations. Phys. B: Cond. Matter **407**(13), 2632–2636 (2012)
55. L. Sponza, V. Véniard, F. Sottile, C. Giorgetti, L. Reining, Role of localized electrons in electron-hole interaction: the case of $SrTiO_3$. Phys. Rev. B **87**(23), 235102 (2013)
56. P.K. Gogoi, L. Sponza, D. Schmidt, T.C. Asmara, C. Diao, J.C.W. Lim, S.M. Poh, S.-I. Kimura, P.E. Trevisanutto, V. Olevano, A. Rusydi, Anomalous excitons and screenings unveiling strong electronic correlations in $SrTi_{1-x}Nb_xO_3$ ($0 \leq x \leq 0.005$). Phys. Rev. B **92**(3), 035119 (2015)
57. S. Schmitt-Rink, D.S. Chemla, D.A.B. Miller, Linear and nonlinear optical properties of semiconductor quantum wells. Adv. Phys. **38**(2), 89–188 (1989)
58. S. Galambosi, L. Wirtz, J.A. Soininen, J. Serrano, A. Marini, K. Watanabe, T. Taniguchi, S. Huotari, A. Rubio, K. Hämäläinen, Anisotropic excitonic effects in the energy loss function of hexagonal boron nitride. Phys. Rev. B **83**(8), 081413 (2011)
59. N. Serpone, D. Lawless, R. Khairutdinov, Size effects on the photophysical properties of colloidal anatase TiO_2 particles: size quantization versus direct transitions in this indirect semiconductor? J. Phys. Chem. **99**(45), 16646–16654 (1995)
60. S. Monticone, R. Tufeu, A.V. Kanaev, E. Scolan, C. Sanchez, Quantum size effect in TiO_2 nanoparticles: does it exist? Appl. Surf. Sci. **162**, 565–570 (2000)
61. H. Haug, S. Schmitt-Rink, Basic mechanisms of the optical nonlinearities of semiconductors near the band edge. JOSA B **2**(7), 1135–1142 (1985)
62. V.P. Zhukov, E.V. Chulkov, Ab initio calculations of the electron-phonon interaction and characteristics of large polarons in rutile and anatase. Phys. Solid State **56**(7), 1302–1309 (2014)
63. E. Baldini, T. Palmieri, E. Pomarico, G. Auböck, M. Chergui. Clocking the ultrafast electron cooling in anatase titanium dioxide nanoparticles. ACS Photonics (2018) https://doi.org/10.1021/acsphotonics.7b00945
64. D.P. Colombo, K.A. Roussel, J. Saeh, D.E. Skinner, J.J. Cavaleri, R.M. Bowman, Femtosecond study of the intensity dependence of electron-hole dynamics in TiO_2 nanoclusters. Chem. Phys. Lett. **232**(3), 207–214 (1995)

65. A. Furube, T. Asahi, H. Masuhara, H. Yamashita, M. Anpo, Charge carrier dynamics of standard TiO_2 catalysts revealed by femtosecond diffuse reflectance spectroscopy. J. Phys. Chem. B **103**(16), 3120–3127 (1999)
66. X. Yang, N. Tamai, How fast is interfacial hole transfer? In situ monitoring of carrier dynamics in anatase TiO_2 nanoparticles by femtosecond laser spectroscopy. Phys. Chem. Chem. Phys. **3**(16), 3393–3398 (2001)
67. Y. Tamaki, A. Furube, R. Katoh, M. Murai, K. Hara, H. Arakawa, M. Tachiya, Trapping dynamics of electrons and holes in a nanocrystalline TiO_2 film revealed by femtosecond visible/near-infrared transient absorption spectroscopy. C. R. Chim. **9**(2), 268–274 (2006)
68. Y. Tamaki, K. Hara, R. Katoh, M. Tachiya, A. Furube, Femtosecond visible-to-IR spectroscopy of TiO_2 nanocrystalline films: elucidation of the electron mobility before deep trapping. J. Phys. Chem. C **113**(27), 11741–11746 (2009)
69. Y. Yamada, Y. Kanemitsu, Determination of electron and hole lifetimes of rutile and anatase TiO_2 single crystals. Appl. Phys. Lett. **101**(13), 133907 (2012)
70. H. Matsuzaki, Y. Matsui, R. Uchida, H. Yada, T. Terashige, B.-S. Li, A. Sawa, M. Kawasaki, Y. Tokura, H. Okamoto, Photocarrier dynamics in anatase TiO_2 investigated by pump-probe absorption spectroscopy. Jpn. J. Appl. Phys. **115**(5), 053514 (2014)
71. F. Nunzi, F. De Angelis, A. Selloni, Ab initio simulation of the absorption spectra of photoexcited carriers in TiO_2 nanoparticles. J. Phys. Chem. Lett. **7**(18), 3597–3602 (2016)
72. P. Zawadzki, Absorption spectra of trapped holes in anatase TiO_2. J. Phys. Chem. C **117**(17), 8647–8651 (2013)
73. M. Watanabe, S. Sasaki, T. Hayashi, Time-resolved study of photoluminescence in anatase TiO_2. J. Lumin. **87**, 1234–1236 (2000)
74. M. Watanabe, T. Hayashi, Time-resolved study of self-trapped exciton luminescence in anatase TiO_2 under two-photon excitation. J. Lumin. **112**(1), 88–91 (2005)
75. K. Wakabayashi, Y. Yamaguchi, T. Sekiya, S. Kurita, Time-resolved luminescence spectra in colorless anatase TiO_2 single crystal. J. Lumin. **112**(1), 50–53 (2005)
76. N. Harada, M. Goto, K. Iijima, H. Sakama, N. Ichikawa, H. Kunugita, K. Ema, Time-resolved luminescence of TiO_2 powders with different crystal structures. Jpn. J. Appl. Phys. **46**(7R), 4170 (2007)
77. L. Cavigli, F. Bogani, A. Vinattieri, V. Faso, G. Baldi, Volume versus surface-mediated recombination in anatase TiO_2 nanoparticles. J. Appl. Phys. **106**(5), 053516 (2009)
78. L. Cavigli, F. Bogani, A. Vinattieri, L. Cortese, M. Colocci, V. Faso, G. Baldi, Carrier recombination dynamics in anatase TiO_2 nanoparticles. Solid State Sci. **12**(11), 1877–1880 (2010)
79. G. Fuchs, C. Schiedel, A. Hangleiter, V. Härle, F. Scholz, Auger recombination in strained and unstrained InGaAs/InGaAsP multiple quantum-well lasers. Appl. Phys. Lett. **62**(4), 396–398 (1993)
80. V.I. Klimov, A.A. Mikhailovsky, D.W. McBranch, C.A. Leatherdale, M.G. Bawendi, Quantization of multiparticle Auger rates in semiconductor quantum dots. Science **287**(5455), 1011–1013 (2000)
81. F. Wang, Y. Wu, M.S. Hybertsen, T.F. Heinz, Auger recombination of excitons in one-dimensional systems. Phys. Rev. B **73**(24), 245424 (2006)
82. D. Sun, Y. Rao, G.A. Reider, G. Chen, Y. You, L. Brézin, A.R. Harutyunyan, T.F. Heinz, Observation of rapid exciton-exciton annihilation in monolayer molybdenum disulfide. Nano Lett. **14**(10), 5625–5629 (2014)
83. H. Schweizer, A. Forchel, A. Hangleiter, S. Schmitt-Rink, J.P. Löwenau, H. Haug, Ionization of the direct-gap exciton in photoexcited germanium. Phys. Rev. Lett. **51**, 698–701 (1983)
84. W.F. Zhang, M.S. Zhang, Z. Yin, Q. Chen, Photoluminescence in anatase titanium dioxide nanocrystals. Appl. Phys. B Lasers Opt. **70**(2), 261–265 (2000)
85. F.J. Knorr, C.C. Mercado, K.L. McHale, Trap-state distributions and carrier transport in pure and mixed-phase TiO_2: influence of contacting solvent and interphasial electron transfer. J. Phys. Chem. C **112**(33), 12786–12794 (2008)
86. C.C. Mercado, F.J. Knorr, J.L. McHale, S.M. Usmani, A.S. Ichimura, L.V. Saraf, Location of hole and electron traps on nanocrystalline anatase TiO_2. J. Phys. Chem. C **116**(19), 10796–10804 (2012)

87. P.T. Landsberg, *Recombination in Semiconductors* (Cambridge University Press, 2003)
88. E.M. Bothschafter, A. Paarmann, E.S. Zijlstra, N. Karpowicz, M.E. Garcia, R. Kienberger, R. Ernstorfer, Ultrafast evolution of the excited-state potential energy surface of TiO_2 single crystals induced by carrier cooling. Phys. Rev. Lett. **110**(6), 067402 (2013)
89. T. Hitosugi, H. Kamisaka, K. Yamashita, H. Nogawa, Y. Furubayashi, S. Nakao, N. Yamada, A. Chikamatsu, H. Kumigashira, M. Oshima, Electronic band structure of transparent conductor: Nb-doped anatase TiO_2. Appl. Phys. Exp. **1**(11), 111203 (2008)
90. Herbert Fröhlich, Hans Pelzer, S. Zienau, XX. Properties of slow electrons in polar materials. Lond. Edinb. Dublin Philos. Mag. J. Sci. **41**(314), 221–242 (1950)
91. E. Baldini, A. Dominguez, L. Chiodo, E. Sheveleva, M. Yazdi-Rizi, C. Bernhard, A. Rubio, M. Chergui, Anomalous anisotropic exciton temperature dependence in rutile TiO_2. Phys. Rev. B **96**, 041204 (2017)
92. J.T. Devreese, S.N. Klimin, J.L.M. van Mechelen, D. van der Marel, Many-body large polaron optical conductivity in $SrTi_{1-x}Nb_xO_3$. Phys. Rev. B **81**(12), 125119 (2010)
93. B.K. Ridley, *Quantum Processes in Semiconductors* (Oxford University Press, 2013)
94. M. Betz, G. Göger, A. Leitenstorfer, K. Ortner, C.R. Becker, G. Böhm, A. Laubereau, Ultrafast electron-phonon scattering in semiconductors studied by nondegenerate four-wave mixing. Phys. Rev. B **60**(16), R11265 (1999)
95. M. Betz, G. Göger, A. Laubereau, P. Gartner, L. Bányai, H. Haug, K. Ortner, C.R. Becker, A. Leitenstorfer, Subthreshold carrier-LO phonon dynamics in semiconductors with intermediate polaron coupling: a purely quantum kinetic relaxation channel. Phys. Rev. Lett. **86**(20), 4684 (2001)
96. U. Bockelmann, G. Bastard, Phonon scattering and energy relaxation in two-, one-, and zero-dimensional electron gases. Phys. Rev. B **42**(14), 8947 (1990)
97. E. Baldini, L. Chiodo, A. Dominguez, M. Palummo, S. Moser, M. Yazdi-Rizi, G. Auböck, B.P.P. Mallett, H. Berger, A. Magrez, C. Bernhard, M. Grioni, A. Rubio, M. Chergui. Strongly bound excitons in anatase TiO_2 single crystals and nanoparticles. Nat. Commun. **8** (2017)
98. Y.U. Peter, M. Cardona, *Fundamentals of Semiconductors: Physics and Materials Properties* (Springer Science & Business Media, 2010)
99. F. Giustino, Electron-phonon interactions from first principles. Rev. Mod. Phys. **89**, 015003 (2017)
100. P.B. Allen, M. Cardona, Theory of the temperature dependence of the direct gap of germanium. Phys. Rev. B **23**(4), 1495 (1981)
101. R. Merlin, Generating coherent THz phonons with light pulses. Solid State Commun. **102**(2), 207–220 (1997)
102. P. Ruello, V.E. Gusev, Physical mechanisms of coherent acoustic phonons generation by ultrafast laser action. Ultrasonics **56**, 21–35 (2015)
103. L. Brillouin, Diffusion de la lumiére et des rayons x par un corps transparent homogène. Influence de l'agitation termique. Ann. Phys. (Paris) **17**(88–122), 21 (1922)
104. C. Thomsen, H.T. Grahn, H.J. Maris, J. Tauc, Surface generation and detection of phonons by picosecond light pulses. Phys. Rev. B **34**(6), 4129 (1986)
105. J.H. Hodak, A. Henglein, G.V. Hartland, Photophysics of nanometer sized metal particles: electron-phonon coupling and coherent excitation of breathing vibrational modes. J. Phys. Chem. B **104**(43), 9954–9965 (2000)
106. N. Del Fatti, C. Voisin, M. Achermann, S. Tzortzakis, D. Christofilos, F. Vallée, Nonequilibrium electron dynamics in noble metals. Phys. Rev. B **61**(24), 16956 (2000)
107. T.D. Krauss, F.W. Wise, Coherent acoustic phonons in a semiconductor quantum dot. Phys. Rev. Lett. **79**(25), 5102 (1997)
108. P. Verma, W. Cordts, G. Irmer, J. Monecke, Acoustic vibrations of semiconductor nanocrystals in doped glasses. Phys. Rev. B **60**(8), 5778 (1999)
109. G.W. Chern, C.K. Sun, G.D. Sanders, C.J. Stanton, Generation of coherent acoustic phonons in nitride-based semiconductor nanostructures, in *Ultrafast Dynamical Processes in Semiconductors* (Springer, 2004), pp. 339–394

110. D. Rossi, L.E. Camacho-Forero, G. Ramos-Sánchez, J.H. Han, J. Cheon, P. Balbuena, D.H. Son, Anisotropic electron-phonon coupling in colloidal layered TiS_2 nanodiscs observed via coherent acoustic phonons. J. Phys. Chem. C **119**(13), 7436–7442 (2015)
111. H. Lamb, On the vibrations of an elastic sphere. Proc. Lond. Math. Soc. **1**(1), 189–212 (1881)
112. N. Nishiguchi, T. Sakuma, Vibrational spectrum and specific heat of fine particles. Solid State Commun. **38**(11), 1073–1077 (1981)
113. A. Tamura, K. Higeta, T. Ichinokawa, Lattice vibrations and specific heat of a small particle. J. Phys. C Solid State Phys. **15**(24), 4975 (1982)
114. M. Ivanda, K. Furić, S. Musić, M. Ristić, M. Gotić, D. Ristić, A.M. Tonejc, I. Djerdj, M. Mattarelli, M. Montagna et al., Low wavenumber Raman scattering of nanoparticles and nanocomposite materials. J. Raman. Spectrosc. **38**(6), 647–659 (2007)
115. M.H. Rittmann-Frank, C.J. Milne, J. Rittmann, M. Reinhard, T.J. Penfold, M. Chergui, Mapping of the photoinduced electron traps in TiO_2 by picosecond x-ray absorption spectroscopy. Angew. Chem. Int. Ed. **53**(23), 5858–5862 (2014)
116. C. Thomsen, J. Strait, Z. Vardeny, H.J. Maris, J. Tauc, J.J. Hauser, Coherent phonon generation and detection by picosecond light pulses. Phys. Rev. Lett. **53**(10), 989 (1984)
117. O. Matsuda, O.B. Wright, D.H. Hurley, V.E. Gusev, K. Shimizu, Coherent shear phonon generation and detection with ultrashort optical pulses. Phys. Rev. Lett. **93**(9), 095501 (2004)
118. Y.-C. Wen, T.-S. Ko, T.-H. Lu, H.-C. Kuo, J.-I. Chyi, C.-K. Sun, Photogeneration of coherent shear phonons in orientated wurtzite semiconductors by piezoelectric coupling. Phys. Rev. B **80**(19), 195201 (2009)
119. Y.-X. Yan, E.B. Gamble Jr., K.A. Nelson, Impulsive stimulated scattering: general importance in femtosecond laser pulse interactions with matter, and spectroscopic applications. J. Chem. Phys. **83**(11), 5391–5399 (1985)
120. H. Tanaka, T. Sonehara, S. Takagi, A new phase-coherent light scattering method: first observation of complex Brillouin spectra. Phys. Rev. Lett. **79**, 881–884 (1997)
121. C.V. Korff Schmising, A. Harpoeth, N. Zhavoronkov, Z. Ansari, C. Aku-Leh, M. Woerner, T. Elsaesser, M. Bargheer, M. Schmidbauer, I. Vrejoiu et al., Ultrafast magnetostriction and phonon-mediated stress in a photoexcited ferromagnet. Phys. Rev. B **78**(6):060404 (2008)
122. W.-J. Yin, S. Chen, J.-H. Yang, X.-G. Gong, Y. Yan, S.-H. Wei, Effective band gap narrowing of anatase TiO_2 by strain along a soft crystal direction. Appl. Phys. Lett. **96**(22), 221901 (2010)
123. S.J. Smith, R. Stevens, S. Liu, G. Li, A. Navrotsky, J. Boerio-Goates, B.F. Woodfield, Heat capacities and thermodynamic functions of TiO_2 anatase and rutile: analysis of phase stability. Am. Miner. **94**(2–3), 236–243 (2009)
124. T.Y. Chen, C.H. Hsia, H.S. Son, D.H. Son, Ultrafast energy transfer and strong dynamic noncondon effect on ligand field transitions by coherent phonon in γ-Fe_2O_3 nanocrystals. J. Am. Chem. Soc. **129**(35), 10829–10836 (2007)
125. K. Ishii, S. Takeuchi, T. Tahara, Pronounced non-Condon effect as the origin of the quantum beat observed in the time-resolved absorption signal from excited-state cis-stilbene. J. Phys. Chem. A **112**(11), 2219–2227 (2008)
126. A. Hagfeldt, M. Grätzel, Molecular photovoltaics. Acc. Chem. Res. **33**(5), 269–277 (2000)
127. M. Grätzel, Molecular photovoltaics mimic photosynthesis. Eur. Biophys. J. Biophys. Lett. **40**, 37–37 (2011)
128. M.K. Nazeeruddin, E. Baranoff, M. Grätzel, Dye-sensitized solar cells: a brief overview. Sol. Energy **85**(6), 1172–1178 (2011)
129. K. Kalyanasundaram, S.M. Zakeeruddin, M. Grätzel, Photonic and optoelectronic devices based on mesoscopic thin films. Chim. Int. J. Chem. **65**(9), 738–742 (2011)
130. A.L. Linsebigler, G. Lu, J.T. Yates Jr., Photocatalysis on TiO_2 surfaces: principles, mechanisms, and selected results. Chem. Rev. **95**(3), 735–758 (1995)
131. A. Kojima, K. Teshima, Y. Shirai, T. Miyasaka, Organometal halide perovskites as visible-light sensitizers for photovoltaic cells. J. Am. Chem. Soc. **131**(17), 6050–6051 (2009)
132. K. Nakata, A. Fujishima, TiO_2 photocatalysis: design and applications. J. Photochem. Photobiol. C Photochem. Rev. **13**(3), 169–189 (2012)

133. M.M. Lee, J. Teuscher, T. Miyasaka, T.N. Murakami, H.J. Snaith, Efficient hybrid solar cells based on meso-superstructured organometal halide perovskites. Science **338**(6107), 643–647 (2012)
134. G. Hodes, Perovskite-based solar cells. Science **342**(6156), 317–318 (2013)
135. M. Liu, M.B. Johnston, H.J. Snaith, Efficient planar heterojunction perovskite solar cells by vapour deposition. Nature **501**(7467), 395–398 (2013)
136. A. Marchioro, J. Teuscher, D. Friedrich, M. Kunst, R. Van De Krol, T. Moehl, M. Grätzel, J.E. Moser, Unravelling the mechanism of photoinduced charge transfer processes in lead iodide perovskite solar cells. Nat. Photonics **8**(3), 250–255 (2014)
137. S.D. Stranks, G.E. Eperon, G. Grancini, C. Menelaou, M.J. Alcocer, T. Leijtens, L.M. Herz, A. Petrozza, H.J. Snaith, Electron-hole diffusion lengths exceeding 1 micrometer in an organometal trihalide perovskite absorber. Science **342**(6156), 341–344 (2013)
138. A. Furube, L. Du, K. Hara, R. Katoh, M. Tachiya, Ultrafast plasmon-induced electron transfer from gold nanodots into TiO_2 nanoparticles. J. Am. Chem. Soc. **129**(48), 14852–14853 (2007)
139. L. Du, A. Furube, K. Hara, R. Katoh, M. Tachiya. Mechanisms of plasmon-induced charge separation and recombination at gold nanoparticle supported on different size TiO_2 film systems, in *Photonics Asia 2007* (International Society for Optics and Photonics, 2007), pp. 68310W–68310W–10
140. J.M. Rehm, G.L. McLendon, Y. Nagasawa, K. Yoshihara, J. Moser, M. Grätzel, Femtosecond electron-transfer dynamics at a sensitizing dye-semiconductor (TiO_2) interface. J. Phys. Chem. **100**(23), 9577–9578 (1996)
141. F. Willig, R. Eichberger, N.S. Sundaresan, B.A. Parkinson, Experimental time scale of Gerischer's distribution curves for electron-transfer reactions at semiconductor electrodes. J. Am. Chem. Soc. **112**(7), 2702–2707 (1990)
142. Y. Rosenwaks, B.R. Thacker, R.K. Ahrenkiel, A.J. Nozik, Electron transfer dynamics at P-gallium arsenide/liquid interfaces. J. Phys. Chem. **96**(25), 10096–10098 (1992)
143. T.A. Heimer, G.J. Meyer, Luminescence of charge transfer sensitizers anchored to metal oxide nanoparticles. J. Lumin. **70**(1), 468–478 (1996)
144. O. Bräm, A. Cannizzo, M. Chergui, Ultrafast fluorescence studies of dye sensitized solar cells. Phys. Chem. Chem. Phys. **14**(22), 7934–7937 (2012)
145. R. Huber, S. Spörlein, J.E. Moser, M. Grätzel, J. Wachtveitl, The role of surface states in the ultrafast photoinduced electron transfer from sensitizing dye molecules to semiconductor colloids. J. Phys. Chem. B **104**(38), 8995–9003 (2000)
146. J. Kallioinen, G. Benkö, V. Sundström, J.E. Korppi-Tommola, A.P. Yartsev, Electron transfer from the singlet and triplet excited states of $Ru(dcbpy)_2(NCS)_2$ into nanocrystalline TiO_2 thin films. J. Phys. Chem. B **106**(17), 4396–4404 (2002)
147. G. Benkö, P. Myllyperkiö, J. Pan, A.P. Yartsev, V. Sundström, Photoinduced electron injection from $Ru(dcbpy)_2$ NCS_2 to SnO_2 and TiO_2 nanocrystalline films. J. Am. Chem. Soc. **125**(5), 1118–1119 (2003)
148. J. Kallioinen, G. Benkö, P. Myllyperkiö, L. Khriachtchev, B. Skårman, R. Wallenberg, M. Tuomikoski, J. Korppi-Tommola, V. Sundström, A.P. Yartsev, Photoinduced ultrafast dynamics of $Ru(dcbpy)_2(NCS)_2$-sensitized nanocrystalline TiO_2 films: the influence of sample preparation and experimental conditions. J. Phys. Chem. B **108**(20), 6365–6373 (2004)
149. R. Katoh, A. Furube, A.V. Barzykin, H. Arakawa, M. Tachiya, Kinetics and mechanism of electron injection and charge recombination in dye-sensitized nanocrystalline semiconductors. Coord. Chem. Rev. **248**(13), 1195–1213 (2004)
150. A. Furube, Y. Tamaki, M. Murai, K. Hara, R. Katoh, M. Tachiya, Femtosecond visible-to-IR spectroscopy of TiO_2 nanocrystalline films: dynamics of UV-generated charge carrier relaxation at different excitation wavelengths, in *NanoScience+ Engineering* (International Society for Optics and Photonics, 2007), pp. 66430J–66430J–9
151. M. Pellnor, P. Myllyperkiö, J. Korppi-Tommola, A. Yartsev, V. Sundström, Photoinduced interfacial electron injection in Run3–TiO_2 thin films: resolving picosecond timescale injection from the triplet state of the protonated and deprotonated dyes. Chem. Phys. Lett. **462**(4), 205–208 (2008)

152. L. Du, A. Furube, K. Hara, R. Katoh, M. Tachiya, Mechanism of particle size effect on electron injection efficiency in ruthenium dye-sensitized TiO_2 nanoparticle films. J. Phys. Chem. C **114**(18), 8135–8143 (2010)
153. J. Teuscher, J.D. Décoppet, A. Punzi, A.M. Zakeeruddin, J.E. Moser, M. Grätzel, Photoinduced interfacial electron injection dynamics in dye-sensitized solar cells under photovoltaic operating conditions. J. Phys. Chem. Lett. **3**(24), 3786–3790 (2012)
154. N.A. Anderson, T. Lian, Ultrafast electron injection from metal polypyridyl complexes to metal-oxide nanocrystalline thin films. Coord. Chem. Rev. **248**(13), 1231–1246 (2004)
155. H. Němec, P. Kužel, V. Sundström, Far-infrared response of free charge carriers localized in semiconductor nanoparticles. Phys. Rev. B **79**(11), 115309 (2009)
156. H. Němec, J. Rochford, O. Taratula, E. Galoppini, P. Kužel, T. Polívka, A. Yartsev, V. Sundström, Influence of the electron-cation interaction on electron mobility in dye-sensitized ZnO and TiO_2 nanocrystals: a study using ultrafast terahertz spectroscopy. Phys. Rev. Lett. **104**(19), 197401 (2010)
157. J.J.H. Pijpers, R. Ulbricht, S. Derossi, J.N.H. Reek, M. Bonn, Picosecond Electron injection dynamics in dye-sensitized oxides in the presence of electrolyte. J. Phys. Chem. C **115**(5), 2578–2584 (2011)
158. C.F. Negre, R.L. Milot, L.A. Martini, W. Ding, R.H. Crabtree, C.A. Schmuttenmaer, V.S. Batista, Efficiency of interfacial electron transfer from Zn-porphyrin dyes into TiO_2 correlated to the linker single molecule conductance. J. Phys. Chem. C **117**(46), 24462–24470 (2013)
159. Y. Wang, J.B. Asbury, T. Lian, Ultrafast excited-state dynamics of $Re(co)_3cl(dcbpy)$ in solution and on nanocrystalline TiO_2 and ZrO_2 thin films. J. Phys. Chem. A **104**(18), 4291–4299 (2000)
160. J.E. Katz, B. Gilbert, X. Zhang, K. Attenkofer, R.W. Falcone, G.A. Waychunas, Observation of transient iron (ii) formation in dye-sensitized iron oxide nanoparticles by time-resolved x-ray spectroscopy. J. Phys. Chem. Lett. **1**(9), 1372–1376 (2010)
161. J.E. Katz, X. Zhang, K. Attenkofer, K.W. Chapman, C. Frandsen, P. Zarzycki, K.M. Rosso, R.W. Falcone, G.A. Waychunas, B. Gilbert, Electron small polarons and their mobility in iron (oxyhydr) oxide nanoparticles. Science **337**(6099), 1200–1203 (2012)
162. M. Chergui, Time-resolved X-ray spectroscopies of chemical systems: new perspectives. Struct. Dyn. **3**(3), 031001 (2016)
163. F.G. Santomauro, A. Lübcke, J. Rittmann, E. Baldini, A. Ferrer, M. Silatani, P. Zimmermann, S. Grübel, J.A. Johnson, S.O. Mariager, Femtosecond x-ray absorption study of electron localization in photoexcited anatase TiO_2. Sci. Rep. **5** (2015)
164. L. Dworak, S. Roth, J. Wachtveitl, Charge transfer-induced state filling in CdSe quantum dot-alizarin complexes. J. Phys. Chem. C **121**(5), 2613–2619 (2017)
165. E. Baldini, T. Palmieri, T. Rossi, M. Oppermann, E. Pomarico, G. Auböck, M. Chergui, Interfacial electron injection probed by a substrate-specific excitonic signature. J. Am. Chem. Soc. **139**(33), 11584–11589 (2017)
166. M.K. Nazeeruddin, A. Kay, I. Rodicio, R. Humphry-Baker, E. Müller, P. Liska, N. Vlachopoulos, M. Grätzel, Conversion of light to electricity by Cis-X2bis (2, 2'-bipyridyl-4, 4'-dicarboxylate) ruthenium (II) charge-transfer sensitizers (X= Cl-, Br-, I-, CN-, and SCN-) on nanocrystalline titanium dioxide electrodes. J. Am. Chem. Soc. **115**(14), 6382–6390 (1993)
167. O. Bräm, F. Messina, A.M. El-Zohry, A. Cannizzo, M. Chergui, Polychromatic femtosecond fluorescence studies of metal–polypyridine complexes in solution. Chem. Phys. **393**(1), 51–57 (2012)
168. G. Auböck, M. Chergui, Sub-50-fs photoinduced spin crossover in [Fe(bpy)3]2+ apex. Nat. Chem. **7**(8), 1–5 (2015)
169. A. Namekawa, R. Katoh, Exciton annihilation in dye-sensitized nanocrystalline semiconductor films. Chem. Phys. Lett. **659**(C):154–158 (2016)
170. A.N. Tarnovsky, W. Gawelda, M. Johnson, C. Bressler, M. Chergui, Photexcitation of aqueous ruthenium (ii)-Tris-(2, 2'-Bipyridine) with high-intensity femtosecond laser pulses. J. Phys. Chem. B **110**(51), 26497–26505 (2006)

171. K. Kalyanasundaram, Photophysics, photochemistry and solar energy conversion with tris (bipyridyl) ruthenium (ii) and its analogues. Coord. Chem. Rev. **46**, 159–244 (1982)
172. J. Andersson, F. Puntoriero, S. Serroni, A. Yartsev, T. Pascher, T. Polívka, S. Campagna, V. Sundström, Ultrafast singlet energy transfer competes with intersystem crossing in a multicenter transition metal polypyridine complex. Chem. Phys. Lett. **386**(4), 336–341 (2004)
173. G. Benkö, J. Kallioinen, P. Myllyperkiö, F. Trif, J.E. Korppi-Tommola, A.P. Yartsev, V. Sundström, V. Sundström, Interligand electron transfer determines triplet excited state electron injection in RuN3-sensitized TiO_2 films. J. Phys. Chem. B **108**(9), 2862–2867 (2004)
174. H. Long, G. Yang, A. Chen, Y. Li, P. Lu, Femtosecond z-scan measurement of third-order optical nonlinearities in anatase TiO_2 thin films. Opt. Commun. **282**(9), 1815–1818 (2009)
175. S. Griesse-Nascimento, O. Reshef, M. Moebius, C. Evans, E. Mazur, Nonlinear optics in TiO_2 nanoscale waveguides, in *Nano-Optics: Principles Enabling Basic Research and Applications* (Springer, 2017), pp. 449–449
176. S.K. Das, C. Schwanke, A. Pfuch, W. Seeber, M. Bock, G. Steinmeyer, T. Elsaesser, R. Grunwald, Highly efficient THG in TiO_2 nanolayers for third-order pulse characterization. Opt. Exp. **19**(18), 16985–16995 (2011)
177. H.G. Yang, C.H. Sun, S.Z. Qiao, J. Zou, G. Liu, S.C. Smith, H.M. Cheng, G.Q. Lu, Anatase TiO_2 single crystals with a large percentage of reactive facets. Nature **453**(7195), 638–641 (2008)
178. G. Giorgi, M. Palummo, L. Chiodo, K. Yamashita, Excitons at the (001) surface of anatase: spatial behavior and optical signatures. Phys. Rev. B **84**(7), 073404 (2011)
179. M. Palummo, G. Giorgi, L. Chiodo, A. Rubio, K. Yamashita, The nature of radiative transitions in TiO_2-based nanosheets. J. Phys. Chem. C **116**(34), 18495–18503 (2012)

Chapter 5
Probing the Electron-Phonon Interaction in Correlated Electron Systems

One of the long-standing questions in cuprate physics concerns the role that the electron-phonon interaction plays across the phase diagram.[1]

On one side, it is well established that intermediate-to-strong electron-electron correlations represent the essential ingredient to rationalize the electronic structure of the undoped parent compounds [1, 2] and the emergence of a variety of exotic phenomena in the UD region of the phase diagram. With respect to the insulating parent compound, nowadays there is an almost general consensus in the classification of its electronic properties within the CT insulator scenario [3, 4]. As a consequence, a body of theoretical work is devoted to understanding whether a strongly correlated model for the CuO_2 planes alone, such as the 2D Hubbard or the t-J Hamiltonian, can capture the low-energy physics of these materials. Among the most successful results of these models, we can cite the prediction of the renormalized charge dynamics [1, 5] and the opening of a spin gap [6, 7]. At the same time, one has to be aware that these models represent simplified schemes that rely on a number of assumptions. One of these assumptions consists in neglecting the electron-phonon interaction, which can be justified in first instance by the lack of a substantial isotope effect in the cuprates for the emergence of high-T_C superconductivity [8].

On the other hand, the presence of an intermediate-to-strong electron-phonon interaction cannot be neglected a priori. In similarly complex TMOs, like the manganites and the nickelates, the electron-phonon coupling is known to be at play in a variety of effects such as polaronic transport [9, 10] and CDW formation [11]. In cuprates, it is nowadays established that this fundamental interaction cannot be responsible for the SC properties, as the dominant mechanism behind Cooper pair formation does not involve a net saving of ionic kinetic energy as in BCS materials [12, 13]. However, the electron-phonon interaction can lie at the origin of other

[1] Parts of Chap. 5 are reprinted with permission from A. Mann et al., Physical Review B 92, 035147. Copyright 2015 American Physical Society.

E. Baldini, *Nonequilibrium Dynamics of Collective Excitations in Quantum Materials*,
Springer Theses, https://doi.org/10.1007/978-3-319-77498-5_5

emergent phenomena competing with superconductivity, and thus can contribute to shape the phase diagram. Motivated by this idea, a number of experiments attempted to clarify the role of the electron-phonon coupling in cuprates. Broad boson sidebands were discovered in the ARPES spectra of La_2CuO_4 and interpreted as the signature of polaronic coupling between specific lattice modes and the charge carriers [14]. The computed spectral distribution of the electron-phonon coupling was even found to be sufficiently strong to induce the self-trapping of the charge carriers. In this regard, the most coupled optical phonons in the system have been identified with the La mode at 20 meV, the apical O mode at 60–70 meV and the O (half)-breathing mode at 85 meV [14]. In support to the hypothesis of a sizeable interaction, high-resolution ARPES data on a variety of *p*-type doped cuprates concluded that the quasiparticles are strongly coupled to phonons in the frequency range 40–80 meV [15–17]. A sudden and dramatic change in the quasiparticle velocity well above T_C, manifested as a kink in the energy-momentum dispersion along the nodal direction, and a concomitant drop in the quasiparticle scattering rate were interpreted as fingerprints of strong interactions with phonon modes. At the same time, the observation of anomalous phonon dispersions in IXS [18], the softening of a phonon peak in INS [19] and the presence of features in tunnelling spectra [20] indicated a significant role played by the lattice degrees of freedom in the cuprates. Also the equilibrium optical conductivity $\sigma_1(\omega)$ of insulating and weakly-doped cuprates revealed the presence of structures that can be described only within the strong electron-boson coupling regime. For example, the feature associated with the CT excitation in the undoped parent compound has been successfully reproduced with a model of interacting electron-polaron and hole-polaron pairs [21]. In addition, the low-energy $\sigma_1(\omega)$ of weakly-doped cuprates reveals a broad feature at 0.5 eV, known as the "MIR band". The origin of such a feature has been subject of huge controversy in the field [22–24], until a promising explanation has been offered by the numerical solution of the t-J-Holstein model [25]. This involves the incoherent motion of a hole subjected to the interplay between the electron-electron correlations and electron-phonon interaction. Finally, phonons may be responsible for charge instabilities, in the form of stripes [26], CDWs [27, 28] and electronic phase separation [29]. As various physical observables in the cuprates are differently affected by phonon effects, the energy- and momentum structure of the electron-phonon coupling must play an important role.

From these arguments, one intriguing possibility that is being explored in cuprate physics consists in the existence of a non-trivial interplay between high-energy electron-electron correlations and the low-energy electron-phonon interaction [30]. This interplay poses new challenges for theory and experiment. On the theory side, the solution of the t-J-Holstein Hamiltonian is providing novel insights into the low-energy charge dynamics, as this model is considered as a suitable candidate to mimic the coupling of the charge with both magnetic fluctuations and quantum phonons [25, 31–34]. On the experimental side, the advent of nonequilibrium methods based on the pump-probe scheme is shedding light on the coupling among different electronic and structural excitations on the basis of their characteristic timescales. In the last decade, several ultrafast optical studies have been performed over a broad spectral range in order to monitor the nonequilibrium evolution of the in-plane optical

response in the undoped parent compounds La_2CuO_4, Nd_2CuO_4 and $YBa_2Cu_3O_6$ [35–38]. Using this approach, it was found that a transient metallic state establishes for 40 fs upon photodoping the CT insulating state in Nd_2CuO_4 and La_2CuO_4 at RT [36, 37]. Subsequently, due to the strong electron-phonon coupling, the charge dynamics are governed by carrier localization, resulting in the emergence of MIR absorption bands. More recent measurements of ultrafast broadband optical spectroscopy focused more accurately on the dressing process of the quasiparticles in $La_2CuO_{4+\delta}$ [38]. In this regard, the use of sub-gap photoexcitation unravelled the ultrafast build-up of the effective interaction between the charge carriers and the bosonic field.

Despite unveiling the effectiveness of the electron-phonon interaction in undoped cuprates, all the above experiments have only offered an indirect signature of the phononic field dressing the charge excitations. Moreover, as the effect of the carrier dressing is apparent in the incoherent response of the pump-probe signal, these measurements only provide an average insight into the electron-boson coupling caused by the interaction with all bosonic modes. This calls for the development of a novel approach to extract *quantitative* information on the electron-boson matrix elements for *specific* collective modes.

An elegant method to investigate this coupling is to carefully tailor the pump excitation in an ultrafast experiment, in order to trigger specific coherent collective modes. As observed in Chap. 2, coherent modes that can be studied include Raman-active electronic and lattice excitations, which in undoped cuprates are respectively represented by bi-magnons and optical phonons [39]. Once these modes are set out-of-equilibrium, the effects of the coherent bosonic field on the high-energy optical spectrum of the material can be probed in a broad energy region by a delayed optical pulse. Direct information on the coupling between a specific collective mode and the high-energy electronic excitations in the accessible spectral range can be retrieved from the evaluation of the energy-dependent Raman matrix element of the coherent mode. In regard to Raman-active phonons, this approach would provide a conclusive estimate of the electron-phonon coupling strength projected at the Γ point of the BZ. In principle, this quantity can be extracted also in the frequency domain via spontaneous Raman scattering, but with very demanding experiments performed at different laser wavelengths [40]. Ultrafast broadband optical spectroscopy can obtain the same information in a single experiment.

Using this technique, the dream is to estimate the electron-phonon coupling strength for several lattice modes of interest across the whole cuprate phase diagram and to possibly extend this concept to the case of the coherent Bogoliubov QPs at $2\Delta_{SC}$ (where Δ_{SC} denotes the size of the SC gap along a particular Raman scattering symmetry), thus evaluating the coupling of the SC condensate to other excitations [41, 42]. To address this phenomenology, in the framework of this Thesis, we design several ultrafast broadband optical experiments on the prototypical CT insulator La_2CuO_4 in the visible spectral range. The main properties of this material are described in Sect. 5.1, putting emphasis on its electronic structure. The steady-state optical characterization of the system is offered in Sect. 5.2, while the analysis of the Raman spectra, crucial for the interpretation of the pump-probe experiments, is

given in Sect. 5.3. Finally, Sect. 5.4 is devoted to the low-temperature nonequilibrium response that the system exhibits upon a photoexcitation below or above the CT gap. Contrary to previous studies [35–38], we explore both the *a*- and *c*-axis reflectivity response in a broad spectral range, by tuning the probe beam polarization along the [100] and [001] crystallographic directions of La_2CuO_4. Our approach allows to reveal the ultrafast incoherent renormalization of the optical properties and the emergence of specific coherent optical phonons with A_g symmetry. In addition, we extract the Raman matrix elements of such modes, which serve as a benchmark for the estimate of the electron-phonon matrix elements via a phenomenological approach or ab initio techniques. This is the subject of Sect. 5.5, while conclusions are given in Sect. 5.6. Our study paves the route to a systematic investigation of the interplay between structural/charge fluctuations and electronic excitations in complex TMOs.

5.1 La_2CuO_4

La_2CuO_4 is one of the simplest insulating copper oxides that exhibit high-T_C superconductivity upon hole doping. In this material, the 2D network of corner-sharing CuO_4 units, typical of all SC cuprates, is accompanied by two additional O atoms (named apical O) below and above each CuO_4 plaquette. As a consequence, the main building block of La_2CuO_4 is represented by CuO_6 octahedra, which are elongated along the apical oxygens due to the JT distortion. Above 560 K, the high-temperature structural phase of La_2CuO_4 is tetragonal, while below this temperature, an orthorhombic distortion occurs and the crystal lowers its symmetry to orthorhombic. The low temperature crystal structure and the schematics of the Cu-O network are shown in Fig. 5.1a, b, respectively. The single spin on the in-plane Cu^{2+} ions undergoes AFM ordering below the Néel temperature $T_N = 320$ K. In the following, the origin of such AFM ordering will be clarified in relation to the electronic properties of this material.

Indeed, to gain more insights into the open problems associated with cuprate physics, it is pivotal to have a detailed comprehension of the undoped parent compound electronic structure. Conventional band theory fails in providing a reliable description of undoped cuprates, since it predicts the occurrence of a metallic behaviour. Thus, we start with a simplified ionic model, which neglects the hybridization effect among the Cu and O orbitals. The formal valence of Cu atoms is 2+, which leads to a $3d^9$ configuration, with a single hole in the 3*d* orbitals. In the crystal field of La_2CuO_4, the hole is located in the $3d_{x^2-y^2}$ orbital and it is localized on the Cu sites due to the strong on-site Coulomb interaction U. The latter arises due to the localized nature of Cu 3*d* orbitals. As a consequence, a single spin is localized on each Cu ion, while the O ion has a closed shell with a $2p^6$ configuration.

The opening of a gap in this simple model can come from two distinct processes [43]. The first mechanism involves the motion of one localized hole from a Cu ion to another Cu ion (intersite *d*-*d* excitation), while the second phenomenon implies that the localized hole moves to one of the O ions (intersite *p*-*d* excitation). In the

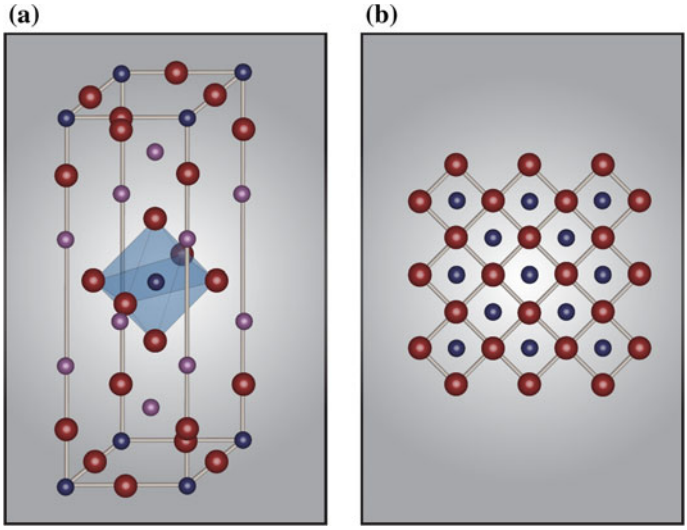

Fig. 5.1 **a** Crystallographic structure of La_2CuO_4, showing its low-temperature orthorhombic unit cell. The Cu atoms are depicted in blue, the O atoms in red and the La atoms in violet. **b** Schematics of the 2D network of corner-sharing CuO_4 units

former case, the total energy change is represented by the Coulomb interaction U itself, while in the latter case it is governed by the CT energy Δ for transferring a hole from the cation to the anion. The insulating behaviour arises as a result of the local blocking of the electron propagation and it is not related to any specific form of AFM long-range order. The AFM long-range order emerges instead as a secondary instability. According to the ZSA scheme [3], the lowest energy between the U and Δ scales determines whether the material can be regarded to as a Mott-Hubbard or a CT insulator. In the Mott-Hubbard insulator picture, the Mott gap U separates the Upper Hubbard Band (UHB) and the Lower Hubbard Band (LHB), and the O $2p$ band lies below the LHB; in contrast, in the CT insulator picture, the CT gap Δ separates the O $2p$ band from the UHB, and the LHB lies below the O $2p$ band. The simplified DOS arising from these two basic frameworks is shown in Fig. 5.2a, b. To establish the correct scenario for the cuprates, the ionic model itself does not prove to be sufficient and the support of experimental data becomes crucial. As many spectroscopic methods extracted $U \sim 8\,\text{eV}$ and $\Delta \sim 2$ eV, a CT insulator scenario was established for this class of compounds.

To capture the low-energy physics arising upon hole doping, several studies have shown that the one-band Hubbard model alone can describe some qualitative properties of the Cu-O layers [1, 6, 7, 24]. The Hubbard Hamiltonian [44] reads

$$H = -t \sum_{<i,j>,\sigma} (c^{\dagger}_{i,\sigma} c_{j,\sigma} + c^{\dagger}_{j,\sigma} c_{i,\sigma}) + U \sum_{i=1}^{N} n_{i\uparrow} n_{i\downarrow} - \mu \sum_{j} (n_{j\uparrow} + n_{j\downarrow}), \quad (5.1)$$

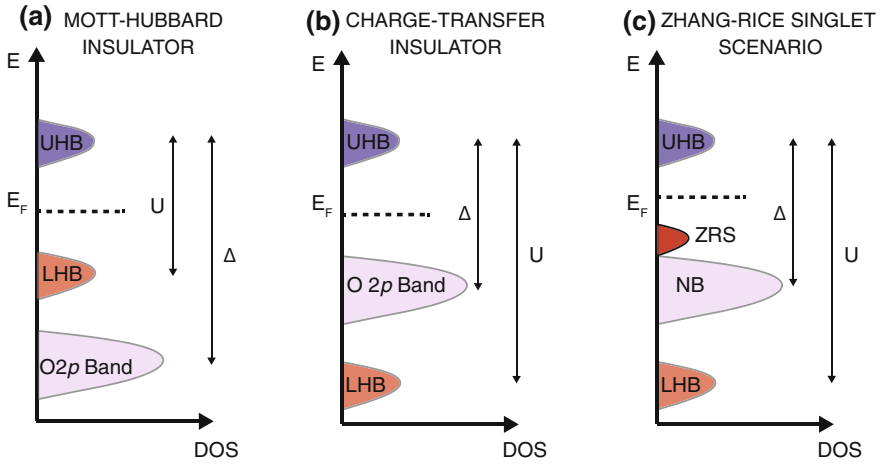

Fig. 5.2 Schematic DOS in the **a** Mott-Hubbard insulator; **b** CT insulator scenario; **c** ZRS scenario. UHB = Upper Hubbard Band, LHB = Lower Hubbard Band, ZRS = Zhang-Rice singlet

where the first sum runs over the nearest neighbour sites $< i, j >$, the $c^{\dagger}_{i,\sigma}$ is the operator that creates an electron of spin σ on the lattice site i, $c_{i,\sigma}$ is the operator that annihilates an electron of spin σ on the lattice site i and $n_{i,\sigma} = c^{\dagger}_{i,\sigma} c_{i,\sigma}$ is the number operator. The final term contains a chemical potential μ which controls the filling. The main parameters that enter the Hubbard Hamiltonian are the hopping integral t and the on-site Coulomb repulsion U, which can be taken from the experimental data or derived by some ab initio computational technique. The Hubbard model provides a rough estimate of the strength of the electronic correlations in cuprates. Within a one-band Hubbard description, parametrized by a bandwidth W $\approx 8t$ and a Coulomb repulsion U, the insulating gap of the paramagnetic insulator is $U - W$ and the superexchange interaction is $J = 4t^2/U$. As in the cuprates U is replaced by the Δ energy scale of 2 eV and J is 0.1 eV, the repulsion can be estimated on the order of $U/W \approx 1.5$, which is above but not far from the Mott boundary $U \approx W$. This implies that insulating cuprates are in a regime of intermediate correlation strengths, which represents a very complex scenario to model with respect to the two extreme regimes. Up to this point, we have neglected the presence of hybridization effects. However, within the framework of CT insulators, hybridization is expected to play even a more significant role and should be accounted for when describing the electronic states of cuprates through a model Hamiltonian. It is generally accepted that the relevant degrees of freedom are the $2p_\sigma$ ($2p_x$ or $2p_y$) Wannier orbitals on the in-plane O ions and the Wannier $3d_{x^2-y^2}$ orbital on the Cu ion, due to the large overlap between their wavefunctions. As a consequence, the minimum model that can be built for the CuO_4 unit is the so-called Emery model [22, 45], which is widely known as the three-band Hubbard model (due to the three orbitals involved) or the d-p model (due to the inclusion of d and p orbitals).

Within the latter framework, important findings have been achieved concerning the low-energy electronic structure of undoped cuprates upon electron or hole creation. The DOS of a CT insulator shown in Fig. 5.2b is indeed a very primitive one and it is tempting to refer to the filled O band as of the non-bonding type. However, this picture becomes very misleading in the presence of intermediate-to-strong correlations, since it does not take into account the possible interactions related to the creation of holes and electrons in the single-particle excitation spectrum. Indeed, it is presumed that the holes are introduced into the O $2p_\sigma$ orbitals and possess a strong coupling in spin and symmetry with the localized hole on the Cu $3d_{x^2-y^2}$ orbitals. This leads to a new bound (or impurity-like) state, known as Zhang-Rice singlet (ZRS) state, that splits-off from the O $2p$ band [46]. The modified DOS is shown in Fig. 5.2c, where a new band of hybrid character separates from the O non-bonding $2p$ band. The representation of the ZRS state is provided in Fig. 5.3. As a consequence, the lowest unbound interband charge excitation in the optical spectrum involves the transfer of a hole localized on a Cu $3d_{x^2-y^2}$ site to an O $2p_\sigma$ orbital. The hole forms in turn a ZRS state which is coupled to an adjacent localized Cu $3d_{x^2-y^2}$ hole, thus giving rise to a non-local excitation involving the ZRS state and the UHB. This model also allows understanding the disappearance of the AFM ordering upon hole doping. The O hole is coupled to a single Cu but in reality it can interact with neighbouring ones as well, leading to a ferromagnetic (FM) contribution to the net coupling between Cu spins and balancing the AFM superexchange.

In the last decade, a new promising route for advancing the understanding of the electronic structure of cuprates has come from the development of Dynamical Mean Field Theory (DMFT) [47] and its extensions [48, 49]. In particular, the use of DMFT with electronic-structure methods such as LDA allows combining the ab initio and the model Hamiltonian viewpoints within the LDA + DMFT multiband framework. This technique has been used to refine the estimate of the correlation strength in cuprates and to describe the electron-hole asymmetry arising in these materials. These issues are still highly debated, as new calculations have identified the undoped parent compounds of electron-doped cuprates (like Nd_2CuO_4) as Slater insulators [50], while the undoped parent compounds of hole-doped cuprates (like La_2CuO_4) as

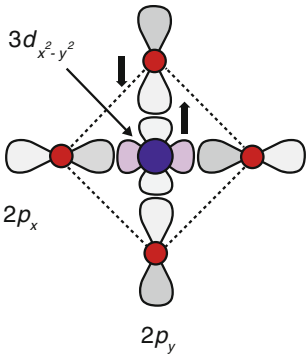

Fig. 5.3 Representation of the ZRS state presumed to be formed by strong AFM coupling of an O hole with that localised on Cu^{2+}. The relative signs of the different orbital lobes is indicated by the shading

CT insulators [51]. In the Slater insulator picture, the insulating behaviour does not originate from the strong Coulomb repulsion, but arises as a result of the doubling of the unit cell caused by AFM long-range order. In this case, the AFM order is the *cause* and not the *consequence* of the gap opening.

Current state-of-the-art LDA + DMFT calculations for La_2CuO_4 are based on a six-band model, in order to take into account the $d_{3z^2-r^2}$, p_z and p_{-z} orbitals associated with the Cu ion and the apical O ions. Indeed, these orbitals are expected to play a role in La_2CuO_4 and not in Nd_2CuO_4 due to the presence of the apical O atoms. The momentum-resolved single-particle spectral function of La_2CuO_4, computed within this method, is displayed in Fig. 5.4a, while the partial DOS in Fig. 5.4b, c. The data are adapted from Ref. [52]. A direct gap of 1.80 eV can be observed at the M point of the BZ and the partial DOS shows two dispersive features, the UHB and the ZRS band below the E_F. The LHB is separated from the UHB by the U energy scale. Consistent with the explanation of the three-band Hubbard model provided above, the ZRS arises from an admixture of O and Cu characters. In addition, the $p_{\pm z}$ and $d_{3z^2-r^2}$ orbitals have a strong weight between -4 and -1 eV and the in-plane O orbitals are located at -5 eV. In addition, the additional $p_{\pm z}$ and $d_{3z^2-r^2}$ orbitals hybridize with the ZRS. Direct comparison of the computed spectral function with data extracted from the experiments is not straightforward. The reason is twofold: (i) Performing ARPES measurements on the insulating La_2CuO_4 is a challenge by itself, due to the absence of a Fermi surface. When a small amount of doping is introduced, the experimental band mapping can be performed, but the renormalization of the spectral function can be rather strong; (ii) Once ARPES is successfully performed

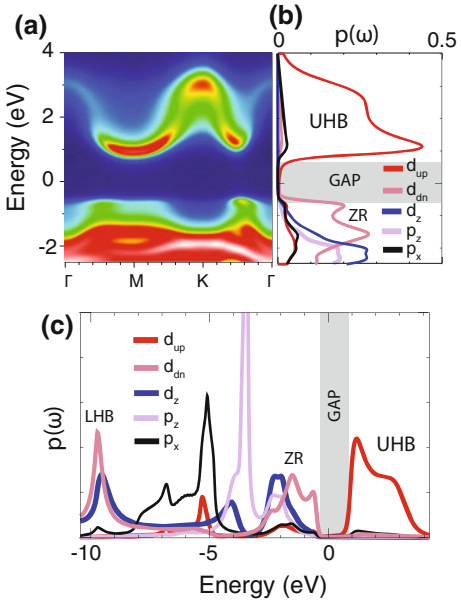

Fig. 5.4 **a** Energy-dependent spectral function A(k,ω) obtained by LDA + DMFT of a six-band model description of La_2CuO_4. **b** Partial DOS of the $d_{x^2-y^2}$, $d_{3z^2-r^2}$, $p_{x,y}$ and $p_{\pm z}$ orbitals, in which a direct gap of 1.80 eV can be observed. **c** Partial DOS on a large energy scale. The LHB is located at -10 eV and the UBH is also shown. Adapted from Ref. [52]

(as in Ref. [14]), incoherent satellites due to the strong electron-phonon coupling emerge in the spectral function. The current level of theory cannot account for the effects produced by such a strong electron-boson coupling.

Concerning the latter point, we have already highlighted in the Introduction to this Chapter the importance of the electron-boson coupling for interpreting the origin of specific features in the one-particle and two-particle excitation spectra. The new frontier for both theory and experiment is to unravel the subtle interplay between the electronic correlations and the electron-boson coupling and understand how these two phenomena concur to promote carrier localization in this class of solids. As already anticipated, the presence of strong electron-boson coupling has a remarkable manifestation in the electrodynamic properties of La_2CuO_4, which are presented in the following section.

5.2 Steady-State Optical Properties

As indicated above, a complete characterization of the two-particle excitation spectrum of La_2CuO_4 under equilibrium conditions is highly desirable to reveal the energy scale of the CT excitation and the importance of the electron-phonon coupling. Moreover, in view of our pump-probe experiment, the knowledge of the steady-state optical spectrum is crucial to understand how the photoexcitation renormalizes the high-energy optical properties of the system. Hence, in this Section, we report on the anisotropic optical response of an (010)-oriented La_2CuO_4 single crystal, and describe the electrodynamic properties of the material.

Figure 5.5 shows the real part of the optical conductivity (σ_1), measured at 10 K with light polarized parallel to the a- (blue curve) and c-axis (red curve) of the crystal, respectively. We observe that σ_{1a} is dominated by an intense feature at 2.25 eV.

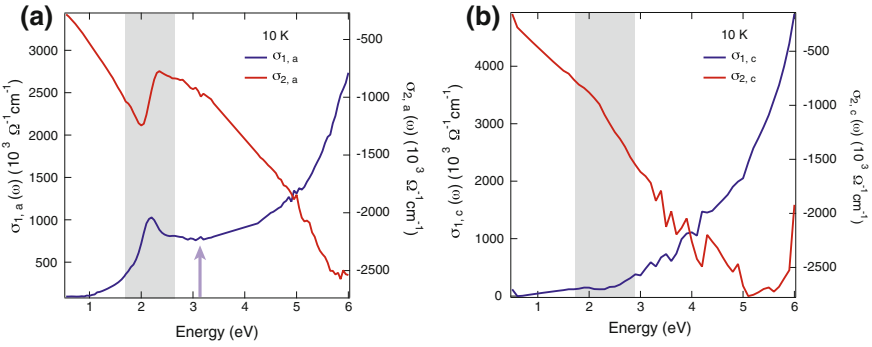

Fig. 5.5 Real part of the optical conductivity along the **a** *a*- (blue curve) and **b** *c*-axis (red curve), measured via spectroscopic ellipsometry at 10 K. The grey shaded areas refer to the spectral ranges monitored by the broadband probe

Preliminary studies assigned this structure to a resonance corresponding to the fundamental CT gap of the material [4, 21]. This interband transition can be considered as a non-local CT excitation, since it involves at least two CuO_4 units. In addition, temperature-dependent studies modelled it as resulting from the interaction between an electron-polaron and a hole-polaron, coupled to each other by a short-range electron-hole interaction [21]. This picture has been recently refined via RIXS, by mapping the dispersion of the elementary excitations far from the long-wavelength limit of optics [53, 54]. It was concluded that the resonance is a weakly dispersive CT exciton, strongly coupled to the phonon bath. The optical spectrum at higher energies (2.50–3.50 eV) has been ascribed to mixed charge excitations from the O $2p$ states to the Cu $3d$ states in the upper Hubbard band (UHB) and to La $5d/4f$ states [4]. Remarkably, upon hole-doping by substitution of Sr for La, only the low-energy spectrum below 3.00 eV undergoes a strong renormalization. SW is transferred from the CT excitation to low energies and gives rise to a two-component response, as will be discussed in detail in Sect. 5.4.

The c-axis optical response retains instead a featureless shape that monotonically increases with energy, which is representative of a particle-hole continuum and confirms the two-dimensional nature of the charge excitations. This spectrum reflects a more insulating behavior of the system along the c-axis and, differently from the in-plane response, chemical doping leads to the formation of a band around ∼2.00–2.50 eV and does not result in a Drude peak [4, 55]. The suppression of the charge excitations along the c-axis allows to track phonon-related features even in the SC state [4, 55]. This, again, represents the signature of a highly semiconducting behavior in the direction perpendicular to the CuO_2 planes. Only in the heavily doped materials ($x \geq 0.18$), the scenario substantially changes and the system becomes an anisotropic 3D metal. Despite these studies, a consensus has not been reached on the origin of the c-axis electrodynamics of insulating cuprates. In Sect. 5.4.2, we show how our nonequilibrium approach provides preliminary results with this respect. Future calculations of the c-axis optical conductivity via six-band DMFT are therefore required to refine our study.

5.3 Spontaneous Raman Scattering

To provide a deeper interpretation of our nonequilibrium data, we also discuss the spontaneous Raman scattering response of La_2CuO_4. This has been the subject of intensive studies in literature, especially in relation to its modification upon chemical doping [39, 56–59]. In the undoped parent compound, the Raman spectra comprise a magnetic and a phononic response. Indeed, the CT insulating nature of this material leads to AFM order as a secondary instability, thus giving rise to well defined features due to Raman-active magnetic modes. This becomes apparent in the B_{1g} Raman scattering channel in the form of a broad bimagnon spectral feature [39]. In La_2CuO_4, the bimagnon feature at RT peaks at ∼385 meV and extends over a wide energy range from 230 to 580 meV. Importantly, this can be used as a direct measure of the effective

exchange interaction J^*, which is estimated at ∼129 meV [39]. Since the bimagnon excitation lies at relatively high energies, this mode cannot be triggered coherently in our nonequilibrium study, due to limitations in our time resolution. Thus, we restrict our description to phononic Raman scattering below the energy of 90 meV, i.e. the range accessible by our pump-probe experiment. In this regard, we put emphasis only to the totally-symmetric (A_g) scattering channel, as this will manifest in our nonequilibrium response. When pumping above the CT gap to create particle-hole pairs in the material, only the bosonic modes of A_g symmetry are expected to couple to the photoexcited charge density via the displacive excitation. When pumping below the CT gap, in principle also modes with different symmetries can be generated via the ISRS mechanism [60]. However, we will show that no modes with symmetries rather than A_g appear in our $\Delta R/R$ data.

From group theory considerations, the orthorhombic phase of La_2CuO_4 admits 5 phonons with A_g symmetry. In spontaneous Raman scattering, a clean study of these totally-symmetric response can be obtained only in the (c, c) scattering geometry. In principle, the A_g symmetry configuration can be also obtained from the (x,x), (a,a), (x,y) and (a, b) spectra by the calculation: $[(x, x) + (a, a) - (x, y) - (a, b)]/2$. However, it was observed that the number of Raman-active peaks exceeds the 5 phonon modes allowed by group theory. This implies that some mechanism makes the forbidden B_{2g} and B_{3g} modes active also in this channel [57]. As a result, performing spontaneous Raman scattering in the (c, c) configuration has led to the correct identification of the 5 A_g modes [56, 59]. The Raman spectrum at 6 K is shown in Fig. 5.6, as measured in Ref. [56], and all the mode quantum energies are listed in Table 5.1. Among the main results obtained by Raman studies of the vibrational modes of La_2CuO_4, we can mention the temperature dependence of the mode at 15.5 meV in the A_g scattering channel (staggered rotational mode of CuO_6 octahedra), as a partial softening of the mode is observed in the proximity of the

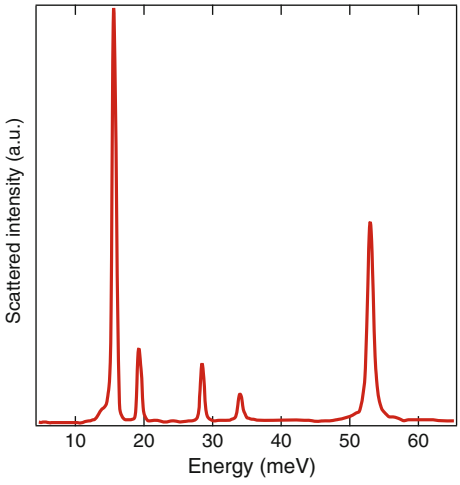

Fig. 5.6 Spontaneous Raman scattering spectrum of La_2CuO_4 in the (c, c) geometry, measured using a monochromatic laser with a photon energy of 2.41 eV. The temperature is 6 K and the data have been adapted from Ref. [56]

High-Temperature Tetragonal to Low-Temperature Orthorhombic structural phase transition [57–59]. Hence, this mode represents the soft phonon associated with the structural phase transition and undergoes a strong damping for increasing temperature and doping. More importantly, in the insulating parent compound, it shows a pronounced anomaly in its energy and linewidth around 280–300 K. As this temperature is far from the structural phase transition temperature (560 K) and coincides instead with the Néel temperature of the crystal, this is a strong evidence for a sizeable coupling between the AFM ordering and the lattice at small doping levels. Since the soft mode involves the tilting vibrations of the apical O atoms, the emergence of the AFM ordering in the CuO_2 planes is likely to modify the tilting angle [59].

In addition to this result, tentative assignments of the other phonon modes were given in a number of Raman studies [39, 57, 61] and calculations of the phonon dispersion [62–64]. However, the detailed eigenvectors at $\mathbf{q} = 0$ have never been systematically reported. To provide an accurate characterization of these modes, we calculated the phonon spectrum of La_2CuO_4 using DFT–LDA. The details of the calculations are reported in Appendix C.3.1. The theoretical values are given in Table 5.1 for a direct comparison with the experimental energies. The energies of the 5 A_g modes are in good agreement with the values extracted from the experiment. The eigenvectors are shown in Fig. 5.7 and the final assignments are also provided in Table 5.1. Having established the eigenvectors of the A_g modes allows us to perform

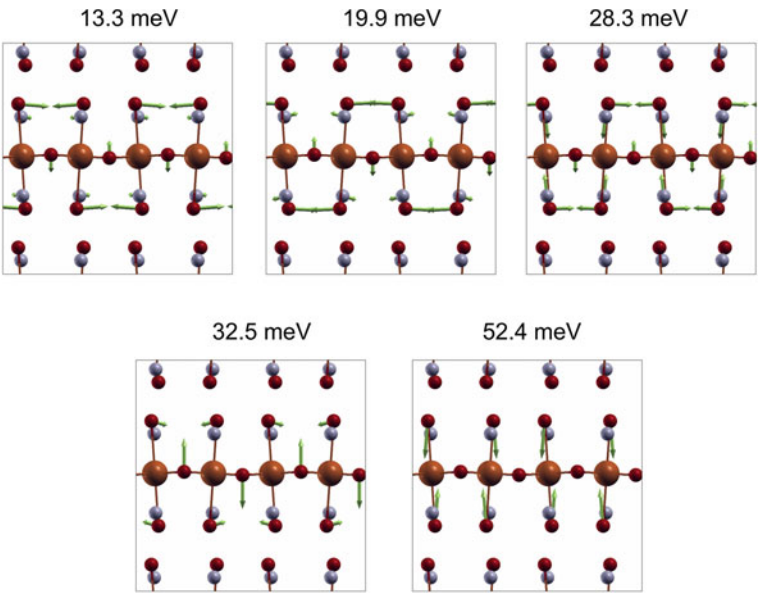

Fig. 5.7 Calculated eigenvectors of the 5 A_g modes of La_2CuO_4 at $\mathbf{q} = 0$. The corresponding energies are indicated in the figure. Brown atoms refer to Cu, red atoms to O and violet atoms to La. The phonon spectrum has been computed using DFT–LDA

Table 5.1 Experimental and theoretical values of the energy of the 5 A_g modes in La_2CuO_4, together with their assignments. The experimental values have been obtained from Ref. [56], while the theoretical values have been calculated via DFT in this work

Label	Experiment (meV)	Theory (meV)	Assignment
I	15.5	13.3	Staggered rotational mode of CuO_6 octahedra With in-phase La vibration
I	19.3	19.9	Staggered rotational mode of CuO_6 octahedra Without-of-phase La vibration
III	28.5	28.3	In phase vibration between La and apical O
IV	34.0	32.5	Vibrations of the in-plane O along the *c*-axis
V	53.0	52.4	Breathing mode of the apical O

the nonequilibrium experiment for mapping the emergence of specific Raman-active modes of interest, as discussed in the following section.

5.4 Ultrafast Broadband Optical Spectroscopy

In Sect. 5.2, we highlighted the role played by the electron-phonon interaction on the electrodynamics of La_2CuO_4. Elucidating how the electron-phonon coupling affects the charge dynamics in this material is of primary importance, especially in relation to the fate of this interaction in the presence of an excess carrier density. A powerful method to reveal the details of the carrier dynamics in real time is represented by ultrafast broadband optical spectroscopy. As underlined in Chap. 2 and demonstrated in Chap. 4, photoexciting an insulator above the gap using an ultrashort laser pulse leads to the creation of particle-hole pairs in the material. The nonequilibrium particle-hole density subsequently undergoes intraband relaxation via distinct scattering channels with all the other degrees of freedom in the system. As a result, the carriers can remain delocalized through the crystal lattice, forming a transient metallic state, or can become localized/trapped to specific lattice sites. Eventually, the recombination of the particle-hole density proceeds via radiative or non-radiative processes [65].

In conventional band semiconductors/insulators, the main scattering channel for the photoexcited carrier density is the one with optical phonons. The carriers remain delocalized in the material and give rise to a sizeable Drude response for tens of picoseconds. The localization process is typically driven by the presence of impurities and defects that bind the carriers in the proximity of specific lattice sites [66–68]. This, in turn, produces characteristic absorption features in the infrared/visible range,

which can persist for hundreds of picoseconds or even nanoseconds. This scenario has to be slightly refined in the presence of intermediate-to-strong electron-phonon coupling, as the intraband relaxation to the band edges can become extremely fast (see Chap. 4 and Ref. [69]) and polaronic bands are expected to emerge in the MIR range for low carrier densities, similarly to the effects produced by chemical doping [70]. Increasing the carrier density leads to the screening of the electron-phonon interaction and one might observe the transition from a polaron gas to a (transient) weakly correlated metal [71]. From this discussion, one can conclude that the response of band semiconductors/insulators to photoexcitation is nowadays quite well understood. This is mainly due to the simpler physics governing these materials, in which the bands can be considered as "rigid", i.e. almost independent of filling and temperature.

Still elusive is instead the physics emerging upon photoexcitation of a strongly correlated system governed by Mott physics, as the photodoping process can cause a strong renormalization of the bands. First of all, we have to underline that every system has its own peculiar features compared to others, thus making the description far from being general. While VO_2 has been extensively studied in relation to its metal-to-insulator phase transition at 340 K [72, 73], the undoped manganites possess an orbitally ordered GS and, in some cases, exotic spin ordered patterns [74]. In addition, photoexciting a Mott-Hubbard insulator across the intersite d-d gap is expected to differ from photoexciting a CT insulator across its intersite p-d gap, due to the hybridization effects that manifest in the presence of the O orbitals. Finally, a non-trivial interplay between Mott and Peierls physics can also emerge in some materials. To correctly predict and interpret the response of a Mott insulator to an ultrashort laser pulse, state-of-the-art theoretical calculations are becoming a promising tool. In the last years, the pioneering extension of DMFT under nonequilibrium conditions has provided insights into the metal-to-insulator phase transition [75], the thermalization dynamics [76, 77] and the modification of the exchange interaction upon photoexcitation [78]. Despite representing a breakthrough in the theoretical study of Mott insulators, these models cannot account for the complexity of the many-body problem in these materials. Due to the variety of effects displayed by these solids, in the following we restrict our discussion only to the case of undoped cuprates.

As already described above, an almost general consensus exists in considering these materials as CT insulators. As such, AFM order emerges as a second instability and involves the Cu^{2+} ions on the CuO_4 plaquettes. Thus, one can expect that, upon creation of particle-hole pairs, the intraband relaxation involves the energy exchange of carriers with both high-energy spin fluctuations and phonons, leading to the ultrafast thermalization of the photoexcited particle-hole pairs. In addition, the freezing of carrier motion can emerge as a result of a variety of processes, namely Coulomb-induced localization, (spin- or phonon-driven) polaronic coupling or trapping to impurity/defect sites. To elucidate the hierarchy of these phenomena resulting from above-gap photoexcitation, in the last decade, ultrafast broadband optical spectroscopy has been applied to the undoped parent compounds La_2CuO_4, Nd_2CuO_4 and $YBa_2Cu_3O_6$ [35–37]. All these studies measured the differential transmittance

$\Delta T/T$ of undoped cuprate thin films, which can be more easily related to the transient absorption ΔA occurring upon photoexcitation. These experiment consistently reported a transfer of SW from the high-energy to the low-energy region, with the establishment of a very rapid Drude (coherent) response and a delayed rise of incoherent absorption bands in the MIR (well distinguishable in Nd_2CuO_4, Fig. 5.8a). This response embodies one of the paradigm of the cuprates, i.e. the coexistence of itinerant and localized carriers upon chemical doping, as evidenced by steady-state optics [4]. As a result, the salient feature is the presence of a two-component low-energy contribution for lightly doped compounds, formed by a Drude-like band centred at $\omega = 0$ and broad structures in the MIR. From the nonequilibrium experiment, the MIR features have been assigned to electron- and hole-polaron absorption bands, as indicated in Fig. 5.8b. This is remarkably different from the *extrinsic* photoinduced absorption bands observed on the millisecond timescale, which are related to charge localization on impurity/defect sites [79].

Therefore, photoexciting an undoped cuprate across the CT gap leads to a photodoping effect which retains some features in common with the chemical doping process and can possibly influence the material properties on the ultrafast timescale. In this regard, photoinduced phase transitions from insulator to metal have been reported in organics [80, 81] and other CT insulators [82]. In La_2CuO_4, the photoinduced metallic states rapidly decays within 40 fs (Fig. 5.9a, b) and the carrier density freeze due to strong electron-boson coupling (Fig. 5.9c). Such polaronic carriers relax within 100 ps and the heating of the system proceeds on longer timescales (Fig. 5.9d).

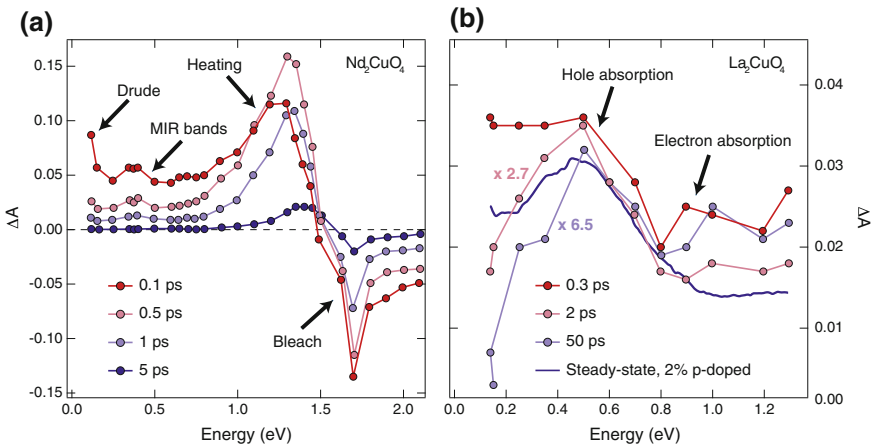

Fig. 5.8 **a** Transient absorption spectra of Nd_2CuO_4 for different time delays after pump photoexcitation above the gap at RT. The ultrafast Drude response, the MIR bands, the spectral features related to heating and the bleach of the CT gap are indicated. **b** Normalized transient absorption spectra of La_2CuO_4 for different time delays after pump photoexcitation above the gap at RT. The MIR bands are assigned to hole- and electron-polaron bands. A comparison with the steady-state absorption spectrum of p-doped $La_{1-x}Sr_xCuO_4$ (x = 0.02) is also shown. The data are adapted from Ref. [37]

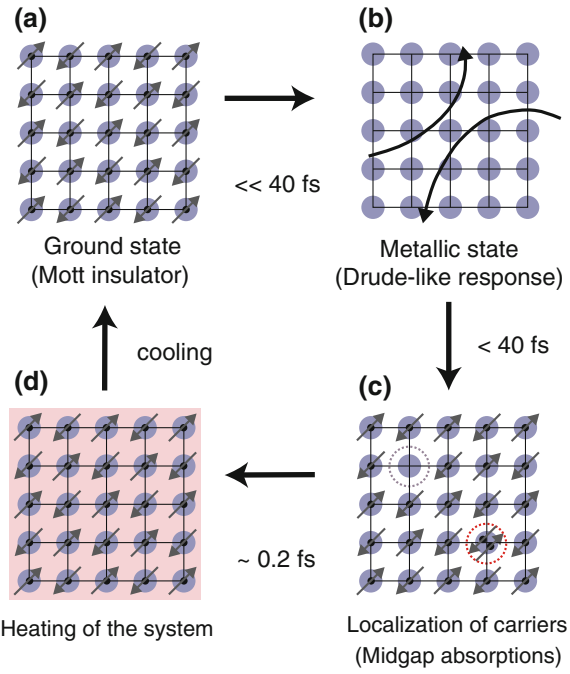

Fig. 5.9 Cartoon of the different phenomena characterising the charge dynamics in undoped cuprates. **a** GS of the system, governed by Mott physics. **b** Photoinduced metallic states that give rise to the Drude response on a 40 fs timescale. **c** Charge localisation into polaronic states. **d** Heating of the system after photocarrier recombinations. The scheme has been adapted from Ref. [37]

Importantly, while the coherent Drude and midgap spectral features are observed to rise and decay with their characteristic timescales, the depletion of the SW above the CT gap reflects the timescales of all processes in the material. This is a crucial aspect, as the time resolution of ultrafast spectroscopy in the visible spectral range is higher than in the infrared, thus leading to the detection of very short transients like the one caused by the Drude response.

More recently, the different impact of below- and above-gap photoexcitation on the in-plane $\Delta R/R$ has been studied in $La_2CuO_{4+\delta}$ (where $\delta = 5 \times 10^{-3}$) [38]. It was discovered that photoexciting the material along the *a*-axis with a pump photon energy at 0.95 or at 1.40 eV in the linear regime leads to an "*instantaneous*" rise time of the signal followed by an ultrafast decay. This was found to be in contrast with the response retrieved for above-gap excitation at 2.25 or 3.10 eV, which possesses a slower rise time. The difference between the two photoexcited states is also encoded in the spectral response, as the CT feature for the sub-gap excitation undergoes a rapid blueshift within the first 100–150 fs and finally reaches the spectral response for above-gap excitation. This effect was rationalized in the framework of the Hubbard-Holstein Hamiltonian, by introducing the effects of the electromagnetic field by means of a classical vector potential. This leads to the distinction between a non-adiabatic regime, describing real transitions between electronic states, and an adiabatic regime, where the response comes from the deformation of the wavefunction by the electric field of light. In the latter scenario, the system relaxes back to

the GS once the effect of the pump pulse is over. According to this picture, sub-gap excitation produces an ultrafast reaction of the bosonic field, leading to a coherent dressing of the charge carriers before the thermal response takes the control of the energy flow in the system. This effect results from the presence of a small excess oxygen content $\delta = 5 \times 10^{-3}$, as this is at the origin of a non-vanishing optical conductivity below the gap. These tail states arise from the interaction between the excess charge and the bosonic degree of freedom [34].

All these experiments reinforce the idea that the electron-boson coupling plays a vital role in the nonequilibrium response of La_2CuO_4. For this reason, ultrafast broadband optical spectroscopy can be considered as an ideal tool for unveiling the interplay between the photoexcited charge density and the phonon field in a correlated electron material. Inspired by these experiments, here we design a methodology to reveal a clear and direct signature of the phonon modes participating to the dynamics, and we reach a first quantitative estimate of the electron-phonon coupling for specific lattice modes. Our approach relies on performing a polarization dependence in the nonequilibrium experiment, exciting or detecting also the out-of-plane response of the material. In Sect. 5.4.1, we first focus on the below-gap excitation regime, by pumping a slightly doped (010)-oriented single crystal of $La_2CuO_{4+\delta}$ (where $\delta = 3 \times 10^{-3}$) with a photon energy of 1.55' eV. Finally, in Sect. 5.4.2, we concentrate on the above-gap excitation regime, in which we photoexcite a stoichiometric (010)-oriented single crystal of La_2CuO_4 with a photon energy of 3.10 eV. In both situations, we observe a clear signature of the lattice modes of the system. This allows us to gain insights into the generation mechanism of these modes, being the ISRS process or the long-lived perturbation of the electronic GS [83].

5.4.1 Below-Gap Excitation

In this section, we describe the first set of experiments, in which we use a slightly-doped (010)-oriented single crystal of $La_2CuO_{4+\delta}$, with $\delta = 3 \times 10^{-3}$. This doping value corresponds to a very small hole content of $p = 0.006$. The pump photoexcitation is tuned at 1.55 eV and its polarization is varied to explore both the *a*- and *c*-axis. The broadband probe covers instead the region 1.75–2.75 eV and its polarization is set along the *a*-axis, in order to monitor the spectrum of the in-plane CT excitation.

Figure 5.10a, c display the colour-coded maps of the $\Delta R/R$ response as a function of the probe photon energy and of the time delay between pump and probe at 10 K, for a pump polarization along the *a*- and *c*-axis, respectively. The absorbed pump fluence is estimated around 6.7 mJ/cm^2. In both pump polarization configurations, the *a*-axis $\Delta R/R$ response is dominated by a negative feature emerging in correspondence to the CT excitation, around the probe photon energy of 2.15 eV probe. We observe that the qualitative shape of the response is in agreement with the results of a previous ultrafast broadband optical spectroscopy study in which the pump photon energy was set at 0.95 and 1.40 eV [38]. Figure 5.10b, d show the

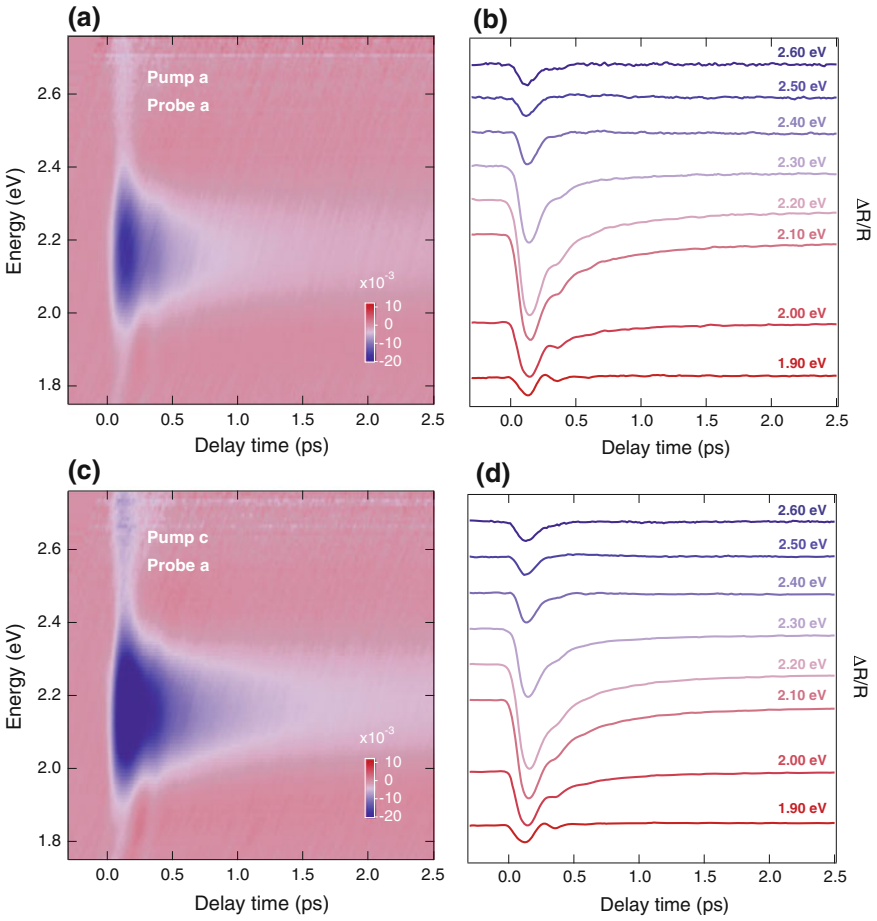

Fig. 5.10 **a**, **c** Colour-coded maps of ΔR/R at 10 K with in-plane probe polarization and (**a**) in-plane, **c** out-of-plane pump polarization. The pump photon energy is 1.55 eV and the absorbed pump fluence is 6.7 mJ/cm^2. **b**, **d** Temporal traces at specific probe photon energies of the respective ΔR/R maps. Each temporal trace results from the integration over 0.10 eV around the indicated probe photon energy

ΔR/R temporal traces selected at specific probe photon energies. Under both pump polarization conditions, the dynamics are characterized by the presence of a prompt (albeit not resolution-limited) rise, followed by a fast relaxation of ∼500 fs. These dynamics are slower than those reported in Ref. [38], and thus evidence a sizeable absorption from our sample. However, contrary to previous experiments, a coherent oscillation is found to modulate the ΔR/R response across the whole probed region. This can be clearly distinguished in the low-energy region of the probed spectral range, in which the incoherent background becomes less pronounced. Notably, the coherent response evolves as a sine function, which is the fingerprint of an ISRS-type

of generation mechanism for the collective bosonic mode involved. By repeating the same experiments also at RT, we confirm the persistence of this oscillating mode, though with reduced coherence.

To elucidate whether this coherent excitation affects also the c-axis $\Delta R/R$ response, we perform a separate experiment where we tune the polarization of the probe beam. Figure 5.11a, b display the colour-coded maps of $\Delta R/R$ as a function of the probe photon energy and of the time delay between pump and probe at 10 K, for a pump polarization along the a- and c-axis, respectively. We observe that the signal is extremely weak and it is completely related to a leakage of the a-axis CT excitation, due to a non-perfect alignment of the probe polarization along the c-axis. This result is remarkable, since it demonstrates the absence of a sizeable long-lived incoherent variation of the out-of-plane reflectivity when $La_2CuO_{4+\delta}$ is pumped below the CT gap at 1.55 eV even in the presence of a slight doping. In addition, no coherent oscillation (other than the one arising from the leakage of the a-axis) is detected within the framework of ISRS.

As the presence of this oscillation modulating the a-axis reflectivity is a novel feature of the nonequilibrium dynamics of $La_2CuO_{4+\delta}$, in the following we specifically focus on this observable. The aim is to reveal its origin and establish its coupling with the high-energy CT excitation. First, as anticipated above, this feature remained undetected in previous ultrafast broadband optical experiments [38]. We tend not to attribute this effect to the lower cross-section for the generation of this mode when the material is pumped at 0.90 eV or 1.40 eV rather than 1.55 eV. Our pump photon energy lies very close to the one at 1.40 eV and it is extremely unlikely that the Raman cross-section is abruptly modified across this small spectral range. Also the temperature at which the experiments are performed does not play a role, as our response at RT bears the signature of the oscillation. Therefore, this effect might be

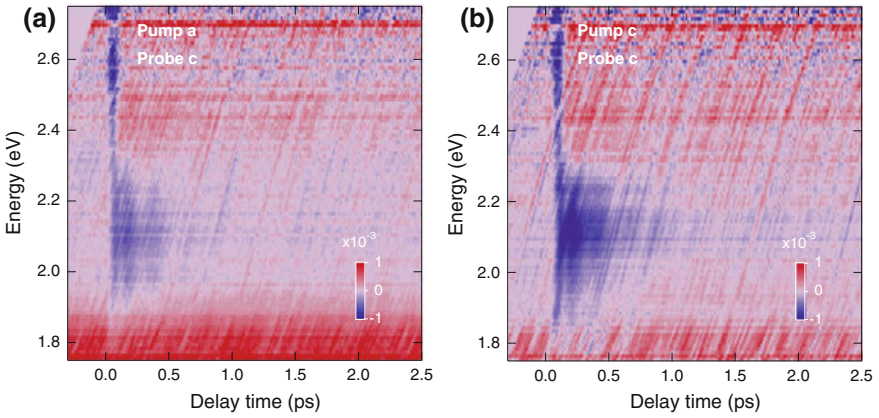

Fig. 5.11 Colour-coded maps of $\Delta R/R$ at 10 K with out-of-plane probe polarization and **a** in-plane, **b** out-of-plane pump polarization. The pump photon energy is 1.55 eV and the absorbed pump fluence is 6.7 mJ/cm^2

ascribed to the value of the absorbed fluence or the lack of a fine sampling of the temporal response in the previous experiments.

To assign the mode, we perform a Fourier transform (FT) analysis of the residuals obtained from a multiexponential fit of the incoherent response at 1.90 eV, where the oscillation possesses a higher contrast. The FTs for a pump polarization along the *a*- and *c*-axis are shown in Fig. 5.12 in blue and pink, respectively. In both polarization channels, we observe the appearance of a sharp peak around the energy of 19 $\pm$ 1.47 meV. This peak finds an excellent correspondence with the A_g Raman-active mode labelled II in Table 5.1. This mode is associated with the staggered rotation of the CuO_6 octahedra, accompanied by a prominent out-of-phase vibration of the La ion. In our experiments, the use a broadband probe allows to study the spectral dependence of the coherent phonon amplitude (hereafter called the Raman matrix element), which plays a fundamental role in the evaluation of the electron-phonon matrix elements related to this specific collective mode.

To extract the Raman matrix element from our $\Delta R/R$ response, two alternative methods can be implemented: (i) A global fit analysis of the incoherent response across the whole spectral region, followed by a FT analysis of the residuals; (ii) A singular value decomposition (SVD) procedure. The latter algorithm is more efficient when the amplitude of the oscillations is rather small compared to the incoherent background, as it filters the noise and reduces the fit dimensionality (identifying the minimum number of uncorrelated components that describe the response). Here, we adopt this second approach to treat the $\Delta R/R$ data, restricting to the analysis of the response obtained for a pump excitation along the *c*-axis. The general principles behind SVD and the details of its application on our $\Delta R/R$ data are reported in Appendix C.3.2. We just remark that this method enables the decomposition of the

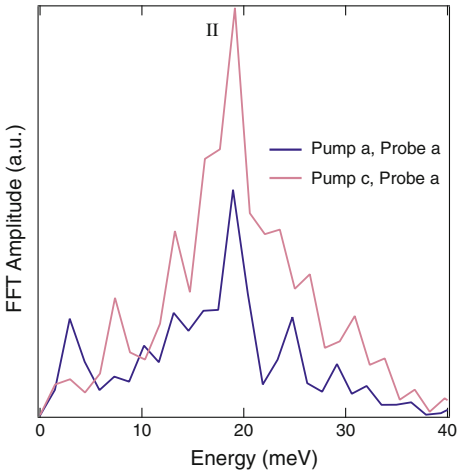

Fig. 5.12 FT analysis of the residuals from a multiexponential fit of the temporal trace at 1.90 eV, integrated over 200 meV. The blue and the pink curves refer to a pump polarization along the *a*- and *c*-axis, respectively

$\Delta R/R$ response into a relaxation (incoherent) part and an oscillatory (coherent) part, according to

$$\left(\frac{\Delta R}{R}\right)(t, E) = \left(\frac{\Delta R}{R}\right)^{\text{rel}}(t, E) + \left(\frac{\Delta R}{R}\right)^{\text{osc}}(t, E). \tag{5.2}$$

In our analysis, the main features of the data are reconstructed using SVD up to second rank. The results for the data reconstruction is shown in Fig. 5.13a, while the relaxation and oscillatory contributions are shown in Fig. 5.13b, c, respectively. We observe that the reconstructed map well agrees with the measured response of Fig. 5.10c and displays a strong reduction of the noise level. Moreover, the SVD provides a precise separation of the two contributions, allowing for a better subtraction of the incoherent peak inside the oscillatory response and delivering the energy dependence of the oscillation in a straightforward way.

The temporal evolution of the coherent component extracted from the SVD is shown in Fig. 5.14a. In agreement with the direct observation in Fig. 5.10b, d, the oscillation follows a damped sine function, which confirms an ISRS type of excitation mechanism (as illustrated in Chap. 2). The energy profile of the coherent component is instead mapped in Fig. 5.14b as a blue curve. Such energy profile is selected in correspondence to the time delay t_{max} at which the oscillation displays its maximum amplitude. We observe that the spectral response is characterized by a resonance around 2.10 eV. The energy profile for the same oscillation observed with the pump polarized along the *a*-axis is also shown (red curve). Due to the lower oscillation-to-background ratio, it can only be obtained at a few energy values, integrating over a wide energy range for each point. As discussed in detail in Chap. 2, the *absolute* Raman profile for a coherent mode can be retrieved only when the pump and the probe beams have the same polarization, while its shape depends solely on the probe direction. Consistent with this argument, we observe very similar lineshapes between the two Raman matrix elements shown in Fig. 5.14b. Therefore, it is sufficient to

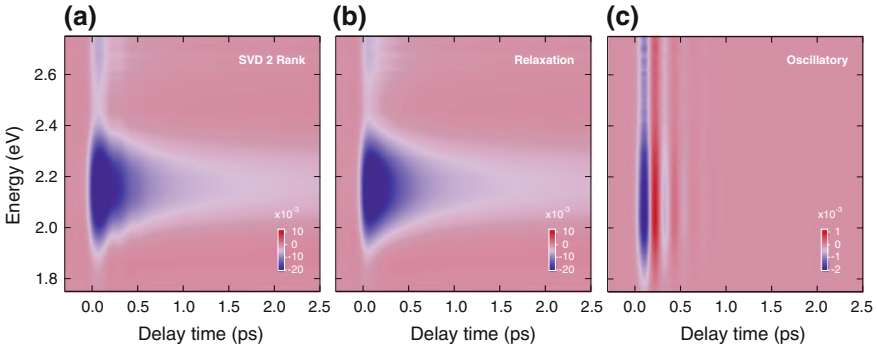

Fig. 5.13 Reconstruction of the data using the SVD results up to second rank. **a** Reconstructed data. **b** Relaxation and **c** oscillatory contributions

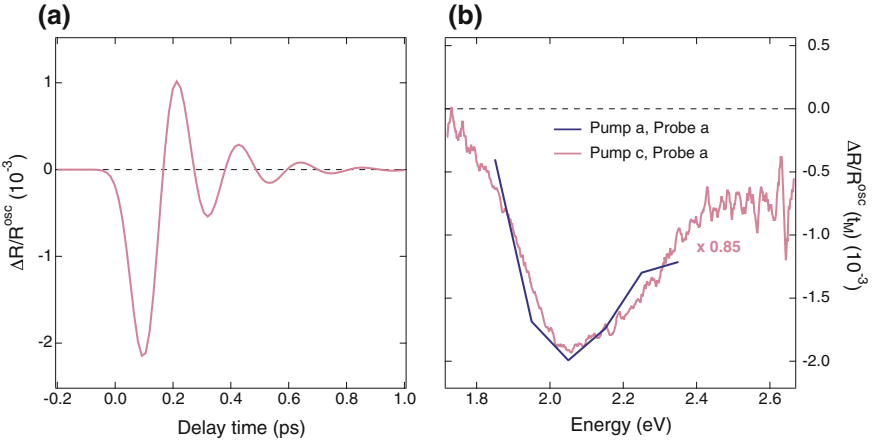

Fig. 5.14 **a** Oscillatory contribution obtained from the SVD at a probe photon energy of 2.10 eV. **b** ΔR/R energy profile of the coherent oscillation at $t = t_{max}$ for in-plane (blue) and out-of-plane (pink) excitation. The data with out-of-plane pump excitations are rescaled to match the intensity of the data with in-plane pump polarization

rescale the profile for the pump beam polarized along the *c*-axis to match the intensity of the case with the pump polarized along the *a*-axis. This allows the full ΔR/R profile to be obtained as if the pump was polarized along the *a*-axis.

Extracting the experimental Raman matrix element for the coherent optical phonon II opens the doors to the evaluation of the electron-phonon coupling for this specific lattice mode. In this regard, proper modeling of the optical response is required at a phenomenological or ab initio level. In the specific case of this single coherent optical phonon that is revealed upon below-gap photoexcitation, the presence of a slight amount of doping hinders a complete and reliable estimate of the electron-phonon matrix elements within the framework of six-band DMFT, as too computationally demanding. Therefore, to treat this case, we make use of a simple phenomenological theory that offers preliminary quantitative results. The theoretical analysis is reported in Sect. 5.5.1. Here, we proceed to describe a second class of experiments in the above-gap excitation regime, which allow us to go beyond the results presented in the current section and set the basis for a complete treatment via ab initio methods.

5.4.2 Above-Gap Excitation

The experiments performed in the previous section shed light on the strengths and the limitations of our approach. On one hand, the power of our methodology relies in the detection of the changes produced on the material high-energy CT excitation by a specific low-energy phonon mode, thus gaining selective insights into the

electron-phonon interaction. On the other hand, the small doping present in the sample prevents from a straightforward application of ab initio techniques to provide a microscopic evaluation of the electron-phonon matrix elements. Moreover, as the coherent optical phonon discussed in the previous section was triggered via the ISRS mechanism, it was coupled to a *virtual* charge density. Typically, one is also interested in evaluating the coupling between a *real* charge density that is generated upon above-gap excitation and the coherent optical phonons. Indeed, the question whether the photoexcited charge density across the gap possesses a large coupling to the optical phonon modes is particularly intriguing and still open. These arguments call for the evaluation of the nonequilibrium dynamics of the purely undoped La_2CuO_4 in response to a pump photon energy $\hbar\omega > 2.10\,\text{eV}$.

To overcome these limitations, we conceive a second set of experiments on a purely undoped (010)-oriented La_2CuO_4 to access the details of the anisotropic ultrafast dynamics and reveal the possible coupling of the photoexcited particle-hole excitations with the other A_g lattice modes. To this end, we tune the pump photoexcitation at 3.10 eV and perform a detailed polarization dependence at 10 K. When the pump polarization is set along the *a*-axis, the pump photon energy lies above the in-plane CT gap, thus promoting an electron in the UHB and leaving a hole behind in the O 2*p* band. On the contrary, when the pump polarization is set along the *c*-axis, excitations in the particle-hole continuum are generated. The changes in the material reflectivity are subsequently probed with a broadband continuum, which gives access to the high-energy electrodynamics of the system.

Figure 5.15a, c display the colour-coded maps of the $\Delta R/R$ response as a function of the probe photon energy and of the time delay between pump and probe at 10 K, for a probe polarization along the *a*- and *c*-axis, respectively. In both cases, the pump polarization is set along the *a*-axis and the absorbed pump fluence is estimated around $4.5\,\text{mJ/cm}^2$. The *a*-axis $\Delta R/R$ response is again characterized by the negative feature associated with the CT excitation around 2.15 eV. This response is consistent with previous studies of the in-plane charge dynamics [38]. Compared to the below-gap excitation scenario, the signal is one order of magnitude higher because of the increased sample absorption and the higher density of photoexcited particle-hole pairs. In addition, the high-energy region of the spectrum displays a sign inversion around 0.5 ps. The dynamics are governed by four relaxation time constants, which can be estimated at ∼60 fs, 1.6, 3.5 and 54 ps. The *c*-axis $\Delta R/R$ response in Fig. 5.15c shows instead a more complex behaviour, with two distinct regions of negative and positive photoinduced changes. These features are well displayed by selecting specific temporal traces across the probed spectral range, as evidenced in Fig. 5.15d. An extremely fast signal appears in the rise of the response during the first hundreds of femtoseconds, causing a sign inversion across the spectrum. The subsequent relaxation dynamics comprises a fast decay of 60 fs which is dominant in the low-energy side of the spectrum, an intermediate decay of 1.6 ps and a longer relaxation of 9 ps. On top of this incoherent response, a prominent oscillatory pattern clearly emerges across the whole spectrum.

To unravel the degree of anisotropy governing the *a*- and *c*-axis response, we compare two temporal traces selected from the colour-coded maps of Fig. 5.15a, c.

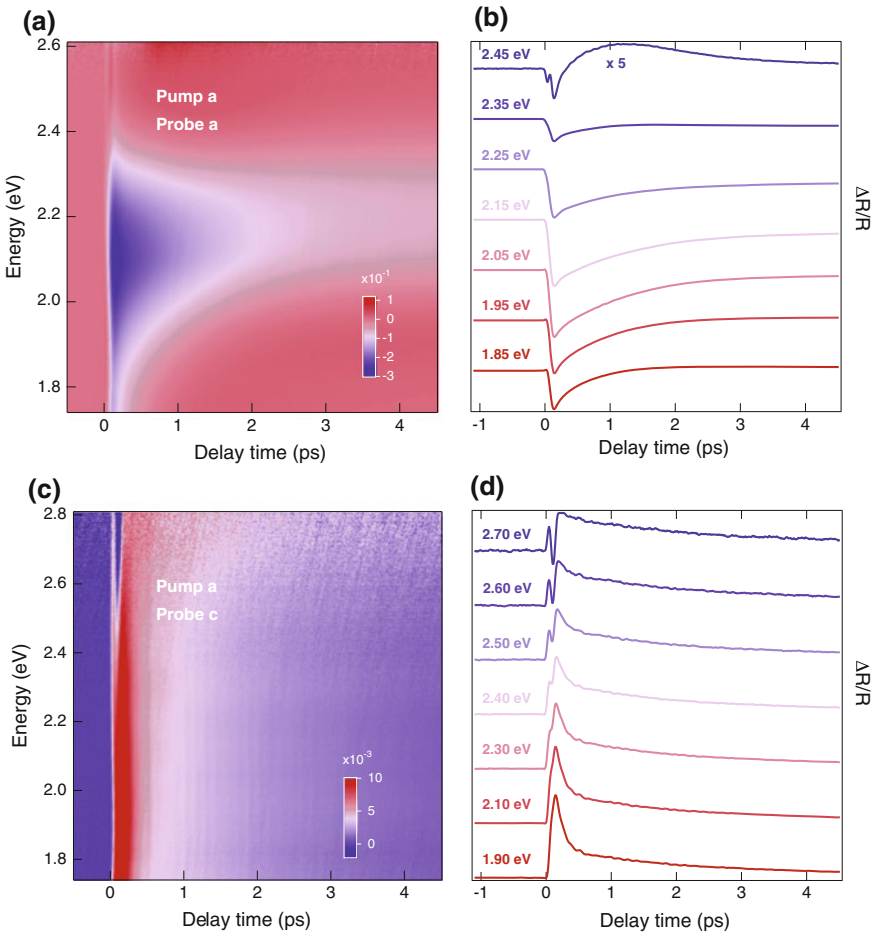

Fig. 5.15 **a**, **c** Colour-coded maps of ΔR/R at 10 K with in-plane pump polarization and **a** in-plane, **c** out-of-plane probe polarization. The pump photon energy is 3.10 eV and the absorbed pump fluence is 4.5 mJ/cm^2. **b**, **d** Temporal traces at specific probe photon energies of the respective ΔR/R maps. Each temporal trace results from the integration over 0.10 eV around the indicated probe photon energy

The results are shown in Fig. 5.16, in which the *c*-axis response has been multiplied by a factor of −20 to reach the amplitude of the *a*-axis response. It is evident that the *c*-axis relaxation dynamics is faster than its *a*-axis counterpart, which represents a signature of a more insulating behaviour shown by the out-of-plane charge transport. We also observe that, in the in-plane dynamics, the high signal intensity resulting from the CT excitation hides a clear manifestation of the coherent oscillations. In contrast, in the out-of-plane dynamics, a beating among several coherent modes is clearly distinguished and found to persist up to several picoseconds. The higher contrast for

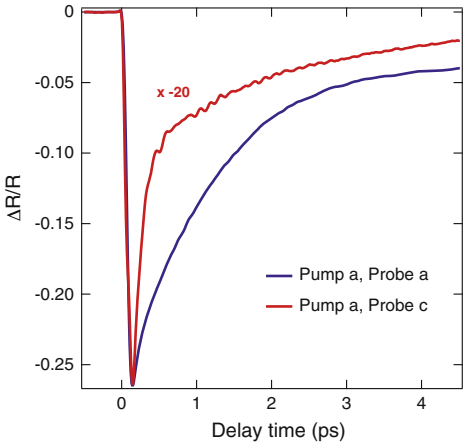

Fig. 5.16 Comparison between the in-plane (blue trace) and out-of-plane (red trace) temporal evolution at 2.10 eV upon in-plane photoexcitation. The pump photon energy is 3.10 eV and the absorbed pump fluence is 4.5 mJ/cm^2

the coherent modes along this probe polarization channel is related to the suppression of the incoherent excitations, which is also due to the more insulating character of the material along this axis. We will address the complete characterization of the coherent response later in this section. Here, we first gain complementary perspectives on the ultrafast incoherent dynamics from the analysis of the temporal evolution of the ΔR/R spectrum. We observe from Fig. 5.15d that the high-energy region of the spectrum is characterized by a very rapid response, which generates a spike-like feature in the first 80 fs. Thus, to identify peculiar trends in the evolution of the ultrafast response, we analyse the ΔR/R spectra by separating different temporal regimes.

Figure 5.17 shows the dynamics of the *a*-axis ΔR/R spectrum at different delay times. Panel (**a**) collects the transient spectra from 50 to 80 fs (corresponding to the first part of signal rise), in which the most remarkable feature is the emergence of an isosbestic point at 2.43 eV. Panel (**b**) shows the subsequent behaviour from 100 to 140 fs (still in correspondence to the rise of the signal), in which the spectral feature of the CT excitation does not modify its shape but undergoes a continuous redshift with time. Panel (**c**) depicts the first part of the relaxation dynamics between 140 fs and 1500 fs, in which the CT feature gradually modifies its shape and blueshifts over time; as a result, two positive wings develop at the edges of the detection window. Finally, for time delays larger than 1500 fs, two new isosbestic points set in at 1.83 and 2.32 eV.

We apply the same method of analysis to the *c*-axis ΔR/R response. This allows us to separate again the spectral evolution into four different temporal windows, as shown in Fig. 5.18. We observe the presence of an isosbestic point at 2.40 eV in the transient spectra from 50 to 80 fs (Panel (a)), accompanied by the development of a featureless ultrafast response. This featureless ΔR/R signal is monotonically decreasing for increasing photon energies and undergoes a continuous blueshift with time between 100 and 140 fs (Panel (b)). The relaxation dynamics sets in at 140 fs and can be divided into two distinct temporal windows. Between 140 and 300

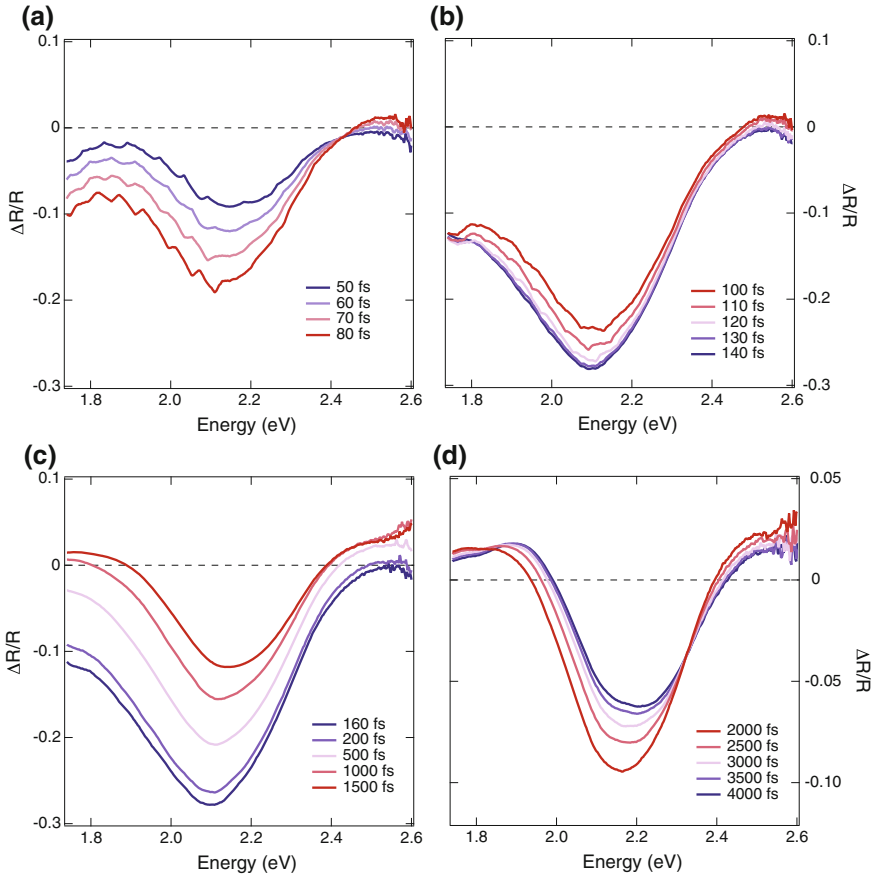

Fig. 5.17 In-plane ΔR/R spectrum at different delay times: **a** 50–80 fs, corresponding to the first rise of the signal; **b** 100–140 fs, which is still in correspondence to the rise; **c** 160–1500 fs, which represents the first step of the relaxation dynamics; **d** > 1500 fs, which shows the long-time relaxation of the in-plane response

fs the spectrum modifies its shape and approaches a constant behaviour (Panel (c)). Finally, for time delays larger than 300 fs, the ΔR/R response maintains a flat shape and simply decreases its weight over time.

Direct comparison of the spectral evolution along the *a*- and *c*-axis reveals insightful information on the microscopic phenomena occurring on our ultrafast timescale. First, we observe that both the in-plane and out-of-plane spectral responses are characterized by the presence of isosbestic points. When the isosbestic point manifests in the rise of the signal, it indicates that SW is redistributed from high- to low-energies around that particular energy; when the isosbestic point emerges in the decay, it reveals how the high-energy SW is recovered after the dynamical evolution of the system [4, 84]. In addition, two very rapid processes are found to emerge in the rise

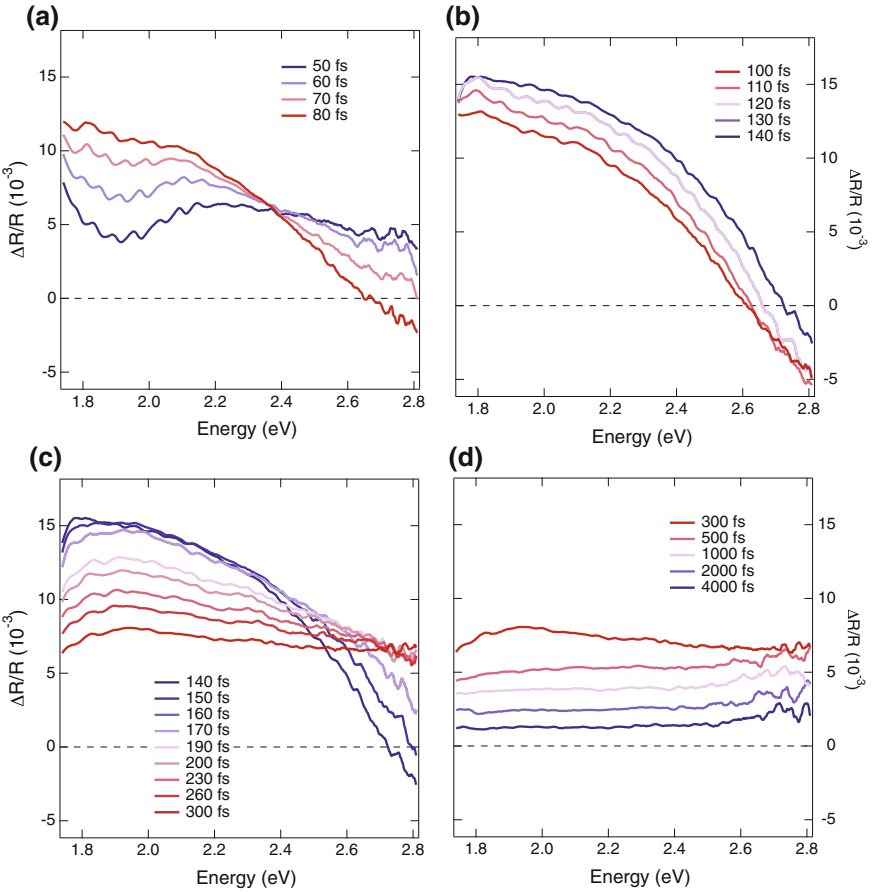

Fig. 5.18 Out-of-plane ΔR/R spectrum at different delay times: **a** 50–80 fs, corresponding to the first rise of the signal; **b** 100–140 fs, which is still in correspondence to the rise; **c** 140–300 fs, which represents the first step of the relaxation dynamics; (d) >300 fs, which shows the long-time relaxation of the out-of-plane response

of the response, within 140 fs. Due to the timescales involved, these phenomena must be of electronic origin. Consistent with this idea, a recent ultrafast broadband optical spectroscopy extending to the FIR spectral range identified the emergence of a photoinduced Drude contribution in the in-plane response of La_2CuO_4, which is the signature of a transient metallic state developing in the system. It was observed that SW is transferred from the high- to the low-energy region of the spectrum, giving rise to a bleach of the CT feature and to the rise of the Drude peak. As a result, both ΔA and ΔR/R in the region of the CT excitation start developing a negative sign in the transient spectra, in agreement with our *a*-axis response at early time delays. This bleach can be easily explained by assuming that the photoexcited carrier density within the O 2*p* band and the UHB block the CT transitions monitored by the probe

beam via a Pauli blocking mechanism. Remarkably, the similar timescale involved in the rise of the out-of-plane response strongly indicates that the transient metallic state at early time delays has an isotropic nature and induces a coherent transport of carriers also along the *c*-axis. At 140 fs the relaxation dynamics starts to occur: The coherence of the photoinduced charge fluctuation is maintained up to this time and the nonequilibrium charge density couples to the coherent optical modes manifesting in the decay of the transient signal. For long time-delays two positive features emerge at both the low- and high-energy tails of the spectrum, whose origin lies in the thermal heating of the sample upon pump photon absorption. The CT peak also undergoes a blueshift with time, as thermalization of the lattice proceeds (Fig. 5.17d). Along the *c*-axis, the thermal response of the material sets in already at 300 fs, as evidenced by the flat background in $\Delta R/R$ that decreases over time.

We finally address the coherent response emerging in the $\Delta R/R$ signal. An enlarged version of the temporal dynamics in the low-energy side of the *c*-axis spectrum is shown in Fig. 5.19a, in which the oscillatory pattern can be clearly distinguished. The trace has been integrated between 1.80 eV and 2.20 eV to reduce the noise level affecting the signal. Figure 5.19b displays the FT of the residuals obtained by fitting the relaxation dynamics.

From the FT analysis, we identify the presence of 5 collective modes taking part to the coherent dynamics triggered by the in-plane CT excitation. Their energies correspond to 15.2, 18.8, 28.7, 34.0 and 53.8 meV and are in perfect agreement with those of the 5 A_g modes reported in Table 5.1 (within the energy resolution of our FT, which is ± 0.9 meV). It is important to highlight that the appearance of the Raman-active coherent phonon modes occurs upon the excitation of real (i.e. not virtual) electronic transitions in the material. In other words, the system is opaque to

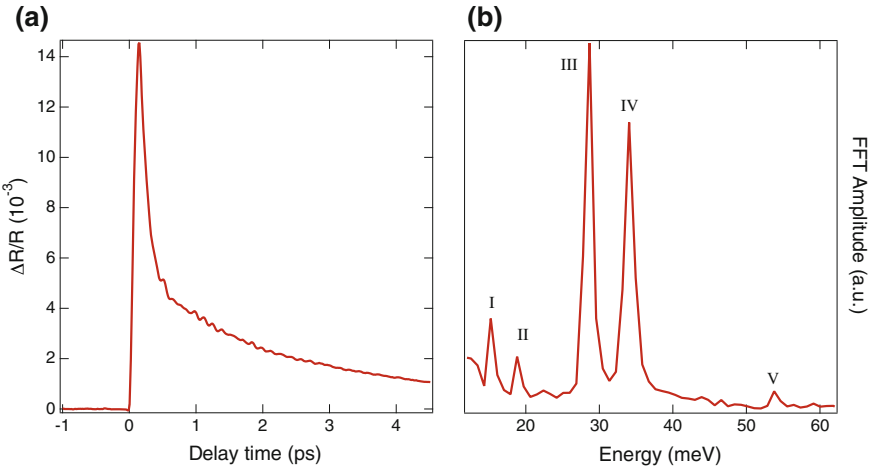

Fig. 5.19 **a** Temporal dynamics and **b** FT of the spectral region around 2.00 eV, averaged between 1.80 and 2.20 eV

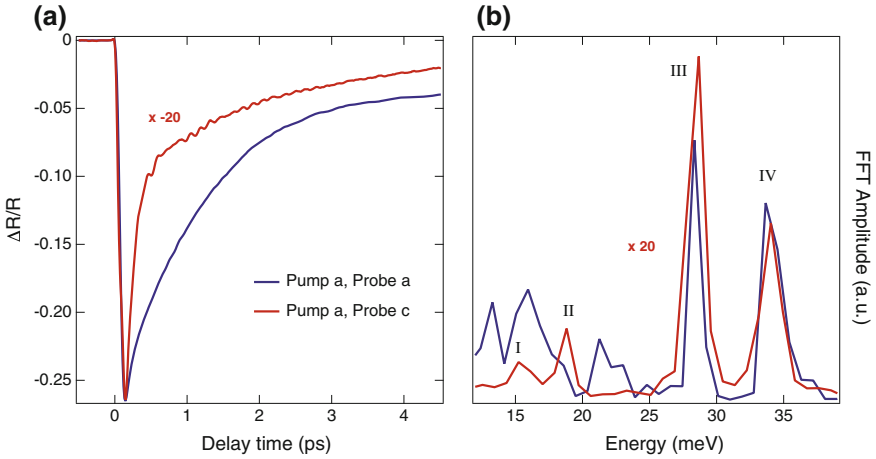

Fig. 5.20 Comparison between the in-plane (blue trace) and out-of-plane (red trace) coherent response at 2.10 eV upon in-plane photoexcitation. The pump photon energy is 3.10 eV and the absorbed pump fluence is 4.5 mJ/cm^2. **a** Temporal traces. **b** FT analysis

the pump photon energy. Hence, the origin of the totally-symmetric coherent optical phonons may lie in their coupling with a real charge fluctuation characterized by the same symmetry and promoted by the pump photoexcitation. In such a displacive scenario, a different Raman tensor comes into play with respect to the typical one describing the ISRS process that involves virtual electronic transitions [85]. As a result, the phonon amplitudes depend both on the pump photon energy and on the carrier relaxation time. More interestingly, in an anisotropic material, the Raman tensors are expected to be highly anisotropic and the coherent response can differ for the specific pump and probe polarizations selected in an experiment.

Before extracting the *c*-axis Raman profiles across the spectrum, we elucidate whether the observed coherent optical phonons have also an impact on the *a*-axis response of the material. To this aim, we perform the FT analysis of the two temporal traces selected around 2.10 eV (Fig. 5.20). As already observed, the coherent response is largely suppressed in the *a*-axis dynamics, as a consequence of the strong incoherent background arising from particle-hole excitations across the CT gap. Of the 5 A_g phonons modulating the *c*-axis reflectivity, only 2 of them (III and IV) have also a sizeable influence on the in-plane electrodynamics, namely the in-phase vibration of the La and apical O atoms and the vibrations of the in-plane O atoms along the *c*-axis. In contrast, no clear evidence of the mode II triggered via below-gap excitation is found. Due to the strong background, the *a*-axis Raman profiles for the observed phonons cannot be tracked.

Therefore, in the following, we only concentrate on the *c*-axis response and extract the mode Raman matrix elements. Since, to our knowledge, no resonant Raman experiment on La_2CuO_4 has ever been reported in literature, our Raman matrix elements could provide novel information about the origin of the *c*-axis electrodynamics

in La_2CuO_4. Indeed, the resonant enhancement of a mode in a specific spectral region elucidates the orbitals that play a central role in the underlying interband transitions. Given the high visibility of the modes with respect to the incoherent background and the presence of multiple modes, here the global fit analysis is preferable compared to the SVD. We select twenty temporal traces from the map displayed in Fig. 5.15c and perform the global fit by imposing the same relaxation times across the monitored spectral region. By calculating the FT of the residuals, we reconstruct the Raman profiles, which are shown in Fig. 5.21. The low intensity of mode V prevents us from extracting its energy dependence. We underline that identical results can be obtained by decreasing the absorbed fluence down to 1.7 mJ/cm^2, which represents the threshold allowed by the sensitivity of our pump-probe experiment.

As evident from Fig. 5.21, the coherent response of our pump-probe data is dominated by the optical phonon III, corresponding to the in-phase vibration between La and apical O atoms. The intensity of this mode shows a first feature around ∼2 eV, followed by a marked increase towards 2.70–2.80 eV. This Raman profile follows the spectral behaviour of the absorptive part of the optical conductivity (Fig. 5.5b), thus suggesting a displacive mechanism at play for this mode. The strong enhancement of the mode towards high energies is in agreement with the argument that the *c*-axis electrodynamics in the 2.60–3.00 eV spectral region is dominated by CT excitations from Cu to apical O states [4, 42, 55]. More interestingly, this mode was also revealed in the *c*-axis $\Delta R/R$ response of optimally-doped (OP) $La_{1.85}Sr_{0.15}CuO_4$ upon in-plane photoexcitation at 1.55 eV [41, 42]. Consistent with our measurements, also in this SC cuprate such phonon was found to resonate around 2.70–2.80 eV and its spectral fingerprint in the FTs was overlapped to a broad electronic background related to the Bogoliubov excitations at $2\Delta_{SC}$.

Mode IV, corresponding to the vibrations of the in-plane O along the *c*-axis, produce a sizeable effect in the region between 1.80 and 2.50 eV and resonate around

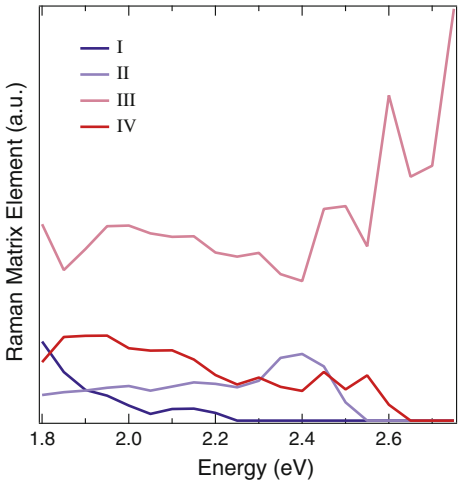

Fig. 5.21 Raman matrix elements for the 4 A_g modes extracted through a global fit analysis of the $\Delta R/R$ map at 10 K

2.00 eV. Thus, the resonant enhancement of both phonons III and IV around 2.00 eV allows us to conclude that the underlying interband transition is modulated by displacements along the *c*-axis of the material. Thus, the origin of this interband transition may lie in the transfer of a hole from a Cu atoms to a planar O of a contiguous plane. The estimate of the Madelung energy for such a process (∼2.00 eV) supports this scenario [42].

Mode II is the one retrieved by pumping the slightly-doped material at 1.55 eV (see Sect. 5.4.1). Differently from that experiment, in which we could only study the impact of this mode on the *a*-axis electrodynamics, here we can access its coupling to the *c*-axis charge excitations. While the phase of the mode for below-gap photoexcitation clearly indicated an ISRS mechanism at play, here the simultaneous emergence of several phonons hinders a reliable estimate of the individual phases. Based solely on the Raman profile analysis, it is difficult to identify the generation mechanism of mode II. An analogous situation applies with respect to the soft mode I, which manifests an increased strength in the low-energy region of the probed spectrum.

To establish whether the coherent response gets amplified or suppressed upon a change in the pump polarization, we finally measure the *c*-axis ΔR/R response while the material is pumped along the same axis at 3.10 eV. Figure 5.22a shows the colour-coded map of ΔR/R at 10 K as a function of probe photon energy and time delay between pump and probe. The absorbed pump fluence is set on purpose at ∼5.5 mJ/cm^2, i.e. exceeding the values used for the in-plane photoexcitation. Despite the higher fluence, we observe a weaker ΔR/R intensity, with dramatic changes also in the level of the modulation produced by the coherent lattice modes. In Fig. 5.22b,

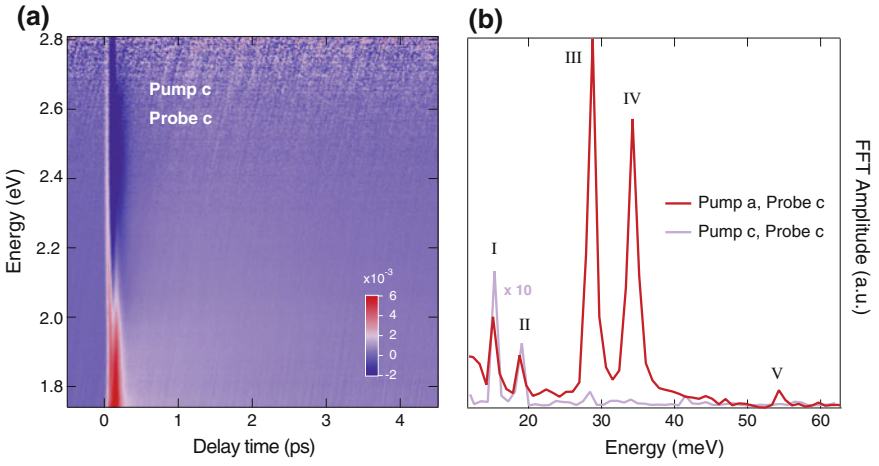

Fig. 5.22 **a** Colour-coded map of ΔR/R at 10 K with out-of-plane pump polarization and out-of-plane probe polarization. The pump photon energy is 3.10 eV and the absorbed pump fluence is 5.5 mJ/cm^2. **b** Comparison between the FTs of the spectral region around 2.00 eV (averaged between 1.80 and 2.20 eV), obtained upon in-plane (red curve) and out-of-plane (violet curve) photoexcitation

we show the FT of the residuals from a multiexponential fit of a temporal trace between 1.80 and 2.20 eV (violet curve) and its comparison with the FT obtained upon in-plane photoexcitation (red curve). Remarkably, when the material is pumped along the *c*-axis, only modes I and II are efficiently triggered, while modes III and IV are strongly suppressed or completely absent. This polarization analysis confirms the large anisotropy of the Raman profiles along the *a*- and *c*-axis of La_2CuO_4. In addition, irrespective of the details behind the generation mechanism of the observed phonon modes, we conclude that the photoexcited charge density in the CuO_2 planes strongly couples at least with the phonon modes III and IV, leading to a periodic structural elongation and compression of the CuO_6 octahedra along the *c*-axis. To explain this behaviour, a possible scenario is proposed in Sect. 5.6.

The complete mapping of the Raman profiles along the *c*-axis opens novel perspectives in the evaluation of the electron-phonon matrix elements for all A_g modes of La_2CuO_4 from ab initio calculations. This is of pivotal importance in the evaluation of possibly strongly coupled modes that can contribute to polaronic distortions. As La_2CuO_4 is governed by Mott physics, an ideal approach to address this problem is to reproduce its electrodynamics by means of DMFT. We discuss the current status of the calculations for our system in Sect. 5.5.2.

5.5 Extracting the Electron-Phonon Matrix Elements

In this Section, we set the basis for a complete evaluation of the electron-phonon matrix elements in a correlated electron system. To start from a simple situation, in Sect. 5.5.1 we present a phenomenological model in the case of the coherent optical phonon II triggered in $La_2CuO_{4+\delta}$ via ISRS for below-gap excitation. The model represents the first step towards more detailed ab initio estimates (Sect. 5.5.2).

5.5.1 Phenomenological Theory

Our approach is based on fitting the data of Fig. 5.14b using a phenomenological model of the in-plane dielectric function ε. In particular, we rely on a theory in which the final state of the optical absorption process consists of electron and hole polarons coupled to each other by a short range potential [21]. Hence, the absorption edge of $La_2CuO_{4+\delta}$ is modelled in terms of transitions between a VB and a CB modified by Coulomb interactions, which for simplicity are described by a momentum-independent matrix element U_{eh}, yielding

$$\varepsilon(E) = \varepsilon_\infty + s \cdot \frac{G(E)}{1 - U_{eh} G(E)}. \tag{5.3}$$

Here, the oscillator strength is parametrized by $s = 4\pi e^2 x_{eh}^2 / v_{Cu}$, where x_{eh} is a dipole matrix element between the Wannier orbitals of the two bands and v_{Cu} is the volume per Cu atom. We also define the electron-hole Green's function

$$G(E) \equiv \frac{2}{W} \int_{E_g}^{E_g+W} dE' \left(\frac{1}{E + E' + i\Gamma/2} - \frac{1}{E - E' + i\Gamma/2} \right), \tag{5.4}$$

where, due to the 2D character of the system, we assume a flat joint DOS $D = 2/W$ confined to a band of width W above the gap energy E_g. The bandwidth W of the absorption band is the sum of the electronic (single-particle) hole and electron bandwidths. The linewidth of the transition is given by half the (two-particle) phenomenological damping Γ, which we assume has a simple linear dependence on the frequency, $\Gamma = a + b \cdot E$. Notice that, rigorously speaking, this model holds for a stoichiometric compound, while the measured sample a small oxygen surplus. As discussed in Ref. [85], the small opacity caused by the excess oxygen introduces an imaginary component into the Raman tensor for the generation of the phonon. However, the doping is so small that its effect can be phenomenologically absorbed in small changes of the damping and other parameters.

According to the Born-Oppenheimer approximation, it is assumed that the electronic parameters of the model, like the DOS D and bandgap energy E_g, depend parametrically on the coherent ionic motion excited by the pump pulse. In our study, the equilibrium optical response of the slightly doped compound (Fig. 5.23, red curves) and the $\Delta R/R$ profile at the maximum of the oscillation (at time t_{max}, Fig. 5.24a) can be simultaneously fitted with only two parameter changes, $\delta E_g = 6.4$ meV, $\delta D = 4.6 \cdot 10^{-3}$ eV^{-1}. Physically, these are also the parameters expected

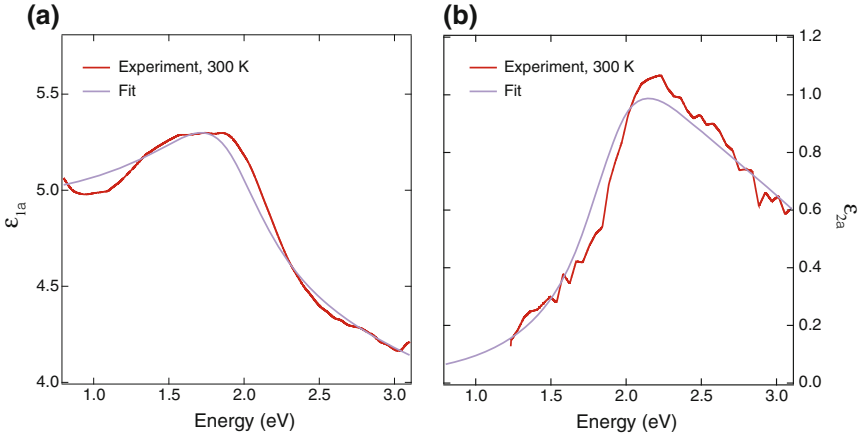

Fig. 5.23 **a** Real and **b** imaginary parts of the dielectric function along the *a*-axis (red curves), measured via SE at RT. The violet lines are fit to the data with the model of Ref. [21]

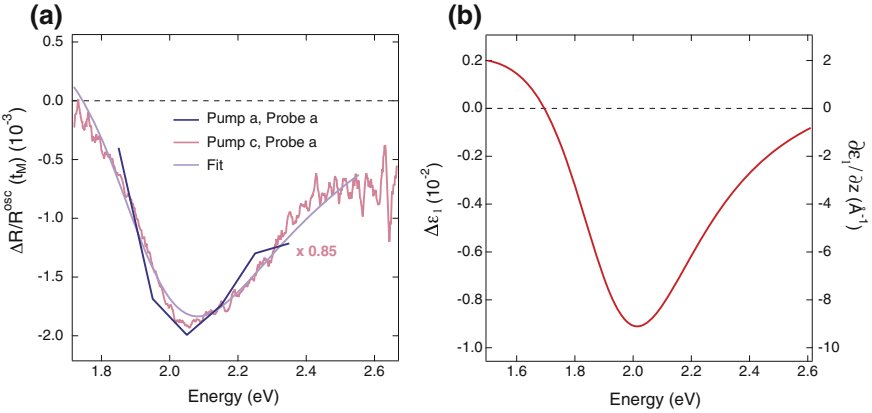

Fig. 5.24 **a** ΔR/R energy profile of the coherent oscillation at t = t_{max} for in-plane (blue) and out-of-plane (pink) excitation. The data with out-of-plane pump excitations are rescaled to match the intensity of the data with in-plane pump polarization. **b** Differential dielectric function $\Delta\epsilon_1$ corresponding to in-plane pump and probe polarizations at t = t_{max} (left scale). The absolute right scale was obtained as explained in the text

to be most sensitive to the La displacement involved in the phonon eigenvector. Figure 5.24b shows the differential dielectric function $\Delta\varepsilon_1$ corresponding to the oscillation amplitude at t_{max}. Neglecting the absorption part, we can represent its value at the pump energy as $\Delta\varepsilon(E_L) = \frac{\partial\varepsilon}{\partial z}(E_L)z_{max} = 1.8 \times 10^{-3}$. This equation, together with Eq. (2.14) (using for M the mass of one La atom moving in the volume $v_i = v_c/4$, v_c being the orthorhombic unit cell volume), yields a maximum amplitude $z_{max} = 1.0 \times 10^{-3}$ Å. We can use this value to calculate the absolute Raman profile $\partial\varepsilon/\partial z \equiv \Delta\varepsilon(E)/z_{max}$, shown in the right scale in Fig. 5.24b.

We are also able to evaluate the electron-phonon matrix elements $\partial E_g/\partial z \equiv \delta E_g/z_{max} = 6.4$ eV Å^{-1} describing the change of the CT gap with the La motion, and $\partial D/\partial z \equiv \delta D/z_{max} = 4.6$ eV^{-1} Å^{-1} describing the change in DOS. We point out that we fit the static data at 300 K of the slightly doped compound together with time-resolved data at 10 K. In spite of this discrepancy, the curves in Fig. 5.23 imply that the fit tends to an even lower energy for the CT peak, corresponding to an even higher temperature. A possible explanation for this is given by the very high electronic temperatures that are reached upon laser excitation.

To check the reliability of our estimate, we also use a simple ionic model and assume $\partial E_g/\partial z$ is approximately given by the change of the difference in Madelung energy among planar Cu and O atoms when the La is moved in the z direction. In this model, we neglect the displacement of the La ion along the x direction, as the displacement along z is the one that mostly affects the Madelung energies ε_{Cu} and ε_O of the Cu and O atoms in the *ab*-plane, changing the CT energy $\Delta = \varepsilon_{Cu} - \varepsilon_O \equiv E_g$ [86], as well as the DOS $D(\omega)$ in the band with width W. The electron-phonon matrix element $\partial E_g/\partial z$, reflecting the change in Madelung energies due to the displacement of ions along the z direction, can be easily estimated in point charge approximation.

To this end, we consider the effect of the displacement δz of the La atoms closest to the CuO_4 plaquette on the in-plane CT energy Δ. The atoms in question are the ones sitting above and below the plaquette. The energy Δ is given by difference in Madelung energies of the Cu and O atoms, $\Delta = \varepsilon_{Cu} - \varepsilon_O \equiv E_g$ [86]. Therefore, Δ is given as a function of the shortest La distance z from the Cu-O plane by

$$\begin{aligned}\Delta(z) &= \frac{Ze^2}{4\pi\varepsilon_0\varepsilon_R}\cdot\left(\frac{+4}{d_{La-Cu}}+\frac{-8}{d_{La-O}}\right)\\ &= \frac{Ze^2}{4\pi\varepsilon_0\varepsilon_R}\cdot\left(\frac{4}{\sqrt{\frac{a^2}{2}+z^2}}-\frac{8}{\sqrt{\frac{a^2}{4}+z^2}}\right),\end{aligned} \tag{5.5}$$

with the La charge $Z = 3$ and the unit cell length $a = 3.8$ Å, which is equivalent to twice the in-plane Cu-O distance. Note that there are two La atoms closest to each CuO_4 plaquette which are nearest neighbours to two Cu atoms and four O atoms each and that the Cu and O atoms carry a single charge, yielding the factors 4 and 8 in Eq. (5.5). For the relative dielectric constant ε_R, we use the value $\varepsilon_1(E_{CT}) = 5.3$ at the CT energy (see Fig. 5.23(a)) to account for screening effects. Using the equilibrium distance $z_0 = 1.79$ Å, we find an electron-phonon matrix element of $\frac{\partial E_g}{\partial z} \equiv \frac{\partial \Delta}{\partial z} = 4.3$ eV Å^{-1}, which is slightly lower than the previous value. We attribute this small discrepancy to the combination of two effects: (i) Our ionic model neglects the rotation of the CuO_6 octahedra involved in the phonon eigenvector; (ii) The strong covalency of the Cu-O bond, which makes the CT energy less sensitive to the change of Madelung energy with respect to what the simplified ionic estimate suggests.

In conclusion, in this Section we demonstrated that the combination of our ultrafast broadband optical spectroscopy data with suitable phenomenological modelling allows us to evaluate the sensitivity of the electronic Hamiltonian parameters to a specific lattice motion. The step further in our approach is represented by the application of first-principles calculations, since a more accurate quantitative estimate can be provided. We discuss this possibility in the following section.

5.5.2 *Ab Initio Calculations*

The final goal of our study will be to reproduce from first-principles how the *c*-axis optical response of the material reacts to selective displacements of the unit cell following the eigenvectors of the coherently excited optical modes. In this way, a direct comparison with the experiment can be obtained and the impact of the coherent motion on the different parameters of the electronic Hamiltonian unravelled. This is a formidable task in a correlated electron system such as La_2CuO_4, and thus calls for the use of state-of-the-art computational techniques. At the time of writing, the calculations are being performed and hold promise for understanding the elusive *c*-axis charge dynamics of undoped cuprates. We expect to clarify whether the

electron-phonon coupling strength is particularly strong for specific modes, leading to the localization of carriers as small polarons. A similar finding would also rationalise the origin of the broad boson sidebands observed in ARPES data [14].

5.6 Conclusions

In this chapter, our experimental method revealed novel aspects associated with the structural dynamics occurring in an undoped cuprate upon photoexcitation. Differently from previous broadband pump-probe experiments [35–38], the use of a systematic polarization dependence leads us to identify the impact of coherently generated Raman-active optical phonons on the *a*- and *c*-axis electrodynamic response of the material.

When the pump photon energy is tuned below the fundamental CT gap, one specific Raman-active coherent optical phonon has been observed. The combination of SVD and a theoretical treatment at the phenomenological level has enabled us to evaluate the electron-phonon matrix elements for this specific mode, overcoming the limitations of spontaneous Raman scattering measurements. In the past, a similar framework has been applied to simple semiconductors without electron-electron correlations [87, 88]. Extending this approach to correlated electron systems represents a new area of research, as it can provide insights into the electron-phonon coupling strength projected at the Γ point of the BZ and elucidate the existence of small polarons in many materials.

Concerning this latter point, more interesting results can be obtained when a real charge density is photoexcited in the system. In the past, this scenario has been explored by pumping undoped cuprates above the fundamental CT gap and monitoring the in-plane dynamical response in a broad spectral range from the FIR to the visible [35–37]. The rapid disappearance of the Drude response and the emergence of incoherent MIR bands suggested the freezing of the charge motion by the simultaneous action of electron-electron correlations and electron-boson coupling [25]. In our experiments, we go beyond the established results, by mapping a complex coherent structural rearrangement following the generation of particle-hole excitations on the CuO_2 planes. In this regard, it is pivotal to clarify the effect produced by the photoexcitation at 3.10 eV. Once the photons of the pump interact with the material, an excitation across the CT gap is performed, leading to the creation of electrons in the UHB and holes in the O 2*p* band. One possibility is that this type of excitation locally removes the JT distortion on the CuO_6 octahedra via the anti-JT effect. This picture has been explored theoretically in a number of works upon chemical doping (i.e. hole addition), showing how the apical O in the CuO_6 octahedra tends to approach the Cu^{2+} ions in order to gain attractive electrostatic energy. As a result, the elongated CuO_6 octahedra shrink upon hole doping. In our situation, the interaction with light at 3.10 eV has been demonstrated to *photodope* the system. Despite representing a two-particle process and being characterized by different properties compared to chemical doping, photodoping is expected to lead to a

similar removal of the local JT distortion. The pronounced coherences found upon in-plane photoexcitation may embody the fingerprint of the structural reorganisation that the lattice undergoes to save energy. In particular, the dominant phonon mode involves the coherent motion of the apical O and the La atoms along the *c*-axis, i.e. a displacement that is likely to follow the removal of the JT distortion. Remarkably, the Raman profile of this mode suggests the involvement of a displacive mechanism behind the phonon generation, thus reinforcing the idea of the strong coupling to the photogenerated carrier density. Consistent with this explanation, recent experiments on $La_{1.85}Sr_{0.15}CuO_4$ clearly showed the occurrence of a cosinusoidal response of this mode around a probe photon energy of 2.70 eV [41]. In La_2CuO_4, of particular interest is also the appearance of the apical O breathing mode, despite its low intensity. To shed light on the controversial aspect of small polaron formation in La_2CuO_4, the support of DMFT calculations will be crucial for extracting the electron-phonon matrix elements of all modes observed in the nonequilibrium response.

The extension of this framework across the phase diagram of $La_{2-x}Sr_xCuO_4$ also paves the way to understand how the electron-phonon coupling is renormalized upon hole doping. More interestingly, the investigation of other Raman-active excitations, such as bi-magnons or the coherent Bogoliubov QPs, will allow unravelling new details about the mechanism at the heart of high-T_C superconductivity. With this respect, performing experiments in a broad MIR range is of primary importance, in order to verify the presence of resonances associated with the Bogoliubov QPs in relation to the "MIR scenario" [12, 89, 90].

Finally, knowing the details of the Raman profile allows selecting the suitable pump photon energy at which the applied force on the collective mode of interest reaches its maximum strength. As a consequence, elucidating the Raman profiles of coherent modes opens the doors to the manipulation and control of the material properties on an ultrafast timescale.

References

1. P.W. Anderson, The resonating valence bond state in La_2CuO_4 and superconductivity. Science **235**(4793), 1196–1198 (1987)
2. A. Fujimori, E. Takayama-Muromachi, Y. Uchida, B. Okai, Spectroscopic evidence for strongly correlated electronic states in La-Sr-Cu and Y-Ba-Cu oxides. Phys. Rev. B **35**(16), 8814 (1987)
3. J. Zaanen, G.A. Sawatzky, J.W. Allen, Band gaps and electronic structure of transition-metal compounds. Phys. Rev. Lett. **55**(4), 418 (1985)
4. S. Uchida, T. Ido, H. Takagi, T. Arima, Y. Tokura, S. Tajima, Optical spectra of $La_{2-x}Sr_xCuO_4$: effect of carrier doping on the electronic structure of the CuO_2 plane. Phys. Rev. B **43**(10), 7942 (1991)
5. Z.-X. Shen, G.A. Sawatzky, Novel electronic structure of cuprate superconductors revealed by the anomalous spectral lineshape in ARPES experiments. Phys. Stat. Sol. (b) **215**(1), 523–529 (1999)
6. I. Affleck, J.B. Marston, Large-n limit of the Heisenberg-Hubbard Model: implications for high-T_c superconductors. Phys. Rev. B **37**(7), 3774 (1988)
7. G. Kotliar, J. Liu, Superexchange mechanism and d-wave superconductivity. Phys. Rev. B **38**(7), 5142 (1988)

8. J.P. Franck, D.M. Ginsberg. Physical properties of high temperature superconductors IV. World Sci, Singapore, p. 189 (1994)
9. Y. Tokura, N. Nagaosa, Orbital physics in transition-metal oxides. Science **288**(5465), 462–468 (2000)
10. Y. Yamada, O. Hino, S. Nohdo, R. Kanao, T. Inami, S. Katano, Polaron ordering in low-doping $La_{1-x}Sr_xMnO_3$. Phys. Rev. Lett. **77**(5), 904 (1996)
11. J.M. Tranquada, D.J. Buttrey, V. Sachan, J.E. Lorenzo, Simultaneous ordering of holes and spins in $La_2NiO_{4.125}$. Phys. Rev. Lett. **73**(7), 1003 (1994)
12. A.J. Leggett, A "midinfrared" scenario for cuprate superconductivity. Proc. Natl. Acad. Sci. **96**(15), 8365–8372 (1999)
13. P.W. Anderson, Is there glue in cuprate superconductors? Science **316**(5832), 1705–1707 (2007)
14. O. Rösch, O. Gunnarsson, X.J. Zhou, T. Yoshida, T. Sasagawa, A. Fujimori, Z. Hussain, Z.X. Shen, S. Uchida, Polaronic behavior of undoped high-T_c cuprate superconductors from angle-resolved photoemission spectra. Phys. Rev. Lett. **95**(22), 227002 (2005)
15. A. Lanzara, P.V. Bogdanov, X.J. Zhou, S.A. Kellar, D.L. Feng, E.D. Lu, T. Yoshida, H. Eisaki, A. Fujimori, K. Kishio et al., Evidence for ubiquitous strong electron-phonon coupling in high-temperature superconductors. Nature **412**(6846), 510–514 (2001)
16. G.-H. Gweon, T. Sasagawa, S.Y. Zhou, J. Graf, H. Takagi, D.-H. Lee, A. Lanzara, An unusual isotope effect in a high-transition-temperature superconductor. Nature **430**(6996), 187–190 (2004)
17. T. Kondo, R. Khasanov, J. Karpinski, S.M. Kazakov, N.D. Zhigadlo, Z. Bukowski, M. Shi, A. Bendounan, Y. Sassa, J. Chang, S. Pailhés, J. Mesot, J. Schmalian, H. Keller, A. Kaminski, Anomalies in the Fermi surface and band dispersion of quasi-one-dimensional CuO chains in the high-temperature superconductor $YBa_2Cu_4O_8$. Phys. Rev. Lett. **105**(26), 267003 (2010)
18. M. d'Astuto, P.K. Mang, P. Giura, A. Shukla, P. Ghigna, A. Mirone, M. Braden, M. Greven, M. Krisch, F. Sette, Anomalous dispersion of longitudinal optical phonons in $Nd_{1.86}Ce_{0.14}CuO_{4+\delta}$ determined by inelastic x-ray scattering. Phys. Rev. Lett. **88**(16), 167002 (2002)
19. D. Reznik, L. Pintschovius, M. Ito, S. Iikubo, M. Sato, H. Goka, M. Fujita, K. Yamada, G.D. Gu, J.M. Tranquada, Electron-phonon coupling reflecting dynamic charge inhomogeneity in copper oxide superconductors. Nature **440**(7088), 1170–1173 (2006)
20. J. Lee, K. Fujita, K. McElroy, J.A. Slezak, M. Wang, Y. Aiura, H. Bando, M. Ishikado, T. Masui, J.-X. Zhu et al., Interplay of electron-lattice interactions and superconductivity in $Bi_2Sr_2CaCu_2O_{8+\delta}$. Nature **442**(7102), 546–550 (2006)
21. J.P. Falck, A. Levy, M.A. Kastner, R.J. Birgeneau, Charge-transfer spectrum and its temperature dependence in La_2CuO_4. Phys. Rev. Lett. **69**(7), 1109 (1992)
22. C.M. Varma, S. Schmitt-Rink, E. Abrahams, Charge transfer excitations and superconductivity in "ionic" metals. Sol. State Comm. **62**(10), 681–685 (1987)
23. T.M. Rice, F.C. Zhang, Frequency-dependent conductivity from carriers in Mott insulators. Phys. Rev. B **39**(1), 815 (1989)
24. J. Inoue, S. Maekawa, Dynamics of holes in antiferromagnetic state. J. Phys. Soc. Jpn. **59**(6), 2110–2123 (1990)
25. A.S. Mishchenko, N. Nagaosa, Z.-X. Shen, G. De Filippis, V. Cataudella, T.P. Devereaux, C. Bernhard, K.W. Kim, J. Zaanen, Charge dynamics of doped holes in high T_c cuprate superconductors: a clue from optical conductivity. Phys. Rev. Lett. **100**(16), 166401 (2008)
26. J.M. Tranquada, B.J. Sternlieb, J.D. Axe, Y. Nakamura, S. Uchida, Evidence for stripe correlations of spins and holes in copper oxide superconductors. Nature **375**(6532), 561–563 (1995)
27. G. Ghiringhelli, M. Le Tacon, M. Minola, S. Blanco-Canosa, C. Mazzoli, N.B. Brookes, G.M. De Luca, A. Frano, D.G. Hawthorn, F. He, Long-range incommensurate charge fluctuations in (Y, Nd)$Ba_2Cu_3O_{6+x}$. Science **303**(6096), 821–825 (2012)
28. J. Chang, E. Blackburn, A.T. Holmes, N.B. Christensen, J. Larsen, J. Mesot, R. Liang, D.A. Bonn, W.N. Hardy, A. Watenphul, Direct observation of competition between superconductivity and charge density wave order in $YBa_2Cu_3O_{6.67}$. Nat. Phys. **8**(12), 871–876 (2012)

29. J. Lorenzana, C. Castellani, C. Di Castro, Phase separation frustrated by the long-range Coulomb interaction. I. Theory. Phys. Rev. B **64**(23), 235127 (2001)
30. Z.X. Shen, A. Lanzara, S. Ishihara, N. Nagaosa, Role of the electron-phonon interaction in the strongly correlated cuprate superconductors. Phil. Mag. B **82**(13), 1349–1368 (2002)
31. J. Callaway, D.P. Chen, D.G. Kanhere, Q. Li, Pairing in finite cluster models. Physica B **163**(1–3), 127–128 (1990)
32. C.J. Thompson, T. Matsubara, A unified statistical mechanical approach to high-temperature superconductivity, in *Studies of High Temperature Superconductors* (1991)
33. A. Macridin, G.A. Sawatzky, M. Jarrell, Two-dimensional Hubbard-Holstein bipolaron. Phys. Rev. B **69**(24), 245111 (2004)
34. G. De Filippis, V. Cataudella, E.A. Nowadnick, T.P. Devereaux, A.S. Mishchenko, N. Nagaosa, Quantum dynamics of the Hubbard-Holstein model in equilibrium and nonequilibrium: application to pump-probe phenomena. Phys. Rev. Lett. **109**(17), 176402 (2012)
35. O. Matsuda, O.B. Wright, D.H. Hurley, V.E. Gusev, K. Shimizu, Coherent shear phonon generation and detection with ultrashort optical pulses. Phys. Rev. Lett. **93**(9), 095501 (2004)
36. H. Okamoto, T. Miyagoe, K. Kobayashi, H. Uemura, H. Nishioka, H. Matsuzaki, A. Sawa, Y. Tokura, Ultrafast charge dynamics in photoexcited Nd_2CuO_4 and La_2CuO_4 cuprate compounds investigated by femtosecond absorption spectroscopy. Phys. Rev. B **82**(6), 060513 (2010)
37. H. Okamoto, T. Miyagoe, K. Kobayashi, H. Uemura, H. Nishioka, H. Matsuzaki, A. Sawa, Y. Tokura, Photoinduced transition from mott insulator to metal in the undoped cuprates Nd_2CuO_4 and La_2CuO_4. Phys. Rev. B **83**(12), 125102 (2011)
38. F. Novelli, G. De Filippis, V. Cataudella, M. Esposito, I. Vergara, F. Cilento, E. Sindici, A. Amaricci, C. Giannetti, D. Prabhakaran et al., Witnessing the formation and relaxation of dressed quasi-particles in a strongly correlated electron system. Nat. Comm., 5 (2014)
39. S. Sugai, H. Suzuki, Y. Takayanagi, T. Hosokawa, N. Hayamizu, Carrier-density-dependent momentum shift of the coherent peak and the LO phonon mode in p-type high-T_c superconductors. Phys. Rev. B **68**(18), 184504 (2003)
40. E.T. Heyen, S.N. Rashkeev, I.I. Mazin, O.K. Andersen, R. Liu, M. Cardona, O. Jepsen, Resonant Raman scattering in $YBa_2Cu_3O_7$: band theory and experiment. Phys. Rev. Lett. **65**, 3048–3051 (1990)
41. B. Mansart, J. Lorenzana, A. Mann, A. Odeh, M. Scarongella, M. Chergui, F. Carbone, Coupling of a high-energy excitation to superconducting quasiparticles in a cuprate from coherent charge fluctuation spectroscopy. Proc. Natl. Acad. Sci. **110**(12), 4539–4544 (2013)
42. J. Lorenzana, B. Mansart, A. Mann, A. Odeh, M. Chergui, F. Carbone, Investigating pairing interactions with coherent charge fluctuation spectroscopy. Eur. Phys. J. Spec. Top. **222**(5), 1223–1239 (2013)
43. J. Zaanen, G.A. Sawatzky, The electronic structure and super exchange interactions in transition-metal compounds. Can. J. Phys. **65**(10), 1262–1271 (1987)
44. J. Hubbard, Electron correlations in narrow energy bands, in *Proceedings of the Royal Society of London a: Mathematical, Physical and Engineering Sciences*, vol. 276, pp. 238–257. The Royal Society (1963)
45. V.J. Emery, Theory of high-T_c superconductivity in oxides. Phys. Rev. Lett. **58**(26), 2794 (1987)
46. F.C. Zhang, T.M. Rice, Effective Hamiltonian for the superconducting Cu oxides. Phys. Rev. B **37**(7), 3759 (1988)
47. A. Georges, G. Kotliar, W. Krauth, M.J. Rozenberg, Dynamical mean-field theory of strongly correlated fermion systems and the limit of infinite dimensions. Rev. Mod. Phys. **68**(1), 13 (1996)
48. G. Kotliar, S.Y. Savrasov, K. Haule, V.S. Oudovenko, O. Parcollet, C.A. Marianetti, Electronic structure calculations with dynamical mean-field theory. Rev. Mod. Phys. **78**(3), 865 (2006)
49. T. Maier, M. Jarrell, T. Pruschke, M.H. Hettler, Quantum cluster theories. Rev. Mod. Phys. **77**(3), 1027 (2005)
50. C. Weber, K. Haule, G. Kotliar, Strength of correlations in electron-and hole-doped cuprates. Nat. Phys. **6**(8), 574–578 (2010)

51. C. Weber, K. Haule, G. Kotliar, Optical weights and waterfalls in doped charge-transfer insulators: a local density approximation and dynamical mean-field theory study of $La_{2-x}Sr_xCuO_4$. Phys. Rev. B **78**(13), 134519 (2008)
52. C. Weber, K. Haule, G. Kotliar, Apical oxygens and correlation strength in electron-and hole-doped copper oxides. Phys. Rev. B **82**(12), 125107 (2010)
53. D.S. Ellis, J.P. Hill, S. Wakimoto, R.J. Birgeneau, D. Casa, T. Gog, Y.-J. Kim, Charge-transfer exciton in La_2CuO_4 probed with resonant inelastic x-ray scattering. Phys. Rev. B **77**(6), 060501 (2008)
54. E. Collart, A. Shukla, J.P. Rueff, P. Leininger, H. Ishii, I. Jarrige, Y.Q. Cai, S.-W. Cheong, G. Dhalenne, Localized and delocalized excitons: resonant inelastic x-ray scattering in $La_{2-x}Sr_xNiO_4$ and $La_{2-x}Sr_xCuO_4$. Phys. Rev. Lett. **96**(15), 157004 (2006)
55. S. Uchida, K. Tamasaku, S. Tajima, c-Axis optical spectra and charge dynamics in $La_{2-x}Sr_xCuO_4$. Phys. Rev. B **53**(21), 14558 (1996)
56. S. Nimori, S. Sakita, F. Nakamura, T. Fujita, H. Hata, N. Ogita, M. Udagawa, Electron-phonon interaction in $La_{2-x}Sr_xCuO_4$ investigated by Raman scattering. Phys. Rev. B **62**(6), 4142 (2000)
57. S. Sugai, Phonon Raman scattering in $(La_{1-x}Sr_x)_2CuO_4$ single crystals. Phys. Rev. B **39**(7), 4306 (1989)
58. W.H. Weber, C.R. Peters, E.M. Logothetis, Raman studies of lanthanum cuprate superconductors. J. Opt. Soc. Am. B **6**(3), 455–464 (1989)
59. E. Liarokapis, E. Siranidi, D. Lampakis, K. Conder, C. Panagopoulos, Lattice effects in the $La_{2-x}Sr_xCuO_4$ compounds. J. Phys.: Condens. Matter **20**(43), 434233 (2008)
60. C.J. Stevens, D. Smith, C. Chen, J.F. Ryan, B. Podobnik, D. Mihailovic, G.A. Wagner, J.E. Evetts, Evidence for two-component high-temperature superconductivity in the femtosecond optical response of $YBa_2Cu_3O_{7-\delta}$. Phys. Rev. Lett. **78**(11), 2212 (1997)
61. D. Lampakis, D. Palles, E. Liarokapis, C. Panagopoulos, J.R. Cooper, H. Ehrenberg, T. Hartmann, Phase transitions and Raman spectra correlations in $La_{2-x}Sr_xCuO_4$ ($0.0 < \sim X < \sim 0.45$). Phys. Rev. B **62**(13), 8811 (2000)
62. M. Mostoller, J. Zhang, A.M. Rao, P.C. Eklund, Lattice vibrations in La_2CuO_4. Phys. Rev. B **41**(10), 6488 (1990)
63. S.L. Chaplot, W. Reichardt, L. Pintschovius, N. Pyka, Common interatomic potential model for the lattice dynamics of several cuprates. Phys. Rev. B **52**(10), 7230 (1995)
64. C.-Z. Wang, R. Yu, H. Krakauer, First-principles calculations of phonon dispersion and lattice dynamics in La_2CuO_4. Phys. Rev. B **59**(14), 9278 (1999)
65. A. Othonos, Probing ultrafast carrier and phonon dynamics in semiconductors. Jpn. J. Appl. Phys. **83**(4), 1789–1830 (1998)
66. A. Furube, T. Asahi, H. Masuhara, H. Yamashita, M. Anpo, Charge carrier dynamics of standard TiO_2 catalysts revealed by femtosecond diffuse reflectance spectroscopy. J. Phys. Chem. B **103**(16), 3120–3127 (1999)
67. Y. Tamaki, A. Furube, R. Katoh, M. Murai, K. Hara, H. Arakawa, M. Tachiya, Trapping dynamics of electrons and holes in a nanocrystalline TiO_2 film revealed by femtosecond visible/near-infrared transient absorption spectroscopy. Cr. Chim. **9**(2), 268–274 (2006)
68. Y. Tamaki, K. Hara, R. Katoh, M. Tachiya, A. Furube, Femtosecond visible-to-IR spectroscopy of TiO_2 nanocrystalline films: elucidation of the electron mobility before deep trapping. J. Phys. Chem. C **113**(27), 11741–11746 (2009)
69. V.P. Zhukov, E.V. Chulkov, Ab initio calculations of the electron-phonon interaction and characteristics of large polarons in rutile and anatase. Phys. Sol. State **56**(7), 1302–1309 (2014)
70. J.T. Devreese, S.N. Klimin, J.L.M. van Mechelen, D. van der Marel, Many-body large polaron optical conductivity in $SrTi_{1-x}Nb_xO_3$. Phys. Rev. B **81**(12), 125119 (2010)
71. S. Moser, L. Moreschini, J. Jaćimović, O.S. Barišić, H. Berger, A. Magrez, Y.J. Chang, K.S. Kim, A. Bostwick, E. Rotenberg, Tunable polaronic conduction in anatase TiO_2. Phys. Rev. Lett. **110**(19), 196403 (2013)
72. A. Cavalleri, C. Tóth, C.W. Siders, J.A. Squier, F. Ráksi, P. Forget, J.C. Kieffer, Femtosecond structural dynamics in VO_2 during an ultrafast solid-solid phase transition. Phys. Rev. Lett. **87**(23), 237401 (2001)

73. D.J. Hilton, R.P. Prasankumar, S. Fourmaux, A. Cavalleri, D. Brassard, M.A. El Khakani, J.C. Kieffer, A.J. Taylor, R.D. Averitt, Enhanced photosusceptibility near T_c for the light-induced insulator-to-metal phase transition in vanadium dioxide. Phys. Rev. Lett. **99**(22), 226401 (2007)
74. J.A. Johnson, T. Kubacka, M.C. Hoffmann, C. Vicario, S. de Jong, P. Beaud, S. Grübel, S.-W. Huang, L. Huber, Y.W. Windsor, E.M. Bothschafter, L. Rettig, M. Ramakrishnan, A. Alberca, L. Patthey, Y.-D. Chuang, J.J. Turner, G.L. Dakovski, W.-S. Lee, M.P. Minitti, W. Schlotter, R.G. Moore, C.P. Hauri, S.M. Koohpayeh, V. Scagnoli, G. Ingold, S.L. Johnson, U. Staub, Magnetic order dynamics in optically excited multiferroic $TbMnO_3$. Phys. Rev. B **92**, 184429 (2015)
75. M. Eckstein, P. Werner, Photoinduced states in a Mott insulator. Phys. Rev. Lett. **110**, 126401 (2013)
76. M. Eckstein, P. Werner, Thermalization of a pump-excited Mott insulator. Phys. Rev. B **84**, 035122 (2011)
77. P. Werner, K. Held, M. Eckstein, Role of impact ionization in the thermalization of photoexcited Mott insulators. Phys. Rev. B **90**, 235102 (2014)
78. J.H. Mentink, M. Eckstein, Ultrafast quenching of the exchange interaction in a Mott insulator. Phys. Rev. Lett. **113**, 057201 (2014)
79. Y.H. Kim, S.-W. Cheong, Z. Fisk, Dynamics of photogenerated charge carriers in cuprates. Phys. Rev. Lett. **67**, 2227–2230 (1991)
80. H. Okamoto, H. Matsuzaki, T. Wakabayashi, Y. Takahashi, T. Hasegawa, Photoinduced metallic state mediated by spin-charge separation in a one-dimensional organic Mott insulator. Phys. Rev. Lett. **98**(3), 037401 (2007)
81. S. Wall, D. Brida, S.R. Clark, H.P. Ehrke, D. Jaksch, A. Ardavan, S. Bonora, H. Uemura, Y. Takahashi, T. Hasegawa et al., Quantum interference between charge excitation paths in a solid-state Mott insulator. Nat. Phys. **7**(2), 114–118 (2011)
82. S. Iwai, M. Ono, A. Maeda, H. Matsuzaki, H. Kishida, H. Okamoto, Y. Tokura, Ultrafast optical switching to a metallic state by photoinduced Mott transition in a halogen-bridged nickel-chain compound. Phys. Rev. Lett. **91**(5), 057401 (2003)
83. T.E. Stevens, J. Kuhl, R. Merlin, Coherent phonon generation and the two stimulated Raman tensors. Phys. Rev. B **65**(14), 144304 (2002)
84. M. Eckstein, M. Kollar, D. Vollhardt, Isosbestic points in the spectral function of correlated electrons. J. Low Temp. Phys. **147**(3–4), 279–293 (2007)
85. J.J. Li, J. Chen, D.A. Reis, S. Fahy, R. Merlin, Optical probing of ultrafast electronic decay in Bi and Sb with slow phonons. Phys. Rev. Lett. **110**(4), 047401 (2013)
86. F. Carbone, N. Gedik, J. Lorenzana, A.H. Zewail, Real-time observation of cuprates structural dynamics by ultrafast electron crystallography. (Adv. Cond. Matt, Phys. 2010)
87. C.A.D. Roeser, A.M.-T. Kim, J.P. Callan, L. Huang, E.N. Glezer, Y. Siegal, E. Mazur, Femtosecond time-resolved dielectric function measurements by dual-angle reflectometry. Rev. Sci. Instr. **74**(7), 3413–3422 (2003)
88. S.I. Kudryashov, M. Kandyla, C.A.D. Roeser, E. Mazur, Intraband and interband optical deformation potentials in femtosecond-laser-excited α-Te. Phys. Rev. B **75**(8), 085207 (2007)
89. A.J. Leggett, Where is the energy saved in cuprate superconductivity? J. Phys. Chem. Solids **59**(10), 1729–1732 (1998)
90. A.J. Leggett, Cuprate superconductivity: dependence of T_C on the c-axis layering structure. Phys. Rev. Lett. **83**(2), 392 (1999)

Chapter 6
Disentangling the Signatures of Precursor Superconductivity in Cuprates

The short coherence length ($\xi_0 \sim 1$ nm) of Cooper pairs in cuprate high-T_C superconductors allows for a variety of fascinating phenomena in contrast to low-T_C materials, which have homogeneous SC properties on length scales of the order of several hundreds or thousands of nanometers [1]. On one hand, superconductivity and other electronic states can coexist in cuprates, with disorder tipping the balance on a local scale [2]. On the other hand, thermal and quantum fluctuations of the SC order parameter can play an important role because of the reduced dimensionality (layered structure) of the material. Thus, understanding the interplay between SC fluctuations, inhomogeneities, competing orders and reduced dimensionality remains a major challenge in cuprate physics.

Several temperature scales have been identified in the cuprates phase diagram (Fig. 6.1a), which presumably result from the above interplay, but whose precise meaning is far from being understood. Below T^*, the PG state appears (Fig. 6.1a, grey circles) [3–6]. Early ideas [7–9] suggested that the PG reflected the presence of pairing correlations without long-range phase coherence. Another line of thought postulates the existence of a different kind of incipient electronic order [10–18] competing with superconductivity. Traces of such orders have been seen in different regions of the phase diagram, as stripes [19, 20], nematic [21], time-reversal symmetry breaking [22] and incommensurate CDWs [17, 23–25].

More recent experiments give support to the competing scenario, by showing a temperature scale for precursor effects with a doping dependence quite different from T^*. For example, STM reveals that local pairing correlations can be detected up to several tens of kelvin above T_C at optimal doping (Fig. 6.1a, brown squares) [26, 27]. ARPES provides a similar temperature scale [28, 29]. In addition, local probes show the inhomogeneous nature of the phenomena [26, 27, 30]. Nernst effect [31] (Fig. 6.1a, violet triangles) and magnetization measurements [32] (Fig. 6.1a, violet

Parts of Chap. 6 are reprinted with permission from E. Balding et al., Physical Review B 95, 024501. Copyright 2017 American Physical Society.

E. Baldini, *Nonequilibrium Dynamics of Collective Excitations in Quantum Materials*, Springer Theses, https://doi.org/10.1007/978-3-319-77498-5_6

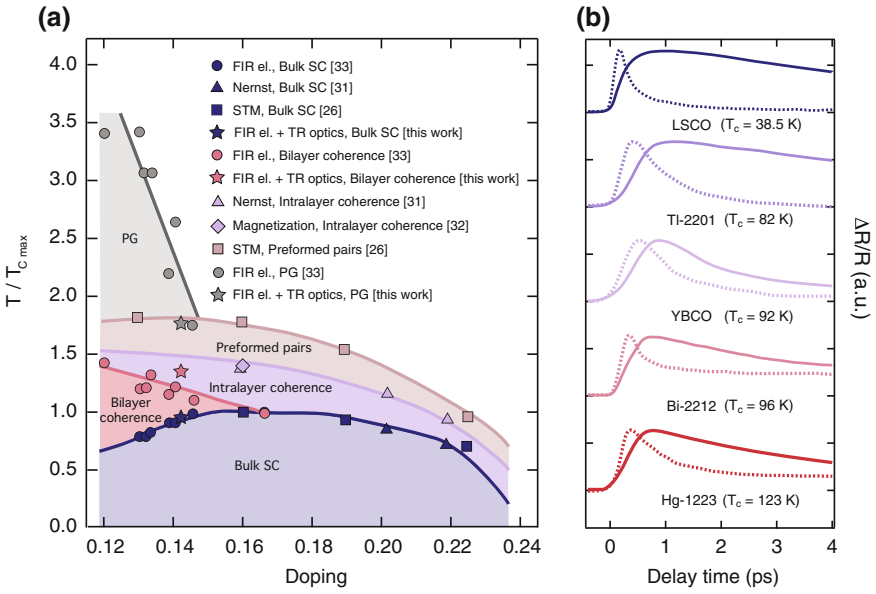

Fig. 6.1 **a** Phase diagram for bilayer cuprates displaying the temperature scale for precursor SC phenomena. The data points have been obtained by a number of experimental studies: STM [26], Nernst effect [31], magnetization [32], FIR SE [33] and this work. Symbols and colours are highlighted in the label. **b** Normalized single-wavelength $\Delta R/R$ traces collected in the SC (solid lines) and normal (dashed lines) states on different OP cuprates under comparable experimental conditions. Data have been adapted from Refs. [34–37]. The T_C for each material is indicated in the figure

diamonds) show another crossover line where precursor diamagnetic effects appear, requiring some degree of intralayer coherence.

In the case of bilayer materials, the FIR *c*-axis conductivity provides additional information. The response can be well described by a multilayer model of coupled bilayers separated by poorly conducting regions [33, 38]. In this case, precursor effects appear as an increase in the Drude SW due to the coherent transport between neighboring layers. Such a bilayer coherence requires substantial intralayer coherence to set in first, and indeed it appears closer to T_C (Fig. 6.1a, red circles). For example, in OP materials, the onset of the bilayer coherence coincides with T_C and only in the UD samples the bilayer onset temperature (T_{ONS}) separates from T_C, remaining always clearly below the PG temperature T^* [33, 39].

In the previous Chapters, we showed that a powerful strategy for disentangling the interplay between different competing states is to separate their contributions directly in real time via pump-probe spectroscopy. This technique allows to perturb the equilibrium between different states with a pump pulse and to subsequently study their incoherent recovery time or the dynamics of coherent modes linked to the perturbed states. In this regard, special attention has been reserved to the transient optical

response of cuprate superconductors in the near-infrared/visible spectral range [34–37, 40–50]. In OP cuprates, pump-probe spectroscopy provides a simple picture, as shown in Fig. 6.1b, where we collect a number of single-wavelength transient reflectivity ($\Delta R/R$) data below T_C (solid lines) and above T_C (dashed lines) on a variety of OP materials under comparable experimental conditions [34–37]. In the normal-state above T_C, a fast relaxation of several hundreds of femtoseconds appears. This is typically attributed to the cooling of a hot quasi-equilibrium electron gas, giving rise to a response similar to that observed in metals (the PG signal does not manifest in OP cuprates, see Fig. 6.1a. Below T_C, the dynamics is instead dominated by a slow relaxation component τ_{QP} of several picoseconds, attributed to the recombination of Bogoliubov quasiparticles (QPs) into pairs. Indeed, the relaxation dynamics of this QP response is very well described by the Rothwarf-Taylor model [46, 51] and is directly related to the recovery of the SC gap detected by nonequilibrium low-energy probes [52–59]. That said, one should be aware that the Rothwarf-Taylor model was derived for long coherence length superconductors and the possibility to disorder the phase of preformed pairs in cuprates may bring new physics.

In UD samples a more complex behaviour occurs, due to the emergence of a multi-component response. Indeed, the QP recombination dynamics across the SC gap is accompanied by an additional fast decay time τ_{PG} lasting several hundreds of femtoseconds. Since this component vanishes at T^*, it has been ascribed to the recombination of the carriers subjected to PG correlations. Finally, superimposed to these relaxations, a very long decay time τ_H of several nanoseconds appears, usually interpreted either as a pump-induced heating effect [35, 36, 40, 44, 46, 49] or as the signature of a photoinduced absorption from localized carriers [37, 42, 43]. Pioneering experiments also suggested the possibility to detect precursor effects within the PG phase of UD cuprates, by monitoring the evolution of the QP signal above T_C [44]. In contrast to OP cuprates, in UD samples this component persists well above T_C.

In Chap. 2, we also highlighted that another strength of pump-probe optical spectroscopy consists in the possibility to reveal the ultrafast dynamics and the intrinsic properties of specific Raman-active collective modes [34, 41, 47, 48, 50, 60], which are coherently excited via the ISRS process or by a long-lived perturbation of the electronic GS [61]. Interestingly, several of these modes have strong intensity and energy anomalies at T_C, which suggest that they can be used as probes of pairing correlations [41, 48, 50]. Similar anomalies are seen in spontaneous Raman scattering [62].

All these results make ultrafast spectroscopy a suitable candidate to study the dynamics of precursor SC effects. Here, we perform a combination of FIR SE and femtosecond broadband optical spectroscopy as a function of temperature to identify different spectroscopic features associated with the precursor SC state in an UD cuprate. As a model system, we select a high-quality single crystal of slightly UD $NdBa_2Cu_3O_{7-\delta}$ (NBCO), which is isostructural to $YBa_2Cu_3O_{7-\delta}$ (YBCO) and has a sufficiently large difference between T_C (93.5 K) and T^* (170 K) while being close to optimal doping [63]. Therefore, it is the ideal playground for identifying the spectral

fingerprint of the QP signal above T_C and for testing how its coherent collective modes react to the possible existence of precursor phenomena.

In the following, Sect. 6.1 is devoted to the description of the properties and the electronic structure of the 123-family of cuprates. The steady-state optical measurements are presented in Sect. 6.2 and provide an initial estimate of the three temperature scales T_C, T_{ONS} and T^* by means of a local electric field-analysis of the FIR conductivity and via the temperature dependence of the B_{1u} O bending mode [33]. In contrast, the T_{ONS} and T^* temperature scales do not emerge under equilibrium conditions in the SW analysis performed over the visible spectral range. To rationalize the outcome of the nonequilibrium experiments, in Sect. 6.3 we provide a description of significant electronic and phononic effects detected by spontaneous Raman scattering. Finally, the ultrafast broadband optical spectroscopy experiments are reported in Sect. 6.4. Here, we reveal the QP response over a large spectral range, showing that this signature persists well above T_C and vanishes only above T_{ONS}. Simultaneously, two coherent collective modes (i.e. the Ba and Cu phonon modes) undergo an anomalous renormalization of their intensity at T_{ONS} and not close to T_C as in OP compounds. Our data suggest that a precursor SC state manifests above T_C, where bilayer coherence is established among planes containing pre-formed pairs.

6.1 $NdBa_2Cu_3O_{7-\delta}$

The compound NBCO belongs to the so-called "123-family of cuprates", which exhibit high-T_C superconductivity at temperatures as high as 100 K. The highest T_C in this class of compounds is retrieved in the case of a small amount of oxygen deficiency, $\delta \sim 0.1$, in the formula $RBa_2Cu_3O_{7-\delta}$ (where R is a rare-earth ion). This slightly less than half-full condition (where $\delta = 0$ for half-full) implies that there are missing electrons near E_F, leading to a hole-type conductivity. We first discuss the details of the 123-family crystal structure, as it has strong implications on the electronic structure of this compound compared to the case of $La_{2-x}(Sr,Ba)_xCuO_4$ discussed in Chap. 5. The orthorhombic unit cell of a prototypical crystal of the 123-family is shown in Fig. 6.2a. Three planes containing Cu and O are sandwiched between two planes containing Ba and O and one plane containing the rare-earth ion R. The atoms are puckered in the two CuO_2 planes that have the R plane between them. The other plane, typically referred to as the CuO plane or the "chains", consists of -Cu-O-Cu-O- atoms along the *b* axis. Remarkably, both the CuO_2 planes and the CuO chains contribute to the SC properties. Focusing on the local environment of each Cu ion, the chain Cu(1) ion is square planar-coordinated and the two coppers Cu(2) and Cu(3) in the plane exhibit fivefold pyramidal coordination.

For the purpose of this book, it is pivotal to discuss the current status of understanding of the electronic structure of the 123-family. Differently from other cuprates that retain a body-centered crystal structure, this class of compounds has a structure of the aligned type, thus resulting in a simpler BZ. However, the structural units of these bilayer compounds reflect in a higher degree of complexity of their electronic struc-

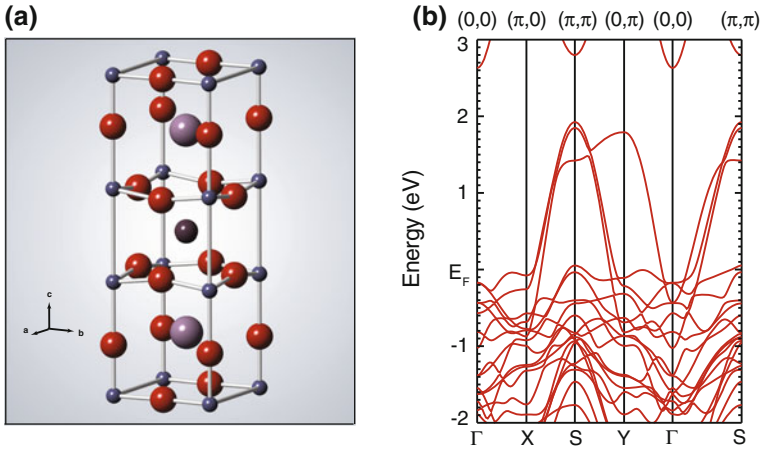

Fig. 6.2 **a** Crystallographic structure of RBCO, showing its orthorhombic unit cell. The Cu atoms are depicted in blue, the O atoms in red, the Ba atoms in pink and the rare-earth atoms R in dark violet. **b** In-plane electronic structure ($k_z = 0$) for $YBa_2Cu_3O_7$ calculated using DFT-LDA. The calculations have been adapted from Ref. [64]

ture compared to the case of the monolayer $La_{2-x}(Sr, Ba)_xCuO_4$ cuprates discussed in the previous Chapter. This complexity becomes evident already in the band structure calculated using the the LDA functional [64–66], which is shown for $YBa_2Cu_3O_7$ in Fig. 6.2b along the principal directions connecting the high-symmetry points of the BZ in the central ($k_z = 0$) horizontal plane. The calculations are adapted from Ref. [64]. In contrast to all layered cuprates, where one hybrid $pd\sigma^*$ band derived from the CuO_2 planes is found to cross E_F, here we observe that *two* narrow CuO_2 plane-related bands, almost identical in shape, rise far above E_F at the corner point S (π, π) of the BZ and undergo a strong dispersion. A much broader chain band also disperses between S and Y far above E_F and originates from the Cu-O σ bonds along the chains (formed from the O p_y and Cu $d_{x^2-y^2}$ orbitals). Another chain band rises slightly above E_F at S, undergoing very little dispersion. Oxygen deficiency in the sample depopulates the chains, leading to the absence of the chain bands in the insulating parent compound $RBa_2Cu_3O_6$ [64]. Along k_z, a substantial lack of dispersion is present in the bands, which implies a very large effective mass and a low conductivity in the z direction [65].

Although DFT-LDA allows to capture some basic features of the physics of cuprates, the independent-particle picture fails in the description of the insulating parent compound and of the UD samples. In this region of the phase diagram, intermediate-to-strong electronic correlations give rise to a plethora of phenomena, among which the CT insulating nature of the undoped system, the emergence of the PG and CDW states and the pronounced SW redistribution that occurs upon doping the CT insulator [67]. In this regard, experimental measurements based on ARPES have been key to refine our understanding of the cuprate low-energy electronic struc-

ture [68]. However, the investigation of the 123-family of cuprates has always been rather problematic, due to the natural crystal twinning and the higher bulky-like nature that leads to a poor quality of the cleaved surface. These issues have been overcome in the last years, thus allowing ARPES to investigate also YBCO across the phase diagram [69, 70]. This calls for additional developments from the theory side. At the time of writing, the combination of the LDA framework with DMFT represents the most promising avenue to capture the physics of strongly correlated quantum systems from a computational perspective [71–73]. Compared to the calculations we introduced in the previous Chapter on the undoped parent compound La_2CuO_4, two complications arise in the case of a slightly-UD crystal of the 123-family: (i) The presence of the hole doping, which leads to the normal-state metallic behaviour of the system and causes a strong renormalization of the electronic structure; (ii) The presence of the bilayer CuO_2 structure and of the CuO chains, which increases the number of bands characterizing the electronic structure of the material and contributing to its electrodynamic response.

The challenge of studying the renormalization of the electronic structure upon hole doping has already been addressed by a 6-band LDA+DMFT approach in the simpler case of $La_{2-x}Sr_xCuO_4$ [74]. The momentum resolved spectral functions and the corresponding integrated spectral functions for a hole doping of $x = 0.1$ and $x = 0.2$ are displayed in Fig. 6.3a, c and b, d, respectively, and adapted from Ref. [74]. One can observe the collapse of the CT gap presented in Fig. 5.4 of Chap. 5 and a marked redistribution of SW in the proximity of E_F. In particular, at $x = 0.1$, the ZRS has developed an incoherent contribution and a narrow coherent QP peak at E_F. Remarkably, the latter is not resolved by static mean-field theories like Hartree-Fock and it represents a feature arising from the inclusion of correlations. The black vertical arrows highlight the location of the direct transitions from occupied to unoccupied states that give rise to the high-energy features in the optical conductivity spectra.

The inclusion of a multi-band bilayer model for performing a complete DMFT calculation is instead a formidable task. Advances towards this goal have extended

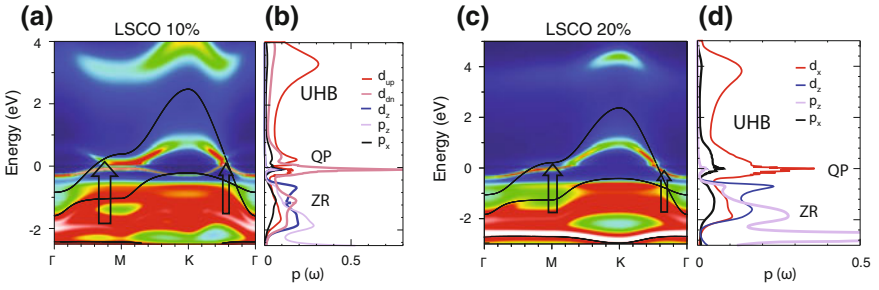

Fig. 6.3 **a**, **c** Energy- and momentum-dependent spectral function $A(k,\omega)$ obtained by LDA+DMFT of a six-band model description of doped $La_{2-x}Sr_xCuO_4$ for **a** $x = 0.1$, **c** $x = 0.2$. The solid black lines refer to LDA calculations. **b**, **d** Partial DOS of the $d_{x^2-y^2}$, $d_{3z^2-r^2}$, $p_{x,y}$, and p_z orbitals for **b** $x = 0.1$, **d** $x = 0.2$. Adapted from Ref. [74]

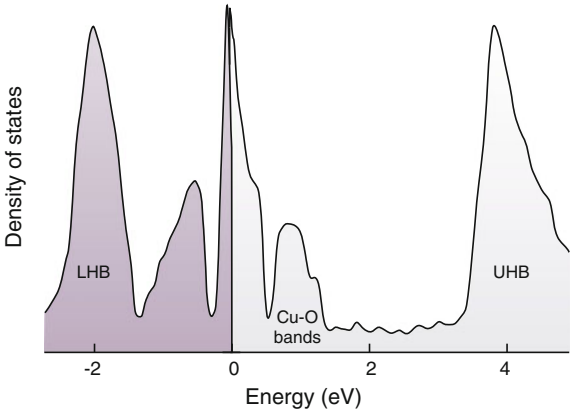

Fig. 6.4 Schematic illustration of the DOS for the 123-family of cuprates. The DOS is adapted from DMFT calculations [50]. UHB = Upper Hubbard Band, LHB = Lower Hubbard Band

the Hubbard model to account for a bilayer structure on a square lattice [75–78]. Such an approach is being investigated as a promising minimal model for describing the salient features of 123-family of cuprates, especially after the discovery of bilayer band splitting in ARPES experiments on YBCO [69]. More recently, the DFT band structure of YBCO has been combined with a DMFT treatment of the Coulomb interaction, including $d_{x^2-y^2}$ orbital and an on-site Coulomb repulsion on Cu of $U_d = 4.8$ eV. The calculated DOS is displayed as a function of energy in Fig. 6.4. The primary effect of the electronic correlations is to shift SW to a LHB and an UHB, which coexist with a low-energy structure corresponding to itinerant carriers with a renormalized bandwidth. In the following Section, we highlight how this electronic structure relates to the high-energy transitions observed in the optical spectra of the 123-family of cuprates. In Sect. 6.4, we make extensive use of the current knowledge on the electronic structure of these compounds to design a nonequilibrium experiment for getting insights into low-energy phenomena using high-energy photons and tracking the renormalization of specific collective modes.

6.2 Steady-State Optical Properties

To discover novel observables related to the existence of precursor SC correlations under nonequilibrium conditions and disentangle their contribution from the PG response, it is first pivotal to illustrate the steady-state electrodynamics of our NBCO sample. The reason behind this preliminary analysis is twofold: (i) To identify the possible manifestation of the precursor SC phenomena at equilibrium and locate our sample in the phase diagram of Fig. 6.1a; (ii) To carefully select the pump and probe photon energies, by assigning the high-energy features in the in-plane optical spectrum and relating them to the current status of understanding of the electronic structure. Thus, we first describe the *c*-axis FIR spectra of NBCO in Sect. 6.2.1, and we proceed with the study of the in-plane optical spectra in Sect. 6.2.2.

6.2.1 Far-Infrared Spectroscopic Ellipsometry

In the introduction to this Chapter, we have observed that FIR SE represents a very sensitive technique to reveal the three temperature scales T_C, T_{ONS} and T^* (Fig. 6.1, blue, red and grey circles). Indeed, when performed along the *c*-axis, FIR SE probes the opening of a gap in the DOS of a cuprate, especially near the antinodal region of the Fermi-surface where a PG develops below T^* in UD samples [63, 66]. This is due to the strong *k*-dependence of the perpendicular hopping matrix element for the transfer of charge carriers between the CuO_2 bilayer units (across the BaO and CuO chain layers). The formation of the SC gap below T_C gives rise to an additional weaker suppression of the conductivity and to a pronounced mode at finite frequency, known as the transverse Josephson plasma mode [63]. The latter arises from the layered structure which is composed of two closely spaced CuO_2 layer (bilayer unit) and a spacer layer that consists of two BaO layers and the CuO chain layer. The transverse plasma mode is very sensitive to the coherence of the electron transport between the CuO_2 layers of the individual bilayer units and thus to the onset of SC correlations, even if they are short-ranged and strongly fluctuating. Moreover, the presence of the Josephson plasma mode significantly affects the energy of the phonon mode related to the bending of the in-plane O and Cu ions, making it another sensitive observable to precursor SC phenomena [33, 39].

In this section, we perform FIR SE on our NBCO sample and measure its *c*-axis optical conductivity $\sigma_c(\omega) = \sigma_{1,c}(\omega) + i\sigma_{2,c}(\omega)$. Figure 6.5a, b show our data as a function of temperature. As expected from previous works [33, 38, 39, 63, 79], the contribution of the electronic excitations is strongly reduced in $\sigma_{1,c}(\omega)$ and sharp phonon modes prominently emerge on top of the residual electronic background. The B_{1u} mode at ∼39 meV is caused by the Cu-O bond bending involving an in-

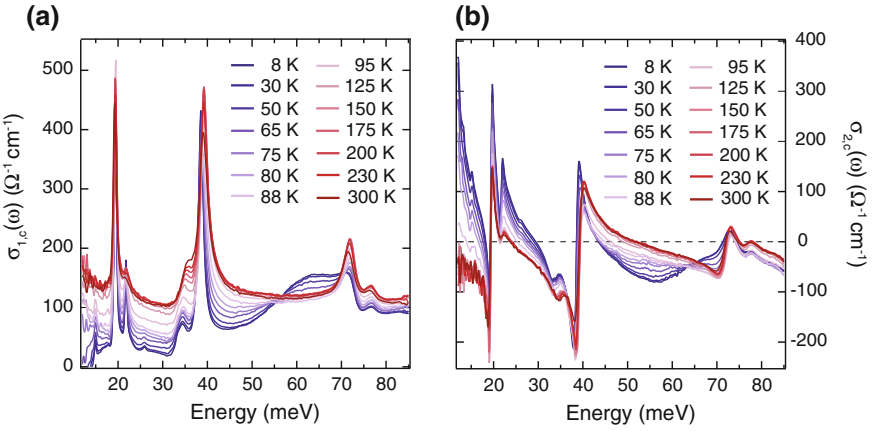

Fig. 6.5 **a** Real and **b** imaginary part of the *c*-axis optical conductivity in the FIR measured by SE as a function of temperature

phase motion of all O ions within the cuprate bilayer, while the mode at 71 meV is related to the collective vibrations of the apical O ions located between the bilayers and the chains. As the temperature is reduced below T_C, a broad absorption feature becomes evident around ∼65 meV and is related to the establishment of the transverse Josephson plasma mode.

As a first step in our analysis, we proceed to identify the T_C and T^* temperature scales of our sample via the analysis of $\sigma_{1,c}(\omega)$. For our purposes, we only focus on the evaluation of the partial SW in the 12.5–85.0 meV region as a function of temperature. We calculate the SW as

$$SW = \int_{12.5meV}^{85meV} \sigma_{1,c}(\omega) d\omega \tag{6.1}$$

In Fig. 6.6 the temperature dependence of the SW is shown. As expected from previous studies [63], we observe that the SW decreases well above T_C. This "missing" SW is a characteristic feature of the PG and provides an estimate of T^*. According to our data, we can determine $T_C \sim 94$ K and $T^* \sim 170$ K, as indicated in Fig. 6.6.

Subsequently, we estimate the T_{ONS} temperature scale by applying the same analysis performed in Ref. [33]. In particular, we focus on the central energy and linewidth of the B_{1u} phonon at ∼39 meV. As anticipated above, this mode is also affected by the onset of the bilayer coherence, which modifies the local fields on the CuO_2 layers [33, 39]. Figure 6.7a shows the temperature evolution of the phonon peak position

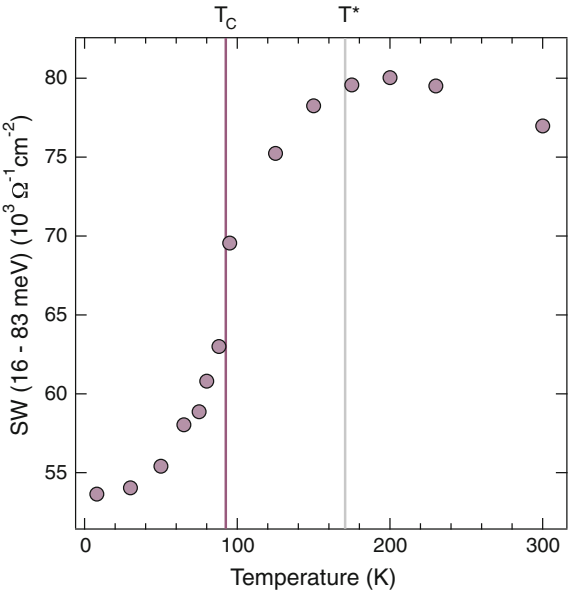

Fig. 6.6 Temperature dependence of the *c*-axis SW, calculated over the FIR spectral range covered by SE (12.5–85.0 meV). The violet and grey vertical lines mark the estimated T_C and T^* respectively

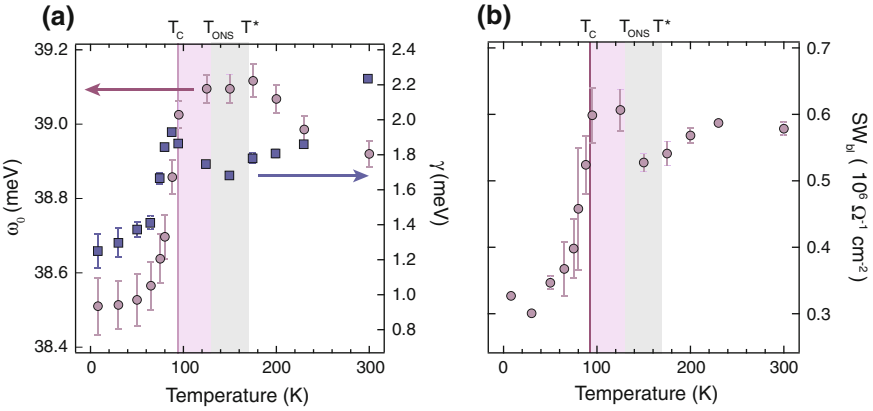

Fig. 6.7 **a** Temperature evolution of the B_{1u} O bending mode frequency (violet circles) and linewidth (blue squares), showing an anomalous behaviour between T_C and T_{ONS}. The violet vertical line marks the value of T_C and the violet (grey) shaded area highlights the temperature region characterized by incoherent pairing (PG) correlations. **b** Temperature dependence of the low-energy SW of the bilayer conductivity

and linewidth, revealing a renormalization in the temperature range between 110 and 140 K that signifies the onset of the bilayer coherence between these temperatures.

The T_{ONS} scale is also estimated by a local electric field analysis of the data using the so-called multilayer model [33, 38]. Within this model, T_{ONS} is associated with the temperature below which the bilayer conductivity starts to exhibit an increase [33, 80]. For $T_C < T < T_{ONS}$, the condensation of pairs with a finite correlation lifetime enhances the coherence among the neighbouring planes of a bilayer and thus gives rise to an increase in the low-energy SW. In the model, the real and imaginary parts of the conductivity are simultaneously fitted using the multilayer model in the energy range from 16 to 370 meV. The parameters describing the phonons are fitted at 300 K and kept fixed at all lower temperatures, allowing only for a small reduction in the width and a blueshift of the peak energy due to thermal effects. Figure 6.7b shows the SW of the low-energy component of the bilayer conductivity. There is a significant increase in the low-energy SW below 150 K, before it decreases again below 95 K due to the opening of a full SC gap (which is accompanied by a transfer of SW into a δ function at zero energy). The resulting estimate of T_{ONS}, between 110 and 140 K, is therefore consistent with the value extracted from the B_{1u} phonon analysis.

The three temperature scales obtained for our NBCO single crystal are displayed by star symbols in the phase diagram of Fig. 6.1a. The slight shifts of our values with respect to those reported in the phase diagram can be associated with a different scaling shown by NBCO single crystals compared to YBCO.

6.2.2 *Visible Spectroscopic Ellipsometry*

In the previous section, we observed the appearance of three temperature scales (T_C, T_{ONS} and T^*) in the *c*-axis FIR spectra of our sample, as the latter are particularly sensitive to the low-energy charge dynamics in the material. Since one of the paradigms of strongly correlated quantum systems is the complex interplay between low- and high-energy scales, another important spectral region to monitor is represented by the near-infrared to UV range. Indeed, in the past, many studies reported the observation of peculiar effects taking place at T_C in the equilibrium in-plane optical response even at high-energies [81–84], which were interpreted as a fingerprint of "Mottness" [85, 86]. To prove the validity of this scenario and test whether the optical spectra at high energies are also sensitive to the T_{ONS} and T^* temperature scales, we measured the in-plane optical conductivity $\sigma_{ab}(\omega) = \sigma_{1,ab}(\omega) + i\sigma_{2,ab}(\omega)$ from the near-infrared to the UV via broadband SE. The results are shown in Fig. 6.8a, b. The energy of the monochromatic pump (red arrow) and of the broadband probe (grey shaded area), used in the nonequilibrium experiment, are also highlighted in Fig. 6.8a.

We first observe that the measured response agrees well with previously reported data for the 123-family of cuprates [81, 87]. The spectral range below 1.00 eV has been modelled including a Drude-like contribution and a MIR component [87]. The feature at 1.40 eV sharpens with decreasing temperature, and is closely followed by a weaker satellite at 1.77 eV; it has been ascribed to a CT excitation in the CuO_2 planes and represents a remnant of the fundamental absorption gap that emerges in the same spectral region in the undoped parent compound. A second prominent peak can be observed around 2.60 eV, which progressively loses SW with decreasing temperature. Linear Muffin-Tin Orbital calculations assigned this peak to an interband transition

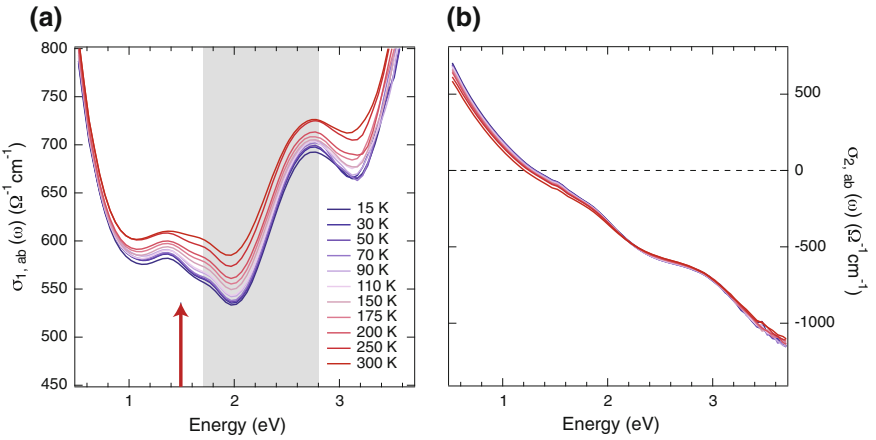

Fig. 6.8 **a** Real and **b** imaginary part of the in-plane optical conductivity at selected temperatures. The red arrow indicates the photon energy of the pump pulse used in the nonequilibrium experiment, while the grey shaded area refers to the spectral range monitored by the broadband probe pulse

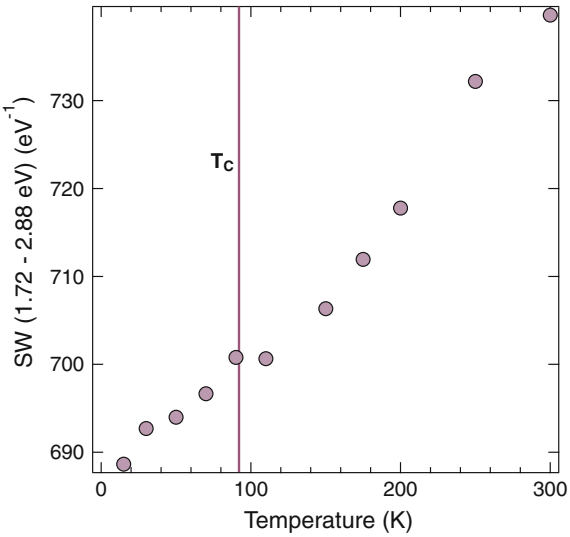

Fig. 6.9 Temperature evolution of the SW calculated over the region highlighted by the grey shaded area (1.72–2.88 eV). T_C is indicated on the figure as a violet vertical line

into the antibonding Cu(2)-O(2)-O(3) band, with the initial state being found in a manifold of strongly dispersive bands [88]. This interpretation has been recently refined by DMFT calculations, which described it as a charge excitation from the LHB to E_F in OP YBCO [50].

Figure 6.9 shows the partial SW integrated over the region covered by the grey shaded area (1.72–2.88 eV) as a function of temperature. We observe that the partial SW drops with decreasing temperature and reveals a kink around T_C. Remarkably, no features are instead seen between T_C and T^*. This observation proves that the high-energy equilibrium excitation spectrum of NBCO is not affected by the emergence of precursor SC and PG states. Later, we will show that this paradigm breaks down when $\Delta R/R$ of the material is monitored under nonequilibrium conditions via the pump-probe technique, as precursor and PG phenomena cause a renormalization of different spectroscopic observables in the material.

To introduce the experiments at nonequilibrium, we need to rely on the equilibrium reflectance $R(\omega)$ of our single crystal, which can be directly calculated from the SE data. Figure 6.10 displays the steady-state $R(\omega)$ as a function of temperature, limited in the spectral range that is monitored by our pump-probe experiment (1.73–2.80 eV). Importantly, we observe that $R(\omega)$ increases its value in the whole spectral range when the temperature is increased. This implies that the thermal component in the $\Delta R/R$ response measured by the pump-probe experiment must be characterized by a positive sign over the visible region.

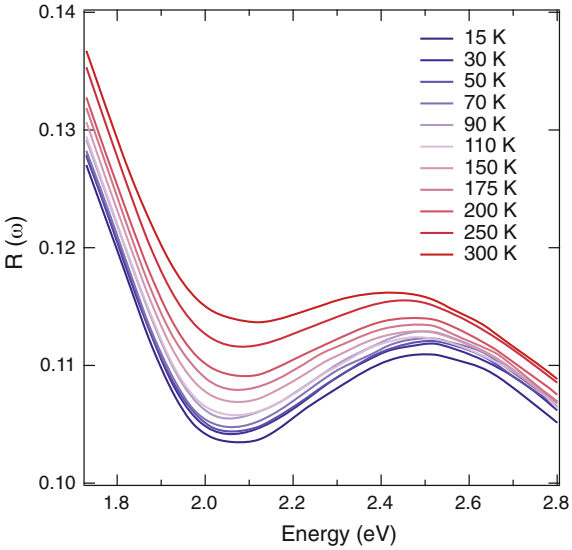

Fig. 6.10 Temperature dependence of the in-plane reflectance, R(ω), as calculated from the SE data. The displayed spectral range is limited to the one of the pump-probe experiment

6.3 Spontaneous Raman Scattering

The main purpose of this work is to get novel insights into low-energy phenomena in strongly interacting and correlated quantum systems by monitoring the nonequilibrium dynamics of specific collective excitations in these materials. To this end, in Chaps. 3 and 4, the explored collective excitations were lying at high energy and thus their renormalization became accessible to a probe pulse covering the visible or the UV spectral range. In Chap. 5, we observed instead that a different subsets of low-energy collective excitations can be coherently generated in the material via the ISRS process of via a displacive excitation [61, 89–91]. As these collective modes are Raman-active, it becomes crucial to analyse the spontaneous Raman scattering response of the system in order to assign possible coherent modes emerging under nonequilibrium conditions and provide a direct comparison between the two techniques.

In this Section, we discuss the spontaneous Raman scattering response of the 123-family of cuprates to identify possible modes of interest for our ultrafast broadband optical spectroscopy experiment. As already observed in Chap. 3, one of the most intriguing Raman-active excitations in all superconductors is represented by the pairing-breaking (coherent) peak, which has an electronic origin and arises from the breaking of the Cooper pairs in the SC state during the scattering process [92, 93]. Setting this excitation out of equilibrium and probing the consequent changes in the optical properties in a broad range is particularly desirable, as it allows studying how the perturbed condensate affects other elementary excitations on different energy scales and obtaining information on potential pairing actors in superconductivity [47, 94]. Within this framework, in OP LSCO it was found that the SC quasiparticles

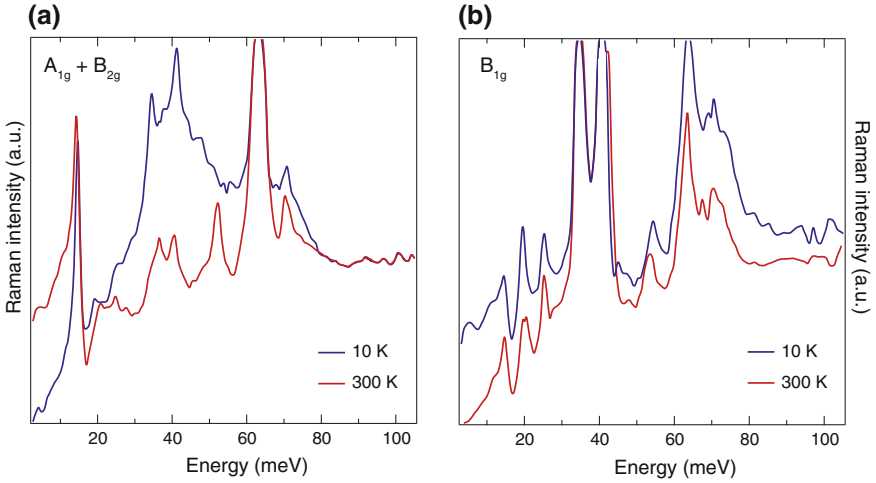

Fig. 6.11 Spontaneous Raman scattering data in the **a** $A_{1g} + B_{2g}$ and **b** B_{1g} scattering geometry for an OP single crystal of NBCO at temperature above (red lines) and below (blue lines) $T_C = 95$ K. The data have been adapted from Ref. [95]

are strongly coupled to a high-energy excitation lying on the Mott scale at 2.60 eV, thus shedding light on the importance of non-retarded interactions in the onset or breaking of superconductivity in cuprates [47]. Other collective modes of interest in superconductors are the optical phonons, as their renormalization gives insights into subtle SC-induced many-body processes in the material. Therefore, in the following, we focus on the salient features detected by electronic and phononic Raman scattering in the 123-family.

Electronic Raman scattering studies on OP NBCO identified the substantial anisotropy of the SC gap, as evidenced from the Raman shift associated with the pair-breaking peak in two different symmetry configurations [95]. These results are shown in Fig. 6.11a, b which have been adapted from Ref. [95]. In the $A_{1g} + B_{2g}$ channel, the pair-breaking peak was found to arise at 10 K around ∼41 meV, while in the B_{1g} scattering channel the electronic continuum peaks around ∼72 meV. This prominent anisotropy is a signature of the *d*-wave symmetry of the SC gap in high-T_C cuprates [92, 93]. Phononic Raman scattering experiments in OP YBCO identified instead remarkable effects associated with the temperature dependence of several normal modes [62, 96]. The low-energy Raman spectrum in the $A_{1g} + B_{1g}$ scattering geometry is displayed in Fig. 6.12a. Sudden anomalies in the intensities of the A_{1g} Ba (∼14.5 meV), A_{1g} Cu (∼19.5 meV) and B_{1g} out-of-phase O(2)-O(3) (∼42.3 meV) modes were observed upon lowering the temperature below T_C (Fig. 6.12b, c, d). This effect has been studied for different laser polarizations and excitation energies [62, 97]. A strong enhancement of the Ba mode was found in the $A_{1g} + B_{1g}$ scattering configuration and a resonant effect was observed under excitation with 2.00 eV photon energy. This intensity renormalization of the Ba mode could be associated

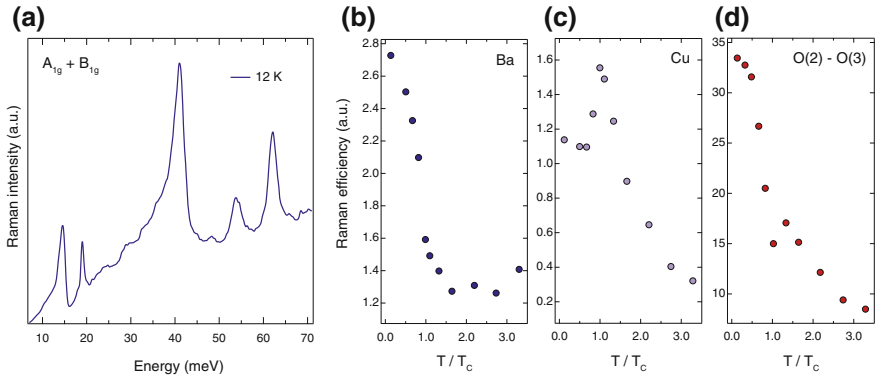

Fig. 6.12 **a** Spontaneous Raman scattering data in the $A_{1g} + B_{1g}$ scattering geometry for an OP single crystal of YBCO at 12 K. (**b**, **c**, **d**) Temperature dependence of the Raman efficiency for the **b** Ba **c** planar Cu and **d** out-of-phase O(2)-O(3) modes. The data have been adapted from Ref. [62]

neither with a redistribution of the electronic continuum in the SC state, nor with the superconductivity-induced modification of the laser penetration depth. Thus, the enhancement of this Raman-active phonon could be only related to the establishment of the SC state inside the crystal, which leads to a different Raman scattering mechanism [97]. Several possibilities have been proposed for explaining the renormalization of the Ba mode: (i) Changes in the lattice subsystem in the SC state, as even small variations of the interatomic distance can cause huge changes in the Raman matrix element; (ii) The appearance of the SC gap, which may have an impact on the interband transition energies, thus modifying the Raman matrix element; (iii) The redistribution of Cooper pairs between the CuO_2 planes and the CuO chains, which can also affect the matrix elements. Irrespective of the microscopic mechanism behind this renormalization, the Ba mode represents a very sensitive probe of pairing correlations. Remarkably for our results, all temperature-dependent low-frequency Raman scattering studies reported in literature have been performed in OP cuprates [62, 96–98], in which there is little or no coherence among the bilayers above T_C (Fig. 6.1a).

Thus, the above discussion on spontaneous Raman scattering provides valuable information to design our pump-probe experiment and reveal the possible interplay between collective structural modes and superconductivity. A crucial requirement to set these modes out of equilibrium is that the pump pulse duration is shorter than the period of the oscillations. While the phonon modes can be easily accessed by our experiment, the pair-breaking mode needs separate discussion. Indeed, due to its high energy (i.e. small period), it cannot be coherently triggered when the $A_{1g}+B_{1g}$ Raman symmetry configuration is selected, as our time resolution is limited to $\sim$50 fs. As a result, to possibly excite and detect this mode, in our nonequilibrium experiment the

pump and probe polarizations have to be set along the [110] crystallographic directions. This gives access to the $A_{1g} + B_{2g}$ Raman symmetry configuration, comprising both the A_{1g} phonons of interest and the pair-breaking mode in the SC state.

6.4 Ultrafast Broadband Optical Spectroscopy

In this Section, we demonstrate that setting superconductivity out of equilibrium via femtosecond light excitation offers a fertile route for disentangling the different temperature scales in our slightly-UD cuprate and evidence the existence of precursor SC phenomena.

In our time-resolved optical study, we tune the pump photon energy to be resonant with the interband charge excitation that promotes particle-hole pairs across E_F towards high-energy states [44, 50]. Afterwards, we monitor the optical reflectivity change $\Delta R/R$ in a broad spectral region between 1.70 and 2.80 eV. As observed above, this spectral range includes the absorption feature at 2.60 eV, involving occupied states in the LHB and unoccupied states close to E_F [50]. A pictorial illustration of the pump-probe experiment is offered in Fig. 6.13, where the one-particle DOS computed by DMFT (adapted from Ref. [50]) is shown together with the optical transitions promoted by our pump and probe pulses.

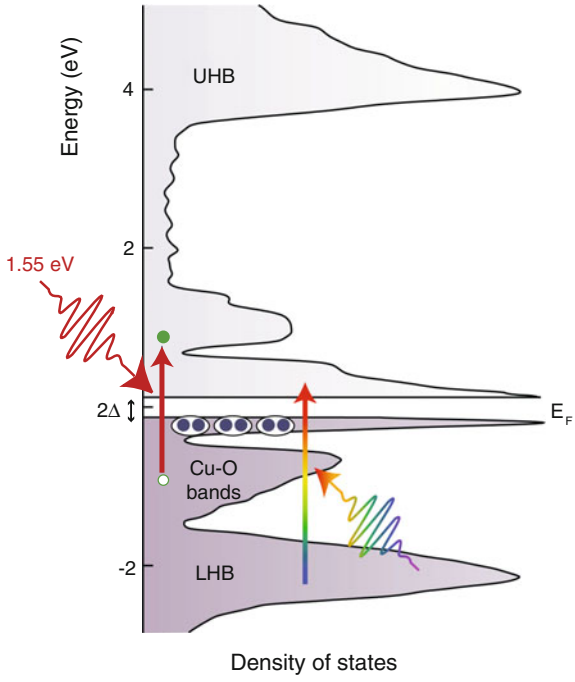

Fig. 6.13 Schematic illustration of the DOS for the 123-family of cuprates. The DOS is adapted from DMFT calculations [50]. The pump photon energy at 1.55 eV is depicted in dark red and the white light continuum probe is represented with a rainbow arrow. The photogenerated particle-hole pairs across E_F are displayed in green, the pairs close to E_F in blue. UHB = Upper Hubbard Band, LHB = Lower Hubbard Band

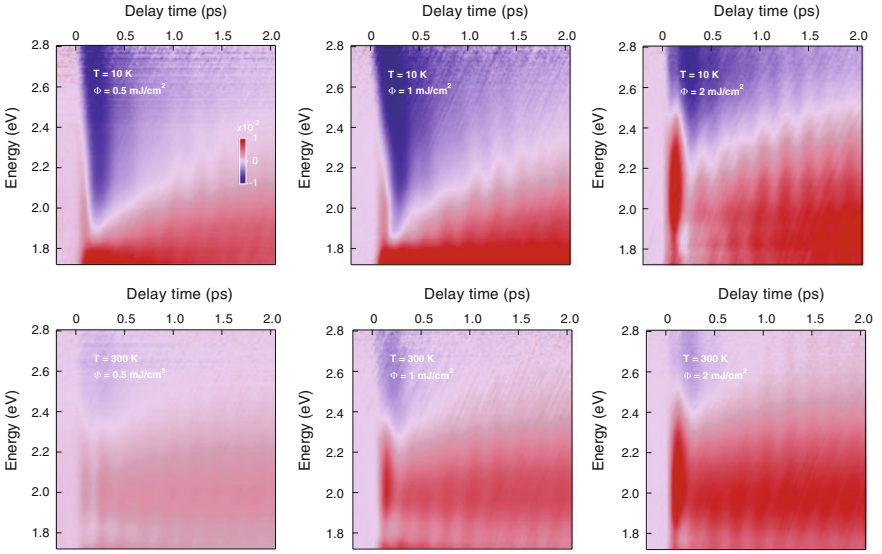

Fig. 6.14 Fluence dependence of $\Delta R/R$, displayed as a function of the probe photon energy and of the time delay between pump and probe. The temperatures of 10 and 300 K and the values of the absorbed fluence of 0.5, 1 and 2 mJ/cm^2 are indicated in the labels

6.4.1 Fluence Dependence

Before performing a detailed temperature dependence, a compromise between the data acquisition rate and the intensity of the laser pump pulse has to be found. Indeed, high signal-to-noise ratio at all temperatures is desirable, but the pump intensity should be maintained below the threshold for the complete vaporization of the condensate below T_C. To this end, we perform a fluence dependence of the in-plane $\Delta R/R$ for establishing the suitable fluence to be used in the temperature dependence.

Figure 6.14 displays the colour-coded maps of $\Delta R/R$ at 10 and 300 K for some representative values of the absorbed fluence (indicated in the labels). We identify the absorbed fluence of 0.35 mJ/cm^2 as the highest one at which the response maintains linearity in the SC state. This absorbed fluence value can be considered large when compared to the typical fluences that are sufficient for driving $La_{2-x}Sr_xCuO_4$ and $Bi_2Sr_2CaCu_2O_{8+x}$ into the normal state. However, 123-family of cuprates has been demonstrated to tolerate high levels of absorbed laser fluence before the total vaporization of the condensate takes place [54]. As a larger number of pump photons are delivered onto the sample, the spectral response of NBCO at 10 K starts displaying a positive contribution around 2.10 eV and strongly differs from the low-fluence regime. The rise of this spectroscopic feature represents the signature of a highly thermal nonequilibrium state driven by the pump pulse, which resembles the signal measured at 300 K. The linearity in the normal state at 300 K is instead maintained over a wider absorbed fluence range, as previously observed in literature

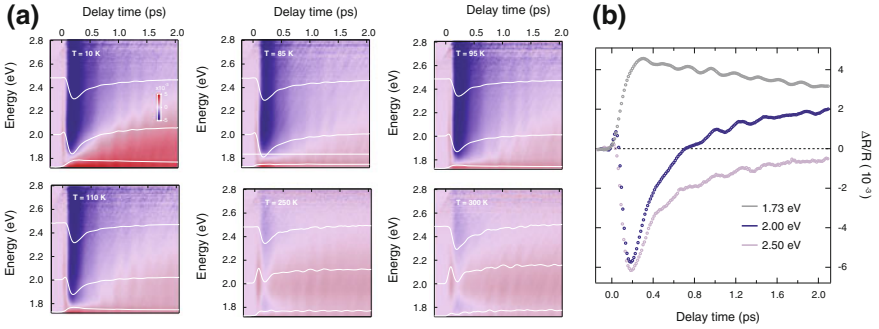

Fig. 6.15 **a** Colour-coded maps of ΔR/R as a function of the probe photon energy and time delay between pump and probe. The pump photon energy is set at 1.55 eV and the absorbed fluence corresponds to ∼0.3 mJ/cm^2. The temperatures are indicated in the labels. **b** Temporal traces at 10 K for fixed probe photon energies of 1.73, 2.00 and 2.50 eV

for $Bi_2Sr_2CaCu_2O_{8+x}$ [99]. Based on the above arguments, we choose an absorbed fluence of 0.3 mJ/cm^2 to perform the temperature dependence.

6.4.2 Temperature Dependence

Figure 6.15a displays the colour-coded maps of ΔR/R as a function of the probe photon energy and time delay between pump and probe for some representative temperatures (10, 85, 95, 110, 250 and 300 K). The temporal dynamics of ΔR/R at 10 K are displayed in Fig. 6.15b for selected probe photon energies (1.73, 2.00 and 2.50 eV). The signal around 2.00 eV comprises a first, resolution-limited positive rise, followed by a second, delayed negative contribution that shows the maximum change of the response around 200 fs. Subsequently, a fast decay of the negative contribution takes place and the response becomes positive at larger time delays. This pattern characterizes the signal across the whole spectrum, but the relative weights of the positive and negative components are strongly dependent on the probe photon energy. On top of this incoherent response, an oscillation can be detected in the whole spectrum and ascribed to the coherent excitation of collective bosonic modes. We measure a complete temperature-dependence of ΔR/R at 16 temperatures, as shown in Fig. 6.16.

6.4.3 Global Fit Analysis

As a first step in our analysis, we perform a global fit of ΔR/R as a function of time in order to disentangle the contributions of the different processes occurring on our ultrafast timescale. Eleven temporal traces are selected from each map of the

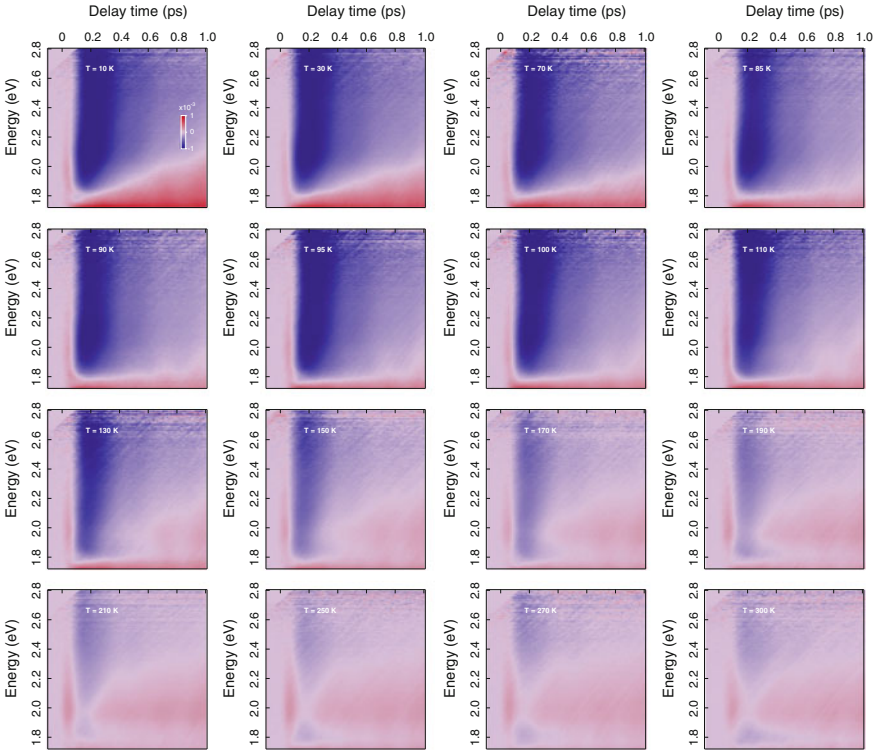

Fig. 6.16 Measured temperature dependence of ΔR/R as a function of the probe photon energy and of the time delay between pump and probe. The absorbed fluence is 0.3 mJ/cm^2 and the temperatures are listed as labels in the maps

temperature dependence and fitted simultaneously by imposing the same time constants. Different models with gradual complexity have been implemented to obtain a satisfactory fit of the incoherent response. At low temperatures, no converging fit is obtained by using only two exponential functions. Hence, the easiest model that captures the incoherent dynamics consists of three exponential functions convolved with a Gaussian accounting for the temporal shape of the pump pulse. Whereas a resolution-limited rise characterizes the first exponential term, a delayed rise has to be used for the other two components to correctly reproduce the early dynamics. The function that is used for fitting the data is

$$f(t) = f_H(t) + f_{PG}(t) + f_{QP}(t) = e^{\frac{-t^2}{\tau_{R_1}}} * A_H e^{-\frac{t-t_{D_1}}{\tau_H}} + e^{\frac{-t^2}{\tau_{R_2}}} * \left[A_{PG} e^{-\frac{t-t_{D_2}}{\tau_{PG}}} + A_{QP} e^{-\frac{t-t_{D_2}}{\tau_{QP}}} \right] \tag{6.2}$$

where A_H, A_{PG} and A_{QP} are the amplitudes of the three exponential functions; τ_{R_1} and τ_{R_2} are the rise times of the exponential functions; τ_H, τ_{PG} and τ_{QP} are the relaxation constants of the three exponentials; t_{D_1} and t_{D_2} are delay parameters with respect to the zero time.

The function presented in Eq. 6.2 allows to reproduce both the early temporal dynamics, represented by the resolution-limited positive rise, and the delayed negative contribution whose maximum amplitude occurs around 200 fs. Depending on the temperature, the extracted values for the time constants varied in the following way: $\tau_{PG} = 150 \div 250$ fs ($\pm 4 \div 9$ fs), $\tau_{QP} = 4 \div 6$ ps ($\pm 0.65 \div 1.6$ ps), $\tau_H = 34 \div 50$ ps ($\pm 10 \div 21$ ps). These time constants match the ones reported in the literature [35–37, 40, 44, 49, 52, 54], corresponding to the PG response τ_{PG} (hundreds of femtoseconds), the QP response τ_{QP} (several picoseconds) and the long-lived component τ_H (hundreds of picoseconds). The large uncertainty on τ_H is due to the limited temporal window probed in our experiment.

In such a model function, the exponential term with relaxation constant τ_H embodies the response of localized carriers which remain trapped in a long-lived state [42, 43]; the two exponential terms with delay t_{D_2} represent the conventional PG and QP response reported in all pump-probe spectroscopy experiments. We remark that simpler fit functions (not accounting for the two separate rise times and the two separate delays) do not result in a convergent fit. Hence, although the microscopic explanation for the long-lived component might not be related to an ultrafast localization of charge carriers, we first make use of Eq. 6.2 for fitting the data in an accurate way, as it represents the simplest fit function with the smallest number of free parameters. Below in this paragraph, we also show that another fit function can be used to successfully reproduce our data at all temperatures, by describing a long-lived bolometric response. At high temperatures, the data can instead be fitted using only two exponential functions, in agreement with the results obtained in the literature of pump-probe spectroscopy for the analysis of the normal state.

Figure 6.17 displays the experimental temporal traces cut around 1.90 eV, together with the results of the global fit analysis. In each panel, the result of the fit is super-

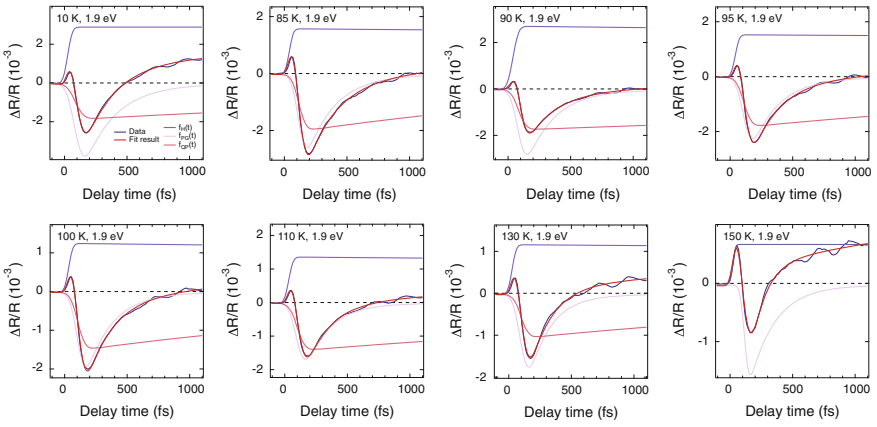

Fig. 6.17 Results of the global fit analysis on the temporal trace at 1.90 eV for different temperatures (10, 85, 90, 95, 100, 110, 130, 150 K). The experimental data are indicated in blue, the results of the global fit in red. The remaining curves represent the separate contributions to the fitting function

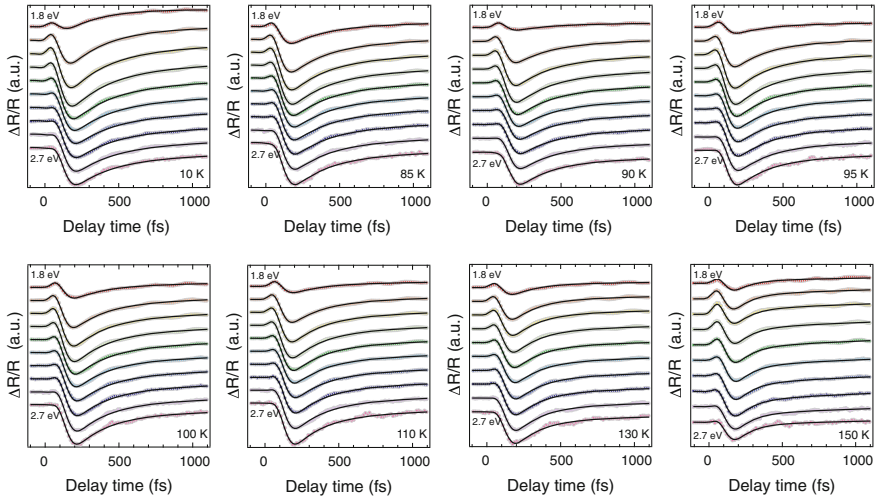

Fig. 6.18 Global fit analysis of the temporal traces at 10, 85, 90, 95, 100, 110, 130, 150 K for different probe photon energies (from 1.80 eV at the top of the graphs to 2.70 eV at the bottom, with a constant spacing of 0.10 eV)

imposed to the experimental data, and the decomposition of the final fit function into its separate contributions is given as well. The results are shown at different temperatures (10, 85, 90, 95, 100, 110, 130, 150 K). In Fig. 6.18 we prove the stability of the global fit across the whole probed spectral region. Every panel shows the eleven experimental temporal traces (coloured traces) in which the broad spectrum has been cut, together with the results of the global fit (black curves superimposed). The red curve at the top of each graph is the temporal trace at 1.80 eV, while the purple curve at the bottom is the temporal trace at 2.70 eV. We observe that the model used to fit the data is very accurate across the broad spectrum and catches the detailed features characterizing the early dynamics of the transient response.

As anticipated above, we also use a second approach for fitting the experimental data, which involves a Gaussian pulse-like contribution for capturing the early dynamics, a slowly rising long-lived component and the two delayed exponential functions of the previous model. The separate contributions are depicted in Fig. 6.19 for the temporal trace at 1.90 eV at 10 K. In this case, the Gaussian pulse is used to model the initial metallic contribution setting after the interaction of the pump with the sample, following the model of Okamoto et al. [100]. The delayed negative exponential functions still embody the PG and QP response, decaying with time constants τ_{PG} and τ_{QP}. The long-lived component instead corresponds to the bolometric (heating) response of the sample, which sets after the thermalization of the excited carriers has occurred. Although the use of this fit function leads to a satisfactory description of the experimental data, the number of free parameters is larger than the function proposed in the previous model. In any case, the use of this second fitting approach does not change the outcome of our analysis in a substantial way.

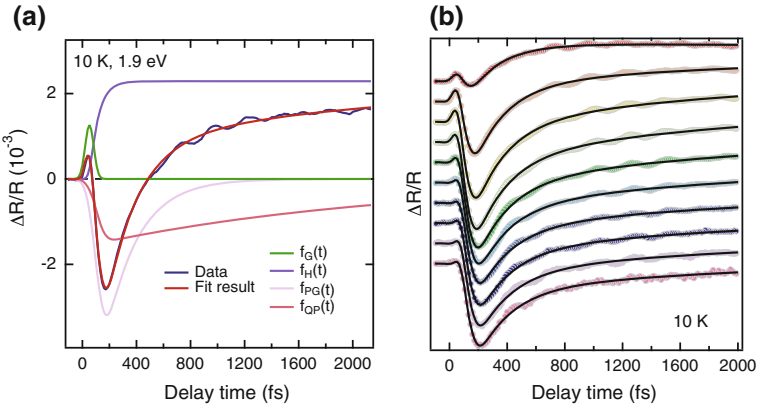

Fig. 6.19 **a** Results of the global fit analysis on the temporal trace at 1.90 eV and 10 K. The experimental data are indicated in blue, the results of the global fit in red. The remaining curves represent the separate contributions to the fitting function. **b** Global fit analysis of the temporal traces at 10 K for different probe photon energies (from 1.80 eV at the top of the graphs to 2.70 eV at the bottom, with a constant spacing of 0.10 eV)

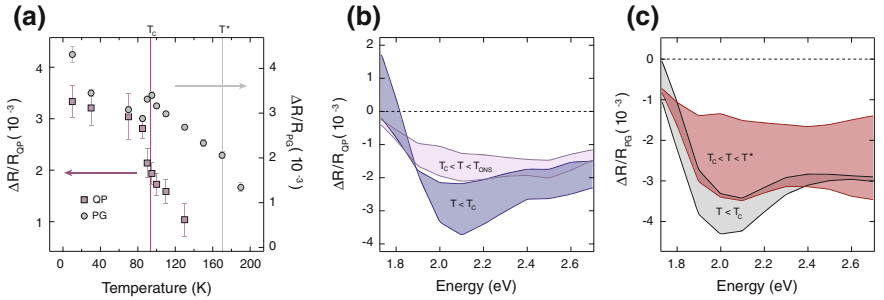

Fig. 6.20 **a** Temperature evolution of the QP (violet squares) and PG (grey circles) contributions to ΔR/R at 2.00 eV probe photon energy, as extracted from the global fit analysis. The vertical violet and grey lines identify the temperature scales T_C and T^*, respectively. **b**, **c** ΔR/R spectra of the QP and PG response obtained from the global fit analysis. Different colour shadings are used to identify the temperature regions below T_C (blue), and between T_C and T_{ONS} (violet) for the QP response or below T_C (grey), and between T_C and T^* (red) for the PG response

When iterated for all the measured ΔR/R maps, the global fit analysis allows to track the separate temperature evolution of the QP and PG responses. In Fig. 6.20a we show their temperature dependences for a selected probe photon energy of 2.00 eV, at which detailed single-wavelength pump-probe studies on OP YBCO have been reported [40, 41]. Interestingly, in our UD sample, the presence of the QP response is detected even above T_C, up to a temperature $T_{ONS} \sim 130$ K, which we associate with the onset of a precursor SC state and which is consistent with the previous equilibrium analysis. The faster PG contribution instead sets in near T^* and increases its weight down to T_C.

In contrast to single-wavelength pump-probe studies, our broadband probe pulse retrieves the whole $\Delta R/R$ spectrum of each contribution. The $\Delta R/R$ spectrum of the QP response obtained from the global fit is shown in Fig. 6.20b, where, for clarity, we group the spectra below T_C and between T_C and T_{ONS} in different colour shadings. Figure 6.20c displays the spectrum of the PG component in the temperature ranges below T_C and between T_C and T^*. By resolving the whole optical spectrum, we can observe that the QP response exhibits a sign reversal at 1.80 eV. It undergoes a continuous decrease in its amplitude with increasing temperature only in two spectral ranges, below 1.75 eV and around 2.00–2.10 eV. These results are fully consistent with previous experiments performed around 1.55 and 2.00 eV [44], and demonstrate that the temperature dependence of low-energy phenomena in cuprates can be easily tracked by these specific high-energy photons in a manner similar to low-energy probes [52, 54]. Although the measured $\Delta R/R$ spectra represent a mixture of the dispersive and absorptive parts of the system's dielectric function, its identification allows one to determine the transient optical conductivity response, as shown below. This unique capability of broadband ultrafast optical spectroscopy enables us to overcome the limitations of single-wavelength studies and provides a deeper connection with the material's electronic structure.

6.4.4 Transient Optical Conductivity

As anticipated above, the use of a continuum probe can provide quantitative information on the microscopic processes affecting the visible spectral range of our cuprate. A useful quantity that can be extracted from the nonequilibrium experiment is the transient complex optical conductivity $\Delta\sigma/\sigma = \Delta\sigma_1/\sigma_1 + i\Delta\sigma_2/\sigma_2$. This can be calculated without the need of a KK transform by relying on our steady-state SE data in the visible range (reported in Sect. 6.2.2) as a starting point and performing a Drude-Lorentz analysis of the $\Delta R/R$ maps at the different temperatures. In particular, the determination of the real part $\Delta\sigma_1/\sigma_1$ gives access to the temporal evolution of the SW in the visible range.

In Fig. 6.21a, b we plot $\Delta\sigma_1/\sigma_1$ at 10 K as a function of probe photon energy and time delay. A prominent drop is found in a wide energy range between 1.90 and 2.80 eV at early time delays. In contrast, for energies below 1.80 eV, a positive contribution emerges and progressively dominates the higher energy range. The response at early time delays strongly differs from the one expected from a simple transient heating of the crystal, which would display a positive sign across the whole measured spectrum. Hence, we can already assume that the pump pulse predominantly acts on the crystal as a non-thermal perturbation, creating a nonequilibrium distribution of hot carriers across E_F. Figure 6.22a, b display the temporal traces and the transient spectrum of $\Delta\sigma_1/\sigma_1$ at 10 K, which have been cut from the maps displayed in Fig. 6.21a, b. Similarly, Fig. 6.22c, d display the temporal traces and the transient spectrum of $\Delta\sigma_2/\sigma_2$ at 10 K.

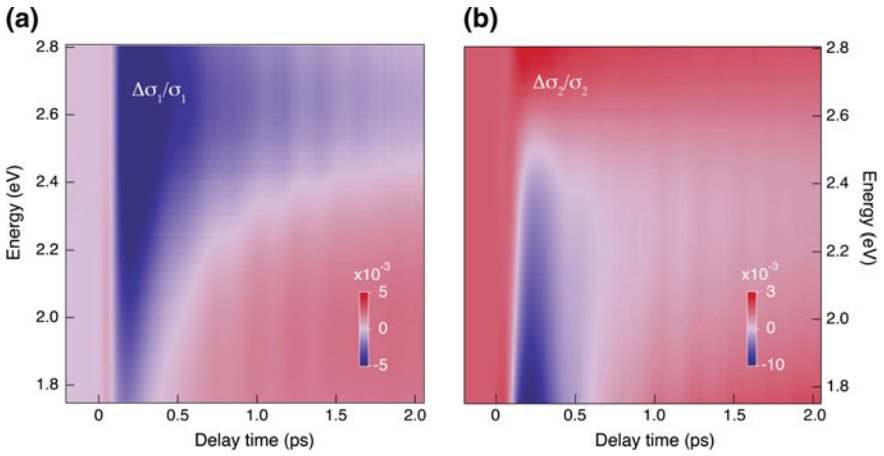

Fig. 6.21 Calculated transient optical conductivity **a** $\Delta\sigma_1/\sigma_1$ and **b** $\Delta\sigma_2/\sigma_2$ at 10 K as a function of probe photon energy and of time delay between pump and probe

To unravel the effects produced by each separate ultrafast process on $\Delta\sigma_1/\sigma_1$, we select ten temporal traces across the broadband spectral range and we perform a global fit analysis, by imposing the same model used for the global fit of ΔR/R. This global fit allows us to isolate the spectral fingerprints of the three separate components emerging in our nonequilibrium experiment. These spectral components are shown in Fig. 6.23, in which we use the same nomenclature given in Eq. 6.2. We observe that A_H provides a positive contribution to $\Delta\sigma_1/\sigma_1$, while A_{PG} and A_{QP} are at the origin of the decreased $\Delta\sigma_1/\sigma_1$ which is dominating in the traces and spectra of Fig. 6.22.

Here, we can contribute to the discussion concerning the long-live component, which has been previously assigned either to a pump-induced heating effect or as the signature of an excited-state absorption from localized (polaronic) carriers [42, 43]. Indeed, in Fig. 6.24 we compare the effect produced on σ_1 by this long-lived component in the nonequilibrium experiment and the variation in σ_1 provided by a static increase of the crystal temperature (from 10 to 30 K). We observe an excellent matching between the two trends, which suggests that the long-lived component corresponds to the bolometric response of our sample. Notice that this assignment implies that the correct model to fit the data is the one described in Fig. 6.19a, as the rise of the bolometric response is strictly correlated to the thermalization of the hot charge carriers after the initial excitation.

Finally, in Fig. 6.25, we present the effects produced by each separate component on the equilibrium σ_1. In each panel, the variation occurring in σ_1 has been multiplied by a factor 5 to make the change distinguishable. We observe that both the PG and QP responses remove SW in the visible region, redistributing it most likely to lower energy [54].

The long-lived component of the response provides an increase of the SW that is mostly flat and can be reproduced from the steady-state σ_1 by assuming a simple

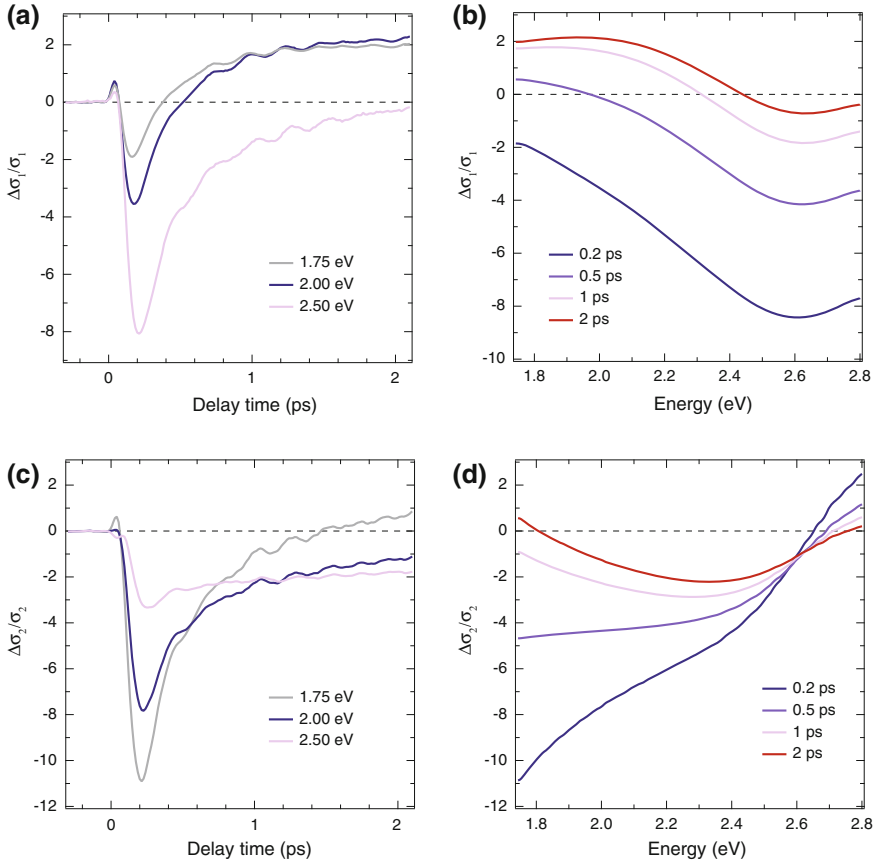

Fig. 6.22 **a**, **c** Temporal traces of $\Delta\sigma_1/\sigma_1$ ($\Delta\sigma_2/\sigma_2$) at 10 K for fixed probe photon energies of 1.75, 2.00 and 2.50 eV **b**, **d** Transient spectrum of $\Delta\sigma_1/\sigma_1$ ($\Delta\sigma_2/\sigma_2$) at 10 K for selected delay times of 0.2, 0.5, 1 and 2 ps

heating of the crystal. In contrast, the QP and PG contributions are responsible for the pronounced decrease of the SW in the visible (peaked around the interband transition at 2.70 eV) and manifest their maximum amplitude around 200 fs, suggesting the occurrence of a delayed response. This indicates that the photoinduced hot carriers decay within 200 fs to the proximity of E_F. A fraction of the energy released in this fast relaxation is conveyed to the particles subjected to SC and PG correlations, providing a channel for their excitation. Since these excited particles accumulate close to E_F, the final states associated with the high-energy interband transitions from the LHB to E_F result occupied. This explains why the broadband probe experiences a reduced absorption in the visible range due to a Pauli blocking mechanism. The SW removed in the visible range is typically transferred to low energy, contributing to the onset of

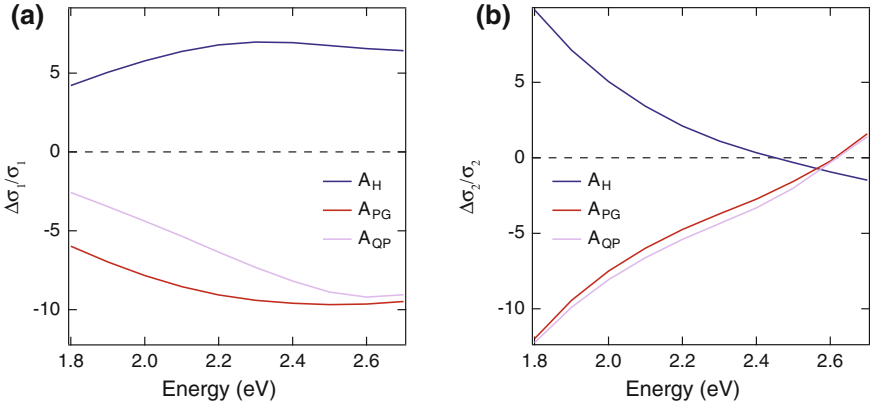

Fig. 6.23 Transient optical conductivity spectra of the three components obtained from the global fit analysis. **a** $\Delta\sigma_1/\sigma_1$; **b** $\Delta\sigma_2/\sigma_2$

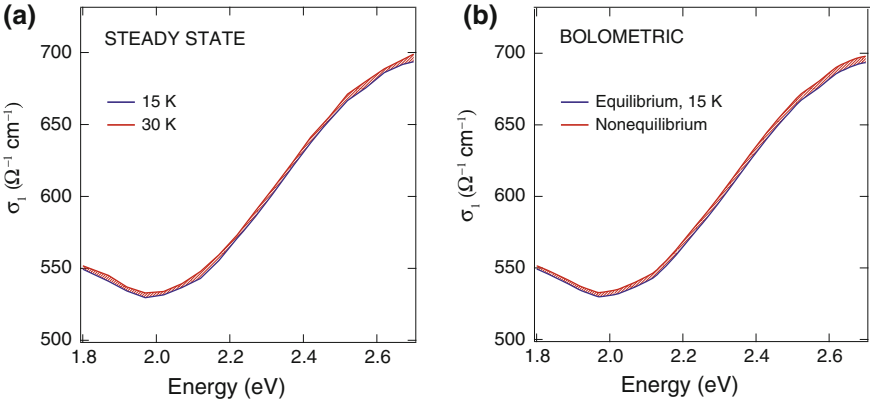

Fig. 6.24 **a** Steady-state optical conductivity measured by SE in the visible range at 15 K (blue curve) and 30 K (red curve). **b** Effect produced on the equilibrium σ_1 (represented in blue) by the long-lived component in the transient signal. This can be identified as the bolometric response of the crystal after photoexcitation

a transient Drude response [54] and possibly opening new channels that are inactive at equilibrium.

The determination of $\Delta\sigma_1/\sigma_1$ at all temperatures allows following the temperature evolution of the change in SW (ΔSW) in the probed range, as displayed in Fig. 6.26 for a time delay of 200 fs. Remarkably, ΔSW displays its maximum absolute intensity in the SC state and shows a first kink in the proximity T_C, which can be related to the opening of the SC gap. As the temperature is increased above T_C, ΔSW reduces its value, which is indicative for the occurrence of a rapid crossover. A pronounced recovery of ΔSW is found around T_{ONS}, as the QP response from the precursor state ceases to contribute to the loss of SW in the probed spectral range. Finally, as the

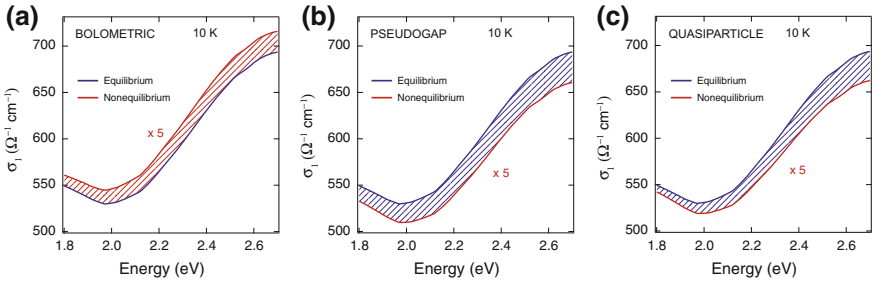

Fig. 6.25 Effects produced on the equilibrium σ_1 (represented as blue lines) by **a** the bolometric, **b** the PG and **c** the QP responses. The nonequilibrium σ_1 is drawn as a red curve and the added (removed) SW is depicted by the red (blue) filled area

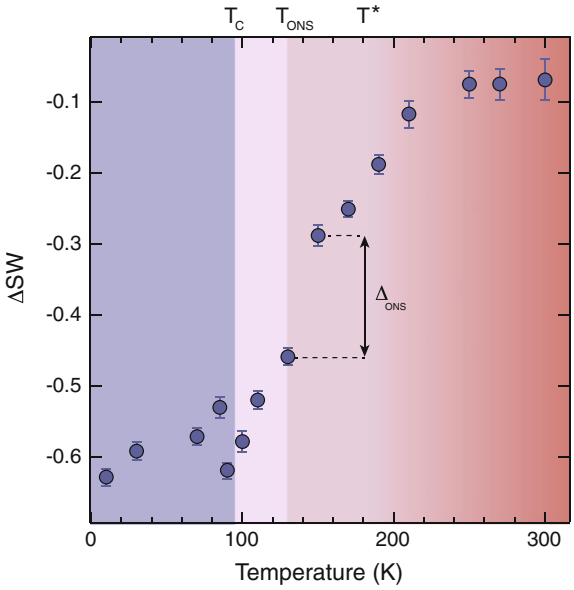

Fig. 6.26 Temperature evolution of the nonequilibrium SW (ΔSW) integrated over the whole probe spectrum at 200 fs delay time. The blue shaded region highlights the temperature range where the material is SC, the violet region depicts the precursor state and the gradient red region represents the crossover from the PG phase to the normal state of the material. The respective temperature scales T_C, T_{ONS} and T^* are indicated on top. The Δ_{ONS} parameter is indicated on the graph and identifies the difference existing between the ΔSW at 150 and 130 K for a time delay of 200 fs

temperature approaches T^*, a second crossover takes place and the response stabilizes around a vanishing constant value. Thus, by selecting the difference between $\Delta SW(t = 200\ fs)$ at 150 and 130 K, our experiment measures the amount of SW "lost" in the visible range due to the existence of QPs in the precursor state. This quantity, which we name Δ_{ONS}, also contains a minor contribution from the particles subjected to PG correlations, since the amplitude of their nonequilibrium response varies (although slightly) with temperature. Recently, it has been shown that three-pulse experiments can directly disentangle these two contributions in time without the need of a subtraction procedure [49]. In this scheme, a first pulse is used to selectively melt the SC condensate, and the recovery dynamics is measured via a conventional two-pulse pump-probe. This technique has been demonstrated using a single colour for the three pulses, but we expect that its future extension to a broadband detection can contribute to refine the current value of Δ_{ONS}. However, already from our analysis of the incoherent response, we can conclude that signatures of the precursor state above T_C emerge in the nonequilibrium experiment.

6.4.5 Coherent Optical Phonon Anomalies

In the previous Sections, we focused on the incoherent response of the pump-probe data, which represents a direct spectroscopic signature of the fermionic excitations associated with the QP or the PG responses. Here, we concentrate instead on the temperature evolution shown by the coherent pump-probe response, which provides direct access to specific Raman-active collective modes of the material. The interplay between fermionic and bosonic excitations is one of the key feature of a many-body system and the bosonic collective modes can strongly couple to the fermionic particles and get renormalized as a result of many-body interactions. In this scenario, one expects the emergence of anomalies in the bosonic spectrum as the external temperature is modified.

To prove this idea, we corroborate the analysis above by investigating how the coherently excited Raman-active modes in our $\Delta R/R$ spectra renormalize their features as a function of temperature. First, we provide an assignment of the collective modes emerging in our data by performing a FT analysis of the residuals from the global fit. In Fig. 6.27a, we show the FTs around the probe photon energy of 2.10 eV at the selected temperatures of 10, 110, 130 and 300 K, which clearly reveal the presence of the two separate peaks. This observation implies that two separate modes are influencing the high-energy electrodynamics of our UD cuprate. The energies of the two peaks are $\sim$14.5 and $\sim$19.5 meV at 10 K and undergo a gradual softening as the temperature is increased. The peaks can be assigned to the A_{1g} Raman-active optical phonons involving the *c*-axis vibrations of the Ba and Cu ions, respectively (see Sect. 6.3). The atomic displacements are shown in Fig. 6.27b. No further peaks are observed at higher energy in the FTs, thus implying the possible absence of other phonon modes and, most importantly, of the pair-breaking mode expected at $\sim$41 meV. The latter may be strongly damped or simply resonate in a spectral

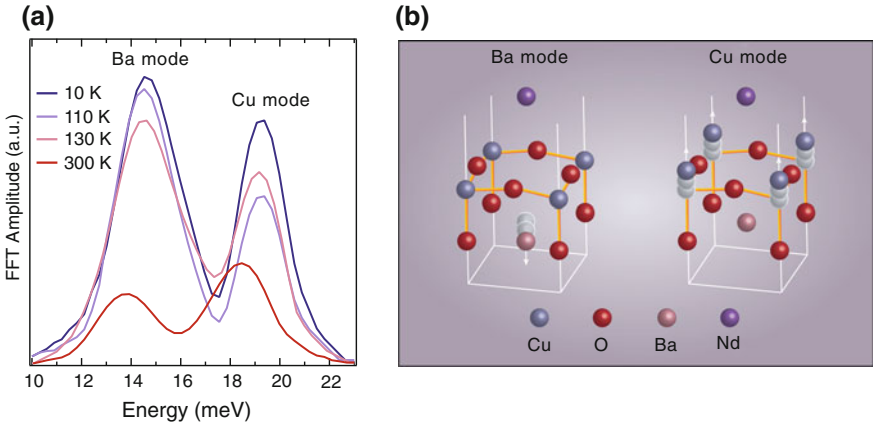

Fig. 6.27 **a** FT analysis of the residuals obtained from the global fit at selected temperatures and a probe photon energy of 2.10 eV. The two modes at ∼15 and ∼19 meV correspond to the coherent A_{1g} Ba and Cu phonons, respectively. **b** Atomic displacements of the Raman-active A_{1g} phonons involving *c*-axis vibrations of the Ba and Cu ions

region outside our probing range. Therefore, in the following, we concentrate on the analysis of the two coherent optical phonons that are clearly distinguishable in our nonequilibrium experiment.

In the past, such modes have been extensively discussed in spontaneous Raman scattering and time-resolved pump-probe spectroscopy of OP YBCO [41, 50, 62, 96]. These two experimental techniques provide the same information concerning the frequency of the phonon modes, but they measure distinct states of the phonon system. Spontaneous Raman scattering measures an equilibrium response of the system. In pump-probe spectroscopy, the collective modes are instead brought into a coherent state by the pump pulse via an impulsive or displacive mechanism [61] and therefore they may be influenced by the nonequilibirum distribution of carriers and by nonlinear effects.

In OP YBCO both experimental methods consistently observed: (i) The softening of the Cu and Ba phonon frequencies for increasing temperatures; and (ii) An anomalous intensity increase of the Ba mode when the crystal entered the SC phase at T_C. While in spontaneous Raman scattering the latter effect has been explained as a superconductivity-induced resonant process (in which the Raman cross-section is renormalized by self-energy effects, see Sect. 6.3), a different explanation has been provided by pump-probe spectroscopy. The anomalous temperature dependence of the Ba mode was demonstrated to follow the same behaviour of the QP response, suggesting that the driving force behind the coherent excitation is represented by the change in the density of broken pairs [41]. This displacive mechanism at the origin of the coherent Ba mode has also been invoked by theoretical calculations [101]. In this scenario, the pair-breaking process instantaneously removes pairing energy from the energy balance determining the equilibrium ionic conditions, eventually triggering the coherent lattice motion. This explains why the coherent oscillation of

the Ba mode in OP YBCO vanishes together with the QP signal as soon as T_C is crossed. Beyond such phenomenological models, recent ab initio calculations found a high sensitivity of the DOS at E_F to the displacement of the Ba ion [50]. Such strong electron-phonon coupling suggests that a perturbation of the low-energy electronic states can trigger the coherent motion of the Ba mode. Irrespective of the details of the excitation process, there is a firm experimental evidence that the Ba mode is a sensitive probe of the pairing correlations.

Distinct conclusions were drawn by spontaneous Raman scattering and pump-probe spectroscopy concerning the temperature behaviour of the Cu mode in OP samples [41, 62]. While in static Raman the Cu mode was found to display a peak at T_C [62], in pump-probe spectroscopy the peak anomaly was found well-above T_C and a clear temperature dependence could not be identified [41]. In addition, *ab initio* calculations predicted this mode to be only weakly coupled to the low-energy electronic states [50].

All the above observations were reported in OP YBCO, in which there is little or no coherence among the bilayers above T_C (Fig. 6.1a). In UD samples of the 123-family, the presence of bilayer coherence above T_C is therefore expected to play a major role in modifying the intensity anomaly at least of the Ba mode. In the following, we track the intensity of the Ba and Cu peaks in the FT as a function of temperature. To this end, we take advantage of a unique feature of our technique over spontaneous Raman scattering and single-wavelength pump-probe studies, which is the direct access to the energy dependent Raman matrix elements of all collective modes affecting the visible range [50, 60]. Revealing the shape of the Raman matrix elements enables us to track the temperature dependence of the coherent modes in a spectral region where they resonate with specific electronic excitations and can be clearly distinguished. The Raman matrix elements of the Ba (blue curve) and Cu (red curve) modes at 10 K across the probed range are shown in Fig. 6.28.

We observe that at 2.00 eV the Ba mode intensity is larger than the Cu mode intensity by a factor 1.7. This is consistent with the results reported by single-wavelength

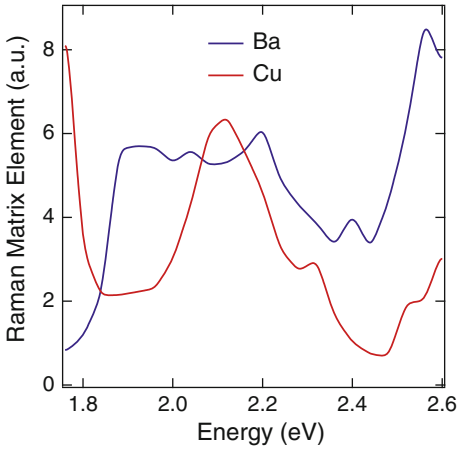

Fig. 6.28 Raman matrix elements of the Ba (blue curve) and Cu (red curve) modes at 10 K, as determined from the FT analysis as a function of the probe photon energy

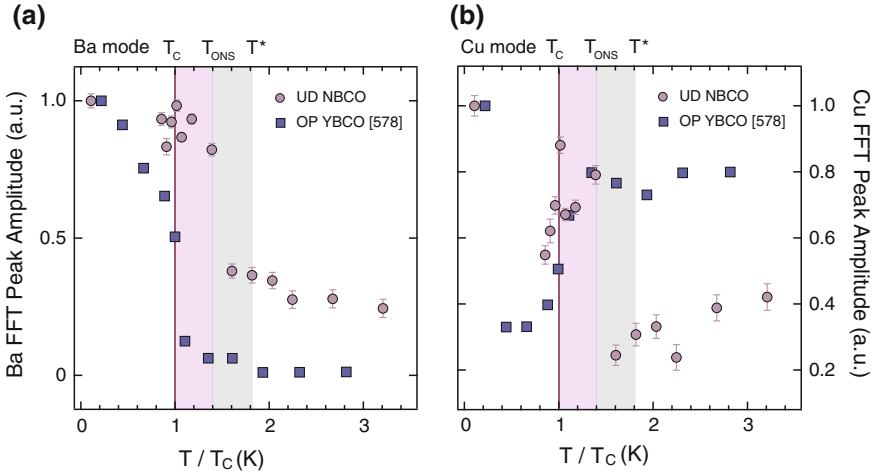

Fig. 6.29 Temperature dependence of the **a** Ba and **b** Cu mode amplitudes in OP YBCO (blue squares) and UD NBCO (violet circles). The data for OP YBCO have been extracted from Ref. [41]. The violet vertical line identifies the T_C temperature scale, while the violet (grey) shaded area highlights the temperature region of NBCO which is subjected to incoherent pairing (PG) correlations

pump-probe spectroscopy at 2.00 eV, in which the low-temperature signal was found to be dominated by the contribution of the Ba mode [41]. The general trend described by our Raman matrix elements also agrees with early spontaneous Raman scattering experiments performed at varying laser photon energies [62]. Finally, it is worth noting the resonant behaviour displayed by the Cu mode for probe photon energies below 1.80 eV, i.e. outside our probed spectral range. This finds a natural explanation in the proximity of the spectroscopic feature at 1.40–1.77 eV (Fig. 6.8), which has been associated with the reminiscence of the CT excitation in the CuO_2 planes. We remark that the shape of the determined Raman matrix elements are very similar to the ones reported in Ref. [50] for OP YBCO.

In Fig. 6.29a, b we track the temperature dependence of the Ba and Cu mode intensities in our slightly UD NBCO around a probe photon energy where they resonate and we compare it with the trends reported in the literature on OP YBCO [41, 62]. The data are normalized with respect to the lowest temperature value and are displayed as a function of the normalized temperature T/T_C. The temperature scales T_{ONS} and T^* extracted from the analysis of the incoherent response of our slightly UD NBCO sample are also highlighted.

Interestingly, in the UD crystal, we find that the Ba mode persists well above T_C and loses intensity only in the proximity of T_{ONS} (Fig. 6.29a). This anomaly indicates that the Ba mode intensity is sensitive to the stabilization of the bilayer coherence, as expected from the above discussion. Hence, we attribute the large intensity change displayed by the Ba mode to the establishment of the precursor SC state, consistent with the emergence of the QP component in the incoherent pump-probe response. An alternative possibility will also be proposed in the final

discussion. The temperature dependence of the Cu phonon amplitude is instead more complex (Fig. 6.29b). It shows a peak exactly at T_C, similarly to what was reported by spontaneous Raman scattering (Sect. 6.3), followed by an additional jump at T_{ONS}, which was not previously observed in OP YBCO. This temperature dependence of the Cu mode intensity appears to follow the low-energy component of the bilayer conductivity (Fig. 6.7b). One can speculate that this component is mimicked by a similar electronic contribution in the electronic Raman response, according to the so-called Shastry-Shraiman relation [102, 103]. Then, the dependence of the Cu phonon amplitude could be due to a resonant effect with the electronic background at the frequency of the Cu mode, which suggests again the coupling among coherent modes and the local SC response of the system.

6.5 Conclusions

In our broadband ultrafast optical study we reveal evidence within three independent observables that suggest the emergence of a precursor SC state in the UD regime at a temperature scale T_{ONS}, such that $T_C < T_{ONS} < T^*$. In particular, these observables include the persistence of the QP response up to T_{ONS}, a prominent jump in the QP SW in the vicinity of this temperature scale and the anomalies of the coherent Ba and Cu mode intensity at T_{ONS} and not at T_C as in OP cuprates. We remark that all these effects are simultaneously detected in the same transient spectra, providing a clear evidence for the development of an electronic state that affects the optical response of the system and that can be unambiguously disentangled from the PG correlations on the basis of their distinct relaxation timescales. The interpretation of such an electronic state in terms of precursor SC correlations is based on the matching between the T_{ONS} scale under nonequilibrium conditions and the temperature extracted from FIR SE of the same UD single crystal. Indeed, FIR SE demonstrates that the intra-bilayer response becomes more coherent below T_{ONS} and that this trend is just enhanced below T_C. In the past, the application of a magnetic field has also been shown to counteract this trend, both below T_C and T_{ONS} [33]. Although this effect is a clear evidence for enhanced SC correlations below T_{ONS}, it does not exclude the possibility that the precursor SC state is coupled to another kind of fluctuating order, e.g. CDW or SDW [33]. This idea is reinforced when the portions of the YBCO phase diagram characterized by SC- and CDW-correlations are compared, revealing a remarkable correspondence between the T_{ONS} temperature scales associated with the two phenomena [33, 104]. As an example, in YBCO Ortho-VIII ($T_C = 67$ K), the precursor SC state temperature $T_{ONS} = 130$ K measured by FIR SE [33] matches the temperature scale at which the CDW state has been detected by resonant elastic x-ray scattering [104]. Consistent with this scenario, recent single-wavelength pump-probe experiments propose that the superfluid in UD cuprates can be considered as a condensate of coherently-mixed particle-particle and particle-hole pairs (particle-hole quadruplets), whose origin lies in a coupled SC-CDW order parameter [105]. In the specific case of the 123-family of cuprates, one can also speculate

that the coupling between the coherent Ba mode and the SC state is mediated by the competition among the latter and the CDW. As shown in Ref. [48], the repulsive interaction between the CDW and SC order parameters works as an efficient mechanism to establish the CDW in the SC state. Since the CDW is naturally a charged mode, it will couple strongly to all lattice phonons with the appropriate symmetry. Hence, once the CDW is established, coherent phonons will be also triggered due to their mutual coupling.

A complete understanding of this possibly intertwined precursor state setting at T_{ONS} and of its dynamical fluctuations will become possible only upon its direct imaging with sub-picosecond time resolution. In this perspective, the development of techniques as time-resolved STM and cryo-Lorentz microscopy is expected to play a crucial role [106–108].

References

1. M. Tinkham, *Introduction to Superconductivity: (Dover Books on Physics)*, vol I (2004)
2. K.M. Lang, V. Madhavan, J.E. Hoffman, E.W. Hudson, H. Eisaki, S. Uchida, J.C. Davis, Imaging the granular structure of high-T_C superconductivity in underdoped $Bi_2Sr_2CaCu_2O_{8+\delta}$. Nature **415**(6870), 412–416 (2002)
3. W.W. Warren Jr., R.E. Walstedt, G.F. Brennert, R.J. Cava, R. Tycko, R.F. Bell, G. Dabbagh, Cu spin dynamics and superconducting precursor effects in planes above T_C in $YBa_2Cu_3O_{6.7}$. Phys. Rev. Lett. **62**(10), 1193 (1989)
4. H. Alloul, T. Ohno, P. Mendels, ^{89}Y NMR evidence for a Fermi-liquid behavior in $YBa_2Cu_3O_{6+x}$. Phys. Rev. Lett. **63**(16), 1700 (1989)
5. M. Takigawa, A.P. Reyes, P.C. Hammel, J.D. Thompson, R.H. Heffner, Z. Fisk, K.C. Ott, Cu and O NMR studies of the magnetic properties of $YBa_2Cu_3O_{6.63}$ ($T_C = 62$ K). Phys. Rev. B **43**(1), 247 (1991)
6. J.W. Loram, K.A. Mirza, J.R. Cooper, W.Y. Liang, Electronic specific heat of $YBa_2Cu_3O_{6+x}$ from 1.8 to 300 K. Phys. Rev. Lett. **71**(11), 1740 (1993)
7. V.J. Emery, S.A. Kivelson, Importance of phase fluctuations in superconductors with small superfluid density. Nature **374**(6521), 434–437 (1995)
8. I. Kosztin, Q. Chen, Y.-J. Kao, K. Levin, Pair excitations, collective modes, and gauge invariance in the BCS-Bose-Einstein crossover scenario. Phys. Rev. B **61**(17), 11662 (2000)
9. M. Shi, A. Bendounan, E. Razzoli, S. Rosenkranz, M.R. Norman, J.C. Campuzano, J. Chang, M.Månsson, Y. Sassa, T. Claesson, O. Tjernberg, L. Patthey, N. Momono, M. Oda, M. Ido, S. Guerrero, C. Mudry, J. Mesot, Spectroscopic evidence for preformed Cooper pairs in the pseudogap phase of cuprates. EPL (Europhys. Lett.), 88(2):27008 (2009)
10. J. Zaanen, O. Gunnarsson, Charged magnetic domain lines and the magnetism of high-T_C oxides. Phys. Rev. B **40**(10), 7391 (1989)
11. V.J. Emery, S.A. Kivelson, Frustrated electronic phase separation and high-temperature superconductors. Phys. C Supercond. **209**(4), 597–621 (1993)
12. C. Castellani, C. Di Castro, M. Grilli, Singular quasiparticle scattering in the proximity of charge instabilities. Phys. Rev. Lett. **75**(25), 4650 (1995)
13. L. Benfatto, S. Caprara, C. Di Castro, Gap and pseudogap evolution within the charge-ordering scenario for superconducting cuprates. Eur. Phys. J. B **17**(1), 95–102 (2000)
14. C. Nayak, Density-wave states of nonzero angular momentum. Phys. Rev. B **62**(8), 4880 (2000)
15. A.V. Chubukov, J. Schmalian, Temperature variation of the pseudogap in underdoped cuprates. Phys. Rev. B **57**(18), R11085 (1998)

16. C.M. Varma, Pseudogap phase and the quantum-critical point in copper-oxide metals. Phys. Rev. Lett. **83**(17), 3538 (1999)
17. R. Comin, A. Frano, M.M. Yee, Y. Yoshida, H. Eisaki, E. Schierle, E. Weschke, R. Sutarto, F. He, A. Soumyanarayanan, Y. He, M. Le Tacon, I.S. Elfimov, J.E. Hoffmann, G.A. Sawatzky, B. Keimer, A. Damascelli, Charge order driven by Fermi-arc instability in $Bi_2Sr_{2-x}La_x\ CuO_{6=\delta}$. Science **343**(6169), 390–392 (2014)
18. M. Capati, S. Caprara, C. Di Castro, M. Grilli, G. Seibold, J. Lorenzana, Electronic polymers and soft-matter-like broken symmetries in underdoped cuprates. Nat. Comm. **6**, 7691 (2015)
19. J.M. Tranquada, B.J. Sternlieb, J.D. Axe, Y. Nakamura, S. Uchida, Evidence for stripe correlations of spins and holes in copper oxide superconductors. Nature **375**(6532), 561–563 (1995)
20. A. Bianconi, N.L. Saini, A. Lanzara, M. Missori, T. Rossetti, H. Oyanagi, H. Yamaguchi, K. Oka, T. Ito, Determination of the local lattice distortions in the CuO_2 plane of $La_{1.85}Sr_{0.15}CuO_4$. Phys. Rev. Lett. **76**(18), 3412 (1996)
21. V. Hinkov, D. Haug, B. Fauqué, P. Bourges, Y. Sidis, A. Ivanov, C. Bernhard, C.T. Lin, B. Keimer, Electronic liquid crystal state in the high-temperature superconductor $YBa_2Cu_3O_{6.45}$. Science **319**(5863), 597–600 (2008)
22. B. Fauqué, Y. Sidis, V. Hinkov, S. Pailhes, C.T. Lin, X. Chaud, P. Bourges, Magnetic order in the pseudogap phase of high-T_c superconductors. Phys. Rev. Lett. **96**(19), 197001 (2006)
23. M. Vershinin, S. Misra, S. Ono, Y. Abe, Y. Ando, A. Yazdani, Local ordering in the pseudogap state of the high-T_c superconductor $Bi_2Sr_2CaCu_2O_{8+\delta}$. Science **303**(5666), 1995–1998 (2004)
24. G. Ghiringhelli, M. Le Tacon, M. Minola, S. Blanco-Canosa, C. Mazzoli, N.B. Brookes, G.M. De Luca, A. Frano, D.G. Hawthorn, F. He, Long-range incommensurate charge fluctuations in (Y, Nd)$Ba_2Cu_3O_{6+x}$. Science **303**(6096), 821–825 (2012)
25. M. Hashimoto, E.A. Nowadnick, R.-H. He, I.M. Vishik, B. Moritz, K. Yu He, R.G. Tanaka, DLu Moore, Y. Yoshida, Direct spectroscopic evidence for phase competition between the pseudogap and superconductivity in $Bi_2Sr_2CaCu_2O_{8+\delta}$. Nat. Mat. **14**(1), 37–42 (2015)
26. K.K. Gomes, A.N. Pasupathy, A. Pushp, S. Ono, Y. Ando, A. Yazdani, Visualizing pair formation on the atomic scale in the high-T_C superconductor $Bi_2Sr_2CaCu_2O_{8+\delta}$. Nature **447**(7144), 569–572 (2007)
27. A. Yazdani, Visualizing pair formation on the atomic scale and the search for the mechanism of superconductivity in high-T_C cuprates. J. Phys. Cond. Matt. **21**(16), 164214 (2009)
28. T. Kondo, Y. Hamaya, A.D. Palczewski, T. Takeuchi, J.S. Wen, Z.J. Xu, G. Gu, J. Schmalian, A. Kaminski, Disentangling Cooper-pair formation above the transition temperature from the pseudogap state in the cuprates. Nat. Phys. **7**(1), 21–25 (2011)
29. T. Kondo, W. Malaeb, Y. Ishida, T. Sasagawa, H. Sakamoto, T. Takeuchi, T. Tohyama, S. Shin, Point nodes persisting far beyond T_C in Bi2212. Nat. Comm. **6**, 7699 (2015)
30. I. Iguchi, T. Yamaguchi, A. Sugimoto, Diamagnetic activity above T_C as a precursor to superconductivity in $La_{2-x}Sr_xCuO_4$ thin films. Nature **412**(6845), 420–423 (2001)
31. Y. Wang, L. Li, N.P. Ong, Nernst effect in high-T_C superconductors. Phys. Rev. B **73**(2), 024510 (2006)
32. L. Li, Y. Wang, S. Komiya, S. Ono, Y. Ando, G.D. Gu, N.P. Ong, Diamagnetism and Cooper pairing above T_C in cuprates. Phys. Rev. B **81**(5), 054510 (2010)
33. A. Dubroka, M. Rössle, K.W. Kim, V.K. Malik, D. Munzar, D.N. Basov, A.A. Schafgans, S.J. Moon, C.T. Lin, D. Haug, Evidence of a precursor superconducting phase at temperatures as high as 180 K in $RBa_2Cu_3O_{7-\delta}$ (R = Y, Gd, Eu) superconducting crystals from infrared spectroscopy. Phys. Rev. Lett. **106**(4), 047006 (2011)
34. D.H. Torchinsky, F. Mahmood, A.T. Bollinger, I. Božović, N. Gedik, Fluctuating charge-density waves in a cuprate superconductor. Nat. Mat. **12**(5), 387–391 (2013)
35. C. Giannetti, F. Cilento, S. Dal Conte, G. Coslovich, G. Ferrini, H. Molegraaf, M. Raichle, R. Liang, H. Eisaki, M. Greven et al., Revealing the high-energy electronic excitations underlying the onset of high-temperature superconductivity in cuprates. Nat. Comm. **2**, 353 (2011)

36. D.C. Smith, P. Gay, D.Z. Wang, J.H. Wang, Z.F. Ren, J.F. Ryan, Ultrafast quasiparticle dynamics in $Tl_2Ba_2CuO_{6+\delta}$. Phys. C Supercond. **341**, 2219–2220 (2000)
37. D. Mihailovic, J. Demsar, R. Hudej, V.V. Kabanov, T. Wolf, J. Karpinski, Quasiparticle relaxation dynamics in cuprates and lifetimes of low-energy states: femtosecond data from underdoped to overdoped YBCO and mercury compounds. Phys. C Supercond. **341**, 1731–1734 (2000)
38. D. van der Marel, A. Tsvetkov, Transverse optical plasmons in layered superconductors. Czech. J. Phys. **46**(6), 3165–3168 (1996)
39. E. Uykur, K. Tanaka, T. Masui, S. Miyasaka, S. Tajima, Persistence of the superconducting condensate far above the critical temperature of $YBa_2(Cu, Zn)_3O_y$ revealed by c-axis optical conductivity measurements for several Zn concentrations and carrier doping levels. Phys. Rev. Lett. **112**(12), 127003 (2014)
40. S.G. Han, Z.V. Vardeny, K.S. Wong, O.G. Symko, G. Koren, Femtosecond optical detection of quasiparticle dynamics in high-T_C $YBa_2Cu_3O_{7-\delta}$ superconducting thin films. Phys. Rev. Lett. **65**(21), 2708 (1990)
41. W. Albrecht, Th Kruse, H. Kurz, Time-resolved observation of coherent phonons in superconducting $YBa_2Cu_3O_{7-\delta}$ thin films. Phys. Rev. Lett. **69**(9), 1451 (1992)
42. T.N. Thomas, C.J. Stevens, A.J.S. Choudhary, J.F. Ryan, D. Mihailovic, T. Mertelj, L. Forró, G. Wagner, J.E. Evetts, Photoexcited carrier relaxation and localization in $Bi_2Sr_2Ca_{1-y}Y_yCu_2O_8$ and $YBa_2Cu_3O_{7-\delta}$: a study by femtosecond time-resolved spectroscopy. Phys. Rev. B **53**(18), 12436 (1996)
43. C.J. Stevens, D. Smith, C. Chen, J.F. Ryan, B. Podobnik, D. Mihailovic, G.A. Wagner, J.E. Evetts, Evidence for two-component high-temperature superconductivity in the femtosecond optical response of $YBa_2Cu_3O_{7-\delta}$. Phys. Rev. Lett. **78**(11), 2212 (1997)
44. D. Mihailovic, B. Podobnik, J. Demsar, G. Wagner, J. Evetts, Divergence of the quasiparticle lifetime with doping and evidence for pre-formed pairs below T^* in $YBa_2Cu_3O_{7-\delta}$ direct measurements by femtosecond time-resolved spectroscopy. J. Phys. Chem. Sol. **59**(10), 1937–1941 (1998)
45. J. Demsar, B. Podobnik, V.V. Kabanov, Th Wolf, D. Mihailovic, Superconducting gap Δ_C, the pseudogap Δ_P, and pair fluctuations above T_C in overdoped $Y_{1-x}Ca_xBa_2Cu_3O_{7-\delta}$ from femtosecond time-domain spectroscopy. Phys. Rev. Lett. **82**(24), 4918 (1999)
46. N. Gedik, P. Blake, R.C. Spitzer, J. Orenstein, R. Liang, D.A. Bonn, W.N. Hardy, Single-quasiparticle stability and quasiparticle-pair decay in $YBa_2Cu_3O_{6.5}$. Phys. Rev. B **70**(1), 014504 (2004)
47. B. Mansart, J. Lorenzana, A. Mann, A. Odeh, M. Scarongella, M. Chergui, F. Carbone, Coupling of a high-energy excitation to superconducting quasiparticles in a cuprate from coherent charge fluctuation spectroscopy. Proc. Natl. Acad. Sci. **110**(12), 4539–4544 (2013)
48. J.P. Hinton, J.D. Koralek, Y.M. Lu, A. Vishwanath, J. Orenstein, D.A. Bonn, W.N. Hardy, R. Liang, New collective mode in $YBa_2Cu_3O_{6+x}$ observed by time-domain reflectometry. Phys. Rev. B **88**(6), 060508 (2013)
49. I. Madan, T. Kurosawa, Y. Toda, M. Oda, T. Mertelj, P. Kusar, D. Mihailovic. Separating pairing from quantum phase coherence dynamics above the superconducting transition by femtosecond spectroscopy. Nat. Sci. Rep., 4 (2014)
50. F. Novelli, G. Giovannetti, A. Avella, F. Cilento, L. Patthey, M. Radovic, M. Capone, F. Parmigiani, D. Fausti, Localized vibrations in superconducting $YBa_2Cu_3O_7$ revealed by ultrafast optical coherent spectroscopy. Phys. Rev. B **95**(17), 174524 (2017)
51. V.V. Kabanov, J. Demsar, D. Mihailovic, Kinetics of a superconductor excited with a femtosecond optical pulse. Phys. Rev. Lett. **95**(14), 147002 (2005)
52. R.A. Kaindl, M. Woerner, T. Elsaesser, D.C. Smith, J.F. Ryan, G.A. Farnan, M.P. McCurry, D.G. Walmsley, Ultrafast mid-infrared response of $YBa_2Cu_3O_{7-\delta}$. Science **287**(5452), 470–473 (2000)
53. R.P. Saichu, I. Mahns, A. Goos, S. Binder, P. May, S.G. Singer, B. Schulz, A. Rusydi, J. Unterhinninghofen, D. Manske, Two-component dynamics of the order parameter of high temperature $Bi_2Sr_2CaCu_2O_{8+\delta}$ Superconductors revealed by time-resolved Raman scattering. Phys. Rev. Lett. **102**(17), 177004 (2009)

54. A. Pashkin, M. Porer, M. Beyer, Kyung W. Kim, A. Dubroka, C. Bernhard, X. Yao, Y. Dagan, R. Hackl, A. Erb, Femtosecond response of quasiparticles and phonons in superconducting $YBa_2Cu_3O_{7-\delta}$ studied by wideband terahertz spectroscopy. Phys. Rev. Lett. **105**(6), 067001 (2010)
55. R. Cortés, L. Rettig, Y. Yoshida, H. Eisaki, M. Wolf, U. Bovensiepen, Momentum-resolved ultrafast electron dynamics in superconducting $Bi_2Sr_2CaCu_2O_{8+\delta}$. Phys. Rev. Lett. **107**(9), 097002 (2011)
56. C.L. Smallwood, J.P. Hinton, C. Jozwiak, W. Zhang, J.D. Koralek, H. Eisaki, D.-H. Lee, J. Orenstein, A. Lanzara, Tracking Cooper pairs in a cuprate superconductor by ultrafast angle-resolved photoemission. Science **336**(6085), 1137–1139 (2012)
57. J. Graf, C. Jozwiak, C.L. Smallwood, H. Eisaki, R.A. Kaindl, D.-H. Lee, A. Lanzara, Nodal quasiparticle meltdown in ultrahigh-resolution pump-probe angle-resolved photoemission. Nat. Phys. **7**(10), 805–809 (2011)
58. W. Zhang, C.L. Smallwood, C. Jozwiak, T.L. Miller, Y. Yoshida, H. Eisaki, D.-H. Lee, A. Lanzara, Signatures of superconductivity and pseudogap formation in nonequilibrium nodal quasiparticles revealed by ultrafast angle-resolved photoemission. Phys. Rev. B **88**(24), 245132 (2013)
59. W. Zhang, C. Hwang, C.L. Smallwood, T.L. Miller, G. Affeldt, K. Kurashima, C. Jozwiak, H. Eisaki, T. Adachi, Y. Koike, Ultrafast quenching of electron-boson interaction and superconducting gap in a cuprate superconductor. Nat. Comm. **5**, 4959 (2014)
60. A. Mann, E. Baldini, A. Tramontana, E. Pomjakushina, K. Conder, C. Arrell, F. van Mourik, J. Lorenzana, F. Carbone, Probing the electron-phonon interaction in correlated systems with coherent lattice fluctuation spectroscopy. Phys. Rev. B **92**(3), 035147 (2015)
61. T.E. Stevens, J. Kuhl, R. Merlin, Coherent phonon generation and the two stimulated Raman tensors. Phys. Rev. B **65**(14), 144304 (2002)
62. B. Friedl, C. Thomsen, H.-U. Habermeier, M. Cardona, Intensity anomalies of Raman-active phonons in the superconducting state of $YBa_2Cu_3O_{7-\delta}$. Sol. State Comm. **78**(4), 291–294 (1991)
63. L. Yu, D. Munzar, A.V. Boris, P. Yordanov, J. Chaloupka, T. Wolf, C.T. Lin, B. Keimer, C. Bernhard, Evidence for two separate energy gaps in underdoped high-temperature cuprate superconductors from broadband infrared ellipsometry. Phys. Rev. Lett. **100**(17), 177004 (2008)
64. I.S. Elfimov, G.A. Sawatzky, A. Damascelli, Theory of Fermi-surface pockets and correlation effects in underdoped $YBa_2Cu_3O_{6.5}$. Phys. Rev. B **77**(6), 060504 (2008)
65. W.E. Pickett, R.E. Cohen, H. Krakauer, Precise band structure and Fermi-surface calculation for $YBa_2Cu_3O_7$: importance of three-dimensional dispersion. Phys. Rev. B **42**(13), 8764 (1990)
66. O.K. Andersen, A.I. Liechtenstein, O. Jepsen, F. Paulsen, LDA energy bands, low-energy Hamiltonians, t', t", $t_\perp$ (k), and $J_\perp$. J. Phys. Chem. Sol. **56**(12), 1573–1591 (1995)
67. A. Toschi, M. Capone, Optical sum rule anomalies in the cuprates: interplay between strong correlation and electronic band structure. Phys. Rev. B **77**(1), 014518 (2008)
68. A. Damascelli, Z. Hussain, Z.-X. Shen, Angle-resolved photoemission studies of the cuprate superconductors. Rev. Mod. Phys. **75**, 473–541 (2003)
69. D. Fournier, G. Levy, Y. Pennec, J.L. McChesney, A. Bostwick, E. Rotenberg, R. Liang, W.N. Hardy, D.A. Bonn, I.S. Elfimov, A. Damascelli, Loss of nodal quasiparticle integrity in underdoped $YBa_2Cu_3O_{6+x}$. Nat. Phys. **6**(11), 905–911 (2010)
70. Y. Sassa, M. Radović, M. Månsson, E. Razzoli, X. Y. Cui, S. Pailhes, S. Guerrero, M. Shi, P. R. Willmott, F. Miletto Granozio, J. Mesot, M. R. Norman, L. Patthey, L. Patthey, Ortho-II band folding in $YBa_2Cu_3O_{7-\delta}$ films revealed by angle-resolved photoemission. Phys. Rev. B **83**(14), 140511 (2011)
71. A. Georges, G. Kotliar, W. Krauth, M.J. Rozenberg, Dynamical mean-field theory of strongly correlated fermion systems and the limit of infinite dimensions. Rev. Mod. Phys. **68**(1), 13 (1996)

72. G. Kotliar, S.Y. Savrasov, K. Haule, V.S. Oudovenko, O. Parcollet, C.A. Marianetti, Electronic structure calculations with dynamical mean-field theory. Rev. Mod. Phys. **78**(3), 865 (2006)
73. T. Maier, M. Jarrell, T. Pruschke, M.H. Hettler, Quantum cluster theories. Rev. Mod. Phys. **77**(3), 1027 (2005)
74. C. Weber, K. Haule, G. Kotliar, Apical oxygens and correlation strength in electron-and hole-doped copper oxides. Phys. Rev. B **82**(12), 125107 (2010)
75. A. Fuhrmann, D. Heilmann, H. Monien, From Mott insulator to band insulator: a dynamical mean-field theory study. Phys. Rev. B **73**(24), 245118 (2006)
76. H. Hafermann, M.I. Katsnelson, A.I. Lichtenstein, Metal-insulator transition by suppression of spin fluctuations. EPL (Europhys. Lett.), 85(3):37006 (2009)
77. S.S. Kancharla, S. Okamoto, Band insulator to Mott insulator transition in a bilayer Hubbard model. Phys. Rev. B **75**(19), 193103 (2007)
78. H. Lee, Y.-Z. Zhang, H.O. Jeschke, R. Valentí, Competition between band and Mott insulators in the bilayer Hubbard model: a dynamical cluster approximation study. Phys. Rev. B **89**(3), 035139 (2014)
79. D. Munzar, C. Bernhard, A. Golnik, J. Humlíček, M. Cardona, Anomalies of the infrared-active phonons in underdoped $YBa_2Cu_3O_y$ as evidence for the intra-bilayer Josephson effect. Sol. State Comm. **112**(7), 365–369 (1999)
80. J. Corson, R. Mallozzi, J. Orenstein, J.N. Eckstein, I. Bozovic, Vanishing of phase coherence in underdoped $Bi_2Sr_2CaCu_2O_{8+\delta}$. Nature **398**(6724), 221–223 (1999)
81. J. Bäckström, D. Budelmann, R. Rauer, M. Rübhausen, H. Rodriguez, H. Adrian, Optical properties of $YBa_2Cu_3O_{7-\delta}$ and $PrBa_2Cu_3O_{7-\delta}$ films: high-energy correlations and metallicity. Phys. Rev. B **70**(17), 174502 (2004)
82. M. Rübhausen, A. Gozar, M.V. Klein, P. Guptasarma, D.G. Hinks, Superconductivity-induced optical changes for energies of 100δ in the cuprates. Phys. Rev. B **63**(22), 224514 (2001)
83. H.J.A. Molegraaf, C. Presura, D. Van Der Marel, P.H. Kes, M. Li, Superconductivity-induced transfer of in-plane spectral weight in $Bi_2Sr_2CaCu_2O_{8+\delta}$. Science **295**(5563), 2239–2241 (2002)
84. A.V. Boris, N.N. Kovaleva, O.V. Dolgov, T. Holden, C.T. Lin, B. Keimer, C. Bernhard, In-plane spectral weight shift of charge carriers in $YBa_2Cu_3O_{6.9}$. Science **304**(5671), 708–710 (2004)
85. T.D. Stanescu, P. Phillips, Pseudogap in doped Mott insulators is the near-neighbor analogue of the Mott gap. Phys. Rev. Lett. **91**(1), 017002 (2003)
86. F. Carbone, A.B. Kuzmenko, H.J. Molegraaf, E. Van Heumen, V. Lukovac, F. Marsiglio, D. van der Marel, K. Haule, G. Kotliar, H. Berger, Doping dependence of the redistribution of optical spectral weight in $Bi_2Sr_2CaCu_2O_{8+\delta}$. Phys. Rev. B **74**(6), 064510 (2006)
87. S.L. Cooper, D. Reznik, A. Kotz, M.A. Karlow, R. Liu, M.V. Klein, W.C. Lee, J. Giapintzakis, D.M. Ginsberg, B.W. Veal, Optical studies of the a-, b-, and c-axis charge dynamics in $YBa_2Cu_3O_{6+x}$. Phys. Rev. B **47**(13), 8233 (1993)
88. J. Kircher, M.K. Kelly, S. Rashkeev, M. Alouani, D. Fuchs, M. Cardona, Anisotropy and oxygen-stoichiometry dependence of the dielectric tensor of $YBa_2Cu_3O_{7-\delta}$ ($0 \leq \delta \leq 1$). Phys. Rev. B **44**(1), 217 (1991)
89. R. Merlin, Generating coherent THz phonons with light pulses. Sol. State Comm. **102**(2), 207–220 (1997)
90. H.J. Zeiger, J. Vidal, T.K. Cheng, E.P. Ippen, G. Dresselhaus, M.S. Dresselhaus, Theory for displacive excitation of coherent phonons. Phys. Rev. B **45**(2), 768 (1992)
91. J.J. Li, J. Chen, D.A. Reis, S. Fahy, R. Merlin, Optical probing of ultrafast electronic decay in Bi and Sb with slow phonons. Phys. Rev. Lett. **110**(4), 047401 (2013)
92. S. Sugai, H. Suzuki, Y. Takayanagi, T. Hosokawa, N. Hayamizu, Carrier-density-dependent momentum shift of the coherent peak and the LO phonon mode in p-type high-T_c superconductors. Phys. Rev. B **68**(18), 184504 (2003)
93. S. Sugai, Y. Takayanagi, N. Hayamizu, T. Muroi, R. Shiozaki, J. Nohara, K. Takenaka, K. Okazaki, Superconducting pairing and the pseudogap in the nematic dynamical stripe phase of $La_{2-x}Sr_xCuO_4$. J. Phys-Condens. Mat. **25**(47), 475701 (2013)

94. J. Lorenzana, B. Mansart, A. Mann, A. Odeh, M. Chergui, F. Carbone, Investigating pairing interactions with coherent charge fluctuation spectroscopy. Eur. Phys. J. Spec. Top. **222**(5), 1223–1239 (2013)
95. O.V. Misochko, K. Kuroda, N. Koshizuka, Superconducting gap anisotropy and phonon anomalies in single crystal $NdBa_2Cu_3O_{7-x}$. Phys. Rev. B **56**(14), 9116 (1997)
96. O.V. Misochko, K. Kisoda, K. Sakai, S. Nakashima, Dynamics of low-frequency phonons in the $YBa_2Cu_3O_{7-x}$ superconductor studied by time-and frequency-domain spectroscopies. Phys. Rev. B **61**(6), 4305 (2000)
97. O.V. Misochko, E.Y. Sherman, N. Umesaki, K. Sakai, S. Nakashima, Superconductivity-induced phonon anomalies in high-T_C superconductors: a Raman intensity study. Phys. Rev. B **59**(17), 11495 (1999)
98. O.V. Misochko, Anisotropy of the Raman scattering measured in the xy plane of a nontwinned $YBa_2Cu_3O_{7-x}$ single crystal. J. Exp. Theor. Phys. **94**(2), 345–349 (2002)
99. C. Giannetti, G. Coslovich, F. Cilento, G. Ferrini, H. Eisaki, N. Kaneko, M. Greven, F. Parmigiani, Discontinuity of the ultrafast electronic response of underdoped superconducting $Bi_2Sr_2CaCu_2O_{8+\delta}$ strongly excited by ultrashort light pulses. Phys. Rev. B **79**(22), 224502 (2009)
100. H. Okamoto, T. Miyagoe, K. Kobayashi, H. Uemura, H. Nishioka, H. Matsuzaki, A. Sawa, Y. Tokura, Photoinduced transition from Mott insulator to metal in the undoped cuprates Nd_2CuO_4 and La_2CuO_4. Phys. Rev. B **83**(12), 125102 (2011)
101. I.I. Mazin, A.I. Liechtenstein, O. Jepsen, O.K. Andersen, C.O. Rodriguez, Displacive excitation of coherent phonons in $YBa_2Cu_3O_{7-\delta}$. Phys. Rev. B **49**(13), 9210 (1994)
102. B.S. Shastry, B.I. Shraiman, Theory of Raman scattering in Mott-Hubbard systems. Phys. Rev. Lett. **65**(8), 1068 (1990)
103. T.P. Devereaux, R. Hackl, Inelastic light scattering from correlated electrons. Rev. Mod. Phys. **79**(1), 175 (2007)
104. J. Chang, E. Blackburn, A.T. Holmes, N.B. Christensen, J. Larsen, J. Mesot, R. Liang, D.A. Bonn, W.N. Hardy, A. Watenphul, Direct observation of competition between superconductivity and charge density wave order in $YBa_2Cu_3O_{6.67}$. Nat. Phys. **8**(12), 871–876 (2012)
105. J.P. Hinton, E. Thewalt, Z. Alpichshev, F. Mahmood, J.D. Koralek, M.K. Chan, M.J. Veit, C.J. Dorow, N. Barisć, A.F. Kemper, The rate of quasiparticle recombination probes the onset of coherence in cuprate superconductors. Nat. Sci. Rep., **6** (2016)
106. Y. Terada, S. Yoshida, O. Takeuchi, H. Shigekawa, Real-space imaging of transient carrier dynamics by nanoscale pump-probe microscopy. Nat. Phot. **4**(12), 869–874 (2010)
107. T.L. Cocker, V. Jelic, M. Gupta, S.J. Molesky, J.A.J. Burgess, G. De Los Reyes, L.V. Titova, Y.Y. Tsui, M.R. Freeman, F. A. Hegmann, An ultrafast terahertz scanning tunnelling microscope. Nat. Phot. **7**(8), 620–625 (2013)
108. J. Rajeswari, P. Huang, G.F. Mancini, Y. Murooka, T. Latychevskaia, D. McGrouther, M. Cantoni, E. Baldini, J.S. White, A. Magrez, T. Giamarchi, H.M. Rønnow, F. Carbone, Filming the formation and fluctuation of skyrmion domains by cryo-Lorentz transmission electron microscopy. Proc. Natl. Acad. Sci. **112**(46), 14212–14217 (2015)

Chapter 7
Lattice-Mediated Magnetic Order Melting in Multiferroic Mott Insulators

One fascinating topic in the field of nonequilibrium dynamics concerns the manipulation and control of magnetic order using ultrashort laser pulses. This subject has rapidly improved in the last decade, due to its relevance for modern data storage and processing technology [1]. The ultimate success of this research field is intimately related to the comprehension of the response that a specific magnetic material will exhibit upon the interaction with a tailored light pulse. Being able to predict the pathway followed by the energy and the angular momentum from the initial photons to the spin degrees of freedom can pave the route to the development of novel materials with superior functionalities. However, despite huge efforts, this problem is still open, as the ultrafast interaction sets a material in a highly nonequilibrium state and leads to the failure of the conventional thermodynamic description of magnetic phenomena. Under these conditions, a wealth of effects can take place depending on the nature of the interaction and the properties of a specific magnetic material.

First pioneering experiments in the field were performed on FM materials using 60 fs laser pulses, which resulted in a sub-picosecond demagnetization of the film [2–5]. Subsequent experiments also demonstrated the possibility to optically generate coherent magnetic precession [6, 7], laser-induced spin reorientation [8, 9] or even modifications of the magnetic structure within 1 ps [10, 11]. These experiments led to the identification of two main mechanisms through which photons are absorbed by the material and influence its magnetic order: (i) A thermal effect, in which the change in the magnetic order corresponds to that of the spin temperature. Light does not couple directly to spins, but exchanges energy into the electronic and phonon subsystems. As a result, the magnetic order dynamics is determined by internal equilibration processes, such as the electron-electron, electron-phonon and electron-spin interactions. While in itinerant ferromagnets this energy exchange can proceed even on a timescale of 50 fs, in dielectric ferromagnets it can last for several nanoseconds due to the absence of a direct electron-spin coupling; (ii) A non-thermal effect, which involves the absorption of the pump photons by some electronic states having a direct influence on the magnetic parameters. This interaction is instantaneous but the parameters cause a motion of the magnetic moments that obeys the usual precession behaviour.

E. Baldini, *Nonequilibrium Dynamics of Collective Excitations in Quantum Materials*,
Springer Theses, https://doi.org/10.1007/978-3-319-77498-5_7

As anticipated in Chap. 2, to model the complexity of the magnetic order dynamics, a simple three-temperature model has been widely used, where the three temperatures are assigned to three separate but interacting reservoirs, i.e. the electrons, the lattice and the spins. However, this assignment is possible only if a certain equilibrium is assumed within the considered subsystem. Given the short time scales, this assumption is not always valid, imposing a limit on the applicability of this model.

In the last years, the field of ultrafast magnetism has broadened its horizons beyond weakly correlated ferromagnets, extending the investigation to the class of strongly correlated quantum systems. These materials offer an intricate interplay among the charge, spin, orbital and lattice degrees of freedom, posing new challenges to the comprehension of the ultrafast dynamics. More remarkably, a variety of materials display emergent magnetic phenomena that involve exotic spin patterns at low temperatures. Of particular interest is the class of solids known as "frustrated magnets", in which competing interactions between spins preclude simple magnetic orders. This, in turn, may lead to AFM spiral spin structures and, consequently, to an electric polarization. This peculiar type of multiferroicity is highly desirable, as one can use electric fields to switch magnetic order or magnetic fields to switch the spontaneous electric polarization.

One of the most valuable probes of the magnetic order dynamics is time-resolved resonant x-ray scattering (trREXS), which nowadays can reach a time resolution of 100 fs in slicing facilities at third-generation synchrotron sources and in free-electron lasers. After the photoexcitation with an ultrashort laser pulse, a soft x-ray probe tuned to a resonance can provide the highest sensitivity to spin, orbital, and charge order in combination with element selectivity. In regard to the magnetic order dynamics, using this technique on $La_{0.5}Sr_{1.5}MnO_4$ upon ultrafast resonant excitation of an infrared-active phonon mode, the magnetic order was observed to reduce within a few ps [12]. A similar timescale was retrieved in the realization of a magnetic phase transition from the collinear commensurate phase to the spiral incommensurate phase of CuO after photoexcitation at 1.55 eV [13]. These preliminary experiments established a characteristic timescale for the magnetic disordering of a strongly correlated system with exotic spin pattern. In this context, an unexpected phenomenon has been recently observed by trREXS in $TbMnO_3$ [14, 15], which is a prototypical example of type-II multiferroic chiral magnet. In these experiments, optical excitation in the near-infrared/visible range has been shown to lead to a delayed melting of the long-range magnetic order on a time scale of $\sim$20 ps [14]. Time-resolved measurements of magnetic x-ray scattering have suggested that the loss of magnetic order and the associated Mn 3*d* orbital reconstruction follows a quasi-adiabatic pathway from the cycloidal phase through an intermediate sinusoidal phase, similar to what is seen when slowly increasing the temperature [15]. Unlike the situation seen in thermal equilibirum, the wavevector of the spin ordering in the intermediate sinusoidal phase remains at a value equivalent to the cycloidal ordering wavevector. A direct coupling between magnetic and orbital orders was also found by monitoring the orbital reconstruction induced by the spin ordering [15]. Although these studies shed light on various mechanisms occurring in $TbMnO_3$ upon photoexcitation, a complete microscopic explanation for the delayed demagnetization process is still lacking. The slow

dynamics imply a delayed transfer of energy from the photoexcited carriers to the spin system, which is at odds with the behaviour observed in other correlated oxides with long-range spin order [12, 13]. As such, the dynamic bottleneck may be due to the lattice or to the spin system itself, or to a combination of both.

A promising route to elucidate the energy pathway and the possible involvement of other degrees of freedom in the melting process is to perform ultrafast optical spectroscopy with a combination of broad detection window and high temporal resolution. A broad detection window becomes crucial when large shifts of the optical SW are induced by magnetic ordering phenomena. Despite being an indirect probe of magnetism, it is well established that photons in the optical range can access magnetic and other complex ordering phenomena, as changes of the symmetry in a system upon ordering are often reflected in the optical properties of the material. This effect is at play in the insulating perovskite manganites and manifests on the *d*-*d* intersite transitions of the optical spectrum [16]. A high temporal resolution is key to overcome the limitations imposed by trREXS experiments. Improving the time resolution below 50 fs can reveal the timescales on which the excited electronic states redistribute their excess energy and unveil the fingerprint, if any, of specific collective modes of the lattice or the spin subsystems. Thus, by applying our nonequilibrium approach with 45 fs time resolution, we can elucidate how the energy exchange among several degrees of freedom proceeds in a $TbMnO_3$ single crystal after photoexcitation at 1.55 eV. In this Chapter, after introducing the properties of $TbMnO_3$ in Sect. 7.1, we first focus on the steady-state optical properties of the material in Sect. 7.2. Section 7.3 is devoted to the description of the spontaneous Raman scattering data, as these will be crucial for the interpretation of the pump-probe experiment. Next, in Sect. 7.4, we perturb the system out-of-equilibrium and interrogate the spectro-temporal signatures for the melting of the long-range AFM order on long timescales. By means of our ultrafast time resolution, we disentangle the dynamics of the different degrees of freedom in the system and observe a complex collective response of the lattice. The latter precedes the magnetic order melting and is interpreted as the fingerprint of the formation of anti-JT polarons in the material. We finally conclude with Sect. 7.5, providing a complete picture of the ultrafast dynamics following photoexcitation of $TbMnO_3$ using a 1.55 eV laser pulse.

7.1 $TbMnO_3$

The class of perovskite $RMnO_3$ manganites (where R is a rare-earth ion) represents a family of strongly correlated electron systems that displays rich phase diagrams and exhibits a number of intriguing cooperative phenomena. The complexity behind the behaviour of these materials is the result of the strong coupling between charge, orbital, magnetic and lattice degrees of freedom. This subtle interplay lies at the origin of the peculiar ordering patterns characterizing each manganite. The simplest manganite belonging to this family, $LaMnO_3$, possesses an orthorhombic crystal structure, a C-type orbital ordering below T_{OO} = 750–800 K and an A-type spin

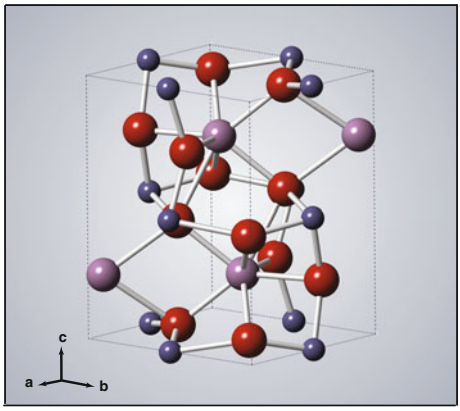

Fig. 7.1 Crystallographic structure of $TbMnO_3$, showing its orthorhombic unit cell. The Mn atoms are depicted in blue, the O atoms in red and the Tb atoms in violet

ordering below the Néel temperature $T_N = 140$ K [17, 18]. As already illustrated in Fig. 1.4 of Chap. 1, upon substitution of the La ion with other R ions, these compounds undergo pronounced structural and magnetic ordering changes [17]. Indeed, to compensate for the strain produced by the modified ionic radius, the ideal perovskite structure undergoes a strong cooperative lattice distortion, in which the octahedra rotate collectively about the orthorhombic <010> and <001> direction [19]. The degree of lattice distortion affects the tilting of the Mn-O-Mn bond and determines in turn the magnetic properties of the crystal, as shown in Fig. 1.4. The crystal structure eventually modifies from orthorhombic ($R = La - Dy$) to hexagonal ($R = Ho - Lu$) when the size of the R ion reaches a threshold. Sitting at the boundary of this structural phase transition lie $TbMnO_3$ and $DyMnO_3$, in which the orthorhombic perovskite structure lowers its symmetry to the most-distorted *Pbnm* $GdFeO_3$-type lattice.

The $GdFeO_3$-distorted structure, represented in Fig. 7.1b, is at the origin of the exotic spin ordering patterns and mutiferroic properties characterizing $TbMnO_3$ and $DyMnO_3$. In regard to the magnetic properties, it is the delicate balance between different types of exchange interactions that stabilizes complex long-range spin ordering patterns. In particular, the sign, character and strength of the superexchange interaction is affected by the geometry of the Mn-O-Mn bond, crystalline symmetry, orbital occupation and intermediate ligands and can be phenomenologically determined via the Goodenough-Anderson-Kanamori rules [20–23]. In distorted manganites, many competing exchange paths can exist between nearest neighbour and next nearest neighbour Mn ions and this can lead to magnetic frustration of the Mn^{3+} spin degree of freedom [17]. In $TbMnO_3$, it is this magnetic frustration that causes the exotic long-range spin ordering patterns unraveled by neutron scattering [24–26] and REXS [27–29]. At RT, this material is paramagnetic, as no spin order is observed. When the temperature is decreased below $T_{ONS} = 100$ K, short-range spin correlations start developing, and a magnetic and structural fluctuating regime dominates a wide temperature range. The first magnetic phase transition is observed at $T_{N1} = 42$ K with the establishment of a paraelectric SDW state, in which a sinusoidal AFM spin structure forms along the *b*-axis (Fig. 7.2a). A second magnetic phase transition occurs around

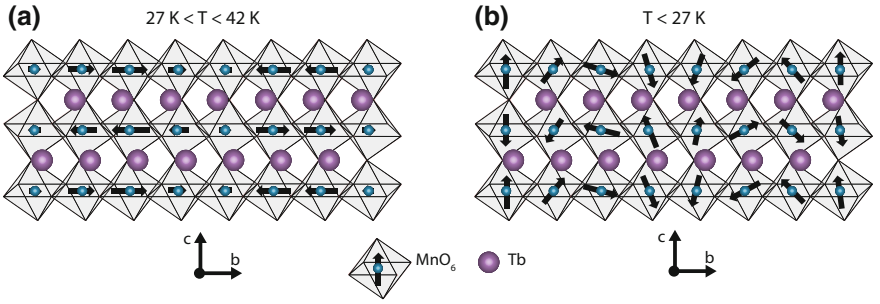

Fig. 7.2 Schematic representation of spin order in $TbMnO_3$ (**a**) in the paraelectric SDW state (27 K < T < 42 K) and **b** in the spin cycloid phase (T < 27 K). Mn atoms are represented in blue, Tb atoms in violet and O atoms are omitted at the vertices of the MnO_6 octahedra. The ellipticity in **b** has been neglected

T_{N2} = 27 K, at which the spins on the Mn^{3+} sites order in a spin cycloid in the *bc* plane (Fig. 7.2b). The spin cycloid order builds on top of the pre-existing SDW-like order and the Tb spins follow the ordering of the Mn spins. An additional transition related to the 4*f* spins of the Tb^{3+} ions is finally observed at 7 K [25, 30].

The existence of more than one magnetic phase transition suggests that several magnetic interactions are simultaneously competing in this system and at the origin of the magnetic frustration. Besides the nearest neighbour and next-nearest neighbour AFM superexchange that we have already mentioned, the Dzyaloshinskii-Moriya interaction and the biquadratic interaction are also expected to play a crucial role [31, 32]. Moreover, it is well established that, in all magnetically ordered phases of $TbMnO_3$, the Mn spins possess a FM order along the *b*-axis and an AFM order along the *c*-axis. The cycloid spin ordering has a remarkable impact on the properties of the low temperature phase, representing the source of multiferroicity in $TbMnO_3$. Indeed, this spiral order creates a spontaneous ferroelectric polarization along the *c*-axis due to the inverse Dzyaloshinskii-Moriya interaction, further stabilized by the atomic displacements [25, 30, 33]. In other words, it is the spin-order breaking inversion symmetry that drives the ferroelectric order, and thus multiferroicity in $TbMnO_3$ is of the "improper" type (also known as "type II"). This is a rare situation, since two ferroic orders of different kind (one magnetic, one electric) coexist and are mutually connected via magnetoelectric coupling. In Sect. 7.3, we will describe how this spin-charge coupling leads also to the emergence of exotic hybrid collective modes in the system.

From the above discussion, it becomes evident that the coupling among several degrees of freedom makes multiferroic manganites the natural playground where to test the capabilities of ultrafast spectroscopy. In this regard, crucial to the interpretation of the experiments performed under nonequilibrium conditions is the clarification the electronic properties of these compounds. Hence, in the following, we focus on the electronic structure of the $RMnO_3$ manganites, putting strong emphasis on $TbMnO_3$. We start with a simplified ionic model, which neglects the hybridization

effect among the Mn and O orbitals [19]. In an ideal perovskite $RMnO_3$ manganite, the Mn^{3+} ion has an electronic configuration d^4 and sits in the octahedral environment of six O anions. While the crystal-field effect splits the Mn d-levels into a set of three degenerate t_{2g} and two degenerate e_g orbitals, the high-spin d^4 configuration leads to the JT structural distortion and lifts the t_{2g} and e_g degeneracy. When the displacement involves a particular axis of the octahedron, it gives rise to a static JT effect, but at high temperatures the distortion can switch from one axis to another, generating a dynamic mechanism. Irrespective of the particular axis of distortion, in a crystal lattice the JT effect sets in a cooperative way from unit cell to unit cell, leading to the establishment of an orbital order in the system [19]. As a consequence, while the GS properties of many correlated materials can be described by considering only the charge and spin degrees of freedom, in manganites the orbital state also plays a relevant role. Clear evidence for the strength of this effect in manganites is provided by the very high orbital ordering temperatures T_{OO} (from 750–800 K for $LaMnO_3$ to 1500 K for $TbMnO_3$) [18]. In the specific case of $TbMnO_3$, the orbital order involves mainly the $|y^2>$ state, with some admixture from the $|x^2 - z^2>$ state, leading to a JT elongation along the y axis [18].

The following step in the description of the electronic structure involves the inclusion of the hybridization between the O p orbitals and the Mn d orbitals. In this regard, differently from other strongly correlated quantum systems, a major breakthrough in understanding the electronic structure of the manganites has been made by optical spectroscopy [16, 34, 35]. Despite offering only indirect information on the material DOS, optical spectroscopy and especially SE remains one of the most efficient techniques to inspect the material electronic structure, especially when momentum-resolved information on the single-particle excitation spectrum cannot be easily retrieved by ARPES. In the case of manganites, the detailed and quantitative analysis of the temperature-dependent optical conductivity provided strong indication that the insulating gap is of Mott-Hubbard origin rather than of p-d CT character [16, 34]. These pioneering works triggered a variety of theoretical and additional optical studies to elucidate the fine structure emerging in the experimental spectra, which is a clear manifestation of the intrinsic complexity of this material. At the time of writing, the origin of the fine structure in the manganite optical spectrum is a subject of intense debate [16, 35–37]. The main difficulty regards the presence of numerous degrees of freedom that can concur to generate the observed optical transitions. Thus, the main questions that remain open regard the role of the initial and final states associated with these transitions, and the possible involvement of intra-atomic correlations and lattice relaxation. This topic is widely discussed in Sect. 7.2. An increasing number of ab initio calculations is also emerging for describing the electronic structure of undoped manganites of the $RMnO_3$ family, using DFT + U (based on LDA or GGA) [38, 39]. Despite being still far from capturing all the details of the optical data, these computational techniques are rapidly contributing to the comprehension of the origin behind the main elementary excitations of the material. In the next Section, we will make use of DFT + U calculations to assign the coarse features of the optical conductivity spectrum of $TbMnO_3$.

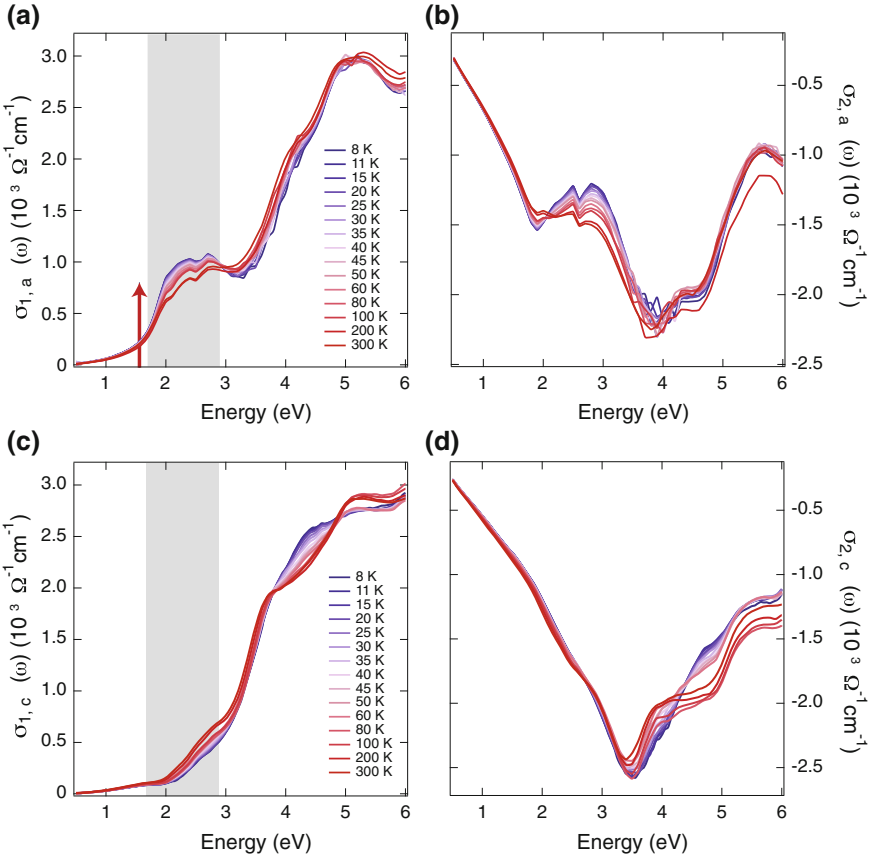

Fig. 7.3 Temperature dependence of the **a**, **c** real $\sigma_1(\omega)$ and **b**, **d** imaginary $\sigma_2(\omega)$ parts of the complex optical conductivity of $TbMnO_3$; **a**, **b** refer to the optical response for light polarized along the a-axis, **c**, **d** for light polarized along the c-axis. The red arrow indicates the pump photoexcitation at 1.55 eV in the nonequilibrium experiment. The grey shaded area represents the spectral region monitored by the probe along the two different axes

7.2 Steady-State Optical Properties

A crucial prerequisite for our nonequilibrium study consists in the measurement and comprehension of the steady-state optical properties of $TbMnO_3$. To this aim, in this Section we present the temperature dependent anisotropic optical response of an untwinned (010)-oriented single crystal of $TbMnO_3$, as measured by SE in the spectral range between 0.50–6.00 eV.

Figure 7.3a–d shows the temperature dependence of the real- ($\sigma_1(\omega)$) and imaginary ($\sigma_2(\omega)$) parts of the optical conductivity, measured with light polarized parallel to the a- (**E** ∥ a) and c-axis (**E** ∥ c) of the crystal. We observe a marked anisotropy

between the $\sigma_a(\omega)$ and $\sigma_c(\omega)$ response, which confirms the complete detwinning of our $TbMnO_3$ single crystal. The $\sigma_{1a}(\omega)$ spectrum is featureless in the near-infrared region and is dominated by two broad absorption bands, centred around 2.45 and 5.15 eV. The two optical bands are found to persist in the proximity of these characteristic energies at all measured temperatures. However, as the temperature is increased from 8 to 300 K, a number of smaller spectral features emerge on top of the optical band at 2.45 eV. In contrast, the $\sigma_{1c}(\omega)$ spectrum presents a tail-like structure covering the $2.00 - 3.00$ eV region and a complex feature evolving with temperature between 3.80 and 6.00 eV. The latter consists of an optical band centered around 4.50 eV at 8 K, which progressively loses SW for increasing temperature and splits into two well distinguished features at 3.90 and 5.15 eV above 25 K. Our anisotropic $\sigma(\omega)$ response is in agreement with the one reported in a previous study on untwinned $TbMnO_3$ single crystals [40]. Nevertheless, in our SE experiment, we access a broader spectral range of $\sigma(\omega)$, which allows for the observation of a clear temperature evolution in the c-axis response between 4.00 and 6.00 eV.

To provide a detailed description of the steady-state optical response of $TbMnO_3$, we first rely on the conclusions drawn by other works in literature on orthorhombic manganites. Indeed, in the last decade, the optical spectrum of the insulating (i.e. undoped) manganites has been subject of intensive theoretical and experimental studies [16, 34–37, 40–46]. The main goals were to clarify the origin of the different bands manifesting in the spectra and to identify possible signatures of the magnetic ordering on the optical response of the material. Particular attention has been devoted to $LaMnO_3$, which represents the manganite of the $RMnO_3$ family with the lowest degree of structural distortion from the ideal perovskite (Fig. 7.1).

Early normal-incidence reflectivity studies [41–43] assigned both the low-energy and high-energy bands along the b-axis to p-d CT excitations, thus concluding that $LaMnO_3$ is a CT insulator in the ZSA picture [47]. Other works instead assigned the low-energy feature to the JT orbiton excitation or d-d crystal field transitions [48]. The orbiton model predicts the formation of self-trapped orbital defects in the orbital ordered GS, which behave similarly to Frenkel excitons in molecular crystals and provide optical absorption at specific photon energies. Later, temperature-dependent measurements of normal-incidence reflectivity revealed a pronounced rearrangement of SW between the two bands, suggesting a strong involvement of the CT hopping between nearest-neighbour Mn^{3+} ions (i.e. intersite d-d transitions) [44]. However, it was just with the combined use of temperature dependent SE and modelling that a link between the anisotropic SW in the optical spectra and the spin correlations manifesting in the system was unraveled [16, 34]. A strong redistribution of SW was found to occur close to the Néel temperature $T_N = 140$ K and the anisotropic behaviour of this SW transfer could be traced back to the characteristic magnetic ordering pattern setting in the material. The use of a superexchange model quantitatively reproduced the SW transfer induced by the establishment of the magnetic order, leading to the assignment of the optical bands appearing in the spectra. It was concluded that the broad low-energy band in the ab-plane response of $LaMnO_3$ originates from intersite Mn^{3+} d-d CT transitions (i.e. $d_i^4\, d_j^4 \rightarrow d_i^3\, d_j^5$ between neighbouring i and j Mn ions), preserving the electronic spin state. It is therefore a high-spin (HS) transition

that becomes favoured in the AFM phase. The *c*-axis low-energy optical response is instead governed by the CT between Hund states of neighbour Mn^{3+} ions with antiparallel spin. Thus, it involves a low-spin (LS) transition. In contrast, the more isotropic high-energy band was attributed to the manifold of CT transitions from O $2p$ to Mn $3d$ levels. As anticipated in the previous Section, such an assignment has a profound consequence for the interpretation of the perovskite manganites electronic structure, as it implies that $LaMnO_3$ is a Mott-Hubbard insulator and not a *p*-*d* CT insulator [47]. The HS band should be then interpreted as an intersite *d*-*d* CT transition across the Mott gap, between the LHB and the UHB. The same conclusion was drawn by calculations based on the orbitally-degenerate Hubbard model [49]. In addition, a clear manifestation of the *d*-*d* CT origin of the low-energy band came from the resonant enhancement at 2.00 eV of the B_{2g} breathing mode in spontaneous Raman scattering, as this mode strongly modulates the intersite *d*-*d* CT [50].

Here, we confirm the latter assignments by employing DFT calculations of the electronic structure and the optical properties of $TbMnO_3$. The exchange-correlation potential were treated using GGA + U, where U was set at 3 and 6 eV for Mn 3d and Tb 4f orbitals, respectively. The computational details are reported in the Appendix C. The calculated equilibrium optical responses along the *a*- and *c*-axes are shown in Fig. 7.4a, b together with the experimental data measured at 8 K. For the *a*-axis response we see a relatively good agreement between our calcualtions and the experiment. For the *c*-axis response the agreement is mostly qualitative but does capture the rough position and magnitude of the increase in absorption with increasing energy. Based on the calculated electronic DOS, the low-energy feature is identified with intersite *d*-*d* transitions while the higher energy feature is identified with CT excitation from O $2p$ to Mn $3d$ levels. These combined experimental-theoretical efforts clarify the coarse features of the optical spectrum, but the origin of the fine

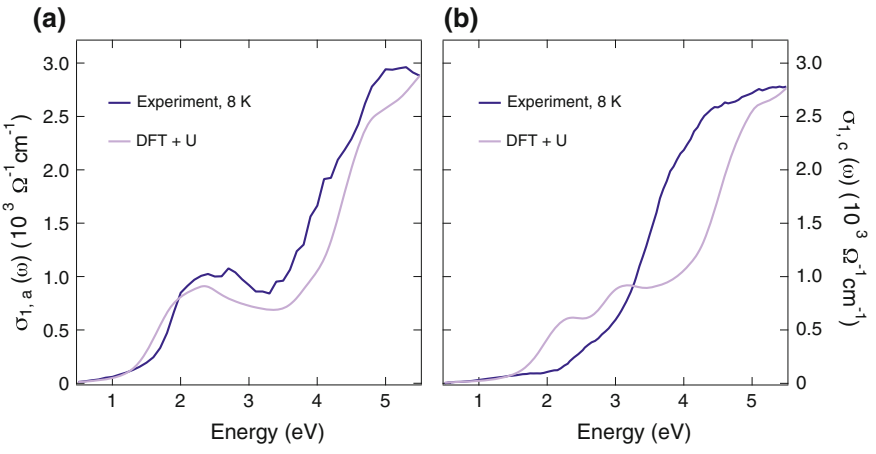

Fig. 7.4 Comparison between $\sigma_1(\omega)$ of $TbMnO_3$ measured at 8 K (blue curve) and computed from DFT + U calculations (violet curve): **a** *a*-axis response; **b** *c*-axis response

structure of the HS band remained largely unexplained. Recently, several authors have attemped to better understand this fine structure by combining new SE experiment and theoretical calculations. The fine structure has been first attributed to Mn^{3+} *d-d* crystal field transitions split by the JT effect [36]. More significantly, a very complete and detailed study assigned a dual nature (*d-d* and *p-d*) to the fundamental optical gap, since this is also characterized by forbidden/weakly-allowed *p-d* transitions that act as a precursor to the strong dipole-allowed *p-d* CT transition at higher energies [35]. Thus, the fine structure reflects these *p-d* transitions overlapped to the *d-d* HS absorption band, giving rise to an intermediate regime between the *p-d* CT and the Mott-Hubbard insulator in the ZSA scheme [47]. A more recent interpretation relate the fine structure to quantum rotor orbital excitations for the e_g electron of Mn^{3+} ions, disturbed by the lattice anharmonicity [37]. Therefore, the issue of the fine structure in the absorption spectrum is still an open one and will be also addressed by our nonequilibrium experiment in Sect. 7.4.3.

Differently from $LaMnO_3$, $TbMnO_3$ retains such a fine structure of the *d-d* HS band even at very low temperatures, as evident in the high-resolution spectrum of $\sigma_{1,a}(\omega)$ in Fig. 7.5. Moreover, the centre of mass of the HS optical band in $TbMnO_3$ is shifted towards higher energies than the corresponding one in $LaMnO_3$. The latter effect is a general one in the electrodynamics of manganites. It is observed that for decreasing radius of the R ion, the low-energy band decreases its SW and blueshifts from 2.00 to 2.20 eV, consistent with our data. This effect has been explained by assuming that the JT distortion increases for smaller R ion sizes, thus enhancing the value of the *d-d* CT energy [35].

As our ultrafast study in the following Sections involves the measurements of the transient reflectivity ($\Delta R/R$) of the $TbMnO_3$ crystal, it is relevant to calculate the anisotropic reflectivity spectrum under equilibrium conditions from the SE measurements. Figure 7.6a, b shows the temperature-dependent reflectivity spectra along the

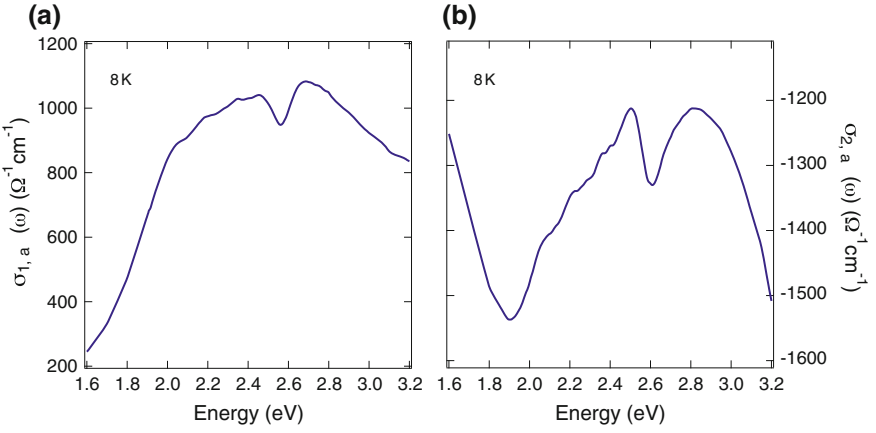

Fig. 7.5 **a** Real $\sigma_{1a}(\omega)$ and **b** imaginary $\sigma_{2a}(\omega)$ parts of the *a*-axis complex optical conductivity of $TbMnO_3$, measured at 8 K via SE

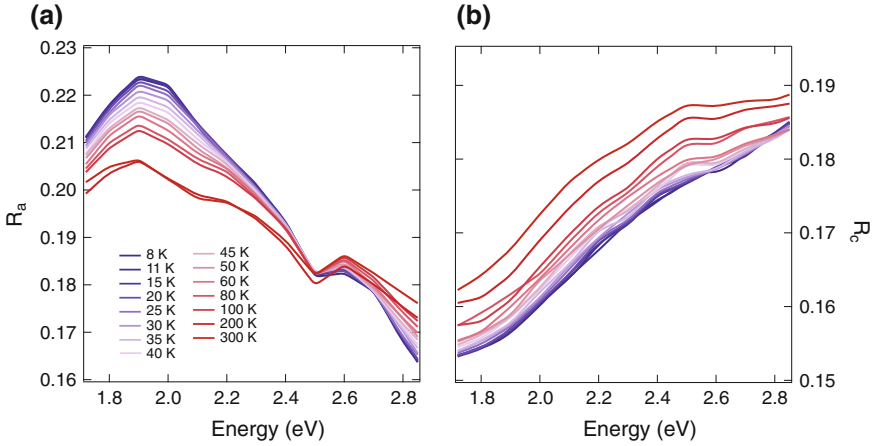

Fig. 7.6 Temperature dependence of the **a** *a*-axis (**b**) *c*-axis reflectivity of $TbMnO_3$

a- and *c*-axis, respectively. The spectral range presented is limited to the one covered by the broadband probe in the nonequilibrium experiment. The reflectivity along the *a*-axis comprises a pronounced feature centred around 1.90 eV and is characterized by the presence of a fine structure on top. A second feature emerges around 2.60 eV, separated from the former by a dip in the reflectivity. Along the *c*-axis, the reflectivity monotonically increases its value for higher energies and shows a more structured spectrum in the 2.40–2.80 eV spectral region. More remarkably, consistent with the SW shifts identified in the previous discussion, we observe an opposite trend of the reflectivity as a function of temperature for the two different axes. For increasing temperatures, the *a*-axis reflectivity undergoes a prominent drop, while the *c*-axis reflectivity increases over the whole spectral range. We will see in Sect. 7.4 that this aspect enters into play in the interpretation of the pump-probe data.

7.3 Spontaneous Raman Scattering

To address the magnetic order dynamics in our $TbMnO_3$ crystal, the same experimental conditions of previous trREXS measurements reported in literature must be reproduced [14]. This implies photoexciting the system with an *a*-axis polarized pump beam at 1.55 eV, lying on the tail of the intersite *d*-*d* transition of the material (as indicated by the red arrow in Fig. 7.3). In these conditions, we can assume that a *real* charge density will be created in the system, corresponding to charge excitations across the Mott gap [16]. This charge density may subsequently couple to Raman-active modes of A_g symmetry via the displacive mechanism, thus generating a coherent response in the time domain [51]. However, we cannot exclude a priori that the pump pulse may act also non-resonantly via an ISRS mechanism, as we

have observed in Chap. 5 for La_2CuO_4 upon below-gap excitation. This can possibly lead to the generation of coherent modes even with different symmetry than A_g [52]. Based on these arguments, before introducing our experiment under nonequilibrium conditions, it is therefore crucial to show and clarify the Raman spectrum of the material, as measured by polarized spontaneous Raman scattering. In this way, possible modes of interest for our ultrafast broadband optical spectroscopy experiment can be identified.

The most intriguing feature appearing in the Raman spectra of $TbMnO_3$ is represented by the emergence of exotic collective modes, known as electromagnons, when the crystal is maintained in its multiferroic phase below 28 K. Electromagnons are hybrid magnon-phonon excitations exhibiting an oscillatory electric-dipole moment which is activated by the electric (and not magnetic) component of an incident light field [54]. In other words, it is the electric field that leads to the motion of the spins. These excitations can be observed both in FIR/THz spectroscopy [55–57] and spontaneous Raman scattering [53, 58]. Due to their nature, in FIR/THz spectroscopy electromagnons are activated by the electric field of light, differently from conventional magnetic modes that are excited via the magnetic field component. In spontaneous Raman scattering their observation is instead indirect, as the magnetic field does not couple directly to magnetic excitations and the electric field does via the spin-orbit coupling. Figure 7.7a, b summarises one of the main results obtained by spontaneous Raman scattering in the absence of an external magnetic field, adapted from Ref. [53]. When the electric field is set along the *b*-axis, two electromagnons arise at 3.86 and 7.94 meV and both correspond to propagating modes of the spins out of the cycloid plane. When the electric field is set along the *c*-axis, a single broad electromagnon peak is observed around 3.56 meV.

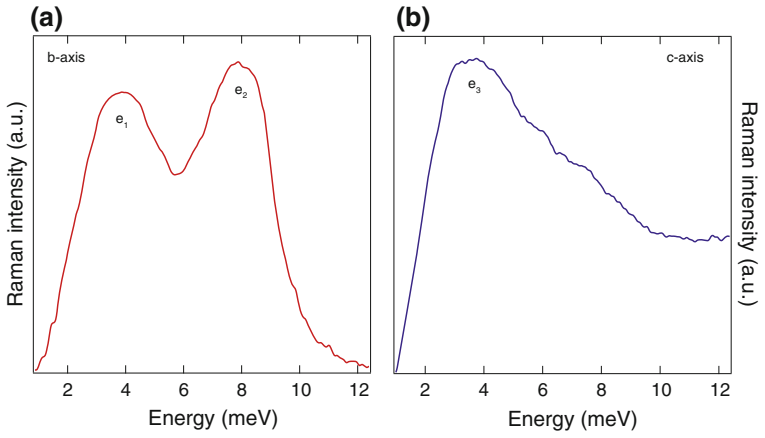

Fig. 7.7 **a**, **b** Raman spectra at 10 K on a (100)-oriented $TbMnO_3$ single crystal, as measured in Ref. [53]. The electric field of the incident light is polarized along the **a** *b*-axis **b** *c*-axis, respectively. The symbols e_1, e_2 and e_3 refer to electromagnon modes

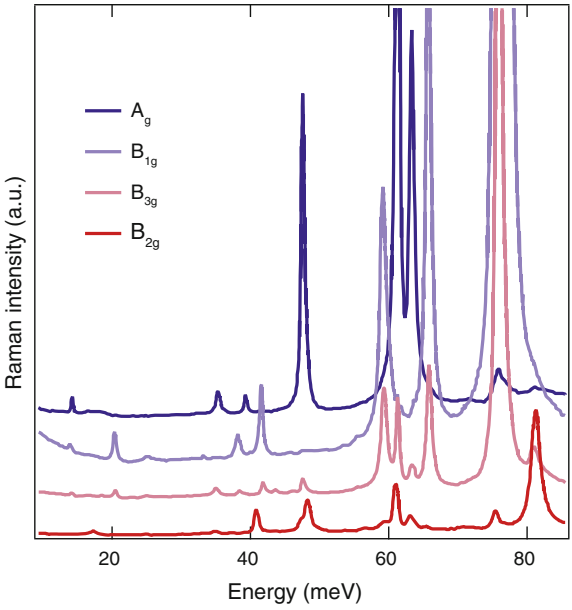

Fig. 7.8 Polarized Raman spectra of $TbMnO_3$ phonon modes at 10 K for different symmetries. The data have been adapted from Ref. [53]

Extensive experimental and theoretical studies in literature have also addressed the phononic Raman spectrum of $TbMnO_3$, which covers the 12–80 meV spectral range [53, 59–62]. Since in an ideal perovskite no Raman-active modes are allowed by symmetry, in $RMnO_3$ it is the deviation from the ideal lattice that leads to Raman activity. As a result, the activation of each Raman mode can be related to the value of one or two types of basic distortion of the normal perovskite (i.e. the rotations of MnO_6 octahedra around [101] or [010] directions, the JT distortion or the shift of R atoms). In the *Pbnm* space group of $TbMnO_3$, the Raman-active normal modes allowed from group theory considerations are 24. These phonon modes are classified in terms of their symmetries as: $\Gamma_{Raman} = 7A_g + 7B_{1g} + 5B_{2g} + 5B_{3g}$. Figure 7.8 shows the polarized Raman spectra of the phonon modes in $TbMnO_3$ at 10 K. The data are adapted from Ref. [53], which reports all the measured phonon energies and compares them with the results of previous calculations. Here, for our purposes, we provide only the assignments of the 7 A_g modes, as some of them will play an important role in the nonequilibrium dynamics upon photoexcitation (Sect. 7.4.3). Some representative eigenvectors are illustrated in Fig. 7.9, while the nomenclatures at the Γ point and assignments are summarised in Table 7.1. Mn ions do not participate with any Raman mode, as they are located at inversion centers, while the Tb and the apical O(1) ions display the same kind of movements. Particularly important are the $A_g(1)$ mode (anti-stretching vibration of the O atoms in the xz planes), and the $A_g(4)$ mode (rotation of the MnO_6 octahedra), as these are directly associated with the structural distortion from the cubic symmetry. Another remarkable effect that becomes more prominent for decreasing size of the R ion is the mixing of the character between

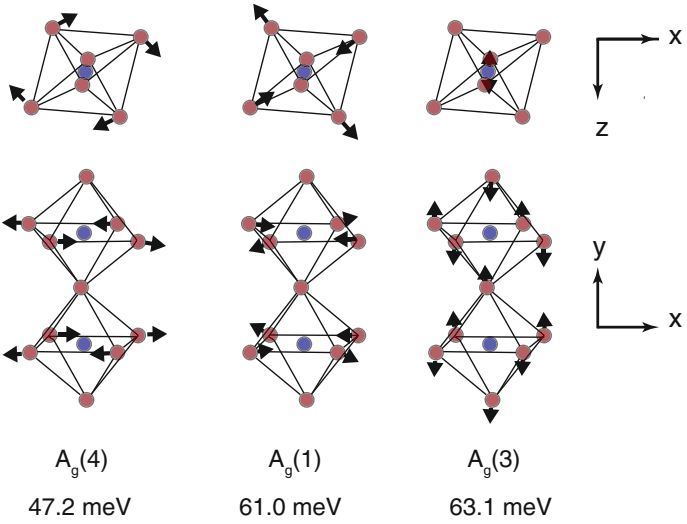

Fig. 7.9 Eigenvectors of four A_g modes of $TbMnO_3$ at $\mathbf{q} = 0$. The corresponding energies are indicated in the figure. Blue atoms refer to Mn, red atoms to O and violet atoms to Tb. The assignments are taken from Ref. [61]

Table 7.1 Nomenclature at the Γ point of the BZ, experimental values of the energy and assignment of the 7 A_g modes of $TbMnO_3$

Nomenclature at Γ	Experiment (meV)	Assignment
$A_g(5)$	14.0	Motion of the Tb^{3+} atom along z
$A_g(6)$	18.1	Motion of the Tb^{3+} atom along x
$A_g(2)$	35.1	In-phase y-rotation of the MnO_6 octahedra
$A_g(7)$	39.1	Motion of the apical O(1) atoms along x
$A_g(4)$	47.2	Anti-phase rotation of the MnO_6 octahedra
$A_g(1)$	61.0	JT in-phase stretching of O(2) atoms in the xz plane
$A_g(3)$	63.1	Out-of-phase bending of MnO_6 octahedra

several Raman modes [60, 61]. This mixing arises at all temperatures especially for the $A_g(1)$ and $A_g(3)$ modes, as they become very close in frequency. The coupling constant between the two modes in $TbMnO_3$ has been evaluated ∼2.5 meV.

In the spontaneous Raman scattering literature of $TbMnO_3$, the effects of the different magnetic phase transitions on the phonon modes have also been investigated by performing a detailed temperature dependence [53, 62]. In the absence of strong couplings, phase transitions and critical phenomena, the phonon frequency measured in a Raman scattering experiment typically undergoes a softening as the temperature is increased, due to the dilation of the unit cell. However, in a magnetic system with strong electron-phonon and spin-phonon couplings, the temperature-dependent behaviour of a phonon mode at frequency ω can be expressed as [63]

$$\omega(T) = \omega(0) + (\Delta\omega)_{qh}(T) + (\Delta\omega)_{anh}(T) + (\Delta\omega)_{el-ph}(T) + (\Delta\omega)_{sp-ph}(T) \quad (7.1)$$

where $(\Delta\omega)_{qh}$(T) is the change in the phonon frequency due to a change in the lattice parameters of the unit cell (known as the quasi-harmonic effect), $(\Delta\omega)_{anh}$(T) is the intrinsic anharmonic contribution, $(\Delta\omega)_{el-ph}$(T) is the renormalization induced on the phonon frequency by the electron-phonon coupling and $(\Delta\omega)_{sp-ph}$(T) is the renormalization induced on the phonon frequency by the spin-phonon coupling, caused by the modulation of the exchange integral (J) by lattice vibrations. The subtle interplay among all these terms can result in complex temperature dependences displayed by the phonon modes. Consistent with this scenario, two phonon modes in $TbMnO_3$, $A_g(7)$ (at 39 meV) and $B_{2g}(3)$ (at 41 meV) were found to undergo an anomalous behaviour as the temperature was increased from 10 K, which was tentatively described as a manifestation of strong spin-phonon coupling [53].

Another significant question addressed via spontaneous Raman scattering regards the nature of the ferroelectric transition in $TbMnO_3$. In an ionic displacement scenario, a soft phonon mode is indeed expected to manifest. Remarkably, a partial softening behaviour was observed for the $A_g(5)$ phonon mode (at 14 meV) at the ferroelectric transition temperature T_{N2} (Fig. 7.10) [53]. As indicated above, the ferroelectric transition is a consequence of a magnetic transition from an incommensurate to a commensurate order, in which the spin modulation becomes a cycloid. All Raman studies in literature assign the $A_g(5)$ mode and the $A_g(6)$ modes to the vibrations of the Tb^{3+} ion [53, 59, 64], since they are also observed in other isostructural compounds such as $TbFeO_3$ [65]. However, while Ref. [53] cites that the eigenvector of the $A_g(5)$ mode involves the motion of the Tb^{3+} ion along z, the original assign-

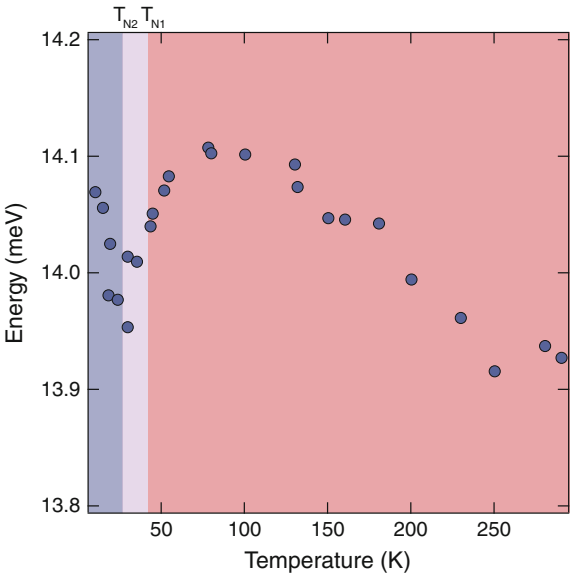

Fig. 7.10 Temperature dependence of the $A_g(5)$ phonon energy, taken from Ref. [53]. Different colour shadings indicate the temperature ranges for distinct phases in the material: The region in blue represents the low-temperature spin-cycloid ferroelectric phase, the region in violet the SDW phase and the region in red the high-temperature paramagnetic phase. The mode involves the vibration of the Tb^{3+} ions along the *c*-axis of the crystal and it is observed to undergo a partial softening at the ferroelectric transition temperature T_{N2}

ment on orthorhombic manganites predicted a motion of the Tb^{3+} ion along x [64]. In view of the following discussion, we tend to agree with the former interpretation, thus indicating this assignment in Table 7.1. The observation of a partial softening of this mode can indeed be connected to recent x-ray diffraction studies that have measured the displacement of the Tb^{3+} along z and have concluded that this displacement gives rise to a quarter of the polarization magnitude [66]. Thus, the partial softening of the mode can be considered as one of the signature of the ferroelectric phase transition and indicates some involvement of an ionic displacement at the origin of the ferroelectric polarization. The additional contribution to the total polarization may instead have an electronic origin.

In conclusion, in this Section we provided a detailed description of the salient features associated with the collective modes of $TbMnO_3$, as detected by spontaneous Raman scattering. We will make an extensive use of the conclusions drawn by spontaneous Raman scattering for the interpretation of our pump-probe experiment, since our high-energy photons can access the low-energy Raman-active collective modes of the system via the ISRS process or via a long-lived perturbation of the electronic GS [67]. In the following Section, we introduce our experiment under nonequilibrium conditions. The coherent response of the system and its relation with spontaneous Raman scattering will be instead treated in Sect. 7.4.3.

7.4 Ultrafast Broadband Optical Spectroscopy

In this Section, we present an extensive study of the magnetic order dynamics occurring in the same detwinned (010)-oriented single crystal of $TbMnO_3$ measured via SE. In our experiments, we drive the system out-of-equilibrium using an ultrashort 1.55 eV pump pulse, which mimics the experimental conditions of previous trREXS studies reported in literature [14]. The pump beam is polarized along the *a*-axis and it mainly promotes intersite *d*-*d* transitions [16]. The possibility that the excitation of *p*-*d* CT transitions could lead to the magnetic dynamics was ruled out via trREXS experiments by observing the persistence of the average scattering cross-section intensity. Although this argument does not exclude that tails of the *p*-*d* CT excitation could contribute to other channels probed in the optical range, in the following we will assume that the main effect of photoexcitation is to promote intersite *d*-*d* transitions. This is also consistent with our optical conductivity data of Fig. 7.3a, in which we indicate a red arrow at 1.55 eV to mark the energy at which the system is photoexcited. After the interaction with the pump pulse, the ultrafast variation of the material reflectivity is monitored over a broad visible range, extending from 1.72 to 2.85 eV, along both the *a*- and *c*-axis. This is highlighted by a grey shaded area in Fig. 7.3a, c. As described in Sect. 7.2, this spectral region involves the intersite HS and LS *d*-*d* transitions along the *a*- and *c*-axis, respectively [16]. Such optical features are very sensitive to the establishment or disappearance of the magnetic order in the crystal, and thus represent a suitable observable for tracking the magnetic order dynamics with high time resolution.

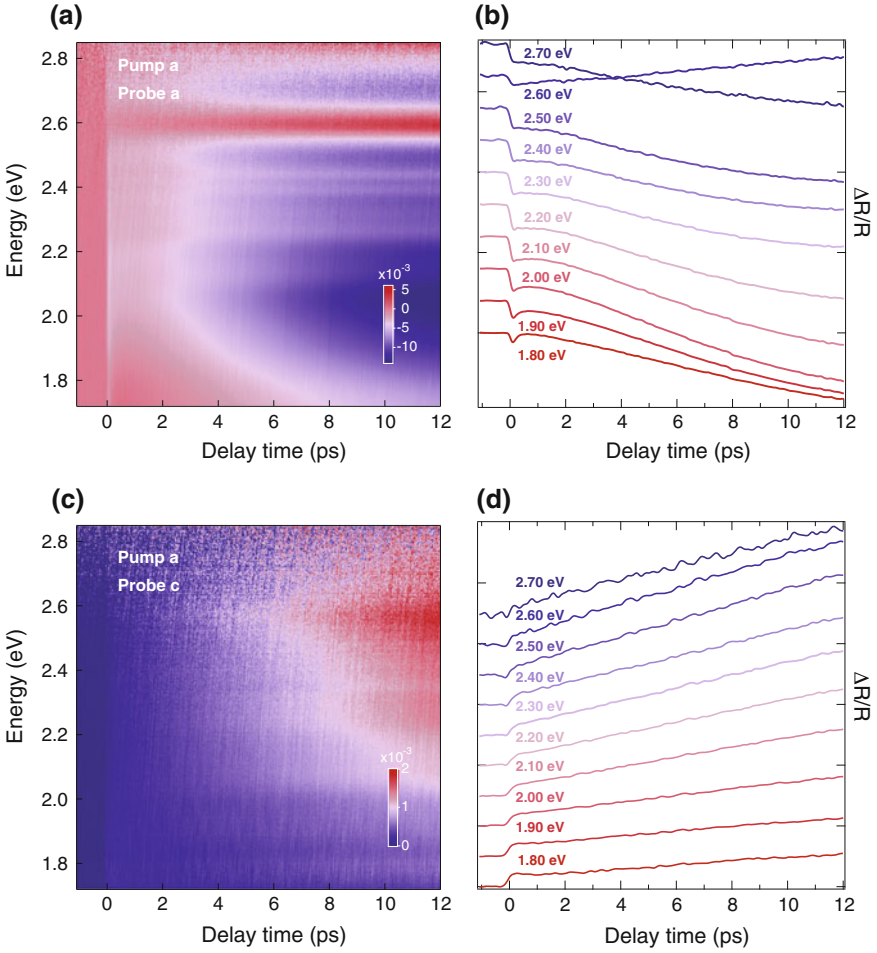

Fig. 7.11 **a**, **c** Colour-coded maps of ΔR/R at 8 K with *a*-axis pump polarization and **a** *a*-axis, **c** *c*-axis probe polarization. The pump photon energy is 1.55 eV and the absorbed pump fluence is 4.4 mJ/cm^2. **b**, **d** Temporal traces at specific probe photon energies of the respective ΔR/R maps. Each temporal trace results from the integration over 0.10 eV around the indicated probe photon energy

Figure 7.11a, c displays the colour-coded maps of the ΔR/R response as a function of the probe photon energy and of the time delay between pump and probe at 8 K, for a probe polarization along the *a*- and *c*-axis respectively. In both cases, the pump polarization lies along the *a*-axis and the absorbed pump fluence is estimated around 4.4 mJ/cm^2. Importantly, in this set of measurements, the dynamics have been detected up to 14 ps with a temporal resolution of ∼26 fs.

The *a*-axis ΔR/R response shows the emergence of a main negative feature in correspondence to the HS intersite *d*-*d* transition, which increases its absolute weight

over time. The spectral shape of this optical band becomes more structured over time, displaying a series of satellites. Simultaneously, a very sharp feature emerges around 2.60 eV and changes the sign of $\Delta R/R$ to positive. In contrast, the *c*-axis response undergoes a remarkably different behaviour. It is dominated by a positive signal, which increases for longer time delays and shows a maximum close to 2.60 eV.

More insightful information on the temporal dynamics can be gained by selecting different temporal traces at representative photon energies from the colour-coded maps of Fig. 7.11a, c. These temporal traces are collected and shown in Fig. 7.11b, d. We first consider the dynamics seen for probe light polarized along the crystal a-axis. Here we see that for all probe photon energies at short times there is a sudden decrease in reflectivity which reaches a local minimum at approximately 190 fs. This time scale is significantly longer than the 45 fs response time of the apparatus. After this fast decrease, there is a fast partial recovery of the reflectivity that is characterized by a time scale of several hundred femtoseconds, a recovery that is particularly evident at lower photon energies (e.g. 1.80 eV). After this partial recovery, the reflectivity changes more slowly. For most photon energies this change is a slow decrease in reflectivity that continues beyond the time window of our measurement. At 2.60 eV, however, the reflectivity instead increases. Here, a negative-to-positive crossover clearly develops after 3.8 ps, as anticipated by the colour-coded map in Fig. 7.11a. Along the *c*-axis, the temporal traces show a markedly different behaviour. The rise time of the signal is ~400 fs and all temporal traces undergo a long increase of the response amplitude over time. Here the distinction between a short-lived component and a delayed one is not pronounced and no changes of sign appear over time. Probing in a broad spectral range allows us to go beyond the results obtained by previous two-colour pump-probe experiments on $TbMnO_3$, in which the fast component in the *a*-axis response was not detected [68]. The apparent absence of the prompt rise in $\Delta R/R$ along the *a*-axis served as the basis for a phenomenological model that could describe the observed ultrafast dynamics. Already at this stage our data contradict one of the main conclusions of Ref. [68].

To get more quantitative information on the timescales governing the dynamics, we perform a fit of some representative temporal traces at 8 K. For this purpose, we select the temporal traces around a probe photon energy of 1.80 eV, as in this region the short-lived component becomes more apparent. These traces are shown as violet curves in Fig. 7.12a, b along the *a*- and *c*-axis, respectively. Among the several models that can be implemented for capturing the dynamics, the simplest one consists of three exponential functions convolved with a Gaussian accounting for the temporal shape of the pump pulse. The shortest lived component appears immediately after the pump photoexcitation, whereas the other two components display a slow rise. The function that is used for fitting the data is:

$$f(t) = u(t)\Big[f_1(t) + f_2(t) + f_m(t)\Big] = u(t)\Big[e^{\frac{-t^2}{\tau_{R_1}}} * A_1 e^{-\frac{t-t_{D_1}}{\tau_1}} + \Big(1 - e^{\frac{-t^2}{\tau_{R_2}}}\Big) * \Big[A_2 e^{-\frac{t-t_{D_2}}{\tau_2}} + A_m e^{-\frac{t-t_{D_2}}{\tau_m}}\Big]\Big] \tag{7.2}$$

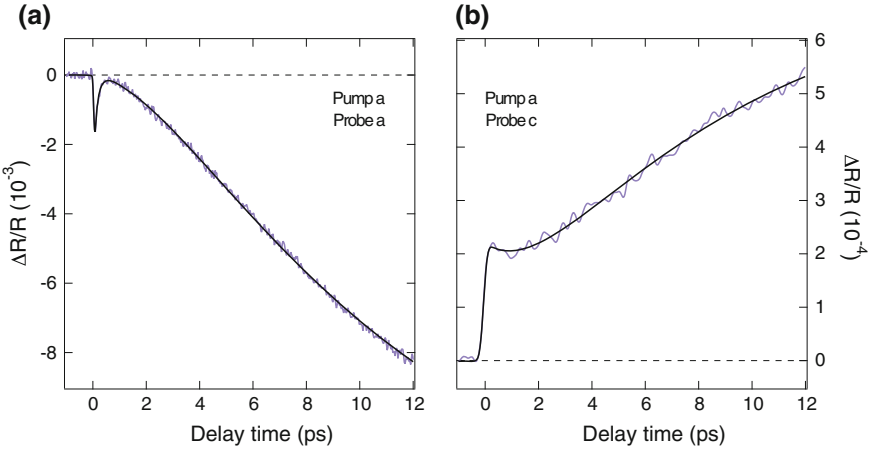

Fig. 7.12 Temporal traces of the ΔR/R response at 8 K along the **a** *a*- and **b** *c*-axis, resulting from the integration over 0.10 eV around the probe photon energy of 1.80 eV. In both cases, the pump polarization lies along the *a*-axis and the absorbed pump fluence is estimated around 4.4 mJ/cm^2. The black lines represent the results of the fit based on our model function

where u(t) is a step function that has u = 0 for t < 0 and u = 1 for t ≥ 0 A_1, A_2 and A_m are the amplitudes of the three exponential functions; τ_{R_1} and τ_{R_2} are the rise times of the exponential functions; τ_1, τ_2 and τ_m are the relaxation constants of the three exponentials; t_{D_1} and t_{D_2} are delay parameters with respect to the zero time. While all three exponential functions are necessary for fitting the *a*-axis response, only two of them are sufficient to reproduce the *c*-axis dynamics. The results of the fit are shown in Fig. 7.12a, b as black lines superposed on the original data. The timescales retrieved along the *a*-axis are $\tau_1 = 120 \pm 10$ fs, $\tau_2 = 3 \pm 0.7$ ps and $\tau_m = 9 \pm 1.5$ ps, while those along the *c*-axis are $\tau_1 = 2 \pm 0.5$ ps and $\tau_m = 9 \pm 0.5$ ps. A larger uncertainty is expected on τ_m due to the limited temporal window of ∼12 ps probed in our experiment. Between the two axes, we notice a strong mismatch in the time constant τ_1 and a perfect correspondence in the time constant τ_m. Considering the *a*-axis response alone, the emerging picture of the temporal dynamics reconciles the results of separate two-colour pump-probe experiments performed in the past [68, 69]. Analysis of a high time-resolution experiment on LaMnO3 attributed a short-lived component similar in time-scale to our τ_1 to electron thermalization, while the intermediate time-scale τ_2 was interpreted as electron-phonon relaxation [69]. Another experiment on $TbMnO_3$ had significantly worse time resolution and considered only the slowest component of the time-resolved changes along both axes (corresponding to our τ_m), interpreting this as the time scale for melting of magnetic order [68]. Despite observing also the faster component along the *c*-axis, the latter experiment explicitly neglected it due to the difficulty in fitting the data. Using our model function, we find this component to decay with a time constant of $\tau_1 = 2$ ps,

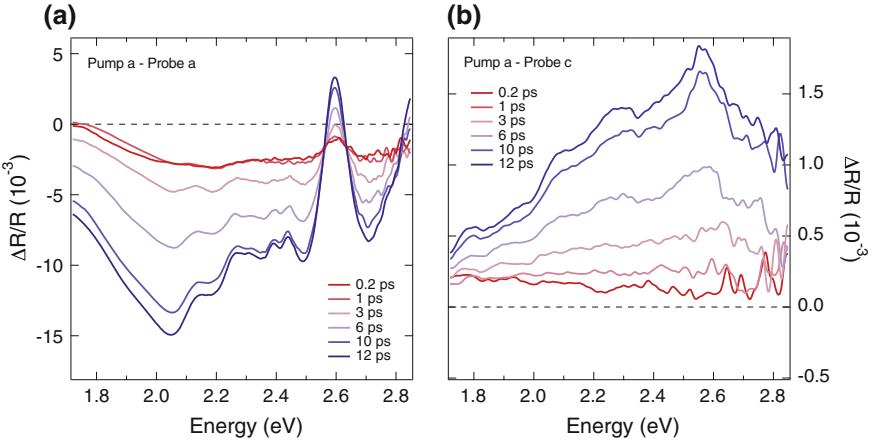

Fig. 7.13 Transient spectrum of $\Delta R/R$ at different delay times for a probe polarization set along **a** the *a*-axis, **b** the *c*-axis. The pump photon energy is 1.55 eV and the absorbed pump fluence is 4.4 mJ/cm^2

which is one order of magnitude larger than expected from a typical electron-electron thermalization timescale.

As an alternative way of examining the data, in Fig. 7.13a, b we show the spectral evolution of $\Delta R/R$ at different time delays along the *a*- and *c*-axis, respectively. In Fig. 7.13a, the *a*-axis $\Delta R/R$ spectrum for early time delays is almost featureless and shows only a broad structure around 2.60 eV. As time evolves, a fine peak-dip structure clearly emerges in the spectrum, with shoulders covering the range from 2.05 to 2.50 eV. These features coincide with the fine structure superposed on the *d*-*d* HS absorption band, which can also be observed in the steady-state reflectivity spectrum of Fig. 7.6a. At 2.60 eV the former broad feature sharpens and increases its weight until the sign of the response is reversed. Above 2.85 eV the $\Delta R/R$ response changes sign and becomes positive, as evidenced by the gradual redshift of the zero-crossing energy at the edge of the probed spectrum. In Fig. 7.13b, the *c*-axis $\Delta R/R$ spectrum for early time delays appears as a featureless background, while for long time delays some fine structure also arises. Remarkably, these features are not apparent under steady-state conditions (Fig. 7.6b) and cannot be related to a leakage of the *a*-axis response, since their energies are well distinct from the ones of the *a*-axis fine structure. Thus, we conclude that our pump-probe experiment provides a higher contrast to resolve elementary excitations that lie hidden in the equilibrium spectra. However, at this stage, no insightful information can be retrieved on the origin of this fine structure characterizing the two-particle excitation spectrum of $TbMnO_3$. Later, in Sect. 7.4.3, we will show that a strong indication about the character of these elementary excitations is obtained by analysing the coherent response emerging in the pump-probe traces.

From this preliminary analysis, we can conclude that the photoexcitation of $TbMnO_3$ along the *a*-axis with a pump photon energy of 1.55 eV leads to an overall reduction of the reflectivity along the *a*-axis, accompanied by an increase of the reflectivity along the *c*-axis. This anisotropic behaviour goes beyond the results of previous two-colour pump-probe measurements performed at different temperatures [68]. In these experiments, the pump pulse was set at 3.00 eV, thus at the edge between the intersite *d*-*d* transitions and the tail of the CT transition, while the probe pulse at 1.50 eV was monitoring the lowest tail of the HS and LS bands in the material. As a consequence, the probe was not capable of revealing the details of the ultrafast electronic response at early time delays, nor of providing spectrally resolved information across the whole spectral region of the intersite *d*-*d* excitations. In the following, we demonstrate instead that our approach bridges the gap between the conclusions drawn by ultrafast two-colour optical spectroscopy and trREXS experiments, thus providing a unified picture of the nonequilibrium dynamics triggered by a near-infrared pump pulse.

7.4.1 Temperature Dependence

To monitor how the spectral signature of the *a*-axis HS band varies in the nonequilibrium experiment across the two magnetic phase transitions, we perform a complete temperature dependence of $\Delta R/R$. The colour-coded maps of $\Delta R/R$ are shown in Fig. 7.14, where the different temperature values are also indicated. We observe that the fine structure of the low-energy band manifesting at 8 K is gradually lost as the temperature is increased. A strong variation of the intensity of the response also occurs and the measured changes become smaller than the noise level above 100 K.

The fine structure of the low-energy optical band of $TbMnO_3$ becomes more evident when the long time delay $\Delta R/R$ spectra are directly compared at different temperatures. These spectra are diplayed in Fig. 7.15a for a time delay of 13 ps and are vertically shifted among them of a constant value for clarity. The temporal evolution of the system around the probe photon energy of 2.20 eV is displayed in 7.15b at the different temperatures. Upon entering the magnetic phase below T_{N1}, the spin-order melting dynamics slow down dramatically, as already observed previously [68]. This increase in the τ_m time constant for decreasing temperature was assigned to the signature of a photoinduced magnon-assisted hopping along the *c*-axis of the material, which leads to an increase in the magnon number density and in turn affects both the *a*- and *c*-axis optical response. In the following, we will show that our data support instead a scenario in which lattice reorganization following the formation of small polarons is the source of the bottleneck observed in the spin order melting of $TbMnO_3$.

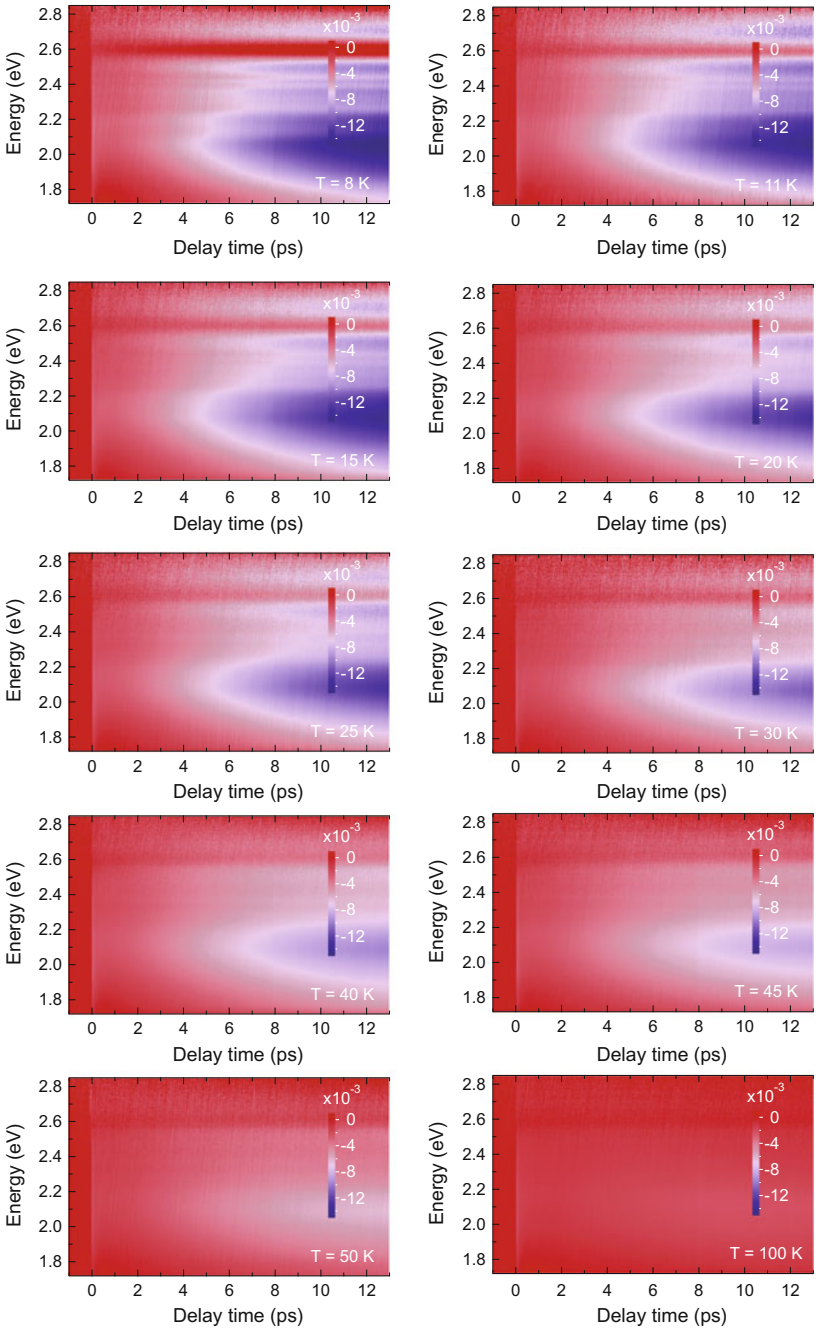

Fig. 7.14 Temperature dependence of $\Delta R/R$ as a function of probe photon energy and time delay between pump and probe. The temperatures are indicated in the labels and the absorbed pump fluence is 4.4 mJ/cm^2

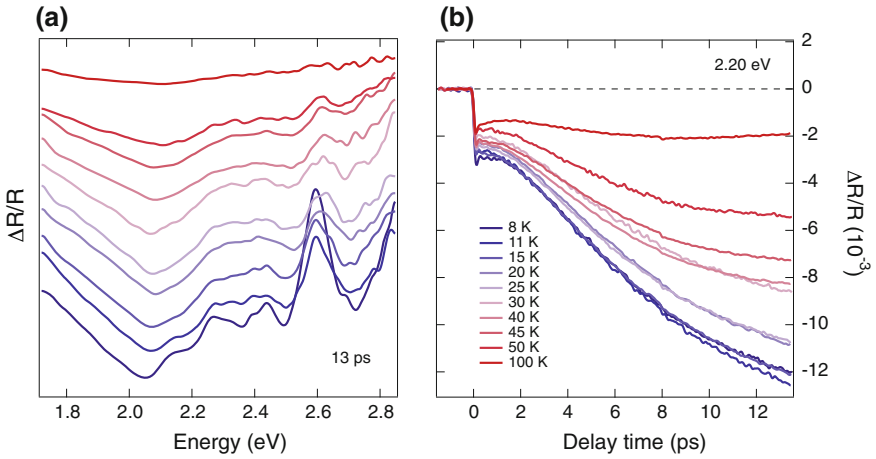

Fig. 7.15 **a** Temperature dependence of the ΔR/R spectrum for a time delay of 13 ps. **b** Temperature dependence of the ΔR/R temporal traces for a probe photon energy of 2.20 eV. The temperatures are indicated in the labels and all curves have been cut from the maps of Fig. 7.14

7.4.2 Transient Optical Conductivity

As highlighted in Sect. 7.2, the spectral region of the *a*-axis HS optical band is an extremely sensitive probe of magnetic correlations in the insulating perovskite manganites [16]. We can then expect that measurements of optical properties in this frequency range can give us some information on the dynamics associated with magnetic order changes. The useful quantity that has to be extracted from the nonequilibrium experiment is the transient complex optical conductivity $\Delta\sigma = \Delta\sigma_1 + \mathrm{i}\,\Delta\sigma_2$. This can be calculated without the need of a KK transform by relying on our steady-state SE data of Fig. 7.3a as a starting point and performing a Drude-Lorentz analysis of the ΔR/R maps at the different temperatures. As a consequence, the determination of the real part $\Delta\sigma_1$ gives access to the temporal evolution of the SW in the visible range.

In Fig. 7.16 we show the calculated $\Delta\sigma_1$ at all temperatures, as a function of probe photon energy and time delay. At low temperatures, a prominent drop dominates the whole spectral range especially at large time delays. As the temperature increases, the absolute strength of the response becomes smaller and declines to the order of our sensitivity close to 100 K. The determination of $\Delta\sigma_1$ at all temperatures allows following the temporal evolution of the change in SW (ΔSW) over the probed range. The dynamics of ΔSW are overlapped to all colour-coded maps of $\Delta\sigma_1$ in Fig. 7.16.

A direct comparison among the ΔSW temporal dynamics at the different temperatures is established in Fig. 7.17a. Here, our primary interest is to reveal whether the magnetic order dynamics gives rise to detectable temperature anomalies in ΔSW at long time delays. For this reason, we track the value of ΔSW at 12 ps for the different temperatures and we collect the results in Fig. 7.17b. For clarity, we also

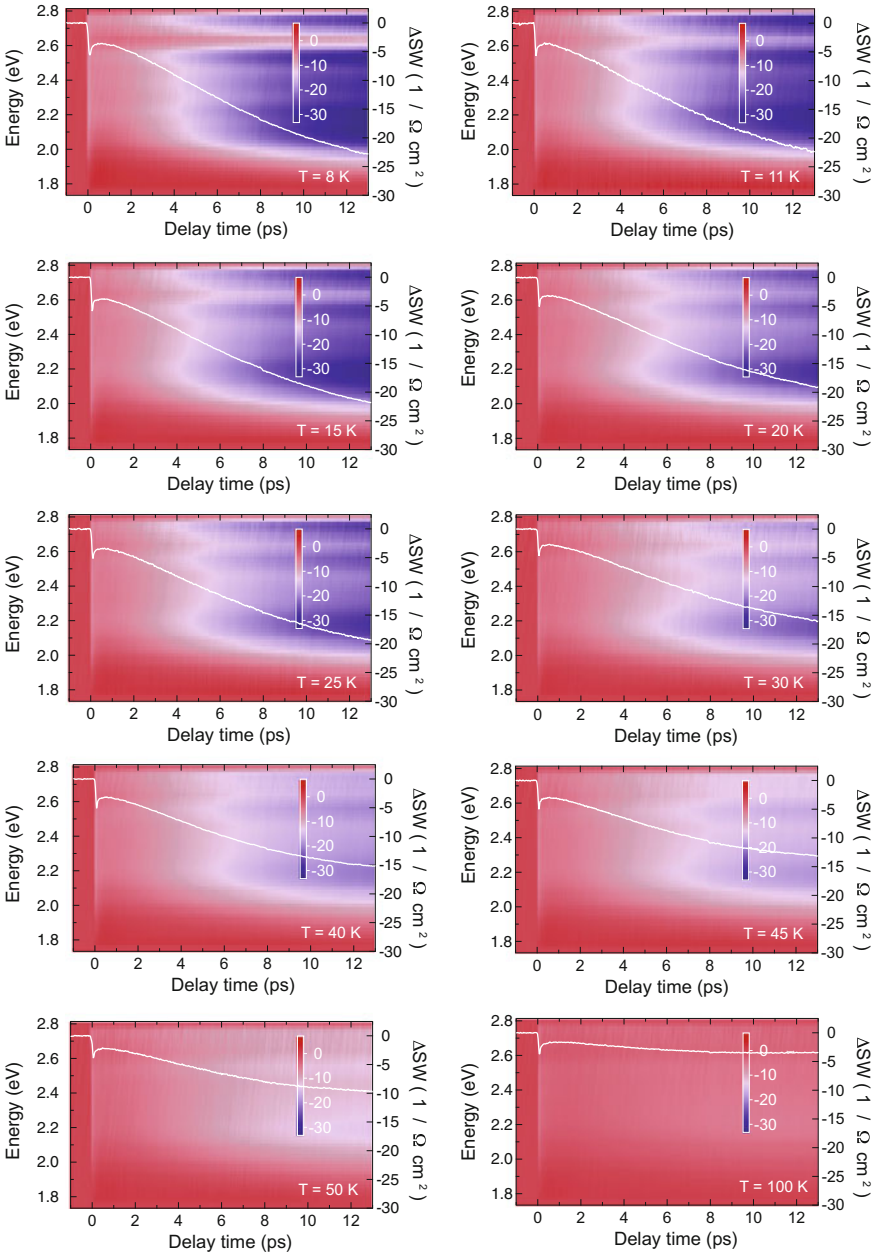

Fig. 7.16 Temperature dependence of the transient optical conductivity $\Delta\sigma_1$ as a function of probe photon energy and time delay between pump and probe. Every map also shows the temporal evolution of the nonequilibrium SW (ΔSW), which is calculated by computing the integral of the corresponding $\Delta\sigma_1$ map over the whole probed range. The temperatures are indicated in the labels and the absorbed pump fluence is 4.4 mJ/cm^2

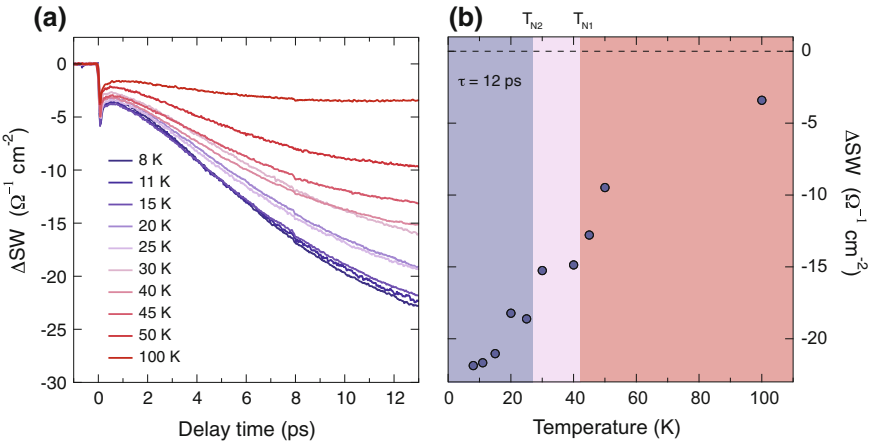

Fig. 7.17 **a** Comparison of the nonequilibrium ΔSW temporal dynamics at different temperatures, which are indicated in the label. At every time delay, the SW is calculated by computing the integral of the corresponding $\Delta\sigma_1$ map over the whole probed spectral range. The absorbed pump fluence is 4.4 mJ/cm^2. **b** Temperature evolution of the nonequilibrium SW integrated over the whole probe spectrum at 12 ps delay time. The blue shaded region highlights the temperature range where the material is in the multiferroic spin-cycloid phase, the violet region depicts the region where the SDW phase emerges and the red region represents the paramagnetic phase with short-range spin correlations. The respective temperature scales T_{N2} and T_{N1} are indicated on top

indicate the T_{N1} and T_{N2} temperature scales by highlighting different temperature regions with distinct colours. Starting from high temperatures, we observe that the ΔSW decreases its value more rapidly when approaching the first magnetic phase transition and shows a change in slope at the T_{N1} temperature scale. A more prominent anomaly sets in close to the second magnetic phase transition at T_{N2}, involving the presence of a kink. While the change in slope at T_{N1} had been already detected at the single-wavelength ΔR/R level [68], the anomaly emerging at T_{N2} is a completely novel feature that can be accessed only when the whole spectral region of the intersite *d-d* transitions is covered by the probe pulse.

7.4.3 Coherent Collective Response

The detection of a dynamical SW transfer associated with the loss of magnetic order in photoexcited $TbMnO_3$ provides new insights into the nonequilibrium response of the material. However, this observable represents an indirect effect of the order parameter melting on the optical properties of the system. As such, our measurements only suggest that a delayed transfer of thermal energy from the excited carriers to the spin system is at play in the material, consistent with previous experimental results. Thus, the microscopic mechanism behind the magnetic order melting remains unclear.

One scenario that has been envisioned behind the delayed energy transfer is related to relaxation of the JT distortion, with the subsequent localization of the carriers in the form of small polarons. The charge localization would hinder magnon-assisted hopping and therefore would require that the energy transfer to the spin system to be mediated by changes in the lattice structure.

This represents a crucial aspect, since the polaronic behaviour of the charge carriers is widely recognized as one of the peculiarities of the orthorhombic manganites [70–72]. Indeed, doping carriers [73] or photoexciting the intersite *d*-*d* CT transitions in perovskite manganites is predicted to lead to the creation of the so-called anti-JT polarons [74]. Similar effects are envisioned when the *p*-*d* CT transitions are photoexcited [75]. As the lattice shows a cooperative JT distortion, the presence of an extra charge (i.e. electron or hole) on the Mn^{3+} ions can produce a strong structural rearrangement to locally remove and relax the JT distortion. In this way, the system tries to minimize the energy cost generated by the existence of additional charge in a collectively JT-distorted crystal. This site acts as a defect that becomes strongly pinned, since the hopping to other Mn^{3+} sites requires moving along the lattice distortion. In magnetically ordered phases, also the spin degree of freedom can be affected by the charge localization, as the polaron is expected to produce canting of the spins from their natural directions. Behaving similarly to a defect, the anti-JT polaron is a prototypical example of a small (Holstein) polaron and, as such, it involves the presence of a local deformation around the self-trapped carrier [76, 77]. As pointed out in Chap. 1, the local symmetry associated with the displacement of an Holstein polaron is expected to retain a totally symmetric character.

To investigate the validity of this scenario, we search for the signatures of coherent optical phonon modes with totally symmetric character that are coupled to the photoexcited carriers and signal a rearrangement of the lattice structure consistent with the relaxation of the JT distortion. Here, we go beyond the results of Sect. 7.3 and monitor the *a*-axis $\Delta R/R$ at 8 K by decreasing the time step for the detection to $\sim$13 fs.

Figure 7.18a, b shows some representative temporal traces and the FTs of the residuals from the fit of the incoherent response when the absorbed pump fluence for is 2.2 mJ/cm^2. The probe photon energies at which these traces have been selected are indicated in the labels. Remarkably, the initial ultrafast relaxation of the electronic response is now clearly resolved, displaying a sharp and well-defined negative peak. Simultaneously, a coherent beating among several modes emerges in the time-domain during the electronic relaxation and persists up to 4 ps (see the inset of Fig. 7.18c). By performing a FT analysis of the residuals from the fit, we are able to identify the presence of at least two peaks that can be ascribed to coherent modes, which are centred around an energy of 47.2 meV and 61.0 meV, respectively. However, these FT suffer from a low signal-to-noise ratio, as the measured signal lies within our detection limit.

For this reason, the measurements have been repeated by increasing the absorbed pump fluence to 4.4 mJ/cm^2, mimicking the conditions of the experiment performed in the previous Paragraphs. The results are shown in Fig. 7.18c, d. From the FT analysis, we identify the presence of four collective modes taking part to the coher-

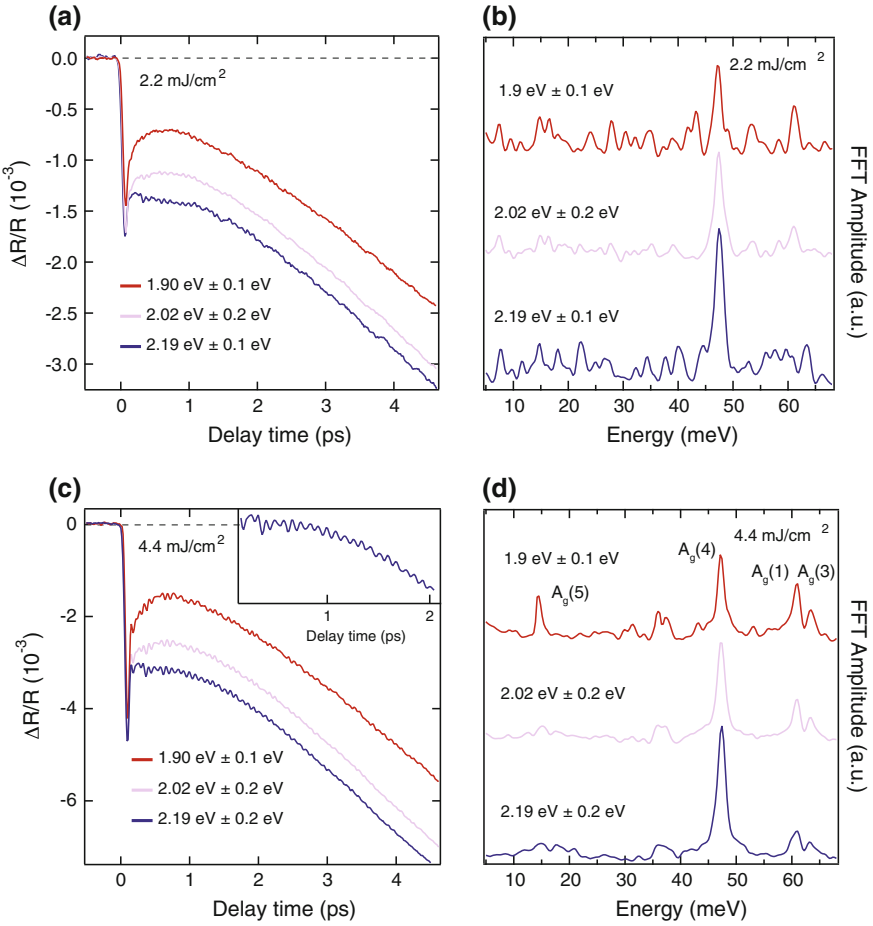

Fig. 7.18 **a**, **c** Temporal dynamics and **b**, **d** FT of the spectral response at 1.90, 2.02 and 2.19 eV, averaged over the region indicated in the label. The pump polarization is set along the *a*-axis. The absorbed pump fluence for **a**, **b** is 2.2 mJ/cm^2 and for **c**, **d** is 4.4 mJ/cm^2. The assignment of the coherent modes is given in (**d**)

ent dynamics triggered by the intersite *d*-*d* excitation. Their energies correspond to 14.5 meV ($A_g(5)$ mode), 47.2 meV ($A_g(4)$ mode), 61.0 meV ($A_g(1)$ mode) and 63.4 meV ($A_g(3)$ mode) and are indicative of four of the seven A_g modes detected by spontaneous Raman scattering (as shown in Sect. 7.3). In particular, $A_g(5)$ corresponds to the soft mode involving the displacement of the Tb^{3+} ion, $A_g(4)$ to the rotation of the MnO_6 octahedra, $A_g(1)$ to the anti-stretching JT vibrations of the O atoms in the xz plane and $A_g(3)$ to the bending of MnO_6 octahedra. On the other hand, the doublet structure centered around 35–37 meV in the FT may arise from the convolution of the peaks associated with the $A_g(2)$ and $A_g(7)$ modes, which are known to be strongly intermixed in $TbMnO_3$ [60]. Indeed, this feature is found to

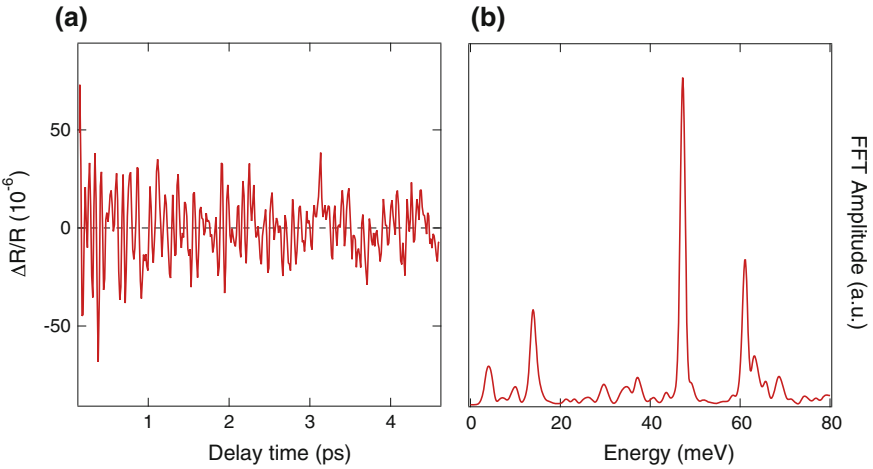

Fig. 7.19 **a** Residuals from a multiexponential fit of the temporal trace at 1.85 eV, integrated over 250 meV. **b** FT analysis of the residuals shown in panel (**a**)

persist over the probed spectral range, despite becoming broader as the probe photon energy is tuned above 2.00 eV. For the purpose of our discussion, we avoid any speculation in the absence of a clear spectroscopic observable, thus neglecting the presence of this feature.

We also put more emphasis on the low-energy probe region, where all modes appear simultaneously. By integrating the temporal trace over a broader spectral region of 250 meV around 1.85 eV and subtracting the background, we retrieve the residuals displayed in Fig. 7.19a. Here, we show the richness of the response generated by the beating among the different modes. The FT analysis of these residuals is shown in Fig. 7.19b. Remarkably, we do not detect the signature of any coherent electromagnon excitation neither in these temporal traces, nor in those measured up to ∼14 ps. Thus, we confirm that only four coherent A_g phonon modes resonate without ambiguity in the proximity to the *d*-*d* HS intersite absorption band.

To test whether the coherent modes modulating the *a*-axis reflectivity can be excited even under other pump polarization conditions, we perform a separate experiment at 8 K where the pump beam is polarized along the *c*-axis. In these conditions, the pump photon energy at 1.55 eV can promote intersite *d*-*d* transitions along the *c*-axis, as it is resonant with the tail of the *c*-axis LS *d*-*d* absorption feature shown in Fig. 7.3c. The colour-coded map of the *a*-axis ΔR/R is presented in Fig. 7.20a as a function of probe photon energy and time delay between pump and probe. Despite the weak *c*-axis absorption, we retrieve a sizable ΔR/R signal, retaining the same spectral shape of the response in Fig. 7.18a, c. Some representative temporal traces selected from the map are displayed in Fig. 7.20b and demonstrate the emergence and persistence of the coherent response even for a pump polarization along the *c*-axis.

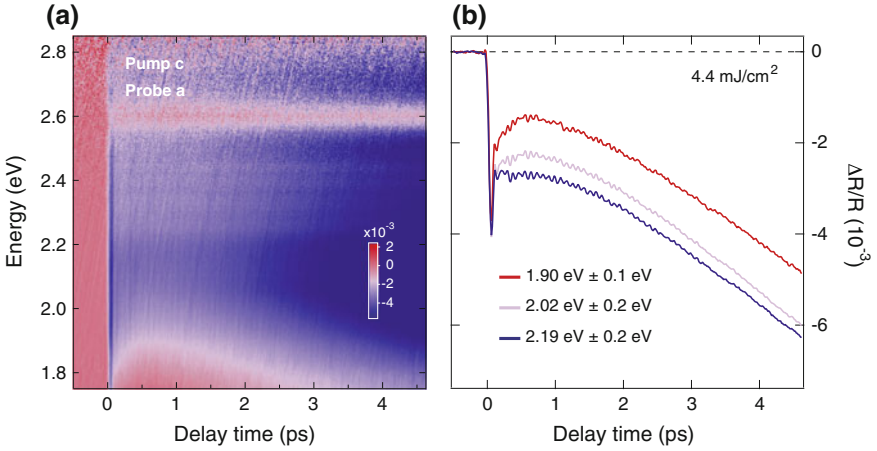

Fig. 7.20 **a** Colour-coded maps of ΔR/R at 8 K with *c*-axis pump polarization and *a*-axis probe polarization. The pump photon energy is 1.55 eV and the absorbed pump fluence is 4.4 mJ/cm^2. **b** Temporal dynamics of the spectral response at 1.90, 2.02 and 2.19 eV, averaged over the region indicated in the label

The FT analysis of the residuals from a fit of the incoherent response confirms the presence of all previously listed phonon modes.

The use of a broadband probe in our experiment enables us to extract useful information concerning the Raman matrix elements of the coherent optical phonons at the delivered pump fluence, i.e. the spectral dependence of each phonon amplitude across the monitored spectral range. We select twenty-two temporal traces from the map at 8 K with fine time-step over the 1.74−2.63 eV spectral range and we proceed to fit the incoherent background. By calculating the FT of the residuals, we reconstruct the results shown in Fig. 7.21a. Although the low intensity of the Tb^{3+} ion mode at 14.5 meV prevent us from extracting its Raman matrix element, we can conclude that this mode mainly resonates with the low-energy spectral region close to 1.90 eV (Fig. 7.19b).

We observe that the Raman matrix element of the $A_g(4)$ mode dominates the response and resonates over a broad spectral region from 1.90 to 2.50 eV. The spectral dependences of the $A_g(1)$ and $A_g(3)$ modes retain instead the same shape, with a weaker amplitude compared to the $A_g(4)$ mode. In addition, these two phonons emerge more clearly in the spectral region around 2.0 eV. One can observe that some structures appear on top of the overall spectral dependence of the three modes. While we cannot confirm that a similar fine structure is effectively present on the $A_g(1)$ and $A_g(3)$ modes matrix elements due to lower amplitude of these phonons, in the case of the $A_g(4)$ mode the peak-and-dip features could have a real origin. To test the reliability of this result, we also track the spectral dependence of the $A_g(4)$ mode in the measurement with the pump polarization set along the *c*-axis of our single crystal. The Raman matrix elements are reported in Fig. 7.21b, where we observe an excellent matching between the shapes of the two responses and confirm the presence of the fine

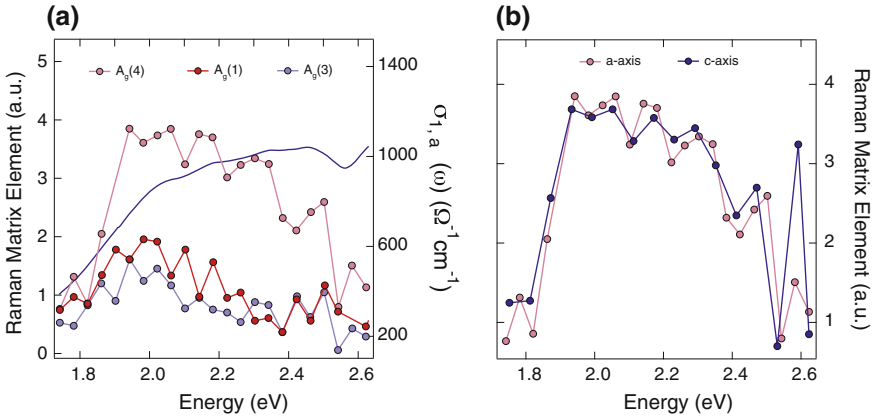

Fig. 7.21 **a** Raman matrix elements for the three A_g modes extracted through a global fit analysis of the a-axis $\Delta R/R$ map at 8 K. The pump polarization is set along the a-axis and the absorbed pump fluence is 4.4 mJ/cm^2. For comparison, the real part of the a-axis optical conductivity $\sigma_{1,a}$, measured at 8 K via SE, is displayed in blue over the same spectral range. **b** Raman matrix elements for the Ag(4) mode for different polarizations of the pump beam

structure. To clarify the possible origin of these features, we proceed comparing the real and imaginary parts of the a-axis optical conductivity, $\sigma_{1,a}$ and $\sigma_{2,a}$, as measured via high-resolution SE at 8 K (see Fig. 7.5a, b). We notice a good correspondence with the absorptive part of the optical conductivity, which is also plotted in Fig. 7.21a for comparison. Also the peak-dip structures found in the Raman matrix element of the $A_g(4)$ mode have a good correspondence with the fine structure manifesting on top of the low-energy a-axis absorption band of $TbMnO_3$. For example, this behaviour is well evidenced by the dip around 2.54 eV in the Raman matrix element, which appears in the proximity of the 2.57 eV dip in the equilibrium optical conductivity. All these features imply that the elementary excitations associated with the fine structure undergo a renormalization of their spectral properties upon a collective anti-phase rotation of the MnO_6 octahedra. This observation may have remarkable consequences, as it can contribute to the debate on the origin of the fine structure of the d-d HS band in the manganite absorption spectra. As described in detail in Sect. 7.2, three main explanations have been provided about the origin of the fine structure: (i) HS and LS intersite d-d CT transitions involving different types of d orbitals, leading to conclude that orthorhombic manganites are Mott-Hubbard insulators [16, 34, 45]; (ii) Forbidden/weak dipole allowed p-d CT transitions acting as precursors to the strong dipole allowed p-d CT transition at high energy, leading to conclude a duality of the gap nature in the ZSA scheme [35]; (iii) Quantum rotor orbital excitations for the e_g electron of Mn^{3+} ions disturbed by lattice anharmonicity [37]. In our experiment, the $A_g(4)$ mode corresponds to the out-of-phase rotation of the MnO_6 octahedra. Resonant Raman experiments confirmed this assignment by observing a weak signal of this mode in correspondence to the visible range and a strong enhancement for deep-UV radiation [50]. This is due to the fact that the

rotational vibrations are not expected to strongly couple to the JT e_g orbitals but can be enhanced in the vicinity of *p-d* CT transitions involving the O orbitals. Here, the out-of-phase rotation mode dominates the coherent response in the visible spectral range when a *real* charge density is created by the 1.55 eV pulse and its Raman profile is able to disentangle the fine structure on top of the *d-d* HS CT transition. This suggests that the elementary excitations associated with the fine structure may be satellites of *p-d* CT transitions, i.e. precursors to the dipole-allowed *p-d* transition in the deep-UV. Within this framework, our experiment supports the scenario of a dual gap nature for the orthorhombic manganites of the $RMnO_3$ family [47]. In addition, to our knowledge, no other ultrafast measurements on solids previously detected a comparable fine structure in the spectral response characterizing an optical phonon mode. The observation of coherent optical phonons in the nonequilibrium dynamics of $TbMnO_3$ and the consequent extraction of their Raman matrix elements opens intriguing perspectives in the evaluation of the electron-phonon coupling for all these modes, albeit projected at the Γ point, in the spirit of what we described in Chap. 5 for La_2CuO_4.

The emergence of these coherent collective modes with a well-defined symmetry allows us to propose an explanation of the ultrafast magnetic order dynamics occurring in the spin cycloid phase of $TbMnO_3$. In the past, a two-colour ($\hbar\omega_{pump}$ = 1.90 eV and $\hbar\omega_{pump}$ = 1.95 eV) pump-probe study with a time resolution of 10 fs revealed the presence of the $A_g(4)$ and $A_g(1)$ modes in the ultrafast response of $LaMnO_3$ [69]. The $A_g(5)$ and $A_g(3)$ modes were not detected. In this experiment, the pump photon energy was tuned to be resonant with the intersite *d-d* transition, thus promoting the CT between two neighbouring Mn^{3+} sites and creating locally Mn^{2+}-Mn^{4+} sites. Moreover, a detailed temperature study of the ΔR/R was performed in order to track the relevant parameters of the coherent modes, such as the oscillation amplitude and the damping rates. Surprisingly, both $A_g(4)$ and $A_g(1)$ modes were found to sharply increase their intensity below T_N and to undergo a pronounced decrease of their damping rates when the temperature was reduced toward T_N. Although this experiment did not provide any information on the ultrafast magnetic order dynamics occurring in the material, it was concluded that the generation mechanism of the two modes proceeds via the displacive excitation. The trigger mechanism of mode $A_g(1)$ (anti-stretching JT mode) was explained by observing that the Mn^{2+} and Mn^{4+} ions are no longer JT active, leading to a relaxation of the JT distortion that launches the coherent mode. Importantly, as we will discuss later, the disruption of the regular, pure Mn^{3+} arrangements has been addressed from the theory perspective [74], leading to the scenario of anti-JT polaron formation. The excitation of mode $A_g(4)$ (out-of-phase rotation of the MnO_6 octahedra) was instead interpreted by invoking the Goodenough-Anderson-Kanamori rules [20–23]. In the ES of the manganite, the presence of neighbouring Mn^{3+}-Mn^{4+} sites gives rise to two empty e_g orbitals. Hence, according to the Goodenough-Anderson-Kanamori rules, the exchange interaction J becomes negative. In a similar way, the presence of neighbouring Mn^{2+}-Mn^{3+} sites leads to two half-filled e_g levels, providing again a negative J. The change in sign of the J results in the establishment of a force to reduce the Mn-O-Mn semicovalent bond length. This can be achieved by both the

relaxation of the JT distortion and by reducing the bond angle to give a straighter bond, which in turn excite the coherent mode. In other words, the renormalization of J under nonequilibrium conditions triggers the coherent lattice motion via the displacive mechanism.

As already observed above, modes $A_g(5)$ and $A_g(3)$ were not observed in the nonequilibrium dynamics of $LaMnO_3$, and thus they represent novel features detected by our measurement. The experimental parameters (time resolution, and pump/probe photon energy) used in Ref. [69] were indeed suitable for revealing the presence, if any, of both modes. This suggests that these coherent modes are a peculiar feature of the ultrafast dynamics of $TbMnO_3$, which possesses a high degree of distortion compared to $LaMnO_3$ and displays multiferroicity. Given the complex beating among the different modes, extracting the phase of each individual mode (to distinguish whether the temporal behaviour is a sine or a cosine function) becomes a challenge. Hence, to explain the appearance of modes $A_g(5)$ and $A_g(3)$, we rely on additional considerations.

Concerning mode $A_g(3)$, we base our arguments on spontaneous Raman scattering data for the series of orthorhombic $RMnO_3$ manganites. It has been found that the stretching $A_g(1)$ and bending $A_g(3)$ modes, while uncorrelated for R = La, display a pronounced mixing for R = Sm, Eu, Gd, Tb [60]. This effect is due to the proximity between their phonon energies when the unit cell becomes highly distorted. Two phonon modes of same symmetries and close energies can be considered as coupled quantum oscillators, whose frequencies are given by

$$\hbar\omega_{1,2} = \frac{\hbar\omega' + \hbar\omega''}{2} \pm \sqrt{\frac{(\hbar\omega' - \hbar\omega'')^2}{4} + \frac{V^2}{4}} \tag{7.3}$$

where $\hbar\omega'$ and $\hbar\omega''$ are the mode energies without coupling and V is the coupling constant. From spontaneous Raman scattering, V can be estimated ~2.5 meV. This leads us to conclude that, in our nonequilibrium experiment, the coherent excitation of mode $A_g(3)$ is strictly connected to the coherent excitation of mode $A_g(1)$, as the two modes are mutually dependent.

The generation mechanism of the coherent $A_g(5)$ mode is instead more subtle. As discussed in Sect. 7.3, this mode corresponds to the vibration of the Tb^{3+} ion along the *c*-axis and has been identified as a partially soft phonon mode associated with the ferroelectric transition [53]. In the past, ferroelectric phase transitions have been widely investigated via pump-probe spectroscopy to track the dynamics of coherent soft modes in order-disorder type perovskites (such as $KNbO_3$ and $SrTiO_3$) [78–80] and in displacive type ferroelectrics (such as GeTe) [81]. While in the first class of materials the generation mechanism of the soft modes has been associated to ISRS, in the second class a displacive excitation has been proposed. In our experiment, the use of a broad detection window can help clarifying the generation mechanism of our coherent mode. As indicated in Fig. 7.21, we are not able to extract a Raman matrix element for this mode across the whole monitored spectral region, since the mode is found to strongly resonate only in the low-energy wing of the visible spectrum (around 1.90 eV). In this region, the absorptive part of the optical conductivity is

weak and featureless, suggesting that the displacive character of the exctiation is weak. Consistent with this hypothesis, we observe that the 1.90 eV region in which the $A_g(5)$ mode resonates corresponds to the pronounced dip found in the dispersive part of the optical conductivity (Fig. 7.5b). This leads us to conclude that the ISRS scenario rationalizes the excitation mechanism of this partially softened mode in $TbMnO_3$.

7.5 Conclusions

In this Chapter we have applied ultrafast broadband optical spectroscopy to study the sequence of events leading to spin-order melting in laser-excited multiferroic $TbMnO_3$. Similar to what we observed in other Chapters of this Thesis on different materials, probing the spectro-temporal evolution of the system using high-energy photons is key to the correct interpretation of the ultrafast dynamics. In this particular case, the probe pulse covers the interesting spectral range associated with the Mott-Hubbard gap of $TbMnO_3$. This is the ideal region in which to detect the complex interplay between different degrees of freedom, as the low-energy phenomena in a strongly correlated quantum system dramatically influence its high-energy electrodynamics. Here, our observations allow us mapping the pathway that the energy follows from the initial pump photons to the spin system of $TbMnO_3$.

The interaction between the pump pulse at 1.55 eV and the system leads to the excitation of an intersite *d*-*d* CT transition, corresponding to an optical excitation across the fundamental Mott-Hubbard gap. In other words, the excitation locally promotes the creation of Mn^{2+}-Mn^{4+} sites, leading to the disruption of the regular Mn^{3+} arrangement and to the relaxation of the JT distortion. In this scenario, anti-JT small polarons are expected to form, producing a local distortion in the MnO_6 octahedra [74]. A pictorial representation of the photoexcitation process and the formation of anti-JT polarons is given in Fig. 7.22. The change in the lattice structure is reflected in the emergence of the coherent $A_g(1)$ anti-stretching JT mode and of the $A_g(3)$ bending mode, to which the $A_g(1)$ is strongly mixed. Simultaneously, the photoexcited charge density couples via the exchange interaction to the $A_g(4)$ mode, corresponding to the out-of-phase rotation of the MnO_6 octahedra. Also this structural mode may be involved in the distortion associated with the anti-JT polaron formation. Therefore, we propose that these coherent modes represent the signatures of the creation of anti-JT polarons in $TbMnO_3$. The formation of such a relatively long-lived self-trapped charge hinders magnon-assisted hopping and thus requires the energy transfer to the spin system to be mediated by the rearrangement of the lattice structure. Consistent with this idea, the signal associated with the melting of the long-range magnetic order rises within several picoseconds and, at our absorbed pump fluence, the complete melting of the magnetic order is expected to take place within 22 ps [14]. We expect polaronic effects to manifest also when the initial photoexcitation couples to the *p*-*d* CT transition, as the *d*-orbitals will be again influenced by the presence of an extra charge. Similar experiments exploring a pump

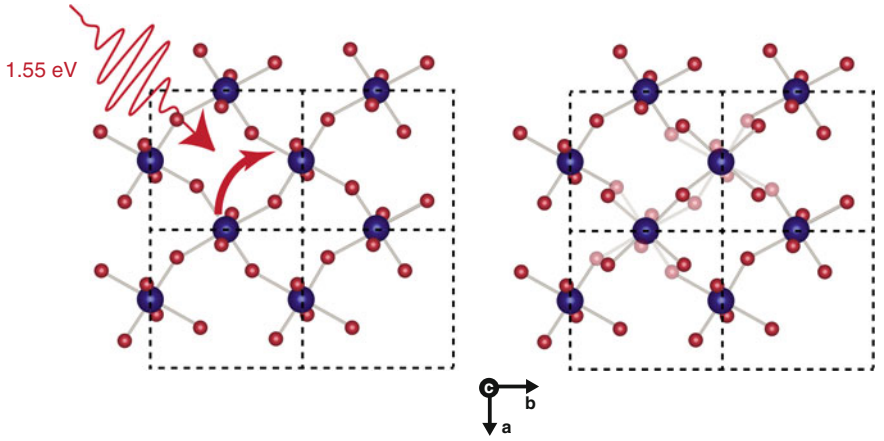

Fig. 7.22 Schematic illustration of the lattice displacement associated with the creation of an anti-JT polaron upon photoexcitation of the system via an intersite *d*-*d* CT transition

photon energy at 3.10 eV confirm the insensitivity of the magnetic order response to the details of the initial photoexcitation [15, 68].

The scenario proposed above reconciles the results reported in different experiments, suggesting the crucial involvement of the lattice behind the spin-order melting. More importantly, as the coherent optical phonons were previously detected in $LaMnO_3$, it is reasonable to believe that the same phenomenology is effectively at play in all undoped orthorhombic manganites. Indeed, the pronounced coherences appear in both $LaMnO_3$ and $TbMnO_3$, which represent the least and the most distorted orthorhombic manganites of the $RMnO_3$ family, respectively. A different microscopic mechanism may be at play in the hexagonal manganites of the $RMnO_3$ family, as the hexagonal crystal field splitting lifts the *d*-orbital degeneracy in a different fashion [82, 83]. In this case, a pump pulse at 1.55 eV promotes an *on-site d-d* transition of the Mn electron, which leaves the total charge unchanged and does not change the polaronic potential [84].

We remark that novel features are also unveiled by our nonequilibrium experiment on $TbMnO_3$. A remarkable one is associated with the fine structure that emerges in the Raman matrix element of the $A_g(4)$ mode, which is indicative of a *p*-*d* CT origin behind the elementary excitations giving rise to such fine structure. According to this scenario, the parent orthorhombic manganites of the $RMnO_3$ family are characterized by a dual nature in the ZSA scheme and cannot be sorted neither into the Mott-Hubbard insulator nor into the CT insulator regime [47]. In addition to this, two previously undetected coherent phonon modes are found to participate to the ultrafast evolution of the system after the photoexcitation. In particular, the $A_g(5)$ mode corresponds to a partially soft phonon associated with the ferroelectric phase transition. We speculate that this mode is generated via the ISRS mechanism, similarly to the behaviour observed in the order-disorder perovskite ferroelectrics [78–80]. We sug-

gest that temperature dependent studies of this partially soft mode may unveil new intriguing aspects on the origin of the magnetoelectric coupling in this multiferroic material and shed light on the fate of the ferroelectric order parameter following the photoexcitation. One interesting open question is whether the ferroelectric and the magnetic order parameters decouple simultaneously after the interaction with the pump pulse and follow separate temporal evolution in the system. In this regard, our measurements set the basis for revealing the dynamics of the ferroelectric polarization in the spin-cycloid magnetic phase with more sensitive ultrafast methods, such as time-resolved second harmonic generation spectroscopy [85] and microscopy [86].

References

1. A. Kirilyuk, A.V. Kimel, T. Rasing, Ultrafast optical manipulation of magnetic order. Rev. Mod. Phys. **82**(3), 2731 (2010)
2. E. Beaurepaire, J.-C. Merle, A. Daunois, J.-Y. Bigot, Ultrafast spin dynamics in ferromagnetic nickel. Phys. Rev. Lett. **76**(22), 4250 (1996)
3. J. Hohlfeld, E. Matthias, R. Knorren, K.H. Bennemann, Nonequilibrium magnetization dynamics of nickel. Phys. Rev. Lett. **78**(25), 4861 (1997)
4. A. Scholl, L. Baumgarten, R. Jacquemin, W. Eberhardt, Ultrafast spin dynamics of ferromagnetic thin films observed by fs spin-resolved two-photon photoemission. Phys. Rev. Lett. **79**(25), 5146 (1997)
5. J. Güdde, U. Conrad, V. Jähnke, J. Hohlfeld, E. Matthias, Magnetization dynamics of Ni and Co films on Cu(001) and of bulk nickel surfaces. Phys. Rev. B **59**(10), R6608 (1999)
6. G. Ju, A.V. Nurmikko, R.F.C. Farrow, R.F. Marks, M.J. Carey, B.A. Gurney, Ultrafast time resolved photoinduced magnetization rotation in a ferromagnetic/antiferromagnetic exchange coupled system. Phys. Rev. Lett. **82**(18), 3705 (1999)
7. M. Van Kampen, C. Jozsa, J.T. Kohlhepp, P. LeClair, L. Lagae, W.J.M. De Jonge, B. Koopmans, All-optical probe of coherent spin waves. Phys. Rev. Lett. **88**(22), 227201 (2002)
8. A.V. Kimel, A. Kirilyuk, A. Tsvetkov, R.V. Pisarev, T. Rasing, Laser-induced ultrafast spin reorientation in the antiferromagnet $TmFeO_3$. Nature **429**(6994), 850–853 (2004)
9. J.-Y. Bigot, M. Vomir, L.H.F. Andrade, E. Beaurepaire, Ultrafast magnetization dynamics in ferromagnetic cobalt: the role of the anisotropy. Chem. Phys. **318**(1), 137–146 (2005)
10. G. Ju, J. Hohlfeld, B. Bergman, R.J.M. van de Veerdonk, O.N. Mryasov, J.-Y. Kim, X. Wu, D. Weller, B. Koopmans, Ultrafast generation of ferromagnetic order via a laser-induced phase transformation in FeRh thin films. Phys. Rev. Lett. **93**, 197403 (2004)
11. J.-U. Thiele, M.s Buess, C.H. Back, Spin dynamics of the antiferromagnetic-to-ferromagnetic phase transition in FeRh on a sub-picosecond time scale. Appl. Phys. Lett. **85**(14) (2004)
12. M. Först, R.I. Tobey, S. Wall, H. Bromberger, V. Khanna, A.L. Cavalieri, Y.-D. Chuang, W.S. Lee, R. Moore, W.F. Schlotter, J.J. Turner, O. Krupin, M. Trigo, H. Zheng, J.F. Mitchell, S.S. Dhesi, J.P. Hill, A. Cavalleri, Driving magnetic order in a manganite by ultrafast lattice excitation. Phys. Rev. B **84**, 241104 (2011)
13. S.L. Johnson, R.A. De Souza, U. Staub, P. Beaud, E. Möhr-Vorobeva, G. Ingold, A. Caviezel, V. Scagnoli, W.F. Schlotter, J.J. Turner et al., Femtosecond dynamics of the collinear-to-spiral antiferromagnetic phase transition in CuO. Phys. Rev. Lett. **108**(3), 037203 (2012)
14. J.A. Johnson, T. Kubacka, M.C. Hoffmann, C. Vicario, S. de Jong, P. Beaud, S. Grübel, S.-W. Huang, L. Huber, Y.W. Windsor, E.M. Bothschafter, L. Rettig, M. Ramakrishnan, A. Alberca, L. Patthey, Y.-D. Chuang, J.J. Turner, G.L. Dakovski, W.-S. Lee, M.P. Minitti, W. Schlotter, R.G. Moore, C.P. Hauri, S.M. Koohpayeh, V. Scagnoli, G. Ingold, S.L. Johnson, U. Staub, Magnetic order dynamics in optically excited multiferroic $TbMnO_3$. Phys. Rev. B **92**, 184429 (2015)

15. E.M. Bothschafter, E. Abreu, L. Rettig, T. Kubacka, S. Parchenko, M. Porer, C. Dornes, Y.W. Windsor, M. Ramakrishnan, A. Alberca, S. Manz, J. Saari, S.M. Koohpayeh, M. Fiebig, T. Forrest, P. Werner, S.S. Dhesi, S.L. Johnson, U Staub, Dynamic pathway of the photoinduced phase transition of $TbMnO_3$. Phys. Rev. B **96**, 184414 (2017)
16. N.N. Kovaleva, A.V. Boris, C. Bernhard, A. Kulakov, A. Pimenov, A.M. Balbashov, G. Khaliullin, B. Keimer, Spin-controlled Mott-Hubbard bands in $LaMnO_3$ probed by optical ellipsometry. Phys. Rev. Lett. **93**(14), 147204 (2004)
17. T. Kimura, S. Ishihara, H. Shintani, T. Arima, K.T. Takahashi, K. Ishizaka, Y. Tokura, Distorted perovskite with e_g^1 configuration as a frustrated spin system. Phys. Rev. B **68**(6), 060403 (2003)
18. J.-S. Zhou, J.B. Goodenough, Unusual evolution of the magnetic interactions versus structural distortions in $RMnO_3$ perovskites. Phys. Rev. Lett. **96**(24), 247202 (2006)
19. D. Khomskii, *Transition Metal Compounds* (Cambridge University Press, Cambridge, 2014)
20. P.W. Anderson, Antiferromagnetism. Theory of superexchange interaction. Phys. Rev. **79**(2), 350 (1950)
21. J.B. Goodenough, Theory of the role of covalence in the perovskite-type manganites [La, M (II)] MnO_3. Phys. Rev. **100**(2), 564 (1955)
22. J.B. Goodenough, An interpretation of the magnetic properties of the perovskite-type mixed crystals $La_{1-x}Sr_xCoO_{3-\lambda}$. J. Phys. Chem. Solids **6**(2–3), 287–297 (1958)
23. J. Kanamori, Superexchange interaction and symmetry properties of electron orbitals. J. Phys. Chem. Solids. **10**(2–3), 87–98 (1959)
24. S. Quezel, F. Tcheou, J. Rossat-Mignod, G. Quezel, E. Roudaut, Magnetic structure of the perovskite-like compound $TbMnO_3$. Phys. B+ C **86**, 916–918 (1977)
25. M. Kenzelmann, A.B. Harris, S. Jonas, C. Broholm, J. Schefer, S.B. Kim, C.L. Zhang, S.-W. Cheong, O.P. Vajk, J.W. Lynn, Magnetic inversion symmetry breaking and ferroelectricity in $TbMnO_3$. Phys. Rev. Lett. **95**(8), 087206 (2005)
26. D. Senff, P. Link, K. Hradil, A. Hiess, L.P. Regnault, Y. Sidis, N. Aliouane, D.N. Argyriou, M. Braden, Magnetic excitations in multiferroic $TbMnO_3$: evidence for a hybridized soft mode. Phys. Rev. Lett. **98**(13), 137206 (2007)
27. S.B. Wilkins, T.R. Forrest, T.A.W. Beale, S.R. Bland, H.C. Walker, D. Mannix, F. Yakhou, D. Prabhakaran, A.T. Boothroyd, J.P. Hill et al., Nature of the magnetic order and origin of induced ferroelectricity in $TbMnO_3$. Phys. Rev. Lett. **103**(20), 207602 (2009)
28. H.C. Walker, F. Fabrizi, L. Paolasini, F. de Bergevin, D. Prabhakaran, A.T. Boothroyd, D.F. McMorrow, Circularly polarized x-ray scattering investigation of spin-lattice coupling in $TbMnO_3$ in crossed electric and magnetic fields. Phys. Rev. B **88**(21), 214415 (2013)
29. S.W. Lovesey, V. Scagnoli, M. Garganourakis, S.M. Koohpayeh, C. Detlefs, U. Staub, Melting of chiral order in terbium manganate ($TbMnO_3$) observed with resonant x-ray Bragg diffraction. J. Phys-Condens. Mat. **25**(36), 362202 (2013)
30. T. Kimura, T. Goto, H. Shintani, K. Ishizaka, T. Arima, Y. Tokura, Magnetic control of ferroelectric polarization. Nature **426**(6962), 55–58 (2003)
31. I.A. Sergienko, E. Dagotto, Role of the Dzyaloshinskii-Moriya interaction in multiferroic perovskites. Phys. Rev. B **73**(9), 094434 (2006)
32. N.S. Fedorova, C. Ederer, N.A. Spaldin, A. Scaramucci, Biquadratic and ring exchange interactions in orthorhombic perovskite manganites. Phys. Rev. B **91**(16), 165122 (2015)
33. T. Goto, T. Kimura, G. Lawes, A.P. Ramirez, Y. Tokura, Ferroelectricity and giant magnetocapacitance in perovskite rare-earth manganites. Phys. Rev. Lett. **92**(25), 257201 (2004)
34. N.N. Kovaleva, A.M. Oleś, A.M. Balbashov, A. Maljuk, D.N. Argyriou, G. Khaliullin, B. Keimer, Low-energy Mott-Hubbard excitations in $LaMnO_3$ probed by optical ellipsometry. Phys. Rev. B **81**(23), 235130 (2010)
35. A.S. Moskvin, A.A. Makhnev, L.V. Nomerovannaya, N.N. Loshkareva, A.M. Balbashov, Interplay of p-d and d-d charge transfer transitions in rare-earth perovskite manganites. Phys. Rev. B **82**(3), 035106 (2010)
36. J.F. Lawler, J.G. Lunney, J.M.D. Coey, Magneto-optic Faraday effect in $(La_{1-x}Ca_x)MnO_3$ films. Appl. Phys. Lett. **65**(23), 3017–3018 (1994)

37. N.N. Kovaleva, K.I. Kugel, Z. Potůček, O.E. Kusmartseva, N.S. Goryachev, Z. Bryknar, E.I. Demikhov, V.A. Trepakov, A. Dejneka, F.V. Kusmartsev, A.M. Stoneham, Optical evidence of quantum rotor orbital excitations in orthorhombic manganites. J. Exp. Theor. Phys. **122**(5), 890–901 (2016)
38. K.H. Ahn, A.J. Millis, Effects of magnetic ordering on the anisotropy and temperature dependence of the optical conductivity in $LaMnO_3$: a tight-binding approach. Phys. Rev. B **61**(20), 13545 (2000)
39. P. Ravindran, A. Kjekshus, H. Fjellvåg, A. Delin, O. Eriksson, Ground-state and excited-state properties of $LaMnO_3$ from full-potential calculations. Phys. Rev. B **65**(6), 064445 (2002)
40. M. Bastjan, S.G. Singer, G. Neuber, S. Eller, N. Aliouane, D.N. Argyriou, S.L. Cooper, M. Rübhausen, Magneto-optical study of the spin-polarized electronic states in multiferroic $TbMnO_3$. Phys. Rev. B **77**(19), 193105 (2008)
41. Y. Okimoto, T. Katsufuji, T. Ishikawa, T. Arima, Y. Tokura, Variation of electronic structure in $La_{1-x}Sr_xMnO_3$ f ($0 \leq x \leq 0.3$) as investigated by optical conductivity spectra. Phys. Rev. B **55**(7), 4206 (1997)
42. K. Takenaka, K. Iida, Y. Sawaki, S. Sugai, Y. Moritomo, A. Nakamura, Optical reflectivity spectra measured on cleaved surfaces of $La_{1-x}Sr_xMnO_3$: evidence against extremely small Drude weight. J. Phys. Soc. Jpn. **68**(6), 1828–1831 (1999)
43. K. Tobe, T. Kimura, Y. Okimoto, Y. Tokura, Anisotropic optical spectra in a detwinned $LaMnO_3$ crystal. Phys. Rev. B **64**(18), 184421 (2001)
44. M.A. Quijada, J.R. Simpson, L. Vasiliu-Doloc, J.W. Lynn, H.D. Drew, Y.M. Mukovskii, S.G. Karabashev, Temperature dependence of low-lying electronic excitations of $LaMnO_3$. Phys. Rev. B **64**(22), 224426 (2001)
45. A. Nucara, F.M. Granozio, M. Radovic, F.M. Vitucci, P. Maselli, R. Fittipaldi, A. Vecchione, P. Calvani, Optical investigation of $LaMnO_3$ thin films: a study of the 2-eV band. Eur. Phys. J. B **79**(4), 435–441 (2011)
46. M.W. Kim, S.J. Moon, J.H. Jung, J. Yu, S. Parashar, P. Murugavel, J.H. Lee, T.W. Noh, Effect of orbital rotation and mixing on the optical properties of orthorhombic $RMnO_3$ (R= La, Pr, Nd, Gd, and Tb). Phys. Rev. Lett. **96**(24), 247205 (2006)
47. J. Zaanen, G.A. Sawatzky, J.W. Allen, Band gaps and electronic structure of transition-metal compounds. Phys. Rev. Lett. **55**(4), 418 (1985)
48. P.B. Allen, V. Perebeinos, Self-trapped exciton and Franck-Condon spectra predicted in $LaMnO_3$. Phys. Rev. Lett. **83**(23), 4828 (1999)
49. J.S. Lee, M.W. Kim, T.W. Noh, Optical excitations of transition-metal oxides under the orbital multiplicity effects. New J. Phys. **7**(1), 147 (2005)
50. R. Krüger, B. Schulz, S. Naler, R. Rauer, D. Budelmann, J. Bäckström, K.H. Kim, S.W. Cheong, V. Perebeinos, M. Rübhausen, Orbital ordering in $LaMnO_3$ investigated by resonance Raman spectroscopy. Phys. Rev. Lett. **92**(9), 097203 (2004)
51. H.J. Zeiger, J. Vidal, T.K. Cheng, E.P. Ippen, G. Dresselhaus, M.S. Dresselhaus, Theory for displacive excitation of coherent phonons. Phys. Rev. B **45**(2), 768 (1992)
52. R. Merlin, Generating coherent THz phonons with light pulses. Sol. State Comm. **102**(2), 207–220 (1997)
53. P. Rovillain, J. Liu, M. Cazayous, Y. Gallais, M.-A. Measson, H. Sakata, A. Sacuto, Electromagnon and phonon excitations in multiferroic $TbMnO_3$. Phys. Rev. B **86**, 014437 (2012)
54. G.A. Smolenskiĭ, I.E. Chupis, Ferroelectromagnets. Sov. Phys. Uspekhi **25**(7), 475 (1982)
55. A.B. Sushkov, R. Valdés Aguilar, S. Park, S.-W. Cheong, H.D. Drew, Electromagnons in multiferroic YMn_2O_5 and $TbMn_2O_5$. Phys. Rev. Lett. **98**, 027202 (2007)
56. Y. Takahashi, N. Kida, Y. Yamasaki, J. Fujioka, T. Arima, R. Shimano, S. Miyahara, M. Mochizuki, N. Furukawa, Y. Tokura, Evidence for an electric-dipole active continuum band of spin excitations in multiferroic $TbMnO_3$. Phys. Rev. Lett. **101**, 187201 (2008)
57. A. Pimenov, A.A. Mukhin, V.Y. Ivanov, V.D. Travkin, A.M. Balbashov, A. Loidl, Possible evidence for electromagnons in multiferroic manganites. Nat. Phys. **2**(2), 97–100 (2006)
58. P. Rovillain, M. Cazayous, Y. Gallais, A. Sacuto, M.-A. Measson, H. Sakata, Magnetoelectric excitations in multiferroic $TbMnO_3$ by Raman scattering. Phys. Rev. B **81**, 054428 (2010)

59. L. Martín-Carrón, A. de Andrés, M.J. Martínez-Lope, M.T. Casais, J.A. Alonso, Raman phonons as a probe of disorder, fluctuations, and local structure in doped and undoped orthorhombic and rhombohedral manganites. Phys. Rev. B **66**, 174303 (2002)
60. M.N. Iliev, M.V. Abrashev, J. Laverdiere, S. Jandl, M.M. Gospodinov, Y.-Q. Wang, Y.-Y. Sun, Distortion-dependent Raman spectra and mode mixing in $RMnO_3$ perovskites (R = La, Pr, Nd, Sm, Eu, Gd, Tb, Dy, Ho, Y). Phys. Rev. B **73**(6), 064302 (2006)
61. J. Laverdiere, S. Jandl, A.A. Mukhin, V.Y. Ivanov, V.G. Ivanov, M.N. Iliev, Spin-phonon coupling in orthorhombic $RMnO_3$ (R = Pr, Nd, Sm, Eu, Gd, Tb, Dy, Ho, Y): a Raman study. Phys. Rev. B **73**(21), 214301 (2006)
62. P. Kumar, S. Saha, D.V.S. Muthu, J.R. Sahu, A.K. Sood, C.N.R. Rao, Raman evidence for orbiton-mediated multiphonon scattering in multiferroic $TbMnO_3$. J. Phys.-Condens. Mat. **22**(11), 115403 (2010)
63. W. Hayes, R. Loudon, *Scattering of Light by Crystals*. Courier Corporation (2012)
64. M.N. Iliev, M.V. Abrashev, H.-G. Lee, V.N. Popov, Y.Y. Sun, C. Thomsen, R.L. Meng, C.W. Chu, Raman spectroscopy of orthorhombic perovskitelike $YMnO_3$ and $LaMnO_3$. Phys. Rev. B **57**, 2872–2877 (1998)
65. S. Venugopalan, M. Dutta, A.K. Ramdas, J.P. Remeika, Magnetic and vibrational excitations in rare-earth orthoferrites: a Raman scattering study. Phys. Rev. B **31**, 1490–1497 (1985)
66. H.C. Walker, F. Fabrizi, L. Paolasini, F. de Bergevin, J. Herrero-Martin, A.T. Boothroyd, D. Prabhakaran, D.F. McMorrow, Femtoscale magnetically induced lattice distortions in multiferroic $TbMnO_3$. Science **333**(6047), 1273–1276 (2011)
67. T.E. Stevens, J. Kuhl, R. Merlin, Coherent phonon generation and the two stimulated Raman tensors. Phys. Rev. B **65**(14), 144304 (2002)
68. I.P. Handayani, R.I. Tobey, J. Janusonis, D.A. Mazurenko, N. Mufti, A.A. Nugroho, M.O. Tjia, T.T.M. Palstra, P.H.M. van Loosdrecht, Dynamics of photo-excited electrons in magnetically ordered $TbMnO_3$. J. Phys.-Condens. Mat. **25**(11), 116007 (2013)
69. S. Wall, D. Prabhakaran, A.T. Boothroyd, A. Cavalleri, Ultrafast coupling between light, coherent lattice vibrations, and the magnetic structure of semicovalent $LaMnO_3$. Phys. Rev. Lett. **103**(9), 097402 (2009)
70. Y. Yamada, O. Hino, S. Nohdo, R. Kanao, T. Inami, S. Katano, Polaron ordering in low-doping $La_{1-x}Sr_xMnO_3$. Phys. Rev. Lett. **77**(5), 904 (1996)
71. S. Shimomura, N. Wakabayashi, H. Kuwahara, Y. Tokura, X-ray diffuse scattering due to polarons in a colossal magnetoresistive manganite. Phys. Rev. Lett. **83**(21), 4389 (1999)
72. A. Daoud-Aladine, J. Rodriguez-Carvajal, L. Pinsard-Gaudart, M.T. Fernandez-Diaz, A. Revcolevschi, Zener polaron ordering in half-doped manganites. Phys. Rev. Lett. **89**(9), 097205 (2002)
73. S. Mildner, J. Hoffmann, P.E. Blöchl, S. Techert, C. Jooss, Temperature-and doping-dependent optical absorption in the small-polaron system $Pr_{1-x}Ca_xMnO_3$. Phys. Rev. B **92**(3), 035145 (2015)
74. P.B. Allen, V. Perebeinos, Anti-Jahn-Teller polaron in $LaMnO_3$. Phys. Rev. B **60**(15), 10747 (1999)
75. T. Mertelj, D. Kuščer, M. Kosec, D. Mihailovic, Photoinduced infrared absorption in $(La_{1-x}Sr_xMn)_{1-\delta}O_3$: changes of the small polaron binding energy with doping. Phys. Rev. B **61**(22), 15102 (2000)
76. T. Holstein, Studies of polaron motion: part I. The molecular-crystal model. Ann. Phys. **8**(3), 325–342 (1959)
77. T. Holstein, Studies of polaron motion: part II. The "small" polaron. Ann. Phys. **8**(3), 343–389 (1959)
78. T.P. Dougherty, G.P. Wiederrecht, K.A. Nelson, M.H. Garrett, H.P. Jensen, C. Warde, Femtosecond resolution of soft mode dynamics in structural phase transitions. Science **258**(5083), 770–774 (1992)
79. T.P. Dougherty, G.P. Wiederrecht, K.A. Nelson, M.H. Garrett, H.P. Jenssen, C. Warde, Femtosecond time-resolved spectroscopy of soft modes in structural phase transitions of perovskites. Phys. Rev. B **50**(13), 8996 (1994)

80. T. Kohmoto, K. Tada, T. Moriyasu, Y. Fukuda, Observation of coherent phonons in strontium titanate: structural phase transition and ultrafast dynamics of the soft modes. Phys. Rev. B **74**(6), 064303 (2006)
81. M. Hase, M. Kitajima, S. Nakashima, K. Mizoguchi, Forcibly driven coherent soft phonons in GeTe with intense THz-rate pump fields. Appl. Phys. Lett. **83**(24), 4921–4923 (2003)
82. R.C. Rai, J. Cao, J.L. Musfeldt, S.B. Kim, S.-W. Cheong, X. Wei, Spin-charge coupling and the high-energy magnetodielectric effect in hexagonal $HoMnO_3$. Phys. Rev. B **75**(18), 184414 (2007)
83. A.B. Souchkov, J.R. Simpson, M. Quijada, H. Ishibashi, N. Hur, J.S. Ahn, S.W. Cheong, A.J. Millis, H.D. Drew, Exchange interaction effects on the optical properties of $LuMnO_3$. Phys. Rev. Lett. **91**(2), 027203 (2003)
84. P. Bowlan, S.A. Trugman, J. Bowlan, J.-X. Zhu, N.J. Hur, A.J. Taylor, D.A. Yarotski, R.P. Prasankumar, Probing ultrafast spin dynamics through a magnon resonance in the antiferromagnetic multiferroic $HoMnO_3$. Phys. Rev. B **94**, 100404 (2016)
85. R. Mankowsky, A. von Hoegen, M. Först, A. Cavalleri, Ultrafast reversal of the ferroelectric polarization. Phys. Rev. Lett. **118**, 197601 (2017)
86. M. Matsubara, S. Manz, M. Mochizuki, T. Kubacka, A. Iyama, N. Aliouane, T. Kimura, S.L. Johnson, D. Meier, M. Fiebig, Magnetoelectric domain control in multiferroic $TbMnO_3$. Science **348**(6239), 1112–1115 (2015)

Conclusions and Future Directions

In the Introduction, we underlined the importance of adopting a novel strategy to gain insights into the dynamical properties of matter. Probing matter in a nonequilibrium state goes beyond the paradigm of conventional steady-state methods. In the latter approach, the external stimuli are applied for a long enough time for the system to reach a steady state which may or may not correspond to the real GS. In contrast, when the perturbation is faster than the relaxation time of the system, one can map the hierarchy of processes occurring during the path towards equilibrium, thus accessing the dynamics of broken symmetry phases.

One of the most successful examples of nonequilibrium approach is offered by ultracold atoms in optical lattices, as the lifetime of the ES is so long that the evolution from an ES to a statistical ensemble can be mapped in real time. Adopting an analogous framework in real materials has become a reality thanks to huge advances in ultrafast laser science. The development of novel techniques, such as pump-probe THz, trARPES, trREXS and time-resolved TEM, is paving the route to the selective observation of phenomena with a direct link to the GS properties of the material. Indeed, when the perturbation is kept within the linear regime, the ES one can reach corresponds to that probed a steady-state experiment, thus giving access to similar information. In addition, when the degrees of freedom in a system are strongly intertwined, the nonequilibrium approach offers a straightforward tool to disentangle them in the time domain on the basis of their characteristic relaxation timescales. On the contrary, when larger perturbations are applied beyond the linear regime, one can also discover exotic nonlinear phenomena that are not accessible under equilibrium conditions. In this regard, the outstanding results achieved in the field of photoinduced phase transitions and hidden states of matter are intimately linking this field of research to possible technological developments. These successes have rapidly led to a change of perspective in a broad part of the condensed matter physics community and triggered the interest of many theorists to address the nonequilibrium many-body problem at extreme timescales. Eventually, this "ultrafast revolution" has also motivated governments in justifying the efforts of building large-scale facilities devoted to ultrafast x-ray science. This leads us to conclude that ultrafast spectroscopy should

E. Baldini, *Nonequilibrium Dynamics of Collective Excitations in Quantum Materials*,
Springer Theses, https://doi.org/10.1007/978-3-319-77498-5

not be considered as an avant-garde technique anymore, but as a precious tool for the study of quantum processes in matter.

In this Thesis, we have put special emphasis on ultrafast broadband optical spectroscopy and tried to demonstrate that this technique is a fertile route for revealing the emergence of specific collective excitations either in the frequency or in the time domain. By mapping the dynamics of these collective excitations, novel information on the low-energy response of complex materials could be unveiled, despite the use of high-energy photons in the optical regime. For example, the observation of the dynamics of the longitudinal plasmon in MgB_2 allowed us to track the interband scattering mechanism between distinct electronic subsystems, while the discovery of strongly bound excitons in anatase TiO_2 has given access to the ultrafast carrier dynamics even at very short timescales; the observation of coherent optical phonons in the time domain resulted in the determination of the electron-phonon coupling in La_2CuO_4, in the detection of precursor superconducting phenomena in $NdBa_2Cu_3O_{7-\delta}$ and in the understanding of the magnetic order melting dynamics in $TbMnO_3$. These results demonstrate how collective excitations can be used as very sensitive probes of their environment and can provide insights into the magnitude and dynamics of interactions and correlations in complex materials beyond conventional band theory. The main question that remains open concerns the fate of this technique, in relation to its strengths and limitations.

Due to its bulk sensitivity, ultrafast broadband optical spectroscopy is ideal for probing the properties of strongly correlated electron systems, but would fail in revealing insightful information on topological phases of matter, which are characterized by the emergence of topological surface states. Therefore, we expect that the field of strongly correlated electron systems will continue to benefit from the application of this technique to probe the electronic properties of newly discovered materials. In this regard, it is highly desirable to broaden the detection window towards different spectral ranges rather than the visible and the UV. For example, the extension towards the MIR/FIR/THz has become a reality in ultrafast spectroscopy since more than a decade ago, but its systematic applications on correlated electron systems has been limited to a few studies. Moreover, the advancement to the 2D spectroscopy framework holds promise especially to unravel interaction and correlation effects among coherent collective excitations (triggered via the ISRS) in the time domain and collective modes in the frequency domain (*e.g.* infrared-active phonons, magnons...). Finally, two are the main limitations associated with this technique: (i) It represents an indirect probe of quantum phenomena, as the two particle excitation spectrum of the material is mapped; (ii) It is restricted at $\mathbf{q} = 0$ for detecting high-energy collective modes in the frequency domain and for generating low-enegy coherent collective modes in the time domain. To overcome this intrinsic limitation of optics, key is the development of x-ray or electron-based techniques such as trRIXS and trEELS. The "*spontaneous*" version of trRIXS and the use of trEELS are ideal to extend the **q**-range of the collective excitations probed in the frequency domain, thus revealing how their energy-momentum dispersion relation is renormalized over time. Some pioneering experiments have already demonstrated remarkable results with this respect. The more challenging "*impulsive stimulated*" version of trRIXS

would instead pave the route to the generation of coherent collective modes at finite **q**, thus opening new fascinating frontiers in the spectroscopy and control of these excitations.

Thus, we naturally conclude saying that a bright future is in front of both fundamental and applied research dealing with the interaction of ultrashort laser pulses with complex matter.

Appendix A
Sample Preparation

A.1 MgB_2

High-quality MgB_2 thin films were grown using hybrid physical-chemical vapor deposition at a substrate temperature of 730 °C, hydrogen carrier gas pressure of 40 Torr, hydrogen flow rate of 400 sccm, and diborane mixture (5% B_2H_6 in H_2) flow rate of 20 sccm. The corresponding deposition rate was 55 nm/min. The resulting thin film was a parallelepiped with a (0001)-oriented surface of 5 mm × 5 mm and a thickness of 200 nm along the *c*-axis. This thickness was controlled by the deposition time (220 s). Epitaxial MgB_2 films were deposited directly on SiC-(0001) substrate. After the MgB_2 deposition, the sides of the substrate were cleaned with 10% hydrogen chloride acid to remove the MgB_2 deposit. The structure of the MgB_2 thin films was characterized by x-ray diffraction and cross-sectional TEM using a JEOL 2100 LaB6 operated at 200 kV. The DC transport properties were measured using the four-probe van der Pauw method.

It is well established that surface contamination by exposure to air strongly reduces the absolute reflectivity of MgB_2, decreasing the value of the plasma frequency over time [1–4]. To prevent the measurements to suffer from this effect, the sample was stored in a vacuum environment before being introduced in the cryostat for the ultrafast optical experiments. During the transfer from the sample container to the cryostat, the thin film was kept in an argon flow until vacuum was produced in the cryostat. Finally, during the measurements at low temperatures, to counteract the adsorption of carbon oxide compounds on the MgB_2 thin film surface, the sample was warmed up above ∼230 K after about 2 h at low temperatures to restore the reflectivity of its surface.

E. Baldini, *Nonequilibrium Dynamics of Collective Excitations in Quantum Materials*,
Springer Theses, https://doi.org/10.1007/978-3-319-77498-5

A.2 Anatase TiO_2

A.2.1 Single Crystals

High-quality single crystals of anatase TiO_2 were produced by a chemical transport method from anatase powder and NH_4Cl as transport agent, similar to the procedure described in Ref. [5]. In detail, 0.5 g of high-purity anatase TiO_2 powder were sealed in a 3 mm thick, 2 cm large and 20 cm long quartz ampoule together with 150 mg of NH_4Cl, previously dried at 60 °C under dynamic vacuum for one night, and 400 mbar of electronic grade HCl. The ampoules were placed in a horizontal tubular two-zone furnace and heated very slowly to 740 °C at the source, and 610 °C at the deposition zone. After 2 weeks, millimeter-sized crystals with a bi-pyramidal shape were collected and cut into rectangular bars (typically $0.8 \times 0.6 \times 0.15$ mm^3). The raw anatase TiO_2 single crystals were characterized through transport and Reflection High-Energy Electron Diffraction measurements, as in Ref. [6]. The doping level was estimated $n = 2 \times 10^{19}$ cm^{-3}. Cu-doped anatase TiO_2 single crystals were obtained by annealing raw anatase TiO_2 single crystals in O_2 at 700 °C for 6 days in the presence of Cu vapors. The pristine (reduced) form of anatase TiO_2 was instead obtained by annealing the *n*-doped anatase TiO_2 crystals at 700 °C for 10 days under 950 mbar of CO.

The pristine anatase TiO_2 single crystal was also polished along a (010)-oriented surface, in order to be used in the SE measurement. The surface roughness of this crystal was estimated via atomic force microscopy. Figure A.1a, b show two images taken under the atomic force microscope. The average surface roughness of the polished surface was found around 0.9 nm.

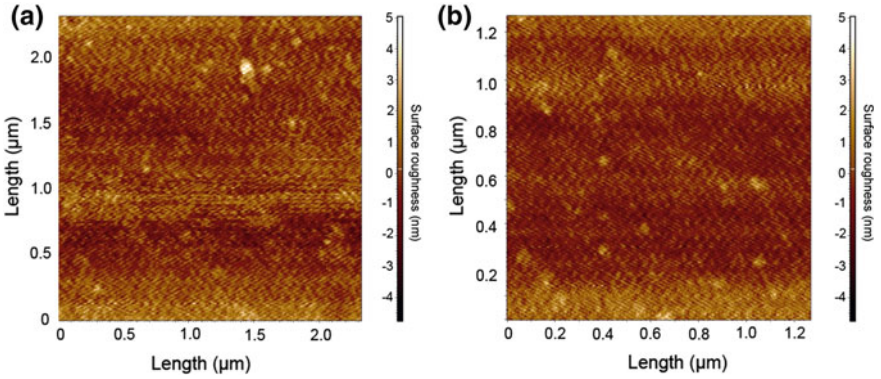

Fig. A.1 (**a**, **b**) Roughness characterization of the (010)-oriented polished surface of the reduced anatase TiO_2 single crystal used for the SE measurement. The images are taken using atomic force microscopy and the average surface roughness is estimated around 0.9 nm

A.2.2 Nanoparticles

The $TiO2_2$ NPs were prepared using the sol-gel method [7]. The synthesis was carried out in a glove box under argon atmosphere. Titanium isopropoxide (Sigma Aldrich, 99.999% purity) was used as precursor and was mixed with 10 ml of 2-propanol. This mixture was added dropwise under vigorous stirring to cold acidic water (2 °C, 250 ml H_2O, 18 MΩ, mixed with 80 ml glacial acetic acid, final pH 2). At the beginning the mixture looked turbid, but after stirring it in an ice bath for 12 h, it became transparent as the amorphous NPs were formed. Half of the mixture was left stirring for days to stabilize the NPs. The other half was peptized at 80 °C for about 2 h until the liquid turned into a transparent gel. The gel was autoclaved at 230 °C for 12 h. During this process the previous amorphous TiO_2 sample became denser and underwent a phase transition, resulting in anatase TiO_2 NPs. After the autoclave, the NPs have precipitated to the bottom of the container. They were separated from the supernatant and added to 100 ml acidic water (pH 2) to obtain a white colloidal solution with a final concentration of ca. 337 mM. In Ref. [8], we reported the details of the sample characterization by means of x-ray diffraction and TEM. Using these techniques, the good quality of the anatase phase and the spherical shape (with an average diameter of approximately 25 nm) of the NPs were demonstrated. The doping of the NPs is unknown.

Concerning the experiments with dye-sensitized anatase TiO_2 NPs, the dye N719 was purchased from Solaronix and dissolved in dimethylformamide to achieve an optical density of 0.4 at a photon energy of 2.25 eV. For the dye-sensitized anatase TiO_2 NPs, we used the ruthenium N719 dye (Di-tetrabutylammonium cis-bis (isothiocyanate)bis(2,2'-bipyridyl-4,4'-dicarboxylate) ruthenium(II)) adsorbed onto the NPs. To achieve a monolayer of dye on the NP at a concentration of 5 g/L, a solution of 170 mg of N719 in 10 ml DMF was mixed with the NPs for half a day. To ensure that no unbound N719 molecules remain, the suspension was left still for several days, in order to let the sensitized-NPs precipitate and then washed several times with DMF. Under the assumption that the NPs are spherically shaped with a diameter between 10 and 20 nm and that the N719 footprint is about 20 Å, we can deduce that a monolayer covering a NP consists of 300 to 350 dye molecules.

The steady-state absorption specta reported in Figs. 4.14 and 4.28 were recorded at RT using a commercial UV-VIS-NIR spectrometer (Shimadzu, UV-3600). Before measuring the absorption spectrum of the sample, a reference spectrum of the pure solvent (acidic water, pH 2) was taken to check its transparency in the investigated spectral range.

A.3 $La_2CuO_{4+\delta}$

A slightly doped single crystal of $La_2CuO_{4+\delta}$ was grown as follows. Polycrystalline La_2CuO_4 samples were prepared by a solid state reaction. The starting materials La_2O_3 and CuO with 99.99% purity were mixed and ground. This process was

followed by a heat treatment in air at 900–1050 °C for at least 70 h with several intermediate grindings. The phase purity of the resulting compound was checked with a conventional x-ray diffractometer. The resulting powder was hydrostatically pressed into rods (7 mm in diameter) and subsequently sintered at 1150 °C for 20 h. The crystal growth was carried out using an optical floating zone furnace (FZ-T-10000-H-IV-VP-PC, Crystal System Corp., Japan) with four 300-W halogen lamps as heat sources. The growing conditions were as follows: The growth rate was 1 mm/h, the feeding and seeding rods were rotated at about 15 rpm in opposite directions to ensure the liquid's homogeneity, and an oxygen and argon mixture at 3 bar pressure was applied during growth. The as-grown crystals were post-annealed at 850 °C in order to release the internal stress and to adjust the oxygen content. One crystal was oriented in a Laue diffractometer, cut along a plane containing the *a* and *c* axes and polished to optical quality. The Néel temperature was determined to be $T_N = 260$ K, which corresponds to a doping $\delta = 3 \times 10^{-3}$ and a hole content $p = 6 \times 10^{-3}$. After the first set of measurements on the slightly doped sample, the crystal was annealed for 48 h to remove part of the excess oxygen. After the treatment, the Néel temperature increased to $T_N = 307$ K, which well agrees with the typical value found in purely undoped compounds.

A.4 $NdBa_2Cu_3O_{7-\delta}$

High-quality single crystals of $NdBa_2Cu_3O_{7-\delta}$ were flux-grown in an Y-stabilized zirconia crucible and under low oxygen partial pressure to avoid spurious substitution of the Nd ion onto the Ba site [9]. The resulting crystal was a parallelepiped with dimensions 5.5 mm × 4 mm × 1 mm along the *a*, *b* and *c* axes, respectively. The sample was annealed in oxygen for ten days at 370 °C resulting in a SC transition temperature of $T_C = 93.5$ K, as measured by dc magnetisation, and a sharp transition width of 1.5 K. All crystal surfaces were mechanically polished to optical grade using diamond powder paste.

A.5 $TbMnO_3$

High-quality, stoichiometric $TbMnO_3$ single crystals were grown by the optical floating zone technique at the zoning rate of 0.5 mm/h with rotation rate of 15 rpm for the growing crystal and 0 rpm for the feed rod under static argon. The crystal was oriented using Laue backscattering and cut to expose the (010) face with an approximately 3° miscut. The surface of the sample was polished and afterwards the sample was annealed in air in 650 °C for 110 h. The dimensions of the crystal are approximately 2 mm × 2 mm × 3 mm along the *a*, *b* and *c* axes, respectively. The *Pbnm* orthorhombic convention is used to describe the crystal axes.

Appendix B
Additional Experimental Methods

B.1 Angle-Resolved Photoemission Spectroscopy

Angle-resolved photoemission spectroscopy (ARPES) is one of the most direct techniques aimed at measuring the electronic structure of solids. In this method, a sample is illuminated with sufficiently high photon energy radiation, leading to the photoemission of electrons with a distribution of kinetic energies and angles. By measuring the kinetic energy and angular distribution, insightful information on both the energy and momentum of the electrons propagating inside a material can be retrieved. This technique represents an advanced version of photoelectron spectroscopy, which is a photon in-electron out experiment used for probing the valence- or the core-level structure of a material. A detailed description of the ARPES process is out of the scope of this Thesis. Here we briefly introduce the method and put emphasis on how the information is retrieved. More specific and excellent reviews/books are given at Ref. [10, 11].

In ARPES, the beam of monochromatized UV or x-ray radiation that interacts with the sample is supplied either by a gas-discharge lamp, by a laser (laser-based ARPES) or by a synchrotron beamline (synchrotron-based ARPES). As a result of the interaction, electrons are emitted via the photoelectric effect and escape in vacuum with a broad distribution of emission angles and kinetic energies. While in photoemission spectroscopy the emitted electrons are collected over a broad (angle-integrated) acceptance angle, in ARPES an electron energy analyzer with a finite acceptance angle is used, leading to the measurement of the electron kinetic energy for a given emission angle. Using this approach, the wave vector or momentum $\mathbf{K} = \mathbf{p}/\hbar$ of the photoelectrons in vacuum is completely determined, as its modulus is $\mathbf{K} = \sqrt{2mE_{kin}}/\hbar$ and its components parallel ($\mathbf{K}_{\parallel} = \mathbf{K}_x + \mathbf{K}_y$) and perpendicular ($\mathbf{K}_{\perp} = \mathbf{K}_z$) to the sample surface can be obtained in terms of the polar and azimuthal emission angles of the experiment

$$K_x = \frac{1}{\hbar}\sqrt{2mE_{kin}}\sin\theta\cos\phi, \tag{B.1}$$

E. Baldini, *Nonequilibrium Dynamics of Collective Excitations in Quantum Materials*,
Springer Theses, https://doi.org/10.1007/978-3-319-77498-5

$$K_y = \frac{1}{\hbar}\sqrt{2mE_{kin}}\sin\theta\sin\phi, \tag{B.2}$$

$$K_z = \frac{1}{\hbar}\sqrt{2mE_{kin}}\cos\theta. \tag{B.3}$$

The final goal is to extract the energy-momentum dispersion relations E(**k**) of the solid under study, i.e. the relation between the binding energy and momentum **k** for the electrons propagating inside the material, starting from the measured E_{kin} and **K** of the photoelectrons in vacuum. In this regard, the total energy and momentum conservation laws have to be applied. Within the framework of non-interacting electrons in a solid, the measured photoelectron kinetic energy has a simple relation to the binding energy of the electronic state inside the solid. More difficult is to retrieve full information on the crystal electronic momentum **k**. Indeed, because of the translational symmetry in the xy plane across the surface, only the parallel component of the electron momentum is conserved in the photoemission spectrum, leading to

$$\mathbf{k}_{\parallel} = \mathbf{K}_{\parallel} = \frac{1}{\hbar}\sqrt{2mE_{kin}}\sin\theta, \tag{B.4}$$

where $\mathbf{k}_{\parallel}$ is the component parallel to the surface of the electron crystal momentum. As $\mathbf{k}_{\perp}$ is not conserved, a different approach is required for mapping the 3D dispersion E(**k**) relation of the solid. One possibility is to make an assumption concerning the final states involved in the photoemission process using the nearly-free-electron dispersion for the final bulk Bloch states, as discussed in Ref. [10].

In the framework of this Thesis, we used synchrotron-based ARPES for revealing the electronic structure of anatase TiO_2 in Chap. 4. These measurements were performed at the Electronic Structure Factory endstation on beamline 7.0.1 at the Advanced Light Source, Berkeley, USA. A raw anatase TiO_2 single crystal was polished and cleaned in a buffered 5% fluoridic acid solution before introducing it into the ultra-high vacuum system ($< 10^{-10}$ mbar). The crystal was annealed in 35 mbar of oxygen at 400 °C for 30 min before the ARPES experiments. The results are shown and discussed in Sect. 4.2.

B.2 Steady-State Spectroscopic Ellipsometry

SE is an optical technique that provides a detailed and reliable characterization of a material's dielectric properties. This method measures the change experienced by the polarization of a light beam when the latter is reflected under non-normal incidence from a sample surface. In the last decades, SE has established as a more powerful alternative to normal-incidence reflectivity, which was conventionally used for measuring the dielectric properties of a material. Several are the advantages of SE over normal-incidence reflectivity measurements: (i) In SE, suitable extrapolations and a KK analysis are not required to obtain the complex optical constants; (ii) SE

measures the intensity modulation rather than the absolute intensity of the reflected light and therefore it does not require the measurement of a reference sample for calibration; (iii) SE is not restricted to a single angle of incidence like typical reflectivity measurements, thus enabling the optimization of the angle for each individual sample in order to obtain maximum sensitivity; (iv) In the UV, SE is less sensitive to the surface roughness of the sample than normal-incidence reflectivity.

In contrast, the main drawback is that SE is experimentally more demanding than reflectivity, especially in the infrared region where high-quality polarizers operating in a broad region of frequencies are difficult to fabricate. Also concerning SE, we just present the working principle behind this technique, citing Ref. [12] for a complete treatment of the subject.

Figure B.1 illustrates the basic scheme of SE. A linearly polarized light beam is incident on the sample. The electric field components parallel (E_p) and perpendicular (E_s) to the plane of incidence are in phase with each other. According to the Fresnel equations, E_p and E_s undergo different attenuations and phase shifts upon reflection of the beam from the sample surface. As a consequence, a change of the polarization state of the beam arises. In general, the reflected beam is elliptically polarized and SE measures the difference in phase shift (Δ) and amplitude ratio ($\tan(\psi)$) of the reflected beam components E_p^r and E_s^r. These quantities are independent and defined from the ratio of the Fresnel reflection coefficients for the parallel (r_p) and the perpendicular (r_s) components of the light beam

$$\rho = \frac{r_s}{r_p} = \tan(\psi) \cdot e^{i\Delta}, \tag{B.5}$$

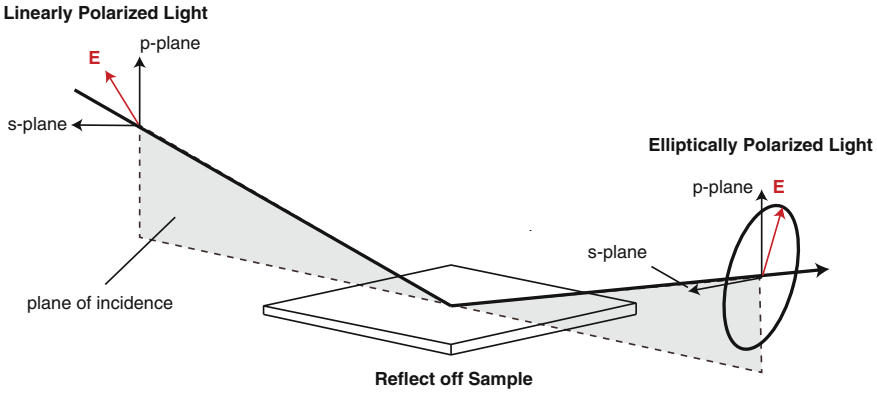

Fig. B.1 Schematic view of the principle of SE. An incoming light beam is linearly polarized and interacts with the sample. After the reflection under a certain angle, a change in polarization occurs and the outgoing beam becomes elliptically polarized

with $\tan(\psi) = r_p/r_s$ and $\Delta = \delta_p - \delta_s$. Thus, in the case of SE, the relevant quantities are the reflection coefficients r_p and r_s. For a bulk sample, these are given by

$$r_p = \frac{E_p^r}{E_p^i} = \frac{N_1 \cos(\Theta_0) - N_0 \cos(\Theta_1)}{N_1 \cos(\Theta_0) + N_0 \cos(\Theta_1)} = |r_p| \cdot e^{i\delta_p}, \tag{B.6}$$

$$r_s = \frac{E_s^r}{E_s^i} = \frac{N_0 \cos(\Theta_1) - N_1 \cos(\Theta_1)}{N_0 \cos(\Theta_0) + N_1 \cos(\Theta_1)} = |r_s| \cdot e^{i\delta_s}, \tag{B.7}$$

where $N_0(\omega) = n_0(\omega) + i\, k_0(\omega)$ is the complex index of refraction of the medium surrounding the sample, $N_1(\omega) = n_1(\omega) + i\, k_1(\omega)$ is the complex index of refraction of the sample, Θ_0 is the angle of incidence with respect to the normal to the sample surface in the initial medium, Θ_1 is the transmission angle with respect to the normal to the sample surface. The angles Θ_0 and Θ_1 are determined from Snell's law $N_0 \cdot \sin(\Theta_0) = N_1 \cdot \sin(\Theta_1)$. As the complex index of refraction and dielectric function are related via $\epsilon = N^2$, the complex dielectric function of the material is obtained directly from

$$\epsilon = \sin^2(\Theta_0)\left[1 + \tan(\Theta_0)\left(\frac{1-\rho}{1+\rho}\right)^2\right]. \tag{B.8}$$

In the framework of this Thesis, SE was used to measure the complex dielectric function of the investigated samples. As our primary interest was devoted to the high-energy dielectric properties of the materials, the static characterization via SE has been performed in a broad spectral range from 1.50 to 5.50 eV. In the specific case of MgB_2 (Sect. 3.2) we relied on RT SE data published in literature [2]; in the case of all the other materials, we performed temperature-dependent SE. During the measurements, a commercial Woollam VASE ellipsometer was used. The sample was mounted in a helium flow cryostat, allowing measurements from RT down to 10 K. At cryogenic temperatures, the data were acquired at a pressure of $<10^{-8}$ mbar, in order to prevent the occurrence of ice-condensation onto the sample. Anisotropy corrections were performed using standard numerical procedures [13] and diffraction effects at low frequency were accounted for using the method developed by Humlíček et al. [14]. In the case of the anatase TiO_2 single crystals (Sect. 4.3), the data have been further corrected to account for the surface roughness of the sample, which was estimated around 0.9 nm by means of atomic force microscopy (see Appendix A.2.1).

Finally, in the case of NBCO, we also performed complementary FIR SE measurements to obtain the complex optical conductivity of the sample along the *c*-axis over the 12.5–85.0 meV spectral range (Sect. 6.2). To this end, we used a home-built ellipsometer attached to a Bruker fast-Fourier spectrometer at the infrared beam line of the ANKA synchrotron at the Karlsruhe Institute for Technology, Germany.

Appendix C
Additional Analysis and Calculations

C.1 MgB_2

In this Section, we present the details of the ab initio calculations supporting our ultrafast broadband optical spectroscopy data on MgB_2 (Chap. 3).

C.1.1 Time-Dependent Quantum Mechanical Calculations

A quantum mechanical time-dependent method was used to evolve the electronic wavefunction with the propagator proposed in Refs. [15–18]. The evolution of the electronic wavefunction is therefore calculated with a generalized Cayley algorithm, based on a Dyson-like expansion of the time-evolution operator [19]. Numerically, the time-dependent Schrödinger equation is solved by the Cranck-Nicolson approximation method [20, 21], based on expressing the exponential operator $e^{H\Delta t}$ with second-order accuracy. It uses the commonly recommended finite differences scheme to approximate the solutions of the time-dependent Schrödinger equation in complex multiscale phenomena. This is a unitary and stable approach, which conserves probability and preserves orthogonality; moreover, as an O(N) method, it is particularly appropriate to investigate large systems, such as complex materials and biological molecules.

The propagator contains the unperturbed Hamiltonian at a certain k point of the crystal periodic structure, $H^0(k)$, plus the perturbing Hamitonian, H', representing the interaction of the applied electromagnetic field with the crystal dipole moment matrix of the periodic system. It reads

$$\Psi_j(t+\Delta t,k)=\left(1+\frac{iH(k)\Delta t}{2\hbar}\right)^{-1}\left(1-\frac{iH(k)\Delta t}{2\hbar}\right)\Psi_j(t,k). \tag{C.1}$$

E. Baldini, *Nonequilibrium Dynamics of Collective Excitations in Quantum Materials*,
Springer Theses, https://doi.org/10.1007/978-3-319-77498-5

The initial electronic wavefunction, $\Psi(t_0, k)$, is the matrix of crystal orbitals of the periodic system at a specific k point, built as a linear combination of Bloch orbitals extended over the entire crystalline solid. The Bloch orbitals are, in turn, a linear combination of a set of basis functions. Δt is the time step, H(k) is the Hamiltonian of a specific k point in the reciprocal space, $H(k) = H^0(k) + H'$. The perturbing Hamiltonian is then calculated as a product of the electric field and the crystal dipole moment, here written as

$$H(t) = -D\ E(t)\ \sin(\omega t)\ e^{-t/\tau}, \tag{C.2}$$

where D is the dipole moment matrix between crystal orbitals, ω is the frequency of the incoming photon, E(t) is the electric field amplitude or field envelope (here kept constant in time) and τ is the pulse duration (here set at 6 fs). The calculations are carried out in the crystal orbital framework. The field polarization can be chosen during simulations. The crystal orbitals coefficients of $\Psi(t, k)$ are updated at each time step under the effect of the external field. The propagation is carried out starting from crystal orbitals orthonormalized by the Löwdin transformation.

This approach allows to gain a detailed microscopic description of the ultrafast electronic response of the system, which can be followed in terms of a large number of observables (i.e. time-dependent electron density distribution, crystal orbital occupancies, dipole moment changes and relative absorption spectra). In the past, it has been successfully employed also to investigate the photolytic splitting of water ice by vacuum-UV light [22], the dynamics of photoactivated chemical bonding [23], ET processes [24], photoinduced dissociation [25], nonlinear optical properties [26], mono- and multi-photon excitations [27], and photoelectron spectra of coronene [28]. Using this technique, we investigate the ultrafast changes of the MgB_2 band structure during the first 40 fs after photoexcitation at selected critical momentum points of the BZ.

The electronic GS of the structures were calculated with the Gaussian 09 [29] suite of programs with periodic boundary conditions. The nuclear geometries are frozen during the electron wavepacket dynamics so that the pure electron reorganization of the system wavefunction is investigated. The MgB_2 calculations were run on the hexagonal AlB_2-type lattice structure [30], with space group P6/mmm and lattice parameters, a = 3.084 Å and c = 3.522 Å, using the Perdew-Burke-Ernzerhof (PBE) functional [31] implemented in Gaussian09. A 724 k-points grid in the reciprocal space was created. The basis sets applied were the Small Split-Valence 3-21SP function for Mg atoms and the 6-31G for B atoms. The results of the calculations are presented in Chap. 3.

C.1.2 Effect of Lattice Expansion on the c-Axis Plasmon

We simulated the effect of the increased lattice temperature on the c-axis plasmon peak energy by calculating the excitation spectrum at different lattice parameters.

Two models for the MgB_2 lattice parameter expansion were employed. In the first case, we obtained the lattice parameters by considering a 3D lattice expansion. Here, at a fixed volume value, the c/a ratio was optimized using the Vienna Ab Initio Simulation Package [32, 33] with GGA as in the PBE scheme for the exchange-correlation functional [31]. The interaction between the ion cores and valence electrons was described by the projector augmented-wave method [34]. In the second case, we performed calculations for the uniaxial c-axis expansion, i.e. varying the lattice constant only in this direction and maintaining the in-plane lattice constant fixed.

The collective electronic excitations of a bulk solid can be traced [35, 36] to the peaks in the loss function $L(\mathbf{q}, \omega)$, defined as the imaginary part of the inverse dielectric function

$$L(\mathbf{q}, \omega) = \mathrm{Im}[\epsilon^{-1}(\mathbf{q}, \omega)], \tag{C.3}$$

where $\mathbf{q}$ and ω are momentum and energy, respectively, transferred to the system. The inverse dielectric function ϵ^{-1} is related to the density response function of interacting electrons χ through the integral equation $\epsilon^{-1} = 1 + \upsilon\chi$, where υ is the Coulomb potential. In the framework of the time-dependent DFT [37, 38] χ obeys the integral equation $\chi = \chi^o + \chi^o(\upsilon + \mathrm{K_{xc}})\chi$, where χ^o is the response function for a non-interacting electron system and $\mathrm{K_{xc}}$ accounts for dynamical exchange-correlation effects. The imaginary part of χ^o, which takes a matrix form for a 3D solid, is calculated according to

$$\begin{aligned}\mathrm{Im}[\chi^o_{\mathbf{G}\mathbf{G}'}(\mathbf{q}, \omega)] = \frac{2}{\Omega}\sum_{\mathbf{k}}^{\mathrm{BZ}}\sum_{nn'}(f_{n\mathbf{k}} - f_{n'\mathbf{k}+\mathbf{q}})\langle\psi_{n\mathbf{k}}|e^{-\mathrm{i}(\mathbf{q}+\mathbf{G})\cdot\mathbf{r}}|\psi_{n'\mathbf{k}+\mathbf{q}}\rangle \\ \langle\psi_{n'\mathbf{k}+\mathbf{q}}|e^{\mathrm{i}(\mathbf{q}+\mathbf{G}')\cdot\mathbf{r}}|\psi_{n\mathbf{k}}\rangle\delta(\varepsilon_{n\mathbf{k}} - \varepsilon_{n'\mathbf{k}+\mathbf{q}} + \omega),\end{aligned} \tag{C.4}$$

where the factor 2 accounts for spin, Ω is the normalization volume, n and n' are the energy band indices, vector $\mathbf{k}$ is in the first BZ, $f_{n\mathbf{k}}$ is the Fermi distribution function, $\varepsilon_{n\mathbf{k}}$ and $\psi_{n\mathbf{k}}$ are Bloch eigenvalues and eigenfunctions of the Kohn-Sham Hamiltonian, respectively. In the numerical calculations, the δ-function in Eq. (C.4) was replaced by a Gaussian with a broadening parameter of 25 meV. Subsequently, the real part of χ^o is obtained from $\mathrm{Im}[\chi^o]$ (evaluated on a discrete mesh of energies ranging from 0 to 25 eV with the step of 2.5 meV) using the KK relation. The single-particle energies and wavefunctions were obtained from the self-consistent solution of the Kohn-Sham equations using the local exchange-correlation potential of Refs. [39, 40]. The electron-ion interaction was described by a nonlocal norm-conserving ionic pseudopotential [41]. In the Fourier expansion of χ^o, χ and ϵ, matrices up to 51 reciprocal lattice vectors $\mathbf{G}$ were included, in such a way to include the local-field effects [42, 43]. In Eq. C.4, we used a $(120 \times 120 \times 60)$ mesh for the $\mathbf{k}$ summation over the first BZ. The sum over n and n' included 30 VBs. For the description of $\mathrm{K_{xc}}$, a RPA (i.e. $\mathrm{K_{xc}} = 0$) was employed. The results of the calculations are presented in Chap. 3.

C.2 Anatase TiO_2

To support our experimental results on anatase TiO_2 (Chap. 4), we performed many-body perturbation theory calculations.

C.2.1 Ab Initio Calculations: Computational Details

Many-body perturbation theory at the level of the GW and BSE [44–46] was employed to compute the band structure and the dielectric response of bulk anatase TiO_2. The GW and BSE calculations were performed on-top of eigenvalues and eigenfunctions obtained from DFT. We used the planewave pseudopotential implementation of DFT as provided by the package Quantum Espresso [47]. GW and BSE calculations were performed with the BerkeleyGW package [48]. We also used the GW + BSE Yambo [49] implementation to verify that the results of our calculations were code independent.

The DFT calculations were done using the GGA as in the PBE scheme for the exchange-correlation functional. The Ti norm-conserving pseudopotential was generated in the Rappe-Rabe-Kaxiras-Joannopoulos scheme [50], including semicore 3*s* and 3*p* states. While standard structural and electronic quantities are already converged in DFT with an energy cutoff of 90 Ry, the energy cutoff used here was raised to 160 Ry to properly include the high number of bands necessary to reach convergence for the many-body evaluated properties. Bulk anatase TiO_2 was modeled on a body-centered tetragonal lattice containing 2 Ti atoms and 4 O atoms (primitive cell) with lattice parameters (optimized at the PBE level) a = b = 3.79 Å and c = 9.66 Å. The experimental lattice constants at RT are a = b = 3.78 Å and c = 9.51 Å. As indicated in Ref. [51], we scaled these parameters to zero temperature via a linear extrapolation of the RT lattice constant [52]. This yields a = b = 3.78 Å and c = 9.49 Å.

The GS electronic density is properly described with a coarse $4 \times 4 \times 4$ *k*-point grid for sampling of the BZ. The GW quasiparticle corrections to the DFT eigenvalues were performed at the one-shot level of theory (G_0W_0). For the computation of the polarizability and inverse dielectric matrices in BerkeleyGW, we employed a total of 2474 CBs and G-vectors with kinetic energies up to 46 Ry, whereas the self-energy operator was computed using 2472 unoccupied bands and a G-vector cutoff energy of 46 Ry and 160 Ry for the screened and bare Coulomb matrices, respectively. The coarse $4 \times 4 \times 4$ *k*-point grid sampling is sufficient for the description of the quasiparticle corrections, while a high number of bands is mandatory to get a proper description of screening effects and many-body corrections. The electronic band structure was finally obtained by interpolating GW corrections on top of a more refined DFT calculation with a $16 \times 16 \times 16$ grid.

The fully converged BSE results shown in Fig. 4.11 were obtained with BerkeleyGW. We used a shifted grid with up to $16 \times 16 \times 16$ *k*-points (4096 irreducible

k-points). The six lowest CBs and six topmost VBs were included to solve the excitonic Hamiltonian. The results are code-independent, as verified by comparing the BerkeleyGW results with those obtained with the Yambo code at the same level of convergence [53]. All results were obtained with the resonant part of the excitonic Hamiltonian (inclusion of the antiresonant part does not lead to significant changes). Spin-polarized calculations were performed to highlight possible dark excitons due to triplet excitations but no measurable differences with respect to the spin-restricted results were obtained.

C.2.2 Frozen-Lattice Results

The calculated GW direct band gap at the Γ point is 4.07 eV, at Z it is 4.13 eV, and the indirect band gap (between Γ and a *k*-point close to X) is 3.61 eV (see Fig. 4.10). The band gap at the middle point of the Γ-Z line is 3.96 eV. These values have been converged up to 5 meV, and the two codes give the same results, despite the use of a different plasmon pole models for the frequency integration in the GW method. The present fully converged minimum GW quasiparticle correction amounts to 1.4 eV, which is smaller than the value of 1.69 eV from Ref. [53] (the difference comes from the smaller number of bands and *k*-points used in Ref. [53]), highlighting the careful and exhaustive convergence evaluation done in the present work.

The symmetry-line along Γ-Z shows nearly parallel dispersion curves for the CB and VB edges. This peculiar shape of electronic states along Γ-Z plays a fundamental role in the optical properties of the material as it dictates the character and binding of the lowest excitons in anatase TiO_2. The nearly parallel dispersion observed in the theoretical band gap allows us to use the direct gap at Γ of 4.07 eV as a very good approximation to estimate the bound direct nature of the exciton to be compared with the experimental data. Due to the band structure shape along the Γ-Z high-symmetry direction, we also underline that an accurate *k*-point sampling is especially critical for the quality of the optical spectra, since the main excitons are built up from optical transitions with contributions from a small region of the BZ. The CB and VB in this region display a wormlike shape aligned along the Γ-Z direction.

In Fig. C.1, we compare the results obtained with the GW implementations in BerkeleyGW and Yambo codes obtained at the same level of accuracy,[1] showing the equivalence between the two implementations. To get the fully converged spectra shown in Fig. 4.11, a denser grid is required. Most importantly, the main effect of the stringent convergence obtained here with respect to *k*-points and number of bands is given by the shape of exciton I (see Fig. C.2). This charge excitation, split in two small peaks at low convergence [53, 54] (or a main peak with a shoulder), becomes a unique, uniform peak, similar to the one observed in the experiment (dark red

[1] Yambo calculations were performed using a $12 \times 12 \times 12$ unshifted grid whereas a randomly shifted grid of $8 \times 8 \times 8$ *k*-points was employed in the BerkeleyGW calculations. Thus, both approaches employ roughly 500 *k*-points.

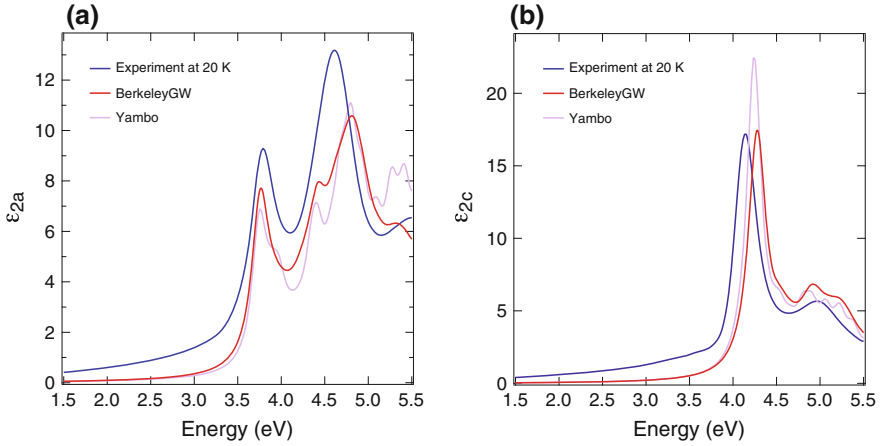

Fig. C.1 Comparison between the experimental SE data (blue curve) and BSE calculations, for light polarized along (**a**) the *a*-axis (**b**) the *c*-axis. Both BerkeleyGW (red curve) and Yambo (violet curve) data are evaluated using the highest convergence parameter values described in the text. For BerkeleyGW they correspond to the best converged spectra (both for peaks shape and position). For Yambo the spectra has been obtained with a less denser *k*-grid [53], for this reason the spectrum shows a spurious shoulder above the main exciton peak, as in the previously published works. The fully-converged spectra (red curves) show a single peak in agreement with the experimental data. For light polarized along the *a*-axis the agreement between the two calculations is excellent

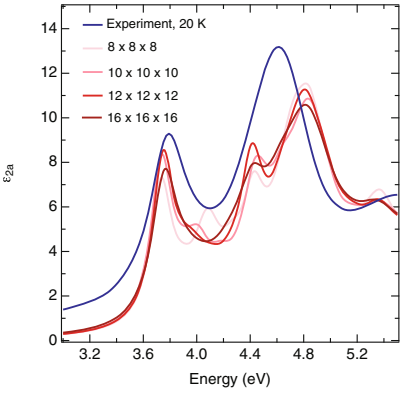

Fig. C.2 Convergence test of the imaginary part of the dielectrid function with respect to the size of the *k*-points grid using the BerkeleyGW code, in red-color scale. For comparison, the experimental data at 20 K are also reported (blue curve). In order to get the proper shape of the spectra we need to use a very large *k*-point grid together with a very large number of bands as described in the text

curve in Fig. C.2). The fine *k*-sampling is needed, since the main optical transitions contributing to exciton I comes from the Γ-Z line, with bands almost parallel and flat. The 2D exciton I for $\mathbf{E} \perp c$ (at 3.76 eV) has indeed a major contribution from the transition from the top of the VB to the bottom of the CB at the middle point in the Γ-Z line. To a lesser extent, significant contributions come from the *k*-points lying along the Γ-Z line and close to it in every direction. The contribution increases gradually when approaching the aforementioned Γ-Z middle point. Even if the GW direct electronic bandgap of 3.96 eV (located at the middle point along the Γ-Z line)

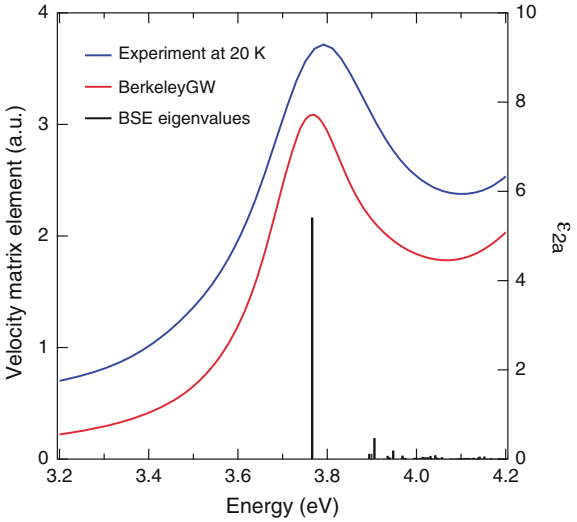

Fig. C.3 Black bars represent the square of the transition matrix elements of the velocity operator along the a-axis ($|\,\mathbf{E}_a \cdot \langle 0|\,\mathbf{v}\,|S\rangle|^2$), corresponding to exciton states S contributing to the peak I. This quantity is related to the oscillator strength f_S by $f_S = (2\,|\,\mathbf{E}_a \cdot \langle 0|\,\mathbf{v}\,|S\rangle|^2)/E_S$, where E_S is the excitation energy corresponding to exciton state S (see ref. 18). Comparison with the experimental ϵ_{2a} (blue curve) and the full-converged BerkeleyGW calculations with a phenomenological Lorentzian broadening of 0.12 eV (red curve)

is used as a reference energy to calculate the exciton E_B, the bound nature of exciton I is still confirmed (with $E_B = 50$ meV). A phenomenological Lorentzian broadening of 0.12 eV was applied to reproduce the experimental spectra. A comparison of the measured spectrum with the bare BSE eigenvalues is displayed in Fig. C.3. It demonstrates that mainly one eigenvalue is contributing to the exciton peak I and that the measured lifetime is not of electronic origin but is due to the strong electron-phonon coupling in this material.

Next, we investigate in detail the slight shift of the calculated exciton III with respect to our experimental value (0.1 eV). Increasing the number of k-points and bands did not allow us to obtain a match to experiment as good as for exciton I. We can also exclude possible effects of anisotropic screening, as increasing the parameters of the local field effects and separating the screening along the a- and c-axis components do not lead to significant changes in the spectrum. The peak maximum seems instead to be related, in a nonlinear manner, to the lattice constants. The a-axis lattice constant from *ab initio* optimization is in excellent agreement with experimental data (3.79 Å vs 3.78 Å), while the c-axis lattice constant is slightly (1%) overestimated. However, when using the experimental lattice parameters, the position of peak III is blueshifted by 0.2 eV from that obtained with the PBE parameters, thus worsening the agreement with experiment.

Finally, the presence of dark excitons in anatase TiO_2 at energies below the bright exciton I at 3.76 eV has been ruled out by our spin-resolved optical BSE calculations. The calculated lowest exciton in anatase TiO_2 is a singlet and it is optically active. This is in contrast with the rutile phase of TiO_2, in which the lowest exciton is an optically dark triplet state [53].

C.2.3 Electron-Phonon and Temperature Effects

To estimate the role of the electron-phonon coupling in the electronic and optical properties of anatase TiO_2, we performed frozen phonon DFT + GW + BSE calculations by separately displacing the ions in the primitive unit cell according to the eigenvector of the E_u and A_{2u} normal modes, which are those possessing the stronger coupling with the electronic degrees of freedom [6, 55]. The displacement of atom j was calculated from the harmonic oscillator mean square displacement at 300 K according to

$$< |u_j(t)|^2 >= \frac{\hbar(1+2n)}{2m_j\omega}, \tag{C.5}$$

where

$$n = \frac{1}{e^{(\hbar\omega/k_BT)} - 1}, \tag{C.6}$$

is the phonon population, T is the temperature, k_B is the Boltzmann constant, m_j is the atomic mass and ω is the phonon frequency.

Our calculations revealed a GW band gap increase of 60 meV (in the case of the E_u mode) and 80 meV (in the case of the A_{2u} mode) at RT, compared to the zero temperature value. Moreover, we corrected this value by considering the lattice expansion effect. By using the thermal expansion coefficient in Ref. [52], we determine that the a and c lattice parameters of anatase TiO_2 increase in 0.1 % and 0.3 %, respectively, from zero temperature to RT. Consideration of both the phonon-induced and thermal expansion-induced effects leads to a net blueshift of the band gap of about 30 meV (in the case of the E_u mode) and 50 meV (in the case of the A_{2u} mode) from zero temperature to RT. This blueshift is opposite to the redshift commonly observed in standard semiconductors, and in accordance with experimental measurements in polar materials [56–59]. A similar trend was recently reported for rutile TiO_2, where the electronic gap (evaluated within the thermal lines method for electron-phonon coupling) has a non-monotonic behaviour with temperature [60]. Additionally, we solved the BSE on top of the temperature-corrected GW and found a net blueshift of roughly 80 meV (in the case of the E_u mode) and 70 meV (in the case of the A_{2u} mode) at RT, which is in line with our SE measurements (blueshift of 40 meV from 20 to 300 K). This confirms the bound character of exciton I.

C.2.4 Direct Exciton in an Indirect Bandgap Material

Anatase TiO_2 is an indirect band gap material with a minimum indirect band gap amounting to 3.46 eV, according to our calculations. This gap is smaller than the optical gap we obtained at the BSE level of theory (3.76 eV). As we demonstrated in Chap. 4, exciton I is bound with respect to the direct gap. Despite this, the exciton should be also considered as resonant with respect to all phonon-mediated indirect transitions. In the frozen-phonon calculations for a single TiO_2 unit cell, the BSE includes only coupling of direct electron-hole transitions with phonons at the Γ point, and hence, possible effects originating from the indirect nature of the material would not be accounted for. A way to incorporate those effects would to perform BSE calculations for a large TiO_2 supercell, where both the indirect- and direct gap are folded into the $\tilde{\Gamma}$ point of the supercell. In such a calculation, frozen atom displacements can couple electron and hole states with different k values in the original sampling of the first BZ via phonons with nonzero q-vectors.

We considered a supercell composed of $3 \times 3 \times 2$ conventional unit cells (12 atoms) which leads to a total of 216 atoms in the supercell. This implies the inclusion of 648 phonons. Although the employed number of phonons is still limited, it provides a first approximation of the effect of the indirect gap in the renormalization of the excitonic peak. We performed two molecular dynamics simulation runs at temperatures of 20 K and 300 K. The MD runs were carried out using a Nosé-Hoover chain thermostat. A total of 5 snapshots were randomly chosen in the interval between 5 and 10 ps of the run for each temperature. To investigate if the position of the excitonic peak changes when accounting for the indirect nature of the material, we performed similar calculations for the primitive unit cell of anatase TiO_2 at the same level of theory and convergence. We obtained a negligible blueshift of 30 meV, which indicates that the indirect band gap nature of anatase TiO_2 does not play a significant role in the exciton properties, beyond adding an Urbach tail at the lower energy side of the peak.

C.3 $La_2CuO_{4+\delta}$

C.3.1 Phonon Calculations

The phonon eigenenergies and eigenvectors were calculated using first-principles DFT linear-response calculations as implemented in the Quantum Espresso package [47]. We used norm-conserving [61] pseudopotentials explicitly including semi-core states [62] for La and Cu, the LDA [40], and a plane-wave cutoff energy of 200 Ry on the kinetic energy. The charge density and dynamical matrices were calculated for the Γ point using a $7 \times 7 \times 7$ Γ-centered Monkhorst-Pack [63] electron-momentum grid and a Gaussian smearing of 0.002 Ry. The convergence with respect to all these parameters has been checked thoroughly. The experimental primitive unit cell [64]

was relaxed prior to the phonon calculation which resulted in a slightly reduced volume (∼1%) typical for LDA calculations.

C.3.2 Singular Value Decomposition of the ΔR/R Maps

In this Paragraph, we provide the details of the analysis performed on the ΔR/R response of Fig. 5.10c. In this regard, we use an algorithm based on SVD to separate the ΔR/R response into a relaxation (incoherent) and an oscillatory (coherent) part, according to

$$\left(\frac{\Delta R}{R}\right)(t, E) = \left(\frac{\Delta R}{R}\right)^{\text{rel}}(t, E) + \left(\frac{\Delta R}{R}\right)^{\text{osc}}(t, E). \tag{C.7}$$

In the following, we present a general algorithm to separate the measured ΔR/R as a function of time delay and photon energy into its different physical components. We start by invoking the large separation of energy (or time) scales of the phenomena observed in real time ($\hbar\omega < 0.10$ eV) and the probed window ($\hbar\omega > 1.70$ eV). In the spirit of the Born-Oppenheimer approximation, we assume that ΔR/R at high energies can be taken as a parametric function of a set of "slow" variables $\xi_\nu(t)$ describing the out-of-equilibrium state produced by the pump. Here, t represents the time delay from the arrival of the pump pulse. Examples of slow variables ξ_ν are ionic displacements and "slow" charge and magnetic fluctuations, either coherent or incoherent. "Fast" fluctuations produced by the pump are either relaxed after the pump passage (∼50 fs) or not resolved. We can thus expand ΔR/R as a function of the high probe energy E and time delay t as

$$\left(\frac{\Delta R}{R}\right)(t, E) = \sum_{i=1}^{N_p} \left(\frac{\partial \log R}{\partial \xi_i}\right)(E)\ \ \xi_i(t). \tag{C.8}$$

Typically, the sum can be restricted to a small number N_p of processes which contribute significantly. In particular, the sum can be partitioned into an oscillatory part $\left(\frac{\Delta R}{R}\right)^{\text{osc}}(t, E)$ and a relaxational part $\left(\frac{\Delta R}{R}\right)^{\text{rel}}(t, E)$. Equation C.8 allows to represent the full 2D data in terms of a few time dependencies of the excitation coordinates $\xi_i(t)$ and their associated energy dependencies $\left(\frac{\partial \log R}{\partial \xi_i}\right)(E)$ which can be related to the Raman profile for excitation ξ as in Eq. 2.18.

In principle, one can obtain the decomposition by fitting the experimental data with a model of the form of Eq. C.8, but in practice it is more convenient to use the following algorithm. It is natural to consider the data in Fig. 5.10c as a rectangular matrix $\left(\frac{\Delta R}{R}\right)(t, E)$ of differential reflectivity values with the discrete version of the variables E and t playing the role of indices. SVD relies on the fact that any rectangular matrix $\left(\frac{\Delta R}{R}\right)(t, E) \in \mathbb{R}(m, n)$ (corresponding to data at m time points and n energy values) can be uniquely decomposed into a sum of tensorial vector

products [65] of the form

$$\left(\frac{\Delta R}{R}\right)(t, E) = \sum_{i=1}^{N} \lambda_i u_i'(t) \otimes v_i(E) = \sum_{i=1}^{N} u_i(t) \otimes v_i(E), \tag{C.9}$$

The $\lambda_i \in \mathbb{R}$ are the sorted singular values, $\lambda_1 \geq \lambda_2 \geq \lambda_3 \geq \ldots$, the $\otimes$ denotes the outer product, N is called the rank of the matrix $\left(\frac{\Delta R}{R}\right)$ and $u_i(t) \in \mathbb{R}(m)$ and $v_i(E) \in \mathbb{R}(n)$ are the *canonical* time and energy traces, respectively. In the second form we have absorbed the singular value in the definition of the canonical time trace u_i. By construction, the canonical traces are orthogonal, $v_i \cdot v_j = \delta_{ij}$ and $u_i \cdot u_j = \delta_{ij}\lambda_i^2$. Restricting the sum over i in Eq. C.9, one finds that only a small number of terms are necessary to reproduce the physically relevant signal in $\left(\frac{\Delta R}{R}\right)$ while the rest contribute to the background noise. We can therefore limit the sum to $i = 1, .., N_c \ll N$. Note that the $u_i(t)$, $v_i(E)$ do not correspond directly to the physical quantities in Eq. C.8. This is because the canonical traces are by construction orthogonal while the "*physical traces*" $\left(\frac{\partial \log R}{\partial \xi_i}\right)(E)$, $\xi_i(t)$ do not need to be so. The latter typically consist of incoherent charge relaxations and/or damped phonon oscillations. We thus decompose each of the N_c canonical time traces $u_i(t)$ into N_p physical traces by fitting with a sum of relaxations and damped oscillations representing the physical traces $U_i(t) \propto \xi_i(t)$

$$u_i(t) = \sum_{j=1}^{N_p} a_{ij} U_j(t). \tag{C.10}$$

Substituting this into Eq. C.9, we obtain the decomposition of our data in terms of physical traces

$$\left(\frac{\Delta R}{R}\right)(t, E) = \sum_{j=1}^{N_p} U_j(t) \otimes V_j(E), \tag{C.11}$$

with $V_j(E) = \sum_{i=1}^{N_c} v_i(E) a_{ij}$. We normalize $\sum_{i=1}^{N_c} {a_{ij}}^2 = 1$, which implies unity norm for the physical energy traces, $V_j \cdot V_j = 1$ with $V_j(E) \propto \left(\frac{\partial \log R}{\partial \xi_i}\right)(E)$. Equation C.11 can be separated into a relaxation part and an oscillatory part, according to the character of the model functions $U_j(t)$

$$\left(\frac{\Delta R}{R}\right)(t, E) = \left(\frac{\Delta R}{R}\right)^{\text{rel}}(t, E) + \left(\frac{\Delta R}{R}\right)^{\text{osc}}(t, E). \tag{C.12}$$

For the present data, we find that the oscillation of interest is present in the first two canonical traces $u_i(t)$. Thus, we choose $N_c = 2$. We find that u_1 and u_2 can be fitted accurately with the sum of two exponential decays (u_1) or an exponential decay and a step function (u_2), plus one oscillation, as shown in Figs. C.4a,b. Leaving the frequency of the oscillation to vary independently in the two fits, we find almost

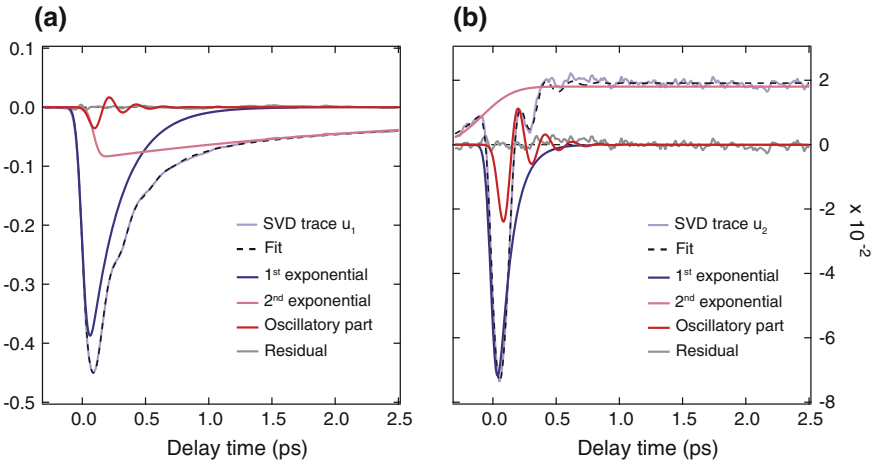

Fig. C.4 Canonical time traces (**a**) $u_1(t)$ and (**b**) $u_2(t)$ obtained from the SVD. The traces have been fitted with a sum of two exponentials and a damped oscillation

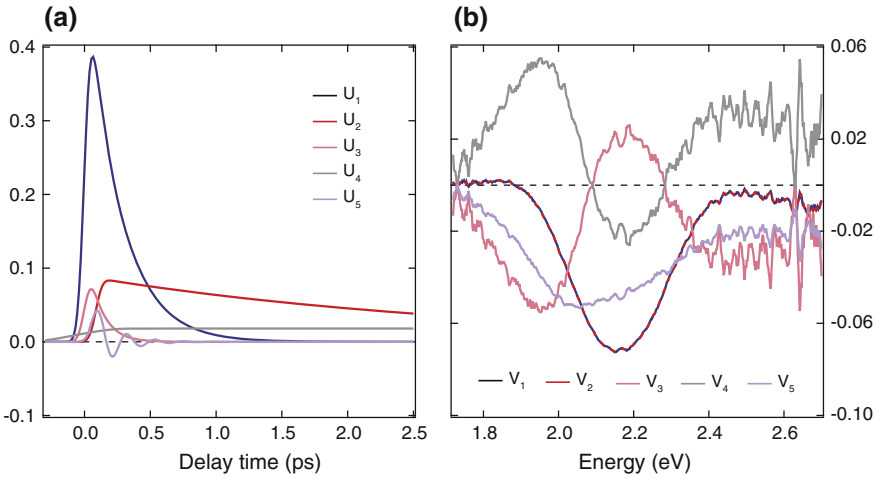

Fig. C.5 Physical traces (**a**) $U_i(t)$, (**b**) $V_i(E)$, extracted from the SVD. The relaxation is included in U_1 to U_4, while the oscillation is represented by U_5. The energy vectors V_i have been smoothed using a sliding average

the same frequency $\hbar\omega = 21$ meV and $\hbar\omega = 20$ meV, respectively. This confirms the presence of the same physical trace in the two leading canonical traces.

Next, we repeat the fit constraining the frequency and the relaxation time to be the same in the oscillatory part so that we can obtain the "weight" of the oscillatory physical trace in each of the two canonical traces. To get an accurate fit we need to introduce introduce a slight delay (18 fs) of the trace u_1 with respect to the trace u_2. We attribute this is to a numerical error caused by small uncertainties in the correc-

tion for group velocity dispersion in the original data. Thus, we neglect this small difference in the analysis.

The physical time traces $U_i(t)$ are shown in Fig. C.5a, where the relaxation is contained in U_1 to U_4, whereas the oscillation is given by U_5. Figure C.5b shows the corresponding energy vectors $V_i(E)$. Note that the oscillatory contribution in the trace U_5 follows a damped sine function, as expected for an ISRS excitation mechanism, even though the phase of the oscillation was left as an independent fit parameter. The energy dependence of the oscillation displayed in Fig. 5.14b is determined by the energy vector V_5 associated with the oscillation.

The reconstruction of the data from the SVD for $N_c = 2$ and its separation into relaxation and oscillatory components is shown in Fig. 5.13. The reconstructed damped oscillation at a fixed probe energy is shown in Fig. 5.14a. The decay time is τ = 170 fs and the energy is $\hbar\omega_0$ = 19.9 meV. As mentioned, the main features of the data are reconstructed even when limiting the SVD to second rank. Compared to the simpler global fit analysis, the SVD is a lot more effective in subtracting the incoherent peak, reduces the noise level, and delivers the energy dependence of the oscillation with ease.

C.4 $TbMnO_3$

The crystal structure used for the DFT + U calculations is orthorhombic with space-group Pnma (a = 0.5838 nm, b = 0.7403 nm, and c = 0.5293 nm). The electronic structure and optical properties of $TbMnO_3$ were carried out using DFT via Wien2k code. The exchange-correlation potential were treated using GGA + U, where U was set at 3 and 6 eV for Mn 3*d* and Tb 4*f* orbitals, respectively. The muffin-tin radii Rmt were 2.2, 1.95, 1.5 a.u. for Tb, Mn, and O atoms, respectively. The maximum angular momentum of the radial wavefunctions was set to 10, and RmtKmax was fixed at 7.0 to determine the basis size.

References

1. Y. Fudamoto, S. Lee, Anisotropic electrodynamics of MgB_2 detected by optical reflectance. Phys. Rev. B **68**(18), 184514 (2003)
2. V. Guritanu, A.B. Kuzmenko, D. van der Marel, S.M. Kazakov, N.D. Zhigadlo, J. Karpinski, Anisotropic optical conductivity and two colors of MgB_2. Phys. Rev. B **73**(10), 104509 (2006)
3. T. Kakeshita, S. Lee, S. Tajima, Anisotropic drude response and the effect of anisotropic C substitution in $Mg(B_{1-x}C_x)_2$. Phys. Rev. Lett. **97**(3), 037002 (2006)
4. A.B. Kuzmenko, Multiband and impurity effects in infrared and optical spectra of MgB_2. Physica C **456**(1), 63–74 (2007)
5. H. Berger, H. Tang, F. Levy, Growth and Raman spectroscopic characterization of TiO_2 anatase single crystals. J. Cryst. Growth **130**(1), 108–112 (1993)

6. S. Moser, L. Moreschini, J. Jaćimović, O.S. Barišić, H. Berger, A. Magrez, Y.J. Chang, K.S. Kim, A. Bostwick, E. Rotenberg, Tunable polaronic conduction in anatase TiO_2. Phys. Rev. Lett. **110**(19), 196403 (2013)
7. S. Mahshid, M.S. Ghamsari, M. Askari, N. Afshar, S. Lahuti, Synthesis of TiO_2 nanoparticles by hydrolysis and peptization of titanium isopropoxide solution. Semicond. Phys. Quantum Electron. Optoelectron. **9**(2), 65–68 (2006)
8. M.H. Rittmann-Frank, C.J. Milne, J. Rittmann, M. Reinhard, T.J. Penfold, M. Chergui, Mapping of the photoinduced electron traps in TiO_2 by picosecond X-ray absorption spectroscopy. Angew. Chem. Int. Ed. **53**(23), 5858–5862 (2014)
9. S.I. Schlachter, U. Tutsch, W.H. Fietz, K.-P. Weiss, H. Leibrock, K. Grube, Th. Wolf, B. Obst, P. Schweiss, H.Wühl, Pressure effect and specific heat of $RBa_2Cu_3O_x$ at distinct charge carrier concentrations: possible influence of stripes. Int. J. Mod. Phys. B, **14**(29n31), 3673–3678 (2000)
10. A. Damascelli, Probing the electronic structure of complex systems by ARPES. Physica Scr. **2004**(T109), 61 (2004)
11. S. Hüfner, *Photoelectron Spectroscopy: Principles and Applications*. (Springer Science & Business Media, 2013)
12. H. Fujiwara, *Spectroscopic Ellipsometry: Principles and Applications*. (Wiley, 2007)
13. D.E. Aspnes, Approximate solution of ellipsometric equations for optically biaxial crystals. JOSA **70**(10), 1275–1277 (1980)
14. J. Humlíček, C. Bernhard, Diffraction effects in infrared ellipsometry of conducting samples. Thin Solid Films **455**, 177–182 (2004)
15. R.E. Allen, Electron-Ion dynamics: a technique for simulating both electronic transitions and ionic motion in molecules and materials. Phys. Rev. B **50**(24), 18629 (1994)
16. J.S. Graves, R.E. Allen, Response of GaAs to fast intense laser pulses. Phys. Rev. B **58**(20), 13627 (1998)
17. B. Torralva, R. Allen, Mechanisms for laser control of chemical reactions. J. Mod. Opt. **49**(3–4), 593–625 (2002)
18. Y. Dou, B.R. Torralva, R.E. Allen, Semiclassical electron-radiation-ion dynamics (SERID) and Cis-Trans photoisomerization of butadiene. J. Mod. Opt. **50**(15–17), 2615–2643 (2003)
19. R.E. Allen, T. Dumitrica, B. Torralva, *Ultrafast Physical Processes in Semiconductors*
20. J. Crank, P. Nicolson, A practical method for numerical evaluation of solutions of partial differential equations of the heat-conduction type, in *Mathematical Proceedings of the Cambridge Philosophical Society*, vol. 43 (Cambridge Univ Press, 1947), pp. 50–67
21. Z. Sun, W. Yang, Communication: an exact short-time solver for the time-dependent schrödinger equation. J. Chem. Phys. **134**(4), 041101 (2011)
22. A. Acocella, G.A. Jones, F. Zerbetto, Excitation energy transfer and low-efficiency photolytic splitting of water ice by vacuum UV light. J. Phys. Chem. Lett. **3**(23), 3610–3615 (2012)
23. A. Acocella, F. Carbone, F. Zerbetto, Quantum study of laser-induced initial activation of graphite-to-diamond conversion. J. Am. Chem. Soc. **132**(35), 12166–12167 (2010)
24. A. Acocella, G.A. Jones, F. Zerbetto, What is adenine doing in photolyase? The Journal of Phys. Chem. B **114**(11), 4101–4106 (2010)
25. G.A. Jones, A. Acocella, F. Zerbetto, On-the-fly, electric-field-driven, coupled electron- nuclear dynamics. J. Phys. Chem. A **112**(40), 9650–9656 (2008)
26. G.A. Jones, A. Acocella, F. Zerbetto, Nonlinear optical properties of C_{60} with explicit time-dependent electron dynamics. Theor. Chem. Acc. **118**(1), 99–106 (2007)
27. A. Acocella, G.A. Jones, F. Zerbetto, Mono-and bichromatic electron dynamics: LiH, a test case. J. Phys. Chem. A **110**(15), 5164–5172 (2006)
28. A. Acocella, M. de Simone, F. Evangelista, M. Coreno, P. Rudolf, F. Zerbetto, Time-Dependent quantum simulation of coronene photoemission spectra. Phys. Chem. Chem. Phys **18**, 13604 (2016)
29. M.J. Frisch, G.W. Trucks, H.B. Schlegel, G.E. Scuseria, M.A. Robb, J.R. Cheeseman, G. Scalmani, V. Barone, B. Mennucci, G.A. Petersson et al., *Gaussian 09* (Revision A. Inc., Wallingford CT, 2009)

30. M.E. Jones, R.E. Marsh, The preparation and structure of magnesium boride, MgB_2. J. Am. Chem. Soc. **76**(5), 1434–1436 (1954)
31. J.P. Perdew, K. Burke, M. Ernzerhof, Generalized gradient approximation made simple. Phys. Rev. Lett. **77**(18), 3865 (1996)
32. G. Kresse, J. Hafner, Ab initio molecular dynamics for open-shell transition metals. Phys. Rev. B **48**(17), 13115 (1993)
33. G. Kresse, J. Furthmüller, Efficient iterative schemes for Ab initio total-energy calculations using a plane-wave basis set. Phys. Rev. B **54**(16), 11169 (1996)
34. G. Kresse, D. Joubert, From ultrasoft pseudopotentials to the projector augmented-wave method. Phys. Rev. B **59**(3), 1758 (1999)
35. D. Pines, P. Nozières, *The Theory of Quantum Liquids: Normal Fermi Liquids*, vol. 1 (WA Benjamin, 1966)
36. G. Giuliani, G. Vignale, *Quantum Theory of the Electron Liquid*. (Cambridge University Press, 2005)
37. E. Runge, E.K. Gross, Density-functional theory for time-dependent systems. Phys. Rev. Lett. **52**(12), 997 (1984)
38. M. Petersilka, U. Gossmann, E. Gross, Excitation energies from time-dependent density-functional theory. Phys. Rev. Lett. **76**(8), 1212 (1996)
39. D.M. Ceperley, B. Alder, Ground state of the electron gas by a stochastic method. Phys. Rev. Lett. **45**(7), 566 (1980)
40. J.P. Perdew, A. Zunger, Self-Interaction correction to density-functional approximations for many-electron systems. Phys. Rev. B **23**(10), 5048 (1981)
41. N. Troullier, J.L. Martins, Efficient pseudopotentials for plane-wave calculations. Phys. Rev. B **43**(3), 1993 (1991)
42. A.L. Adler, Quantum theory of the dielectric constant in real solids. Phys. Rev. **126**(2), 413 (1962)
43. N. Wiser, Dielectric constant with local field effects included. Phys. Rev. **129**(1), 62 (1963)
44. L. Hedin, New method for calculating the one-particle green's function with application to the electron-gas problem. Phys. Rev. **139**(3A), A796 (1965)
45. L. Hedin, S. Lundqvist, *Solid State Physics*, vol. 23, 7. (Academic Press, New York, 1968)
46. G. Onida, L. Reining, A. Rubio, Electronic excitations: density-functional versus many-body green's-function approaches. Rev. Mod. Phys. **74**(2), 601 (2002)
47. P. Giannozzi, S. Baroni, N. Bonini, M. Calandra, R. Car, C. Cavazzoni, D. Ceresoli, G.L. Chiarotti, M. Cococcioni, I. Dabo et al., QUANTUM ESPRESSO: a modular and open-source software project for quantum simulations of materials. J. Phys. Cond. Matt. **21**(39), 395502 (2009)
48. J. Deslippe, G. Samsonidze, D.A. Strubbe, M. Jain, M.L. Cohen, S.G. Louie, BerkeleyGW: a massively parallel computer package for the calculation of the quasiparticle and optical properties of materials and nanostructures. Comput. Phys. Commun. **183**(6), 1269–1289 (2012)
49. A. Marini, C. Hogan, M. Grüning, D. Varsano, Yambo: an ab initio tool for excited state calculations. Comput. Phys. Commun. **180**(8), 1392–1403 (2009)
50. A.M. Rappe, K.M. Rabe, E. Kaxiras, J.D. Joannopoulos, Optimized pseudopotentials. Phys. Rev. B **41**(2), 1227 (1990)
51. M. Cardona. *Electrons and Photons in Solids*. Vol. Honour Fr. Bassani Scuola Norm. Pisa (2001), p. 25
52. K.K. Rao, S.N. Naidu, L. Iyengar, Thermal expansion of rutile and anatase. J. Am. Ceram. Soc. **53**(3), 124–126 (1970)
53. L. Chiodo, J.M. García-Lastra, A. Iacomino, S. Ossicini, J. Zhao, H. Petek, A. Rubio, Self-energy and excitonic effects in the electronic and optical properties of TiO_2 crystalline phases. Phys. Rev. B **82**(4), 045207 (2010)
54. W. Kang, M.S. Hybertsen, Quasiparticle and optical properties of rutile and anatase TiO_2. Phys. Rev. B **82**(8), 085203 (2010)
55. N.A. Deskins, M. Dupuis, Electron transport via polaron hopping in bulk TiO_2: a density functional theory characterization. Phys. Rev. B **75**(19), 195212 (2007)

56. C. Keffer, T.M. Hayes, A. Bienenstock, PbTe Debye-Waller factors and band-gap temperature dependence. Phys. Rev. Lett. **21**(25), 1676 (1968)
57. P.W. Yu, W.J. Anderson, Y.S. Park, Anomalous temperature dependence of the energy gap of $AgGaS_2$. Sol. State Comm. **13**(11), 1883–1887 (1973)
58. M. Rössle, C.N. Wang, P. Marsik, M. Yazdi-Rizi, K.W. Kim, A. Dubroka, I. Marozau, C.W. Schneider, J. Humlíček, D. Baeriswyl, Optical probe of ferroelectric order in bulk and thin-film perovskite titanates. Phys. Rev. B **88**(10), 104110 (2013)
59. M. Cardona, *Renormalization of the Optical Response of Semiconductors by Electron-Phonon Interaction*. ArXiv (2001)
60. B. Monserrat, Correlation effects on electron-phonon coupling in semiconductors: many-body theory along thermal lines. Phys. Rev. B **93**(10), 100301 (2016)
61. M.J.T. Oliveira, F. Nogueira, Generating relativistic pseudo-potentials with explicit incorporation of semi-core states using APE, the atomic pseudo-potentials engine. Comp. Phys. Comm. **178**(7), 524–534 (2008)
62. C.L. Reis, J.M. Pacheco, J.L. Martins, First-principles norm-conserving pseudopotential with explicit incorporation of semicore states. Phys. Rev. B **68**(15), 155111 (2003)
63. H.J. Monkhorst, J.D. Pack, Special points for Brillouin-zone integrations. Phys. Rev. B **13**(12), 5188 (1976)
64. H. Takahashi, H. Shaked, B.A. Hunter, P.G. Radaelli, R.L. Hitterman, D.G. Hinks, J.D. Jorgensen, Structural effects of hydrostatic pressure in orthorhombic $La_{2-x}Sr_xCuO_4$. Phys. Rev. B **50**(5), 3221 (1994)
65. L.N. Trefethen, D. Bau III, *Numerical Linear Algebra*, vol. 50 (Siam, 1997)